CLRC

COUNCIL FOR THE CENTRAL LABORATORY
OF THE RESEARCH COUNCILS

Central Laser Facility
Rutherford Appleton Laboratory
Annual Report 1997-98

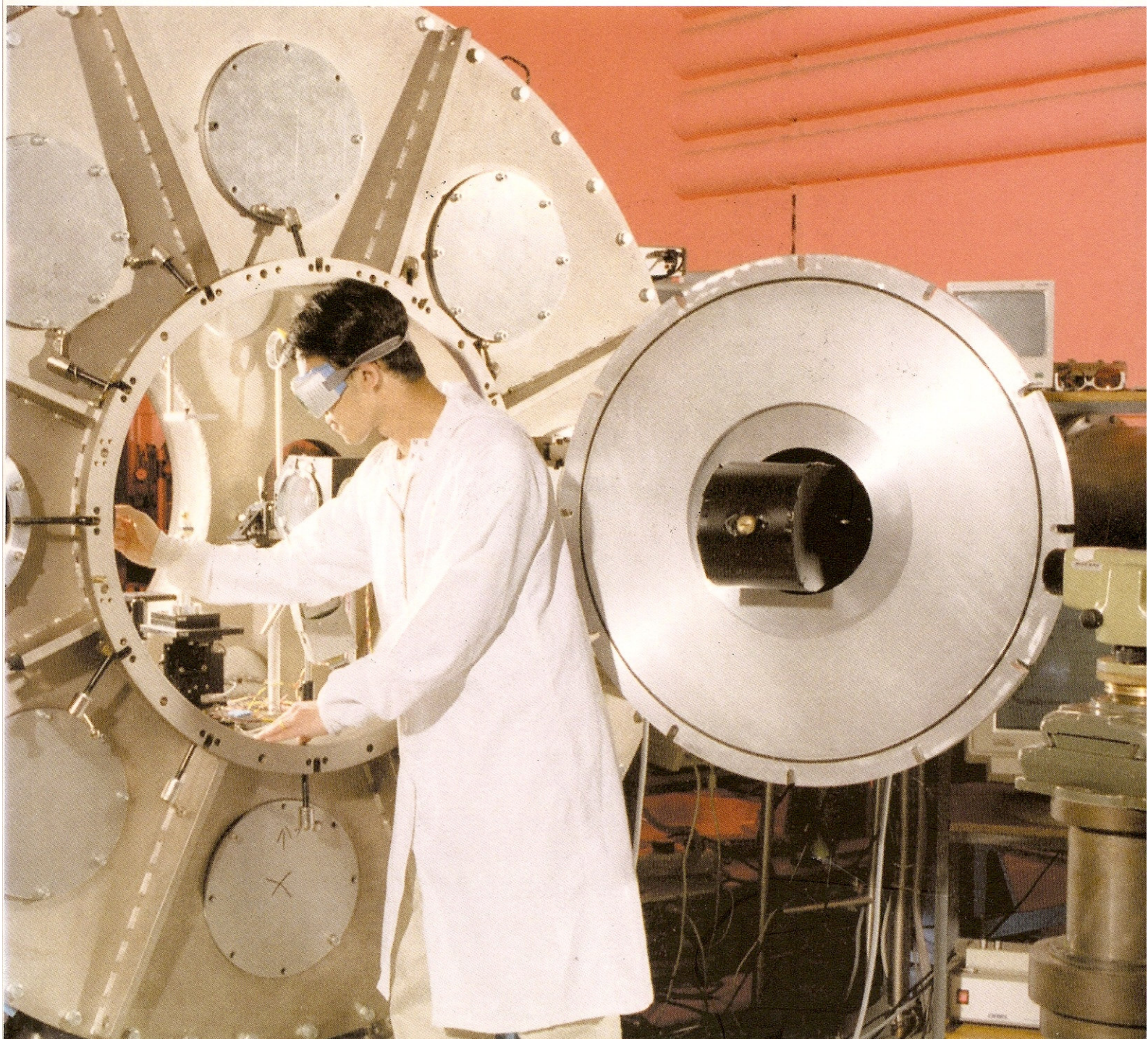

Central Laser Facility

Rutherford Appleton Laboratory

Annual Report 1997/98

Central Laser Facility
Rutherford Appleton Laboratory
Chilton, Didcot
Oxfordshire OX11 0QX
Tel. 44 (0) 1235 445655
Fax. 44 (0) 1235 445888
E-mail. clf@rl.ac.uk
Web site. http://www.clf.rl.ac.uk

RAL Report No. RAL-TR-1998-080

The front and back covers show the new Interaction Chamber in Vulcan's Target Area West.

ISBN 0902376802

Contents

Acknowledgements

The production team for this Annual Report was as follows:

Editor	Brian Wyborn
Overall Co-ordination	Alison Brown
Production	Katharine Horton, Chris Naboulsi, Corriene Walker, Dave Burgess
Chapter Editors	Steven Rose, Tony Parker, Colin Danson
Section Editors	Ric Allott, Margaret Notley, Colin Danson, David Neely, Abdeslem Djaoui, Pavel Matousek, Phil Taday, Waseem Shaikh, Graeme Hirst, Andrew Langley, Ian Ross, Mike Towrie, Andy Kidd
Technical Support	Chris Reason, Edmund Jones, Richard Williams, RAL CLEO Support.

For the second year the CLF Annual Report has been produced as an electronic document. Facility users and staff provided articles as electronic files. Collating, editing and the final document production were carried out on the CLF's file server. There were a few compatibility problems: between different software; different versions of the same software; different hardware platforms; and different printers. However, these were less than last year and the resulting publication has benefited overall.

This report is available on the CLF's Web Page Ref. http://www.clf.rl.ac.uk/.
It is also proposed to produce it on CD Rom.

The document has been reproduced by the RAL Reprographics Section.

Thanks to all the above for their contribution towards producing this report and of course to all the authors for their submissions.

Foreword

M H R Hutchinson.
CLRC Rutherford Appleton Laboratory, Chilton, Didcot, Oxon., OX11 0QX, UK

This report contains scientific accounts of the work which has been carried out at the Central Laser Facility (CLF) both by university users and facility staff during the financial year 1997/98. The year has again been highly productive with important developments both in Vulcan and the Lasers *for* Science Facility (LSF).

One of the most conspicuous developments during the year has been the continued development of the Vulcan laser. In particular, using the technique of chirped pulse amplification, intensities in excess of 10^{19} W/cm^2 have been achieved. This combined with a completely new optical layout and target chamber in Target Area West, which permits the use of synchronised nanosecond and sub-picosecond pulses, has provided a unique facility for the study of a broad range of laser related physics. Examples include x-ray scattering from shock compressed plasmas, the study of plasmas at near solid density and pumping of X-ray laser transitions using long and short pulses.

The diverse and highly successful science programme has continued within the LSF. The 1 kHz dual OPA laser has been used for a variety of ultrafast spectroscopic investigations ranging from studies of electroluminescent films to electron transfer within molecular complexes. The project to develop a 1 TW, 10 Hz, 30 fs source has been successfully completed and projects on multiphoton ionisation and molecular dissociation and realignment have been carried out. The Laser Loan Pool has benefited from an ongoing investment programme in laser and diagnostic equipment which has been funded by EPSRC and has enabled state of the art lasers to be made available to university users in their own laboratories.

During the year, a novel scheme was explored which has the potential for enabling pulses to be amplified which are significantly shorter than the limit set by the bandwidth of the glass amplifying medium of Vulcan. This is called Optical Parametric Chirped Pulse Amplification (OPCPA) and, if the scaling experiments which have yet to be carried out prove to be successful, the technique would enable intensities available from the Vulcan laser to be increased by up to one order of magnitude.

The science being carried out within the CLF by university colleagues from both within the UK and elsewhere in Europe continues to be of the highest quality. Funding of the programme which is principally through EPSRC and the EU depends upon a partnership between the CLF and our users. I believe we can look forward to further successes, both in the development of world-class facilities and the excellence of the science.

Overview of the Central Laser Facility

C B Edwards.

CLRC Rutherford Appleton Laboratory, Chilton, Didcot, Oxon., OX11 0QX. Email C.B.Edwards@RL.AC.UK

Laser Facilities for Users

The Central Laser Facility (CLF) is one of the world's leading centres for research using lasers. Facilities available to users include the multi-TW Vulcan Nd:glass laser, the electron beam pumped krypton fluoride Titania facility, a range of state of the art commercial systems within the Lasers *for* Science Facility and the Laser Loan Pool.

Vulcan

Vulcan is a highly versatile, large-scale Nd:glass laser installation which delivers a maximum of 2.5 kJ of energy in its six 10 cm and two 15 cm beamlines with pulse durations ranging from 100 ps to 20 ns. Two target areas are available, each supporting versatile irradiation geometries ie cluster, line focus, etc. and each equipped with frequency conversion optics to enable both 1 μm and 0.5 μm operation of all beams. Two further target areas are provided for lower energy applications.

An ultra-short pulse (700 fs) ultra-high irradiance (~$5x10^{19}$ Wcm^{-2} on target) Chirped Pulse Amplification (CPA) capability is available, with vacuum propagation to target and reflective beam focusing optics. Additional low energy beams, including sub-picosecond CPA probes, are provided for diagnostics with high temporal resolution. The system is fully characterised and equipped with advanced diagnostics. This facility gives users access to extreme conditions and plasma regimes currently unavailable from other facilities.

Titania

Titania is a unique high power laser installation based on electron beam pumped krypton fluoride excimer laser amplifiers. The facility currently provides high irradiance to target at 249 nm using CPA to generate 1 TW output with pulse durations as short as 350 fs. It is also available in Raman mode in which the KrF laser energy is used to pump a series of Raman amplifiers which generate high brightness, high contrast radiation at 268 nm with pulse durations in the range 20 ps to 100 ps.

Facility time on Titania during the reporting year has been shared between the use of the CPA output for EPSRC and EU funded plasma science, and the development of the Raman mode of the facility.

Lasers *for* Science Facility

The Lasers for Science Facility (LSF) operates a suite of state of the art table-top laser systems and associated instrumentation giving users access to highly tuneable (vuv - ir) and variable pulse width (ns to fs) laser radiation. This includes lasers for ns and ps time-resolved resonance Raman spectroscopy (TR^3), a unique dual wavelength multi-kHz femtosecond synchronised pump-probe apparatus based on Optical Parametric Amplification (OPA) technology, a femtosecond laboratory, a high average power laser plasma x-ray source and a fast gated (100 ps) confocal microscopy laboratory.

Stand-alone, commercial laser systems are available on loan from the Laser Loan Pool for periods of up to 6 months at the user's home laboratory.

Astra (HPHR)

A major EPSRC grant funded programme is under way to develop a terawatt source delivering 30 mJ in 30 fs at a repetition rate of 10 Hz. The first stage is complete and 1 mJ pulses of 50 fs duration have been provided to several user groups during the year.

Customers

The main customers of the Central Laser Facility are the UK Research Councils (primarily EPSRC, BBSRC, NERC), who fund beam time for grant-supported UK University researchers and their overseas collaborators. A small proportion of access is provided by the Research Councils for non-grant funded work to enable rapid access for topical and 'proof of principle' experiments.

The EU provides beam time at the CLF for European researchers through the Large-Scale Facility Access scheme under the TMR programme.

Use by other UK government bodies, commercial enterprises, or any other agency is available at contract rates.

Access to Facilities

A large proportion (typically ~90%) of EPSRC access is provided to grant supported programmes through a ticket mechanism. Such grants specify the amount of facility time required, enabling the full cost of the proposals to be taken into account by the prioritisation panels convened by EPSRC. Successful proposals are allocated "tickets", which guarantee beam time subject only to scheduling considerations. The remaining EPSRC funded beam time is allocated to Direct Access for experiments to assist in the preparation of grant proposals, to demonstrate feasibility, etc. Direct Access experiments are peer reviewed by an expert panel who advise the Director of the CLF on scientific priority, etc. Bids for Direct Access are publicised in scientific journals and on the CLF's Web site. Please contact Prof. Henry Hutchinson (h.hutchinson@rl.ac.uk) for further information on EPSRC sponsored use of the facilities.

Arrangements for funding of beamtime for experiments within the remit of BBSRC and NERC programmes differ from the EPSRC model. Potential applicants working in these areas should contact Dr. Tony Parker (a.w.parker@rl.ac.uk) in the first instance for further information.

Enquires concerning the use of the Laser Loan Pool should be directed to Dr Mike Towrie (m.towrie@rl.ac.uk).

European researchers are eligible for beamtime at the CLF funded by the EU through its Large-Scale Facilities programme. Calls for Proposals are publicised in Europhysics News, Physics Today, etc. and on the CLF's Web site. For information on forthcoming calls for proposals, eligibility criteria, etc. please contact Colin Danson (c.n.danson@rl.ac.uk).

Potential commercial users should contact Dr Graeme Hirst (g.j.hirst@rl.ac.uk) in the first instance for further information.

CLF Web site

Further information on the CLF, its facilities, and the scientific programmes is available on the CLF's Web site at http://www.clf.rl.ac.uk/

Science - High Power Laser Programme

1) Long Pulse Plasma Physics

2) X-Ray Laser Physics

3) Short Pulse Plasma Physics

4) Theory and Computation

Phosphor dopant activation using pulsed KrF laser annealing

E A Mastio, W M Cranton, C B Thomas.

The Nottingham Trent University, Department of Electrical and Electronic Engineering, Burton Street, Nottingham, NG1 4BU.
Email emmanuel.mastio@ntu.ac.uk

Introduction

The aim of the presented work is to investigate and define the optimum Pulsed Laser Annealing (PLA) conditions of phosphor layers i.e. ZnS:Mn for high efficiency thin film electroluminescent (TFEL) devices. Previously demonstrated at The Nottingham Trent University (TNTU) displays group, is that light emission efficiency improvements are obtained by increasing the number of luminescent centres within the phosphor layer, whilst maintaining a pinned Fermi Level within the devices structure [1)]. Conventional thermal annealing has been shown to increase the number of active luminescent centres, but to reduce the density of interface electronic trapping states and thus un-pin the Fermi level which is unsuitable for high efficiency devices. On the other hand, pulsed excimer laser annealing promises a technique to heat the phosphor layer with minimal energy absorption at the interfaces and cladding dielectrics, thereby preventing the detrimental Fermi Level un-pinning effect. Thus, PLA provides a process route to optimise efficiency of red, green and blue electroluminescent phosphors for full colour integrated flat panel displays.

Experimental conditions

Critical to the viability of PLA processing is the definition of the parameters to successfully anneal the phosphor thin films with no ablation [2)]. This has necessitated the construction of a pressure cell to house the target wafer during annealing, since previous work [3)] has demonstrated that it is essential to carry out these experiments with the samples held under inert gas pressure to prevent material loss at high irradiation levels. In [4)], successful PLA of Mn ions implanted ZnS thin films, deposited onto single-crystal Si substrates, was obtained when irradiating under 90 psi of Ne pressure. Reported was the Mn peak photoluminescence (PL) intensity vs. ambient Ne pressure behaviour under 2.8 J/cm^2 laser fluence. Pressure range used at that time was 15 to 90 psi where slight loss of material still occurred for 90 psi and it was suggested that pressures in excess of ~100 psi may have to be employed. Therefore, for the present work, the pressure cell has been constructed to withstand pressures up to 150 psi i.e. 13.42 bars. The cell has been successfully utilised at pressures of 150 psi and to facilitate the accurate positioning of the target wafer in the KrF beam(s), an XZ motion was constructed using two MicroControl stages with ± 10 μm accuracy over 200 mm total travel, capable of supporting 30 kgs (figure 1). PC control of the stepper motor drives allows accurate positioning of specific target areas of the wafer.

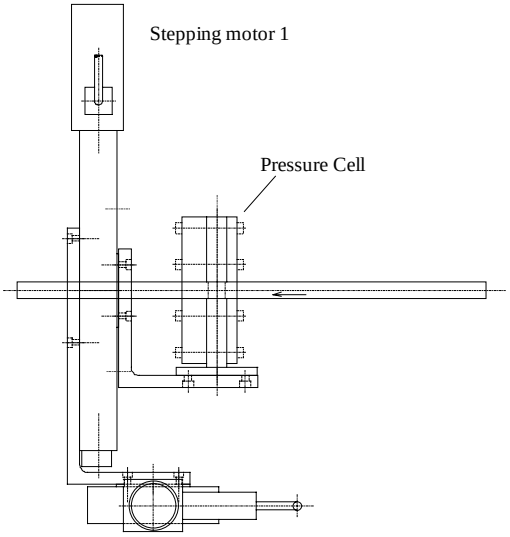

Figure 1. Side view of XZ motion and pressure cell

The presented laser annealing processing has been performed in collaboration with the Central Laser Facility (X-rays lab) and Titania groups using two different KrF excimer lasers. Both lasers are operating at 249 nm wavelength and 20 ns pulse width but the latter has a considerably bigger output beam size. For the initial experimentation at LSF, the effect of energy density was investigated using the system described in [2)]. With a focused beam spot of 3 mm diameter, the energy density could be varied between 53 mJcm^{-2} and 777 mJcm^{-2}. Single and multi-shot irradiation was performed across the ZnS:Mn thin films and the irradiated area was then examined via photoluminescence using a pulsed N_2 laser for excitation and a Minolta LS110 Luminance Meter for measurement. At Titania, laser fluence is varied by blocking one or two beams as shown in figure 2.

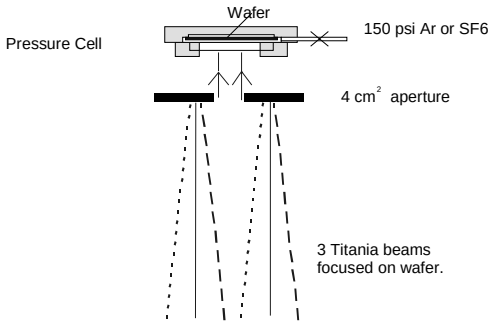

Figure 2. Experimental set-up for Titania irradiation

Results and discussion

So far, seven experimentation weeks have been performed, five at LSF and two at Titania. Tests were carry out onto 25 wafers investigating two different phosphor series, 4 thin film thickness, 3 pre-thermal anneal (TA) temperatures and post-TA effect, 5 laser beam sizes, more than 40 energy densities (Ed) and multi-shot configurations, 5 laser pulse repetition rates, effects on the average roughness (Ra) and two surrounding gas nature and pressures. The figures 3,4 and table1 illustrate the major photoluminescence improvements obtained using the PLA technique.

ZnS sublimes before melting and figure 3 highlights clearly the predicted vaporisation when irradiating at atmospheric pressure. The loss of material being followed by PL reduction (crosses). Single and double shots, with the samples held under 150 psi of Ar pressure, show a linear PL improvement characteristic with different slopes relative to applied energy density. Since the action of several pulses cannot be additive due to the interval between them (nanosecond regime), it can be concluded that the

structure formed on each shot influences subsequent coupling of the radiation to the samples. Therefore, as the Energy density, Ed, is increased, the double shot irradiations benefit from improved coupling due to changes induced by the initial shot.

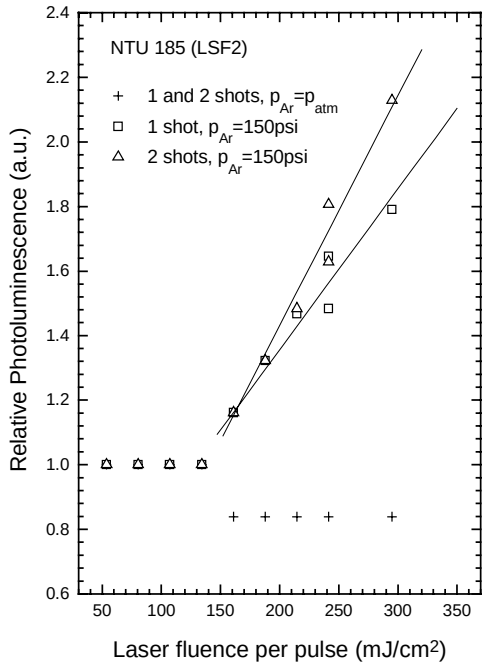

Figure 3. Relative PL vs Ed of 800 nm ZnS:Mn film deposited onto a Si wafer after LA with a 20 ns pulsed KrF excimer laser. Single and double shot irradiation under atmospheric and 150 psi Ar pressure

As shown in figure 4, PL and Ed are still linearly dependent even at high laser fluence level. A one-dimensional thermal model of the PLA processing shows that the luminescent improvement is obtained in the solid state and that linearity is conserved during metallurgic transition [5)].

The experimentation with Titania showed the best PL results (table 1). The larger beam area permits annealing of large regions with a very good beam uniformity. Unfortunately, repeatability and high Ed were not achieved due to KrF gas instabilities into the laser cavity.

Ed per pulse (mJ/cm^2)	259	495	235+265	457+440	483+635
PL(LA)/PL(NA)	1.5	3.0	1.5	3.25	5.5

Table 1. Relative PL vs Ed. Single and double shot irradiation of ZnS:Mn under 150 psi of Ar pressure using Titania laser.

Conclusions

In this work, various routes have been taken in order to improve the PL signal. Demonstrated is a linear dependence between PL improvement factor and laser fluence when irradiating under 150 psi of argon pressure, and therefore, the viability of the laser annealing technique for activating the luminescent dopant of ZnS:Mn phosphors. Noted is that both lasers exhibit this behaviour.

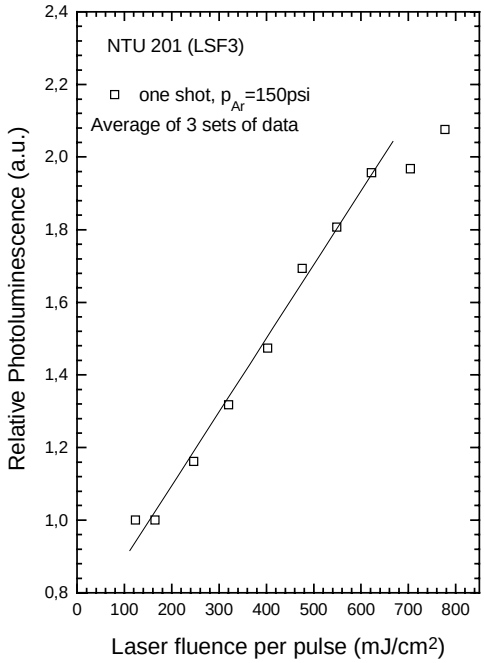

Figure 4. Relative PL vs Ed of 800 nm ZnS:Mn film deposited onto a Si wafer after LA with a 20 ns pulsed KrF excimer laser. Single shot irradiation under 150 psi Ar pressure

To further investigate the luminescent properties of the irradiated phosphor layer, the irradiation technique developed will be applied to thin film structures that can subsequently be fabricated into EL devices. More, the use of energy densities beyond the melting point threshold will be used with the recrystallisation of the poly-ZnS:Mn structure expected to provide an increase of Mn ion luminescence efficiency and light transport in the thin film.

References

1. W.M. Cranton, R. Stevens, C.B. Thomas, A.H. Abdullah, A H, and M.R. Craven
IEE Colloquium on Materials for Displays, (1995)

2. W.M. Cranton, E.A. Mastio, C.B.Thomas, and R. Stevens
CLF-RAL Annual Rep, 147-148(1997),

3. H.S Reehal and C.B Edwards
Annual Rep. Laser Facility Committee, SERC Rutherford and Appleton Labs., 2.17-2.18, (1981).

4. H.S. Reehal and J.M. Gallego, C.B. Edwards
Appl. Phys. Lett., 40 (3), 258-260, (1982)

5. E.A. Mastio, W.M. Cranton, C.B. Thomas, E. Fogarassy, S. de Unamuno
accepted for publication in J. Appl. Surf. Sci. (1998).

X-ray Scattering from a shock compressed plasma

D Riley, NC Woolsey †, D McSherry.

Queens University of Belfast, University Road, Belfast BT7 1NN, Northern Ireland

† Present address: Dept. of Physics, University of York

E Nardi.

Department of Particle Physics, Weizmann Institute of Science Il-76100 Rehovot, Israel

Introduction

An important concept of dense plasma physics is the idea of strong coupling [1-3]. This occurs when the Coulomb energy of interaction between charged species in the plasma is comparable to, or greater than, their kinetic energy due to thermal motion. Often this fact is expressed via the strong coupling parameter, which for ion-ion interactions is given by

$$\Gamma_{ii} = \frac{(Z*e)^2}{R_i k T_i} \qquad (1)$$

where T_i is the ion temperature, R_i is the average ion-ion separation, k is Boltzmann's constant, and Z*e is the average ionic charge. If Γ_{ii} is greater than unity, the plasma is said to be strongly coupled. This coupling leads to short range structure in the relative arrangement of the ions, usually expressed as a pair correlation function, g(r), that gives the average probability of finding an ion in a shell of radius r and thickness dr about a test ion. Using this function, a structure factor for X-ray scattering can be calculated, in a manner similar to the way in which atomic lattice arrangements determine X-ray diffraction patterns for crystalline materials. What this means is that, in principle, we can probe the average short range structure of ions in a plasma by measuring the X-ray scattering cross section as a function of scattering angle [4,5]. This report describes just such an experiment.

Experimental arrangement

Figure 1 illustrates the experimental arrangement schematically. A target foil consisting of 3 μm of Al, coated on both sides with 1 μm of CH is irradiated on each side by three 0.53 μm laser pulses of 0.6 ns FWHM duration. The laser pulses are focused to 1.5 mm diameter spots with phased zone plates [6] (PZP) to form a relatively uniform spot. With approximately 220 J of laser energy each side the peak irradiance is ~10^{13} Wcm^{-2}. The rapid heating of the CH layer to several hundred electronvolts drives multi-Mbar shocks which collide in the centre of the foil, compressing and heating it. For the second part of the experiment, two synchronised 80 ps backlighter beams, are used to irradiate a 1 μm thick Ti disk. This generates an intense source of Ti He-α photons at 4.75 keV with a pulse length similar to the laser pulse duration [7]. A pair of pinholes, 300 and 600 μm in diameter, restricts the the photons hitting the target foil to a narrow cone of 5.7° divergence, illuminating a circle 1.2 mm in diameter centred on the shocked part of the foil. Most of the photons pass through the foil and are detected by a crystal spectrometer consisting of a Si(111) crystal coupled to a CCD camera, placed down a long tube in order to confine the photons from going back into the chamber by scattering off walls and the spectrometer housing. The He-α line is by far the brightest K-shell line and the source is effectively monochromatic for our purposes. Finally, a few of the photons (~1 in 10^6) will be scattered from the shocked foil. These constitute our signal and they are detected by a 16-bit cooled X-ray CCD detector (Andor technology Instaspec IV) with 1024x256 pixels of 27 μm x 27 μm size. This was placed at different positions in the horizontal plane so as to subtend approximately 18° i.e. approximately 3 times the resolution set by the beam divergence.

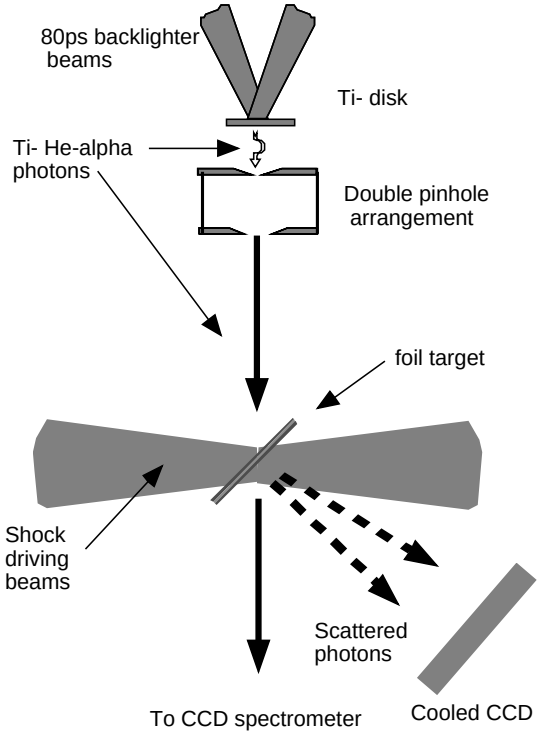

Figure 1. Experimental arrangement

The CCD is sensitive to single X-ray photons. Each electron-hole pair generated in a CCD pixel represents 3.65 eV of absorbed energy. The amplifier is sensitive to 12 electron/hole pairs generated, thus a photon of 4.75 keV generates 109 counts in a pixel. If there are few enough photons incident that the chance of more than one photon being incident on an individual pixel is small then we can histogram the counts from the pixels and obtain a spectrum of detected photons. Due to thermal noise, the resolution of this spectrum is measured to be 5 counts (220 eV). For the histogramming to work, it is important that the background bremsstrahlung generated by the hot laser plasma on the surface of the foil is low enough that the filters on the detector will effectively eliminate this contribution whilst still allowing enough of the scattered He-α photons through to get a usable signal. It is for this reason that we restrict the irradiance on target to 10^{13} Wcm^{-2}. The use of a CH outer coat also helps in this respect since the average charge on the ions is lower than for bare Al foils. In addition, there is a 'tamping effect' that keeps the Al part of the foil under relatively uniform conditions. The contribution of the hot low density CH plasma to the scattering cross section is small due to the fact that not only is the average Z of the plastic lower than Al but the ions are more fully stripped and it is the scattering due to bound electrons that dominates. What is not shown in figure 1 is the screening used to prevent Ti He-α photons from entering the CCD detector via any route other than scatter from the shocked foil. This was checked to be the case with null shots in which only the actual target foil was missing.

Results

We have built up the cross section as a function of angle by histogramming overlapping thirds of the CCD to achieve five data points separated by 3 degrees each. This is shown in figure 2 for three different times relative to the shock driving beam, with the CCD centred at 50°. The error bars in cross section are simply the Poisson statistical counting error. The cross sections are not absolute as the crystals used to measure the He-α beam intensity are not yet calibrated. However, we can see quite clearly that there are differences in the cross sections. A definite peak is seen only for the late time case. However, the earlier time shots show evidence that a peak exists at higher angles not accessible to the experiment.

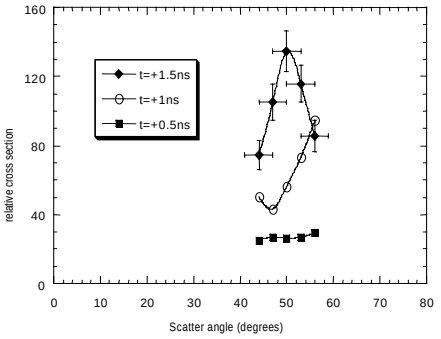

Figure 2. Relative cross sections for three delays

Discussion

We can estimate the expected conditions for all three probing times by running hydrodynamic simulations. The MEDUSA hydrocode[8] has been widely used to simulate laser-plasma interaction and subsequent shock compression. For the high density matter, it has a Thomas-Fermi-Dirac (TFD)[9] equation of state that has quantum corrections to produce low (0.01 Mbar) pressure for cold solid density material. The ionisation balance for the aluminium is also given by the TFD model. A simulation was run with a Gaussian pulse width of 600 ps (FWHM) at a peak irradiance of 1.1×10^{13} Wcm^{-2}. In the simulation the laser is incident from one side only. To simulate the effect of colliding shocks due to two sided irradiation, only one half of the target is simulated with the left hand boundary held fixed. Figure 3 shows the mass averaged values of density and temperature as a function of time. The oscillations early in time are due to rarefractions of the shocks. The temperature at late time is approximately 0.3 eV. At this temperature aluminium under normal atmospheric pressure would evaporate and only a neutral gas cross section, determined by the atomic form factor would be expected.

The scattering cross section has been calculated for conditions relevant to the current experiments. The simulations were carried out as described in references 4 and 5 and some examples are shown in figure 4. The case of 3.7 g/cc and 0.46 eV is relevant to the early time (+0.5 ns) case in the data. The predicted peak is at 72° which is off the experimentally accessible range. However, the slow rise in the observed cross section is consistent with the simulation. However, it does seem that the late time data is consistent broadly with a lower density than the early time data. A lot more work in analysis of the cross sections is needed before any firm conclusions can be drawn. However, an important point is that the experimentally

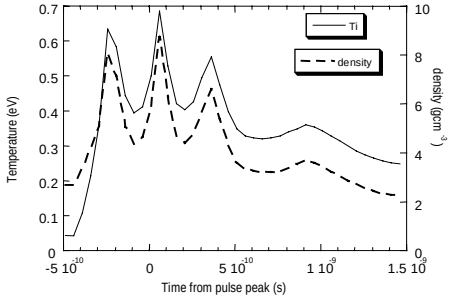

Figure 3. Ion temperature and density predicted by MEDUSA simulation of the shocked foil.

observed peak at 50° suggests a density of less than 1.5 g/cc in contrast to the hydrocode simulation which suggests a value of nearer 2 g/cc. The broadness (~20°) of the peak in the 1.5 g/cc case is related to the lower coupling parameter caused by having an average ionisation of only 1.6. The narrow peak in the late time data suggests a stronger coupling parameter, probably due to a higher temperature leading to higher ionisation. Clearly some more work is needed to assess to what degree the experiment is a test of the hydrocode.

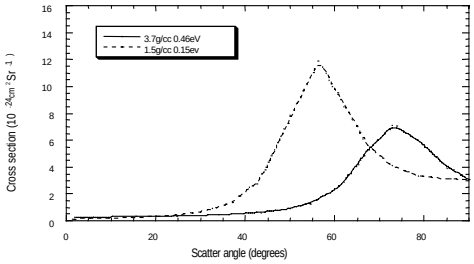

Figure 4. Some examples of simulated X-ray scattering cross sections.

References

1. S Ichimaru,
Rev. Mod. Phys. 51(4) pp1017-1057 (1982)

2. TA Hall et. al.
Phys. Rev. Lett. 60(20) p2034 (1988)

3. AN Mostovych et. al.
Phys. Rev. Lett. 75(8) p1530 (1995)

4. E Nardi,
Phys. Rev. A. 43(4) p1977 (1991)

5. E Nardi, Y Rosenfeld and D Ofer,
J. Phys. Colloq. 49 C7-267 (1988)

6. RM Stevenson et. al.
Optics Letters 19(6) p363 (1994)

7. DW Phillion and CJ Hailey,
Phys. Rev. A 34 p4886 (1986)

8. JP Christiansen, DETF Ashby and KV Roberts,
Computer Phys.Comm. 7, 271 (1974)

9. AR Bell,
Rutherford-Appleton Laboratory Report 80-091 (1980)

X-ray photon yields and intensities from various laser irradiated sources

D McSherry, NC Woolsey †, D Riley.

Queens University of Belfast, University Road Belfast BT7 1NN, Northern Ireland

† Present address: Dept. of Physics, University of York

E Nardi.

Department of Particle Physics, Weizmann Institute of Science Il-76100 Rehovot, Israel

Introduction

Yields of the He α photons ($1s^2$-1s2p) for the laser irradiated sources iron, titanium and vanadium were measured for various laser energies. The 0.53 μm wavelength 25 J laser pulses of 80 ps duration irradiated a focal spot of diameter between 50 and 150 μm. The data presented here taken was during an X-ray scattering study [1), 2)], and was performed using the Vulcan Nd:glass laser system at the Central Laser Facility at the Rutherford Appleton Laboratory.

Experimental arrangement

The experimental arrangement is the same as for the X-ray scattering experiment [1), 2)] as shown in figure 1.

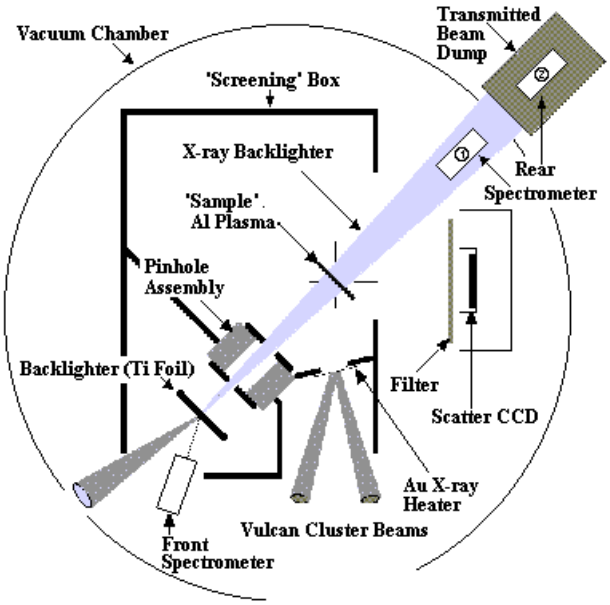

Figure 1. Experiment set-up, not to scale. The beam dump was placed inside the vacuum chamber at the start of the experiment ① and later it was transferred to outside the chamber ②.

The backlighting laser beam illuminated a 3 μm thick titanium, vanadium, or iron foil delivering ~ $2x10^{15}$ W/cm^2 on target. The x-rays produced were collimated into a 5^0 divergent cone by pinholes placed behind the titanium foil. Some x-rays scatter from a heated 1 μm thick aluminium foil placed 20 mm from the titanium foil. The scattered x-rays are detected by a CCD camera at angles away from the normal. These scattered X rays are the study of another paper [1), 2)] and they have been mentioned for completeness.

The number of x-ray photons emitted in the He α transition by the He-like x-ray source was spectrally determined using silicon (111) crystal based spectrometers coupled to cooled CCDs. Two spectrometers were used, photons emitted from both the front, laser irradiated, and the rear side of the x-ray source were detected. The front spectrometer silicon crystal was placed 285 mm from the titanium foil and at 20^0 to normal so that it did not block the incident laser beam. The rear spectrometer was placed at two different positions during this experiment. In the first position the silicon crystal was placed 200 mm from the titanium foil, figure 1,①. At this position we determined signal levels. After several laser shots, and for the X-ray scattering experiment, an X-ray beam dump was attached to the vacuum and the spectrometer moved to 967 mm from the titanium foil, position ② in figure 1. The front spectrometer was filtered with 25 μm Al and 9 μm Be, with an additional layer of 50 or 100 μm of Mylar ($C_{10}H_8O_4$) on some shots. Filtering on the rear spectrometer was different with 25 μm Al and 250 μm Be filters, an additional layer of either 23 μm of Mylar or 17.7 μm of Parylene-C (C_8H_7Cl) was included on some shots. The purpose of this filtering was to prevent soft x-rays and scattered Au M-band radiation swamping the CCD cameras.

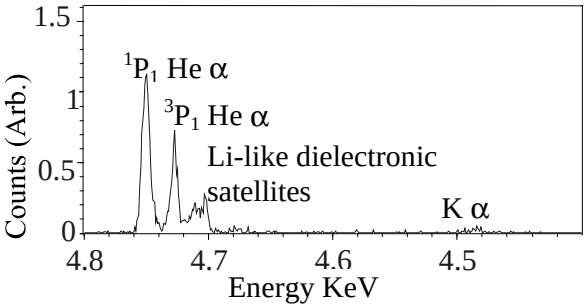

Figure 2. Line emission for the Ti He α transition. Transition energies obtained from Scofield[3] and used to identify the lines and fix the energy scale.

Results

Spectra were recorded for the He α transition for titanium (4749.2 keV), vanadium (5204.6 keV) and iron (6699.5 keV). In some cases the x-ray source was incident on an Al plasma, or a cold Al foil or indeed no plasma for null shots. The incident infrared laser energy and the backlighter focal spot where recorded on each shot.

A typical Ti He α x-ray line spectrum is shown in figure 2. The He-like resonance ($1s^2$-1s2p $^1P_1$), intercombination ($1s^2$-1s2p $^3P_1$) and Li-like dielectronic satellites are resolved.

In order to determine the photon yield in photons per joule-sphere we need to know three things, (1) the total incident green laser energy, (2) the number of photons incident on the CCD integrated over the three lines shown in figure 1, and (3) the solid angle over which the He α radiation falls on to the CCD. The incident laser energy was not measured on a shot to shot basis. However, these values were determined from measured frequency doubling efficiencies. The conversion efficiency of the crystal for a 80 ps laser pulse length was 62 ± 4%, an average of 4 measured values. The number of photons incident on the CCD is determined from the spectra taking into account the He α transmission losses through the various filters and the quantum efficiency of the CCD. The quantum efficiency depends on the energy of the incident photons, and is 70, 62 and 38 percent for the Ti, V and Fe He α photons respectively [4)]. Finally the solid angle is calculated from the angle which the x-ray source subtends at the CCD and from tabulated silicon

crystal reflectivities. The silicon crystals used were assumed to be perfect, with a reflectivities of $5.13x10^{-5}$, $4.38x10^{-5}$ and $4.95x10^{-5}$ radians at 4749.2, 6699.5 and 5204.6 keV [5]. Both crystals were cut from the same source material.

Figure 3 shows the integrated He α photon yields against laser Irradiance for Ti, V, and Fe sources determined from the front spectrometer. Figure 4 shows similar results for the rear spectrometer.

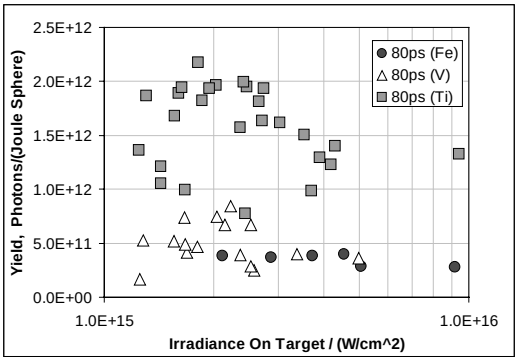

Figure 3. Front spectrometer photon yield vs. laser intensity of the 2p→1s He like lines for Ti, Fe & V target shots with 80 ps pulse length.

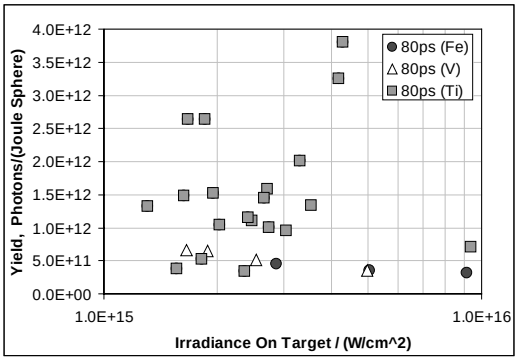

Figure 4. Rear spectrometer photon yield vs. laser intensity of the 2p→1s He like lines for Ti, Fe & V target shots with 80 ps pulse length.

In Figure 5 the ratio of rear and front spectrometer data photon yields as a function of laser Irradiance are compared.

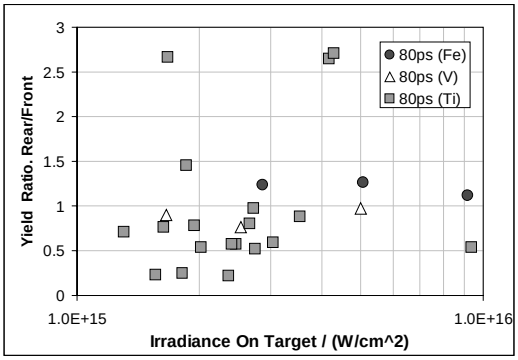

Figure 5. Ratio of front and rear spectrometer photon yield.

Discussion

The Ti results are in broad agreement with the results of Phillion and Hailey [6]. Photon yields typically are between 10^{11} – $2x10^{12}$ Photons/(Joule-Sphere). The average Ti (Z=22) photon yields were larger than the V (Z=23) yields which were in turn bigger then the Fe (Z=26) values. This is expected as the yield falls with increasing atomic number. A large shot to shot variation in photon yield is measured at the same irradiance on target. This may result from shot to shot variations in the focused laser beam profile and possible hot spots in the laser focus. Laser beam smoothing techniques were not applied during this experiment, however, techniques such as random phase plates may reduce hot spot production and reduce the variation in photon yield. Due to large yield variations photon yields were monitored on each shot during the X-ray scattering measurements. This allowed accurate cross-sections to be determined.

We can clearly see from the ratio plot, figure 5, that the He α photon yields are not the same for the front and rear spectrometers for the Ti, V, and Fe targets. The targets are illuminated on the one side only, and effects such as opacity of the plasma should effect the measured yields when comparing front and rear.

We have assumed that the silicon crystals used were perfect however the reflectivities assumed need to be verified by calibrating the crystals. This is a reasonable assumption since silicon is a robust material and crystal manufacture is an advanced process.

In conclusion we have shown typical x-ray photon yields for Ti, V and Fe targets. The yields presented here provide a useful guide when planning experiments were photon numbers are required and this data should prove useful to others in the scientific community.

References

1. NC Woolsey, D Riley and E Nardi,
Rev. Sci. Instrum., 69, 418, 1998.

2. NC Woolsey, D Riley and E Nardi
CLRC Annual Report RAL-TR-97-045, 27 (1998)

3. JH Scofield, Lawarence Livermore National Laboratory,
UCID-16848, (1975)

4. AG MacPhee and CLS Lewis.
CLRC Annual, 135 (1993)

5. BL Henke, EM Gullikson and JC Davis
At. Data Nucl. Data Tables 54 181 (1993)

6. DW Phillion and CJ Hailey,
Phys. Rev. A 34 4886 (1986)

X-ray scattering from a moderately coupled plasma

N C Woolsey†, D McSherry, D Riley.

Department of Physics, The Queen's University of Belfast, Belfast BT7 1NN, Northern Ireland

† Present address: Dept. of Physics, University of York

E Nardi.

Department of Particle Physics, Weizmann Institute of Science Il-76100 Rehovot, Israel

Introduction

In the previous annual report we reported the first experimental measurement of x-ray scattering processes in a plasma[1)]. This experiment demonstrated the feasibility of the technique[2)], and specifically, established this technique as a sensitive method of observing strong coupling phenomena. Following this success a second, experimental measurement of x-ray scattering cross-sections from a radiatively heated plasma has been completed.

The x-ray scattering technique is sensitive to ion-ion correlations, or the structure factor of a plasma. In a weakly coupled plasma the ion cores are screened by the Debye sphere. However, as the density increases, i.e. as the strong coupling regime is approached, the inter-ion core separation may become less than the Debye sphere. At this point ion positions are influenced by neighbouring ions with short range order occurring. X-ray scattering is sensitive to these effects. The technique can be applied to moderately coupled plasmas (i.e. Γ_{ii}~1) as described here or strongly coupled plasma (Γ_{ii}>1) as described in a related article[3)].

Experimental technique

As the experimental technique has been described elsewhere[1,2)], an outline of the experimental technique and modifications follows. A plasma with a moderate ion-ion strong coupling parameter (i.e. Γ_{ii}~1) is formed by radiatively heating a thin, free-standing Al foil. The heating source is a soft x-ray radiation source created by focusing six Vulcan cluster beams onto a 1000 Å thick Au foil. The Au is coated onto a 0.5 µm CH-plastic film. A uniform, 1.5 mm diameter focal spot was created with random phase zone plates to give an irradiance of $3x10^{13}$ Wcm^{-2} in a 1 ns laser pulse. At these irradiances a large area of approximately 80 eV radiation temperature x-ray source consisting of Au P-, O-, and N- band emission was created. Note, the Au M-band was *not* excited. This thermal radiation volumetrically heated a 1 µm thick Al sample placed 6.5 mm from the source.

Synchronized and delayed to the Au soft x-ray source is a second high temperature, short lived, Ti plasma. This backlighting source was ionised to form a He-like plasma with a 80 ps laser pulse focused to $2x10^{15}$ Wcm^{-2}. The x-ray emission is dominated by Ti He-like n=1-2 transition (namely the He_α transition) centred at 4.75 keV. This prolific source of line radiation was collimated with pinholes into a 5° divergent cone and directed onto the Al sample.

The number of incident He_α photons on the Al sample was monitored using a Si(111) spectrometer coupled to a 16-bit CCD detector[4)]. A similar CCD detector was used to record the number of He_α photons scattered by the Al sample. Scattering cross-sections are small (order of 10^{-24}) and the number of scattered photons is roughly 1 in 10^6 incident photons for the experiment. Single photon counting techniques were employed. Careful filtering of the CCD detector was necessary to exclude the soft x-ray background and limit the number of exposed pixels to less than 1 in 10. This is essential to enable reliable single photon detection. The CCD detector was positioned to record scattered photons over a 17° angle on each shot (i.e. approximately 3 times the divergence of the incident x-ray beam) and could placed at angles centred on 20°, and 30°. The detector housing was modified to allow measurements to lower scattering angles.

Reproducible shot-to-shot alignment of target components was possible using an alignment station external to the target chamber and kinematic mounts.

Results

X-ray scattering measurements from cold and radiatively heated Al samples were obtained. In these measurements approximately 1 in 10 pixels on the detector recorded a signal. With knowledge of the sensitivity of the CCD system (i.e. 1 count is equivalent to 12 electron-hole pairs, and a electron-hole pair is created with each 3.65 eV absorbed) the number of single photon events can be histogrammed as a function of energy to produce a spectrum. Examples of x-ray scattering data from radiatively heated Al foils are shown as spectra in figure 1.

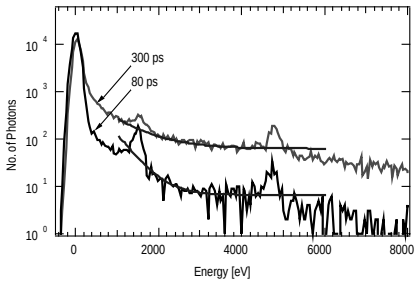

Figure 1. Histograms of scattered photons

In figure 1 the large peak centred on 0 eV indicates 90% of the pixels (1024 x 256 pixels) were empty. The feature between 100 and 2000 eV, including the peak centred at 1510 eV, is due to the spectral nature of the Au soft x-ray source, the transmission of the Be and Al filters covering the CCD, and the Si CCD detector K-edge. The scattered signal is the peak centred at 4750 eV. Peak area after background subtraction gives the number of scattered photons. Absolute and relative x-ray cross-sections as a function of scattering angle and time delay can be extracted. Relative measurements are made by normalizing the number of scattered photons against the number of incident photons measured with the spectrometer, absolute measurements require absolute calibration of the spectrometer.

In order to ensure the scattered signals were real and the scattered signal was a true measure of the cross-section of the evolving Al plasma a series of null shots and cold shots were taken at each scattering angle. The results indicate that the pinhole collimation and shielding was accurately set and did *not* contribute to the scattering. In addition scattering of only the Au x-ray source (i.e. no backlighter) did *not* produce a peak close to 4.7 keV. The cold shots, i.e. the Al foil was not heated but probed by the backlighter, demonstrate the x-ray scattering cross-sections were modified as the heated Al sample evolved.

Relative x-ray scattering cross-sections are shown in figures 2 and 3. In figure 2, three single shot measurements centred at 20° are shown. Two single shot measurements were made with 80 ps temporal resolution (●, and ■) and one at 300 ps (Δ) backlighter duration. Vertical error bars are determined by

statistical uncertainty, horizontal error bars indicate the experimental angular resolution. In figure 3 the 300 ps data set at 20° (Δ and □) is reproduced and compared to 300 ps data centred on 30° (▲).

The CCD detector covered an angle range of 17° on each shot, three times the backlighter beam divergence, by performing a running histogram over a third of the CCD three data points were extracted.

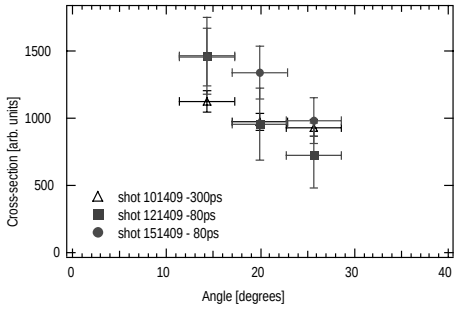

Figure 2. Comparison of 80 and 300 ps results

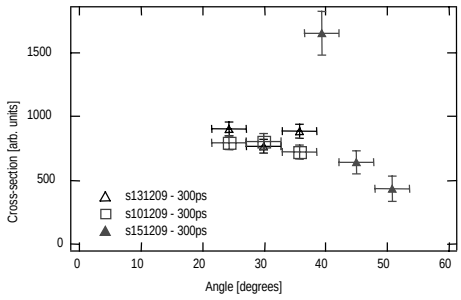

Figure 3. 300 ps cross-sections measurements

Discussion

The results in figures 2 and 3 show the scattering cross-sections decrease with increasing angle: functionally similar to the cross-section expected from a weakly coupled plasma (or ideal gas). Forward scattering cross-sections (i.e. close to 0°) are suppressed for a moderately (and strongly) coupled plasma leading to a peaked cross-section. For moderate coupling short range order is ill defined and inter-ion separation relatively large, a broad peak at low scattering angle is expected. It is possible that measurement at angles closer to 0° would have resolved a peak. Figure 3 suggests the top and high angle wing of such a peak may have been observed, however, the evidence is inconclusive.

From each shot the three points (figures 2 and 3) are smoothly varying. However, shot-to-shot variation is significant, this is in part due to a) statistical noise and b) reproducibility of the scattering plasma conditions.

The need to ensure less than 1 in 10 pixels exposure and allow a 17° coverage limits experimental accuracy. At best 1% statistical uncertainty in the number of detected photons is possible. The He_α intensity above background is maximized to enable efficient filtering of background radiation. Still, many pixels are exposed to background photons impoverishing the statistics; statistical accuracies of approximately 10% for 300 ps and 20% for 80 ps measurements are obtained.

Uniform, as well as reproducible, plasma production is an issue. Modeling indicates the Al surface layer facing the Au x-ray source heats rapidly (to 15 eV) whilst the Al bulk remains cool (~1 eV). The strong density and temperature gradients and variations in the soft x-ray source will lead to shot-to-shot uncertainties.

Absolute x-ray scattering cross-sections require calibration of the crystal spectrometer. Crystal calibrations with accuracies up to 3% can be obtained using a conventional x-ray source and an asymmetric double crystal[5].

Hydrodynamic Modeling

The hydrodynamics of the radiatively heated Al sample is modeled using Med103[6]. Modifications to Med103 include frequency distributed energy absorption using published cold opacity tables[7], incorporation of the Sesame equation of state library[8], and an implementation of a Saha ionisation model based on the work of Heading *et al.*[9]. Frequency distributed radiation sources are taken from the literature[10] and scaled using the Stafan-Boltzmann law, dilution resulting from source to sample separation is included.

Conclusion

Relative x-ray scattering cross-sections have been measured from a radiatively heated Al plasma using a 80 and 300 ps duration, 4.75 keV x-ray source. The scattering data shows a monotonic decrease in the cross-section with angle, although inconclusive evidence of a peak at low angle, indicative of moderate coupling, may be present. Future low angle measurements may confirm this.

Low photon numbers, and the need to ensure the CCD is not overexposed make background elimination and discrimination both important and non-trivial. However photon counting the CCD can be used as a spectrometer which greatly enhances the signal above noise.

The experimental and data analysis procedures continue to be improved. As the hydrodynamic model is developed we will investigate Al sample uniformity. This should improve shot to shot reproducibility. Further development of the CCD may enable angles closer to 0° to be measured

Acknowledgments

The authors thank the staff at the CLF for their expert assistance and Dr. A. G. MacPhee for discussions on CCD detectors. This work was supported by grant GR/K95543 from the UK EPSRC.

References

1. N C Woolsey, D Riley and E Nardi
CLRC Annual Report RAL-TR-97-045, 27 (1998)

2. N C Woolsey, D Riley and E Nardi
Rev. Sci. Instrum. 69 418, (1998)

3. D Riley, D McSherry, N C Woolsey and E Nardi
CLRC Annual Report 97-98

4. D McSherry, N C Woolsey D Riley and E Nardi
CLRC Annual Report 97-98

5. K D Evans, B Leigh and M Lewis
X-ray spectrometry 6 132 (1977)

6. A Djaoui
CLRC Technical Report RAL-TR-96-099

7. B L Henke, E M Gullikson and J C Davis
At. Data Nucl. Data Tables 54 181 (1993)

8. N G Cooper
Los Alamos Scientific Library LALP-83-4 (1993)

9. D Heading, J S Wark, G R Bennett and R W Lee
J. Quant. Spectrosc. Radiat. Transf. 54 167, (1995)

10. C A Back et al.
J. Quant. Spectrosc. Radiat. Transf. 51 19, (1994)

ASE gain and travelling wave model of collisional excitation x-ray lasers

J Y Lin, G J Tallents, A Demir, R Smith.

Department of Physics, University of Essex, Colchester, CO4 3SQ, UK

J Zhang, E Wolfrum.

Department of Physics, Clarendon Laboratory, University of Oxford, Oxford, OX1 3PU, UK

A G MacPhee, C L S Lewis, R M N O'Rourke.

School of Mathematics and Physics, Queen's University of Belfast, Belfast, BT7 1NN, UK

G J Pert.

Department of Physics, University of York, York, YO1 5DD, UK

D Ros, P Zeitoun.

Laboratoire de Spectroscopie Atomique et Ionique, Universite Paris-Sud, 91405 Orsay, Fr

Introduction

Using multiple ~ 100 ps pulse pumping has led to x-ray lasers operating at saturation down to 73 Å [1)]. The other approach of generating high gain and high efficiency x-ray lasers is also demonstrated using a combination of ~ 1 ns long pulse and a few ps short pulse [2)]. Saturated operation of an x-ray laser is important because it means that the maximum power possible for a given volume of excited plasma is extracted by stimulated emission and usually it means a high drive efficiency is achieved. In this report, a modified ASE gain model is used to characterise the saturated Sn x-ray laser output pumped by 75 ps pulse or 3 ps short pulse. Using this simple ASE model, laser output varying with the target length could be accurately calculated and compared with experimental observations. Small signal gain and saturation irradiance can therefore be derived. By incorporating the temporal variation of the signal in the model, travelling effect can also be simulated and explained.

Experiment

The experimental set-up is similar to that described in [1, 2, 5)]. The investigation of saturation and travelling wave effects were undertaken using Sn targets of 2 - 18 mm long and 100 or 200 µm wide stripes coated on glass substrates. To produce a plasma medium longer than 18 mm, double target coupling was used. In double 75 ps pulse pumping, a prepulse with 10% of the total energy on target was produced and delivered 2.2 ns in advance of the main pulse. The peak irradiance of the main pulse on the target was 4×10^{13} W/cm^2. In CPA pulse pumping, a ~ 300 ps background pulse was incident 550 ps earlier than the 3 ps CPA pulse. The peak irradiance for the long pulse and short pulse were 8×10^{12} W/cm^2 and 6×10^{14} W/cm^2 respectively. Travelling wave pumping was only introduced in the CPA pulse pumping by inserting a 300 line/mm grating to tilt the wave front. The primary diagnostic along the target axis was a flat-field grazing incidence x-ray spectrometer with 1200 line/mm aperiodically ruled gratings.

With the optimum double pulse pumping and best coupling (~ 175 µm radial separation) between the two targets, various length of the targets were used to record the variation of the laser output with the length of the gain medium. The pumping irradiances were kept consistent at ~ 2×10^{13} W/cm^2 for Sn targets with less than 15% energy fluctuation. Plasma lengths longer than 18 mm were produced by double target coupling.

The best coupling efficiency between the two targets is measured to be 50 - 70% by comparing the laser output from a single 20 or 22 mm long target with double 14 plus 6 or 8 mm targets with the optimum target separation. The total laser output as a function of the target length for the long (75 ps) pulse pumped Ni-like Sn, x-ray lasers is shown in figure 1.

Gain coefficient

To determine the gain coefficient of x-ray lasers, a simple model for homogenous gain in an amplified spontaneous emission (ASE) laser has been modified and used to calculate the expected x-ray laser intensity variation with the length L of the gain medium for comparison to the experimental measurements (see figure 1). Allowing amplification in both

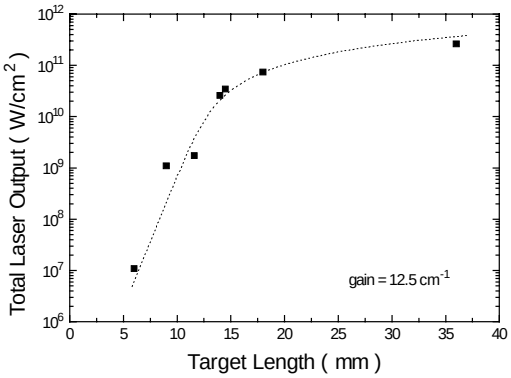

Figure 1. Variations of the total laser output of the Ni-like Sn laser at 120 Å pumped by 75 ps pulses with target length. The dotted lines are the best fits of the model discussed in the text.

directions and assuming that I_s, I_o and G_o are constant along the plasma length and during the x-ray laser transit time, the result is equation (38) from Pert [3)], that is

$$G_oL = (1-2\frac{I_o}{I_s})GL + 2\frac{I_o}{I_s}\alpha(GL) \qquad (1)$$

where G_0 is the peak small signal gain, I_0 is the total spontaneous emission, and I_s is the saturation intensity. If a single direction amplification is applied (i.e. travelling wave pumping), the factor of 2 in equation 1 should be dismissed. The parameter $\alpha(GL)$ takes account of wavelength integration of the laser intensity over an assumed Gaussian gain profile and can be calculated using the Linford [4)] approximation.

$$\alpha(GL) = \left(e^{GL}-1\right)^{3/2} / \left(GLe^{GL}\right)^{1/2} \qquad (2)$$

The output x-ray laser intensity I_l is given by $I_\ell = I_o\alpha(GL)$. Using equation (1) to (2) then gives a complete fit to the experimental Ni-like x-ray laser intensities through saturation. In figure 1, the small signal gain for the 75 ps pulse pumped Ni-like Sn (120Å) x-ray lasers is determined to be 12.5 cm^{-1}. The saturation intensity to spontaneous emission ratio I_s/I_0 is derived to be 3×10^6 for the Sn lasers. This implies an effective gain length product of ~ 15 is required for the Sn laser to reach

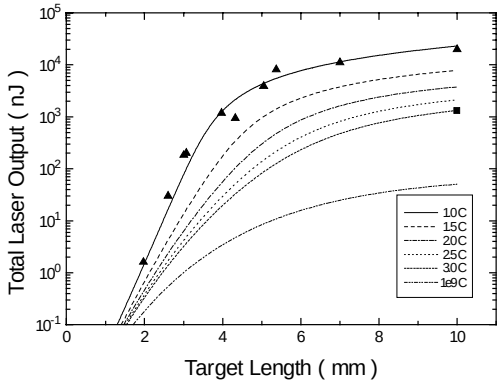

Figure 2. Ni-like Sn x-ray laser output with target length, for various travelling wave speeds. Triangles denote experimental measurements pumped by 1×c travelling wave CPA pulse and the square denotes a CPA pulse with a travelling wave speed 3×c introduced by the focusing system. Assuming a gain decay time ΔT = 10 ps, different travelling wave effects are shown.

saturation. For the CPA pumped Sn laser (figure 2), the small signal gain is determined to be 42 cm^{-1} which is the highest signal gain ever measured in a collisional excitation x-ray laser. The ASE model does not consider refraction, spatial inhomogeneities or other complications possibly present in the plasma and so the small signal gain coefficient derived from the model refers to the spatially averaged value. Overall good fits in figures 1, 2 suggest the simple modified ASE gain model can simulate the saturation characteristics of the laser output well.

The measured saturation irradiances are determined to be ~ 2.9×10^{10} W/cm^2 and 2.5×10^{10} W/cm^2 for 75 ps and 3 ps pulse pumping respectively by fitting equations 1, 2 to the experimental measurements of the laser output (see figures 1, 2). Generally good agreement between the experimental measurements and the theoretical calculations are found [5]. The maximum laser output intensity from the long and short pulse pumped Ni-like Sn lasers is much higher than both the experimental and theoretical saturation intensity, indicating that these lasers are operating well into the saturation region.

It was found that using a simple treatment of ASE gain for a homogeneously broadened gain profile (see equation 1) can predict the variation of the laser output with the length of the gain medium through saturation (figures 1, 2). As mentioned above, the signal gain obtained by fitting equation 1 represents the spatially averaged signal gain because the amplifying laser beams sample different gain regions as they propagate through the whole target. Similarly, if a travelling wave pumping is not applied along the target, a time averaged signal gain is obtained. According to the simulations for 3 ps travelling wave CPA pulse pumped Ne-like Ge x-ray laser [6], a high signal gain is reached during the CPA pulse pumping which then decreases approximately exponentially as collisional redistribution occurs. The gain duration is calculated to last ~ 7 ps (FWHM). To estimate the travelling wave effect for the CPA pulse pumped Ni-like Sn laser, we adopt the gain profile in time from the Ge laser with a peak spatial averaged small signal gain of 42 cm^{-1} as measured in experiment.

Effect of varying pump pulse propagation

If the wave front of the pumping pulse travels along the target with a speed faster than the speed of the amplified x-ray laser beam (i.e. at the light speed c), a smaller local signal gain is sampled as laser beams propagate a longer distance along the gain medium. By taking into account the variation of signal gain coefficient with time, the total laser output for various travelling wave velocities along the target as a function of the target length can be solved numerically by varying the local gain coefficient in equation 1, see figure 2.

It can be seen in figure 2 that when the travelling wave speed is faster than the speed of light, a longer gain medium is required to reach saturation. For the 3×c travelling wave CPA pulse irradiating a 10 mm target, laser output just reaches saturation, but only a ~ 4 mm long target is required to give the same output when a 1×c travelling wave is used. The calculations show that a 3×c travelling wave speed gives a best fit to our measurement without using travelling wave pumping, which is in agreement with our experimental conditions where a 3×c intrinsic travelling wave pumping is produced by the focusing system. Doubling the gain duration to ΔT = 20 ps, calculation shows (figure 3) that even a normal incident wave (travelling wave speed → ∞) gives less than one order of magnitude lower laser output in comparison with the optimum travelling wave pumping. The gain duration is then comparable to the laser propagation time along the target. This suggests the travelling wave effect is much less important in the experiment using 75 ps pumping pulses. A gain duration of 50 - 60 ps is the same as the laser propagation time in an 18 mm long target. Therefore equation 1 without the modification of the travelling wave effect can simply be used to fit the experimental results involving ~ 75 ps drive pulses with a uncertainty factor less than that normally introduced by experimental measurements.

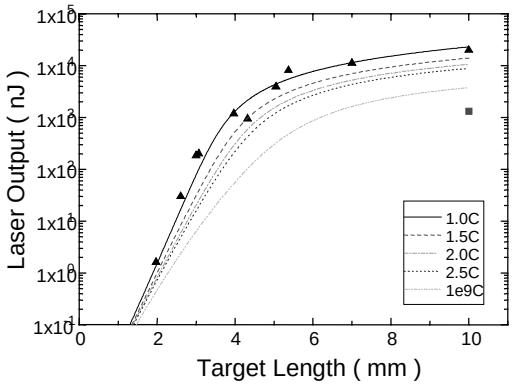

Figure 3. Variations of the Ni-like Sn x-ray laser output with the target length for various travelling wave speed on the target as labelled. The gain decay time ΔT is assumed to be 20 ps.

Conclusions

In conclusion, a simple modified ASE model can be used successfully to calculate the laser output through saturation, and the travelling wave pumping effect. The small signal gain and saturation intensity of the Sn x-ray laser is determined from the best fit. Calculation suggests that the travelling wave effect is only important when the pumping pulse duration is significantly shorter than the x-ray laser beam propagation time.

References

1. J. Zhang et al,
Science **276**, 1097 (1997).

2. M.P. Kalachnikov, et al,
Phys. Rev. A. **57**, 4778 (1998).

3. G.J. Pert,
J. Opt. Soc. Am. B **11**, 1425 (1994).

4. G.J. Linford, E.P. Poressini, W.R. Sooy and M.L. Spaeth,
Appl. Opt. **13**, 379 (1974).

5. J.Y. Lin, et al
Gain saturation of the Ni-like x-ray lasers'
submit to Opt. Comm.

6. J.Y. Lin,
PhD Thesis, University of Essex, 1998.

Optimisation of double pulse pumping for Ni-Like SM x-ray lasers

J Y Lin, G J Tallents, R Smith, G Eker, S J Pestehe.

Department of Physics, University of Essex, Colchester, CO4 3SQ, UK

A G MacPhee, R Keenan, C L S Lewis, R M N O'Rourke.

School of Mathematics and Physics, Queen's University of Belfast, Belfast, BT7 1NN, UK

E Wolfrum, J Zhang, J S Wark.

Clarendon Laboratory, Department of Physics, University of Oxford, Oxford, OX1 3PU, UK

D Neely.

CLRC Rutherford Appleton Laboratory, Chilton, Didcot, Oxon., OX11 0QX, UK

G J Pert.

Department of Physics, University of York, York, YO1 5DD, UK

Introduction

Maximising the efficiency of generating x-ray lasers reduces the driving energy required to produce shorter wavelength x-ray lasing. Using double drive pulses (one prepulse and one main pulse) to pump x-ray lasers has been shown to be able to saturate x-ray laser output of Ni-like Ag (14 nm) [1], In (12.6 nm), Sn (12 nm) [2] and Sm (7.3 nm) [3] at plasma medium lengths 18 ~ 20 mm. With double pulse pumping, the first pulse produces cold plasma from the solid. During the time interval between the prepulse and main pulse, the preformed plasma expands and forms a long scale-length electron density profile. The longer scale-length plasma not only increases the energy absorption of the plasma from the driving laser (main pulse) via inverse Bremsstrahlung absorption, but also produces less refraction of the x-ray laser beam and better propagation within the gain region. Previous studies [4] - [6] suggest that the level of prepulse irradiance and the pulse interval between the prepulse and main pulse determine the electron and ion temperatures, the electron density gradient, the laser gain and the maximum x-ray laser propagation distance in the plasma and that these parameters control the x-ray laser output.

In this report, we have made a systematic experimental study of double pulse pumping of the Ni-like Sm x-ray laser at 7.3 nm. The Ni-like Sm x-ray laser has been successfully demonstrated as the shortest wavelength saturated x-ray laser achieved in the laboratory [3]. To determine the optimum double pulse pumping configuration, double pulses with various pulse ratios (the ratio of the irradiance of the prepulse to main pulse) and pulse intervals (the time between the prepulse and main pulse) were irradiated on single Sm slab targets. The targets were of 14 mm length which is sufficiently short to avoid the laser operating in the saturation region during the optimisation procedures. We expect the gain length product from a single 14 mm target is ≤ 13 [3].

Experimental arrangements

The experiment was carried out at the Rutherford Appleton Laboratory using the Vulcan Nd-glass laser at 1.05 µm. Before entering the pre-amplifiers of the Nd-glass laser chain, the stretched oscillator pulse with a pulse duration of ~ 75 ps was divided by a beam splitter to produce double pulses with adjustable pulse intervals. While keeping the irradiance of the second pulse (main pulse) at the same level, the first pulse's irradiance was controlled by inserting pre-calibrated filters to produce the required pulse ratio (prepulse / main pulse). After the amplifier chain, each of the Vulcan laser beams could deliver up to 22 J (in the main pulse) on the target. Three beams were overlapped onto the target in an 19 mm × 75 µm width line focus by using a combination of three f/2.5 spherical lenses and three f/2.5 off-axis spherical focusing mirrors to produce a peak irradiance of the main pulse on the target of up to ~ 6×10^{13} W/cm^2.

The ratio of the prepulse to main pulse irradiance was monitored by two fast photodiodes in the laser control area and was double-checked by a fast vacuum diode in the target area. For shots with high pulse contrast (>10^2), one photodiode with less filtering was arranged deliberately to be saturated by the main pulse which provides a measurable prepulse signal level to be compared with the main pulse signal measured by the other photodiode.

The targets were 14 mm long flat slabs consisting of 75 µm width and 1 ~ 2 µm thickness samarium stripes coated on glass substrates. The primary on-axis diagnostic was a grazing angle flat field spectrometer with a 1200 lines/mm aperiodically ruled grating. The spectrometer recorded emission from 60 Å to 240 Å wavelength and from –1 mrad to 11 mrad angular deviation in the horizontal direction (perpendicular to the target surface) on an InstaSpec IV back-thinned soft x-ray CCD detector. The collection angle ~1 mrad of the spectrometer in the vertical direction is limited by the entrance slit. The uniformity and the ionisation balance along the line focus was monitored by a space-resolving and time-integrating Bragg crystal spectrometer with a 300 mm convex curvature potassium acid phthalate (KAP) crystal (2d = 26.64 Å). An attached CCD detector recorded the resonance line emissions from 7 Å to 11 Å. For some shots, another crystal spectrometer with a 300 mm curvature KAP crystal was coupled to an x-ray streak camera to measure the time-resolved ionisation balance from the lasing plasma media. The width of the timing slit of the streak camera was set to be 200 µm, which gave a temporal resolution ~ 20 ps.

Results

To determine the best pump pulse configuration for the Ni-like Sm laser, a series of shots using various pulse ratios and pulse intervals were carried out. Keeping the peak irradiance of the main pulse consistently at ~ 5×10^{13} W/cm^2 (with less than a 10% energy fluctuation), the x-ray laser output for each pulse interval is found to peak at various pulse ratios (figure 1). A lower level of prepulse is optimal as the pulse interval is increased. Pumping with the optimum pulse ratio increases the laser output by orders of magnitude compared with unoptimised pulse ratios and pulse intervals.

The brightest Sm x-ray laser has been observed using a 0.5 % prepulse with a pulse interval of 3.5 ns, but the maximum optimised x-ray laser output with pulse intervals of 2.2 ns, 3.5 ns, and 5 ns differ by less than a factor of two (figure 1).

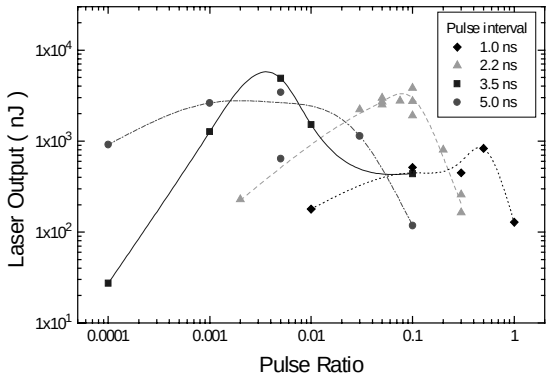

Figure 1. Variations of x-ray laser outputs at 73 Å as a function of the pulse ratios for various pulse intervals. The peak irradiance of the main pulse is fixed at 5×10^{13} W/cm^2.

However, a 1 ns pulse interval gives a factor 4 ~ 7 less signal than that of the optimised laser output for the other pulse intervals.

The beam quality of the brightest Sm x-ray laser pumped by double pulses with a 1 ns pulse interval was found to be similar to those pumped by double pulses with 2.2 ns, 3.5 ns, and 5 ns pulse intervals. The divergence (full width at half maximum) and deflection angle (beam pointing angle relative to the target surface) of the x-ray laser beam were measured to be 2.5 ± 1 mrad and 5 ± 1 mrad respectively, as shown in figure 2. These values are small because of the lack of significant refraction effects in the Ni-like Sm x-ray laser. The short wavelength and flat electron density profiles smoothed by the prepulse mean that refraction is small.

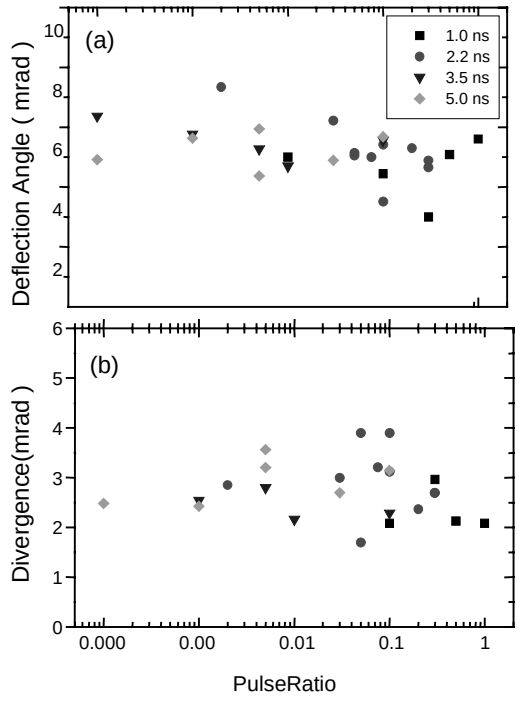

Figure 2. (a) Deflection angle and (b) divergence of the Sm x-ray laser as a function of the pulse ratio for various pulse intervals.

The degree of ionisation of the x-ray lasing plasma was monitored by a keV crystal spectrometer. As the temperature rises in the plasma, we expect more Co-like and higher ionisation stage ions to be generated and consequently stronger band emissions from those ionisation stages. A comparison of time-integrated Sm keV spectra pumped by various pulse ratios with a 3.5 ns pulse interval had been made during the experiment. Experimental observations suggest that Ni-like 4f – 3d emissions show no significant variations, when different pulse ratios are used. However, the Co-like 4f – 3d emissions, and Fe-like and Mn-like band emissions are significantly lower when a small (0.01 %) or large (10 %) prepulse is used. The spectra of the Sm x-ray laser medium pumped by an optimum level of prepulse (0.5 %) implies a hotter plasma because of the strong emission from the higher ionisation stages. Higher temperature in the lasing medium produces a higher excitation rate and thus higher gains.

A typical time-resolved resonance emission of Sm plasma recorded by the streaked keV crystal spectrometer is shown in figure 3. The main driving pulse irradiance is shown schematically on figure 3 assuming that the start of emission corresponds to the start of the laser pulse. In figure 3, 4f – 3d band emissions from the Mn-like and Fe-like ionisation stages peak slightly earlier than those from the Co-like and Ni-like stages do. There is also a significant difference of the emission duration from various ionisation stages. The duration (FWHM) of the Mn-like and Fe-like resonance emissions are ~ 65 ps, which is comparable with the duration of the pumping pulse. In contrast, the resonance emissions from Co-like and Ni-like ions last ~ 85 ps and ~ 100 ps respectively. The Co-like and Ni-like emissions peak later and last longer probably because of recombination from higher ionisation stages after the main drive pulse has switched off.

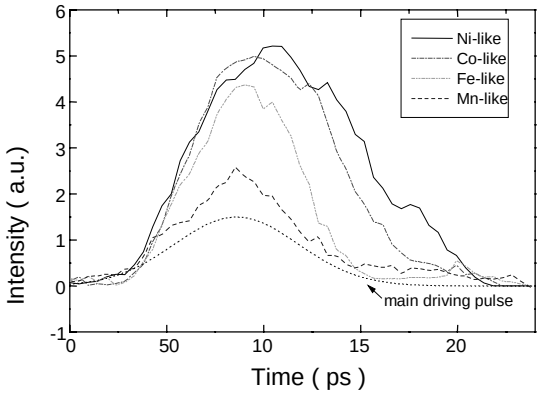

Figure 3. The time-resolved 4f-3d band emissions of Sm from different ionisation stages as labelled. The main laser pulse irradiance is shown schematically as a dotted line.

Discussion

An optimum pulse ratio for x-ray laser output occurs because of a balance between the gain coefficient, the volume of the gain region, and the refraction effects. A small prepulse tends to produce a small volume of preplasma. Although this suggests a high peak temperature and thus high peak gain coefficient when the preplasma is heated by the main pulse, the gain region is small and refraction effects are serious because of the small volume of plasma produced and steep electron density profiles. In contrast, a too large prepulse gives a larger gain region and less refraction in the plasma, but the peak gain is low. It is also found that the optimum pulse ratio decreases with increasing pulse interval (figure 4). A longer pulse interval implies a longer time for the preformed plasma to expand. Although a large scale-length plasma gives a shallower electron density profile, the peak temperature is lower because the main pulse energy has to heat up a larger volume of low-temperature plasma. Hence, a lower level of prepulse is preferred to keep the

plasma at a high temperature to produce gains when a long pulse interval is used.

Simulations [5] suggest that the plasma condition of collisional excitation x-ray lasers pumped by double pulses can be quantified by a parameter, the temperature density (T_e/V_{pre}), where V_{pre} is the volume of the preplasma just before the arrival of the main pulse and T_e is the peak electron temperature during the main pulse irradiation. A higher temperature density than the optimum value implies over-ionisation or a narrow gain region with steep electron density gradients, while a lower temperature density than the optimum gives low gain and thus lower laser output. By assuming the density profile is decided by the prepulse because of the relatively long pulse interval compared with the driving pulse duration and the preplasma undergoes a two dimensional expansion, the volume of the preplasma can be represented as $V_{pre} \sim v^2 T^2$, where v is the ionic sound speed and T is the pulse interval. Since the mass ablation and thus the number of electrons produced by the prepulse is proportional to $v \cdot t$, the lasing electron temperature is then proportional to $T_e \propto I_{main}/v \cdot t$, where t is the prepulse duration and I_{main} is the peak irradiance of the main pulse. If we assume the ionic sound speed is proportional to I_{pre}^a, where I_{pre} is the peak irradiance of the prepulse and a is a constant, the optimum thermal density can be represented as $T_e/V_{pre} \propto I_{main} I_{pre}^{-3a} t^{-1} T^{-2}$. Simulations for the Ne-like Ge x-ray laser suggest a = 1/3, which indicates that the optimum pulse ratio scales as $\left(I_{pre}/I_{main}\right)_{opt} \propto t^{-1}T^{-2}$. In figure 4, the best fit optimum pulse ratio scales as $R_{opt} \propto T^{-3}$, but $R_{opt} \propto T^{-2}$ produces a reasonable fit to the experimental results, particularly for pulse intervals $T \leq 2.2$ ns.

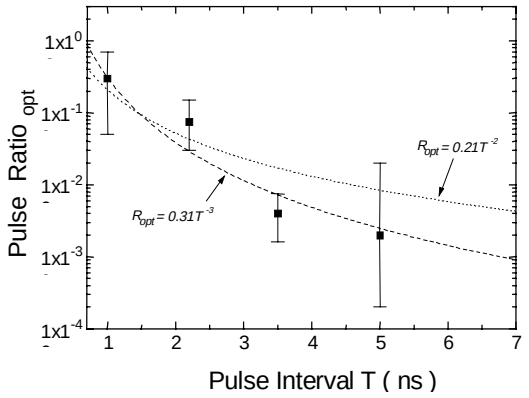

Figure 4. The pulse ratios R_{opt} for optimum x-ray laser output as a function of the pulse interval T. The error bars show the range of R_{opt} giving a factor of two variation of x-ray laser output. The curves show variation of R_{opt} scaling according to $R_{opt} \propto T^{-2}$ (as for [3]) or $R_{opt} \propto T^{-3}$ (the best-fit value).

The x-ray laser output increases as the peak irradiance of the main pulse increases (figure 5). This can be shown to be due to the increase in electron temperature with increasing irradiance. The collisional excitation rate into the upper quantum state of the x-ray lasing transition is approximately proportional to $\sim \exp\left(-\Delta E/kT_e\right)/\left(kT_e\right)^{0.5}$ [7]. If we assume that the electron temperature is proportional to I_{main}/I_{pre}^a as above, the gain coefficient is then proportional to $\exp\left(-bI_{main}^{a-1}\right)/I_{main}^{(1-a)/2}$, where b is a constant. Since the refraction of x-ray lasers is not serious when using a prepulse, the x-ray laser output increases as exponent of the gain coefficient. After fitting this dependence to the experimental data (see figure 5), a is determined as 0.35 ± 0.05, which is consistent with the value described above.

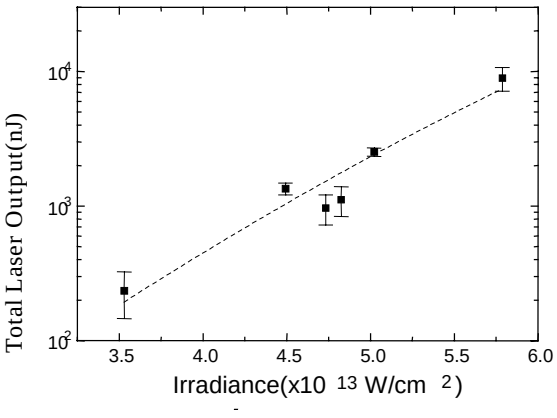

Figure 5. Sm x-ray laser outputs as a function of the peak irradiance of the main pulse. The pulse ratio and pulse interval are fixed at 5% and 2.2 ns respectively. The fitted curve is the expected variation of x-ray laser output taking account of the variation of collisional excitation (see text).

If we assume the prepulse energy is mainly deposited at the critical density, a simple balance of the pressure $P \times$ velocity v and laser irradiance at the critical density gives an ionic acoustic velocity $v \propto I_{pre}^{1/3}$, which also agrees with the scaling value.

Conclusions

The Ni-like Sm x-ray laser pumped by double drive pulses has proved to be an efficient and bright x-ray source at short wavelength. We have demonstrated the first detailed parameter scan of a double pulse pumped Ni-like x-ray laser using a single Sm target. Using an optimum pulse configuration has been shown to increase the x-ray laser outputs by orders of magnitude. The optimum pulse ratio is found to decrease as the pulse interval increases, which agrees with the predictions of a simple model.

References

1. J. Zhang, A.G. MacPhee, J. Nilsen, J. Lin, T.W. Barbee, Jr., C. Danson, M.H. Key, C.L.S Lewis, D. Neely, R.M.N. O'Rourke, G.J. Pert, R. Smith, G.J. Tallents, J.S. Wark, and E. Wolfrum, Phys. Rev. Lett. **78**, 3856 (1997).

2. J. Zhang, A.G. MacPhee, J. Lin, E. Wolfrum, R. Smith, C. Danson, M.H. Key, C.L.S. Lewis, D. Neely, J. Nilsen, G.J. Pert, G.J. Tallents, and J.S. Wark, and P.J. Warwick, Phys. Lett. A **234**, 410 (1997).

3. J. Zhang A.G. MacPhee, J. Lin, E. Wolfrum, R. Smith, C. Danson, M.H. Key, C.L.S. Lewis, D. Neely, J. Nilsen, G.J. Pert, G.J. Tallents, and J.S. Wark. Science **276**, 1097 (1997).

4. G.F. Cairns, C.L.S Lewis, M.J. Lamb, A.G. MacPhee, D. Neely, P. Norreys, M.H. Key, S.B. Healy, P.B. Holden, G.J. Pert, J.A. Plowes, G.J. Tallents, and A. Demir, Opt. Comm. **123**, 777 (1996).

5. J.Y. Lin, G.J. Tallents, A. Demir, S.B. Healy, and G.J. Pert. J. Applied Phys. **83**, 1863 (1998).

6. S.B. Healy, G.F. Cairns, C.L.S. Lewis, G.J. Pert, and J.A. Plowes, IEEE Journal of selected topics in Quantum Electronics, **1**, 949 (1995).

7. R.C. Elton, X-ray lasers, Academic press, London, p.101 (1990).

Spatial Coherence of 23.2 / 23.6 nm Radiation from Multi-element Targets in the Germanium X-ray Laser

R E Burge, G E Slark, M T Browne, X-C Yuan, P Charalambous, X-H Cheng.

Cavendish Laboratory, University of Cambridge, Cambridge, CB3 0HE, UK and Physics Department, King's College London, Strand, London, WC2R 2LS

C L S Lewis, G F Cairns, A G MacPhee.

School of Maths and Physics, Queen's University, Belfast, BT7 1NN

D Neely.

CLRC Rutherford Appleton Laboratory, Chilton, Didcot, Oxon., OX11 OQX

Introduction

The work concerns the optical properties of the lasing lines from the Ge X-ray laser in pursuit of an intense and spatially coherent source for imaging and holographic applications. Neither application can be optimally explored with Ge radiation which is in the 20 nm range of wavelength, because of low specimen penetration, but the principles can be considered relating high source brightness and high spatial coherence to the high temporal coherence available due to the narrow spectral line width. We look forward, as X-ray lasers develop, to reduction in the wavelengths of bright spectral lines with wavelengths in the water window (~2.4 to 4.4 nm) for biological applications and shorter wavelengths for materials applications.

We report here experiments (without prepulse) with the Vulcan laser at RAL on spatial coherence in the horizontal plane of the neon-like Ge X-radiation following single driver pulse irradiation of slab targets. The horizontal plane is the plane containing the optical axis and perpendicular to the target surface. A number of target configurations was examined, namely a two target "injector", the injector followed by a single amplifying target, and the injector followed by a double target amplifier. The intention was to determine what changes in source dimensions accompanied the increased intensity of the 23.2 / 23.6 nm lines of about 70 times [4] when the injector is followed by a single slab amplifier with about double this increase with a two-stage amplifier. We have measured the effective source size for the unresolved 23.2 / 23.6 nm $J = 2 \rightarrow 1$ Ge transitions using the standard [1] Young's double slit method but with an elaborated diagnostic in [2, 3].

Our results must be seen within the context of much experimental work (see [5] for the first study of spatial coherence with the neon-like Se system) and theoretical analysis of the fundamentals of spatial coherence in X-ray laser plasmas (see [6] for summary). Our own recent results for the two target Ge X-ray laser with prepulse [2] have shown marked dependence on divergence angle of apparent source size for 23.2 / 23.6 nm radiation and small dependence on divergence for the 19.6 nm spectral line $J = 0 \rightarrow 1$. Further, for the 23.2 / 23.6 lines in an experiment [3] with a double target without prepulse, on the time dependence of spatial coherence, lower spatial coherence was associated with higher laser intensity and vice-versa.

Experiment

The lay-out of the experiment is shown in figure 1. The injector comprises slab targets A1 and A2 in close proximity and the single and double amplifiers are provided respectively by target A3 acting alone and targets A3 and A4 acting together. Coupling between injector and amplifier, linked by single-pass, was accomplished by relaying the output from A2 by a normal incidence multilayer X-ray mirror selecting the 23.2 / 23.6 nm combined lines. The Ge stripe targets on glass substrates were similar for all four slab targets (18 mm long for A1 and A2, 14 mm for A3 and A4) as has been described e.g [7]. Each target, separately, could be uniformly illuminated by driver laser beams of 1.06 μm wavelength each with pulse energy of ~ 1×10^{13} Wcm 2 and pulse length ~1 ns. The optical pumping of the amplifier was delayed by 4.8 ± 0.1 ns relative to the injector.

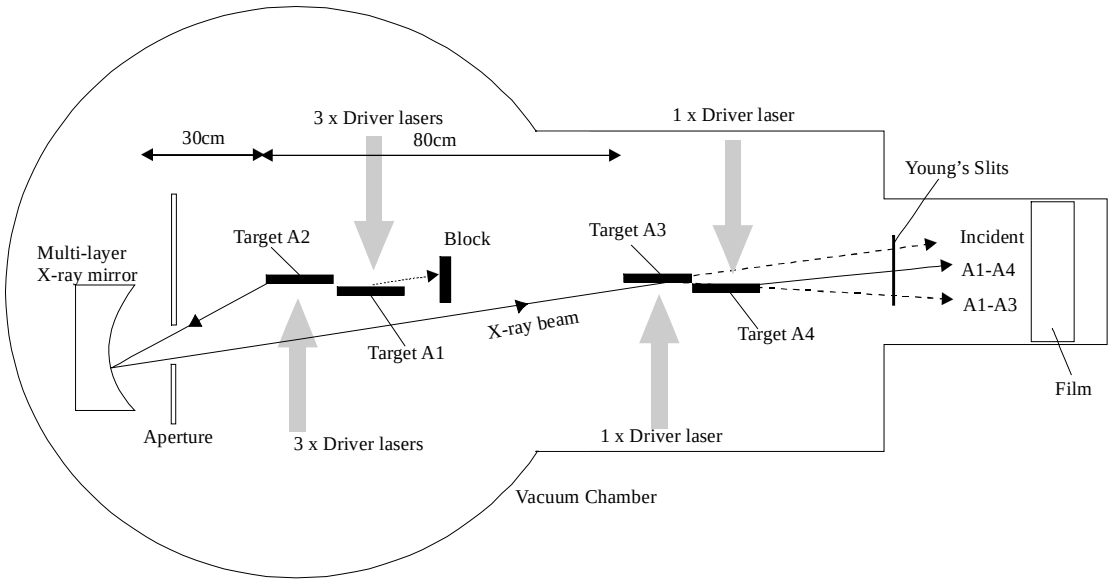

Figure 1. Schematic diagram showing two target injector A1, A2, concave multilayer relay mirror, and two target amplifiers A3 and A4. Direct radiation from the face of the injector nearer the amplifier is blocked when the relay mirror is used. There is a beam limiting aperture to reduce the area of the mirror irradiated in a single pulse: a new mirror area can be brought into place by rotating the mirror. The aperture had no effect on the angular divergence of the laser beam.

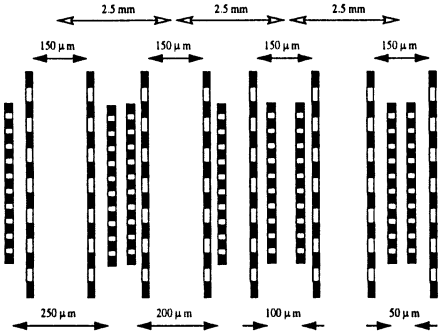

Figure 2. Schematic diagram of diagnostic incorporating dispersion by grating diffraction as well as Young's slit interference.

An example of one of the Young's-slit diagnostics, fabricated in gold by electron- beam lithography is shown in figure 2. This has four pairs of slits set out across the diverging beam in four slit stations. The slits at each station have a common centre and corresponding slits are "laddered" perpendicular to the Young's interference direction with a period of either 4 μm or 2.5 μm with equal land and space ratios to cut out the even diffraction orders. One slit pair at each station has a constant separation of 150 μm; the separation of the second slit pair per station varies from 50 μm to 250 μm as shown. Other diagnostics had 5 or 6 slit pairs with different separations or up to seven slit pairs with constant separation.

All the slit patterns were recorded on film and an example of a result, for the injector with single amplifier, showing interference fringes centred on the positive orders of diffraction gained on Kodak 104.02 film with the diagnostic of figure 2 is shown in figure 3. Visible nearer the pattern centre, in the first diffraction order of the diffraction grating with a 4 μm repeat distance, are the four interference patterns, one per diagnostic station from unresolved 23.2 / 23.6 nm lines and each one from the 150 μm separation Young's slits showing similar patterns with fringes of constant separation. Then further out in the patterns are four first order diffraction patterns due to the 2.5 μm grating repeat, again with the interference patterns overlapping for the two unresolved wavelengths, with fringes of different separations due to the 50 μm, 100 μm, 200 μm and 250 μm separations. The angular distribution of the laser intensity as intercepted by the diagnostic was measured from the variations in the maximum intensities at the angular positions of the centres of each of the Young's interference patterns.

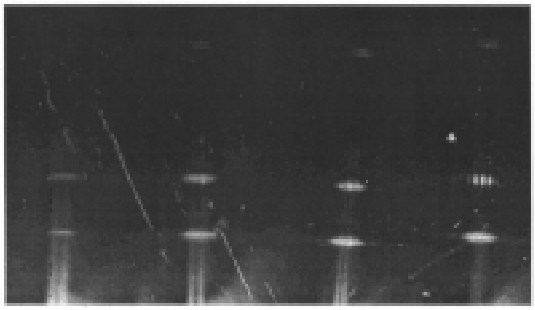

Figure 3. Experimental fringe distributions for 23.2 nm and 23.6 nm radiation and the diagnostic of figure 2.

Experiments were carried out for each of the three separate Ge target configurations each with different separations of source and diagnostic, and diagnostic to film recording. Some dimensions appropriate to experiments with single and double amplifiers are given in figure 1. Otherwise the diagnostic to film distances were between 500 and 700 mm. Photographic records were scanned using a recording microdensitometer and a scanning slit of 5 μm by 50 μm as projected into the plane of the record; conversion of measured optical densities to incident laser intensity accounted for film non linearity.

Coherence Model

The fringe visibility measured at the pattern centre using equal Young's slits is equivalent to the modulus of the complex degree of coherence [1]. In view of the short component separations, the optical results correspond to near field conditions. The measured fringe visibilities were fitted for a given slit separation and known path lengths to the visibilities calculated [2, 3] using a gaussian model for the distribution of intensity for that wavelength at the X-ray laser source of the form $I = I_0 \exp\left(-\frac{x^2}{2\sigma^2}\right)$. Thus a value of the visibility gave directly a value of σ and hence the FWHM = 2.35 σ of the source intensity distribution. Using the model a value of visibility measured for one slit separation can readily be converted to the visibility value for that source size as would be seen at another separation.

We were guided in the choice of a suitable gaussian model by experimental results [8] from spatially resolved direct images of the Ge plasma which show the active region to be centred some 100 μm from the target surface and ~50 μm wide. We took the source model to be a free-standing gaussian intensity distribution with $-4\sigma \le x \le \infty$.

Results and Discussion

The pointing angle, i.e. the angle between the direction of the maximum intensity of the 23.2 / 23.6nm line emission and the symmetry axis of the target arrangement, varied with the target configuration, especially between odd and even numbers of targets, according to the level of refraction compensation, and with some effects of target alignment, with a range from about 3 mrad to 15 mrad. Little change was found in the FWHM of the angular distributions of between 10 and 15 mrad for the three target configurations. Values of the fringe visibilities were taken as averages between the results for the positive and negative diffraction orders and at the same time the angular distributions of intensity were measured. The visibility values for given slit separations were converted to FWHM of the gaussian source distribution.

The FWHM for each target type are plotted in figure 4 for angles of beam deviation centred for each case at the maximum intensity. The angular ranges are governed by the interception of the laser beam by the diagnostic and measurements of spatial coherence have been emphasised towards the conditions of increased refraction in the target plasmas i.e. larger positive angles in figure 4.

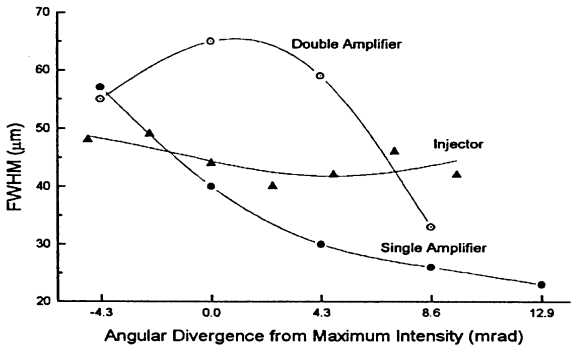

Figure 4. Combined spatial coherence results for injector alone, injector with single target amplifier and injector with double target amplifier. Angular variations centred at angles of maximum X-ray laser intensity.

Large variations of source size across the angular ranges of X-ray laser emission are found in the results with the injector followed by either a single or a double amplifier, but for the injector on its own the source size is roughly constant as measured across the angular range of the beam. From the trends of the curves of figure 4 there seems no doubt that under conditions of strong refraction in the plasma and in agreement with theory [6] the source size is reduced, according to the target configuration, by a factor of up to two; the spread of apparent source size across the beam is also increased following the action of the amplifier(s).

The details of the results of figure 4, as distinct from the general trends, are likely to depend on the precise conditions of beam injection into the amplifiers. There are many variable parameters of the experiment, e.g. target lengths and target separations, axial position of the relay focus mirror which currently produces a magnification of 3.3 on relaying radiation from A2 to A3 with consequential reduction in input angular divergence, alignment of the amplifiers with respect to the injector, time delay of the driver pulses at A3 and A4 relative to the injector etc.

Following from the detailed discussion [4] of the fundamental similarities between the properties of the active plasma medium for polarisation and coherence, and the demonstration that a plane polarised beam produced from the injector output can be amplified without significant depolarisation, it is consistent that the principal effect of the amplifier stages as found in these experiments is to produce a major change in X-ray laser intensity and a relatively small, but experimentally valuable, decrease in apparent source size. The minimum source size, observed for the injector and single amplifier configuration, was 23 μm.

Acknowledgements

We are grateful to the Leverhulme Trust and to AWE, Aldermaston for financial support and to the Engineering and Physical Sciences Research Council for use of the Vulcan laser.

References

1. M Born and E Wolf,
Principles of optics, chap.10,
Perg-amon Press, Oxford, (1993).

2. R E Burge, G E Slark, M T Browne, X-C Yuan,
P Charalambous, X-H Cheng, C L S Lewis, A G MacPhee and D Neely,
J Opt Soc Am B 14, 2742-2751, (1997).

3. R E Burge, G E Slark, M T Browne, X-C Yuan,
P Charalambous, Z An, X-H Cheng, C L S Lewis,
A G MacPhee and D Neely,
J Opt Soc Am B 15, 1620-1626, (1998).

4. B Rus, C L S Lewis, G F Cairns, P Dhez, P Jaegle,
M H Key, D Neely, A G MacPhee, S A Ramsden,
C G Smith, and A Sureau,
Phys Rev A 51, 2316-2327, (1995).

5. J E Trebes, K A Nugent, S Mrowka, R A London,
T W Barbee, M R Carter, J A Koch, B J MacGowan,
D L Matthews, L B DaSilva, G F Stone and M D Feit,
Phys Rev Lett 68, 588-591, (1992).

6. P Amendt, M Strauss and R A London,
Phys Rev A 53, R23-R26, (1996).

7. K Murai, H Shiraga, G Yuan, H Daido, H Azuma, E Miura,
R Kodama, M Takagi, T Kanabe, H Takabe, Y Kato,
D Neely, D M O'Neill and C L S Lewis,
J Opt Soc Am B 11, 2287-2297, (1994).

8. P B Holden, S B Healy, M T M Lightboidy, G J Pert,
J A Plowes, A E Kingston, E Robertson, C L S Lewis, and
D Neely,
J Phys B, At Mol. Opt. Phys. 27, 341-367, (1994).

Time Dependence of Spatial Coherence in the X-ray laser

R E Burge, G E Slark, M T Browne, X-C Yuan, P Charalambous, Z An, X-H Cheng.

Cavendish Laboratory, University of Cambridge, Cambridge, CB3 0HE and Physics Department, King's College London, Strand, London, WC2R 2LS

C L S Lewis, G F Cairns, A G MacPhee.

School of Maths and Physics, Queen's University, Belfast, BT7 1NN

D Neely.

CLRC Rutherford Appleton Laboratory, Chilton, Didcot, Oxon., OX11 0QX

Introduction

The parameter space for the physical description of the spatial coherence of the collisionally excited X-ray laser gets ever more complicated. This is not surprising bearing in mind that the complex degree of spatial coherence, $\mu_{1,2}$, is derived from the source intensity distribution by the van Cittert-Zernicke theorem. Considering the Ge X-ray laser, the subject of the present experiments, much experimental work has been carried out aimed to increase the source brightness and improve the spatial coherence i.e. to make a spatially compact, bright X-ray source for applications. Experimental results include studies of the angular distribution of intensity in various lasing lines , temporal variations of source intensity [1, 2)], the effects of target length and gain conditions in single and multiple targets [3, 4)], the effects of prepulse conditions e.g. [5)], besides the direct measurement of source spatial coherence (for refs see [6, 7)]).

In many experiments advantage is taken of the fact that $|\mu_{1,2}|$ is given directly by the visibility in the interference pattern due to interference when the X-radiation is transmitted by diagnostics based on two equal parallel Young's slits. The angular distribution of spatial coherence can be observed by disposing slit pairs across the angular divergence of the X-ray laser output [7)], for any given target configuration. Such studies may describe the spatial coherence time-averaged over the usual ns or so of the X-ray laser emission following a single pulse of the driver laser(s), which is the usual result, or may, in principle, provide time resolved measurements of the onset and decay of the linked source intensity and spatial coherence. The present study is we believe the first to measure the relationship between the time-dependent intensity and spatial coherence in the X-ray laser. Practical considerations have limited the results to a single divergence angle near the maximum of the angular intensity distribution.

Experimental

A double slab Ge stripe target was set up at the Vulcan laser at the Rutherford Appleton Laboratory as already extensively described [2)] and coherence measurements were made in the horizontal plane i.e. the plane containing the optical axis of the optical arrangement and the normal to the target surface. The total power density on the target was ~ 1.6 x 10^{13} Wcm ^{2} and the driver pulse, approximately of Gaussian shape, had a FWHM of 700 ps. The experimental set-up is shown in figure 1. The unresolved 23.2 / 23.6 nm spectral lines of the lasing Ge plasma were isolated by a multi-layer X-ray mirror by which the interference fringes were imaged with a magnification of ~ 0.5. Interference fringes from a pair of Young's slits, with each slit 20 μm wide and 1 mm long with slit separation of 100 μm, were recorded photographically with a total path length from the source of ~3.5 m, by a streak camera [8)] having spatial resolution of 50 μm and temporal resolution of 50 ps. Fringe visibilities were evaluated by densitometry of the Ilford HP 5 film used in the streak camera. No time fiducial was available and the time origin of the streak camera was set by relating the experimental data to the time development of X-ray laser intensity as derived from plasma modelling [8)].

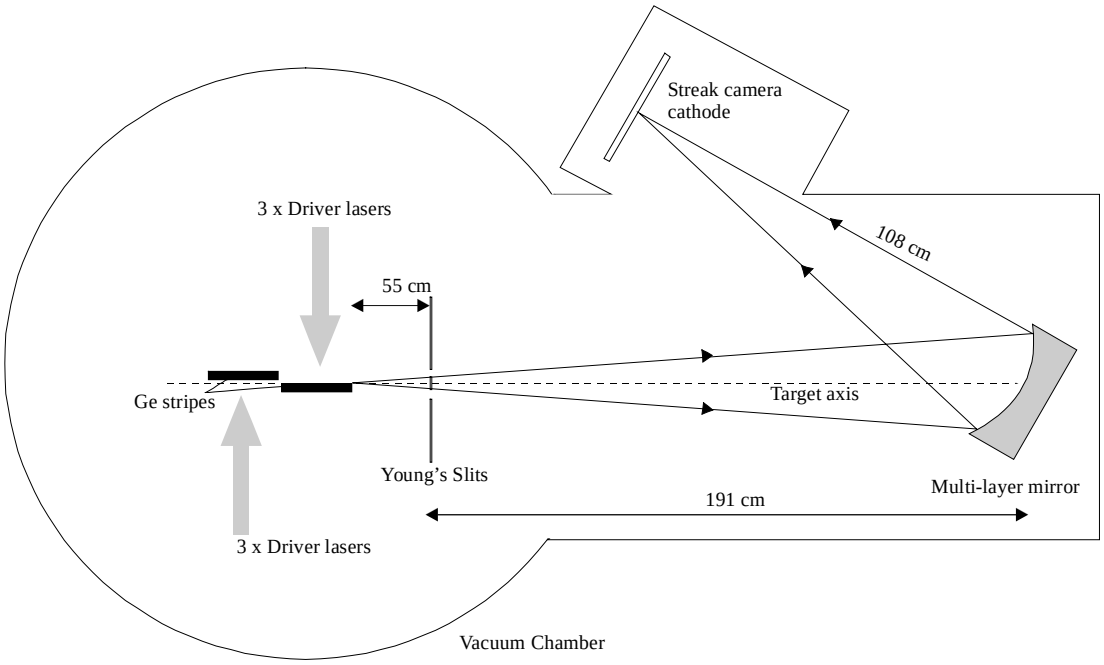

Figure 1. Schematic diagram of optical system at the Vulcan laser.

Results and Discussion

The rate of onset of X-ray laser intensity is shown in figure 2. Combined 23.2 / 23.6 nm radiation was detected over a period extending from ~400 ps after the driver pulse arrived to 1100 ps. The FWHM is ~260 ps, much shorter than the driver pulse, and the development of increasing intensity has a slower build-up than its decay. Measurements of the fringe visibility were possible with acceptable signal to noise ratios for times between 600 ps and 1000 ps after the initiation of the pulse and are shown in figure 3. Also in figure 3 are shown values for the FWHM of the Ge X- ray laser source as derived after fitting to a coherence equation [8)] assuming that the source can be represented by a Gaussian distribution of source intensity.

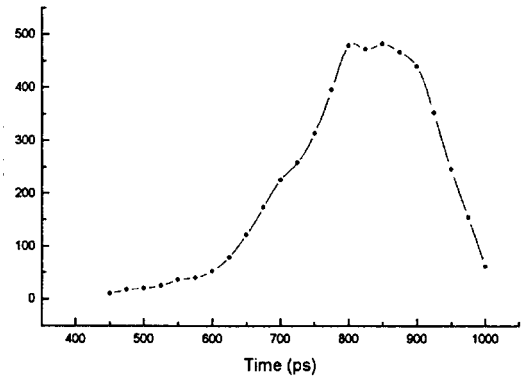

Figure 2. Experimental variation with time of the intensity of the combined 23.2 and 23.6nm X-ray laser lines from a double Ge target. 700 ps pulse irradiation at ~ 1:6 x 10^{13} Wcm ^{2}.

Comparing figures 2 and 3, there is an anti-correlation between the increase of intensity and the change in the visibility of the interference fringes and the reduction of source size. Higher intensity gives lower spatial coherence and vice-versa. The changes in source FWHM show an increase in source size from a starting value of ~65 μm, rising to a slowly varying peak of ~82 μm, and then falling towards 50 μm at the end of the pulse where the intensity is decreasing rapidly. The average value of FWHM is 76 μm.

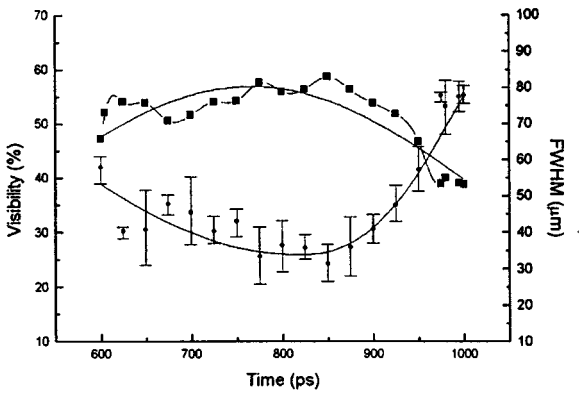

Figure 3. Temporal changes of interference fringe visibility through a single laser pulse. The visibility values are plotted separately for each side of the interference pattern and the average values are also given. Also plotted (square) are the FWHM values gained by interpreting the visibility values on a model with a Gaussian distribution of intensity.

These FWHM values are consistent with the range of published values for the source sizes of neonlike collisional X-ray lasers [8)]. It is not surprising that increased source intensity is gained via an increase in source size, but it is nevertheless disappointing that, for these wavelengths and double target configuration, increased intensity is associated with reduced spatial coherence even though the change with time through the pulse in source FWHM is less than a factor of two.

Acknowledgements

We are grateful to the Leverhulme Trust and to AWE Aldermaston for financial support and to the Engineering and Physical Sciences Research Council for use of the Vulcan laser.

References

1. R Kodama, D Neely, L Dwivedi, M H Key, J Krishnan, C L S Lewis, D O'Neill, P Norreys, G J Pert, S Ramsden, G J Tallents, J Uhomoibi, and J Zhang, Opt Commun. 90, 95-98, (1992).

2. K Murai, H Shiraga, G Yuan, H Daido, H Azuma, E Miura, R Kodama, M Takagi, T Kanabe, Y Kato, D Neely, D M O'Neill, C L S Lewis, and A Djaoui, J Opt Soc Am B, 11, 2287-2297, (1994).

3. C L S Lewis, D Neely, D M O'Neill, J Uhomoibi, M H Key, Y Al Hadithi, and G J Tallents, Opt Commun. 91, 71-76, (1992).

4. A S Wan, J C Moreno, B J MacGowan, S B Libby, J A Koch, J Nilsen, A L Osterheid, J H Scofield, J E Trebes, and R S Walling, Opt. Eng.(Bellingham) 33, 2434-2441, (1994).

5. T Boehly, M Russotto, R S Craxton, R Epstein, B Yaakobi, L B Da Silva, J Nilsen, E A Chandler, L D J Fields, B J MacGowan, D L Matthews, J H Scofield and G Shmikaveg, Phys Rev A 42 6962-6965 (1990).

6. J E Trebes, K A Nugent, S Mrowka, R A London, T W Barbee, M R Carter, J A Koch, B J MacGowan, D L Matthews, L B Da Silva, G F Stone and M D Feit, Phys Rev Lett 68 589-591, (1992).

7. R E Burge, G E Slark, M T Browne, X-C Yuan, P Charalambous, X Cheng, C L S Lewis, A G MacPhee and D Neely, J Opt Soc Am B 14 2742-2751 (1997).

8. R E Burge, G E Slark, M T Browne, X-C Yuan, P Charalambous, Z An, X-H Cheng, C L S Lewis, A G MacPhee and D Neely, J Opt Soc Am B 15 1620-1626 (1997).

Saturation Behaviour of Two X-Ray Lasing Transitions in Ni-Like Dy

G Eker, R Smith, G J Tallents.

Department of Physics, University of Essex, Colchester CO4 3SQ, UK

E Wolfrum, J Zhang.

Department of Physics, Clarendon Laboratory, University of Oxford, Oxford OX1 3PU, UK

S McCabe, G J Pert.

Department of Physics, University of York, York, YO1 5DD, UK

Introduction

Saturation of a gain medium occurs when stimulated emission becomes a significant depopulating process on the upper quantum state population. Saturated operation of an x-ray laser is important because it means that the maximum power possible for a given volume of excited plasma is extracted by stimulated emission, an output sufficiently intense for applications is produced and the laser output is reproducible from shot-to-shot. Saturation of x-ray lasers is usually diagnosed by measuring the laser output as a function of lasing medium length [1)] and by measuring the absolute output irradiance for comparison to calculated saturation irradiances [2)]. Confirmation of saturation can be seen by making the difficult measurement of the lasing line spectral width to check gain narrowing [3)]. There is a need for another independent check of the onset of saturation.

In this paper, we report the first observation of saturated operation for the Ni-like Dy x-ray laser at 5.86 nm and 6.37 nm and describe how the saturation behaviour of the two lasing transitions can act as a signature for saturation in Ni-like x-ray lasers. Ni-like Sm at 7.36 nm was the shortest saturated laser wavelength previously reported [1)]. The Ni-like lasers exhibit gain on two J = 0 → 1 transitions emanating from the same upper quantum state. An equation for saturated gain is found from a rate equation model and by integrating along the gain medium length an expression is found for the variation of the output lasing intensity for the two transitions. We show that experimentally measured laser output for the Ni-like Dy transitions at 5.86 and 6.37 nm wavelengths is well reproduced by the simple modelling if we allow the small signal gain coefficients as fitting parameters.

Experiment

Six beams from the Vulcan 1.06 μm Nd-glass laser with pulse widths of 75 ps were employed in a standard off-axis line focus geometry [4)] to irradiate Dy stripe targets. The targets were pumped using a double pulse configuration in which a prepulse, with 10 - 20% of the total energy, was incident on target 2.2 ns before the main pulse. The prepulse generates a pre-plasma which reduces the density gradients in the direction away from the target surface. This allows for more efficient energy coupling from the main pumping pulse and also serves to reduce refraction effects, which can deflect x-ray photons prematurely out of the gain region. Three beams were focussed by f/2.5 off-axis spherical lenses onto each target plane in a 20 mm length line focus with a width of 100 μm. After taking into account energy loses in the system this arrangement delivered intensities of ~2×10^{13} Wcm^{-2} on target. The stripe targets were of length 18 mm and were set 180º opposed to each other with 150-175 μm separation between the target surfaces. X-ray laser coupling efficiencies of 50 - 80% between the two targets are achieved in this arrangement [1)].

The time-integrated output of the x-ray laser was measured using an axial flatfield spectrometer. Gold reflection filters and an aluminium foil filter were used to spectrally isolate the Ni-like lasing lines at 5.86 nm and 6.37 nm. The spectrometer aberration-corrected concave grating (average line spacing of 1200 lines/mm) at 3º grazing angle incidence imaged the x-ray laser onto the detection plane. An x-ray CCD camera was placed at the focal plane of the grating to record the intensity of the x-ray laser transitions. The X-ray laser output was recorded for a number of gain medium lengths by varying the lengths of the target materials irradiated. For lengths below 18mm, only single targets were used.

Above saturation, reduction of the lower gain coefficient line intensity with increasing gain medium length has been observed (figure 1). It may be seen that once the 5.86 nm line saturates it causes the lower gain 6.37 nm line to also stop increasing in intensity with the length of the gain medium. In the saturation regime, the integrated intensity of the high gain transition increases linearly as a function of plasma length. This process depopulates the common upper lasing level through stimulated emission. The increased depopulation actually causes a net reduction in output for the 6.37 nm line with longer gain medium lengths.

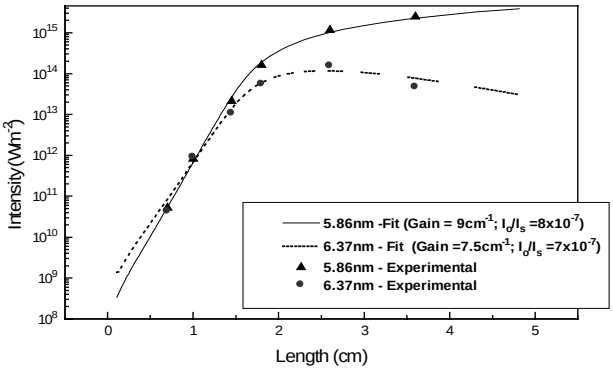

Figure 1. Plot of the output intensity of the 4d-4p J = 0 → 1 lasing lines for the Ni-like Dy x-ray laser as a function of plasma length. The experimental points are shown by the triangle and circle data points for the 5.86 nm and 6.37 nm lasing lines respectively. The solid lines represent the fit from the double line saturation model with the plasma conditions represented in figure 3 and gains of 9 cm^{-1} and 7.5 cm^{-1}.

Rate Equation and 1-D ASE Model

The steady state rate equations for the three levels involved in Ni-like x-ray lasing can be written as:

$$R_1 = N_1\left(\frac{\frac{g_3}{g_1}\sigma_{31}\bar{I}_{31}}{h\upsilon_{31}} + A_{10}\right) - N_3\left(\frac{\sigma_{31}\bar{I}_{31}}{h\upsilon_{31}} + A_{31}\right) \quad (1)$$

$$R_2 = N_2\left(\frac{\frac{g_3}{g_2}\sigma_{32}\bar{I}_{32}}{h\upsilon_{32}} + A_{20}\right) - N_3\left(\frac{\sigma_{32}\bar{I}_{32}}{h\upsilon_{32}} + A_{32}\right) \quad (2)$$

$$R_3 = N_3\left(\frac{\sigma_{31}\bar{I}_{31}}{h\upsilon_{31}} + \frac{\sigma_{32}\bar{I}_{32}}{h\upsilon_{32}} + A_3\right) - N_1\left(\frac{\frac{g_3}{g_1}\sigma_{31}\bar{I}_{31}}{h\upsilon_{31}}\right) - N_2\left(\frac{\frac{g_3}{g_2}\sigma_{32}\bar{I}_{32}}{h\upsilon_{32}}\right) \quad 3)$$

where R_1, R_2 and R_3 are the pumping rates into the excited

quantum states, N_1, N_2 and N_3 represent the populations of the respective energy levels, σ_{ul} is the stimulated emission cross section between level u and l, g_1, g_2 and g_3 are the statistical weights for the levels, A_{ul} is the spontaneous decay rate from level u to l and $h\upsilon_{ul}$ is the transition energy between levels u and l. We write $A_3 = A_{30} + A_{31} + A_{32.}$

The intensity $\bar{I}_{ul}$ for a given lasing line integrated over the emission profile $f(\upsilon)$ is given by:

$$\bar{I}_{ul} = \frac{1}{f(0)}\int I(\upsilon) f(\upsilon) d\upsilon \qquad (4)$$

where $I(\upsilon)$ is the intensity at frequency υ, $f(\upsilon)$ and $f(0)$ are the line shape factors at frequency υ and line centre, respectively.

The gains for the two x-ray lasing transitions are given by:

$$G_{31} = \sigma_{31} g_3 \left(\frac{N_3}{g_3} - \frac{N_1}{g_1} \right), \quad G_{32} = \sigma_{32} g_3 \left(\frac{N_3}{g_3} - \frac{N_2}{g_2} \right) \qquad (5), (6)$$

which upon simultaneously solving Eqs. (1-3) and neglecting non-significant terms can be written as:

$$G_{31} = \frac{g_{31}}{1 + \left(\frac{\bar{I}_{31}}{I_{S1}} + \frac{\bar{I}_{32}}{I_{S2}} \right)}, G_{32} = \frac{g_{32}}{1 + \left(\frac{\bar{I}_{31}}{I_{S1}} + \frac{\bar{I}_{32}}{I_{S2}} \right)} \qquad (7), (8)$$

where the saturation intensities for the two lasing transitions are given as:

$$I_{S1} = \frac{(A_{30} + A_{31} + A_{32}) A_{10} h\nu_1}{\left(A_{10} + \frac{g_3}{g_1}(A_{30} + A_{32}) \right) \sigma_{31}} \qquad (9)$$

$$I_{S2} = \frac{(A_{30} + A_{31} + A_{32}) A_{20} h\nu_2}{\left(A_{20} + \frac{g_3}{g_2}(A_{30} + A_{31}) \right) \sigma_{32}} \qquad (10)$$

and g_{31}, g_{32} are the respective small signal gain coefficients.

The gain coefficient decreases when the lasing intensity is large because stimulated emission becomes an important factor in determining the population of the upper lasing level. Expanding on the analysis of Pert [5], we may establish a relationship between gain and the length of the gain region for both transitions as follows:

$$g_{31}l = \left(1 - 2\frac{I_{O1}}{I_{S1}} \right) G_{31}l - 2\frac{I_{O2}}{I_{S2}} G_{32}l + 2\frac{I_{O1}}{I_{S1}} \alpha(G_{31}l) + 2\frac{I_{O2}}{I_{S2}} \alpha(G_{32}l) \qquad (11)$$

$$g_{32}l = \left(1 - 2\frac{I_{O2}}{I_{S2}} \right) G_{32}l - 2\frac{I_{O1}}{I_{S1}} G_{31}l + 2\frac{I_{O1}}{I_{S1}} \alpha(G_{31}l) + 2\frac{I_{O2}}{I_{S2}} \alpha(G_{32}l) \qquad (12)$$

The parameter $\alpha(Gl)$ takes into account wavelength integration over an assumed Gaussian profile and is given by the Linford approximation [6] as:

$$\alpha(Gl) = \frac{\left(e^{Gl} - 1 \right)^{\frac{3}{2}}}{\left(Gle^{Gl} \right)^{\frac{1}{2}}} \qquad (13)$$

The total emissivity divided by the small signal gain coefficient for each transition is given by:

$$I_{O1} = \frac{A_{31}}{\sigma_{31}} \frac{\Omega}{4\pi} h\nu, \; I_{O2} = \frac{A_{32}}{\sigma_{32}} \frac{\Omega}{4\pi} h\nu \qquad (14), (15)$$

where Ω is the solid angle into which the spontaneous emission is amplified. The output x-ray laser irradiance I_l is given by:

$$I_{l1} = I_{O1}\alpha(G_{31}l), \; I_{l2} = I_{O2}\alpha(G_{32}l) \qquad (16), (17)$$

By subtracting Eqn. (16) from Eqn. (15) we get:

$$G_{32}l = G_{31}l - (g_{31} - g_{32})l \qquad (18)$$

Through combination of Eqns. (11-18), it is possible to plot the intensity of the two lasing lines as a function of plasma length (figure 1).

Numerical simulation of the Ni-like Gadolinium x-ray laser using the 1.5D hydrodynamic and atomic physics code EHYBRID [7] gives the predicted values for the plasma conditions at the position of peak gain. Combining this information with atomic data [8], we may calculate the values for the saturation intensities using Eqns. (9,10) and I_{01} and I_{02} values, using Eqns. (14, 15), for the two lasing lines of Ni-like Dy by assuming that the plasma conditions for lasing with Gd (Z=64) and Dy (Z=66) are similar. We obtain $I_O/I_S = 8\text{x}10^{-7}$ for the higher gain 5.86 nm transition and $I_O/I_S = 7\text{x}10^{-7}$ for the lower gain 6.37 nm transition assuming Doppler broadening for the evaluation of σ_{31} and σ_{32}. The EHYBRID calculated gains are effectively spatially averaged by the propagating x-ray laser beams and will differ for Dy from those shown for Gd. Consequently, we have adjusted the small signal gain coefficient assumed for the model (Eqns. 11-18) to fit the experimental data (figure 1). The best fit values are 9 cm^{-1} and 7.5 cm^{-1} for the 5.86 nm and 6.37 nm lines respectively. Such gains are consistent with the gain profiles peaking at 15 cm^{-1} and 13 cm^{-1} for Gd after allowance for spatial averaging.

Conclusions

To summarise and conclude, saturated lasing has been shown for the first time at wavelengths below 6 nm with the Ni-like Dy x-ray laser. The output dependence of a two transition amplified spontaneous emission x-ray laser with gain medium length was characterised with a simple rate equation and one-dimensional ASE model. The ASE model developed in this paper predicts a drop in intensity for the lower gain transition with the onset of saturation for the higher gain line in approximate agreement with the experimental results. We have shown that such behaviour is symptomatic of the high gain transition operating within the saturation regime.

References

1. J Zhang, A G MacPhee, J Lin, E Wolfrum, R Smith, C Danson, M H Key, D Neely, J Nilsen, G J Pert, G J Tallents, and J S Wark, Science 276, 1097 (1997).
2. J Zhang, P J Warwick, E Wolfrum, M H Key, C Danson, A Demir, S Healy, D H Kalantar, N S Kim, C L S Lewis, J Lin, A G MacPhee, D Neely, J Nilsen, G J Pert, R Smith, G J Tallents, and J S Wark, Phys. Rev. A 54 (1996).
3. J A Koch, B J MacGowan, L B DaSilva, D L Matthews, J H Underwood, P J Batson, and S Mrowka, Phys. Rev. Letts. 68, 3291 (1992).
4. C L S Lewis, D Neely, D M O'Neill, J O Uhomoibhi, M H Key, Y Al Hadithi, G J Tallents, and S A Ransden, Opt. Commun. 91, 71 (1992).
5. G J Pert, J. Opt. Soc. Am. B 11,1425 (1994).
6. G J Linford, E P Poressini, W R Sooy and M L Spaeth, Appl. Opt. 13, 379 (1974)
7. J A Plowes, G J Pert, S B Healy, and D T Toft, Optical and Quantum Electronics 28, 219(1996).
8. H Daido, S Ninomiya, T Imani, Y Okaichi, M Takagi, R Kodama, H Takabe, Y Kato, F Koike, J Nilsen, and K Murai, Intl. J. Mod. Phys B 11, 945 (1997).

Transient Gain in Ni-like Ag using Ultra-Short Heating Pulse

R M N O'Rourke, A G MacPhee, R Keenan, C L S Lewis.
School of Mathematics and Physics, The Queen's University of Belfast, Belfast BT7 1NN. Email r.orourke@qub.ac.uk

A Klisnick, Ph Zeitoun, D. Ros, F Albert, A Carillion, P Fourcade, S Hubert, Pjaeglé, G Jamelot.
LSAI, Université Paris-Sud, France.

P Nickles, K Janulewicz, M Kalashnikov, J Warwick.
Max Born Institute, Berlin, Germany.

J C Chanteloup, E Salmon, C Sauteret, J P Zou.
LULI, École Polytechnique, Palaiseau, France.

Introduction

Recently installed at Ecole Polytechnique, the CPA system has been successfully utilised to demonstrate lasing in Ni-like Ag using an ultra short sub-ps heating pulse and a travelling wave irradiance geometry [1]. Here we report on the new high power laser system at LULI and the results gained from its first use. These experiments were funded under the auspices of the European Union TMR Programme.

New CPA system at LULI

Shown in figure 1 is the new CPA facility at LULI. The output from a Titanium Sapphire oscillator is stretched and passed to the regenerative amplifier. After passing through the rod amplifiers and the final disc amplifier, the stretched pulse is split three ways: firstly, a prepulse of about 0.1%; then a main preforming pulse; and finally the short main heating pulse.

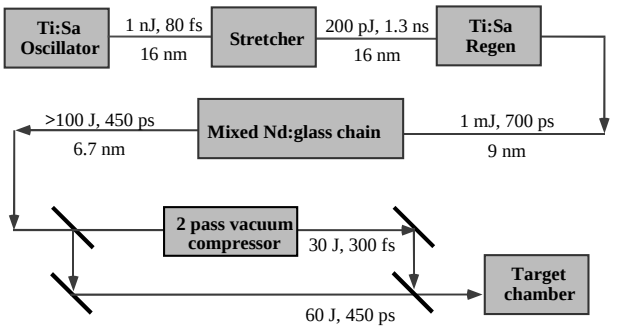

Figure 1. The new CPA chain at LULI.

Method for Generation of the Travelling Wave

An alternative method to that employed at RAL for generating the travelling wave was employed [2]. When the gratings in figure 2 are parallel no travelling wave (apart from that introduced by line focus optics) exists. The travelling wave is introduced by slightly tilting the second grating in the arrangement. In the experiment it was found that tilting the grating by 0.3° was enough to achieve a travelling wave with phase velocity c along the line focus. The second stage is to tune the distance between the gratings to make the plane of best compression coincide with the target plane.

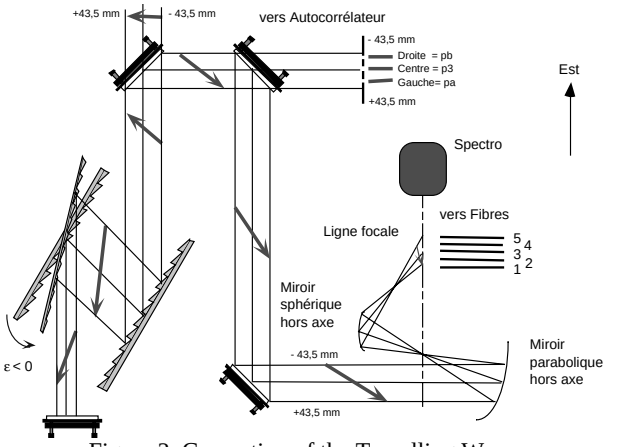

Figure 2. Generation of the Travelling Wave.

As seen in figure 3, the method introduces variation in the pulse duration across the line focus though this is kept to within a factor of two between the wings and the centre of the line focus. The travelling wave velocity was measured experimentally using a set of optical fibres and an ultra-fast optical streak camera as indicated in figures 2 and 4. The pulse durations at the centre and edges of the beam were measured using a second order autocorrelator. Both the Travelling Wave and pulse durations measured agreed with calculations [2].

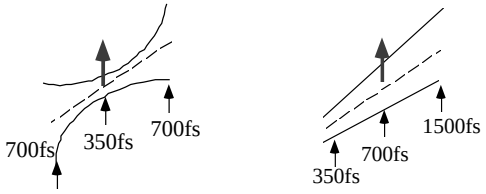

Figure 3. Peripheral Temporal Shearing.

Experiment

The experimental setup is shown in figure 4. A beam splitter had to be employed to recombine the three beams in place of the polariser. This limited the total energy before splitting to 30 J as opposed to 100 J in the original design, reducing to 5 J the CPA energy on target. The main diagnostics were two time integrated flatfield spectrometers positioned at either end of the target to view emission with and against the Travelling Wave.

The pulse configuration comprised a 0.1% pre-pulse of length 450 ps, 3 ns prior to the main preforming pulse also of 450 ps duration. The main heating pulse arrived on target 550 fs after this second pulse and was varied from 350 fs to 1.7 ps duration. The target, a slab of silver 10 mm across, was irradiated by a line focus of 12 mm in length by 70 µm wide. The CPA pulse length was checked prior to data shots using a second order autocorrelator.

Results

Figure 5 is an image taken on the FFS looking at the output in the direction of the Travelling Wave. It shows strong lasing on the Ni-like 4d-4p line in Silver at 139 Å. The pump in this shot comprised a prepulse of 5 mJ (1.3×10^9 Wcm^{-2}) followed by a main preforming pulse of 5 J (1.3×10^{12} Wcm^{-2}) over 450 ps, and finally an ultra-short main heating pulse of 350 fs giving 1.7×10^{15} Wcm^{-2} at beam centre. The peak divergence measured was different than that found on previous experiments at LULI: The 130 ps pumping had yielded XRL divergence of ~2 mrad. The divergence here is far larger at about 13 mrad, as can be seen in the flatfield image. The output angle is also significantly larger (~13 mrad instead of ~4 mrad in the 130 ps experiments) indicating that refraction of the XRL beam is important.

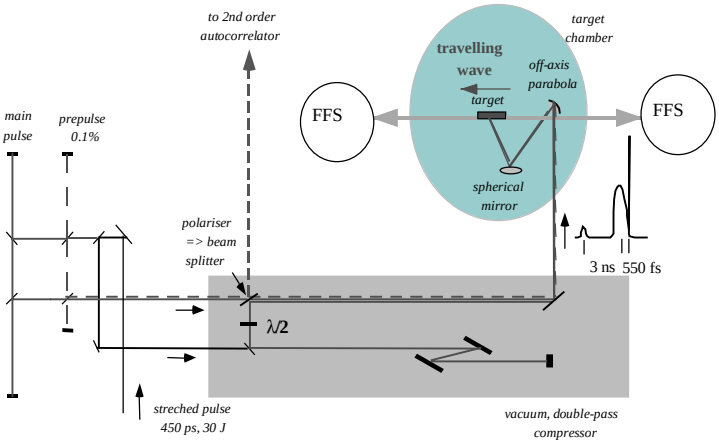

Figure 4. Experimental Setup.

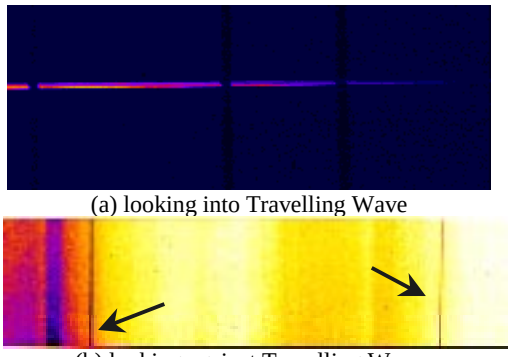

(a) looking into Travelling Wave

(b) looking against Travelling Wave

Figure 7: FFS images with Travelling Wave switched off
(1.7 ps pump).

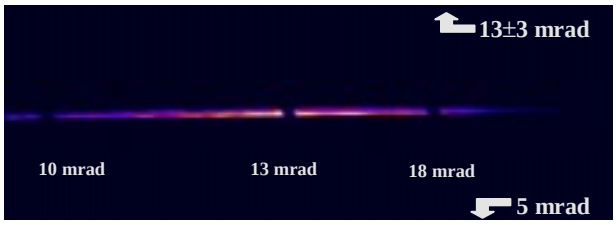

Figure 5. Ni-like Ag lasing line.

Next, using a 500 fs heating pulse, the effectiveness of the travelling wave was tested. With the Travelling Wave switched off an inherent Travelling Wave of 3c present due to the focusing optics. Under these conditions the lasing line disappeared from the FFS looking into the Travelling Wave as shown in figure 6. In both cases (with and without Travelling Wave) the lasing line was absent on the other FFS viewing against the Travelling Wave.

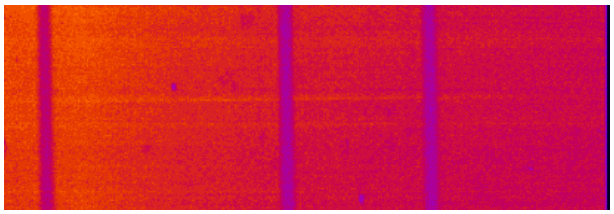

Figure 6. No lasing with Travelling Wave switched off (500 fs pump).

The pump was then changed to 1.7 ps duration and the Travelling Wave was again tested. It was found that the lasing intensity was decreased by a factor of 9 in the direction of the Travelling Wave while being increased by a factor 10 in the direction opposing the Travelling Wave (see figure 7).

Cross calibration of the spectrometers reveals that the ratio of emission with and against the Travelling Wave is about 80.

Finally, a series of shots was taken to provide a gain length scan. Each shot was of 500 fs duration constituting irradiance on target of ~10^{15} Wcm^{-2}. Two sets of data, angular peak and angular integrated, were taken.

As seen in figure 8, exponential increase was obtained up to target lengths of 7 mm, where roll off from the Linford fit occurs. It is thought that this is a result of refraction since the presence of the Travelling Wave prevents effects of finite gain duration. The plots indicate a gain of 14.5 cm^{-1} which yields a maximum GL of 10 at L=7 mm.

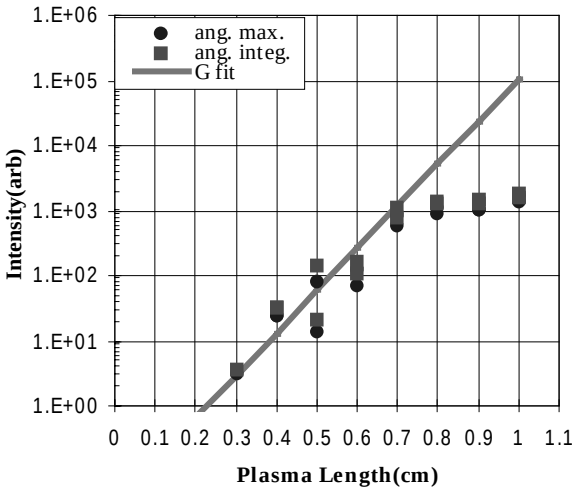

Figure 8. Gain-Length Scan (500 fs pump).

Conclusions

To summarise then, a new CPA system has been installed and successfully utilised at Ecole Polytechnique (LULI). Lasing was achieved in Ni-like Ag using the transient pumping scheme with an ultra-short 350 fs heating pulse The angular characteristics of the XRL using this pump differed from those of the 130 ps pump. The effect of introducing the travelling wave through grating tilt was tested and shown to provide signal enhancement of up to a factor of 80 for the 1.7 ps pump. With ultra-short pumping pulses of the order of 350 fs, the effect of the Travelling Wave was expected to be critical. This assumption was vindicated in that no lasing was seen using a 350 fs pump without Travelling Wave. Finally, a gain of 14.5 cm^{-1} was measured with a main heating pulse of 500 fs.

References

1. A. Klisnick et al,
Proceedings of the 6th International XRL Conference, IOP Publishing, 1998.

2. JC Chanteloup et al,
Proceedings of the 6th International XRL Conference, IOP Publishing, 1998;
Chanteloup et al,
Rapport LULI 1997

Near Frequency Doubling through Four Wave Mixing in Plasma

R M N O'Rourke, C L S Lewis, A Hibbert.

School of Mathematics and Physics, The Queen's University of Belfast, Belfast BT7 1NN. Email r.orourke@qub.ac.uk

Introduction

Progress in the past decade has seen a considerable increase in the output power of XRLs along with an extension of demonstrable saturation to higher Z elements [1]. This, combined with the success of the Ni-like scheme [2], makes viable the option of utilising nonlinear effects to extend the operating wavelengths of our XRLs.

In most media absorption of radiation at soft x-ray wavelength impedes the demonstration of nonlinear effects. One is led, therefore, to consider the home environment of the XRL, plasma, as a candidate medium. This constraint in turn limits experiments to odd order effects only, due to the inversion symmetry of the isotropic plasma. The options presented to us are then: Third Harmonic Generation, Four Wave Sum Sum Mixing or Four Wave Sum Difference Mixing.

THG would require a mixing ion with four equally spaced, dipole connected levels. Even if one was fortuitous enough to find such an ion, analysis by Bjorklund [3] indicates that, in an isotropic medium, this process can be phase matched only under loose focusing thereby reducing the mixed output. Though viable species for FWSSM can be identified, the same phase matching constraints apply here as with THG. FWSDM, though, has a number of identifiable mixing media and can be phase matched under tight focusing.

Four Wave Mixing.

The FWM process involves the combining of three photons, two XRL and one optical, providing an output at a frequency governed by the sum of the constituent input k-vectors. In FWSDM, this amounts to near frequency doubling of the XRL input. The process is illustrated schematically in figure 1.

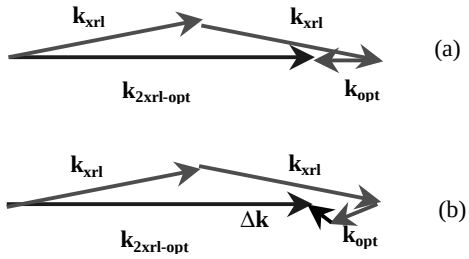

Figure 1. Phase Matching

As we choose to work in a dilute medium, there will be few contributors to the nonlinear effect. Hence resonances to transitions in the mixing medium are sought in addition to the qualification of phase matching. This reduces the selection of suitable ions, due for the most part to the lack of information on highly ionised species. As a result, much of the work done to date, and that presented here, is based on sodium-like ions, which have an energy level structure appropriate to FWSDM.

Figure 1a represents the perfectly phase matched case, where the signal will grow quadratically with distance travelled in the mixing medium. In figure 1b, a phase mis-match has been introduced. This is primarily due to dispersion from the free electrons in the plasma and, to a lesser degree, the difference in the phase velocities of the constituent beams. This implies then that for an optimum phase match, there also exists an optimum electron density. The relationship is as in equation 1 [3, 7].

$$\mathbf{N}_{optimum} = \frac{(b\Delta k)_{opt}}{\alpha b} \qquad (1)$$

The electron density needs to be below critical for the constituent beams and low enough such that angular phase matching can offset dispersion. The graph in figure 2 indicates that for an electron density of 10^{18} cm^{-3}, phase matching is achieved when an angle between the XRL and the optical photon of 0.2° is arranged. This corresponds to an angle of 0.4° between the two XRL photons.

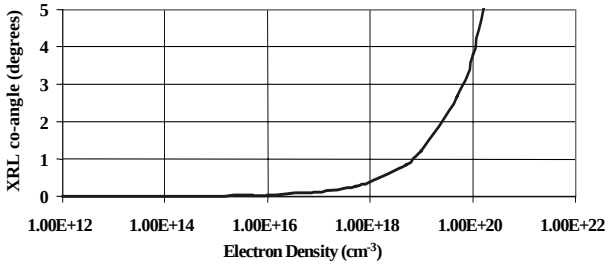

Figure 2. Angular Phase Matching Requirements.

The expression for the FWSDM process can be simplified in the near resonance case [4].

$$\chi^{(3)}(-\omega_\sigma;2\omega_{XRL},\omega_{OPT}) = \frac{1}{6\hbar^3}\sum_{\deg}\mu_{12}\mu_{23}\mu_{34}\mu_{41}\rho_{11}\left[\frac{2}{\omega_{21}-\omega_{XRL}-i\Gamma_{21}}\right]$$
$$\mathrm{X}\left[\frac{1}{\omega_{31}-2\omega_{XRL}-i\Gamma_{31}}\right]\left[\frac{1}{\omega_{41}-(2\omega_{XRL}-\omega_{OPT})-i\Gamma_{41}}\right] \qquad (2)$$

The sum is over the allowed closed loop routes through the energy levels of the ion. As we work on near resonant cases only, it is sufficient to sum over the allowed L-S split levels only. The Γ_{ij} terms represent broadening mechanisms in the plasma. The ρ_{11} term represents the thermal population of the relevant sublevel of level 1. The Grotrian diagram in figure 3 illustrates the process, where two XRL photons excite to level four. The optical photon then stimulates the transition to level three, providing inversion over level one and giving an output at near second harmonic.

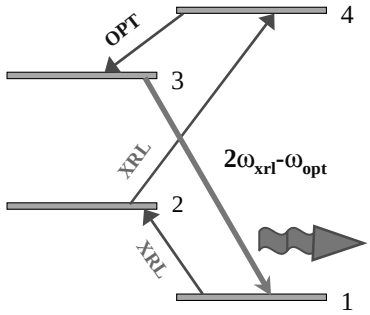

Figure 3. Generic Sodium Grotrian Diagram.

Schemes and Modelling

At Queen's University we have developed the facility to calculate, *ab initio*, the values for the susceptibility of the FWM process. The atomic simulation code SETCIV3, computes values for the energy levels, oscillator strengths and other

parameters of the ion from Hartree-Fock approximations [5]. This code was developed by Prof. A. Hibbert of the Mathematics department. The atomic data agrees with that previously published [6]. From this information, the reduced matrix elements can be calculated and using the Wigner-Eckart theorem, the dipole matrix elements for the various relevant transitions are calculated. A code has also been written to deal with the numerical calculation of the susceptibility. As stated, due to a lack of information, we have been confined to considering only sodium like ions to date (though our codes will presently be modified to include Cu-like and perhaps C-like ions). In table 1 below, we present a selection of new plasma-XRL couples, the emphasis here has been placed on finding resonances to the transitions in the ion, whereas previous publications presented matches with demonstrated XRLs operating the FWSDM process off resonance [7]. In addition, analysis has shown that the process is more critically dependent upon resonance at the shorter wavelengths [4].

Some of the lasing materials suggested may not be those routinely used in laboratories, but as the modelling will show, it is imperative that one try to demonstrate the effect close to resonance, where the susceptibility can be enhanced by up to four orders of magnitude.

Mixing Medium	*XRL*	*Optical*	$\chi^{(3)}$ *(cgs)*	*Output (Angstrom)*
ArVIII(143eV)	Ne-like Ni @ 231.18	Nd 1w @ 1.056μm	10^{-35}	116.86
K IX(176eV)	Ne-like As @ 189	Nd 1w @ 1.056μm	10^{-35}	95.35
K IX(176eV)	Ni-like Mo @ 189.1	Nd 2w @ 0.53μm	10^{-39}	98.29
Ti XII(291eV)	Ni-like Sb @ 114.25	Nd 2w @ 0.53μm	10^{-39}	57.74
V XIII(336eV)	Ne-like Ba @ 97.93	Nd 1w @ 1.056μm	10^{-39}	49.19
V XIII(336eV)	Ni-like Cs @85.9	KrF or Nd at 4w	10^{-38}	43.70
Cr XIV(384eV)	Ni-like Ce @ 85.19	Nd 1w@ 1.056μm	10^{-40}	42.76
Mn XV(435eV)	Ni-like Sm @ 73.55	KrF @ 248nm	10^{-40}	37.32
Fe XVI(488eV)	Ni-like Tb @ 66.29	Nd 1w @1.056μm	10^{-40}	33.25

Table 1. Proposed new FWSDM Schemes.

The final transition from which the near second harmonic is derived has a $\sqrt{2J+1}$ weighting. Therefore, in the calculations of $\chi^{(3)}$, the final transition is set resonant to the j=3/2 level. The susceptibility response curves then take into account in the calculations only those transitions which resonate in a closed loop back to this level. This does not effect the overall numerical values for χ, as the contribution from the j=1/2 loop is typically three to four orders of magnitude lower than that of the 3/2 loop. The results of the modelling agree with those published by Muendel and Hagelstein[4].

Figure 4 exhibits behaviour which one would expect: The first peak is that of the two photon resonance to the 7p level. The structure in this peak is due to the L-S splitting of the level. The second peak, exhibiting no structure, arises from resonance to the 4s level.

Indicated on the curve are two possibly employable XRLs for this particular mixing medium. Both schemes have quite high susceptibilities for FWM. For our case though, in the code it is sometimes more instructive to set a particular wavelength of XRL and then vary the optical wavelength, since this we have somewhat more control over.

The graph in figure 5 is also for sodium like KIX, this time with the XRL set at the wavelength of Ne-like As, and the optical photon energy varying. It shows a somewhat non-critical dependence upon the optical input beam wavelength. This would suggest that employing a tunable optical laser in this scheme would provide a tunable output in the soft X-ray region with applications in spectroscopy. The peak here is due to resonance between 7s and 7p levels.

With respect to executing an experiment though, the materials in this example would present some practical problems: As stated, the phase matching conditions depend on the electron density, control of the density is best provided through use of a gas jet; also the materials themselves (K, As) would require a non trivial amount of care in handling.

An alternative scheme would involve sodium like ArVIII using the Ne-like Ni laser at 231.18 Å. The response curve for this process is shown in figure 6.

For experiment, we wish to know if the output from the mixing plasma will be detectable on our diagnostics. The code has been adapted to compute the output intensity at near doubled frequency. Characteristics are shown in figures 7 & 8.

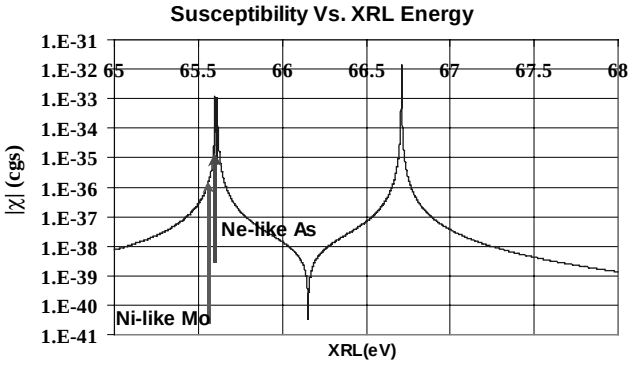

Figure 4. Response curve for KIX.

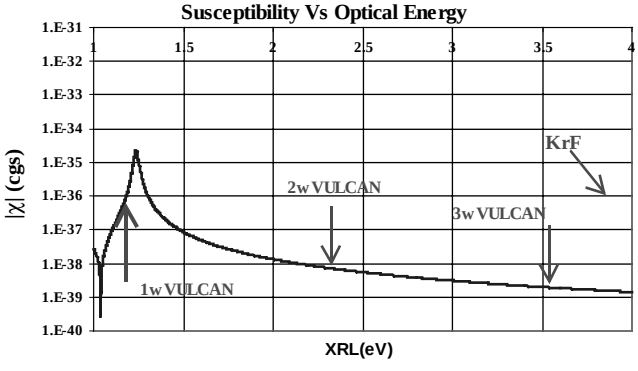

Figure 5. Optical response for KIX.

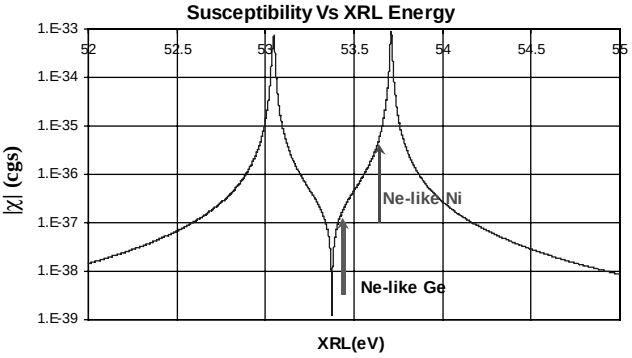

Figure 6. Response curve for ArVIII.

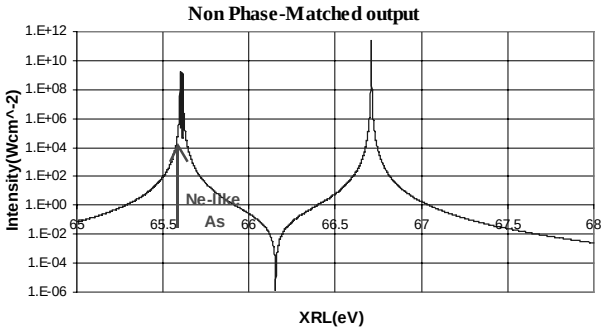

Figure 7. Response curve for KIX.

The safest yardstick for assessing the output is operation in non phase matched mode, this being the worst case scenario. Both curves showing the output intensity are calculated assuming an XRL intensity of 10^{10} Wcm^{-2} and an optical intensity of 10^{12} Wcm^{-2}, at an electron density of 10^{18} cm^{-3}. These parameters should be easily reproduced in the laboratory.

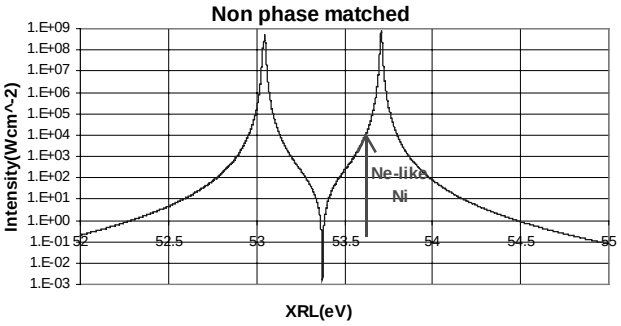

Figure 8. Response curve for ArVIII.

The results indicate that for non-phase matched operation one should expect conversion rates of 10^{-5} and 10^{-6} for the KIX and ArVIII schemes respectively. Allowing for, say, 10^{14} photons from the XRL (this is typical) one should expect about 10^{8} photons at the doubled frequency. For our back thinned CCD we require about 1000 photons per pixel, making detection of the NSH feasible. This is of course the least signal we can possibly expect, being non phase matched. The signal will rise exponentially with propagation in the plasma as long as phase matching is satisfied.

Experimental setup

The experiment is to be carried out on the Vulcan laser facility. Design is incomplete at the time of going to press, therefore a cursory schematic only is presented in figure 9.

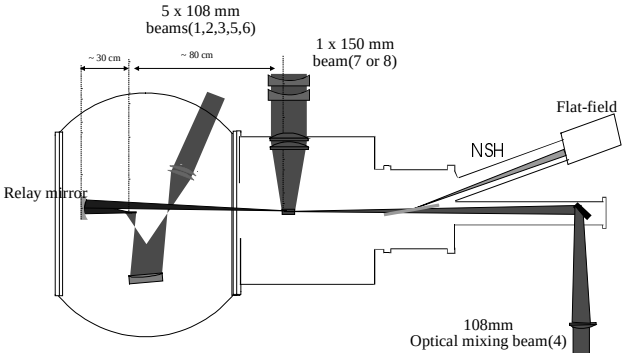

Figure 9. Experimental Schematic.

Recently, five beam target illumination for the production of the XRL has been developed at RAL [8]. This provides a line focus of up to 40 mm and also leaves one of the main six beams free. A longer pulse length is to be employed on the beam ionising the gas jet, while using the remaining 108 mm beam (delayed) for the mixing process (which would have a pulse length suitable for FWM). The gas will be ejected vertically from the base of the chamber and irradiated by a line focus. The output from the XRL will ideally be split using a transmission grating to permit angular phase matching. The XRL photons then combine with the optical mixing beam in the gas jet. Detection of the NSH photons is provided using a thin glass plate at 10°, giving reasonable reflection at both first and near second harmonic into a flat-field spectrometer equipped with a back thinned CCD detector.

Conclusions

New schemes for the FWSDM field have been presented, involving both Ne- and Ni-like XRLs. A viable experimental set-up has been presented. The intensity of a phase matched output at near second harmonic should be easily detectable with current CCDs. The non-critical dependence on optical input suggests the possibility of developing a tunable XRL with application to spectroscopy. It would appear that the time has come for an experiment in this field to be carried out.

References

1. Warwick, J.,
Ph.D. Thesis, Queen's University of Belfast;
Zhang, J., Warwick, J. et al,
Phys. Rev. A, 54, No.6, 1996.

2. Zhang, J. et Al,
Phys. Rev. Lett., 78, 3856, 1997.

3. Bjorklund, G.C.,
IEEE J. Quantum Elect., QE-11, 287 (1975)

4. Muendel, M.H., Hagelstein, P.L.,
Phys. Rev. A, 44, 7573 (1991)

5. Hibbert, A.,
Computational Atomic Physics, (Springer:Berlin),
(ed. K. Bartschat), pp27-64 (1996)

6. Lindgard and Nilsen,
Atomic and Nuclear Data Tables, 19, 533-633, 1977.

7. Shkolnikov, P.L. and Kaplan, A.E.,
Optics Letters, 16, 1153 (1991);
Shkolnikov, P.L. and Kaplan, A.E., Muendel, M.H. and Hagelstein, P.L.,
Appl. Phys. Lett., 61, 2001 (1992);

8. Wolfrum, E. et Al.,
Rutherford Annual Report, 1998.

Observation of Stimulated Optical Scatter in the vicinity of the Fundamental in Ultra-high intensity Laser-solid Interactions

A C Machacek, D M Chambers, J S Wark.

Department of Physics, University of Oxford, Clarendon Laboratory, Parks Road, Oxford OX1 3PU

I Watts, M Zepf, A E Dangor, E Clark, K Krushelnick, M Santala, M Tatarakis.

Imperial College of Science, Technology and Medicine, Prince Consort Road, London SW7 2BZ

P A Norreys, R Allott, C N Danson, D Neely.

CLRC Rutherford Appleton Laboratory, Chilton, Didcot, Oxon., OX11 OQX

R S Marjoribanks.

Department of Physics, McLennan Physical Labs, University of Toronto,Ontario, Canada. M5S 1A7

Introduction

Radiation emitted in the vicinity of the fundamental is relatively straightforward to collect and measure, and hence is invaluable as a diagnostic tool. Such tools are vital if plasma parameters such as density, temperature and scale length are to be known to inform developments in short pulse laser - solid target experiment and theory.

The point of interest here is the position and structure of fractional 'harmonics', often occurring near 3/2 of the incident frequency. The theoretical background to such features is discussed, and the suitability of mechanisms for explaining the observed phenomena is assessed.

Experimental Layout

The experiment was conducted in Target Area West of the Vulcan laser, using the CPA beam 8 as the main beam. Shots of energy 35 J would typically be focused onto the target using either an f/1.6 or f/3.5 parabolic reflector, and in this way, intensities up to 3×10^{19} Wcm^{-2} were obtained. For the purposes of observing the scattered radiation, spectrometers were set up to view the target from a number of directions, as shown in figure 1. Typically Bentham 250 mm focal length monochromators were used, with the exit slit removed, and an Andor 16 bit CCD camera used for capturing the image. To achieve a wide frequency coverage, gratings of 100 lines/mm or 150 lines/mm were used. The most significant spectra were observed by the channel looking along the target surface, that is with $\theta=0$.

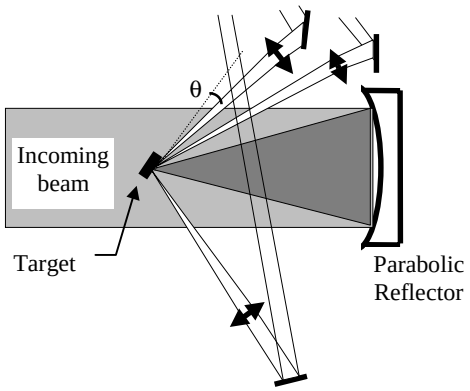

Figure 1. Experimental Arrangement

Observations

Potentially most interesting was the observation of emission in the region of the 3/2 harmonic. A typical spectrum is shown in figure 2 for two different laser pulse energies. Firstly, we note that there is remarkable similarity in the two graphs, and that shot to shot variation is small. Secondly, it is worth pointing out that the position of the peaks was not affected when the target material was changed - although the relative strength of the different peaks did vary. Peaks at 1.65ω, 1.56ω and 1.36ω were particularly common.

Intensities at the central focal spot can be inferred both by CR39 track analysis, and by combining the shot energy (from calorimetry) with the focal spot size (found from a soft X-ray penumbral image). What is seen is that the lower intensity focus actually gives a greater brightness of scatter. There is no paradox once it is realised that the greater scatter was caused by the shot with the greater total energy. This suggests that the scatter is taking place some distance from the critical surface in the underdense region of the plasma, where the size of the focal spot does not greatly affect the intensity. This is in contrast to the critical region, where a doubling in the focal spot diameter corresponds to a quartering in the intensity.

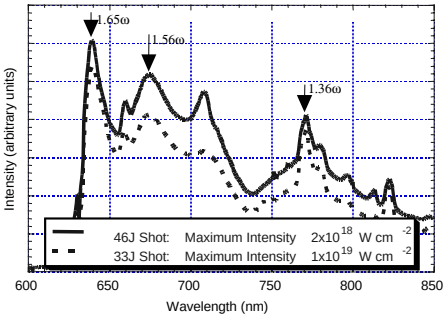

Figure 2. The Intensity Dependence of the Scattering - these spectra are typical for an f/ 1.6 focus

This supposition is confirmed by a comparison of the scattered features with the 3/2 harmonic itself. While no emission actually at 1.50ω is visible in the scattered features, when the angle of view is changed by increasing angle θ to a couple of degrees, considerable radiation at this frequency is seen. Given that the spatial extent of the scattering region is much larger than that producing the emission at 3ω/2, we infer that this region is at a considerably lower density than quarter critical. The absence of 3ω/2 when the target was viewed along its surface may be due to the central focus being in a pit that has been dug by the incident laser beam, which obscures the quarter critical region from a detector viewing the target along its surface. Certainly we do observe considerable emission at 3ω/2

when a 5% prepulse is added 50 ps ahead of the main beam, which is commensurate with the idea that hole-boring is responsible for the lack of 3ω/2 signal along the target surface.

An extra dependency of the observed stimulated scatter is that with f number of focus. Experiments conducted in December 1997 and May 1998 used f/ 3.5 and f/ 1.6 parabolic reflectors respectively: in both experiments the position of the peaks observed was independent of target material, and insensitive to laser intensity at target. Typical spectra are shown in figures 4 and 2 respectively. We see that with the faster focus, there are more peaks visible, while with the f/ 3.5 optic, the fewer peaks are generally broader. The increased breadth of the slow focus

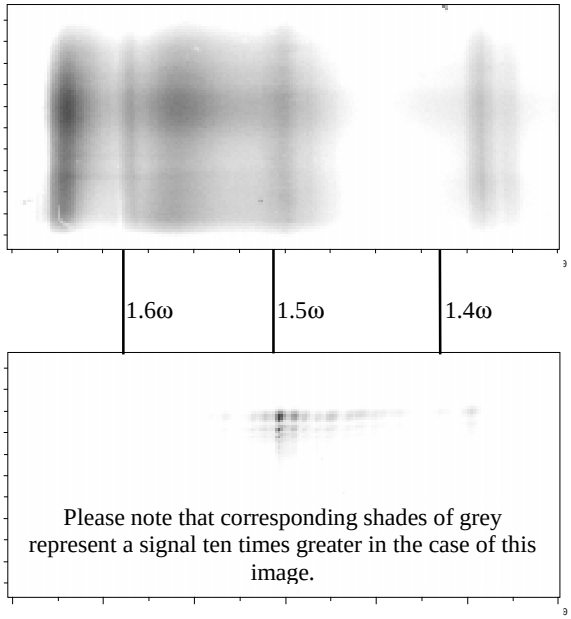

Figure 3. Comparison of scattered radiation (upper) with emission at 3ω/2 coming from the quarter critical surface (lower image)

peaks may be due to the increased intensity in the underdense regions which results from a higher f number: thus allowing more scattering processes to lie above threshold.

Scattering Mechanism

While the origin of the scattering remains unknown to us, and theoretical attempts to understand it are still in progress, some preliminary results may be reported. Traditionally, the emission

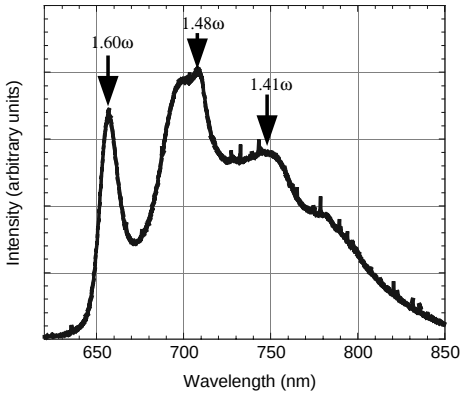

Figure 4. Typical spectrum with an f/ 3.5 focus.

at 3ω/2 has been ascribed to a two-photon process. The first photon undergoes Two Plasmon Decay (TPD), and the resulting plasmons are free to scatter a second photon. It has been shown that if the two photons are parallel, then only radiation at exactly 3ω/2 is produced, however, features at other wavelengths are possible if the two photons are not parallel[1].

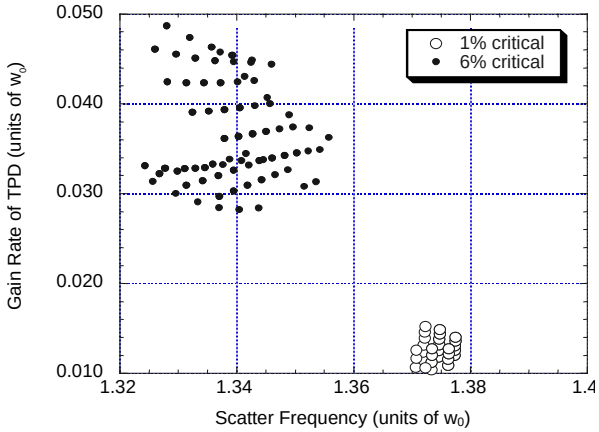

Figure 5. Valid scattering processes for an f/ 1.6 focus using linear instability approximations.

This is more likely to be the case practically, where there exist a variety of possible angles within the focus cone of the laser, even before reflection and other scattering are taken into account.

Using this suggestion, and simple linear treatments for the TPD[2], it is possible to catalogue the processes that are free to produce the observed scatter, given that we restrict the angle between the two photons to be that of the laser cone (18.2° for the case of the f/ 1.6 parabola), and we require the scattered photon to propagate at 45° to the incident beam axis to allow it to be detected by the spectrometer. With this treatment, the possible scattering processes and their gain rates (before compensation due to Landau damping has been taken into account) are shown in figure 5.

We see from this that scattering is predicted in the vicinity of 1.35ω, as observed experimentally. To discover more details regarding the emission at other wavelengths, we are using a more generalized instability analysis, as developed in [3]. We are also developing more advanced theory to predict the behaviour of TPD away from the quarter critical surface, and in the non-linear regime.

We hope that further experiments and a more detailed study may identify the source of the scattering, and may present the community with a diagnostic tool for underdense plasma.

References

1. W Seka *et al*
Phys. Fluids, 28 2570, (1985)

2. W L Kruer
The Physics of Laser Plasma Interactions
Addison Wesley, (1988)

3. B Quesnel *et al*
Phys. Rev. Lett., 78 2132, (1997)
Phys. Plasmas, 4 3358, (1997)

A Spectroscopic Analysis of Near Solid Density Plasmas

R Smith, G J Tallents, S J Pestehe, J Lin, M Tagviashvili.

Department of Physics, University of Essex, Colchester CO4 3SQ,U.K.

G Hirst, S Rose.

CLRC Rutherford Appleton Laboratory, Chilton, Didcot, Oxon., OX11 0QX, U.K.

Introduction

The radiative properties of hot, dense plasmas are of interest in several fields, including studies of Inertial Confinement Fusion (ICF) and astrophysics. The performance of both direct and indirectly-driven ICF implosions is sensitive to the radiative opacity of the target. In astrophysics, the opacity of material in Local Thermodynamic Equilibrium (LTE) is of great interest in studies of stellar structure and evolution. The opacity of the stellar plasma determines the rate of energy transfer from the centre of the star where nuclear reactions provide the energy source, to the outside. As with ICF, all opacity data used as input to such stellar models comes from theoretical calculations.

Within the last ten years, high-power laser experiments employing X-ray heating of a sample[1)] have allowed frequency-resolved opacity measurements to be made and generally good agreement between theory and experiment is found. However, such experiments have been limited to a maximum plasma temperature and density of approximately 100 eV and 10^{-2} gcm^{-3} respectively. Any attempt to extend opacity measurements to the higher energy densities envisaged in ICF implosions would improve our confidence in modelling ICF capsule performance.

Experimental work[2)] has shown that by irradiating an iron layer buried beneath a plastic overlay with intensities of ~10^{17} W/cm^2, it is possible to achieve emission in LTE. Modelling predicts that an overlay of CH confines the iron plasma[3)] thus enabling high energy densities to be reached. However no direct measurement of the conditions in the iron layer have been previously made. In this paper, we will demonstrate that by doping a layer of Fe with a concentration of Al, it is possible to make an accurate measurement of the plasma conditions by x-ray emission spectroscopy. This allows Fe emission in LTE to be characterised for known electron temperatures and densities and will improve the accuracy of theoretical and experimental opacity comparisons.

Method

The experimental setup is shown in figure 1. A 0.1 μm thick pure Al or 20% (by volume) Al impurity in Fe target deposited on a massive ~100 μm thick CHO substrate with a 0.1 μm plastic (CH) overlay was irradiated by the 248 nm, 350 fs CPA pulse from the Titania KrF laser. The layered targets were mounted as 270 μm discs on ~8 μm metal stalks and accurately positioned in the focal plane of the laser under vacuum by using an xyz-motorised target mount and a collinear frequency doubled YAG alignment beam. The laser was focussed onto the target plane with an f/5.27 parabola giving a spot size of 25 μm diameter. The average energy on target was ~300 mJ with irradiances of ~10^{17} W/cm^2. Near field and far field monitors were set up to diagnose the incident laser beam quality.

The focal spot size and position were monitored from shot to shot with an x-ray pinhole camera. The x-ray output emission was spectrally resolved and recorded in the 6-14 Å range with a flat potassium acid phthalate (KAP) (2d = 26.6 Å) crystal time integrated spectrometer with a moderate resolving power ($\lambda/\Delta\lambda \approx 200$). A 25 μm Be filter was placed over the CCD chip to eliminate the effects of scattered optical light. To determine the temperature and density of the plasma, it was necessary for accurate measurements of the relative intensities and line widths of the AlXIII 1s-3p (6.053 Å) and AlXII 1s^2-1s4p (6.31 Å) lines to be made. This was possible through the use of a Von Hamos spectrometer which offers a high resolving power ($\lambda/\Delta\lambda \approx 2000$). The spectrally resolving element in the Von Hamos spectrometer[3, 4)] is a cylindrically curved Pentaerythritol (PET) (2d = 8.742 Å) imaging crystal which collects x-rays over a large solid angle and as a result offers good detection sensitivity. The collected signal is then focussed down onto the detection plane and the wavelengths are dispersed along the line. The extent to which the x-rays are dispersed is determined by the radius of curvature of the crystal. For this experiment a 65 mm radius of curvature was used. The spectral range may be tuned by varying the distance the crystal is away from the target. For the targets of Fe with 20% Al impurity the Von Hamos spectrometer recorded the Al emission while the Fe emission was recorded simultaneously on the flat crystals spectrometer.

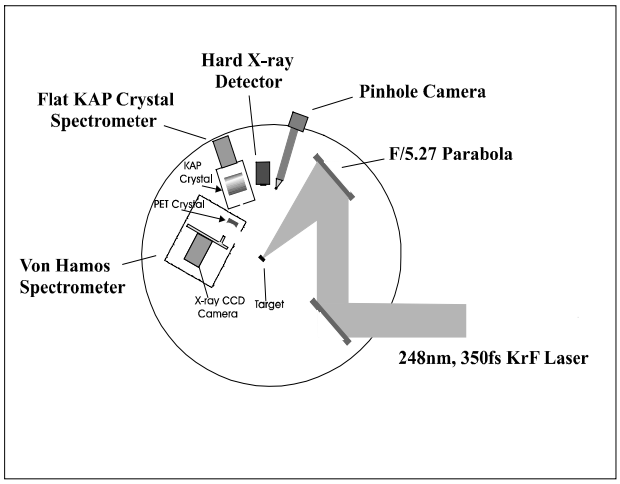

Figure 1. Experimental Setup

It was found that the Titania laser had an inherent amplified spontaneous emission (ASE) with an approximate duration of 100 ns and peak irradiance of 5x10^8 W/cm^2, onto which the CPA pulse was superimposed. In order to determine the effect of this ASE on the spectra, the time between the onset of the ASE and the arrival of the CPA pulse (Δt) was recorded using a photodiode for each shot.

The energy from the incident laser beam is coupled to the target predominantly through the processes of inverse bremsstrahlung and resonance absorption. Inverse bremsstrahlung generates thermal electrons at densities up to the critical density. Energy transport into the target is by diffusive electron thermal conduction[5)] as the electron mean free paths are similar to the scale length of the temperature gradient[6)]. To ensure that this temperature front is spatially uniform, a random phase plate was inserted into the beam to smooth any spatial non-uniformities in the focal spot. Thermal smoothing can also reduce the effects of intensity variations within the beam profile[7, 8)].

The short 248 nm wavelength of the KrF laser is desirable as preheating due to hot electrons decreases with decreasing laser wavelength[9)]. Radiative preheating of the Al layer is also negligible as the plastic overlay is a weak emitter.

Results

The Stark broadened spectral width of the hydrogen-like aluminium line AlXIII 1s-3p is a sensitive indicator for electron density[5] at electron densities above 10^{22} cm^{-3}. The electron temperature within the plasma may be deduced by calculating the ratio of intensities for the AlXIII 1s-3p and AlXII $1s^2$-1s4p lines at 6.053 Å and 6.31 Å, respectively. Using simulated spectra from the FLY code[10], it was possible to calculate these spectral widths and intensity ratios for a given electron temperature and density. Opacity effects on the line intensities were estimated to be negligible as the AlXIII 1s-3p and AlXII $1s^2$-1s4p lines have optical depths less than 0.03. The narrowest line width measured on the Von Hamos spectrometer was 10 mÅ. This value sets the upper limit on the instrument broadening, although the true value is estimated as 5 mÅ from a combination of source broadening and aberrations on the Von Hamos focusing. It was necessary to incorporate instrument broadening into the simulated spectral output from the FLY code. Comparison of FLY calculations with the experimental spectra enabled the dependency of the time-integrated electron temperature and density on the duration of the ASE prepulse, Δt, to be measured (figures 2 and 3). There is a large scatter in the deduced time-integrated electron densities, but a trend towards lower measured densities is apparent as the duration of the ASE pre-pulse increases.

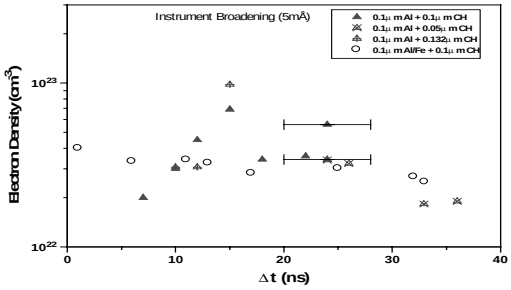

Figure 2. Time-integrated Electron density as a function of the temporal position of the CPA pulse relative to the ASE. The peak time-integrated electron density of ~$1x10^{23}$/cm^3 occurs at $\Delta t \approx 15$ ns. It can be seen that small variations in the thickness of the plastic overlay (as labelled) do not effect the measured electron densities. The timing errors for data points without error bars are typically less than 1 ns.

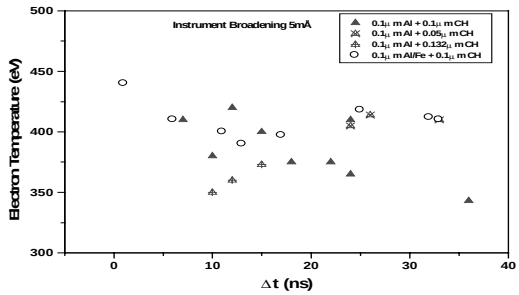

Figure 3. Time-integrated electron temperature as a function of the temporal position of the CPA pulse relative to the ASE for different CH overlay thicknesses (as labelled).

An example of a fit of the FLY output to the experimental spectrum is shown in figure 4. The line splittings of the theoretical FLY spectrum due to stark broadening effects are not seen experimentally, possibly because late time emission as the plasma expands is narrow and fills the central wavelength spectral 'holes'[11]. The measured superthermal temperatures in the range 5-20 keV agree with scaling values[12] and are sufficiently low to ensure that hot electrons have a negligible effect on the heating of the buried layer Al layer.

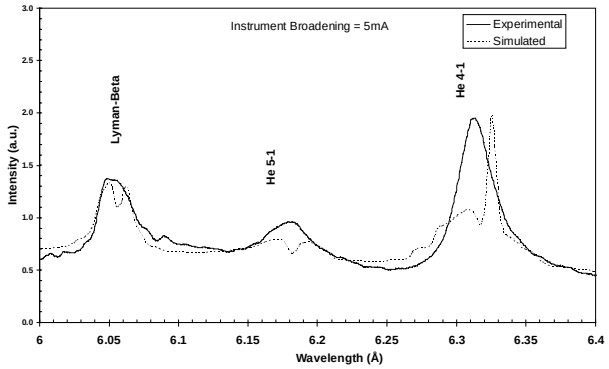

Figure 4. Comparison of experimental spectrum for a tamped Al target and the stimulated FLY spectrum at an electron density of 6.9x 10^{22}/cm^3 and an electron temperature of 400 eV.

Conclusions

We have demonstrated a technique for generating dense near-solid density plasma with electron temperatures of ~400 eV. It was found that the duration of a low intensity prepulse has significant effects on the electron temperature and density. Recording the Al spectrum on the Von Hamos spectrometer and the Fe spectrum on the flat crystal spectrometer simultaneously has allowed us to diagnose the plasma conditions during the Fe emission. The emission of the Fe plasma in LTE for measured values of electron temperature and density compared to existing simulations will allow for a quantitative assessment on the accuracy of iron opacity calculations [2].

References

1. L B DaSilva, B J MacGowan, D R Kania, B A Hammel, C A Back, E Hsieh, R DoyasIglesias, C A Rogers, R W Lee, Phys Rev. Lett. 69, 438 (1992)
2. K Nazir, S J Rose, A Djaoui, G J Tallents, M G Holden, P A Norreys, P Fews, J Zhang, F Failles, Appl. Phys. Lett. 69, 24 (1996)
3. B Yaakobi, R E Turner, H W Schnopper, P O Taylor, Rev. Sci. Instrum. 50, 1609-11 (1979)
4. G J Tallents, B Luther-Davies, M A Horsburgh, Aust. J. Phys., 39, 253 (1986)
5. G J Tallents, M H Key, P Norreys, D Brown, J Dunn, H Baldis, Phys. Rev. A, 40, 2857 (1989)
6. M H Key, Handbook of Plasma Physics, vol. 3, chapter 14, Elsevier Science Publishers B.V. (1991)
7. E M Epperlein, , G J Rickard, A R Bell, Phys. Rev. Lett. 61, 2453 (1998)
8. Y Al-Hadithi, G J Tallents, J Zhang, M H Key, P A Norreys, R Kodama, Phys. Plas. 1, 5 (1994)
9. W C Mead, E M Campbell, K G Estabrook, R E Turner, W L Kruer, P H Y Lee, B Pruett, V C Rupert, K G Tirsell, G L Stadling, F Ze, C E Max, M D Rosen, Phys.Rev. Lett. 47, 1289 (1981)
10. R W Lee, J D Kilkenny, R L Kauffmann, D L Matthews, J. Quant. Spect. & Rad. Ttansfer, 31, 83 (1984)
11. D Riley, L A Gizzi, F Y Khattak, A J MacKinnon, S M Viana, O Willi, Phys. Rev. Lett., 69, 3739 (1992)
12. D W Forslund, J M Kindel, K Lee, Phys. Rev. Lett. 39, 284 (1979)

Vulcan used as a Plasma Accelerator for Nuclear Reactions

K W D Ledingham, T McCanny, P Graham, Xiao Fang, RP Singhal.
Dept of Physics and Astronomy, University of Glasgow, Glasgow G12 8QQ, Scotland

J Magill.
European Commission, Institute for Transuranic Elements, Karlsruhe, Postfach 2340, D-76125, Germany

A J Cresswell, D C W Sanderson.
Scottish Universities Research and Reactor Centre, East Kilbride, Glasgow G75 0QU

R Allott, B Kennedy, D Neely, P A Norreys.
CLRC Rutherford Appleton Laboratory, Chilton, Didcot, Oxon., U.K.

M Santala, E Clark, M Zepf, I Watts, K Krushelnick, M Tatarakis, A E Dangor.
Blackett Laboratory, Imperial College, London SW7 2BZ, UK

A Machecek, J S Wark.
Clarendon Laboratory, Dept of Physics, University of Oxford, OX1 3PU, UK

Introduction

The mechanism of the interaction of charged particles in intense electromagnetic fields has been considered for more than fifty years. This was one of the first explanations put forward by the early workers to explain the origin and energies of cosmic rays [1-3]. Simply the idea is as follows: a charged particle in an intense electromagnetic field is accelerated initially along the direction of the electric field. The vxB force causes the particle's path to be bent into the direction of travel of the wave. In large fields the particle's velocity rapidly approaches the velocity of light and tends to travel with the EM wave gaining energy from it. In astrophysical situations the solar corona was thought to be one of the sources of the electromagnetic waves. These ideas were the counterparts of the machines built on the earth to accelerate particles to high energies.

In 1971 the possibility of accelerating electrons in focused laser fields was first proposed by Feldman and Chiao [4]. They calculated that an electron could gain energies as high as 30 MeV after a single pass through the focus of a diffraction limited laser beam of power 10^{12} W and wavelength 1 μm. Chan [5] similarly calculated that an intense laser beam could be used as an energy booster for relativistic charged particles showing that a 10 MeV electron can absorb 40 MeV from a laser beam of 1 μm wavelength and an electric field of $3x10^{10}$ V/cm in a distance of 1.3 mm.

Recently Tajima and Dawson [6] suggested that a laser electron accelerator could be created when an intense laser pulse produced a wake of plasma oscillations through the action of the non-linear ponderomotive force. They demonstrated through computer simulations that existing glass lasers of 10^{18} W/cm^2 shining on plasmas of densities 10^{18} cm^{-3} could yield electrons of GeV energy per cm of acceleration.

More recently the importance of Raman forward scattering in short pulse high intensity lasers has been realised by a number of authors [7-10] in generating electrons of very high energies in very short distances. The probability of using this technology for the construction of compact accelerators which might find applications where 2-200 MeV electrons or photons are needed was considered.

Many probes have been used for producing nuclear reactions e.g. neutrons, protons, alpha particles and heavier nuclei as well as non nuclear beams such as electrons and gamma rays. It is therefore not surprising that one can induce nuclear reactions using intense light beams. In the mid to late eighties the possibility of producing laser induced fission using laser intensities as high as 10^{21} W/cm^2 was suggested [11-13]. Application of chirped-pulse amplification techniques has revolutionised high power laser technology and has resulted in laser intensities in excess of 10^{19} W/cm^2 being generated. A number of high intensity lasers have been built around the world e.g. Vulcan at the Rutherford Appleton Laboratory, UK and Nova at the Lawrence Livermore National Laboratory, USA which are capable of reaching such intensities. Indeed recently [14] it was announced that intense light beams are capable of transmuting elements and specifically gold was transmuted to platinum and mercury.

This report is presented as a proof of concept that an intense laser beam can be used to induce nuclear reactions.

Experimental

The laser used in these experiments was the Vulcan Nd glass laser at the Rutherford Appleton Laboratory with a wavelength of 1.053 μm. The pulse width was typically 1 ps and with some 40 J in the pulse. The laser beam of p-polarised radiation had dimensions 150 x 88 mm and was focussed on axis using a f /1.7 parabolic mirror. The focal spot had a diameter of about 12-15 μm resulting in laser intensities in excess of 10^{19} W/cm^2. The crater caused by the laser in a lead target of dimensions 10x10x3 mm is shown in figure 1 and has a diameter of about 2 mm. This photograph was taken with a scanning electron multiplier and it is felt the dimensions of the crater and the height and width of the rim can reveal a great deal about the plasma processes involved. When the lead target was replaced with a copper sample of similar dimensions the crater size was reduced by a factor of two. It was noticed that if the laser interacted with the copper target without a lead irradiator, no radioactivity was generated in the Cu target which suggests that the high energy electrons were generating a bremsstrahlung beam in the lead target which then caused subsequent γ induced nuclear reactions. (γ,n) reactions are typically nearly two orders of magnitude larger than (e^-,n) reactions.

The targets were housed in the ultra-short pulse interaction chamber on Vulcan which was evacuated to about 10^{-5} torr and the laser could deliver a pulse every 30 minutes. It took several minutes to take the chamber up to atmospheric pressure and to extract the radioactive samples for analysis and thus at this stage only radioactive samples with half lives greater than a few minutes can be analysed. This is a temporary limitation which will be rectified by a rapid transport system in the future.

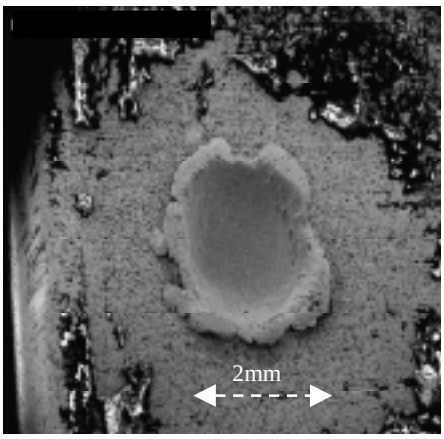

Figure 1. The crater caused by a laser pulse of 40 J interacting with a lead target. The γ beam generated at these intensities is in a direction 180° to the crater and has a continuous distribution energies of many MeV which can induce nuclear reactions.

Results and Discussion

One of the most fundamental photo-nuclear reactions is the (γ,n) reaction which has a Q value of typically > 8 MeV. Such reactions produce proton rich nuclei which decay normally by positron emission or EC. A positron emitting nucleus is very easy to identify unambiguously since the positron annihilates with electrons to produce two 511 keV γ -rays back to back.

In the present experiment, the laser beam was incident on a lead target (3 mm thick) at an angle of 45° as shown in figure 2. Behind the lead target were placed a number of Cu samples of thickness 3 mm from which the angular distribution of the laser induced γ radiation could be determined. The laser beam incident on the lead target generates an MeV γ-ray beam heavily forward collimated as shown in figure 3. [this is the subject of an extended paper to be published elsewhere [15)]. The γ rays irradiated the copper target to produce ^{62}Cu via a ^{63}C(γ,n)Cu^{62} which has a half life of about 10 minutes.

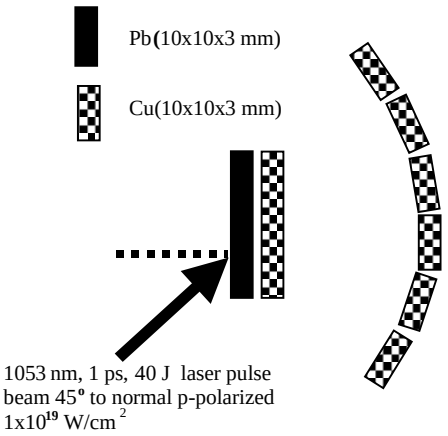

Figure 2. The target arrangement for activation studies. The p-polarized laser beam was incident on the lead target at 45°. The γ beam emerged from the radiator to activate the copper samples.

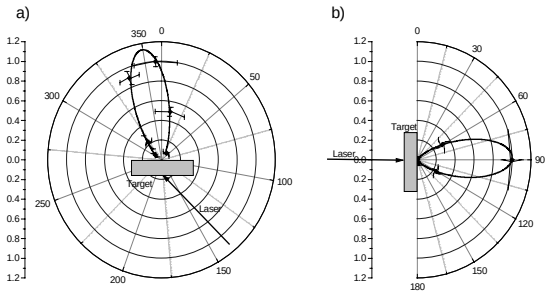

Figure 3. The γ-ray angular distribution above 10 MeV determined by ^{62}Cu activation. The beam is heavily collimated in the forward direction i.e. at right angles to the target plane (a-horizontal, b-vertical plane).

Two large volume NaI scintillators (based on an existing mobile gamma spectrometer) were used in conjunction with a coincidence system. The system was calibrated with ^{58}Co positron activities ranging from 50 to 3200 Bq with the limit of detection of pure β^+ emitters estimated to be a few Bq. The copper samples were placed between the detectors and the summed coincidence spectra were recorded using 120 s live times over periods of several tens of minutes and the net counts in the 1024 keV peak were determined. These were plotted, in figure 4, as a function of time and fitted to exponential decays and the half lives determined. The mean half life for four data sets was 9.63±0.24 minutes which agrees well with the generally accepted value of 9.7 minutes for ^{62}Cu. For the data set with the maximum activity, a long lived component was also visible which was estimated to be several hours presumably from ^{64}Cu.

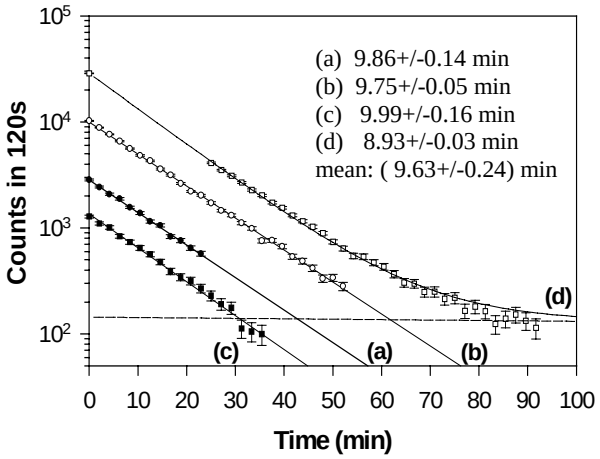

Figure 4. The half lives of Cu^{62} as measured from four different laser shots of nominally the same pulse energy. The mean half life agreed well the accepted value of 9.7 mins. The lead target was also investigated for activity but the (γ,n) reactions in this element produced isotopes with either very short or very long half lives and hence could not be detected.

Conclusions

It has been shown that a high power laser with pulse widths of 1 ps and intensities of about 10^{19} W/cm^2 at a wavelength of 1 μm when interacting with a lead target produces a well collimated beam of γ rays of energies in excess of 10 MeV.

This high energy radiation has been shown to produce a (γ,n) reaction in ^{63}Cu to produce kBq activity of ^{62}Cu. Clearly however many problems have yet to be solved. For example as shown in figure 4 the radioactivity from four different laser pulses, with nominally similar energies, appears to differ by more than an order of magnitude.

It was reported in similar experiments for X-ray production using a much lower energy beam with 120 fs pulses [9], that a low intensity pre-pulse which arises from amplified spontaneous emission precedes the main pulse in time. According to these authors this pre-pulse appears to be necessary for efficient high energy X-ray production. The question of the pre-pulse must be investigated further.

It has thus been demonstrated that high power lasers can be used to induce nuclear reactions. It has been shown that kBq of ^{62}Cu can be generated at 10^{19} W/cm^2. It is hoped that Vulcan will be upgraded to produce laser intensities in excess of 10^{21} W/cm^2 and if the activity scales as the 3/2 power [9] then MBq of activity can be generated with many possible areas of application.

The possibility also exists to produce (e^-,fission) or (γ,fission) reactions and to verify reported calculations [13]. It is therefore very exciting to contemplate the possibility of laser light beams producing radioactive isotopes and point sources of neutrons and fission fragments from the fission reaction.

Other exciting possibilities with an upgraded VULCAN of laser intensities above 10^{20} W/cm^2 are pair creation from ultra-dense plasmas and pion production generated by electrons or photons above 140 MeV.

Much more research is necessary to determine whether plasma particle accelerators can compete with existing accelerators in energy, intensity and quality and in particular whether table top high energy accelerators can be produced using lasers. Even now rather small lasers of pulse energies less than a joule and with pulse lengths of about 50 fs are capable of being focused to laser intensities of about 10^{19} W/cm^2. These lasers have the advantage of being able to be pulsed to repetition rates of about 10 Hz and by integrating many pulses intense radioactive sources may be generated.

Finally as in many scientific endeavours however, the most important results on plasma acceleration may be totally unexpected. The data presented in the present report is the subject of an extended publication dealing specifically with a laser accelerator and its applications [16].

References

1. Menzel D H and Salisbury W W
   Nucleonics 2, 67, (1948)
2. Fermi E
   Phys.Rev. 75, 1169, (1949)
3. McMillan E M
   Phys. Rev. 79, 498, (1950)
4. Feldman M J and Chiao R Y
   Phys.Rev.A , 4, 352, (1971)
5. Chan Y W
   Phys Lett 35A , 305, (1971)
6. Tajima T and Dawson J M
   Phys.Rev.Lett 43, 267, (1979)
7. Joshi C, Tajima T, Dawson J M, Baldis H A , and Ebrahim N A ,
   Phys.Rev.Lett. 47, 1281, (1981)
8. Dawson J M
   Scientific American 260, 34, (1989)
9. Kmetic J D, Gordon III CL , Mackin J J, Lemoff B E Brown G S and Harris S E
   Phys.Rev.Lett 68, 1527, 1992
10. Modean A, Najmudin Z, Dangor, A E , Clayton C E, Marsh K A, Joshi C, Malka V, Darrow C B, Danson C, Neely D, Walsh F N
    Nature 377, 606, (1995).
11. Rhodes C K
    Science 229, 1345 (1985)
12. Lynn J E
    Nature 333, 116 (1988)
13. Boyer K, Luk T S and Rhodes C K
    Phys,Rev.Lett. 60, 557 (1988)
14. Irion, R,
    New Scientist, 18th April, 30, (1998)
15. Santala M, Clark E, Zepf M, Watts I, Beg F N Kruschelnik K, Tatarakis M, Dangor A E, FangX, Graham P, McCanny T, Singhal R P, Ledingham K W D, Cresswell A J, Sanderson D C W, Magill J, Machacek A, Wark J S, Allott R, Kennedy B, Neely D, Norreys P A
    to be published
16. Ledingham K W D et al
    to be published

Transient gain in Ni-like X-ray lasers

AG MacPhee, C L S Lewis, R M N O'Rourke.
School of Mathematics and Physics, The Queen's University of Belfast, Belfast BT7 1NN, UK

J Y Lin, A Demir, G J Tallents.
Department of Physics, University of Essex, Colchester CO4 3SQ, UK

D Neely.
CLRC Rutherford Appleton Laboratory, Chilton, Didcot, Oxon., OX11 OQX, UK

D Ros, Ph Zeitoun.
Laboratoire de Spectroscopie Atomique et Ionique Bâtiment 350, Université Paris-Sud, 91405 Orsay, France

S P McCabe, G J Pert, P Simms.
Department of Physics, University of York, York Y01 5DD, UK

Introduction

Between 1990 and 1995 the efficiency of XRLs has increased by more than 3 orders of magnitude through a combination of novel experimental design and the guidance of detailed theoretical modelling. Scaling to shorter wavelength operation has been achieved through the use of higher Z targets allowing the efficient operation of Ni-like rather than Ne-like ion XRLs. The use of pre-formed plasmas and curved targets have been the principle experimental techniques which have brought the various systems to the state of the art.

More recently, a significant advance in the field has been the demonstration of transient gain at the Max Born Institute in Berlin [1)], and subsequently at the Rutherford Appleton Laboratory in Oxfordshire [2)] in Ne-like systems and at LLNL in Ni-like systems [3)]. In these experiments, a system was developed in which a picosecond scale pulse with intensity approximately 10^{15} Wcm^{-2} was used to pump a pre-formed plasma generated using a ~ns pulse at an intensity of ~10^{12} Wcm^{-2}. The population inversion produced in this way was predicted through modelling to be more than an order of magnitude higher than schemes where the main pulse intensity was of the order 10^{13} Wcm^{-2}. The new technique differs from that of more conventional collision pumped XUV lasers in that gain in the plasma is produced only briefly, rather than in a quasi steady state as happens during the relatively long pulse pumping of the conventional schemes. The short pump pulse rapidly increases the population of the upper lasing state of the Ne-like ions in the plasma, significantly in excess of that attainable with the conventional, lower intensity ~100 ps pulse pumping scheme. This excitation occurs on a timescale too short to allow significant ionisation. Using a travelling wave pumping scheme and the appropriate optical arrangement for a line focus, this transient state can be maintained along the length of a plasma column allowing the pump laser energy stored in the plasma to be depleted by ASE.

Experimental technique

The, simplest, most effective pumping scheme employed two 1.053 μm pumping pulses in a line focus of width 100 μm. Tin coated glass slab targets up to 10 mm in length were irradiated at ~10^{13} Wcm^{-2} (averaged over a 280 ps FWHM Gaussian pulse), followed 550 ps later by a 3 ps CPA pulse at 10^{15} Wcm^{-2}. The photon transit time along a 10 mm target is ~33 ps which is significantly longer than the CPA pulse length. The wavefront of the CPA pulse was therefore tilted to arrive at an angle of 45° to the target plane to match the time of arrival of the short pulse to the propagation of the resulting X-ray laser photons along the plasma column. This was achieved through a combination of the intrinsic wavefront tilt inherent to the off-axis focusing optics and an additional component introduced using a diffraction grating [4)] as shown in figure 1. The grating was situated downstream of the pulse chirping system, which was located at an early stage in the laser amplifier chain. As a result, the change in beam diameter and hence wavefront tilt angle as the pulse propagated through the system had to be taken into account.

Both pulses were derived from the same YLF oscillator. The CPA pulse was compressed prior to entering the target chamber whilst the 280 ps pulse was simply an amplified but uncompressed component. This mode of operation eliminated jitter in the arrival time of the laser pulses. The option of introducing a pre-pulse on the 280 ps beamline was facilitated with beam-splitters and an optical delay line. The pre-280 ps pulse was set to arrive 3.3 ns before the main-280 ps pulse. The pre-pulse generator beam-splitters were chosen so that the pre-pulse accounted for ~(10±2)% of the total beam-line energy recorded for the long pulse.

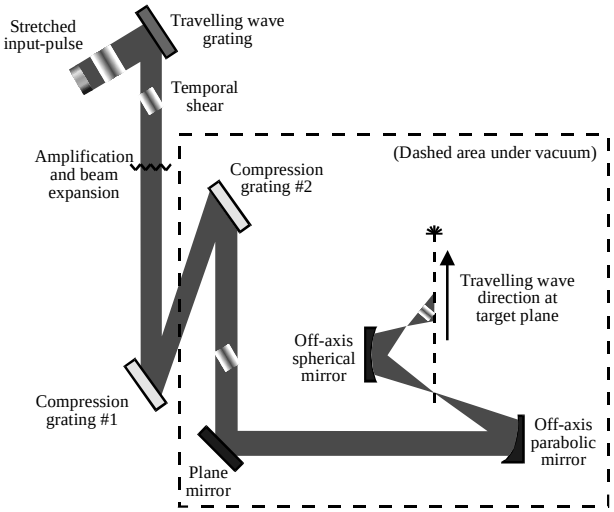

Figure 1. Schematic diagram showing both traveling wave components.

The total path length for the CPA pump beam depended on whether or not we were to use the travelling wave, as the additional grating used to generate it introduced an optical delay. Furthermore, optimum tuning of the pulse stretcher gratings varied depending on whether or not the grating was in. This introduced a further change in path length. The time of arrival of the optical pulses at the target plane was measured during set-up with an S1 streak camera with ~5 ps resolution. Thereafter on a shot to shot basis the beam timing was monitored using X-ray streak records. The CPA pulse length both with and without the travelling wave was measured using a third order auto correlator. Without travelling wave the pulse length was (2.0±0.2) ps, with the travelling wave the pulse was stretched to (3.0±0.2) ps.

The principle diagnostic was a flat field soft X-ray spectrometer using a variable pitch 1200 mm^{-1} 5 m radius concave gold grating and a 16-bit back-thinned CCD system [5]. The spectrometer was mounted axially looking in the direction of the oncoming travelling wave pumped X-ray laser. A similar system was mounted on the other side of the chamber looking in the reverse direction. A Kentech X-ray streak camera was mounted looking transverse to the target plane with a Be-filter and a vertical slit to monitor the pump pulse timing. A time integrated Bragg crystal spectrometer with a 16bit CCD detector [4] was used to monitor the ionisation stages achieved for Ge and Sm.

Results

In the absence of Ni-like Sn (Z=50) resonance line spectra (our standard diagnostic used to monitor such spectra cannot see out to such a long wavelength) it was assumed that the plasma resulting from the first pulse contained an appreciable abundance of Ni-like ions. Indirect evidence of this was provided by keV spectra taken for Sm (Z=62) under similar pumping conditions. Furthermore, from the absence of lasing action in time-integrated measurements of the axial soft X-ray spectra recorded without the CPA pulse, it was confirmed that prior to the arrival of the CPA pulse, the conditions in the plasma were not suitable for gain. Hence it was confirmed that any subsequent lasing action was initiated during the CPA pulse.

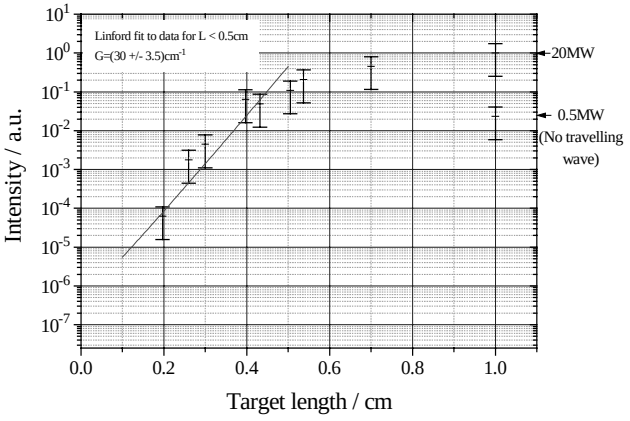

Figure 2. Length scan for Ni-like Sn XRL at 73 Å showing saturation for a target length of ~5 mm.

The system was observed to be insensitive to the use of the 10% pre-pulse. Having established that the pre-pulse had no noticeable effect on the integrated energy from the XRL, the majority of the experiment was conducted without pre-pulse to minimise the number of parameters involved.

Shots were taken on tin with and without pre-pulse where the peak of the CPA pulse arrived at either 50 ps or 550 ps after the peak of the 280 ps pulse. The most effective pumping scheme obtained for the Ni-like Sn system was with the CPA pulse arriving 550 ps after the peak of the long pulse. The 120 Å XRL intensity under these pumping conditions is shown in figure 2 as a function of target length. The beam divergence was ~6 mrad and the beam was refracted ~3.9 mrad off axis.

A shot taken without the travelling wave reduced the XRL intensity by a factor of ~40. This indicates that the system does indeed exhibit transient operation with the gain lasting sufficiently short a time interval that a travelling wave is necessary to efficiently drive a target with greater than ~3 mm length. Spectra recorded in the counter propagating direction to the travelling wave showed no measurable signal with or without the travelling wave pump.

Conclusion

Transient gain and saturated operation of a travelling wave pumped Ni-like X-ray laser has been observed for the first time. This extends the realm of operation of the Ne-like transient gain system first demonstrated at the Max Born Institute in Berlin by Nickles et al. [1] and compliments the more recent systems demonstrated at the Ecole Polytechnique in Paris [6] and the table-top high rep-rate system developed at the LLNL in California [6]. A gain coefficient of ~30 cm^{-1} at 120 Å was produced in a 1cm long Ni-like Sn plasma, sufficient to saturate the $3d^9_{3/2}4d_{3/2}$ J=0 to $3d^9_{5/2}4p_{3/2}$ J=1 transition. A 3 ps travelling wave pump pulse was applied to the plasma 0.5 ns after the peak of a 280 ps pre-forming pulse. Gain was also observed at 73 Å on the same transition in Ni-like Sm [7]. Attempts made to observe gain on the inner shell $1s^22s2p^2_{1/2}2p^4_{3/2}3s$ J=0 to $1s^22s^22p^2_{1/2}2p^3_{3/2}3s$ J=1 transition in Ne-like Ge at 62 Å, according to the conditions prescribed by Healy et al. [8] were unsuccessful in the absence of a 1 ps travelling wave pumping pulse. The modelling suggests that a gain coefficient of ~15 cm^{-1} could be achieved on this transition with the facilities currently available at RAL. The ~30 cm^{-1} gain coefficient observed in the Ni-like Sn scheme meant that only $\sim^1/_2$ of the full energy of the Vulcan laser system was required to saturate gain on the 120 Å transition. Such systems now routinely produce high gain and saturated output on transitions in many Ne-like and Ni-like ions. Although the pump energy required to saturate an XUV laser transition has reduced from ~250 J to ~60 J through use of this technique, the integrated energy of the XUV laser beam is lower, in direct proportion with the pulse duration which is approximately a factor of ~30. However, the reduced pump energy required means that with the rapid development of more efficient short pulse pump lasers, the table top concept of an X-ray laser may now be less remote [3].

References

1. Nickles P.V., Shlyaptsev V.N., Kalachnikov M., Schnurer M., Will I., Sandner W., Phys. Rev. Lett. 78 (14), 2748-2751 (1997)

2. Warwick P.J., Lewis C.L.S., Kalachnikov M.P., Nickles P.V., Schnurer M., Behjat A., Demir A., Tallents G.J., Neely D., Wolfrum E., JOSA B, 15 (6),1808-1814 (1998)

3. Dunn J., Osterheld A.L., Shepherd R., White W.E., Shlyaptsev V.N., Stewart R.E., Phys. Rev. Lett. 80 (13), 2825-2828 (1998)

4. Collier J., Pepler D., Danson D., Warwick J., Lewis C., Neely D., CLF Annual Report 1996/97 (RAL report TR-97-045) 209-210 (1998)

5. Andor Technology Ltd., 9 Millennium Way, Springvale Business Park, Belfast T12 7AL UK

6. Klisnick *et al.*, 6th International Conference on X-Ray Lasers, Aug. 31-Sept 4, Kyoto, Japan (1998)

7. Lewis C.L.S. *et al.*, 6th International Conference on X-ray Lasers, Aug. 31-Sept. 4, Kyoto, Japan, (1998)

8. Healy S.B., Janulewicz K.A., Pert G.J., Opt. Comm., 144, 24-30 (1997)

Transmission of 10 TW, picosecond laser pulses through hollow microtubes

M Borghesi, A J Mackinnon, R Gaillard, O Willi.
Imperial College of Science, Technology and Medicine, London (UK)

A Offenberger.
University of Alberta, Edmonton (Canada)

Introduction

Several important applications require short laser pulses to interact with homogenous plasmas over lengths largely exceeding the natural defocusing distance of the laser beam (Raleigh length). In particular, the propagation of an ultraintense short pulse through a long region of plasma without considerable energy dissipation is a basic requirement of the Fast Ignitor scheme for Inertial Confinement Fusion[1]. In order to confine the laser beam in a small section and achieve the required intensity over several Raleigh lengths, some guiding mechanism is necessary. For pulses at sufficiently high power, relativistic self-guiding can occur, as it has been observed in several experiments[2]. The pulse is guided due to the combination of ponderomotive and relativistic modifications induced in the plasma density profile by the pulse itself. Guiding of short pulses over considerable lengths has also been achieved by using preformed plasma channels[2]. In these experiments, a prepulse, focused in the gas or plasma ahead of the main pulse, provided the necessary refractive index modification .

An alternative approach, not yet widely investigated, is the use of solid guides, namely hollow capillary tubes. In this case the laser pulse is confined within the inner diameter of the guide and propagates through reflections off the inner walls of the tube. The propagation of laser pulses with a power up to 1 TW through glass microcapillary tubes (with diameters in the range 100-200 µm) was first studied by Jackel *et al* [3]. For energies below the breakdown threshold, the propagation occurs through grazing incidence reflections at the dielectric inner surface[4], the reflectivity for each bounce being determined by Fresnel laws. For high intensity pulses, however, an overdense plasma is created at the guide walls ahead of the main pulse, by the pulse's rising edge or by the prepulse. In this case the beam is guided through reflections off the high density plasma (an obliquely incident beam will be reflected at the density $n_e=n_{cr}\cos^2\theta$, where n_{cr} is the critical density and θ the angle of incidence). Since, in principle some energy is absorbed by the plasma at every bounce, a reflection coefficient R can be introduced. The total transmission through the guide will be $T = T_{ins}(R)^N$, where the insertion coefficient T_{ins} represents the fraction of the pulse energy that can be coupled to the guide and N is the number of bounces undergone by the pulse along the length of the guide. Within the guide, a mode structure establishes, depending on its transverse size; a detailed modal analysis of hollow cylindrical waveguides can be found in reference 4.

Guiding of high intensity pulses through solid guides could be of interest in view of alternative approaches to Fast Ignition. In principle, the igniting pulse can be propagated to the high density core of an imploding target, or at least through the coronal plasma region, into a solid waveguide, provided its walls are thick enough to survive the compression. This approach, in principle also applicable to direct drive compression schemes, seems particularly promising for point ignition following indirect-drive compression of a pellet placed inside an holraum. In this case, in order to reach the compressed core, the igniting pulse could propagate through the holraum walls inside a solid capillary tube. Considering the size of holraums presently in use, the guide lengths of interest for these applications are in the 1-10 mm range.

The experiment reported in the following[5] is the first experimental study of guided propagation of 10-20 TW, ps pulses (i.e. in a regime of interest for Fast Ignitor applications) through hollow glass capillary tubes. The energy transmission through the waveguide was measured using capillary tubes of different diameter and length, and high transmittivity were measured (more than 80% of the energy coupled to the guide).

Experimental arrangement

The experiment was carried out using the Vulcan laser operating in the Chirped Phase Amplification mode. The experimental set-up is shown in figure 1. The duration of the 1 µm CPA pulse was 1 ps, with a power on target up to 20 TW. The pulse was superimposed on a 200-300 ps pedestal with a main to prepulse contrast ratio better than 10^{-6} [6]. The targets were pyrex (KG33) hollow capillary tubes, with variable length. Two different sets of targets were used: 40 µm inner diameter targets, with external diameter of 100 µm, and 100 µm inner diameter targets, with external diameter of 550 µm. The targets were mounted on a translation stage, that also allowed rotation in the horizontal and vertical plane. The CPA pulse was focused at the entrance of the waveguide by an f/4.5 Off-Axis-Parabola. The targets were aligned by means of telemicroscope systems, and also by optimising the mode structures observed in the output beam when focusing into the target the CW YLF oscillator beam. The transmitted beam energy was monitored with a contact calorimeter, placed inside the interaction chamber. The transmitted beam was also imaged by a f/2.5 doublet (typically imaging the end plane of the target), collecting a fraction (about 4%) of the energy. A fraction of the uncompressed pulse was recompressed with a separate pair of gratings, duplicated in a KDP crystal and used as a transverse probe. Shadowgrams of the target at different times, before and after interaction, were obtained by suitably delaying the probe pulse, and imaging the target with a microscope objective.

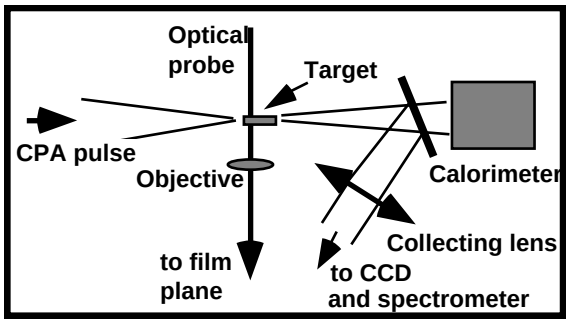

Figure 1. Experimental set-up

Experimental results and discussion

The energy fraction transmitted through the target is plotted in figure 2 as a function of the target length, for the two different diameters used. The energy transmitted through a platinum pinhole 100 µm in diameter is also shown in the data. Despite of some scatter of the data, a consistent behaviour for both sets of measurements clearly emerges from the plot. Even though the transmission appears to decrease with the target length, a sizeable fraction of the laser energy is guided through the guide.

For 100 µm inner diameter targets, transmission as high as 50% was observed for a target length of 10 mm. This corresponds to about 85% of the energy coupled to the guide, if one takes into account the insertion efficiency of 63%, estimated from the 100 µm pinhole transmission data. This relatively low coupling is a consequence of the quality of the focal spot attainable at the highest energy employed. As a matter of fact, the focal spot profile appeared to degenerate as the beam energy was increased above 15 J, with a large fraction of the energy being spread in the beam wings .

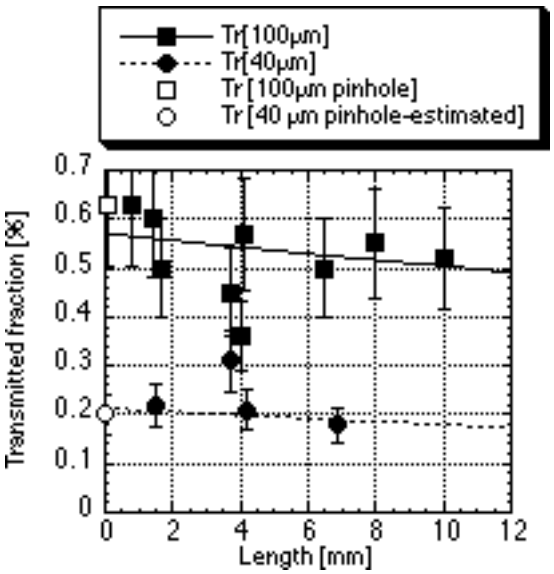

Figure 2. Transmitted energy versus target length for two different target inner diameter, 40 µm (circles) and 100 µm (squares). The measured transmission through a 100 µm pinhole and the estimated transmission through a 40 µm pinhole (see text) are also shown in the graph.

An image of the beam transmitted through a 100 µm pinhole is shown in figure 3. The energy fraction transmitted through a 40 µm pinhole, and consequently the energy coupling to a 40 µm inner diameter guide, have been estimated as 20% of the incident energy, by integrating the intensity distribution of figure 3 over the area of a 20 µm radius disk (shown in the figure as a dashed line). Even in this case one should note that the low coupling to the guide depends only on the poor quality of the focal spot in the conditions of the experiment, and that most of the energy coupled to the guide is transmitted through it.

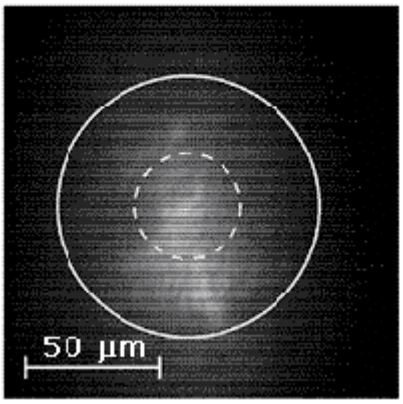

Figure 3. Profile of the beam transmitted through a 100 µm pinhole. The dashed circle indicates the size of a 40 µm diameter pinhole. By integrating the intensity over the area of this circle, the estimated transmission through a 40 µm pinhole (empty circle in the plot of figure 2) is obtained.

A rough estimate of the number of times that the beam is reflected off the plasma walls can be given as N - L/(4f#r), where L is the length of the target, f# the focusing f-number and r the guide inner radius. Consequently, the transmission through the target depends upon the length through the expression $T=T_{ins}R^{L/(4f\#r)}$. A fit of the data using this function has been attempted, including the transmission through a 100 µm diameter pinhole (measured) and through a 40 µm diameter pinhole (estimated) and excluding the two points that most deviated from the general trend.

From the best fits (shown in the graph), an approximated value of the reflectivity R can been obtained, i.e. R=0.98-0.99. Therefore, an absorption of 1-2% of the incident energy for each bounce can be inferred. This is just an order of magnitude estimate, as the effective f-number inside the guide, when the mode structure has been established, will in principle differ from the focusing f-number [3].

The energy is dissipated at the rate of 0.2 cm^{-1}. Though this rate is the same as measured in reference 3, it has to be noted that the measurements here reported were obtained with narrower targets and a smaller focusing f-number than in reference 3. This means that an higher number of bounces per unit length was undergone by the beam and the estimated absorption per bounce was much less than that reported by Jackel [3] (1-2% instead than 15-20%) .

In addition to the transmission diagnostics, transverse optical probing was used for the first time to determine the onset of plasma creation on the guide walls. In fact, as soon as the plasma is formed, the target, initially transparent to the probe radiation, becomes opaque. By suitably delaying the probe pulse with respect to the main beam, breakdown at the channel walls was observed 15-20 ps ahead of the pulse peak. While no plasma appears to be created by the 200 ps pedestal, the breakdown is likely to be initiated by the slowly rising edge of the pulse. The breakdown threshold for glass depends on the laser pulsewidth, and data available for fused silica report the damage threshold for 1 ps pulses as $I_b = 5\ 10^{12}$ W/cm^2 [7]. By simply dividing the power coupled to the guide by the guide section area, one can estimate the laser irradiance at the walls, at the peak of the pulse, as $I_{wp} = 1\text{-}3\ 10^{17}$ W/cm^2. Therefore, $I_b = 1\text{–}5\ 10^{-5}\ I_{wp}$. Published cross correlation measurements of the peak to pedestal contrast ratio for the Vulcan CPA system [5], indicates that a 10^{-5} level is reached 15-20 ps ahead of the peak pulse, consistently with what is deduced from the optical probing measurements.

The plasma, initially cold, is heated up as the laser pulse level rises, but it cannot expand more than a few microns in the few ps between the plasma formation and the peak of the pulse. This is confirmed by the fact that plasma closure does not appear to affect the propagation of the pulse, which interacts throughout all its duration with a short-scale length overdense plasma. In addition, spectra of the radiation transmitted through the guides did not differ significantly from spectra of the unguided radiation. Concerning the low value of absorption per bounce estimated from the data, it is certainly expected that collisional absorption will not be very effective in the conditions of the experiment, due to the high laser irradiance and to the short scale length of the plasma. In addition, classical resonant absorption cannot be very efficient due to the large value of the angle of incidence. Even though classical resonance theory [8] is strictly valid only for $L >> \lambda$ (where L is the scalelength of the plasma), numerical results[9] suggest that, for $L=\lambda$ resonance absorption is still described by a Denisov-like profile, approximately peaking at $\theta=\arcsin(0.8/(2\pi)^{1/3})=25$. Under these conditions a resonance absorption value below a few per cent can be reasonably assumed for $\theta=84$ (i.e. the angle of

incidence on the plasma walls corresponding to the focusing f-number of the experiment). At high irradiance, other collisionless absorption processes could in principle become important even at grazing incidence. In measurements recently reported[10], performed at irradiance exceeding $5\ 10^{17}$ W/cm^2, absorption as high as 80% of the incident radiation was observed at angles of incidence as large as 80, as predicted for absorption via the anomalous skin-effect[11]. However other experiments performed in the same experimental conditions as in reference 11 yielded different results[12], showing a more conventional resonant profile for p-polarised light, with absorption close to zero at very large angles .

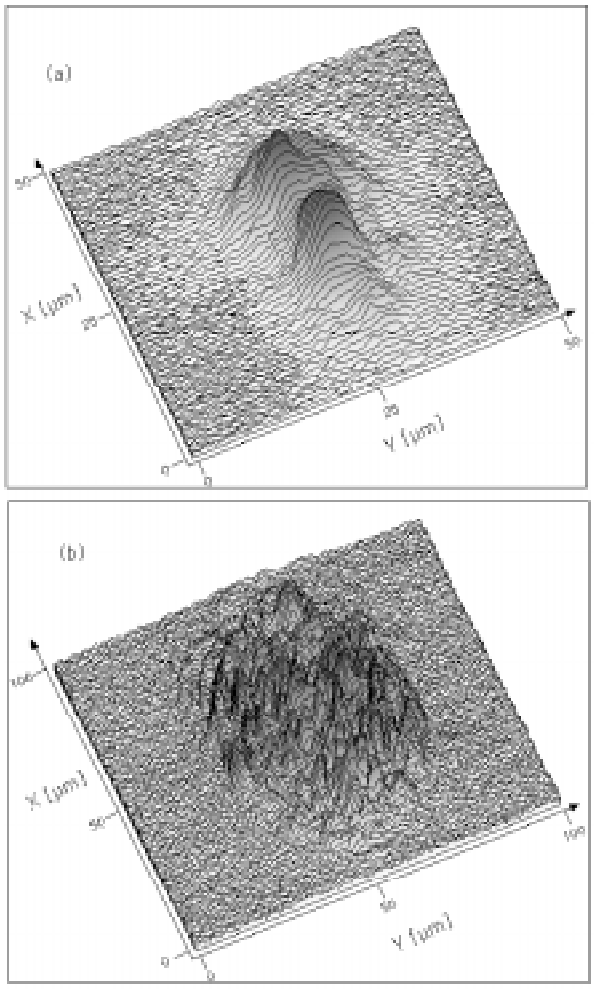

Figure 4. Intensity profile of the beam at the output of a 1.5 mm long target : (a) 100 µm inner diameter;
(b) 40 µm inner diameter.

Images of the beam profile at the guide output provided information concerning the mode structure of the beam during propagation. While several modes were seen when the pulse propagated through 100 µm diameter guides, propagation with no more than two modes was observed through the 40 µm diameter tubes. This can be seen respectively in figure 4(a) and 4(b), where the beam profiles at the end of a 40 µm diameter guide 1.5 mm long and of a 100 µm diameter guide of 4.0 mm length are shown. The efficiency of the guiding is evident if one observes that the size of the unguided beam at such position would be much larger, respectively about 150 and 450 µm. While the different modes present in the multimode structure of figure 4(b) cannot be immediately identified, the intensity pattern of figure 4(a) is, for example, consistent with a combination of the circular electric mode $TE_{0,1}$ and of the hybrid mode $HE_{2,1}$[13]. Again, one should keep in mind that in the experimental conditions of the reported investigation, the limitation in transmitted power is not due to the guiding mechanism, but to the inefficient coupling to the guide. A better quality of the focal spot would certainly improve the coupling, allowing higher power to be transmitted through the guide.

Conclusions

In conclusion, efficient guiding of 10 TW, ps pulses through 40 µm and 100 µm diameter glass capillary tubes has been demonstrated over lengths up to 10 mm (i.e. largely exceeding the Rayleigh length determined by the focusing optics). For both diameters, the pulse propagates with an attenuation coefficient of about 0.2 cm^{-1} and an estimated plasma-wall reflectivity of about 98-99% . Propagation with as few as two modes and output power up to 5 TW has been achieved through the 40 µm diameter guides. Optical probe measurements revealed that a plasma is formed on the guide wall by the rising edge of the pulse 15-20 ps ahead of the pulse peak. These studies are relevant for all applications requiring propagation of laser pulse at high intensity over several Rayleigh length and appear of particular interest for an alternative approach to the Fast Ignitor scheme for ICF, in which the ignitor pulse is driven to the compressed core of the pellet through a solid optical guide. Beside this, hollow capillary tubes provide a way of investigating the propagation of the laser pulse in a channel with overdense plasma walls, a subject also of topical interest for Fast Ignitor applications.

The authors would like to acknowledge the support of the staff of the Rutherford Appleton Laboratory and, in particular, of the Target Preparation Workshop. This work was funded by an EPSRC/MoD grant.

References:

1. M Tabak et al
Phys. Plasmas **1** , 1626 (1994)

2. E Esarey et al
IEEE Trans. Plasma Sci., **24**. 252 (1997) and references within

3. S Jackel et al
Opt. Lett, **20**, 1086 (1995)

4. E A J Marcatili, R A Schmeltzer
Bell Syst. Techn. J. **43**, 1783 (1964)

5. M Borghesi et al
Phys. Rev.E, **57**, R4899 (1998)

6. C N Danson et al
Opt. Comm. **103**, 392 (1993)

7. D Du, X Liu, G Korn and G Mourou
Appl. Phys. Lett. **64**, 3071 (1994)

8. V L Ginzburg
The Propagation of Electromagnetic Waves in Plasmas,
Pergamon Press, NY (1964)

9. O L Landen, D G Stearns and E M Campbell
Phys. Rev. Lett. **63**, 1475 (1989)

10. U Teubner et al
Phys. Rev.E **54**, 4167 (1996)

11. A A Andreev et al
Sov.Phys. JETP **74**, 963 (1992)

12. M Borghesi et al
CLF Annual Report 1994-95 (1995);
R Gaillard, A J Mackinnon, O Willi,
CLF Annual Report 1996-97 , RAL-TR-97-045 (1998)

13. T Sawatari
in N.S. Kapany, J.J. Burke, Optical Waveguides,
Academic Press, NY (1972)

Wave Propagation in Magnetised Overdense Plasmas

R A Cairns, B Rau.

School of Mathematical and Computational Science, University of St Andrews, North Haugh, St Andrews, Fife KY16 9SS.
Email rac@st-andrews.ac.uk, bernhard@dcs.st-andrews.ac.uk

Introduction

Computer simulations [1)] of the interaction of very intense laser pulses with solid density targets indicate that very high magnetic fields, of the order of hundreds of MG, and high electron temperatures, of hundreds of keV, can be produced in the region surrounding the focal spot. We have investigated the linear propagation properties of waves in an overdense plasma with such parameters. The main result of our work is that the propagation characteristics of the wave in the overdense region are very different from those in an unmagnetised plasma and that, in particular, the evanescence length may be very much greater than c/ω_{pe}. This implies that wave energy may penetrate much further into the plasma than might be thought. While our present work is restricted to linear theory in a rather simple geometry, the possibility that magnetic fields may change dramatically the penetration of a wave into a highly overdense plasma has obvious implications for the interpretation of computer simulations and experiments.

Theory

Our analysis is based on the theory of linear wave propagation in hot, magnetised plasmas, the role of high intensity simply being to produce the necessary high magnetic fields and temperatures. We use the weakly relativistic dielectric tensor elements, which are well known and widely applied in the theory of magnetised plasmas [2)]. The weakly relativistic theory assumes a Maxwellian electron distribution and relies on an expansion in which the factor

$$\mu = \frac{mc^2}{T_e} \tag{1}$$

is taken to be large compared to one. It may be expected to give reasonable results as long as the electron temperature does not approach the electron rest energy. Fully relativistic dielectric tensor elements, valid for arbitrary temperature, are available in the literature [2)], but are more complicated to calculate numerically.

Here, we shall only discuss the ordinary (O) mode, since it has a simpler dispersion relation than the extraordinary (X) mode and illustrates the essential features of the theory. We consider propagation perpendicular to the magnetic field, which is both the simplest case and the geometry which seems most appropriate to this problem. The linear dispersion relation for the O mode is

$$n^2 = \varepsilon_{zz}, \tag{2}$$

the magnetic field being assumed, as usual, to be along the *z*-axis. In this formula, *n* is the refractive index of the plasma. In the usual unmagnetised theory we simply have

$$n^2 = 1 - \frac{\omega_{pe}^2}{\omega^2}\ . \tag{3}$$

In weakly relativistic theory, the dielectric tensor we need is given by

$$\varepsilon_{zz} = 1 - \frac{\omega_{pe}^2}{\omega^2}\mu\left\{F_{5/2}(z_0) + \sum_{l=0}^{\infty}\frac{\lambda^l}{2^l\, l!}\left[F_{l+5/2}(z_l) + F_{l+5/2}(z_{-l})\right]\right\} \tag{4}$$

where

$$\lambda = \left(\frac{\omega}{\omega_{ce}}\right)^2 n^2\mu^{-1}, \qquad z_l = \mu\frac{\omega - l\omega_{ce}}{\omega},$$

and the functions *F* (Dnestrovsky functions) are defined, for half-integer *q*, by

$$F_q(z) = -i\int_0^{\infty}\frac{e^{iz\tau}d\tau}{(1-i\tau)^q} \tag{5}$$

for *z* in the upper half complex plane and by analytic continuation elsewhere. They can be related to the well-known plasma dispersion function and expressed in forms more suitable for numerical calculation [2,3)]. The other elements of the dielectric tensor, which are needed for considering the X mode, involve similar series.

For numerical calculation we have taken 40 terms in the series expansion of the dielectric tensor element, having checked that this gives accurate values over the parameter range of interest. Since we now have a polynomial equation of high order, there are many solutions from which we must select the one which we believe to be relevant to the problem. We have done this by beginning with the vacuum root at zero density then following the root to which this connects smoothly as the density increases. This is found to give an unequivocal result in most parameter regimes. As an illustration of the sort or results we find we show below a graph (see figure 1) of the refractive index squared as a function of density with a magnetic field such that $\omega_{ce}/\omega = 0.3$ (corresponding to a field of about 30 MG for one micron radiation) and a temperature of 100 keV.

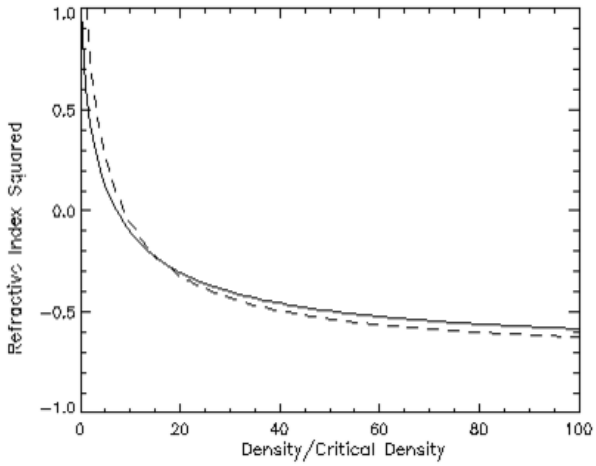

Figure 1. Square of the refractive index as a function of normalized density n_0/n_{crit} for $\omega_{ce}/\omega = 0.3$ and $T_e = 100$ keV. The result for the O-mode is shown in the solid, for the X-mode in the dashed line.

It is clear that for both the O and X modes, the refractive index levels off at a value which is negative, but whose magnitude is much less than given by cold plasma theory. To understand this behaviour we note that the dielectric tensor elements are functions of *k* in a hot, magnetised plasma. Also, in a highly overdense plasma, the dielectric tensor elements contain the large factor $(\omega_{pe}/\omega)^2$. This produces large corrections to the dispersion relation, in contrast to the more familiar underdense plasma regime where hot plasma effects are typically only important near a cyclotron resonance. In our situation the

effects of many cyclotron resonances overlap and contribute to the result.

Computer simulations

We have attempted to investigate this effect using a particle code. The numerical simulations were carried out using a fully relativistic, fully electromagnetic, 2-1/2 dimensional (two spatial, three velocity dimensions) particle–in-cell (PIC) code [4]. Here, a weak electromagnetic pulse ($E_{max} = 0.05 m_e \omega_{laser} c/e$) was initialized in a vacuum region ahead of a pre-ionized, thermal slab of plasma and propagated towards this slab at normal incidence. An external magnetic field directed perpendicularly to the direction of the laser pulse propagation was applied uniformly throughout the simulation region. The plasma was chosen to be only four times overdense ($n_0/n_{crit} = 4$) in order to keep the dimension of the simulation box reasonably low. Furthermore, the plasma thickness was fixed at 0.7 of a laser pulse wavelength to ensure a (theoretically predicted) transmission of laser light at intensities well above the background noise level while keeping the amplitude of the laser pulse within the linear regime. In order to achieve at least qualitative agreement with our theory, the typical Larmor radius of the plasma electrons had to be small compared to the longitudinal extension of the plasma slab. Due to plasma temperatures of up to 125 keV, the applied external magnetic field in our numerical simulations was as large as $B_{ext} = 2 m_e \omega_{pe} c/e$. Finally, in order to achieve a relatively good representation of a hot, Maxwellian plasma electron distribution, the number of macro particles used in our simulations was up to about 14,000 particles per $(c/\omega_{pe})^2$.

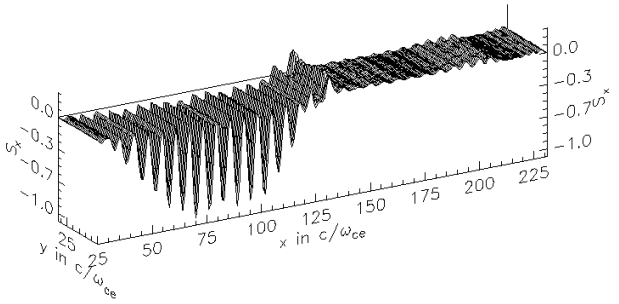

Figure 2. The Poynting flux S_x of the laser pulse after reflection off the dense, hot slab of magnetised plasma in arbitrary units. The plasma slab is located between $x = 123.3\ c/\omega_{pe}$ and $x = 132.1\ c/\omega_{pe}$. The main part of the laser pulse has been reflected off the plasma and is propagating backwards ($S_x<0$). Only a fraction of the initial pulse is transmitted through the dense layer of plasma and continues to propagate forward ($S_x>0$). The peak in the centre of the simulation box results from interference of incoming and reflected laser pulse light due to the reflection of the laser pulse off the overdense slab of plasma.

The same code was run for a total of four cases with low (2 keV) and high (125 keV) electron temperatures and with the external magnetic field B_{ext} switched on and off. The case of the hot, magnetised plasma is shown in figures 2 and 3. The transmission coefficient for the unmagnetised cases can be estimated from cold plasma theory to be of the order of 10^{-6}. In our computer simulations, negligibly small fractions (10^{-6}–10^{-3}) of the initial laser pulse were found to be transmitted through the slab of plasma for these cases. Similarly, the cold, magnetised case held a transmission coefficient both theoretically as well as numerically of about 10^{-3}. For the hot, magnetised case however, we found the transmission of the laser pulse energy to be as high as 6.2% when using the theory outlined above. The numerical simulations showed, in good qualitative agreement with this theory, a transmission coefficient of about 8% (see figure 3). We thus found the transmission of laser light through a slab of overdense plasma to become enhanced if both the electron temperature is high and the plasma is magnetised.

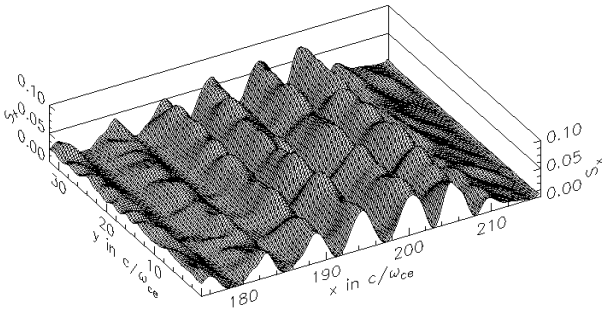

Figure 3. Blow up of the Poynting flux S_x of the transmitted laser light in the same units as in figure 2.

Summary and Conclusions

A study of the linear theory of wave propagation in hot, magnetised plasmas shows that the penetration of wave energy into the overdense region may be over a much longer length scale than would be expected from the usual skin depth, or indeed from anomalous skin depth theory. For the interaction of laser light with plasmas of finite longitudinal extent, this implies much higher transmission coefficients of the light at the original laser pulse frequency when compared to the cold, unmagnetised case. We have shown this behaviour both via numerical integration of the laser light transmission for a given dielectric tensor (see equation (4) for the case of the O-mode) as well as through particle simulation codes. In both cases, we found a transmission of the laser pulse energy to be several orders of magnitude higher than the ones encountered in cold and/or unmagnetised plasmas. In particular, we found the effect of enhanced transmission only to take place if the plasma slab is both hot and magnetised.

In conclusion, we have shown that the propagation characteristics of electromagnetic waves in hot, magnetised plasmas can differ significantly from the cold and/or unmagnetised cases. We have confirmed both theoretically as well as via numerical particle simulations that enhanced transmission through a thin slab of overdense plasma becomes possible if the plasma is both hot and magnetised.

Acknowledgement

This work was supported by the European Commission through the TMR Network SILASI, No. ERBFMRX-CT96-0043.

References

1. S C Wilks, W L Kruer, M Tabak and A B Langdon, Phys Rev. Lett. **69**, 1383, (1992)

2. M Bornatici, R Cano, O de Barbieri and F Engelmann, Nucl. Fus. **23**, 1153 (1983)

3. I P Shkarofsky, Phys. Fluids **9**, 561 and 570 (1966)

4. T Tajima, "Computational Plasma Physics", Addison-Wesley (1989); C K Birdsall and A B Langdon, "Plasma Physics via Computer Simulations", Adam Hilger (1991)

Multiphoton Ionization of Atoms and Molecules using the *R*-matrix-Floquet Theory

D H Glass, J Colgan, P G Burke.

Department of Applied Mathematics and Theoretical Physics, The Queen's University of Belfast, Belfast, BT7 1NN.
Email D.H.Glass@QUB.AC.UK

C J Noble.

CLRC Daresbury Laboratory, Daresbury, Warrington, Cheshire, WA4 4AS

Introduction

The *R*-matrix-Floquet theory[1] enables the interaction of intense laser fields with complex atoms and molecules to be studied in a fully non-perturbative manner. In particular it has been used to study multiphoton ionization, laser-assisted electron-atom scattering, harmonic generation, multiphoton processes involving two incommensurate frequencies and, more recently the multiphoton ionization of diatomic molecules[2]. Taking advantage of *R*-matrix theory the method is able to represent the atomic or molecular structure accurately and so, for example, the role of resonances in the ionization process can be studied in detail. This has permitted a wide range of atoms and negative ions to be considered including H, H^-, He, Ne, Ar, Mg, F^-, Cl^- and Li^-. As well as yielding total ionization rates, partial rates and angular distributions the *R*-matrix-Floquet approach has enabled other phenomena to be considered. Of particular interest has been the study of laser-induced degenerate states (LIDS). After presenting some recent results for the multiphoton detachment of Li^- and LIDS in He a brief description will be given of how the theory has been developed for the molecular case. Then some results will be presented for H_2.

Multiphoton Detachment of Li^-

Recently calculations have been performed[3] on the multiphoton detachment of Li^-. There has been renewed interest in this system in the last few years due to the first observation of resonance structure in the total photodetachment cross section by Berzinsh *et al*[4], who found the region between the $3s\ ^2S^e$ and $3p\ ^2P^o$ thresholds to be dominated by a broad $^1P^o$ resonance.

For the work being considered, the same *R*-matrix basis as that used by Ramsbottom *et al*[5] was adopted. This included five target states and two polarized pseudo-states to account for the polarization of the 2p $^2P^o$ target state. This approximation was found to give a ground state energy as well as target state energies in good agreement with experiment. It also yielded total detachment cross sections in the low intensity limit which were in good agreement with single-photon calculations such as those of Ramsbottom *et al*[5] and with experimental results such as those of Dellwo *et al*[6] who investigated the Wigner cusp-like effect in the energy region near the $2p\ ^2P^o$ threshold. At higher energies the calculations were found to be in agreement with the experiment of Berzinsh *et al*[4] as mentioned above.

Figure 1 shows some two- and three-photon rates at an intensity of 10^{10} Wcm^{-2}. It is found that the structure in the $2s\varepsilon l$ channel at a frequency of 0.0484 au disappears at a lower intensity (see inset). This is explained by a three-photon excitation of a $^1P^o$ resonance near the *3s* threshold accompanied by emission of one photon. This process interferes with the direct two-photon detachment rate and so gives rise to the resonance structure. A large enhancement in three-photon absorption is found at a frequency around 0.055 au and is matched by a decrease in the two-photon rate. In this case one-photon excitation of the residual atom from the $2p\ ^2P^o$ to the $3s\ ^2S^e$ occurs along with two-photon detachment.

Laser-Induced Degenerate States (LIDS) in He

Now some results are considered for the multiphoton ionization of He which continues work from an earlier study[7].In that work

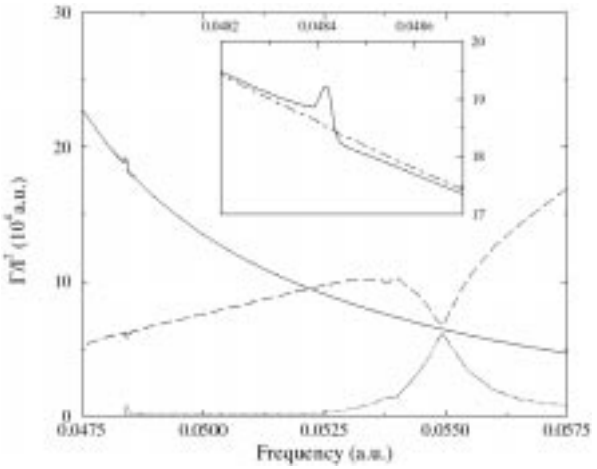

Figure 1. The two-photon rates leaving the residual atom in the *2s*(solid curve) and *2p* (dashed curve) states and the three-photon rate leaving the atom in the *3s* state (dotted curve) divided by the intensity squared are shown for an intensity of 10^{10} Wcm^{-2}. The inset also gives the partial rate leaving the atom in the *2s* state for an intensity of 10^9 Wcm^{-2} (chain curve).

a three-state approximation (1s,2s,2p) was used to describe the He^+ target and was found to give accurate values for the field-free energies and widths of $^1P^o$ autoionizing states. In this approximation there is a double resonance, due to a single photon resonance with the $1s2p\ ^1P^o$ bound state and the three-photon excitation of the ($2s3p$-$3p2s$) $^1P^o$ autoionizing state, which was investigated for intensities up to 10^{13} Wcm^{-2}. Here a LIDS process is investigated at lower intensity as was suggested in that paper.

LIDS occur when two atomic (or molecular) states which are dressed by the laser field become degenerate for a particular value of the intensity and frequency. Such a process is illustrated by figure 2. In each part of the figure a single frequency is considered and the trajectory of each state followed as a function of intensity, with the circle marking the field-free value of the autoionizing state. In a) and b) the frequency is respectively above and below that of a single photon resonance between the states. In a) the autoionizing state takes on the character previously associated with the bound state and vice-versa. In b) each state regains its original character but the effect of the interaction is very noticeable in the autoionizing state as denoted by the loop. In c) and d) the frequencies are once again respectively above and below that of the degeneracy but are now much closer to it. In d) the interaction is very strong but each state just regains its original character while in c) they just manage to change over. This indicates a degeneracy at a frequency of 0.7633345 au and an intensity of 5.4×10^{11} Wcm^{-2}. The work in recent years has demonstrated that LIDS are a common feature of atoms in strong fields.

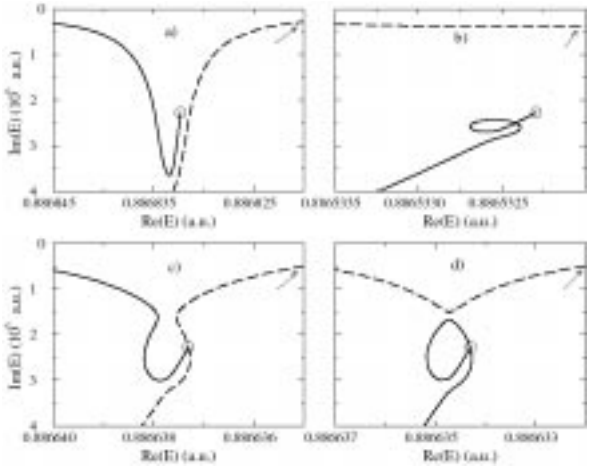

Figure 2. In each part of the figure the real and imaginary parts of the complex energies are shown as a function of intensity for the states which at low intensity correspond to the *1s2p* $^1P^o$ (solid curve) and the (*2s3p-3p2s*) $^1P^o$ (dashed curve) states. The arrow and the circle mark the states at low intensity. The frequency is fixed at 0.7634 au in a), 0.7633 au in b), 0.763335 au in c) and 0.763334 au in d). Intensities between 10^{11} and 10^{12} Wcm^{-2} are considered.

Multiphoton Ionization of Molecules

Recently new developments have been made within *R*-matrix-Floquet theory to treat diatomic molecules. As in the atomic case this involves dividing configuration space into internal and external regions. In the internal region all the electrons lie within a sphere of radius *a* and exchange and correlation effects involving all electrons are included by adopting an antisymmetrized wavefunction. In order to solve this problem use has been made of a general UK molecular *R*-matrix package, which involves a multi-centre expansion and has been used for many years to describe the scattering of electrons by diatomic molecules (see eg Burke *et al*[8]). In the external region one of the electrons lies outside the sphere and exchange between this electron and the remaining target electrons is neglected. A single-centre expansion can be adopted in this region and so use has been made of a computational package developed by Dörr *et al*[9], which has been used in the atomic case.

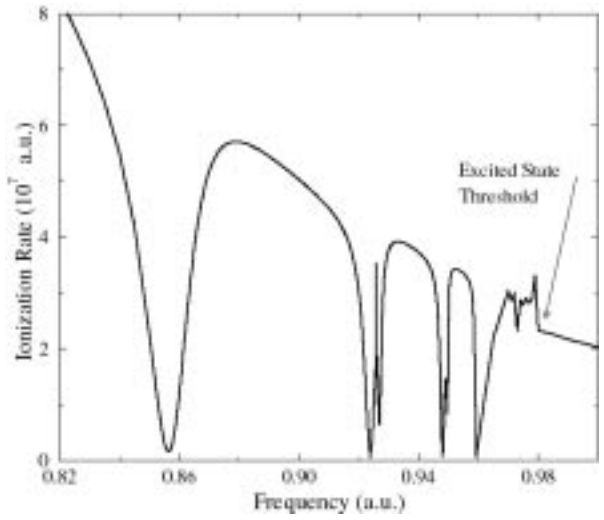

Figure 3. The total ionization rate of H_2 against frequency at an intensity of 10^{11} Wcm^{-2}.

Figure 3 shows results for ionization of H_2 at an intensity of 10^{11} Wcm^{-2} using a two-state approximation for the H_2^+ residual molecular ion. There is a Rydberg series of $^1\Sigma_u^+$ doubly-excited resonance states converging to the $^2\Sigma_u^+$ threshold which arise due to single photon excitation from the H_2 ground state. Other calculations[2] have considered the dissociative ionization of H_2 and also LIDS arising from one- and two-photon processes in the neighbourhood of a double resonance between the ground state, a bound excited state and an autoionizing state.

Conclusions

The results presented here have shown that the *R*-matrix-Floquet approach is able to treat diatomic molecules in the presence of a laser field as well as complex atoms and atomic ions. Future work will involve extending the molecular calculations, continuing work currently underway on the five-photon ionization of He, and also to develop time-dependent approaches to treat shorter pulses and higher intensities.

Acknowledgements

The authors acknowledge with thanks support from the EPSRC through a rolling grant and support by DENI for a studentship to one of us (JC).

References

1. P G Burke et al
J. Phys. B:At. Mol. Opt. Phys., 24 761, (1991)
2. J Colgan et al
Submitted to Comput. Phys. Commun., (1998)
3. D H Glass et al
J. Phys. B: At. Mol. Opt. Phys., 31 L667, (1998)
4. U Berzinsh et al
Phys. Rev. Lett., 74 4795, (1995)
5. C A Ramsbottom et al
J. Phys. B: At. Mol. Opt. Phys., 27 2905, (1994)
6. J Dellwo et al
Phys. Rev. A., 46 3924 (1992)
7. D H Glass et al
J. Phys. B: At. Mol. Opt. Phys., 30 3801 (1997)
8. P G Burke et al
J. Phys. B: At. Mol. Phys., 10 2497 (1977)
9. M Dörr et al
J. Phys. B: At. Mol. Opt. Phys., 25 2809 (1992)

High Harmonic Generation and Population Dynamics

F I Gauthey, P L Knight.

Blackett Laboratory,Imperial College, London SW7 2BZ Email f.gauthey@ic.ac.uk

B M Garraway.

SCOAP & Centre for Theoretical Physics, CPES, University of Sussex, Falmer, Brighton BN1 9QJ

The generation of high harmonics in the spectra of strongly laser-driven atoms has inspired much experimental and theoretical development in the past few years [1)]. The generation of a broad plateau of harmonics appears to be most effective if the laser intensity is such that tunneling of electronic wave packets from the laser-deformed atomic potential is repeated many times in a phase-locked fashion. This observation provides the foundation for the very successful "recollision picture", which provides in particular a widely accepted interpretation of the cut-off energy (in the tunnelling regime) by relating the highest radiated frequency to the maximum kinetic energy which the ionized electron optimally releases when it returns from the continuum and recombines with the atomic core [2)]. Nevertheless, this picture does not give a clear understanding of the origin of the plateau of harmonics. Indeed, most atomic models presently studied, even very simple ones which have no apparent connection with the recollision model, can reproduce high harmonic generation and predict the plateau-cut-off behaviour. In particular, the simplest model of all, that of a strongly driven two-level system, can also predict and reproduce the plateau and cut-off, as well as the characteristics of the phase of harmonics [3)]. Yet this simple model contains no continuum and allows no possibility for any recollision processes, let alone many phase-locked recollisions; it is therefore a very striking example of the generic character of high harmonic generation.

These observations led us to look for another and more generic theoretical approach, which would highlight the more fundamental processes involved in high harmonic generation while giving new tools for its study. We established a picture of periodic crossings [4)], which has allowed us to perform a study of the characteristics of high harmonic generation based on concepts which do not take directly into account the structure of the model atom, but its dynamical properties. The model explicitely contains repeated encounters, phase locked to the laser driving field, which are remarkably reminiscent of the recollision model. The picture of level crossings had already been widely employed in the study of wavepacket dynamics and had proved to be very successful for modelling a large variety of physical problems. Our study allowed us to predict an analytical rule for the cut-off energy of the plateau in harmonic spectra emitted from strongly driven two-level atoms. We described the population dynamics of the system by use of the Landau-Zener theory, in terms of adiabatic and non-adiabatic processes. This revealed that the origin of the plateau structure observed in high harmonic generation is linked to the presence of non-adiabatic effects occuring at each crossing, with adiabatic following between the crossings. We were able to determine the criteria which have to be fulfilled in order to obtain a plateau in high harmonic spectra, in terms of values of the parameters related to the Landau-Zener approach. These are conditions on the crossing duration, which must be very short when compared to the period of the laser field, and on the adiabaticity parameter Λ, which determines the proportion of non-adiabatic effects taking place at each crossing. We also found that the overall intensities of the harmonics in the plateau are directly related to the proportion of non-adiabatic effects occuring at each crossing.

In a more extended study [5)], we found that the height of a particular harmonic of the plateau depends periodically upon the adiabaticity parameter Λ, and shows an alternance of 'peaks' and 'dips'. We related this behaviour to that of probabilities of population transfers, which determine the population evolution, as a function of Λ. We found in particular that the intensity of harmonics is maximal when the time-dependent evolution of the populations form 'Gross structures' determined by the curves on which the values of the populations lie at the antinodes of the laser field. The absence of gross structures in the population dynamics, for example in the case of a totally periodic population evolution, results in much lower harmonic intensities. We determined analytical expressions for the gross structures and transfer probabilities by using the finite Landau Zener model [6)] within an evolution matrix approach.

More generally, the total response of the system fundamentally depends upon the population dynamics and we isolated particular population evolution regimes which give specific characteristics in the spectrum emitted, both for harmonic and hyper-Raman lines. Those population regimes correspond to particular choices of the excitation parameters and are also extremely sensitive upon the initial preparation of the system: hence a way to 'tune' the spectrum accordingly is provided. We are currently developing our analytical study further and are also looking into a possible adaptation of our study to the case of model atoms with a continuum.

References

1. M Protopapas, C H Keitel and P L Knight, Rep. Prog. Phys. 60 , 389 (1997) and references therein
2. M Protopapas, D G Lappas, C H Keitel and P L Knight, Phys. Rev. A 53 , R2933 (1996) and references therein
3. F I Gauthey, C H Keitel , P L Knight and A Maquet, Phys. Rev. A 55 , 615 (1997) and references therein
4. F I Gauthey, B M Garraway and P L Knight, Phys. Rev. A 56 , 3093 (1997)
5. F I Gauthey, B M Garraway and P L Knight, in preparation
6. B M Garraway and N V Vitanov, Phys Rev A 55 , 4418 (1997) and references therein

Non-Perturbative Treatment of Line Broadening in Ar-Filled Microballoon Implosions

P Gauthier, S J Rose.

CLRC Rutherford Appleton Laboratory, Chilton, Didcot, Oxon., OX11 0QX

P Sauvan.

Physique Atomique dans les Plasmas Denses, LULI, CNRS
Université Paris VI, 4 Place Jussieu, 75252 Paris Cedex 05, France and Ecole Polytechnique, 91128, Palaiseau, France

Introduction

We report here a new theoretical analysis of spectroscopic measurements from high density direct-drive implosions performed on the Rochester Omega facility [1]. In these experiments, Ar-filled plastic microballoons were imploded to a simultaneous maximum density and temperature of 40 gcm^{-3} and 800 eV respectively. Theoretical modelling of the time-resolved spectroscopic data was in excellent agreement with experiment, save for an anomalous feature on the high-energy wing (blue side) of He-like Ar $1s^2$-1s2p (Heα). The He-like and H-like lines were observed during a considerable time interval, but the onset of blue satellite-like features only appeared late in the implosion, and was most intense at peak compression where both the density and the temperature peak. Since the spatial extent of the excited-state orbitals at peak compression was comparable to the average interionic spacing, it has been conjectured that this anomalous broadening may indicate the "*initiation of a plasma-solid phase transition*" [1]. Although it will be a work for the future to clearly define if a solid-state-like phase of ionised matter exists, the present analysis, based on a novel treatment of line broadening relevant to very dense plasmas, gives a quantitative interpretation of the observed satellite-like feature in terms of orbital overlapping.

Description of the Model

Our modelling, partly presented elsewhere [2], is based on a description of the electronic structure of the argon plasma at peak compression in terms of molecular wavefunctions. In traditional line shape theories [3], the electronic structure is calculated by modelling the plasma by a set of independent cells, each containing a radiator and N perturbers (N ions + N' free electrons). The perturbers, considered as point charged particles, are treated in classical mechanics, whereas the radiator is described by the quantum theory. The influence of the N ions on the atomic orbitals of the radiator is then taken into account through an external field (Stark effect). This treatment provides an independent atomic and plasma description and does not account for the overlapping of the excited-state orbitals from neighbouring ions that may occur in dense plasmas. In this context, the use of a *N+1*-centre molecular basis provides a better representation of the electronic structure. Such a description also presents the strong advantage of leading to an exact treatment of the multipolar interaction to all orders. In addition, microfield Molecular Dynamics simulations show that the Nearest Neighbour (NN) distribution gives an adequate approximation to the complete microfield distribution, suggesting that a two-centre description of the electronic structure will provide an approximation to the exact many-centre calculation that is relevant [4].

The two-centre electronic structure is calculated using the approach previously employed [2] extended to account for two bound electrons using a simple Molecular Orbital (MO) approach. Free electrons are treated as non-uniform electron gas. To account for the lowering of the ionisation potential, a cylindrically symmetric confining volume is defined from the particular ionic equipotential that satisfies the electrical neutrality condition. The model is self-consistent electrostatically and Ar bound energies and wavefunctions are obtained from an iterative solution procedure of the Schrödinger and Poisson equations for bound and free electrons respectively. Bound states are calculated in the Born-Oppenheimer (BO) approximation. Consequently the bound electron properties depend on the internuclear separation R as a parameter. The BO approximation is valid because for the plasma parameters considered in this work, where the ionic and electronic temperatures are of the same order, the nuclear velocities are much smaller than both the bound and free electronic velocities. Our approach, which accounts for free electron screening, neglects electron correlation. The accuracy of these calculations has been tested to ensure that the bound energy levels go over to the pure He atomic states when the internuclear separation is increased.

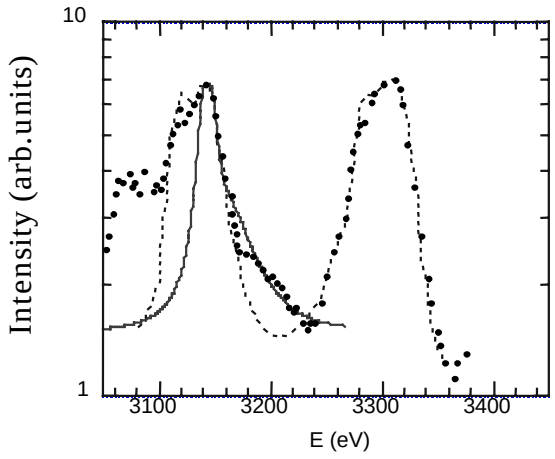

Figure 1. Comparison between Stark- and opacity-broadened theoretical Ar-Heα line profiles and experimental data scanned from Hooper *et al* [1] Contrary to Hooper's fit (---------), the present line shape calculation (_____) is in good agreement with the experimental data in the energy range [3160 eV - 3220 eV]. The present fit was obtained for $N_e = 6.10^{24}$ cm^{-3} and T_e = 800 eV. The low-energy side of the experimental He-like $1s^2$-1s2p is dominated by Li-like satellites, not considered in the present calculation. The experimental background level was taken into account in the computations.

Comparison with experimental data

We compare in figure.1 our calculations of a Stark- and opacity-broadened Heα line profile to the experimental data (scanned from Hooper *et al* [1]). The opacity formula for each Stark line profile employed in our analysis is that appropriate for the normally emergent intensity from a uniformly emitting and absorbing slab [5]. Opacity broadening was accounted for by adjusting the effective optical depth so that the theoretical profile fits the experimental Heα line shape in the core region. The experimental background level was taken into account in our computations. The best fit to the experimental data was found for $N_e = 6.10^{24}$ cm^{-3} and T_e = 800 eV. This is in good agreement with the range of plasma conditions

(i.e. N_e = 4-6.10^{24} cm^{-3}, T_e = 600-900 eV) inferred in reference 1. Computations revealed that the line shape of the blue feature was strongly dependent on the electron density. Increasing the density would broaden the signal and reduce its relative intensity to the resonant component. Although figure 1 shows a quite satisfying agreement between theoretical and experimental line shapes, the theoretical relative intensity of the high-energy satellite-like feature is somewhat higher in the energy region [3160 eV - 3180 eV]. This can be potentially attributed to the density and temperature gradients that may still be present in the experiments as a result of the finite time resolution (t = 60 ps) and not accounted for in the present calculations.

References

1. C.F. Hooper et al,
   Phys. Rev. Letters **63**, 267 (1989).
2. P. Gauthier et al,
   Phys. Rev. E, to be published (July 1998).
3. H. R. Griem,
   «Spectral Line Broadening by Plasmas», Academic Press, New-York (1974).
4. P. Gauthier et al,
   submitted to Phys. Rev. Letters (1998)
5. N. D. Delamater et al,
   Phys. Rev. A **31**, 2460 (1985).

Simulation of Time-Resolved X-ray Diffraction from Shocked Crystals

A Loveridge, J S Wark.

University of Oxford, Clarendon Laboratory, Parks Road, Oxford. OX1 3PU. Email a.loveridge1@physics.ox.ac.uk

A Hauer.

Los Alamos National Laboratory, Los Alamos, NM 87545, U.S.A.

D H Kalantar, SV Weber.

Lawrence Livermore National Laboratory, Livermore, CA 94550, U.S.A.

Introduction

In this report we intend to outline the method of operation of a code we have developed which has the capability of generating simulated time-resolved x-ray diffraction patterns (x-ray streaks), and indicate directions in which we intend to extend this work in the near future. The motivation behind this work is that the lattice dynamics of shocked crystals is not well understood at this time, and so this work is fundamentally interesting, and also there are applications where such a knowledge will prove vital to success - one of which is Inertial Confinement Fusion (ICF).

The current ICF target design employs a crystalline beryllium outer shell, which needs to be uniformly compressed by the shock drive if a clean burn of the deuterium-tritium fuel mixture, and hence energy gain, is to be achieved. During the main stage of the drive the target will be a plasma, however during the start-up phase the target will still be solid, and any instabilities set up in this period will drastically effect the efficiency of the burn. Therefore a detailed knowledge of the dynamics of crystals under shock-drive is of importance.

Also, sub-megabar shocks have been launched into single crystals of silicon and lithium fluoride at the Trident laser facility in Los Alamos, and into silicon at the Nova laser in Livermore, in which the shocks have been observed to propagate. However only a qualitative analysis of the data has been possible at this time.

Theory

The simplest model of x-ray diffraction in crystals is given by Bragg's law:-

$$n\lambda = 2d\mathrm{Sin}\theta_B \tag{1}$$

Its simplicity belies its power to accurately predict the angles of diffraction of any given crystal. Further, when expressed in its differential form:-

$$\frac{\Delta 2d}{2d} = -\Delta\theta\mathrm{Cot}\theta \tag{2}$$

it can incorporate small changes in lattice spacing $\Delta 2d$ caused by the strain we, as shock wave physicists, introduce, and predict the change in diffraction angle $\Delta\theta = \theta - \theta_B$ this causes, where θ is the new angle between the diffracted signal and the crystal surface.

However, this is clearly not a satisfactory model for anything but the most basic of studies. Amongst its faults are that it contains no predictions about the form of the crystal rocking curve (reflection lineshape) and no information about the relative strengths of different reflections. So we must look to a more complicated model, the most appropriate of which is the dynamical model of x-ray diffraction from crystals.

The dynamical theory of x-ray diffraction is the model which must be used when large, perfect crystals are being considered. It was developed initially by Darwin[1)] and modified to include the effects of absorption by Prins[2)]. The wave field within the crystal medium is considered to be made up of the incident beam, the diffracted beam and any secondary diffracted beams, which coherently sum to form the total wave field within the medium. This field interacts with the atoms of the crystal lattice to produce a diffracted signal. For a complete description the reader is referred to the text on the subject by Zachariasen[7)].

The concept of strain within an otherwise perfect single crystal was introduced by Takagi[3,4)] and independently by Taupin[5)] in the 1960's. They achieved this by allowing the $2d$ lattice spacing of the crystal to slowly vary as a function of position within the crystal. This generates an infinite number of differential equations which describe the wave field within the crystal. However this can be reduced to two coupled differential equations if one adopts the case where the wave field contains only two strong components (i.e. the incident and a single diffracted beam). These are known as the Takagi-Taupin equations:-

$$\begin{aligned} i\frac{\lambda}{\pi}\beta_0 \bullet \nabla\mathbf{D}_0(\mathbf{r}) &= \psi_0\mathbf{D}_0(\mathbf{r}) + \psi_H\mathbf{D}_H(\mathbf{r}) \\ i\frac{\lambda}{\pi}\beta_H \bullet \nabla\mathbf{D}_H(\mathbf{r}) &= \psi_0\mathbf{D}_H(\mathbf{r}) + \psi_H\mathbf{D}_0(\mathbf{r}) - \alpha_H\mathbf{D}_H(\mathbf{r}) \end{aligned} \tag{3}$$

where $\mathbf{D}_{0,H}(\mathbf{r})$ are the complex amplitudes of the incident and diffracted waves, $\beta_{0,H}$ are the wave vectors of the incident and diffracted waves, $\psi_{0,H}$ are complex susceptibilities, $\alpha_H = -2(\theta - \theta_B)\mathrm{Sin}\,2\theta_B - \varepsilon\mathrm{Tan}\theta_B$ in the case we are interested in here and ε is the strain perpendicular to the surface of the crystal.

We shall now switch to the more convenient dimensionless units introduced by Zachariasen[7)]. Equation (3) can be specialised by considering the case where α_H depends on only one spatial variable, depth within the crystal. Under these conditions equation (3) reduces to:-

$$i\frac{dX}{dA} = X^2(1+ik) - 2X(y+ig) + (1+ik) \tag{4}$$

where $X(A) = \dfrac{D_H(A)\sqrt{|\gamma_H|}}{D_0(A)\sqrt{|\gamma_0|}}$, A is the dimensionless depth within the crystal, $\gamma_{0,H}$ are the directional cosines of the incident and diffracted beams, $k = \psi''_H / \psi'_H$ (with $\psi_{0,H} = \psi'_{0,H} + i\psi''_{0,H}$), g is the dimensionless absorption parameter and y is the dimensionless deviation from the Bragg angle in dimensionless units.

Wie, Tombrello & Vreeland[6)] showed that this equation could be solved analytically under a layer approximation, so that:-

$$X(A) = \frac{sX_0 + i(B + CX_0)\mathrm{Tan}\left[s(A - A_0)\right]}{s - i(C + BX_0)\mathrm{Tan}\left[(A - A_0)\right]} \tag{5}$$

where $X(A_0) = X_0$, $B = -(1+ik)$, $C = y + ig$ and $s = \sqrt{C^2 - B^2}$. This iterative solution can then be used to build up the rocking curve of a strained crystal.

Time-Resolved Diffraction Code

The starting point for our simulation work is output from the LASNEX[8] hydrodynamic simulation code. LASNEX output is provided by S.V. Weber of the Lawrence Livermore National Laboratory in the form of a series of elastic strain-depth profiles for various times through the duration of the drive laser pulse. The code we have developed takes data of this form and iteratively applies equation (5) for various angles of diffraction around the Bragg angle. In this way, a dynamical rocking curve for each time step, assuming the strain-depth profile provided, can be built up. These rocking curves, when stacked back-to-back, form a simulated x-ray streak of the shock drive process. An example of a simulated streak is given in figure 1.

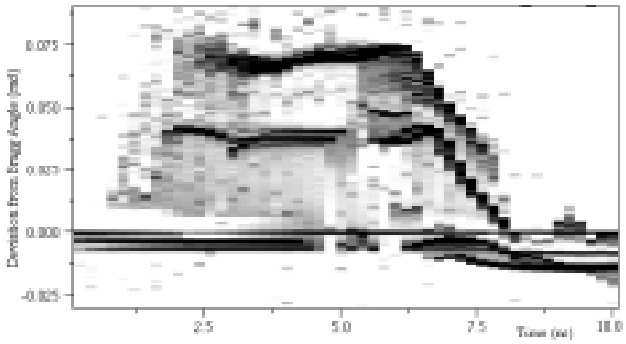

Figure 1. A simulated x-ray streak.

The simulation given in figure 1 assumes a 20 µm thick silicon crystal whose <400> planes are oriented parallel to the front and back faces of the crystal. X-rays from a hohlraum irradiate the back surface of the crystal, driving the shock, and diffraction occurs off the front face. The diffracting x-ray source is assumed to be the $1s2p \rightarrow 1s^2$ transition in helium-like manganese (all of the above are parameters we typically use in experimental work). In it, we can see several interesting features; the twin progagating shocked signals, the drop in intensity of the unshocked signal as the shock reaches the front face of the crystal, and the relaxation that follows. However, the significant point about this simulation is that it is quantitative - it predicts angular shifts and the reflectivity of the various signals, which is something which was previously not possible. This is a unique tool, allowing the people involved with the theoretical work on ICF to directly compare their results with those of the experimental effort.

Experimental Results

In parallel with the simulation work described above, we have been conducting a series of experiments whose purpose is to observe the behavior of crystals under shocked conditions directly. These experiments have been taking place at the Trident laser facility in Los Alamos and the Nova laser at Livermore. An example of the type of time resolved data we have obtained is given in figure 2.

The data in figure 2 was taken on the Trident laser using identical parameters to those used in generating the simulation given in figure 1, with the exception that the shock was generated using a direct drive technique, rather than hohlraum (indirect) drive. Both the shock beam and the beam which drove the x-ray backlighter were 2 ns square pulses, with the start of the x-ray pulse delayed by 2 ns with respect to the start of the shock drive pulse, so that the shock breakout on the front face of the crystal could be observed.

Figure 2 contains many of the features we have just described in figure 1. It has twin shocked signals, a drop in unshocked intensity as the shock reaches the front surface, coinciding with the peak in the shocked signal (indicating that all of the shocked material is strained), and beyond a large, diffuse, relaxation signal. The sharp, vertical feature in the middle of the picture is the "straight through" signal of the camera.

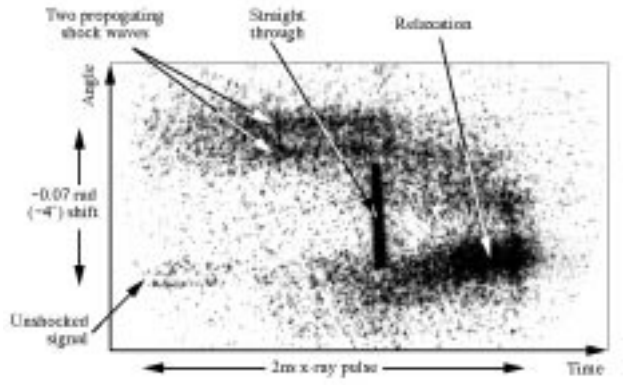

Figure 2. Actual x-ray streak data, taken on Trident shot number 9744.

Future work

Such simulation work as presented above is useful, as it allows direct comparison between simulations and experimental data. However, we intend to use it as a stepping stone to a far more useful code; one will have the capability to extract strain-depth profiles from data of the type given in figure 2. Such a code would prove to be a valuable tool to those interested in studying shock waves in crystals (including, but not limited to, those conducting ICF research) as it would allow direct observation of the shock wave as it propagates.

The way in which such a code would operate is to start with a guessed strain-depth profile, and to use the diffraction code described above to generate a simulated rocking curve based on this. The simulated rocking curve can then be compared with an actual shocked rocking curve and the guessed rocking curve modified accordingly. By repeated application of this process the simulated rocking curve can approach the form of the shocked rocking curve, and the guessed strain-depth profile approach the form of the actual strain-depth profile within the crystal. We have proved this process feasible in the case of monotonic strain-depth profiles, but the technique has yet to be demonstrated in the non-monotonic case.

References

1. Darwin, C. G. (1914). "The theory of x-ray reflexion." Phil. Mag. **27**: 315-33 & 675-91.

2. Prins, J. A. (1930). Zeitschr. f. Phys.(63): 477.

3. Takagi, S. (1962). "Dynamical theory of diffraction applicable to crystals with any kind of small distortions." Acta Cryst. **15**: 1311-2.

4. Takagi, S. (1969). "A dynamical theory of diffraction for a distorted crystal." J. Phys. Soc. Jap. **26**(5): 1239-53.

5. Taupin, D. (1964). "Théorie dynamique de la diffraction des rayons X par les cristaux déformés." Bull. Soc. Franç. Minér. Crist. **87**: 469-511.

6. Wie, C. R., T. A. Tombrello, et al. (1986). "Dynamical x-ray diffraction from nonuniform crystalline films: Application to x-ray rocking curve analysis." J. Appl. Phys. **59**(11): 3743-6.

7. Zachariasen, W. H. (1945). Theory of x-ray diffraction in crystals, John Wiley & Sons.

8. Zimmerman, G. B. and W. L. Kruer (1975). Plasma Phys. Control. Fusion **2**(51).

Effect of a Radiation Field on Ionization in non-LTE Plasma Mixtures

A Djaoui.

CLRC Rutherford Appleton Laboratory, Chilton, Didcot, Oxon., OX11 0QX.

Introduction

The solution of the ionization problem in a typical laser target interaction experiment is complicated because of the existence of many multi-electron ions that can have an extremely large number of excited states. This leads to rate equations that require inversion of impractically large matrices. Furthermore, atomic data is not always available for all quantum states and this has led many authors to develop a variety of simplified and yet adequate models[1,2]. The models rely on either treating a small number of ions and states, or a larger numbers of ions at the expense of averaged (less detailed) states of each ion.

Lee[3] describes such a model for the case of plasmas in steady state. This uses a scaled hydrogenic model but goes beyond the simple average atom model by treating each ionization state and the processes between them explicitly. The plasma is assumed to be optically thin to all photons and no radiative excitation or ionization are taken into account.

In a previous paper[4] we have extended Lee's model to the time dependent case and also generalized its application to mixtures of elements. The calculated ionization for each element in a plasma mixture is consistent with the resulting ambient electron density. This is not the case for models which can only handle a single element and must perform a separate calculation for each element.

In this article we add the effect of radiative excitation and ionization in the presence of a radiation field, either self-emitted by the plasma or externally applied to the plasma. We limit ourselves to Planckian fields, the radiation then being characterized by a temperature. As before we assume that the electron distribution is well approximated by a Maxwellian distribution and no hot electron component is taken into account.

An LTE option (Saha-Boltzmann equations)[5] is provided to allow for cold solid targets as encountered in experiments and to test the high density limit of the non-LTE equations. The resulting code HIMM (Hydrogenic Ionization Model for Mixtures) is applied to typical problems in laser-plasma experiments.

Model

The ionization energies are calculated from More's screening constants and formula[6]. The number of shells included depends on electron density and temperature when continuum lowering is switched on. This is also true of the number of ionization stages since the ground states of low-lying ionization stages may also be pressure ionized.

The ionization potential depression is obtained from a generalized form of the Stewart and Pyatt formula for mixtures. The radius of each ion is calculated under the assumption that if the electron density were uniform, the average volume occupied by each element would contain just Z electrons, where Z is the atomic number of the element. With this prescription, each ion stage of each element has a different value for continuum lowering.

Most of the rates for atomic processes are calculated within the scaled hydrogenic approximation. Collisional excitation rates are taken from either Post[1] or Sampson and Golden[7]. Collisional ionization rates are calculated from the Lotz formula[8]. The rates for the reverse processes are derived from detailed balance.

The radiative spontaneous emission rates and corresponding oscillator strengths are calculated using hydrogenic formulae. Photoexcitation and photoionization rates and the stimulated emissions are derived according to Mihalas[5]. The radiative recombination rates and dielectronic recombination rates are given by Post.

We also include excitation-autoionization from the ground state for the Cu-like[9] and Zn-like[10] ions for elements from selenium to uranium. This last process is found to drastically alter the ionization distribution near the Ni-like stage.

The reverse processes for excitation-autoionization and for dielectronic recombination are not included explicitly. These can be neglected for pure coronal conditions (low densities). In order for the model to recover the LTE value at high densities, the following 'ad-hoc' procedure is used.

The direct solution of the time-dependent rate equations for all species (elements) is complicated. There can be large differences in rate coefficients and this leads to a stiff problem. Stability considerations favor an implicit finite difference scheme, which then requires inversion of large matrices. Our approach is to deal with each species separately within an iterative procedure. Iteration is required whenever continuum lowering is included or when the mass density or atomic number density are specified instead of electron density. With the assumption that energy levels couple to the ground state of the next ionization stage only, the finite difference equations are cast into a tridiagonal form which can be solved efficiently. This assumption is valid when direct ionization from singly excited states dominates. Coupling to excited states of the next ionization stage can occur when inner shell excitation and ionization become significant. Modeling of these processes would require detailed energy levels and cross sections and is beyond the work presented here.

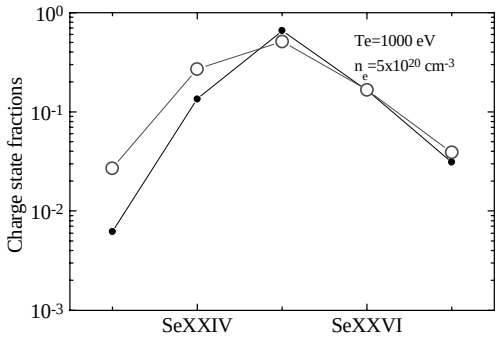

Figure 1. Ionization distribution in selenium

Results

Comparisons:

In figure 1, we compare the non-LTE results from our model to Lee's[3] for a selenium plasma in steady-state and at a fixed electron density and temperature. The empty circles are taken from Lee's work[3] while the dots are the results from our model. Both codes predict the dominance for the Neon-like ionization stage. The small difference between the codes is the result of differences in rate coefficients.

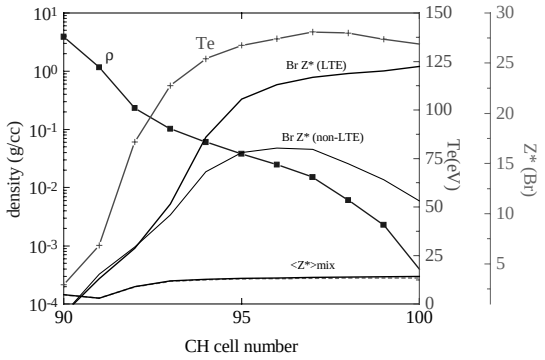

Figure 2. Ionization in brominated plastic when the effects of a radiation field are neglected.

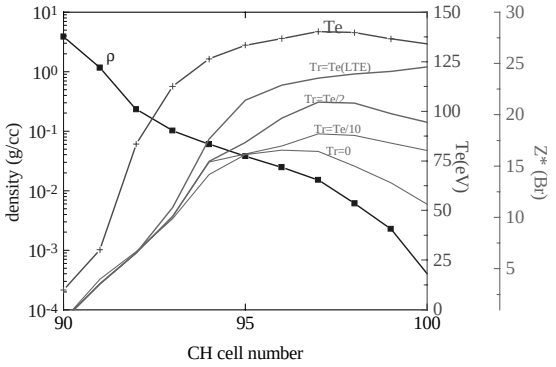

Figure 3. Effect of a radiation field on Br ionization in a brominated plastic.

Effect of radiation field:

Neglect of radiative rates is valid when the plasma is optically thin to all photons. This is no longer the case if an external radiation field (in addition to the plasma self emission) is present. Such situation occurs in the plasma surrounding a capsule which is irradiated by x-rays inside a hohlraum in indirect drive inertial confinement fusion experiments. The outside of the capsule is made of brominated plastic (CH with 0.25% Br and 5% O) shell which is heated with x-rays fom the wall of the hohlraum. The x-rays penetrate through the ablated material and are deposited in the plastic shell. The opacity of the heated material has then a direct effect on the penetration depth of the x-rays and possibly on the performance of the capsule.

Figure 2 shows typical density-temperature conditions as well as the ionization state of the plasma when no radiation is taken into account. Although the non-LTE ionization for Br is quite different from the LTE value the average values <Z*>mix in the plasma (C, H, Br and O) are similar. The low atomic number elements (C, H, and O) in the mixtures are in LTE and since they constitute the major fractional part of the plasma, they effectively determine the average ionization. Br being a minor constituent has no effect on the average ionization but has a much larger opacity. As a result Br has a major contribution to the total opacity. The effect of including a radiation field on the ionization of Br is shown in figure 3. As the radiation temperature approaches the electron temperature (from Tr=0 to Tr=Te) the ionization of Br tends towards LTE. The effects of radiation are more important in the ablated, low density plasma through which x-rays from the hohlraum propagate. The tendency towards LTE in the presence of radiation partly justifies the use of LTE opacities in previous simulation of these ICF capsules. It should be noted however that a more detailed simulation should solve the radiative transfer equation for a local photon spectrum, which should then be used for calculating radiative rates at each point in the plasma.

Summary

A general ionization model for laser produced plasmas which is applicable over a wide range of temperatures and densities is presented. Both LTE and non-LTE equations are solved. The model allows for more than one atomic species, as encountered in many laser-produced plasmas. Energy levels for each shell (having a given principal quantum number), of each ion stage and of each species, are calculated using screening constants. Screened hydrogenic rates are used for most atomic processes. Excitation-autoionization rates are included for Cu-like and Zn-like ions. The effect of a radiation field are also included and are shown to drastically modify the non-LTE, optically thin (Tr=0) results for Br in an ICF target ablator shell.

References

1. Post D.E., Jensen R.V., Tarter C.B., Grasberger W.H. and Lokke W. A.,
At. Data and Nucl. Tables, 20, 397 (1977)

2. Djaoui A. and Rose S.J.,
J. Phys. B: At. Mol. Opt. Phys, 25, 2745 (1992)

3. Lee Y.T.,
J. Quant. Spectrosc. Radiat. Transfer, 38, 131 (1987)

4. Djaoui A.,
J. Quant. Spectrosc. Radiat. Transfer,
'accepted for publication'.

5. Mihalas D.,
Stellar Atmospheres, Freeman, San Fransisco, CA, (1978)

6. More R.M.,
'Atomic physics in inertial confinement fusion',
Applied Atomic Collision Physics, 2,
Academic Press, New York (1982)

7. Sampson D.H. and Golden L.B.,
Astrophys. J., 170, 169 (1971)

8. Lotz W.,
Astrophys. J. Suppl., 14, 207 (1967);
Z. Phys. 216, 241 (1968)

9. Mitnik D., Mandelbaum P., Shwob J.L., Bar-Shalom A., Oreg J., and Godlstein, W. H.,
Phys. Rev. A, 53, 3178 (1996)

10. Mitnik D., Mandelbaum P., Shwob J.L., Bar-Shalom A., and Oreg J.,
Phys. Rev. A, 55, 307 (1997)

11. Osterheld A.L., Young B.K.F., Walling R.S., Goldstein W.H., Scofield J.H., Chen M., Shimkaveg G., Carter M., Shepherd R., MacGowan B.J., Da Silva L., Matthews D., Maxon S., London R. and Stewart R.E.,
Proceedings of Int. Colloquium on X-ray Lasers,
Schliersee, Germany, Inst. Phys. Conf. Ser. No 125: pp 309-314, (1992)

A simple, quick and accurate method of evaluating escape factors

G J Tallents.

Department of Physics, University of Essex, Colchester CO4 3SQ. Email tallg@essex.ac.uk

Simulating the effects of opacity on quantum state populations and the emission of radiation from laser-produced plasmas is often made with hydrodynamic coupled to atomic physics codes such as MEDUSA[1)] and EHYBRID[2)]. The transfer of radiation is calculated using escape factors[3)]. It is possible to evaluate the effects of velocity gradients on the escape factors using the notion of the Doppler decoupling length[4)]. Recent calculations of spectral line profiles using escape factors with Doppler decoupling have been compared with high resolution experimental measurements[5,6)]. In this paper, we illustrate a simple technique for evaluating escape factors which is valid over the optical depth range from 0 to 50 typically found in laser-produced plasmas.

Escape factors have two similar, but not identical[7)] uses in modelling radiation transfer. In one sense, an escape factor is a parameter which multiplies a radiative transition probability to allow for the process of photo-excitation. In the other sense, an escape factor multiplies the emission expected from a plasma if it were optically thin to allow for the effect of opacity. In the astrophysical literature, these two meanings are given different names to distinguish them: respectively, the net radiative bracket and the escape probability[7)]. In the first sense, the escape factor for radiation at a particular wavelength is simply $\exp(-\tau)$,where τ is the optical depth from the element considered to the surface of the plasma. Considering the second sense, the escape factor T_o at a particular wavelength for a plasma of constant source function is given by an integration of the equation of radiative transfer to give

$$T_o = \frac{1-\exp(-\tau_{tot})}{\tau_{tot}} \qquad (1)$$

where τ_{tot} is the optical depth through the plasma. In many calculations, the line intensity integrated over the spectral line profile is required. In the second sense of the escape factor this gives for a Gaussian line profile and constant source function

$$T_1 = \frac{1}{\tau^o_{tot}\sqrt{\pi}} \int_{-\infty}^{\infty} [1-\exp(-\tau^o_{tot} e^{-y^2})]dy = \sum_{m=0}^{\infty} \frac{(-1)^m (\tau^o_{tot})^m}{m!(m+1)^{3/2}} \qquad (2)$$

where τ^o_{tot} is the optical depth at line centre through the plasma. An asymptotic expression valid for $\tau^o_{tot} >> 2$ has been given by Rose[8)], viz.

$$T_1 = \frac{1}{\tau^o_{tot}\sqrt{\pi}} \left\{ 2(\ln \tau^o_{tot})^{1/2} + \frac{\gamma}{(\ln \tau^o_{tot})^{1/2}} - \frac{1}{8}[\gamma^2 + \frac{\pi^2}{6}] \frac{1}{(\ln \tau^o_{tot})^{3/2}} \right\} \qquad (3)$$

where $\gamma = 0.577$ is Euler's constant.

In the first sense of the escape factor, a similar integration over a Gaussian line profile produces

$$T_2 = \frac{1}{\sqrt{\pi}} \int_{-\infty}^{\infty} e^{-y^2} \exp(-\tau_o e^{-y^2}) dy = \sum_{n=0}^{\infty} \frac{(-1)^n (\tau_o)^n}{n!\,(n+1)^{1/2}} \qquad (4)$$

where τ_o is the optical depth from the element considered to the plasma edge at the line centre. A well-known asymptotic expression valid for $\tau_o > 3$ is

$$T_2 = \frac{1}{\tau_o (\pi \ln \tau_o)^{1/2}} \qquad (5)$$

We have found that equations (2) and (4) can be fitted with an expression similar to equation (1) with a simple modification of the optical depth to an 'effective' value. Writing for τ_o or τ^o_{tot}, and dropping the subscipts, we define a new τ' for use in equation (1) such that

$$\tau' = a\,\tau^b \qquad (6)$$

where a and b are parameters determined by the fit of the escape factor of equation (1) form. For T_1, we have a = 0.71, b = 0.87 and for T_2 , a = 1.45, b = 1.25. Equation (1) with this modified optical depth can be evaluated much more quickly than equations (2) and (4) and the fits are accurate to within a few percent for all optical depths less than 50.

Escape factors of the form of equation (1) can be analytically integrated to give average angular values. We assume a planar, one dimensional plasma which is a good approximation for most laser-produced plasmas. The optical depth $\tau(\phi)$ at an angle ϕ to the normal to the plane of symmetry (the target normal for laser produced plasmas) is then

$$\tau(\phi) = \frac{\tau(0)}{\cos\phi} \qquad (7)$$

and the angle averaged escape factor <T> is given by

$$<T> = \int_0^1 T\,du \qquad (8)$$

where u = cosϕ. For an optical depth of the form of equation (6) and escape factor of the form of equation (1), the angle averaged value is given by

$$<T> = \frac{1}{a\tau^b}\left[\frac{1}{b+1} - \frac{E_i(2+1/b, a\tau^b)}{b}\right] \qquad (9)$$

where $E_i(n, y) = \int_1^{\infty} \frac{\exp(-yt)}{t^n} dt$ is the exponential integral. This angle averaged expression can be accurately fitted to an equation of the form of equation (1) provided the optical depth τ is modified, viz.

$$\tau'' = (b+1)a\,\tau^b \qquad (10)$$

Modified escape factors using the above fitting procedure have been incorporated into the EHYBRID code for the evaluation of spectral line intensities emitted in x-ray laser experiments[9,10)]. The effect of velocity gradients can be taken into account by simply integrating the absorption coefficient over the Doppler decoupling length[5,6,9)] to calculate the optical depth or by a similar fitting procedure as outlined here, but with the absorption coefficient scalelength to Doppler decoupling length as an additional parameter in the determination of the a and b coefficients[11)].

References

1. J P Christiansen et al
   Comput. Phys. Commun. 7, 271, (1975)
2. P B Holden et al
   J Phys. B27, 341, (1994).
3. F E Irons
   JQRST 22, 1, (1979)
4. G B Rybicki and D G Hummer
   Astrophys. J 219, 654 (1978)
5. A Djaoui et al
   JQRST 52, 531, (1994)
6. J S Wark et al
   Phys. Rev. Lett. 72, 1826, (1994)
7. F E Irons
   JQRST 45, 217, (1991)
8. S J Rose
   J Phys B31, 2129, (1998)
9. A Demir et al
   Phys Rev E55, 1827, (1997)
10. A Demir et al
    in preparation.
11. G J Tallents and A Demir
    in preparation.

Electron parametric instabilities in short ultra-intense linearly-polarized laser pulses

H C Barr, P Mason, D M Parr.

Department of Physics, University of Essex, Colchester, England, CO4 3SQ. Email barrhc@essex.ac.uk

Introduction

The relativistic mass increase of electrons in ultra-intense laser pulses causes induced transparency of the plasma, saturation of the electron quiver velocity and gives rise to new parametric instability regimes[1-3]. The latter generate laser harmonics and are Raman-like when coupling between light waves is due to density fluctuations or are of the relativistic modulational and filamentation type when the coupling is due to fluctuations in the electron mass increase[4-5]. Laser light of frequency and wavenumber $(\omega_0, \mathbf{k}_0)$ couples any fluctuation at $(\omega,\mathbf{k})$ to a hierarchy of fluctuations at $(\omega+n\omega_0,\ \mathbf{k} + n\mathbf{k}_0)$ where n is an integer. When two or more of these fluctuations simultaneously correspond to resonant modes (or quasimodes) of the laser-plasma system, parametric instability is possible. This is irrespective of whether the laser is circularly polarized (purely harmonic) or linearly polarized (where the anharmonic electron motion is comprised of harmonics $(n\omega_0,n\mathbf{k}_0)$ each of which contribute as pump waves). We adopt an approach which is applicable for any density, laser intensity and polarization, or scattering geometry. Here we show results for the decay of an intense linearly polarized laser pulse in underdense plasma and look at scattering in the plane of polarization.

Method

We perform the analysis in the proper frame of the pulse, i.e. Lorentz-transform to the pulse group velocity $\mathbf{u}=\mathbf{k}_0c^2/\omega_0$. The laser pulse phase becomes $\eta = -\omega_0 t'/\gamma_u$ where $\gamma_u = (1-u^2/c^2)^{-1/2}$ so that the laser, in this frame, appears as a homogeneous oscillation having zero magnetic field. The exact periodic but anharmonic solution is obtained numerically from the non-linear but simple differential equation

$$\ddot{\mathbf{p}}_0 + \omega_{po}^2(\mathbf{p}_0 / \gamma_0 + m\mathbf{u}) = 0 \qquad (1)$$

where the pump wave electron momentum is $\mathbf{p}_0$, the mass increase $\gamma_0=(1+p_0^2/m^2c^2)^{1/2}$ and we define a relativistic plasma frequency $\omega_{pr}(t)=\omega_{po}/\gamma_0^{1/2}(t)$ where ω_{po} is the pulse frame plasma frequency. These pump parameters are time dependent only and give no **k**-space coupling in the linearised equations. When Fourier transformed in space, these can be written in the form (quantities normalized to laser parameters)

$$\ddot{\mathbf{b}} + (\omega_{pr}^2(t) + k^2)\mathbf{b} = ik\mathbf{c}_2(t)(k^2\phi + \omega_{pr}^2(t)(\phi - \dot{\psi})) \qquad (2)$$

$$\dot{\phi} + \omega_{pr}^2(t)\psi = -ik^{-1}c_1(t)(k^2\phi + \omega_{pr}^2(t)(\phi - \dot{\psi})) \qquad (3)$$

$$\dot{\psi} - \phi = -ikc_1(t)\psi + ik^{-1}\mathbf{c}_2(t)\cdot\mathbf{b} \qquad (4)$$

where $\mathbf{b}$ is the magnetic field, ϕ the electric potential and $i\mathbf{k}\phi$ the irrotational part of the electron momentum ($\mathbf{p}=\mathbf{a}+i\mathbf{k}\psi$, $\mathbf{a}$ is the vector potential and $\mathbf{b}=i\mathbf{k}\times\mathbf{a}$). The periodic coupling terms are $c_1(t)=\hat{\mathbf{k}}\cdot\mathbf{p}_0(t)/\gamma_0(t)$, $\mathbf{c}_2(t)=\hat{\mathbf{k}}\times\mathbf{p}_0(t)/\gamma_0(t)$. Since the coefficients are periodic, they admit Floquet solutions whose characteristic exponent gives the dispersion characteristics. The standard procedure is to Fourier analyze in time, obtaining an infinite set of coupled-mode equations whose solution gives the dispersion relation. This requires an *analytic* form for the zero order solution which is only available in certain limiting cases[6].

Here we evolve the above system of ordinary differential equations in time for given values of **k**. The growth is then easily obtained from the time signal after a few e-foldings and the frequencies and mode-structure obtained by applying an Fast Fourier Transform routine to the solution.

Results

Assume a laser pulse propagating in the **x** direction, polarized in the **x-y** plane with amplitude $q = eA_0/mc^2 \approx 8.5\times10^{-10}\lambda_L(\mu m)I_L^{1/2}(Wcm^{-2})$. The dispersion relation in the laboratory frame $\omega_0^2 = \omega_{pr}^2+k_0^2c^2$ becomes $\omega_0' = \omega_{pr}$ in the pulse frame where $\omega_{pr} = \omega_{po}^{lab}/\gamma_a^{1/2}$ and $\gamma_a=(1+q^2/2)^{1/2}$. We consider here scattering in the plane of polarization and choose a density of $n_0=0.1n_c$ where n_c is the laser critical density.

Figure 1 is a contour plot of the normalized pulse-frame growth rate ν'/ω_{pr} plotted in the laboratory frame (k_x,k_y)-plane for intensities ranging from weakly to strongly relativistic. A clear pattern of peak growth lobes is apparent which represent a combination of phase matching and optimal driving. As a guide, the dashed lines are the circles $(k_x-nk_0)^2 + k_y^2 = n(n-2\omega_{pr})$ along which phase matching occurs between a resonant plasma wave $\omega=\omega_{pr}$ and a resonant scattered wave $\omega_s=n\omega_0-\omega_{pr}$ coupled through $n-1$ intermediate non-resonant oscillations. We index each maximum growth lobe as $n.m$ where n refers to the harmonic number (dashed circle) and m is an integer counting the peak growth points in a clockwise direction along circle. This figure exhibits stimulated back, side and forward Raman scattering (SRBS, SRSS, SRBS), the relativistic modulational and filamentation instabilities (RMI, RFI) and includes mode-coupling to all orders and driving by all harmonics in the laser driver. The narrow peaks $n.1$ correspond to SRFS emission emerging at increasingly oblique angles as n rises. The lobe 1.2 is the usual SRBS. The lobes $n.2$ for $n>1$ are SRSS at increasingly oblique directions relative to the backscattering direction. For higher harmonics, new sequences of SRBS and SRSS occur ($m\le(n+3)/2$ for n odd, $m\le(n+2)/2$ for n even). For $q<1$, emission is predominantly at the first harmonic with only weak growth at higher harmonics. Growth at all harmonics rises rapidly with q until $q\approx1$; thereafter a full complement of lobes appears with comparable growth rates over a wide region of **k**-space representing emission into many harmonics and into a set of well-defined scattering angles. There is only a very slow fall-off in growth with harmonic number[1,2]. Although these lobes lie close to the lines predicted by the phase matching argument above, there is significant deviation from weak coupling theory. The growth is such that $\nu \sim\omega \sim \omega_{pr}$ and hence is in an intermediate regime between weakly and strongly coupled.

Figure 2 shows a typical multimode structure of modes of $\omega+n\omega_0$ for the lobe 4.1 which corresponds to scattering into the fourth harmonic at an angle of 51° to the forwards direction. The dominant peak at $\omega=-4\omega_0+\omega_{pr}$ in the vector potential $a(\omega)$ and the peak at $\omega\approx\omega_{pr}$ in the scalar potential $\phi(\omega)$ are resonant scattered and plasma waves respectively coupled through intermediate nonresonant modes; other nonresonant modes outside this range are also generated and need to be included to obtain accurate growth rates.

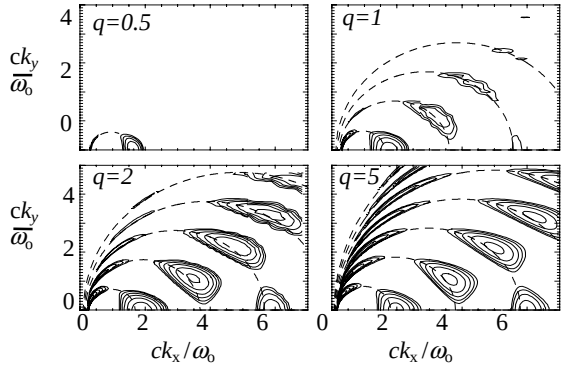

Figure 1. Contour plot of pulse frame growth rate ν'/ω_{pr} versus laboratory (k_x,k_y). Contour range is 0.05(0.02)0.13.

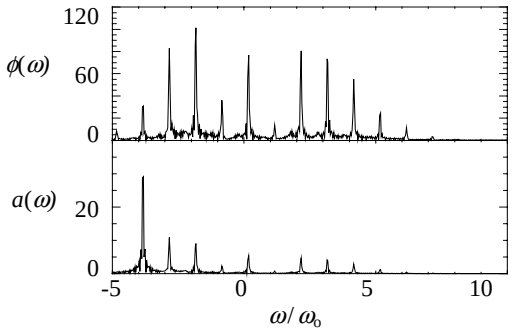

Figure 2. Mode composition of a(ω), $\phi(\omega)$ versus frequency for lobe 4.1 when $q=2$.

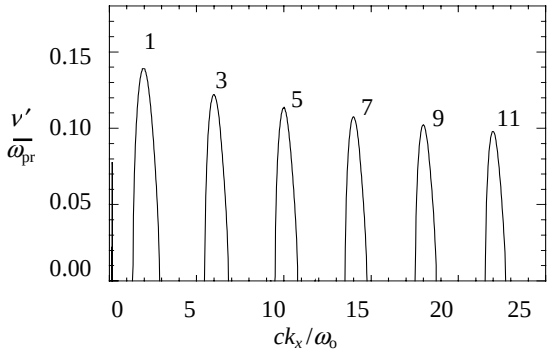

Figure 3. Growth rate ν'/ω_{pr} versus k_x when q=5 for exact back and forward scattering.

Figure 3 shows the growth for $q=5$ in the directly back and forward scattered directions. The very narrow left most peak represents a hybrid of SRFS/RMI in which the two instabilities overlap and interfere to produce a 6-mode instability consisting of Stokes and anti-Stokes EM modes at $\omega_s \approx \omega_0 \pm \omega_{pr}$ and three electrostatic modes at $\omega \approx \omega_{pr}$ and $\omega \approx 2\omega_0 \pm \omega_{pr}$. The second peak (lobe 1.2) is the usual backscattering while the remaining peaks show backscattering at odd harmonics of the laser whose growth decays weakly with harmonic number n.

Figure 4 shows the growth rate for purely relativistic filamentation. This is a coupling of EM modes through nonresonant purely growing transverse fluctuations. Successive peaks represent generation of exact laser harmonics; filamentation at the fundamental dominates where the transverse wavenumber locks at $k_y=0.6\omega_{pr}$ for all $q>1$.

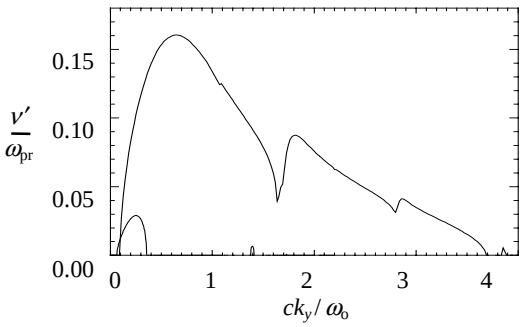

Figure 4. RFI growth rate ν'/ω_{pr} versus k_y for q = 0.5, 5.

Figure 5 indicates the emission angles versus frequency for radiation arising from each of the lobes in figure 1. They show forward scattering $0 < \theta_s < \pi/2$ occurring predominantly into a single angle for each harmonic; this becomes more oblique with increasing harmonic number such that $\theta_s \rightarrow 54°$. In backscattered directions, $\pi/2 < \theta_s < \pi$, emission occurs at m_{max} distinct angles for a given harmonic number n where $m_{max} \le (n+3)/2$ when n is odd, $m_{max} \le (n+2)/2$ for n even.

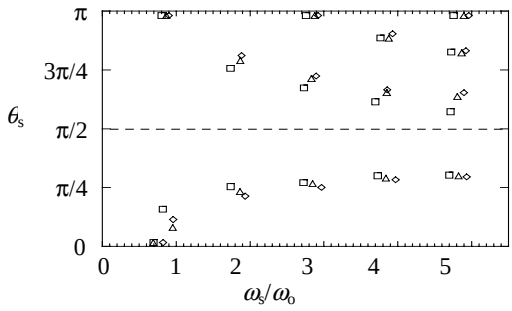

Figure 5. Emission direction versus frequency when q =1(□),2(Δ),5(◊) for each lobe *n.m.*

In conclusion, analysis carried out in the laser pulse proper frame provides a general, rugged and easily applied method for establishing the dispersion characteristics of electron parametric instabilities in which the pump may be anharmonic and the instability involve many modes.

References

1. P. Sprangle and E. Esarey
Phys. Rev. Lett, 67 2021, (1991).

2. A.S. Sakharov and V.I. Kirsanov
Plasma Phys. Rep., 21 596, (1995).

3. J.M. Rax and N.J. Fisch
IEEE Trans. Plasma Sci., 21, 105 (1993);
E. Esarey et al.
IEEE Trans. Plasma Sci., 21, 95 (1993).

4. C.J. McKinstrie and R. Bingham
Phys. Fluids B, 4 2626, (1992).

5. B. Quesnel *et al.*
Phys. Rev. Lett., 78 2132, (1997);
S. Guérin *et al.*
Phys. Plasmas, 2 2807, (1995).

6. A.I. Akhiezar and R.V. Polovin
Sov. Phys. JETP, 3 696, (1956).

Higher Order Effects in Ultra-broadband Multi-frequency Raman Generation

G S McDonald, G H C New, Yuk-Ming Chan.

LASP, Blackett Laboratory, Prince Consort Road, Imperial College, London SW7 2BZ. Email g.mcdonald@ic.ac.uk

L L Losev, A P Lutsenko.

P N Lebedev Physical Institute, Leninsky Prospekt 53, 117924 Moscow

Introduction

Ultra-broadband Multi-frequency Raman Generation (UMRG) is one of the most novel nonlinear optical processes to have emerged over the last few years. With H_2 gas as the Raman medium, our analyses have predicted that nearly 50 distinct frequencies of comparable energy may be generated [1-4]. More recent calculations for UMRG in air at atmospheric pressure, have predicted that beams containing around 150 waves may be attained [5]. Experimental results, that support our overall predictions, are appearing in the literature. However, in some configurations, effects which are additional to the main UMRG process also come into play. We have investigated a range of such higher order effects and their implications for the efficiency of ultra-broadband light generation. We outline here results dealing with two particular higher order effects: competing nonlinear processes and detuning of the UMRG pumps from the Raman resonance of the medium.

Results

Our model equations have been generalized to incorporate a *non-parametric* competing signal and a quantitative study undertaken of its affect on the primary UMRG process. An effective gain-length product for the parasitic process, Z^{eff}, was introduced and a simple analytical model developed for the case of competing processes arising from background noise or amplified spontaneous emission. Model predictions were found to be in good agreement with full numerical simulations, and showed that the efficiency and character of UMRG can effectively drive such parasitic processes below threshold, $Z^{eff} < Z^{th} = 25$ (see figure 1). Moreover, multi-frequency conversion was also found to be robust when competing signals grew from a strong seed, as could arise from the scattering of a UMRG pump beam [6].

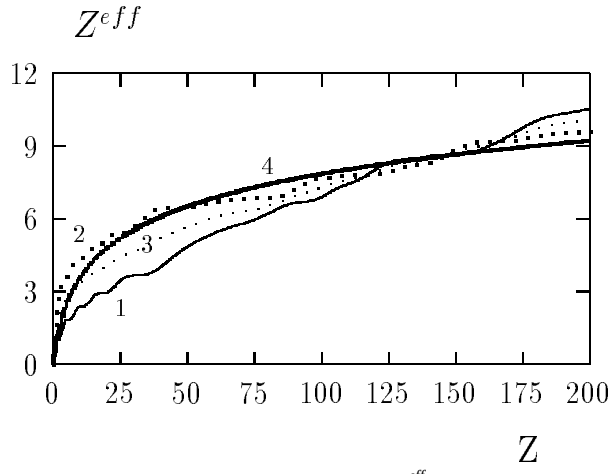

Figure 1. The effective gain-length, Z^{eff}, for competing processes as a function of normalized distance, *Z*. Curves 1-3 are from simulation data while curve 4 is the analytical model

A second key issue is the effectiveness of experimental configurations in which independent oscillator/amplifier chains generate the two-colour pumping for UMRG. In this case, the pumping may not be exactly tuned to the Raman resonance of the nonlinear medium. Thus, detuning has been incorporated into the model equations and analytical and numerical investigations have been undertaken.

For cases of negligible dispersion, we derived an exact analytical solution for the medium polarization wave *P*. This wave defines the parametric gain in the system which, in turn, is directly proportional to the bandwidth generated. We found that this analysis accurately predicts new qualitative and quantitative features of bandwidth generation which arise from detuning of the pump beams (see figure 2).

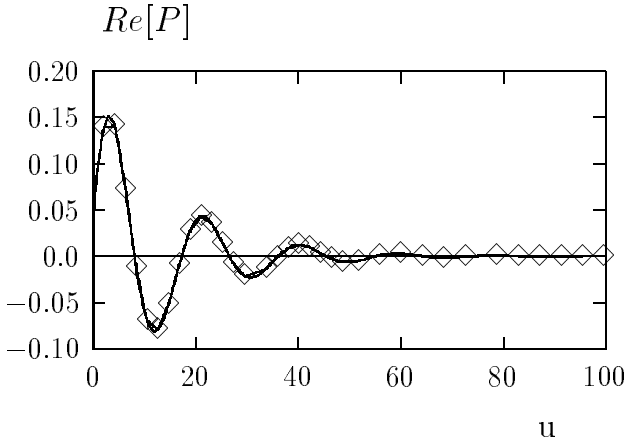

Figure 2. Comparison of analysis and simulation data for the evolution of the real part of the polarization wave when detuned pump beams are employed (*u* is the propagation distance)

While we have shown that non-parametric competing effects need not present any problems, it is also plausible that frequencies of the UMRG spectrum could *parametrically* generate a parasitic wave. Our results on detuning effects have been used to assess this possibility and we found that UMRG can also be robust in this respect.

References

1. L L Losev and A P Lutsenko
Kvantovaya Electron, 20 1054, (1993)

2. G S McDonald, G H C New, L L Losev, A P Lutsenko and M J Shaw
Opt. Lett., 19 1054 (1993)

3. G S McDonald, G H C New, L L Losev, A P Lutsenko and M J Shaw
Inst. Phys. Conf. Series, 140 85 (1995)

4. G S McDonald
Opt. Lett., 20 822, (1995)

5. G S McDonald, G H C New, L L Losev and A P Lutsenko
J. Phys. B, 30 719 (1997)

6. G S McDonald, G H C New, Yuk-Ming Chan, L L Losev and A P Lutsenko
J. Mod. Opt., 45 1099 (1998)

Numerical Investigation of the Absorption of Multipulse Pumping

M Tagviashvili*, G Tallents.

Department of Physics, University of Essex Colchester CO4 3SQ UK Email mado@essex.ac.uk tallg@essex.ac.uk

**Permanent affiliation Institute of Physics, 6 Tamarashvili Str Tbilisi 380027 Georgia Email mado@physics.iberiapac.ge*

Introduction

Enhancement of the efficiency of generating Ne-like X-ray laser output with multipulse irradiation has been demonstrated in several experiments. Various multiple pulse irradiation configurations have been investigated [1, 2] experimentally. Nevertheless, the experimental determination of the optimum pumping pulse configuration parameters such as the time interval between pulses and the intensity of the different pulses is very difficult [2]. Numerical simulations can indicate the optimum pumping condition and elucidate the important physical parameters. However, many X-ray laser simulation codes do not allow for rigorous calculation of the absorption of laser light near the critical density. The code described here [3] ("Kavta") does this with a calculation of the propagation of the laser light by a selfconsistent solution of Maxwell's equations with a hydrodynamical two temperature systems of equations.

Description of the Hydrocode "Kavta"

Plasma dynamics is described via a one dimensional two-temperature hydrocode with electron and ion thermal conductivity, both natural and artificial ion viscosity, relaxation of energy between ions and electrons and ponderomotive force impact on plasma motion. Due to the ponderomotive force, the scale of the hydrodynamical inhomogeneity is of order the scale of the wave length of the laser irradiation and a very fine spatial grid is used to model in detail the shape of the density profile in the expanding plasma. The detailed density and temperature profiles enable the proper calculation of laser fields and absorption in each cell of the grid. Maxwell's equations are solved for normal incident laser irradiation. The ionic populations in the plasma are estimated via a set of atomic rate equations for the population of the ground states.

The equation of state, electron-ion collisional frequency, electrical and heat conductivity are taken into consideration using parameters according to More's [4] model. The target dynamics from the low temperature solid state during the low intensity long pre-pulse to the ideal gas during the high intensity main pulse are thus well modelled.

Computational model

We simulated experiments on the LULI Nd-glass laser system at Ecole Polytechnique in Paris. Three beams at 1.06 μm wavelength were irradiated in a line focus geometry on an iron slab target. Lasing at 25.5 nm with gain coefficient at 15+/– 3 cm^{-1} for a 20 mm long target was achieved. A single pre-pulse and double main pulse was used for the driving beams (option C in the numerical simulations, see table1). Three other laser multipulse configurations modelled in the numerical experiments are (see table 1): single main pulse (A) and multipulses with different intervals of time between pre-pulse and first main pulse (option B and D). The duration of each pulse was equal to 75 ps and the laser irradiation wave length was equal to 1.06 μm. A plane Fe target in the numerical simulations with thickness 13 μm, initial density 7.87 g/cm^3 and initial temperature 0.1e-3 eV was assumed.

Results of numerical simulations

The numerical experiments show that the absorption for the single pulse is low. About 25% of incident energy is absorbed during the single pulse. For the multipulse configuration absorption increases to 80%-90% (figure 1). The maximum electron temperature increases from 170 eV to 550 eV and maximum ionisation from 16 to 18 when a pre-pulse is employed. Figure 2 shows that the plasma density and electron temperature profiles at the end of a single pulse have greater gradient then at the end of the first main pulse with multipulse irradiate. It is evident that multipulse irradiation increases the scale length of density profiles and decreases the refraction of a propagating X-ray laser beam.

N	Intensity Pulse 1 W/cm^{-2}	Interval Pulses 1-2 (ns)	Intensity Pulse 2 W/cm^2	Interval Pulses 2-3 (ns)	Intensity Pulse 3 W/cm^2
A	$1.9x10^{13}$				
B	$1.9x10^{9}$	1.5	$1.9x10^{13}$	0.8	$1.6x10^{13}$
C	$1.9x10^{9}$	2	$1.9x10^{13}$	0.8	$1.6x10^{13}$
D	$1.9x10^{9}$	4	$1.9x10^{13}$	0.8	$1.6x10^{13}$

Table 1. Single (A) and multi (B,C,D,) pulse configurations.

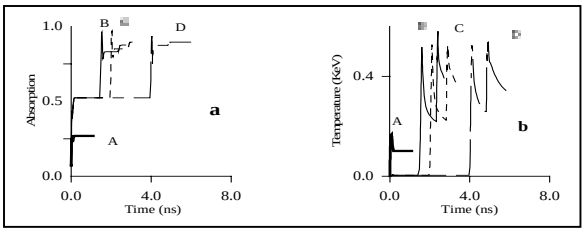

Figure 1. Fraction of absorption (a) and electron temperature (b) for the single pulse (A) and B,C,D multipulses in time.

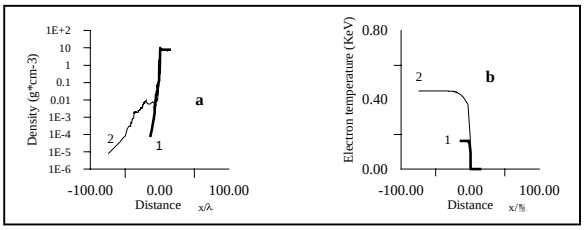

Figure 2. Plasma density (a) and electron temperature (b) profiles at the end of the single pulse (1) and at the end of the first main pulse (2). The laser is assumed incident from the left and the distance scale is in wavelength units (λ=1.06μm)

References

1. R Smith, A MacPhee, G Tallents, Ph Zeitoun, F Albert, A Carillon, P Jaegle, G Jamelot, C L S Lewis, A Klisnick, M Maillard, D Ros, S Sebban. CLF Annual report for 1997, p 36

2. J Y Lin, G J Tallents, A Demir, S B Healy, G Pert, J Appl Physics 83,1863, (1998)

3. N N Demchenko, V B Rozanov, M N Tagviashvili. Sov J Plasma Physics 16 , 812, (1990).

4. R M More. Handbook of Plasma Physics, 3, 63, (1991)

Science – Lasers *for* Science Facility Programme

1) Chemistry

2) Physics

3) Biology

Rate Coefficients for Energy Transfer from High Rotational Levels of NO($X^2\prod_{1/2}$, v = 3) in Collisions with He, Ar and N_2

M Islam, I W M Smith.

School of Chemistry, The University of Birmingham, Edgbaston, Birmingham B15 2TT.
Email islammz@novell5.bham.ac.uk, i.w.m.smith@bham.ac.uk

Introduction

Double resonance (DR) experiments provide a powerful technique of investigating the spectroscopy and dynamics of molecules in specific quantum states. Over the past few years, such methods have been employed in Birmingham in a series of studies on vibrational and rotational energy transfer in collisions involving molecules in selected rovibrational levels [1 - 3]. This state-selection is provided using a pulsed infrared (IR) laser, either an optical parametric oscillator or a difference-frequency laser, which is tuned to an absorption in a fundamental or overtone band of the molecule of interest. The subsequent fate of these excited molecules is examined using a tunable ultraviolet (UV) laser to excite laser-induced fluorescence (LIF) signals. Two kinds of measurement can be made. Either (a) the frequency of the UV probe laser can be fixed, for example to a transition out of the level that is directly populated by the IR pump laser, and the time delay between the two laser pulses can be varied, or (b) the time delay can be fixed and the frequency of the UV laser scanned to record an LIF spectrum. Kinetic experiments of type (a) provide values of the rate coefficients for removal from a particular rovibrational level, usually by rotational energy transfer (RET) as vibrational relaxation is generally much slower. Spectroscopic measurements of type (b) yield state-to-state rate coefficients for transfer between specific pairs of levels. These two laser IRUVDR experiments have been applied to collisions involving HCN, C_2H_2 and NO and the dependence of the rates of collisionally-induced transfer on initial state, collision partner and temperature have been examined.

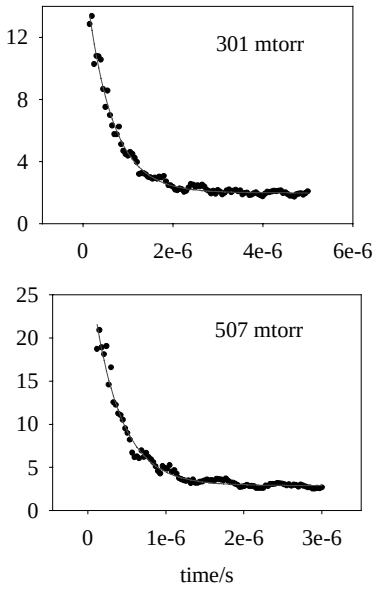

Figure 1. Kinetic traces showing decay of LIF signal following excitation of NO to v =2, J = 40.5

One drawback of the experiments that have been described is that the measurements are limited to rotational levels that have a significant population at the temperature of the experiment. Although rates of RET are quite insensitive to initial J at low and moderate values of J, there is indirect evidence that molecules in high J levels are more resistant to energy transfer as the energy gaps approach or exceed k_BT. Such information would not only be fundamentally interesting but is also important for the interpretation of a number of non-equilibrium media such as that revealed by airglows from the upper atmosphere. The aim in the current project was to measure overall and state-to-state rate coefficients for RET from high rotational levels of NO.

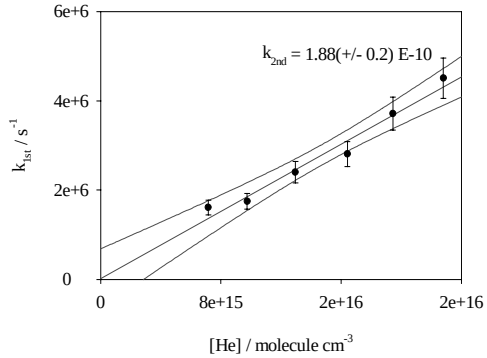

Figure 2. First-order decay constants for NO (v=2, J = 40.5) versus concentration of helium

Experimental Strategy and Procedures

The basis of the experiments was to produce molecules, in this case NO, in high J levels of an excited vibrational level in two, photochemical stages. First, NO was generated with a broad distribution over rotational levels, by pulsed photolysis of NO_2 using radiation at 355 nm. Then, before this non-Boltzmann distribution could relax, the IR pump laser which was tuned to a transition from a high J level in the (2, 0) overtone band of NO was fired promoting molecules to a (v = 2, J) level which was essentially unpopulated by the photolysis process. Finally, the redistribution of these excited molecules was followed using the UV probe laser in the same fashion as in conventional IRUVDR experiments. The overall process can be represented by the equations:

laser 1: $NO_2 + h\nu\ (\lambda = 355\ nm) \rightarrow NO(v, J) + O$

laser 2: $NO\ (v = 0, J) + h\nu\ (\lambda = 2.59\ \mu m) \rightarrow NO\ (v = 2, J+1)$

laser 3: $NO\ (v = 2, J + 1) + h\nu\ (\lambda = 247\ nm) \rightarrow NO(A^2\Sigma^+\ v', J')$

$\downarrow$

$NO\ (X^2\Pi\ v'', J'') + h\nu$

In the present experiments, laser 2, the tunable IR pump, was the difference-frequency mixing Continuum system supplied by the RAL Laser Loan Pool.

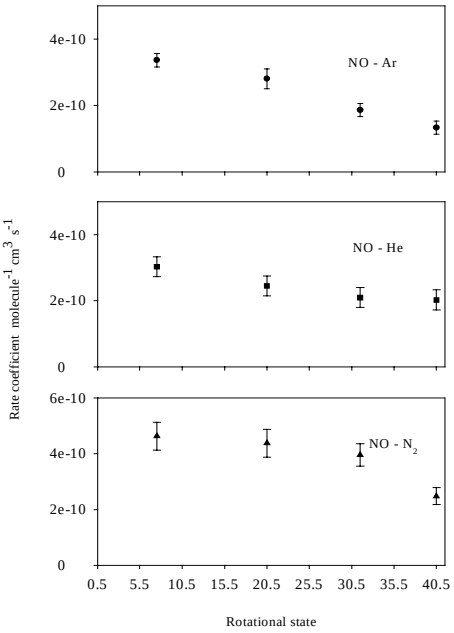

Figure 3. Rate coefficients for overall rotational relaxation for different initial J and different collision partners

Results and Discussion

In the present work, we measured overall and state-to-state rate coefficients for rotational energy transfer in collisions of NO ($X^2\Pi_{1/2}$, v = 3) in rotational levels J = 7.5, 20.5, 31.5 and 40.5 in collisions with He, Ar and N_2 at room temperature. Measurements on J = 7.5 and 20.5 were made using the conventional two-laser IRUVDR technique. Those on J = 40.5 were made using the three-laser method described in the previous section, whilst experiments of both kinds were performed on J = 31.5. Figure 1 shows some kinetic traces of LIF signal versus time reflecting the relaxation from v = 2, J = 40.5 in mixtures of 10% NO in He. Figure 2 shows the first-order rate coefficients obtained from a series of such experiments plotted against the concentration of He yielding, from the gradient, the second-order rate coefficient for relaxation.

The rate coefficients that have been obtained for overall relaxation are plotted against initial rotational level (J_i) in figure 3. For each collision partner, the rate coefficients show a small but significant decrease with J_i, which is in line with what has been inferred from line broadening parameters. The variation is least for NO - He collisions which may be a result of the higher average collision velocities. NO-Ar and NO-N_2 are appreciably less 'sudden' and will appreciate a more rotationally averaged potential.

In addition to the overall rate coefficients for RET, we have measured state-to-state rate coefficients for all combinations of

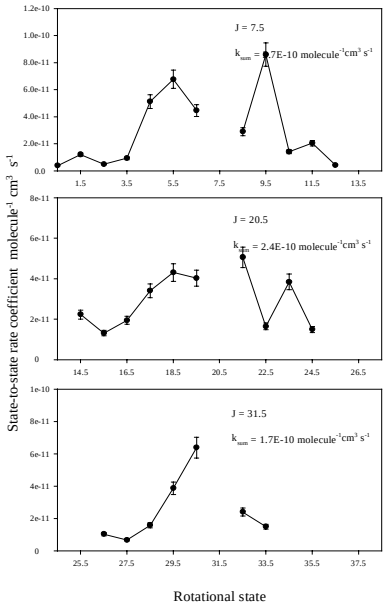

Figure 4. State-to-state rate coefficients for rotational energy transfer in collisions with He

initial rotational level (J_i= 7.5, 20.5, 31.5 and 40.5) and collision partner (He, Ar and N_2). An example of some of these results is shown in figure 4. These rate coefficients show a clear propensity to be dominated increasingly by small ΔJ transitions as J_i increases. This is especially exaggerated for J_i = 40.5. For this level (not shown in figure 4), over 80% of the transfer occurs to J = 39.5

Conclusions and Future Work

We have succeeded in making the first measurements on rotational energy transfer from specific high rotational levels by applying a novel technique using three pulsed lasers. Our experimental results are being compared with theoretical results in an extension of an already fruitful collaboration with M H Alexander. The work reported here is clearly capable of extension in a number of interesting ways. First, we would hope to perform similar experiments in the unique, ultracold environment provided by the CRESU apparatus. This will not diminish our ability to access high rotational levels in NO but will drastically reduce the collision energy, probably resulting in much greater stability of molecules in high J levels. Secondly, this new technique will be applied to similar measurements on OH (from HNO_3 or H_2O_2) or CN (from BrCN). Finally, we intend to examine competition between reaction and relaxation in the cases where a radical in a selected v, J level is produced in the presence of not a chemically inert gas but rather a molecule with which the radical undergoes rapid reaction.

References

1. M. Islam, I.W. M. Smith and J. W. Wiebrecht, J. Phys. Chem., 1994, 98, 9285

2. M. Islam, I.W. M. Smith and J. W. Wiebrecht, J.Chem.Phys., 1995, 98, 9676

3. P. L. James, I. R. Sims and I. W. M. Smith, Chem. Phys. Letters, 1997, 272,

Laser Spectroscopy of Biomolecules and their Hydrated Clusters

J P Simons, E G Robertson, M R Hockridge.
Physical and Theoretical Chemistry Laboratory, South Parks Road, Oxford, OX1 3QZ, UK. Email jpsimons@physchem.ox.ac.uk

Photoinduced Absorption in Thin Oligo(phenylenevinylene) Films

D Oelkrug, H-J Egelhaaf, B Lehr, J Gierschner, L Lüer.

Inst. for Physical Chemistry, Auf der Morgenstelle 8, University of Tübingen, Germany. Email dieter.oelkrug@uni-tuebingen.de

P Matousek, M Towrie.

CLRC Rutherford Appleton Laboratory, Chilton, Didcot, Oxon., OX11 0QX. Email P. Matousek@RL.AC.UK

Introduction

Derivatives of poly(phenylenevinylene)s (PPV) and polythiophenes (PT) are widely investigated as active components in organic electroluminescent devices and field effect transistors [1, 2]. The basic physicochemical processes of creation and recombination of charged intermediates can be investigated with fast spectroscopic techniques [3 - 5].

In this report we describe optical pump-probe experiments on thin films of vapour-deposited oligo(phenylenevinylene)s nPV with n = 2 and 3 vinylene units.

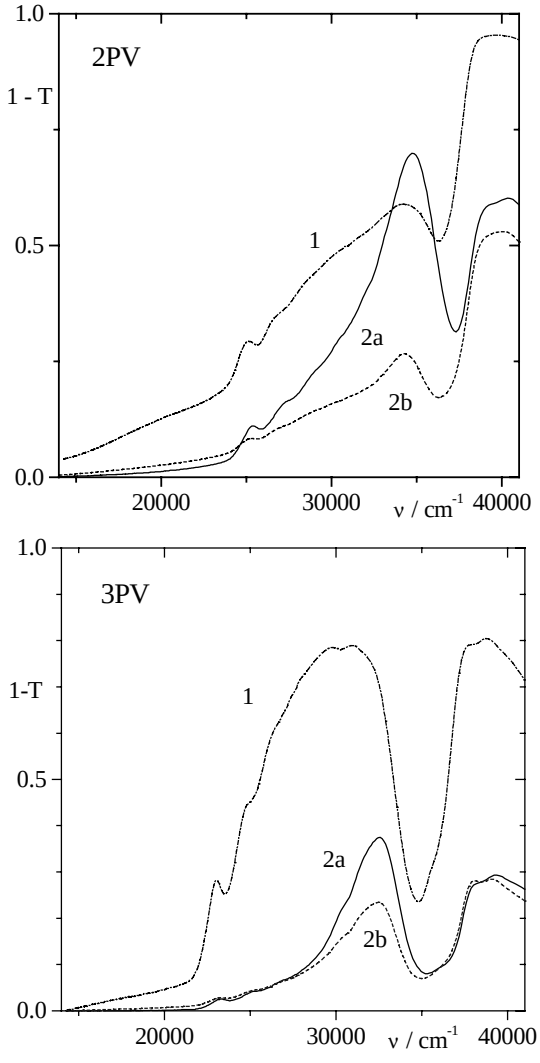

Figure 1. Ground state absorption spectra of 2PV (film thicknesses d = 90 nm (1), d = 55 nm (2)) and 3PV films (d = 70 nm (1), d = 10 nm (2)) on fused silica. Light p-polarized, incident under $\alpha = 0°$ (1, 2b) and $\alpha = 60°$ (2a).

Figure 1 presents the ground state absorption spectra of 2PV and 3PV films on fused silica substrates. The 2PV molecules are highly oriented with their long axes perpendicular to the substrate plane, resulting in strongly anisotropic absorption spectra. The 3PV molecules still show short range intermolecular side-by-side arrangement, but no macroscopic preference with respect to the substrate plane. The spectral position of the main absorption region of 3PV fits very well with the 2nd harmonic of the CLRC femtosecond pump-probe-laser equipment, whereas 2PV absorbs at shorter wavelengths and can be excited only in the weakly absorbing red-edge region. Thus, we concentrate on the results obtained with 3PV films.

Experiments

The samples were prepared by vapor deposition of nPVs under high vacuum onto planar fused silica substrates at film thicknesses of d = 10 – 90 nm.

The OPA system in the Lasers for Science Facility Ultrafast Spectroscopy Laboratory was used at a repetition rate of 40 KHz and provided both pump (ca. 0.02 - 5 $mJcm^{-2}$ at λ = 390 nm) and probe (ca. 0.005 - 0.75 $mJcm^{-2}$) pulses (ca. 600 fs instrument response function). The beams were overlapped at the position of the thin film sample. The pump beam was chopped at ca. 2 kHz, and the probe beam was sampled by two photodiodes, detecting both sample and reference signals. The data were collected, by lock-in amplifier, as kinetic traces at single probe wavelengths, selected by use of interference filters.

Results and Discussion

Two regions with intense transient absorption signals could be distinguished in the wavelength regions of 800 – 1000 nm (region 1) and 550 – 650 nm (region 2). In addition we investigated region 3 at 440 – 500 nm where ground state depletion and stimulated emission can be expected.

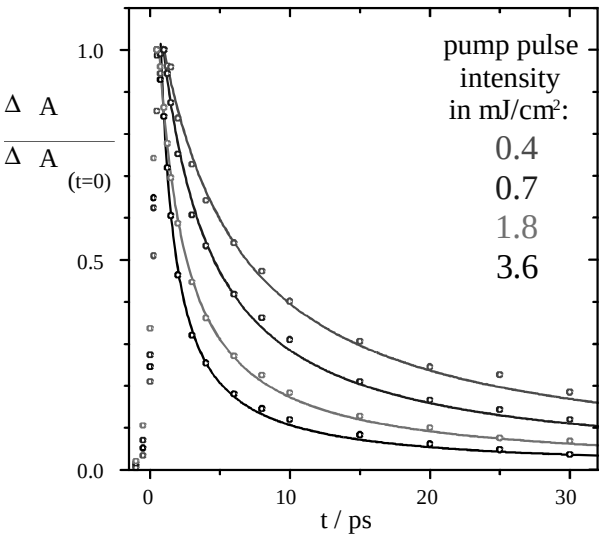

Figure 2. Normalized decay traces of the $S_1 \rightarrow S_n$ absorption of a 3PV film (d = 70 nm) on fused silica at different pump pulse intensities (observed at λ = 900 nm).

The very intense absorption signals, up to $\Delta T/T = 0.3$, obtained in region 1 are assigned to excitonic singlet-singlet absorption ($S_1 \rightarrow S_n$), since a very similar signal can be observed also in dilute 3PV solutions in CH_2Cl_2. The rise and decay kinetics of the $S_1 \rightarrow S_n$ absorption have been monitored at λ = 900 nm.

The main results are presented in figure 2. The normalised decay traces show clearly that the decay kinetics are strongly dependent on the pulse intensity. The decay traces are shorter than in dilute solution by more than one order of magnitude. The excitonic decay in solution is exponential with $\tau \approx 920$ ps, which is identical to the fluorescence decay time

Contrary to region 1, the signal decay curves of region 2 are independent of the laser intensity (figure 3). The rise times are very fast (within the pump pulse width), but the decay is very nonexponential, extending from $\tau_{init} \approx 100\,ps$ to $\tau_{fin} > 10\,ns$.

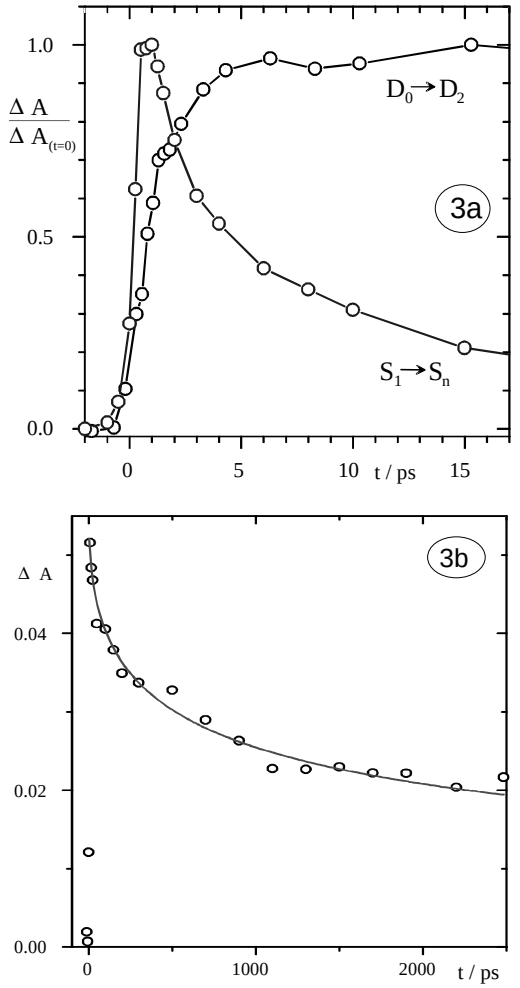

Figure 3. a) Normalized rise curve of the transient absorption of a 3PV film (d = 70 nm) observed at λ = 620 nm (assigned to the $D_0 \rightarrow D_2$ transition in 3PV radical ions) and normalized decay trace of the $S_1 \rightarrow S_n$ absorption.
b) decay of the $D_0 \rightarrow D_2$ absorption.

Kinetic Analysis

All S_1 – S_n decay curves in figure 2 can be analysed with conventional second order kinetics $-\frac{dS_1}{dt} = k_{ss}S_1^2$ inserting a single decay constant of $k_{ss} = (2.8 \pm 0.3) \cdot 10^{12}\,M^{-1}s^{-1}$. Thus, the main part of excited singlets annihilate bimolecularly according to $2S_1 \rightarrow S_n + S_0 \rightarrow S_1 + S_0$. Figure 4 proves this mechanism since the kinetics of ground state recovery is identical with the S_1 decay trace.

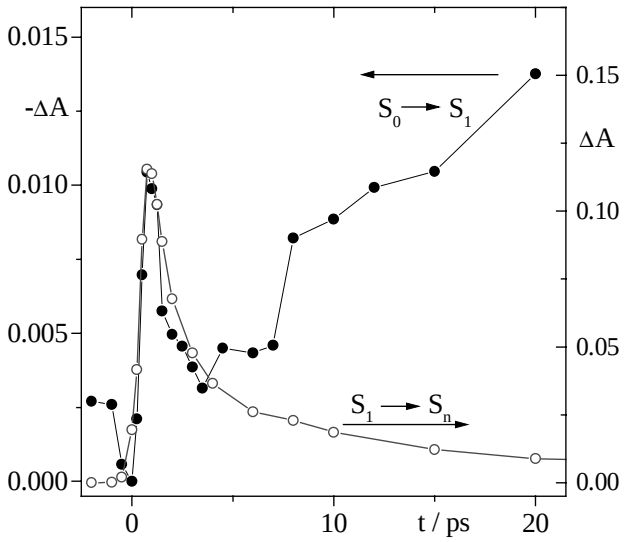

Figure 4. Ground state bleaching and recovery ($S_0 \rightarrow S_1$) of a 3PV film (d = 70 nm) observed at λ = 460 nm, and decay trace of the $S_1 \rightarrow S_n$ absorption.

The rise and decay of figure 3 is tentatively assigned to the formation and decay of radical ions $S_1 + S_0 \rightarrow D^{\bullet +} + D^{\bullet -}$. The formation rate is much faster than the decay rate of S_1 so that it is reasonable to assume that the radical ions can be formed with high yield only from the vibronic S_1 states. The initial fast decay of the radical ions is assigned to geminate recombination since the kinetics is independent of the laser intensity (the long lived radical ions cannot be analysed with the pump-probe technique).

Conclusions and Future Work

The present studies have shown the potential of the pump-probe technique in the elucidation of ultrafast processes in organic thin films. Further work is needed to conclusively assign the observed decay traces to transient species. This will be greatly assisted by spectral detection, e.g. by an optical multichannel analyzing (OMA) system. In order to reduce thermal effects, measurements have to be performed at lower light levels (requiring enhanced signal to noise ratio) and smaller beam spot areas. In order to investigate the effects of oxygen and of temperature on the photophysics of organic films, especially on charge carrier formation and recombination, experiments under high vacuum and at cryogenic temperatures are necessary.

References

1. A.R. Brown, K. Pichler, N.C. Greenham, D.D.C. Bradley, R. H. Friend, P.L. Burn, A.B. Holmes, Synth. Met. 55–57 4117, (1993)

2. D. Oelkrug, A. Tompert, J. Gierschner, H.-J. Egelhaaf, M. Hanack, M. Hohloch, E. Steinhuber, J. Phys. Chem. 102 1902 , (1998)

3. C.H. Lee, G. Yu, D. Moses, A.J. Heeger, Synth. Met. 69 429 , (1995)

4. V.I. Klimov, D.W. McBranch, N.N. Barashkov, J.P. Ferraris, Chem. Phys. Lett., 277 10, (1997)

5. G. Lanzani, S.V. Frolov, P.A. Lane, Z.V. Vardeny, M. Nisoli, S. De Silvestri, Phys. Rev. Lett. 79 3066 , (1997)

Kinetics of ESIPT in 3-hydroxyflavones

S Ameer-Beg, R G Brown.

Centre for Photochemistry, University of Central Lancashire, Preston. Lancs. PR1 2HE.

P Matousek, M Towrie.

CLRC Rutherford Appleton Laboratory, Chilton, Didcot, Oxon., OX11 0QX.

Introduction

It is now well established that the acidity or basicity of certain structural features of molecules are enhanced in the excited state compared to the ground state. If two of these features (one acidic and one basic) are in close proximity to each other in a molecule it is possible, on excitation, for a proton to "hop" from the acidic site to the basic one - excited state intramolecular proton transfer (ESIPT). In most examples of molecules which undergo ESIPT the acidic proton donor is a hydroxyl group and the basic acceptor is a nitrogen atom [1)] or a carbonyl function [2)] An example of the latter is 3-hydroxyflavone (3-HF) where a pyryllium species is produced following ESIPT (Scheme 1).

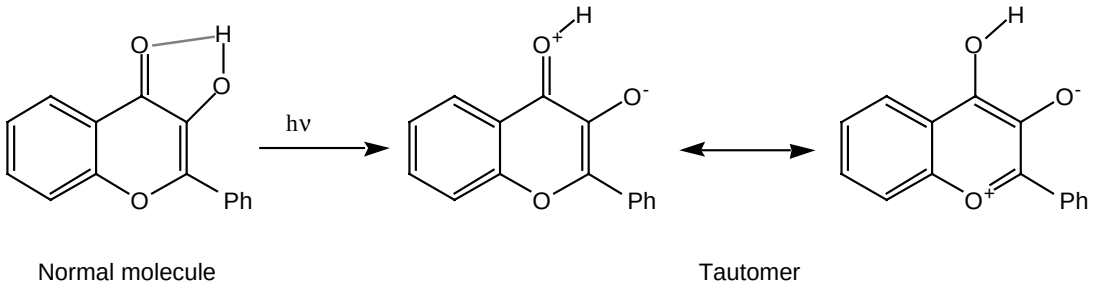

Scheme 1. ESIPT in 3-hydroxyflavone

The excited tautomer produced by ESIPT usually has an energy comparable to or slightly less than the excited state of the normal molecule. However, in the ground state the tautomer is of considerably higher energy than the normal molecule (figure 1). The consequence of these energetics is that the absorption and fluorescence ($h\nu_T$) of the tautomer are considerably red-shifted compared to the normal molecule ($h\nu_N$) and it was the abnormal Stokes' shifts of ≥ 10,000 cm^{-1} which first evoked interest in ESIPT systems.

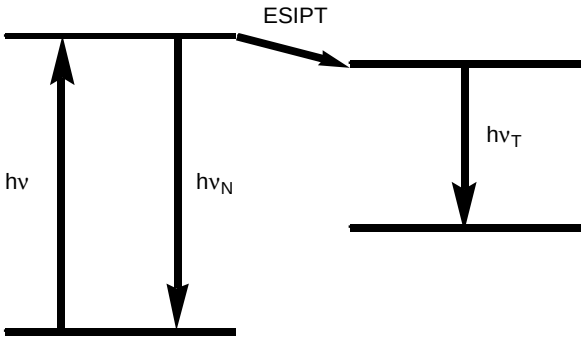

Figure 1. Energetics of ESIPT in 3-hydroxyflavone

These compounds, especially benzotriazoles[2)] and molecules based on 2-hydroxyacetophenone[1)] have been widely used as polymer stabilizers. As a consequence there has been considerable interest in the rate of ESIPT and how this varies with molecular structure. Unfortunately, it has proved very difficult to measure ESIPT rates because the process is so rapid and, for example, experiments where the risetime of the tautomer fluorescence have been determined have only led to lower limits (usually ≈ 10^{11} s^{-1}) being placed on the ESIPT rate constant[1,2)].

However, the development of femtosecond lasers has now provided us with light sources which are sufficiently short-lived such that measurement of ultrafast processes such as ESIPT are now possible and a number of fs pump-probe experiments on ESIPT systems have now been reported.

Harris' group have reported the sub-picosecond risetime of the tautomer fluorescence in 3-hydroxyflavone as 240±50 fs in methylcyclohexane and as ≈ 125 fs in methanol[3)]. They have also invoked the concept of solvent assisted ESIPT to explain the more rapid rate constant observed in the alcoholic solvent. A similar suggestion was also made by Ghiggino *et al.* to explain their data for 2-(2'-hydroxy-5'-methyl)benzotriazole[4)]. The concept is certainly an intriguing one but requires considerably more data to validate it. Elsaesser and co-workers[5)] have also studied the 2-(2'-hydroxy-5'-methyl)-benzotriazole system where ESIPT is found to occur with a rate constant of 10^{13} s^{-1}. They have also found sub-picosecond ESIPT rates for 2-(2'-hydroxyphenyl)benzothiazole in tetrachloroethene. Rates of 170±20 fs[6)] and 160±20 fs[7)] have been reported from measurement of the gain in a probe pulse at 630 nm following 315 nm excitation with a 140 fs FWHM pulse. Arthen-Engeland *et al.* have performed femtosecond pump-probe experiments on the related compound 2-(2'-hydroxyphenyl)benzoxazole in cyclohexane[8)]. A broad transient absorption was detected "which decayed with a time constant of 60±30 fs giving gain in the keto fluorescence band". These experiments provide a good indication of the (extremely rapid) timescale for ESIPT.

We have been able to measure transient spectra over the first few ps following excitation of 3-HF in various solvents[9)]. We have complemented these with a pump-probe study of the kinetics using the femtosecond laser system at the CLF, the results of which are reported here.

Results and Discussion

Transient spectra for 3-HF in cyclohexane[9] reveal new absorption bands at all times immediately after time zero where the trace is essentially flat except for a large spike at the excitation wavelength. At about 500 fs delay between pump and probe a transient is observed which absorbs between 350 and 500 nm with a tail out toward 600 nm. This red-shifts over the next few hundred fs to produce a transient (after 1 ps) which mainly absorbs between 400 and 520 nm with a peak around 470 nm. The transient spectra at later times are all essentially the same shape as the spectrum after 1 ps.

Transient kinetics taken around 450 nm at the CLF reveal a biphasic rise over the first 20 ps. The two components of the rise have lifetimes of 3-4 ps and approximately 100 fs. The latter is shown in figure 2 and is attributed to the actual ESIPT step whereas the slower component (shown in figure 3) is probably due to molecules of 3-HF where the intramolecular hydrogen bond has been broken and the lifetime of 3-4 ps reflects the re-formation of this hydrogen bond.

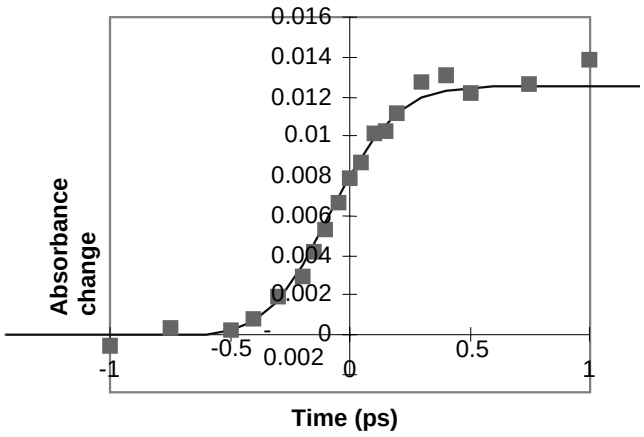

Figure 2. The sub-picosecond risetime of the transient absorption of 3-HF in cyclohexane

Similar measurements were undertaken in ethanol and acetonitrile as solvents and biphasic kinetics were also observed in these solvents. In addition, the faster of the two components in these two solvents also exhibited a risetime of approximately 100 fs, although the risetime of the slower component lay in the range of 5-10 ps. These results conflict with the observations of Schwartz et al[3] who observed a slower rise for the fast component in cyclohexane. This may be due to the presence of water in the solvent or the time resolution of the system and we are hoping to repeat some of these experiments on a system with greater time resolution.

Despite these reservations, these experiments certainly prove that the rate of ESIPT is extremely fast - certainly sub-picosecond- and that correlations of ESIPT rate with molecular structure are now perfectly feasible.

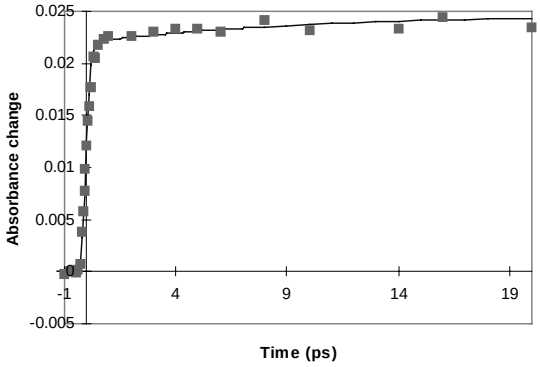

Figure 3. Biphasic transient kinetics of 3-hydroxyflavone in cyclohexane

Acknowledgements

We thank EPSRC for allowing us access to the CLF and the University of Central Lancashire and BNFL plc for a studentship (SA).

References

1. S M Ormson, R G Brown
Prog. React. Kinet. 19 45 (1994)

2. D LeGourrierec, S M Ormson, R G Brown
Prog. React. Kinet. 19 211 (1994)

3. B J Schwartz, L A Peteanu, C B Harris
J. Phys. Chem. 96 3591 (1992)

4. K P Ghiggino, A D Scully, S W Bigger
ACS Symp. Ser. 381 57 (1989)

5. T Elsaesser
"Femtosecond Chemistry Volume 2" (ed. J Manz and L.Wöste), VCH, Weinheim, 1995

6. F Laermer, T Elsaesser, W. Kaiser
Chem. Phys. Lett. 148 119 (1988)

7. W Frey, F Laermer, T Elsaesser
J. Phys. Chem. 95 10391 (1991)

8. Th. Arthen-Engeland, T Bultmann, N P Ernsting, M A Rodriguez, W Thiel
Chem. Phys. 163 43 (1992)

9. S M Ormson, D LeGourrierec, R G Brown, P Foggi
J. Chem. Soc. Chem. Comm. 2133 (1995)

Photo-induced electron transfer in the porphyrin triad H_2TTP-4,4' bipyridinium-ZnOEP$^+$,2ClO_4^- and related dyads

J-M Janot , P Seta.
Laboratoire des Matériaux et Procédés Membranaires, F- 34293 Montpellier Cedex 5. Email janot@admcnrs.cnrs-mop.fr

P Matousek, M Towrie , A Parker.
CLRC Rutherford Appleton Laboratory, Chilton, Didcot, Oxon., OX11 0QX.

Introduction

Substantial efforts have been directed over the past decades towards mimicking the vectorial photo-induced electron transfer and charge separation in photosynthetic reaction centres in view of i) -the desire to understand at the molecular level the mechanism of the primary steps in photosynthesis , ii)- the design and the development of practical systems for light conversion and solar energy storage. One approach for modelling such processes consists in the building of linked donor-acceptor molecules called polyads [1)]. Most of the related studies involve porphyrins and metalloporphyrins because these molecules represent chemically stable models of the chlorophylls of the natural photosynthetic reaction centres where the absorbed light is converted into electrochemical energy by vectorial electron transfers. The stabilisation of the charge separation is generally achieved by the spatial separation of the ion-radicals produced by vectorial electron transfer, which prevents recombination of the electrical charges and by energetic considerations on the potential energy surfaces of the initial and final states described in the Marcus electron transfer theory [2)].

Towards the stabilisation of the charge separation several porphyrins linked to quinone [3)] or to viologen [4)] moieties have been synthesised, the energy level of the charge separated final state (bi-radical) being much lower than the LUMO level, i.e the energy stored in the lower localised singlet excited state of these artificial reaction centres. In the present work we have studied a triad molecule composed of two porphyrins (a zinc and a free base porphyrin) acting as electron donor groups in the photo-excited state of the compound , and located on both sides of a two electrons acceptor group (bipyridinium), which plays the role of an electron trap. We designed this compound to understand how the electron transfer paths (from the porphyrin A or B to the respective adjacent pyridinium acceptor of the bipyridinium V^{2+} linker, see figure1) compete for the charge separation and how these steps are influenced by the possible excitation energy transfer between the two porphyrins of different LUMO levels.

In a previous work [5)] we have shown by fluorescence photon counting experiments that in the triad B- V^{2+}-A as well as in the corresponding dyads B-V^+ and A-V^+ (see figure 1), the fluorescence emission is strongly quenched as compared to those of the corresponding A and B porphyrin monomers. If we take into account electrochemical data obtained with these compounds (oxidation and reduction potentials), two different charge separated states shown in figure 2 are energetically allowed . Thus the shortened fluorescence lifetimes have been tentatively explained as due to the favored electron transfers which produce the radical cations of the porphyrins and reduced forms of the bipyridinium acceptor, that would be evidenced in transient absorption spectroscopy experiments.

During the experiments at RAL we recorded, after excitation of the studied molecules in organic solution with a powerful femtosecond light pulse, the variation of absorption at different wavelengths of the different intermediate states that are formed during the deactivation process. The aim of these experiments is the evaluation of the kinetic parameters of the electron transfer and charge recombination steps from the rises and decays of the transient absorptions.

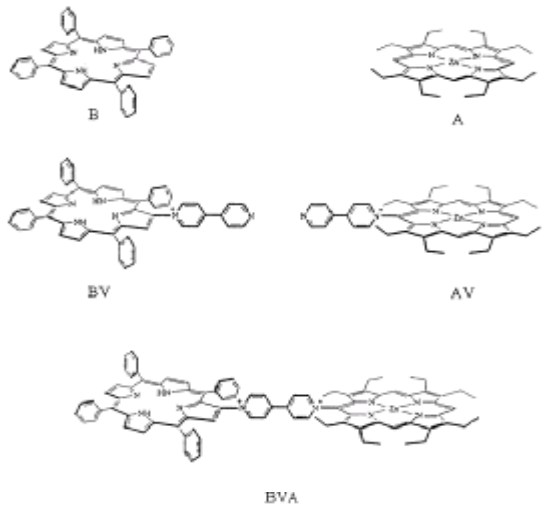

Figure 1. Triad B-V-A, related dyads B-V and A-V and porphyrin monomers B and A.

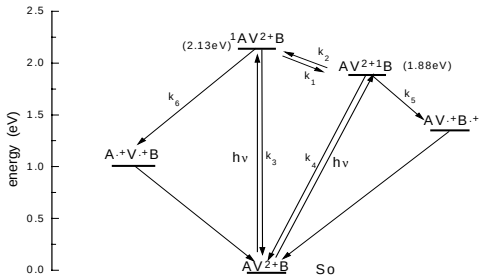

Figure 2. Photoinduced electron transfers scheme

The transient absorption variations recorded for the dyads and the triad are represented in figure 3. The temporal profiles are different according to the values of the probe wavelength. This has to be related to the fact that these variations of absorbance do correspond to a sum of the absorbances of the different intermediate states that are weighted according to their differences in cross sections. These signals are at first characterized by a fast rise in the picosecond time scale, followed by a decay more complex than a single exponential. The decays, at least for the zinc porphyrin dyad and for the triad, are faster than the fluorescence decay times, previously measured [5)]. This means that the shape of the transient absorption signals are not only due to the variations of absorption resulting of the population followed by the deactivation of a unique singlet excited state, but do result from a more complex deactivation scheme. If this was not the case, it should be impossible to explain the shorter decrease of the absorbance in the zinc dyad case as compared to the free base, taking into account the values of the fluorescence lifetimes which vary in the opposite way.

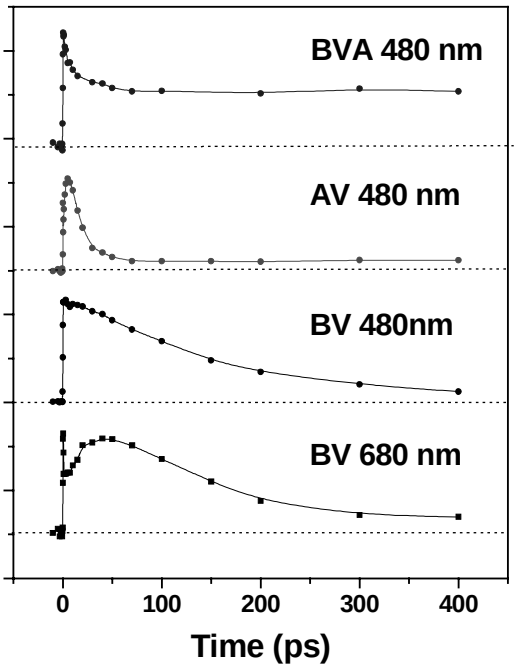

Figure 3. Transient absorption signals recorded after the excitation with a pulse at 415 nm, for the AV, BV dyads and triad AVB. The probe wavelengths are given in the figure.

Thus, after analysis of many different schemes, the mechanism we suggest to explain our data in order to conciliate them with the fluorescence experiments has to incorporate two distinct emitting photo-excited states as drawn in figure 4. The assumption of these two ^{1}S states could be supported by the existence in porphyrins of two well known orthogonal transition moments of the singlet excited state. This effect could be reinforced by the asymmetry imposed by the bipyridinium group.

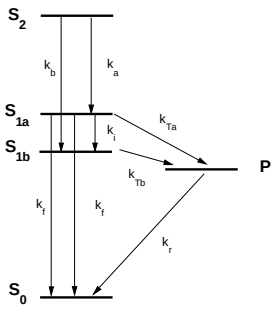

Figure 4. Photoinduced electron transfer scheme used for the fit of the transient absorption signals shown in figure 3.

The main feature of this model is essentially that the upper excited state is rapidly quenched by electron transfer (step with rate constant k_{ta}) giving rise to a quenched luminescence lifetime of about 5-30 ps. This very short lifetime was previously interpreted as scattering light in the luminescence experiments because of the limited time resolution of the single photon counting device (≈20 ps). This upper excited state is in competition with a charge separation process which populates a lower singlet state with a rate constant k_i, from which electron transfer also occurs at a rate lower than that of the upper state (rate constant k_{tb}). The emission of these lower and less populated intermediate states can account for the quenched luminescence observed with these compounds. Thus the major contribution of the upper excited state is the fast charge separation which produces light absorbing radicals, and the population at a minor concentration of a lower excited singlet state which is responsible of the observed luminescence. This model also accounts for the change in the shape of the transient signals with the wavelength of the probe. The variation of absorbance is in fact the difference between the ground state absorption and the sum of the absorbancies of the different intermediate states following the excitation pulse. We know from previous photo-electrochemical experiments that the porphyrin cation radical and the formal acceptor bipyridinium anion mainly absorb at wavelengths longer than 600 nm, which is as a matter of fact the spectral domain where the transient absorption signals present a hump. On the contrary the singlet excited states of the porphyrins have strong absorptions in the 400-500 nm region. According to the model shown in figure 4, the calculated time course of the charge separated state and of the singlet state show that the signals at the lower wavelengths are dominated by the singlet excited states absorptions whereas at longer wavelengths by the radicals. The data collected with the triad resemble those recorded with the zinc porphyrin dyad. However after a fast decay the transient absorption reaches a pseudo steady state of much higher amplitude. As no evidence of triplet state formation was observed in previous experiments, the explanation we propose is the formation of a longer lived charge separation species stabilised by the attraction effect of the remaining positive charge worn by the bipyridinium. The observed faster decay as compared to that of the BV dyad, as well as the occurrence of a stabilisation of the charge separation, accounts for a favoured deactivation of the excitation by the electron path k_6 instead of k_5 (see figure 2).

Conclusion

The transient absorption experiments confirm the possible photoinduced intramolecular charge separation in this family of molecular reaction centres models. The main path for electron transfer in the triad appears to be issued from the localized zinc excited state. However the spectral attribution of the formed porphyrin radicals is not enough accurate to conclude univocally. Thus these conclusions have to be confirmed by the use of a separate powerful technique of radical identification such as transient Raman spectroscopy.

References

1. D Gust and TA Moore
Science, 35 244, (1989)

2. R.A MarcusJ. Chem. Phys. 24 966, (1956) R A Marcus and N Sutin
Biochim.Biophys.Acta, 811 265, (1985)

3. J Liu and J R Bolton J. Phys. Chem, 96 1718, (1992) ;
A D Joran *et al*
Nature, 327 508, (1987)

4. V.Y.Shafirovitch *et al*
Chem. Phys. Lett., 15 24, (1991)

5. M. El Baraka *et al*
Photochem. Photobiol A, 113 163, (1998)

Transient absorption measurements of thiacarbocyanine monomers and phoroisomers adsorbed onto microcrystalline cellulose

LF Vieira Ferreira, A S Oliveira.

Centro de Química-Física Molecular, Complexo I, IST, 1096 Lisboa Codex, Portugal.

P Matousek, M Towrie, AW Parker.

CLRC Rutherford Appleton Laboratory, Chilton, Didcot, Oxon., OX11 0QX, U.K.

D R Worrall, F Wilkinson.

Loughborough University, Loughborough, Leicestershire, LE11 3TU, U.K.

Introduction

In recently published work [1-5] we described the behaviour of several cyanine dyes adsorbed onto a natural polymer, microcrystalline cellulose. In the range of concentrations under study (from 0.005 to 25.0 μmol of dye per gram of cellulose) several cyanines exhibit sandwich type and/or head to tail ground state aggregates. The aggregation is dependent on dye structure and on the degree of hydration of the sample.

Steady-state and laser induced fluorescence emission may provide different emission spectra. For several cyanines under study and for low loadings, only monomers (M*) emit and the two emission spectra are equal within experimental error, while for higher loadings a new emission (N*) was observed arising from a photoisomer generated by the absorption of a initial photon, and excited by the absorption of a second photon. Supralinear dependencies on laser fluence were detected in several cases [1-5].

Apart from this new photoisomer emission, an amplified spontaneous emission process (ASE) was claimed to exist explaining the narrow emission peaks of 3,3´-diethyloxadicarbocyanine iodide both in acetonitrile solution and adsorbed onto microcrystalline cellulose [2].

The present study is a continuation of this work. Transient absorption measurements with picosecond resolution were performed for dry and wet samples of 3,3´-diethylthiacarbocyanine iodide (TCC) and 3,3´-diethyl-9-methylthiacarbocyanine iodide (9-Me-TCC) adsorbed onto microcrystalline cellulose ranging from 0.02 to 15.0 μmol of dye per gram of the substrate, to evaluate both M* and N* lifetimes under the excitation of a powerful picosecond laser system.

Experimental

Ground-state absorption spectra and steady-state or laser induced fluorescence emission spectra of powdered samples were obtained using the methods and apparatus described in refs. 1,2 and references therein. Fluorescence quantum yields for TCC and 9-Me-TCC were determined at room temperature using the method described in ref. 7, with rhodamine 101 adsorbed onto microcrystalline cellulose as reference (ϕ_F=1.0).

Transient absorption measurements of 9-Me-TCC and TCC adsorbed onto microcrystalline cellulose were made by the use of a pump and probe time resolved system, operating with two independent tuneable optical parameter amplifiers described in detail in ref. 6. Excitation pulses were approximately 1 ps halfwidth. The pump wavelength was 534 nm and the probe was 800 nm. The repetition rate was 1.0 kHz and the energy was about 3 μJ per pulse.

Fluorescence emission spectra were also obtained under the same pumping conditions, using as detector a CCD camera coupled to a double grating monochromator [6]. The luminescence produced by the excitation of the picosecond laser was collected with a microscope objective and guided to the entrance of the monochromator by an optical fiber.

Results and Discussion:

Ground state absorption spectra of several samples of TCC and 9-Me-TCC adsorbed onto microcrystalline cellulose are presented in figure 1, where we plot reflectance as a function of wavelength. For both dyes, low loadings simply show monomer absorption and for high loadings (curve 5) 9-Me-TCC exhibits a new absorption band peaking at about 610 nm, which corresponds to J aggregate formation.

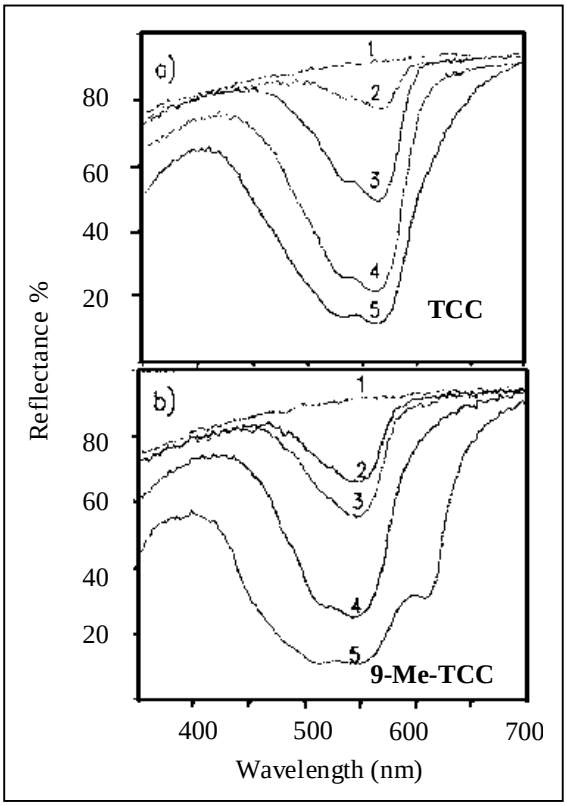

Figure 1. Reflectance spectra for samples of a) TCC and b) 9-Me-TCC adsorbed onto microcrystalline cellulose. Sample concentrations: (1) 0, (2) 0.05, (3) 0.10, (4) 1.0 and (5) 5.2 μmol g^{-1}.

Steady-state fluorescence spectra of TCC samples, excited with a 450W Xenon lamp at 530 nm simply show monomer emission, in contrast with a pulsed excitation (nitrogen laser or YAG laser) which produces both photoisomer emission and ASE. These results are similar to those obtained for 3,3´-dimethylthiacarbocyanine iodide as recently reported [4]. Picosecond laser excitation, with a repetition rate of 1 kHz clearly creates different populations of emissive species, as illustrated in figure 2.

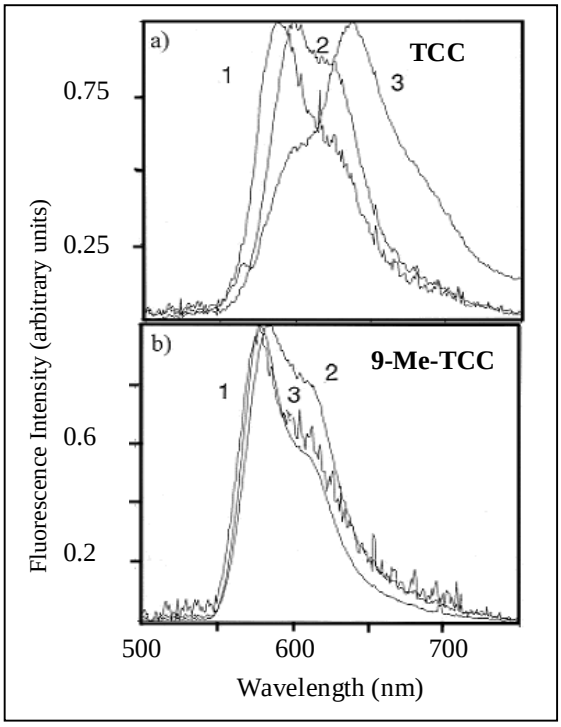

Figure 2. Laser induced fluorescence spectra for samples of a) TCC and b) 9-Me-TCC adsorbed onto microcrystalline cellulose, exciting at 532 nm and as a function of the dye concentration. Sample concentrations: (1) 0.08, (2) 0.5, (3) 10.0 μmol g^{-1}.

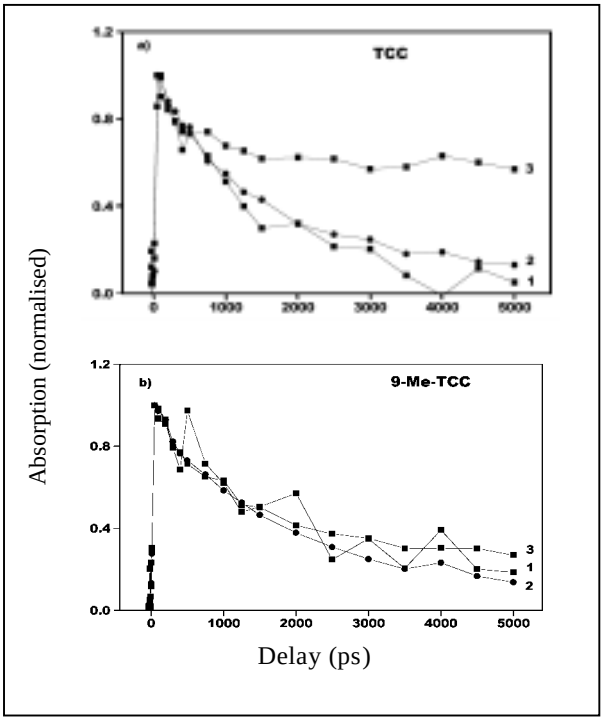

Figure 3. Transient absorption decay curves for samples of a) TCC and b) 9-Me-TCC adsorbed onto microcrystalline cellulose, exciting at 532 nm and as a function of the dye concentration. Sample concentrations: (1) 0.08, (2) 0.5, (3) 10.0 μmol g^{-1}.

Strong photoisomer emission is clearly seen for TCC, while for 9-Me-TCC, mainly monomers emit, without ASE in both cases.

Transient absorption measurements exhibit quite different behaviour for the two dyes, as shown in figure 3 where a long-lived transient absorption attributable to a photoisomer is only observed in the case of TCC.

In conclusion, we have shown that the luminescence properties for the two thiacarbocyanine dyes under study are strongly dependent on dye aggregation (J aggregate formation reduces photoisomerization), and on the characteristics of the excitation source.

References

1. A.S. Oliveira, L.F. Vieira Ferreira, D.R. Worrall, F. Wilkinson. J. Chem. Soc., Faraday Trans., **92** (1996) 4809.
2. L.F. Vieira Ferreira, A.S. Oliveira, D.R. Worrall, F. Wilkinson J. Chem. Soc., Faraday Trans., **92** (1996) 1217.
3. L.F. Vieira Ferreira, A.S. Oliveira, K.H. Henbest, D.R. Worrall, F. Wilkinson. RAL CLF Annual Report, (**1996/97**) 143.
4. A.S. Oliveira, P. Almeida, L.F. Vieira Ferreira. Coll. Czech. Chem. Comm., 00(1998) 000. In Press.
5. L.F. Vieira Ferreira, P.V. Cabral, P. Almeida, A.S. Oliveira, M.J. Reis, A.M. Botelho do Rego. Macromolecules, **30** (1998) 3936
6. M. Towrie, P. Matousek, W. Shaikh, G. Gaborel. RAL CLF Annual Report, (**1996/97**) 219.
7. L.F. Vieira Ferreira, M.R. Freixo, A.R. Garcia, F. Wilkinson J. Chem. Soc. Faraday Trans., **88** (1992) 15.

Detection and identification of low-lying electronic states of simple transition metal compounds

S H Ashworth.

The School of Chemistry, Bristol University, Cantock's Close, Bristol BS8 1TS Email S.H.Ashworth@bristol.ac.uk

Introduction

A series of exploratory experiments were undertaken to prove the efficiency of a spectroscopic source of molecules containing metal atoms [1]. This source will, in future be used in a number of two photon experiments in order to study low lying electronic states in these molecules.

The dichlorides of the transition metals have been subjects of attention in the past [2, 3] as they are the transition metal compounds with the highest vapor pressures. As a result significant vapor pressures can be obtained at temperatures of around 1000 K. Previously a supersonic expansion has been used to obtain vibrationally and rotationally resolved spectra with rotational temperatures as low as 12 K [3] . The wavelength range of observable fluorescence is, however, limited because of the interference of the black–body background from the heated nozzle source.

The new spark discharge source has two big advantages. First there is no thermal background and second, a reaction occurs between metal atoms and a reactant to form gas phase molecules. These molecules are relatively dilute and the majority are able reach the sample volume without condensing. Thus the species one is able to examine are not limited to those with a high vapor pressure.

The series of experiments undertaken sought to confirm that the target molecules, in this case $CuCl_2$ and $NiCl_2$, could be produced efficiently in the new source.

Preliminary experiments

First attempts concentrated on observing Cu atoms sputtered from the cathode. These absorb at 327.5 nm ($^2P_{½}\leftarrow{}^2S_{½}$) and 324.8 nm ($^2P_{½}\leftarrow{}^2S_{½}$) (the ultraviolet) and fluoresce in the green and orange regions of the spectrum. A little searching was required as the signal proved to be very sensitive to the timing of the discharge relative to both the argon gas pulse and the laser. The spectrum is shown in figure 1.

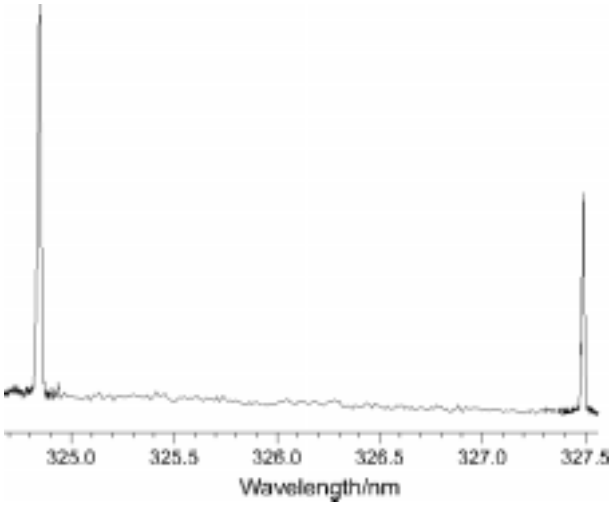

Figure 1. The laser excitation spectrum of copper atoms produced in a discharge source and supersonic expansion. (The change in baseline appearance is due to a scan speed change).

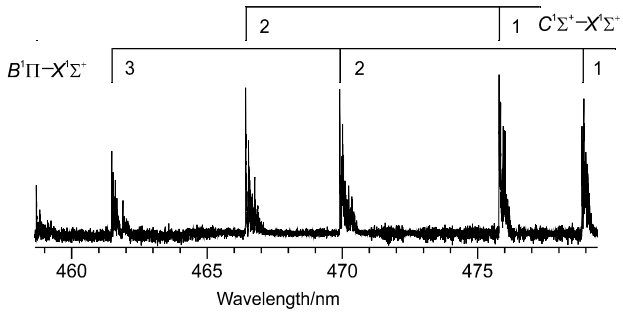

Figure 2. Part of the laser excitation spectrum of CuCl around 470 nm. The combs show the upper state vibrational quantum number.

Second, a stream of chlorine diluted in argon was introduced and fluorescence from CuCl sought. CuCl has some strong systems in the blue region of the spectrum and these were detected. The spectrum obtained is shown in figure 2. Vibrational progressions in the $B^1\Pi–X^1\Sigma^+$ and the $C^1\Sigma^+–X^1\Sigma^+$ band systems can be seen. A pleasing feature of this spectrum is the lack of congestion from sequence bands, which shows that there is little or no excitation in the ground state vibration.

A close up scan of the (2,0) band in the $B^1\Pi–X^1\Sigma^+$ system is shown, with a simulation of this band, in figure 3. The agreement between simulation and experiment is closest using a Lorentzian lineshape with a 0.12 cm^{-1} full width half maximum (FWHM) and a rotational temperature of 40 K. The simulation becomes increasingly bad as one moves to lower frequency. This is because the same rotational constants were used for all isotopomers of CuCl: $^{63}Cu^{35}Cl$, $^{65}Cu^{37}Cl$, $^{65}Cu^{35}Cl$ and, $^{65}Cu^{37}Cl$ which have abundances of 1:0.33:0.43:0.14 respectively.

$CuCl_2$ absorbs strongly in the orange and fluoresces in the red, but this proved quite hard to detect even though all of the

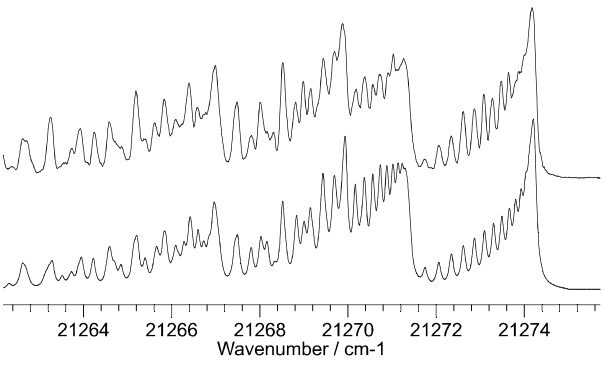

Figure 3. The (2,0) band of the $B^1\Pi–X^1\Sigma^+$ band of CuCl. Upper trace: experimental spectrum. Lower trace: simulated spectrum. The simulation has a Lorentzian linewidth of 0.12 cm^{-1} and a rotational temperature of 40 K

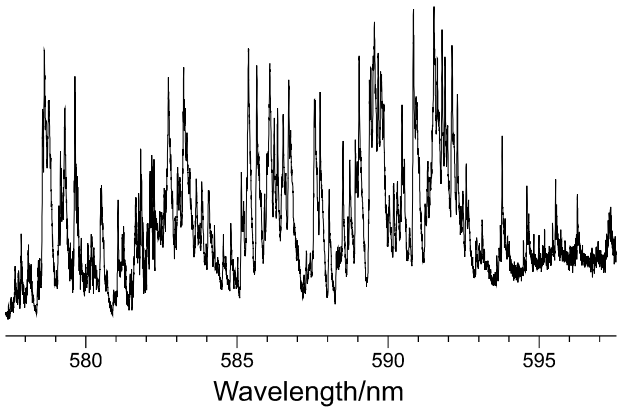

Figure 4. Part of the laser excitation spectrum of $CuCl_2$ around 590 nm

scattered light from the laser could be filtered out. Signals from $CuCl_2$ were, however, observed but these were weaker than hoped. This is probably due to the fact that the equilibrium between CuCl + Cl and $CuCl_2$ is more favourable to CuCl than $CuCl_2$. Part of the spectrum of $CuCl_2$ is shown in figure 4. The complexity of the spectrum implies that there is a degree of vibrational excitation which was not seen in the monochloride. Unfortunately the upper state is not sufficiently well characterized to enable the assignment of these bands to be shown.

Finally searches were made for the 360 nm system of $NiCl_2$. The spectrum which was obtained is shown in figure 5. Unlike the 460 nm system of $NiCl_2$ the 360 nm system is not well understood. It is, however, relatively strong and the equilibrium is in favour of the dichloride, which makes the spectrum straightforward to find. The strong bands shown in figure 5 can be matched to bands in the 360 nm spectrum of $NiCl_2$ but this spectrum looks significantly different from that obtained in the continuous heated expansion source.[5)] This difference is probably giving valuable information, both on the conditions in the supersonic expansion and on the origin of these bands in the spectrum of $NiCl_2$. It is highly likely that more than one electronic state is involved in this band system. If these have significantly different lifetimes the signals from the two states can be told apart using differential gating. This has already been used to good effect in the spectrum of $FeCl_2$.[6)]

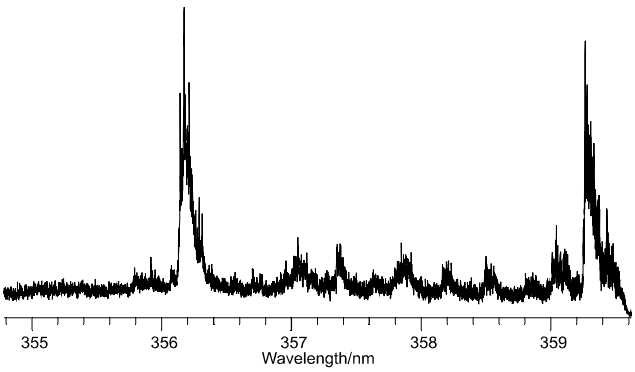

Figure 5. Part of the laser induced fluorescence spectrum obtained around 360 nm from the reaction of Ni atoms with chlorine gas in argon. The spectrum of $NiCl_2$ is expected in this region but this spectrum has not been unambiguously identified, partly because of the lack of calibration lines in this part of the spectrum.

The degenerate four wave mixing (DFWM) signal from $CuCl_2$.

Attempts have been made to observe the DFWM signal from $CuCl_2$ in the phase conjugate geometry. This geometry has the advantage that it is far easier to align than the popular BOXCARS geometry. Two main difficulties were encountered: in the reaction of copper monochloride with chlorine to produce copper dichloride the equilibrium favours the production of the monochloride. It also became clear that the precision of alignment required to separate the signal beam from scattered light was not attainable. Source modifications are currently under way to try to overcome the former so that more target molecules can be produced. Optical mounts and new optics have been purchased to facilitate the latter.

Future work

The work carried out here has laid a solid foundation for a number of future investigations. More recent work has shown that other molecules in the transition metal dichloride series can be usefully studied in this apparatus and there still remains the possibility of four wave mixing experiments. Although a degenerate four wave mixing signal was not detected from $CuCl_2$, once all the necessary improvements have been carried out both degenerate and two–colour four wave mixing remain to be done.

In addition it has also been shown recently that the range of molecules which may be studied is limited to neither transition metals nor chlorides. Given suitable reactants and a metallic wire which can be sputtered this should prove a versatile spectroscopic source.

Acknowledgments

I would like to thank Dr. A. M. Ellis of Leicester University for introducing me to the discharge source technology used here and the EPSRC for an Advanced Fellowship.

References

1. A.J. Bezant, D.J. Turner, G. Dormer and A.M. Ellis J. Chem. Soc. Faraday Trans. 92 3023 (1996)
2. C.W. DeKock and D.M. Gruen J. Chem. Phys., 44 4387-4398 (1966)
3. J.T. Hougen, G. E. Leroi and T.C. James J. Chem. Phys., 34 1670-1677 (1967)
4. S.H. Ashworth, F.J. Grieman and J.M. Brown Chem. Phys. Lett., 175 660 (1990)
5. G. van den Hoek, J.M. Brown J. Mol. Spectrosc., 182 163-177 (1997)
6. S.H. Ashworth (to be published).

Reaction Dynamics with Monoenergetic Atoms

G Hancock.

Physical and Theoretical Chemistry Laboratory, Oxford University.

One of the most significant developments in gas phase reaction dynamics over the past ten years has been in the use of laser prepared reagents to study the stereodynamics of chemical reactions. Polarised laser photolysis of a suitable precursor molecule forms a velocity aligned reagent (generally an atom), and measurements of the polarisation of its reaction products probed by Laser Induced Fluorescence (LIF) or Resonance Enhanced Multiphoton Ionisation (REMPI) can give unprecedented detail about the quantum state resolved dynamics of the reaction. When a diatomic molecule is used as the precursor, then photolysis produces an essentially monoenergetic reagent distribution, as for example in studies of the reactions of H and Cl atoms formed by photolysis of HI [1], HBr [2] and Cl_2 [3]. The aims of the experiments carried out with the loan laser have been to produce a scheme for making monoenergetic O(^{3}P) and N(^{2}D, ^{4}S) atoms by the dissociation through Rydberg states of NO. Reactions of oxygen atoms have relied in the past on the photolysis of the triatomic precursors N_2O [4] and O_3 [5] for O(^{1}D), and NO_2 [6] for O(^{3}P) and this necessarily complicates the interpretation of the measured polarisations, as the atomic reagent now has a range of kinetic energies and possibly a speed dependent anisotropy.

Our experiments first concentrated on the sequential two photon excitation of NO. One photon was used to excite the molecule to the $A^2\Sigma^+$ state near 226 nm, and the second to dissociate from this state via Rydberg levels populated by absorption at 339 nm. The wavelength of the second photon is such that it can be derived from the same dye laser which produces 226 nm radiation: 339 nm is formed by frequency doubling the fundamental output of a pulsed dye laser, and 226 nm from mixing the fundamental and doubled outputs. We have now completed an ion imaging study of this process, in collaboration with Professor Dave Parker's group in Nijmegen. This has been highly successful: we have shown that we form two dissociative channels giving O(^{3}P) atoms in conjunction with N(^{2}D) and N(^{4}S), we have measured the anisotropy parameters for the two processes (essential for unraveling the dissociation dynamics) and have identified the Rydberg predissociative states [7].

We took delivery of the Continuum YAG pumped dye laser in August 1997. Problems with the laser system were severe: the beam quality particularly of the 226 nm output was poor (we used our own mixing crystal, but the major problem appeared to be in the beam quality of the fundamental and doubled outputs). The dye circulators were faulty, and two dye cuvettes failed

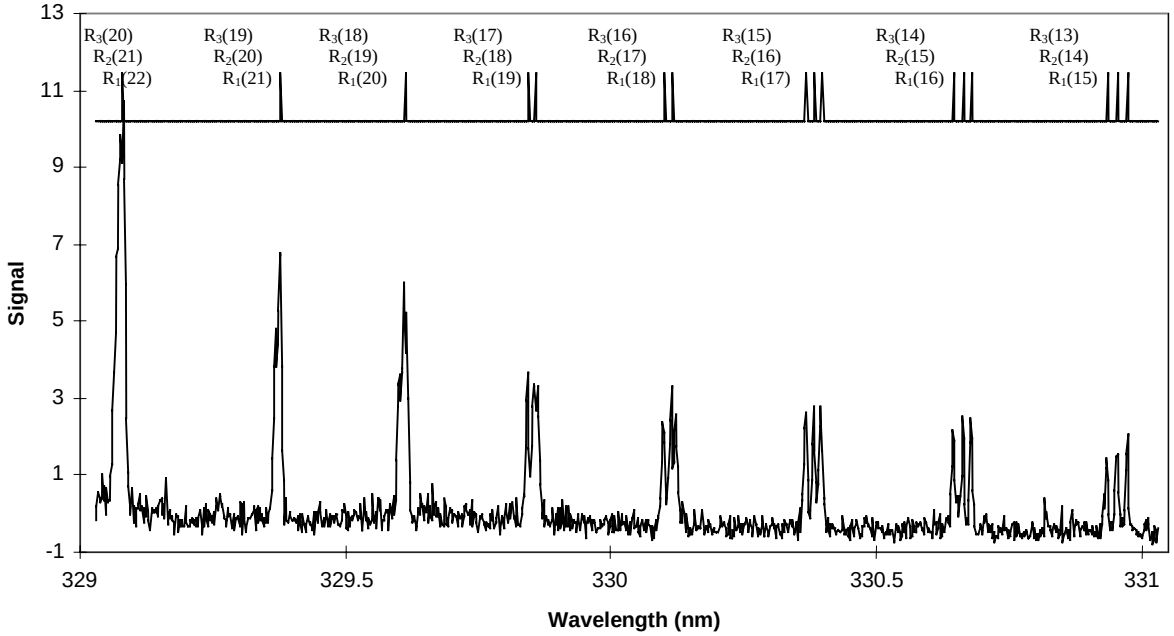

Figure 1. LIF spectrum of NH (v=0) from N(^{2}D) + H_2

We received excellent help from the staff of the CLF, but this could not disguise the fact that the dye laser was not of high enough quality for our needs.

Radiation was eventually obtained, and we tested our 1+1 NO dissociation scheme in the formation of $N(^2D)$ and its reaction with H_2 to form ground state NH, observed by laser induced fluorescence (LIF) at 330 nm. What we immediately found was that the spontaneous fluorescence near 330 nm from the NO A state populated at 226 nm exceeded the small LIF signals, despite the fact that the Franck Condon factors at this wavelength are small. The relatively long lifetime of the A state meant that we could not observe sensible LIF signals.

The Continuum laser was replaced by a LAS dye pumped by a Spectra Physics YAG, with immediate and noticeable improvement in quality and reliability. We correspondingly turned to a different excitation scheme, that of coherent two photon excitation of NO at 275.3 nm, which had previously been used to form $N(^2D)$ in the presence of H_2, with consequent LIF of the NH product under relatively high pressure conditions [8]. Figure 1 shows part of the R branch LIF spectrum that we have observed in this reaction under conditions such that the rotational distribution is nascent. Again we measured the anisotropy parameters from ion imaging experiments [9] which showed that the $N(^2D)$ was largely unaligned, but that changing the wavelength by a small amount resulted in new channel opening for fast and aligned $N(^4S)$ formation. It is hoped that reactions of $N(^4S)$ will be explored in the future.

Measurements of the Doppler profiles of NH were carried out, but the signal to noise ratio was insufficient to enable reliable vector correlations to be measured with the relatively low amount of $N(^2D)$ formed by two photon excitation. The co-product of the photolysis step at 271 nm is fast $O(^3P)$ atoms, and an attempt was made to observe the OH product from the $O(^3P)+CH_4$ reaction, the atom now having enough kinetic energy to surmount the barrier. OH was seen, but it soon became clear that it was the result of uv photolysis of HONO, a persistent impurity in any system containing oxides of nitrogen and H atom donors. Correspondingly the single photon dissociation dynamics of HONO were studied [10], with measurements made of the rotational state distribution and lambda doublet ratios. Results were found to be consistent with previous observations of the dissociation at higher and lower wavelengths.

Our experiments have clearly demonstrated that aligned monoenergetic atoms can be formed from the photolysis of NO with a single laser source. We intend now to explore the use of different techniques for product detection, in particular to move away from LIF in the near uv which, as we have noted, is contaminated with emission from the $A^2\Sigma^+$ state of NO when the sequential dissociation strategy is used.

References

1. N E Shafer, H Xu, R P Tuckett, M.Springer, R N Zare
J. Phys. Chem. 98 3369 (1994)
R Fei, X S Zheng, G E Hall,
J. Phys. Chem. 101 2541 (1997)

2. M Brouard, H .M Lambert, S P Rayner, J P Simons
Mol. Phys. 89 403 (1996)

3. W R Simpson, A J Orr-Ewing, R N Zare,
Chem. Phys. Lett. 212 163. (1993)

4. M Brouard, H M Lambert, J Short, J P Simons
J. Phys. Chem. 99 13571 (1995)
A J Alexander, M Brouard, S P Rayner, J P Simons
Chem. Phys. 207 215 (1996)

5. D S King, D G Sauder, M P Casassa
J. Chem. Phys. 97 8919 (1992)

6. F Green, G Hancock, A J Orr-Ewing
Faraday Discuss. Chem. Soc. 91 79 (1991)
M L Costen, G Hancock, A J Orr-Ewing, D Summerfield
J. Chem. Phys. 100 2754 (1994)

7. B L G Bakker, A T.J B Eppink, D.H Parker, M L Costen,
G Hancock, G A D Ritchie
Chem. Phys. Lett. 283 319 (1998)

8. H Umemoto, K Matsumoto
J. Chem. Soc. Faraday Trans. 92 1315 (1996)
H Umemoto, T Asai, Y Kimura
J. Chem. Phys. 106) 4985 (1997)

9. B L G Bakker, D H Parker, G Hancock, G A D Ritchie
Chem. Phys. Lett. in press.

10. J L Brandwood
Part II Thesis, Oxford University,(1998)

Investigation of Physical Properties of the Liquid/Vapour Interface using Second-Harmonic Generation

A Adam, J G Fordyce, R Spencer-Smith, JG Frey.

Department of Chemistry, University of Southampton

Introduction

It was the intention to measure the dependence of the SHG signal from the H_2SO_4/air interface on acid concentration and the variation of signal with temperature. The use of a completely different laser system to obtain and extend the results previously obtained with the experimental set-up in the Southampton laboratory is an important tool in determining the accuracy of data.

Experimental Arrangement

The Spitfire laser in figure 1 is a regenerative amplifier configured for the chirped pulse amplification of picosecond pulses. This RGA outputs 800 nm pulses at a repetition rate of 1 Khz. The seed is a 200 fs pulse generated by a self mode-locked titanium sapphire laser (Spectra-Physics, Tsunami). After amplification and compression, the output pulses have ~1 ps FWHM pulse duration and ~20 cm^{-1} bandwidth at a central frequency of 800 nm. The pulse energy is in the order of hundreds of microjoules.

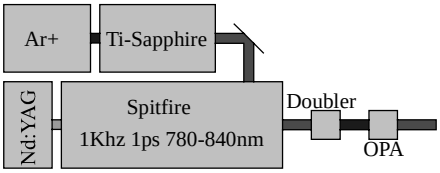

Figure 1. Laser system used at RAL

Even at a moderate energy of 100 μJ per pulse, this resulted in a large peak power being delivered to the sample. Shortly after experimentation began it became clear that a balance had to be achieved between the signal level and the intensity of the beam at the interface. As well as molecular breakdown when focusing tightly, another problem showed up. This was the occurrence of the white light continuum. This happens as a result of self-focussing non-linear effects which are only achieved when using large changes in intensity over short periods of time; conditions which are present in near the focal point of a picosecond laser pulse. The problem with a white light continuum is that light is generated over a very wide range of frequencies. This spectrum includes the frequency being monitored for the detection of SHG. Any second-harmonic signal generated at the interface will be several orders of magnitude less than the continuum signal so this makes detection impossible.

Several things were tried to prevent the generation of the white light including lengthening of the pulse and variation of the input frequency. It was thought that by increasing the temporal duration of the pulse, the effect of reducing the intensity curve with respect to time would keep the conditions below the threshold limits for continuum production. Although the focus could be moved closer to the interface after stretching the beam in this way the problem did not reduce significantly enough to proceed. It was decided to attempt the experiment at an input wavelength of 800 nm. As this is the wavelength of the output light from the Spitfire, this meant we could use this directly, without including the OPA. Whereas the beam quality is not varied much through the OPA, it does reduce the power of the beam. By excluding it from the system, the power delivered could be increased by a factor of ten.

Using the same power as before, the focal point could be moved even further towards the interface before the generation of the white light occurred. However this was not close enough to produce a measurable second-harmonic signal. At this point, there was only one other arrangement to try. This involved using the new, increased, power available to us and to back off the focus to a point before the continuum started.

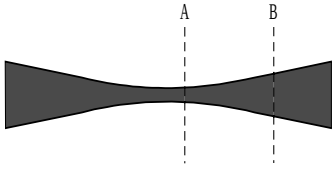

Figure 2. Close-up of focal structure of laser

An explanation of why this set-up was able to produce a measurable second-harmonic signal, while preventing the production of white light, becomes apparent when regarding figure 2. When the interface is located at point A, the angular expansion of the beam is a lot smaller than at point B. In order for a white light continuum to form, the self-focusing effects of the laser beam have to outweigh the defocusing tendency. This condition is easier to achieve at point A than point B as the beam waste at point A is almost parallel.

As it happened, the onset of the white light continuum had a large dependence on the concentration of the sample in question. As the concentration of acid increased, the threshold intensity for the onset of white light generation increased to a point where the focus of the input beam could be moved very close to the interface. This resulted in an enhanced signal to noise ratio when using mid to strong acid concentrations. In all initial cases, the focal point was moved as close as possible to the interface.

Second-harmonic generation is dependent on the intensity of the input beam at the interface. In order to achieve intensity high enough to produce a measurable signal at point B, it was necessary to use all the power available from the Spitfire. The energy used per pulse was ~100 μJ.

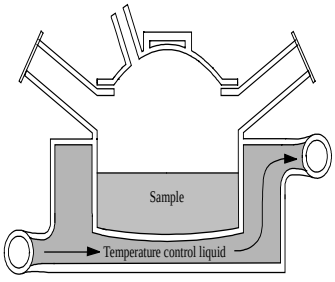

Figure 3. Diagram of improved temperature controlled sample cell

One of the main intentions of the visit to RAL was to measure the effects of temperature changes on the second-harmonic signal. A new cell was constructed, for this purpose, which enabled temperature control of the sample in an enclosed environment; shown in figure 3.

Previous cells for this work have been open to the surrounding environment and allowed loss of the sample as a result of evaporation. This became more of a problem at higher temperatures. Loss by this process meant that the concentration of the sample would be increasing and for systems with large signal dependencies on concentration, this can lead to misleading behaviour.

Sample

Since the time available was very limited, the concentrations of H_2SO_4 to be used for experimentation had to be chosen carefully. Four samples were made up for use at RAL before arrival to ensure accuracy of the concentrations used. The concentrations were decided upon by referral to the data shown here in figure 4:

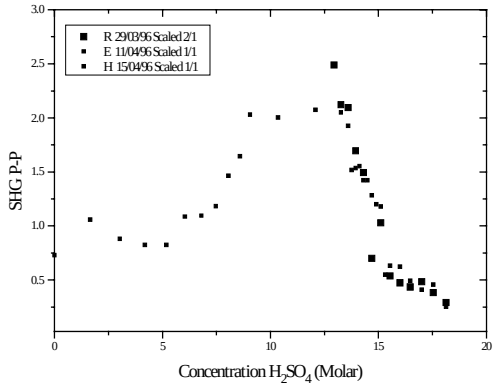

Figure 4. Plot showing previously obtained data for H_2SO_4

The four concentrations used, based on figure 4 were 6M, 12M, 15M and concentrated acid, which was measured to be 18.13M. It was believed that a temperature change induced the concentration curve in figure 4 to shift to the right. If this happened, it would show up, most dramatically, when using the 15M solution.

SHG dependence on the polarisation of the fundamental beam

The plot shown in figure 5, is the behaviour of the second-harmonic signal recorded prior to the RAL visit.

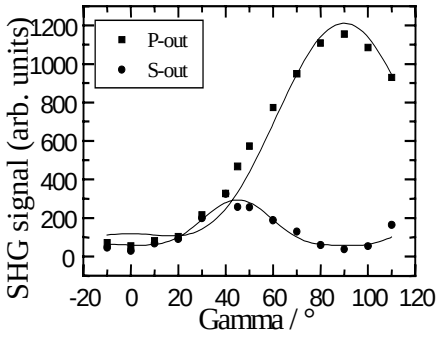

Figure 5. Gamma dependence of 12M H_2SO_4

Table 1 shows the χ ratios found when fitting the curves using equation (1) [1]. This table includes a range of these ratios assuming a different refractive index profile for each value. This range goes from that of the air, to that of the bulk.

$$I_{P-out} = C\left|A^2\cos^4(\gamma) + B^2\sin^4(\gamma) + 2\cos\phi AB\cos^2(\gamma)\sin^2(\gamma)\right|^2 \qquad (1)$$

where: $A = (a_2\chi^{(2)}_{XXZ} + a_3\chi^{(2)}_{ZXX} + a_4\chi^{(2)}_{ZZZ})$

$$B = a_5\chi^{(2)}_{ZXX}$$

$$C = \frac{32\pi^3\omega^2}{c^3}\frac{\sqrt{\varepsilon_1(2\omega)}}{\varepsilon_1(\omega)\left\{\varepsilon(2\omega)\quad\varepsilon_1(2\omega)\sin^2(\theta_1(2\omega))\right\}}$$

The concentration first used to attempt this experiment at RAL was 12M. The results from this are shown here in figure 6.

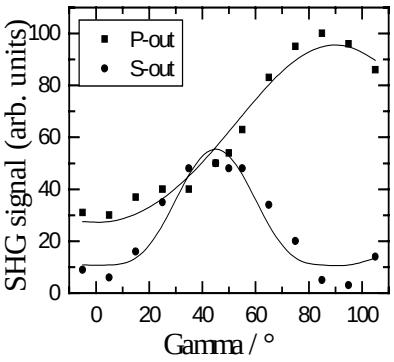

Figure 6. Results from first gamma dependence from RAL at 12M acid concentration

The χ rations calculated from the theoretical fit are presented in table 2

Figures 7-10 and tables 3-6 present the data recorded and analysed for gamma dependencies of 6M, 12M and15M sulfuric acid concentrations.

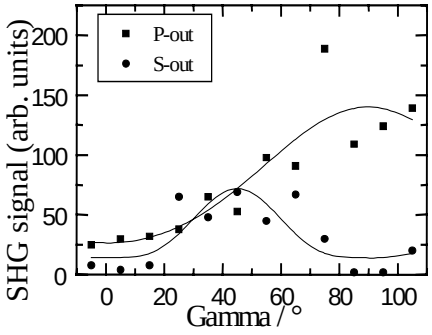

Figure 7. Plot showing gamma dependence curve for 6M sulfuric acid, recorded at RAL

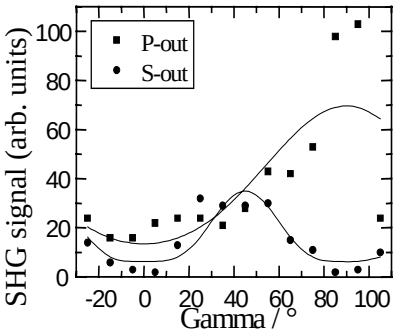

Figure 8. Plot showing second gamma dependence for 12M sulfuric acid, recorded at RAL

Although the values listed in table 4 have a better agreement with those presented in table 1, the scatter of the points suggests that these results are not as reliable as those listed in table 2.

Taking the average value for the two 12M results, the analysed data for a specific refractive index profile is shown in table 6.

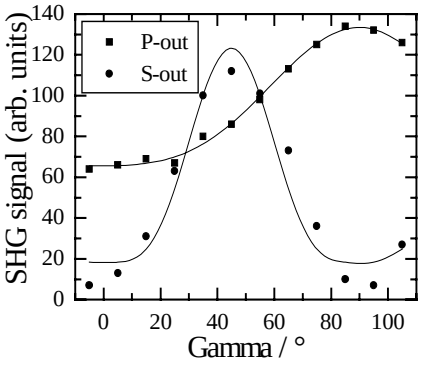

Figure 9. Plot showing second gamma dependence for 15M sulfuric acid, recorded at RAL

A clear trend in the χ ratios can be seen across the concentration range shown. It is interesting to notice that the values of χ_{XXZ} / χ_{ZXX} are much closer to unity than those values found from pure water. This implies that the Kleinmann symmetry rules [2] are being obeyed in the case of sulfuric acid.

Temperature dependence

A new difficulty arose when the temperature dependence experiments were attempted. Signal responses were obtained like the one shown in figure 10.

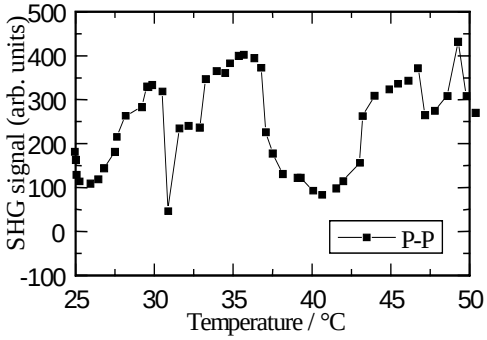

Figure 10. Plot showing response of second-harmonic signal with temperature

Since it was extremely unlikely that this was the true signal dependence on temperature, something else had to be the cause of this strange effect. To eliminate the question of whether or not the new sample cell was the cause, the same experiment was tried using a petri-dish resting on a hot plate. Although this would allow a lot more heat to be exchanged with the environment, it would also show very quickly if this effect were present. It would also indicate if the water bath, used to heat the sample cell, was the cause of the problem. The effect, shown in figure 10, reoccurred so the problem had to lie in the sample.

Expansion of the sample was investigated next. The sample, still in a petri-dish, was mounted onto a vertically adjustable mount. At room temperature, the experiment was performed again and the height of the sample was adjusted finely to simulate thermal expansion. The result was quite astonishing. The signal responded as would be expected from an interference effect. With increasing height of the sample stage, of the order of fractions of millimetres, the signal size increased and decreased dramatically.

The boxcar integrators for the signal and reference were separated to prevent electrical coupling. This went some way to reducing the problem, although it was thought that the cause lay in the primary detection system; namely the PMT and the pre-amp. Both the pre-amp and PMT were exchanged for different units and the strange behaviour reduced again. Finally, at the concentration being used, 12M, the focus was backed off from the interface, even though it was possible to perform the experiment at the original distance without white light being an obvious problem. It was thought that there might have been a minute amount of continuum generation being produced sporadically as the interface moved under thermal expansion, towards and away from the focal point.

Since the amount of light produced from the white light continuum at the second-harmonic wavelength, is several orders of magnitude larger than that produced as a result of SHG, even very small amounts would show up as a huge signal. The focal point was moved further away from the interface, and the behaviour seen in figure 10 decreased appreciably. Unfortunately, the problem could not be eliminated and, when subjected to rapid changes in temperature, reoccurred to a large degree.

With this problem causing misleading results when continual measurements were being made, it seemed that the best way to proceed was to perform the polarisation measurements at high, and low temperatures. This would show up any temperature dependent tendencies of the sample more accurately than by simply measuring the variation of the P-P signal intensity.

The experimental problem shown in figure 10 is reduced if the rate of heating is minimised. As this also increases the time taken to complete an experimental run, the chances of signal degradation are also increased. The plot shown in figure 11 is the only run which yielded reasonably sensible results. Each point is the average of the previous hundred points, to account for a large modulation in signal.

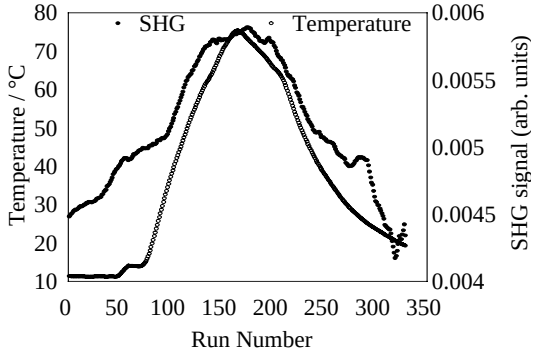

Figure 11. Plot showing variation of P-P signal with temperature for 15M acid

The P-P signal curve shown in figure 11 shows a clear increase with temperature. This curve has been extensively smoothed. Work in Southampton suggested that the curve shown in figure 4 shifts to the right with increasing temperature. The results shown in figure 11 are consistent with this idea.

Figure 11 is re-plotted in figure 12 as a function of temperature.

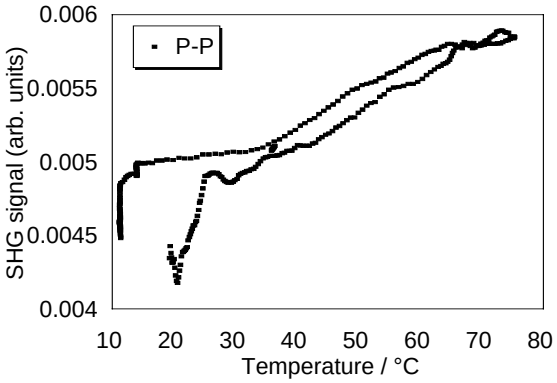

Figure 12. Plot showing variation of P-P signal as a function of temperature

Polarisation measurements were made at a temperature of 85°C was successfully performed at this acid concentration and the results are shown here in figure 13 and tabulated in table 7.

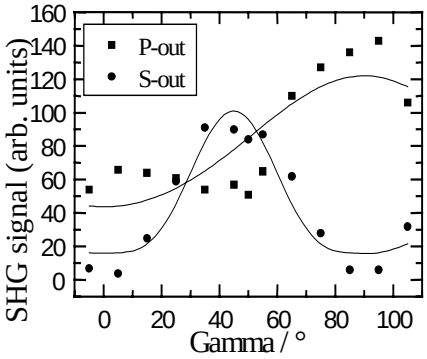

Figure 13. Plot showing gamma dependence for 15M sulfuric acid at 85°C, recorded at RAL

The results from the experiment at 85°C are very interesting. All the χ ratios, shown in table 7, indicate a shift in value *towards* those calculated for lower acid concentrations. In fact, the values presented here are very close to those calculated for the 12M acid experiments. This provides more evidence for a shifting to the right with increasing temperature of the curve shown in figure 4.

Conclusion

The experimental difficulty encountered at RAL meant results for only a very few acid concentrations could be obtained. The great advantage of the system used was with the high repetition rate of the laser. The temperamental nature of the experimental set-up could be offset with the speed at which data could be collected. The results provide further evidence that the profile of the SHG dependence on acid concentration shifts towards higher acid concentrations with increasing temperature.

References

1. Tamburello Luca, P. Herbert, H. Girault,
J. Chem. Soc. Faraday Trans., 1995, **91**(12), 1763-1768

2. D.A.Kleinmann,
Phys. Rev., **126,** (1962), 1977

Input interface index of refraction	1.0000	1.0788	1.1576	1.1972	1.2364	1.3152	1.3940
Output interface index of refraction	1.0000	1.0930	1.1860	1.2323	1.2790	1.3720	1.4650
χ_{ZZZ} / χ_{ZXX}	2.26	3.06	4.05	4.64	5.28	6.76	8.53
χ_{ZZZ} / χ_{XXZ}	2.19	3.04	4.13	4.76	5.47	7.12	9.13
χ_{ZXX} / χ_{XXZ}	0.97	1.00	1.02	1.03	1.04	1.05	1.07

Table 1. Calculated values for χ ratios from Southampton at 12M acid concentration

Input interface index of Refraction	1.0000	1.0788	1.1576	1.1972	1.2364	1.3152	1.3940
Output interface index of Refraction	1.0000	1.0930	1.1860	1.2323	1.2790	1.3720	1.4650
χ_{ZZZ} / χ_{ZXX}	1.39	1.88	2.50	2.85	3.25	4.16	5.25
χ_{ZZZ} / χ_{XXZ}	1.49	2.07	2.80	3.24	3.72	4.84	6.21
χ_{ZXX} / χ_{XXZ}	1.07	1.10	1.12	1.14	1.15	1.16	1.18

Table 2. Calculated values for χ ratios from RAL at 12M acid concentration

Input interface index of refraction	1.0000	1.0741	1.1483	1.1854	1.2224	1.2966	1.3707
Output interface index of refraction	1.0000	1.0836	1.1671	1.2089	1.2507	1.3342	1.4178
χ_{ZZZ} / χ_{ZXX}	1.75	2.33	3.05	3.46	3.92	4.96	6.19
χ_{ZZZ} / χ_{XXZ}	1.63	2.20	2.92	3.34	3.80	4.87	6.15
χ_{ZXX} / χ_{XXZ}	0.93	0.94	0.96	0.97	0.97	0.98	0.99

Table 3. Calculated values for χ ratios from RAL at 6M acid concentration

Input interface index of refraction	1.0000	1.0788	1.1576	1.1972	1.2364	1.3152	1.3940
Output interface index of refraction	1.0000	1.0930	1.1860	1.2323	1.2790	1.3720	1.4650
χ_{ZZZ} / χ_{ZXX}	1.72	2.33	3.10	3.53	4.02	5.15	6.50
χ_{ZZZ} / χ_{XXZ}	1.62	2.25	3.06	3.53	4.05	5.28	6.76
χ_{ZXX} / χ_{XXZ}	0.94	0.97	0.99	1.00	1.01	1.02	1.04

Table 4. Calculated values for χ ratios from RAL at 12M acid concentration

Input interface index of refraction	1.0000	1.0800	1.1601	1.2002	1.2401	1.3202	1.4003
Output interface index of refraction	1.0000	1.1060	1.1932	1.2415	1.2898	1.3864	1.4830
χ_{ZZZ} / χ_{ZXX}	1.15	1.57	2.09	2.39	2.72	3.50	4.42
χ_{ZZZ} / χ_{XXZ}	1.21	1.69	2.31	2.68	3.08	4.04	5.20
χ_{ZXX} / χ_{XXZ}	1.05	1.08	1.11	1.12	1.13	1.16	1.17

Table 5. Calculated values for χ ratios from RAL at 15M acid concentration

Concentration / M	6	12[a]	15
χ_{ZZZ} / χ_{ZXX}	3.46	3.19	2.39
χ_{ZZZ} / χ_{XXZ}	3.34	3.39	2.68
χ_{ZXX} / χ_{XXZ}	0.97	1.07	1.12

Table 6. Variation of χ ratios with concentration, recorded at RAL
(a – averaged values)

Input interface index of refraction	1.0000	1.0800	1.1601	1.2002	1.2401	1.3202	1.4003
Output interface index of refraction	1.0000	1.1060	1.1932	1.2415	1.2898	1.3864	1.4830
χ_{ZZZ} / χ_{ZXX}	1.32	1.79	2.40	2.74	3.12	4.01	5.07
χ_{ZZZ} / χ_{XXZ}	1.30	1.82	2.50	2.89	3.33	4.36	5.61
χ_{ZXX} / χ_{XXZ}	0.99	1.02	1.04	1.06	1.07	1.09	1.11

Table 7. Calculated values for χ ratios from RAL at 15M acid concentration at 85°C

Luminescence imaging microscopy and lifetime mapping using kinetically stable lanthanide (III) complexes

A Beeby, I M Clarkson, S Faulkner, D Parker, J A G Williams.

Department of Chemistry, University of Durham, South Road, Durham, DH1 3LE, UK.

K Henbest, A W Parker.

CLRC Rutherford Appleton Laboratory, Chilton, Didcot, Oxon., OX11 0QX, UK.

T Powell, V Twist.

Department of Physiology, University of Oxford, South Parks Road, Oxford, UK.

Introduction

Time-resolved luminescence microscopy offers many advantages over conventional transmission and fluorescence microscopy. As well as the improved sensitivity inherent in luminescence microscopy, time-resolution offers the possibility of gating out short-lived fluorescence emanating from biological chromophores [1, 2]. To achieve this, the lifetime of the luminescent reporter group must be significantly longer than that of the autofluorescence. While small differences between the lifetimes will suffice, the ideal reporter group should have a lifetime several orders of magnitude longer than that of background fluorescence, i.e. greater than a microsecond .

Sensitized luminescence from lanthanide complexes offers an ideal method, since energy transfer from aromatic chromophores to lanthanide ions is well documented [3] and since lanthanide luminescence tends to be long lived and independent of the degree of sample aeration.

However, little use has been made of such agents in time-resolved microscopy and the few reported examples utilise kinetically unstable complexes based on amino-carboxylate ligands such as DTPA. This is rather surprising given the wide variety of kinetically stable lanthanide complexes which have been synthesised for use in magnetic resonance imaging (MRI), where the additional information provided by high resolution microscopy could provide important information regarding sub-cellular localisation.

Experimental

Systems studied included silica particles, onion cells and guinea pig heart cells stained with either the europium (III) or terbium (III) complex of **1**. Materials stained with Rhodamine 6G were used as a model for autofluorescence. Sample excitation used the 3rd harmonic of a Nd:YAG laser (355 nm). The luminescence was then collected and focussed onto an image intensifier projecting the image onto a CCD camera. Time-resolved measurements were obtained by control of the image intensifier gate period.

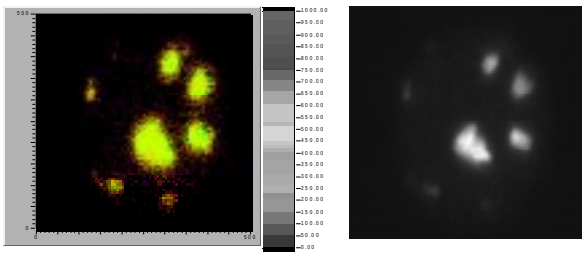

Figure 1.

Results and Discussion

Initial investigations concentrated on demonstrating the possibility of using the complexes in time-resolved imaging. Images of silica particles labelled with europium (III) complex were taken at various time delays allowing a lifetime map to be built up. Figure 1 shows the contrast that can be obtained using time gated imaging and the lifetime map for the europium (III) complex. The lifetimes of the particles correspond closely to that of the complex in solution.

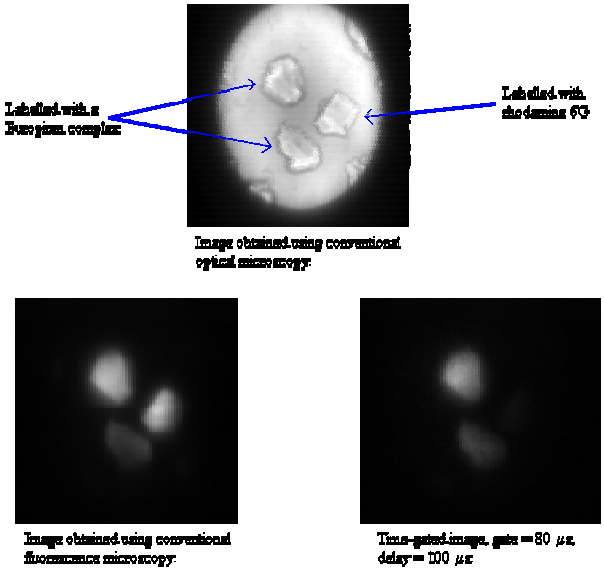

Figure 2.

A more complex experiment involved the study of a sample consisting of a mixture of particles labelled with the europium complex and Rhodamine 6G. Figure 2 shows that the particles were found to be indistinguishable using transmission and fluorescence microscopy. In the time-gated image it can be seen that the Rhodamine 6G labelled particle is no longer visible, demonstrating that the short-lived fluorescence can readily be gated out by such techniques.

Further experiments were performed using onion skin cells and guinea pig heart cells. The guinea pig cells were loaded with complex using electroporation. The images that were obtained showed staining of these cells by our complex and that the autofluorescence could be removed by time-gating techniques.

Conclusions

The work presented here has demonstrated the viability of this technique for the study of lanthanide complexes in a range of environments. We can now apply the method to investigate the bio-distribution of these important materials.

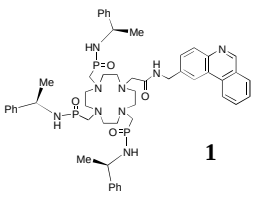

1

References

1. Seveus L, Vailsala M, Syrjanen S, Sandberg M, Kuusisto A, Harju R, Salo J, Hemmila I, Kojola H, Soini E, Cytometry, **1992**, 13, 329.
2. Marriott G, Heidecker M, Diamandis E P, Yanmarriott Y, Biophysical Journal, **1994**, 67, 957
3. Parker D., Williams J. A. G., J. Chem. Soc. Dalton Trans., **1996**, 3631

REMPI studies of the photolysis of physisorbed molecules

C J S M Simpson, P T Griffiths.

Department of Physical and Theoretical Chemistry, Oxford University

M Towrie.

CLRC Rutherford Appleton Laboratory, Chilton, Didcot, Oxon., OX11 0QX.

Introduction

Over the past year, we have extended our previous studies of the photolysis of alkyl nitrites and NO dimers. As before, a transparent, insulating MgF_2 surface was used to avoid surface-induced processes occurring within the adsorbate layer. This allows our experiments to concentrate on the dynamics of the adsorbed molecules.

In these experiments we have been primarily interested in the electronic degree of freedom of the product NO and in the distribution of its angular momentum vector, J, in the laboratory frame.

Experimental

For these experiments, our UHV apparatus was transported to the Rutherford Appleton Laboratory. A base pressure of 2×10^{-10} Torr was achieved using a combination of diffusion pumping and liquid helium and nitrogen cooled cryopumps.

The MgF2 surface was dosed with the equivalent of around four monolayers, and then moved into the path of the photolysis laser beam. For the photolysis step, we used the frequency-doubled output of the Laser for Science Facility's nanosecond OPO, giving a photolysis wavelength between 250 and 400 nm and laser fluences of no more than 0.5 $mJcm^{-2}$.

Following photolysis, NO was desorbed from the surface. It was detected using a two-colour, two-photon REMPI spectroscopy technique. The frequency-doubled output of a dye laser was used for the resonant transition, in this case the X2Π –> A2Σ+ transition, with the electronically excited NO being ionized by a portion of the output 308 nm excimer, which also pumped the dye laser [1]. This provided a very sensitive detection technique, able to detect a partial pressure of 2×10^{-13} Torr of NO with signal-to-noise ratio of 3:1.

Results

1. Λ-doublet population of NO desorbed from NO dimers

NO is an open shell molecule, having a π^1 configuration, and for high-J rotational levels, the orbital can take one of two orientations with respect to the plane of rotation of the molecule [2]. In the first, denoted Π(A'), the lobe is within the plane of rotation. In the other, the Π(A"), the lobe is perpendicular to the plane of rotation. For the F_1 manifold of the ground state, these two orientations correspond to the *e/f* spectroscopic states, and are probed by the R_{11} and Q_{11} transitions respectively.

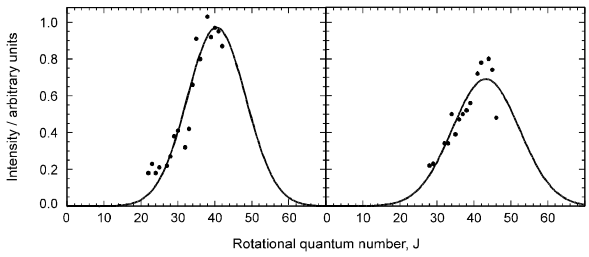

Figure 1. left hand figure: R_{11} transitions; right hand figure Q_{11} transition. The data are fitted to Gaussian functions.

Figure 1 shows the relative intensity of these two transitions for NO desorbed from the photolysis of NO dimers at 250 nm. As can be seen, the R_{11} transitions are considerably stronger than the Q_{11}, indicating preferential population of the Π(A') Λ-doublet. The relative population is 1.4 +/- 0.3.

2 Alignment of NO desorbed from iso-butyl nitrite

Over the past year, we have extended our previous experiments to include a more thorough study of the effect of the polarisation of the photolysis laser on the (v,J) state and yield of desorbed products.

REMPI spectra of NO(v=2) were recorded for a number of different polarisations of both photolysis and detection laser. Through these spectra, we were able to investigate the alignment of the product NO. Alignment is the anisotropic distribution of **J** in the laboratory frame, and is manifest in the different strength of P-Q- and R-branch transitions within the REMPI spectrum [3]. This is because of the well-defined directionality of the transition dipoles with respect to **J**: for high-J states, the Q-branch transition dipole lies parallel to **J**, while that of the P- and R-branches lies perpendicular to **J**.

In our case, we observed strong Q_{11}-branch and weak R_{21} transitions for vertical polarisation of photolysis and detection laser. We consider that this indicates that in this case the product is vertically aligned, i.e. that the **J** vector of the product lies preferentially vertical.

This was confirmed by rotating the plane of polarisation of the detection laser to horizontal, so that the axis of alignment was perpendicular to the plane of polarisation of the detection laser. Stronger P- and R-branch transitions were then observed, as is to be expected if the distribution of **J** is perpendicular to the plane of polarisation of the detection laser (see figure 3 a).

In our experiments, in which the surface was mounted vertically, this mode of desorption may also be described as cartwheeling away from the surface, as shown in the left hand part of Figure 2.

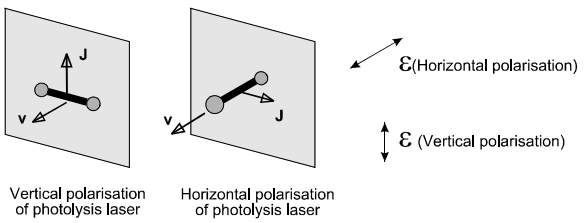

Figure 2. The dependence of the desorption dynamics on the photolysis laser. ε is the electric vector of the plane polarised detection laser.

In our second set of experiments, we studied effect of horizontal polarisation of the photolysis laser. In this case, as shown in figure 3, no significant change in intensity was observed as the polarisation of the detection laser was rotated. Indeed, the ratio of the Q_{11} to R_{21} transitions is constant to within experimental error. There is a small, though significant, change in the ratio of the intensity of the Q_{11} to R_{11} transitions. We consider that

only small changes are observed because the J vector of the product NO makes almost the same angle with respect to both vertical and horizontal planes of polarisation of the detection laser, in contrast to the large changes seen for horizontal polarisation of the photolysis laser. These observations are consistent with a cartwheeling mode of desorption, in which the axis of alignment is horizontal. This is shown in the right hand part of figure 2. As can be seen in this case the **J** vector makes the same angle with both polarisations of the detection laser.

Thus we have found that the axis of alignment in these surface experiments depends on the polarisation of the photolysis laser. In subsequent experiments, we found that the degree of alignment also depends on the polarisation of the photolysis laser, with horizontal polarisation giving a lower degree of alignment than vertical polarisation. This effect has been tentatively assigned to differing degrees of collisional relaxation prior to desorption for the two polarisations, with horizontal polarisation resulting in a greater degree of relaxation. The complete analysis of these results will be given in reference 4.

Conclusions

Our measurements on the NO dimer system have been used to make some suggestions concerning the upper state from which the dissociation occurs. In particular, the preference for the $p\pi$ lobe to lie within the plane of rotation indicates that the photolysis involves in-plane excitation of the planar molecule.

The study of the alignment provides a very sensitive study of the dynamics of the adsorbed molecules. Unfortunately, our apparatus is not particularly well-suited to this study, and our conclusions are only very qualitative. Nevertheless, we have been able to show that vertical polarisation yields vertical alignment of the desorbed NO, and horizontal polarisation yields horizontal alignment. Moreover, the degree of alignment also depends on the polarisation of the laser, being a maximum with vertical polarisation.

References

1. A.E. Wiskerke et al.
   J. Chem. Phys. **102** (1995) 3835.
2. M.H. Alexander and P.J. Dagdigian,
   J. Chem. Phys. **89** (1988) 4325.
3. R. Vasudev, R.N. Zare and R.N. Dixon ,
   J. Chem. Phys **80** (1984) 4863.
4. P.T. Griffiths, C.J.S.M. Simpson and M.Towrie,
   to be submitted to Chem. Phys. Letters.

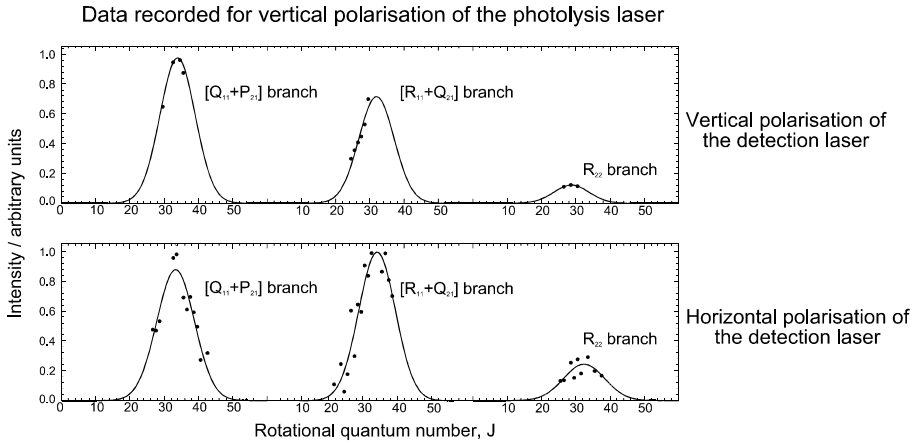

Figure 3a. Comparison of NO branching ratios for vertical and horizontal polarisation of the detection laser and vertical polarisation of the photolysis laser.

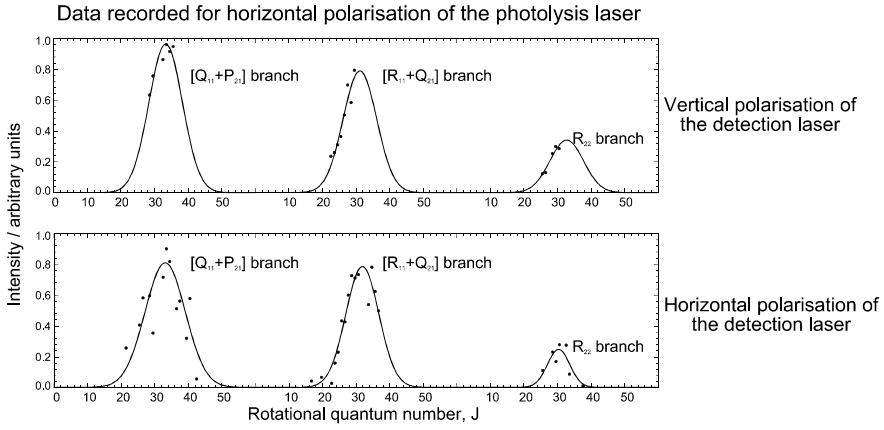

Figure 3b. Comparison of NO branching ratios for vertical and horizontal polarisation of the detection laser and horizontal polarisation of the photolysis laser.

Photophysics of Novel Electropolymerised Indoles

P Jennings, A C Jones, A R Mount.

Department of Chemistry, The University of Edinburgh, West Mains Road, Edinburgh, UK, EH9 3JJ. Email a.c.jones@ed.ac.uk

Introduction

Conjugated polymers are organic semiconductors, the semiconducting behaviour being associated with the π molecular orbitals delocalised along the polymer chain. Most of the interest in conjugated polymers has been concerned with their properties as conducting materials and comparatively little attention has been given to their luminescence properties. Conjugated polymers which have large semiconductor bandgaps can exhibit high photoluminescence quantum yields and there is increasing interest in the excitonic properties of these materials. At present, the best known and most intensively studied example of such a system is poly(p-phenylene vinylene) [1-3]. The electropolymerised 5-substituted indoles which are the subject of this research project are new examples of photoluminescent conjugated polymer systems. The occurrence of efficient luminescence in conjugated polymers has become of technological interest since the discovery that electroluminescence could be produced from poly(phenylene vinylene) in thin-film light-emitting diode structures [2]. Electroluminescent polymer films have potential applications in the development of large-area light-emitting displays.

Recent work in Edinburgh on the electropolymerisation of 5-substituted indoles has shown that the polymerisation proceeds via a trimeric intermediate and that the polymer consists of linked trimer units [4-6]. The trimer intermediate is stable and can be readily isolated. Using laser mass spectrometry and NMR spectroscopy, it has been shown that the trimer has a cyclic structure of the form illustrated in figure 1 [5]. The polymer thus consists of linked cyclic trimer units, rather than a linear chain of monomers as had been supposed previously [7].

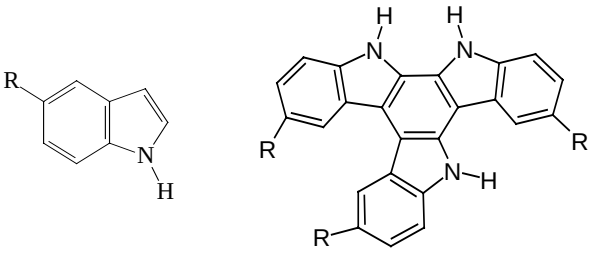

Figure 1. The structure of the 5-substituted indole monomer and trimer.

The aim of this research project was to carry out a detailed investigation of the photophysical properties of these systems with particular emphasis on the factors which influence their photoluminescence efficiency. The electrochemically generated trimers and polymers of a variety of 5-substituted indoles, 5-cyanoindole, indole-5-carboxylic acid, 5-bromoindole, 5-chloroindole and 5-methoxyindole, have been investigated in solution phase and as intact polymer films on the electrode surface, using the techniques of steady state fluorescence spectroscopy and picosecond time-correlated single photon counting.

Experimental

Steady state fluorescence measurments were carried out in Edinburgh using a Spex Fluoromax spectrofluorimeter system. Time-resolved fluorescence measurements were carried out at the CLRC Lasers for Science Facility, using a picosecond mode-locked Nd:YAG-pumped dye laser system and a time-correlated single photon counting system.

Results and Discussion

Solution phase measurements

The emission spectra of the monomer and trimer species are exemplified by those shown in figure 2 for 5-bromoindole. The trimer emission is considerably bathochromically shifted relative to the monomer, consistent with the increase in π-electron delocalisation in the trimer system.

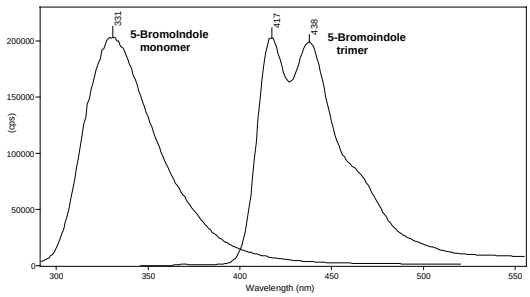

Figure 2. Emission spectra of the monomer and trimer of 5-bromoindole in solution at room temperature.

The relative proportions of trimer and polymer species in the electropolymer film can be controlled using a rotating disc electrode and varying the concentration of the monomer in the background electrolyte [4]. When the working electrode is stationary, transport to the surface is diffusion limited and application of an oxidising potential results in a rapid depletion of monomer at the electrode surface allowing linking of the trimer units on the surface, forming chains of polymer consisting of linked trimers. At high rotation speeds, forced convection occurs, refreshing the supply of monomer at the surface; under these conditions, formation of trimer and film growth is favoured over further oxidation to polymer and the

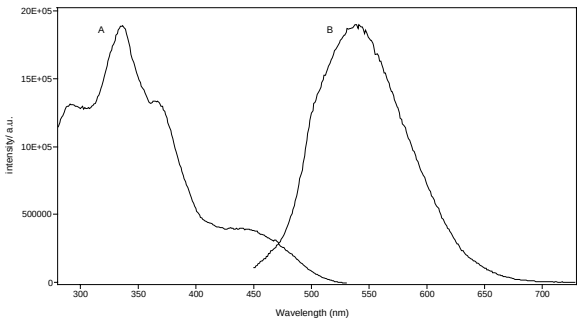

Figure 3. Excitation (A) and emission (B) spectra of 5-bromoindole electropolymer in solution.

resulting film is rich in trimer species. The fluorescence properties of the electropolymer are exemplified in figure 3. The bathochromic shift of the polymer spectrum relative to the trimer indicates exciton delocalisation over conjugation lengths of several trimer units and the broadness of the spectrum reflects the existence of a distribution of conjugation lengths.

The 5-substituted indole monomers and trimers exhibit single exponential fluorescence decays, as expected for single emitting species. The monomers have fluorescence lifetimes of several nanoseconds, comparable with values which have been reported for other indoles [8]. The lifetimes of the trimers are also of

several nanoseconds, similar in magnitude to the lifetimes of the monomers. A typical fluorescence response function and fitted monoexponential decay function for 5-cyanoindole trimer are shown in figure 4.

In contrast, the polymer systems show complex multiexponential decays, as illustrated in figure 4 for 5-cyanoindole electropolymer. Exponential functions with at least 4 lifetime components are required to adequately fit the experimental decay curves of the polymer solutions. This multiexponential decay behaviour is indicative of the presence of a multiplicity of emitting species, consistent with the picture of emission arising from polymer chain segments with a distribution of conjugation lengths. Multiexponential decay curves are observed across the range of emission wavelengths characteristic of the polymer species, whereas at shorter emission wavelengths, characteristic of the trimer species, a single exponential decay function is found.

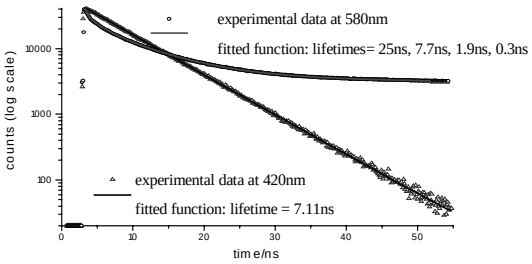

Figure 4. Fluorescence response function for 5-cyanoindole trimer (420nm emission) with fitted monoexponential decay function and for 5-cyanoindole polymer (580nm emission) with fitted 4-exponential function.

Measurements of intact polymer films

As in solution phase, the intact films exhibit broad unstructured emission characteristic of a superposition of many slightly different spectra arising from the existence of a distribution of conjugation lengths. Using a demountable electrode, fluorescence response functions of intact polymer films on the electrode surface were measured. The films are highly fluorescent in the reduced state but non-fluorescent in the oxidised state. The reduced films show complex multiexponential decay kinetics and the lifetimes of the emitting species are substantially shorter than those in solution, showing that the photoluminescence efficiency is decreased. This indicates that interchain interactions enhance non-radiative decay rates. Interchain interactions may influence chain geometry and hence conjugation length. Also, exciton hopping between chains in the polymer film may lead to an increase in non-radiative decay rate as a result of an increased rate of exciton migration to quenching sites.

The fluorescence of non-emitting oxidised films is restored when the films are dissolved, indicating that it is the morphology of the film not the composition of the polymer backbone that is responsible for the quenching of the fluorescence. The oxidised and reduced species in solution show essentially identical fluorescence response functions. The oxidised films are more electronically conducting [9)] than the reduced films and electron transfer is expected to constitute a major non-radiative decay channel in the oxidised intact film.

The quenching of fluorescence by oxidation of the film is reversible, reducing the film again restores the fluorescence. However, oxidation of the film to the point where linking of residual trimers and oligomers to form a more extensive

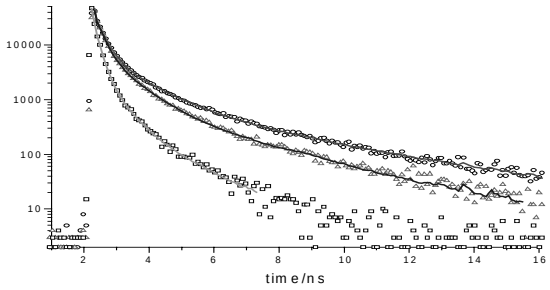

Figure 5. The effect on the fluorescence response function of a 5-cyanoindole film of cycling the potential from reduced to oxidative polymerisation and back to reduced. The top fluorescence response function is for an uncycled film; the middle trace shows the result of one cycle and the bottom trace shows the result of two cycles.

polymer system results in an irreversible decrease in fluorescence lifetimes and hence in photoluminescence efficiency. This is illustrated in figure 5 which shows the effect on the fluorescence response function of repeatedly cycling a film of 5-cyanoindole polymer between reduced and oxidative polymerisation potentials. With repeated cycling. i.e. with increasing chain length and cross-linking, the fluorescence lifetimes become ever shorter until the film becomes non-fluorescent.

Conclusion

The fluorescence properties of a number of 5-substituted indole electroplolymers have been investigated in detail, in solution and as intact polymer films. The electrochemically generated polymer films show intense visible photoluminescence and, therefore, are potential candidates for the development of new electroluminescent materials. The use of picosecond time-resolved fluorescence measurements in conjunction with electrochemical control of the polymerisation conditions has afforded an important insight into the factors which influence the luminescence efficiency of these systems.

References

1. R H Friend, D D.C Bradley, P D Townsend
J. Phys. D 20 1367 (1987)

2. J.H. Burroughs, D.D.C. Bradley, A.R. Brown, R.N. Marks, K. Mackay, R.H. Friend, P.L. Burns and A.B. Holmes, Nature 1990,**347**,539.

3. I.D.W. Samuel, B. Crystall, G. Rumbles, P.L. Burn, A.B. Holmes and R.H. Friend,
Chem. Phys. Lett. 1993,**213**,472.

4. J.G. Mackintosh and A.R. Mount,
J. Chem. Soc. Faraday Trans.1994, **90**, 1121

5. J.G. Mackintosh, C.R. Redpath, A.C. Jones, P.R.R. Langridge-Smith, D. Reed and A.R. Mount,
J. Electroanal Chem. 1994, **375**, 163

6. P. Jennings, A.C. Jones, A.R. Mount and A.D. Thomson,
J. Chem. Soc. Faraday Trans.1997, **93**, 3791

7. P.N. Bartlett, D.H. Dawson and J. Farrington,
J. Chem. Soc. Faraday Trans. 1992, **88**, 2685.

8. S.R. Meech, D. Phillips and A.G. Lee,
Chem. Phys. 1983, **80**, 317.

9. A.R. Mount,
Research in Chemical Kinetics, 1997, **4,** 1

Kinetics of C_2H Radical Reactions at the Temperatures of Interstellar Clouds

D Chastaing, P L James, I R Sims, I W M Smith.

The University of Birmingham, School of Chemistry, Edgbaston, Birmingham, B15 2TT. Email i.r.sims@bham.ac.uk

Introduction

The investigation of reactive and non-reactive molecular collisions in the gas phase at ultra-low temperatures is both of fundamental significance and also of great importance in solving a range of astrochemical problems, especially regarding the improvement of models for molecular synthesis in dense interstellar clouds [1)] and planetary atmospheres. Until very recently, *all* of the rate coefficients included in such models were of dubious reliability, being either calculated theoretically or extrapolated from experimental data obtained at much higher temperatures.

Recently, we have, in collaboration with Dr Bertrand Rowe and his colleagues in Rennes, developed a new technique which has enabled us, for the first time, to measure rate coefficients for bimolecular reactions between electrically neutral species down to temperatures as low as 13 K. We have reviewed progress in gas-phase kinetics at very low temperatures in an article for *Annual Reviews of Physical Chemistry* [2)].

The ethynyl radical, C_2H, is widely observed in dense interstellar clouds, and it is this species' role in the synthesis of cyanopolyynes that was the primary motivation behind this work. The higher members of the series of cyanopolyynes, $H(C)_{2n}CN$ with $n \leq 5$, are the species with the longest carbon chains which have been unequivocally identified in dense interstellar clouds [3), 4)]. In 1992, following on from our earlier work on CN radical reactions with hydrocarbons [5)], we suggested[4)] that these species might be generated by sequences of neutral-neutral reactions involving CN and C_2H (ethynyl) radicals with polyynes and smaller cyanopolyynes; i.e.

$$C_2H + H(C)_{2n}H \rightarrow H(C)_{2n+2}H + H \quad (1a)$$

$$C_2H + H(C)_{2n}CN \rightarrow H(C)_{2n+2}CN + H \quad (1b)$$

$$CN + H(C)_{2n}H \rightarrow H(C)_{2n}CN + H \quad (2)$$

In this work, we set out to measure rate coefficients for reactions of type (1a), as well as other reactions of the C_2H radical, at temperatures as low as 15 K, using laser photochemical techniques in the ultracold environment of the Birmingham CRESU (Cinétique de Réaction en Ecoulement Supersonique Uniforme) apparatus.

Experimental

The heart of the CRESU technique lies in the nature of the isentropic expansion of gas through a convergent-divergent Laval nozzle. It produces a supersonic flow of gas which is uniform in temperature, density and velocity and which endures for several tens of centimetres and hundreds of microseconds. The density of gas in the flow is quite high (10^{16}—10^{17} molecule cm^{-3}) and frequent collisions ensure the maintenance of thermal equilibrium. The rapidity of the expansion and the fact that the gases do not make contact with cold surfaces prevents condensation. A diagram of the Birmingham CRESU apparatus is given elsewhere [6)]. A full description has been published [7)].

The kinetics of C_2H reactions were studied in the ultracold environment of the CRESU apparatus using the pulsed laser photolysis-chemiluminescent marker (PLP-CL) technique. Our first, and most extensive, experiments have been carried out on mixtures containing relatively small concentrations of both C_2H_2 and O_2 diluted in the carrier gas (He, Ar or N_2) for which the particular nozzle was designed. C_2H radicals were generated by the 193 nm excimer laser photolysis of a small fraction of the C_2H_2 and then reacted with both C_2H_2 and O_2:

$$C_2H_2 + h\nu\ (\lambda = 193\ nm) \rightarrow C_2H + H \quad (3)$$

$$C_2H + C_2H_2 \rightarrow \text{products} \quad (4)$$

$$C_2H + O_2 \rightarrow \text{products} \quad (5)$$

Reaction (5) proceeds via a number of channels. Branching ratios are not completely established even at room temperature. However, one minor channel produces $CH(A^2\Delta)$:

$$C_2H + O_2 \rightarrow CH(A^2\Delta) + CO_2 \quad (5a)$$

and the progress of reactions can be followed by observing how the intensity of the $CH(A^2\Delta \rightarrow X^2\Pi)$ chemiluminescence varies with time [6), 8)].

Results

To establish values of the second-order rate coefficients k_4 and k_5, series of experiments were performed in which the concentration of either C_2H_2 or O_2 was varied whilst the other concentration was kept constant. In addition, the reactions of C_2H with C_2H_4 and C_3H_6

$$C_2H + C_2H_4 \rightarrow \text{products} \quad (6)$$

$$C_2H + C_3H_6 \rightarrow \text{products} \quad (7)$$

have been investigated in series of experiments in which different concentrations of these additional reagents were added to mixtures containing constant concentrations of both C_2H_2 and O_2. The temperature-dependence of the rate coefficients for reactions of C_2H with C_2H_2, O_2, C_2H_4 and C_3H_6 are displayed in figure 1.

Discussion

The magnitudes of the rate coefficients for the reactions of C_2H with C_2H_2, C_2H_4 and C_3H_6, their lack of any dependence on pressure and their increase as the temperature is lowered, as well as thermochemical considerations, all point to these reactions proceeding via initial formation of an energised complex which then rapidly loses a H atom, such that

$$C_xH_y + C_2H \rightarrow C_{x+2}H_y + H \quad (8)$$

This proposal parallels that made [5)] for the reactions of CN radicals with unsaturated hydrocarbons, where again the overwhelming evidence is that the radical displaces a H atom in the molecular reagent. The kinetics of the reaction between C_2H and O_2 again suggest that reaction proceeds via the initial formation of a transient energised complex, in this case a substituted peroxy radical, over a potential energy surface on which there is no barrier between reagents and complex. This is undoubtedly the case for the isoelectronic reaction between CN and O_2 [7)]. In the reaction between C_2H and O_2, a number of reaction product pathways are possible on thermochemical grounds but our results shed no light on the branching ratios.

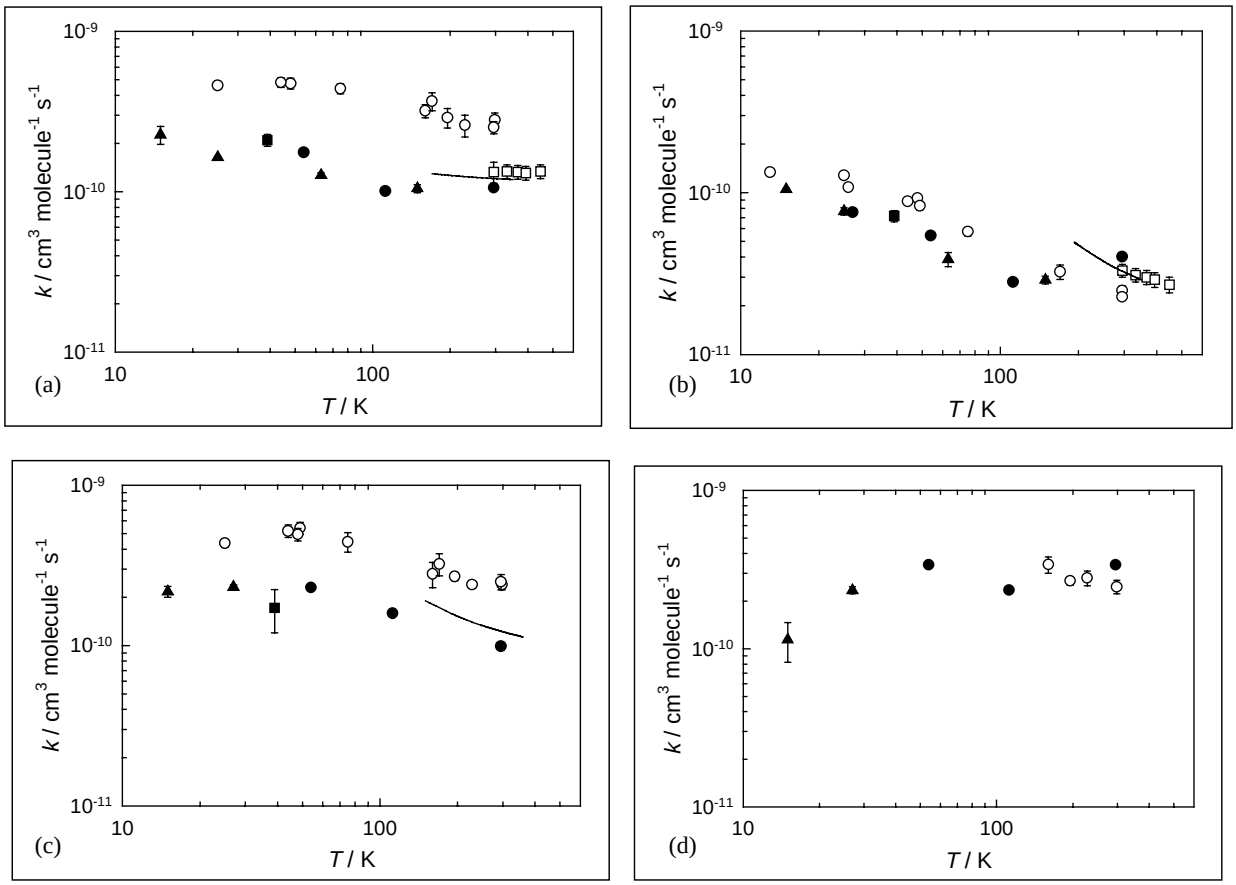

Figure 1. (a)—(d) Rate coefficients k for the reaction of C_2H with C_2H_2, O_2, C_2H_4 and C_3H_6 respectively, plotted on a log-log scale against temperature. The filled symbols show the results of this work: circles (●) denoting Ar carrier gas; squares (■) N_2; and triangles (▲) He. Where applicable, the results of Van Look and Peeters [9] using a comparable chemiluminescent technique are shown as open squares (□), while the results of Leone and co-workers [10 - 12] obtained by an infrared laser absorption technique are shown as a solid line (—). In addition, the combined cell and CRESU results of Sims *et al* [5, 7] for the analogous CN reactions are shown as open circles (○)

A major motivation for this work was our earlier proposal [4] that the kinetics of reactions of C_2H should be similar to those of CN, and therefore that a number of such reactions should contribute to the chemistry of cold interstellar clouds where C_2H and CN are among the most abundant free radicals. In figure 1, we compare the rate coefficients for reactions of C_2H with those measured previously [5] for the corresponding reactions of CN. Our latest data clearly confirm the earlier hypothesis. With the unsaturated hydrocarbons, the reactions of C_2H radicals are somewhat slower than those of CN. This difference may reflect either the slight increase in structural complexity in going from CN to C_2H or the lower dipole moment of C_2H which will mean that the long-range potential between it and a given molecule will be somewhat less strongly attractive than that between CN and the same molecule. Arguments are presented elsewhere [6] to support the extension of these results to the reactions of longer-chain unsaturated species. The present results support the earlier hypothesis that reactions of CN and C_2H with alkynes and cyanoalkynes probably play a major role in the formation and reactions of cyanopolyynes in cold dark interstellar clouds.

We thank the EPSRC and the EU for financial support. The Laser Support Facility Loan Pool provided one of the excimer lasers, for which we express our thanks. We are very grateful to Dr Bertrand Rowe and colleagues at Rennes for valuable discussions.

References

1. W W Duley and D A Williams,
Interstellar Chemistry, Academic Press, New York, (1980)
2. I R Sims and I W M Smith
Ann. Rev. Phys. Chem., 46 109, (1995)
3. M B Bell, *et al*
Astrophys. J., 483 L61 (1997)
4. I R Sims and I W M Smith
J. Chem. Soc., Far. Trans., 89 2166, (1993)
5. I R Sims *et al*
Chem. Phys. Lett., 211 461, (1993)
6. D Chastaing *et al*
Faraday Discuss., 109 165, (1998)
7. I R Sims *et al*
J. Chem. Phys., 100 4229, (1994)
8. K Devriendt *et al*
Chem. Phys. Lett., 261 450, (1996)
9. H Vanlook and J Peeters
J. Phys.Chem., 99 16284, (1995)
10. J O P Pedersen *et al*
J. Phys.Chem., 97 6822, (1993)
11. B J Opansky *et al*
J. Phys.Chem., 97 8583, (1993)
12. B J Opansky and S R Leone
J. Phys.Chem., 100 19904, (1996)

Diffraction Spectroscopy using a 1 kHz Femtosecond-laser Generated X-ray Source

D Klug, I Mercer, R Tompkins.

Department of Chemistry, Imperial College of London, London SW7 2AY. Email D.Klug@ic.ac.uk

P Matousek, M Towrie, A W Parker, I Clark, S Jackson.

CLRC Rutherford Appleton Laboratory, Chilton, Didcot, Oxon., OX11 0QX

Introduction

The experiments were carried out to explore potential opportunities in the area of picosecond/femtosecond time-resolved X-ray spectroscopy by utilising the novel X-ray source technology developed at Imperial College[1)]. The source is based on focusing intense fs laser pulses into a flowing liquid target housed within a vacuum and generates either quasi-continuum or quasi-monochromatic ps pulsed X-ray radiation.

Chief experimental goals were (i) to reproduce IC results at RAL and assess the source performance under conditions specific to the RAL laser system (ii) to optimise the X-ray source (iii) to obtain the diffraction pattern of water (iv) to assess the applicability of the X-ray source at RAL user experiments.

Reproduction of IC Results at RAL

Liquid target in vacuum

The X-ray source developed at IC using fs laser pulses on flowing liquid jets can provide either continuum X-ray radiation in the 10 keV spectral or quasi-monochromatic emission at ~ 9 keV (Cu Kα) using aqueous solutions of copper nitrate. A detailed description of the setup can be found in reference 1. The IC laser produces a 3 times shorter pulse but with lower available energy than the RAL laser. The pulse specifications for the RAL laser used in these experiments was 150 fs pulse duration and 0.9 mJ pulse energy. Both lasers operate at a wavelength of ~ 800 nm.

X-ray emission was successfully obtained at RAL and the IC results were reproduced. Measurements made using the single photon detector (Amptek XR-100T) enabled spectral characterisation of the source and confirmed that a well-defined monochromatic emission at Cu Kα line (~ 9 keV) is available from a concentrated copper nitrite solution in water and quasi-continuum from ethylene glycol.

Optimisation of the X-ray Source

Solid Cu target

The X-ray source was then further optimised to maximize the spectral brightness of the Cu Kα line (~ 9 keV). This line is well suited for probing molecular systems as it closely matches the typical spacing of diffracting 'layers'. The highest Cu Kα flux was obtained from a solid Cu target held in open atmosphere but with the plasma continuously flushed by a He gas jet. The target consisted of a spinning Cu ring (30 rev/s) with diameter ~ 4.2 cm mounted on a sliding stage which moved slowly back and forth with amplitude ~ 2 mm and period ~ 10 s. The laser pulses were focused onto the Cu target using a 3.6 cm focal length achromatic lens. Flowing of helium gas around the focal spot of the laser beam removed debris and avoided plasma build up within the laser interaction region. In the absence of this He gas stream the X-ray production was reduced by more than 2 orders of magnitude.

The absolute X-ray yield from the Cu target was estimated to be 2 - 4 x 10^9 photons/s emitted into 4π solid angle. This was evaluated from a measurement made 240 cm away from the source (a count rate of between 150 - 300 cts/s) and is based on 80 % quantum efficiency and 7 mm^2 sensitive area of the detector. This rate was approximately 100 - 200 times higher than that obtained at RAL using the vacuum chamber and copper nitrite jet.

Diffraction Pattern of Water

A goal of this study was to measure a diffraction pattern of water. This has been identified as a first step towards developing the technique for ps time-resolved X-ray spectroscopy to investigate the ultrafast dynamics occurring in solution phase chemical reactions. Picosecond and femtosecond experiments carried out by others have so far only succeeded in the detection of time-resolved pattern of heavy metals and crystalline structures[2-4)]. These experiments were carried out at similar X-ray fluxes to those used here and required accumulation times of many minutes. Water has a considerably lower diffraction scattering efficiency than the above examples thus, given time constraints and the single channel detector capability, a high throughput arrangement was required in order to produce detectable signals.

Unfortunately, this arrangement was hampered by X-ray photons elastically scattered at least twice from pinhole walls. The background signal levels obtained were similar to the expected diffraction signal. Non-elastically scattered photons could be efficiently rejected using the discriminator capability of the spectrally resolving detector. There is no simple means of subtracting the background produced from elastically scattered photons and this limits the capability of the arrangement to detect a diffraction pattern from water. However, with careful design of the collection system and the use of large area detector arrays it should be possible to produce a diffraction pattern of water within reasonable accumulation times using the flux densities achieved here.

Potential of the X-ray Source at RAL Experiments

Tests were carried out to assess the suitability of the X-ray source for RAL user experiments.

X-ray diffraction pattern of Si (111) sample on reflection

In this experiment a Si(111) crystal was measured in a reflective diffraction setup. The source to sample as well as the sample to source distances were 55 mm. The detector was mounted on a swiveling arm which could be moved through a serious of pre-programmed angles by computer control. The crystal angle was optimized by maximizing the scattering probability. The collected data is presented in figure 1. The expansion of the X ray collection path enabled the reduction of background levels to <1 count/s which was sufficient to detect the useful signal. X-ray diffraction pattern of Au plate on transmission

In this experiment a gold tape with no ordering and thickness ~ 300 μm was used. The diffraction pattern was successfully detected (see figure 2) using the same setup as for the Si(111) crystal experiment apart from using a transmission configuration.. In this case the maximum signal rate was about 4 times lower than that in the above experiment and this resulted in a poorer S/N ratio.

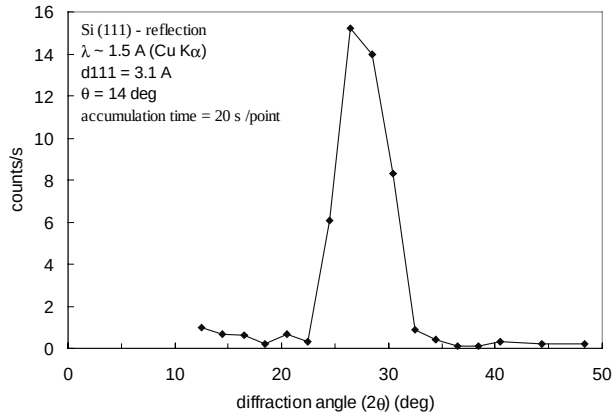

Figure 1. X-ray diffraction pattern of Si (111) measured on reflection using the laser generated X-ray source.

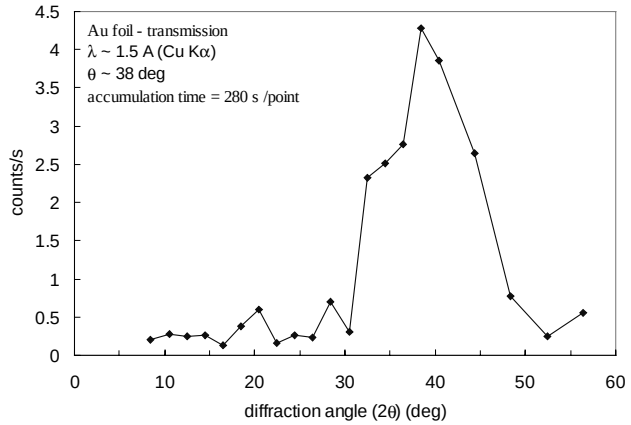

Figure 2. X-ray diffraction pattern of gold tape on transmission using the laser generated X-ray source.

Conclusions

(i) The liquid jet based X-ray source technology developed at IC was successfully transferred to RAL using the longer pulse/higher energy laser. Both broad (continuum) and narrow band (Cu Kα) performance at the $>10^7$ photons/second into 4π were demonstrated.

(ii) The incorporation of a solid copper target boosted the narrow band (Cu Kα) performance to $>10^9$ photons/s into 4π.

(iii) A water diffraction pattern was not obtained due to high noise background and unavailability of reference signal providing the absolute X-ray yield.

(iv) The X-ray source set-up successfully measured the diffraction pattern of gold (randomly oriented) and Si(111) crystal.

In summary, the current source requires further improvements to its yield, detection methods and suppression of the elastically scattered X-ray photon background before it would meet the requirements of experimentalists in the wider Lasers for Science Facility user community. This is believed to be feasible but must ultimately be driven by demand.

However, it has been demonstrated that the diffraction measurements of heavy atom metals and crystals and pump-probe experiments with the existing setup of the type described in references 1,2,3 and 4 are possible.

Acknowledgment

We thank ICE Turcu (RAL) and N.Takeyasu (Department of Chemical Science and Technology at the University of Kyushu, Japan) for expert assistance in the preparation and conduct of experiments.

References

1. R Tompkins
PhD thesis, Imperial College of London, submitted

2. J S Wark, D Riley, N C Woolsey, G Keihn, R R Whitlock
J .Appl.Phys. 68, 4531, (1990)

3. C Rischel, A Rousse, I Uschmann, P-A Albouy, J-P Geindre, P Audebert, J C Gauthier, E Forster, J-L Martin, A Antonetti
Nature 390, 490, (1997)

4. I V Tomov, P Chen, P M Rentzepis
J.Appl.Cryst. 28, 358, (1995)

An Investigation of Polyatomic Molecules in Intense Infrared Laser Beams

K W D Ledingham, R P Singhal, D J Smith, T McCanny, P Graham, H S Kilic [†], W X Peng [‡], S Lwang [#].

Department of Physics & Astronomy, University of Glasgow, Glasgow, G12 8QQ. Scotland, UK.

[†] Permanent address: Department of Physics, University of Selcuk, 42079.Konya, Turkey.
[‡]Permanent Address: Department of Physics, University of Jilin, Changchun, 130023, P.R.China
[#] Present Address: Department of Chemistry, University of Edinburgh, Edinburgh EH9 3JJ, Scotland

A J Langley, P F Taday.

CLRC Rutherford Appleton Laboratory, Didcot, Oxon., OX11 0QX. England, UK

C Kosmidis.

Department of Physics, University of Ioannina, Greece

Introduction

It is well known that stepwise multiphoton ionisation and fragmentation of polyatomic molecules like benzene can yield exclusively parent ions at 10^7 Wcm^{-2} using nanosecond laser pulses in the UV (soft ionization). As the intensity is increased to about 10^9 Wcm^{-2}, dissociation increases dramatically until low mass fragments dominate the spectrum with the parent peak often being missing entirely [1 - 3]. This process is called ladder switching fragmentation. For ladder switching to occur, fragmentation and subsequent photon absorption from the excited state neutral or parent ion must occur within the laser pulse width. On the other hand if the laser pulse is extremely short then the ladder climbing mechanism should dominate. It has been shown [4] that dissociation can largely be suppressed using intense (normally IR) laser beams up to 10^{14} Wcm^{-2} with the parent ion often being the strongest peak. This has also been observed recently for aromatic molecules using intense near-infrared radiation [5, 6].

The multiple ionisation of molecules in intense laser fields has become one of the most active areas of current study in atomic and molecular physics. In particular using picosecond and femtosecond lasers with intensities in the range $10^{14\text{-}16}$ Wcm^{-2}, the electric fields generated are no longer small compared to the binding molecular fields of the valence electrons and hence new physical effects are expected. For example for the irradiation of small molecules in intense laser fields, doubly charged parent ions can be detected and higher charged parent ions are present as transient species [7 - 12]. A special feature of this intense laser field ionization is multielectron ionization followed by dissociation through coulomb explosion of charged fragments [13].

Although the understanding of the interaction of intense laser beams with polyatomic molecules is at a preliminary stage [6], many laboratories are now showing considerable interest. The object of the present work is to demonstrate that a number of polyatomic molecules irradiated by intense laser beams with short laser pulses <90 fs and in the wavelength range 750-790 nm produce multiply charged parent ions and do not fragment appreciably to produce light particles. This was noticed without comment by Cornaggia [8] for C_3H_4 and has recently been demonstrated by Smith et al [14] for benzaldehyde. In this sense the molecules behave more like atoms.

Experimental

In the experiments described in this report the details of the apparatus have been described in a number of previous papers [14 - 17] dealing with one of the applications of this technology, namely femtosecond laser mass spectrometry (FLMS). Suffice it to say that a time of flight mass spectrometer (TOF) was used with unit mass resolution up to 100D. Gases were introduced effusively to the vacuum chamber at pressures up to 10^{-5} torr. A laser beam was focussed with a 100 mm mirror into the sensitive volume of the TOF to irradiate the molecular samples. The specifications of the laser pulses were: pulse width 50-90 fs, wavelengths 750-790 nm with intensities up to $2x10^{15}$ Wcm^{-2}.

Results and Discussion

Figure 1a shows a typical mass spectrum of deuterated benzene (C_6H_5D) with a purity of 98%. The irradiation conditions were $2x10^{15}$ Wcm^{-2} at 50 fs and at 790 nm. From previous work done in our laboratory on benzene[4] at high laser intensities, it was noticed that a strong peak appeared at mass 39 which could be due to the symmetric fragmentation of the parent to $C_3H_3^+$ or the doubly ionised parent mass. With deuterated benzene such an ambiguity was eliminated.

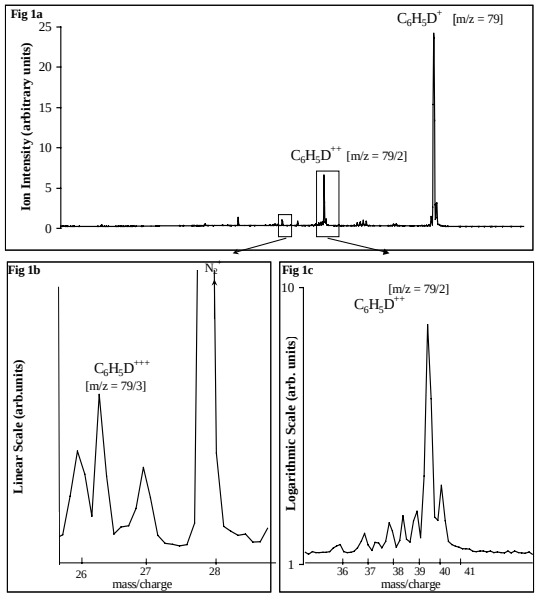

Figure 1. The mass spectrum of deuterated benzene with expanded areas around the 2^+ and 3^+ parent ion. The laser intensity is $2x10^{15}$ Wcm^{-2} with a pulse width of 50 fs and a wavelength of 790 nm.

It can be seen that the parent ion mass (79) is by far the strongest peak in the spectrum. The two expanded areas (b,c) correspond to the 3^+ and 2^+ charged parent ion peaks. The 2^+ peak at m/z=39.5 is the second strongest peak in the spectrum. This graph has been presented in logarithmic form to show clearly the small peaks between m/z=36-40 on either side of the main peak. The 3^+ parent molecule produces an unambigous peak at m/z=26.3. There were impurity peaks at $18(H_20)$, $28(N_2)$ and $32(O_2)$ but these caused no confusion. To the knowledge of the authors, this is the first time that highly ionised parent masses have been observed for medium mass molecules following intense laser irradiation.

It is worth pointing out that the appearance potentials of the 2^+ and 3^+ deuterated benzene are respectively 26 and 44 eV [18] and that the appearance potential for C^+ in the fragmentation of benzene using a UV ns laser is also about 26 eV [1]. The fact that the 2^+ parent ion peak was at least an order of magnitude larger than the carbon ion suggests that the normal fragmentation routes for ns irradiation were being bypassed in the fs irradiations. To return to the double ionised spectrum in figure 1c, the small peaks on either side of the main peak also deserve comment. First of all there are two half mass peaks at 37.5 and 38.5. These correspond to $C_6H_3^{2+}$and $C_6H_3D^{2+}$ respectively and the peak at mass 40 is due principally to the ion $C_5{}^{13}CH_5\ D^{2+}$. This also has the correct carbon isotope ratio for a molecule which contains six carbon atoms (7%). Thus the peaks at mass 38 and 39 are also likely to have a substantial doubly ionised component. The envelope of doubly ionised peaks every half mass corresponding to the parent molecule (M) and a number of (M-nH) satellites seems to be characteristic of polyatomic hydrocarbon molecules when irradiated in the infrared at the high laser intensities $10^{14\text{-}15}$ Wcm^{-2} and the other hydrocarbon molecules presented in this paper all show this doubly ionised cation group. This can always be distinguished from fragments by the small half mass peak at $(M\text{-}13)^{13}C^{2+}$ which must have the correct isotopic ratio. There was little evidence of multiply charged carbon atoms which is characteristic of coulomb explosion for lighter molecules [13].

The intensities of the 1^+, 2^+ and 3^+ parent peaks as well as some of the larger fragments from deuterated benzene are shown as a function of laser intensity in figure 2 at 790 nm and 50 fs pulse width. It would appear that the C_4H_5 and C_5H_4 ion peaks follow the intensity dependence of the parent ion while the 2^+ and 3^+ parent ion peaks have a stronger laser intensity dependence It can be seen in the inset diagram that the ratio of the 1^+ to 2^+ charged peaks is a strong function of the laser intensity. The value at 10^{15} Wcm^{-2} is close to the 1^+ to 2^+ ion ratio for atomic Xenon at similar laser intensities which was carried out under identical experimental conditions to the molecular work.

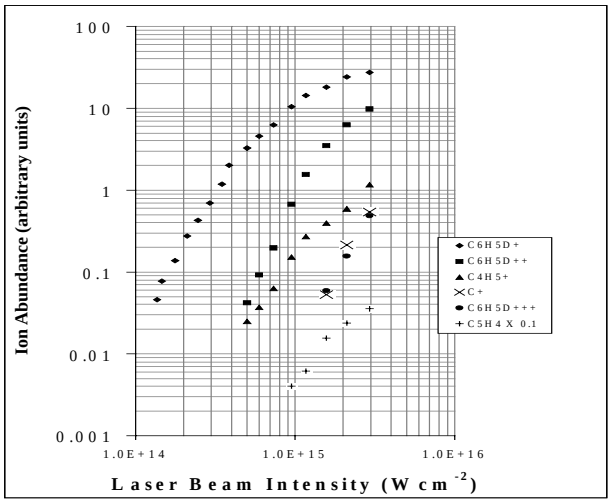

Figure 2. The ion abundances of a number of fragments and multiple charged species from deuterated benzene as a function of laser intensity under the laser conditions mentioned in figure 1. The gradients of the 2^+ and 3^+ ion curves are steeper than the others.

Figure 3 shows the mass spectrum of the linear molecule CS_2 at a laser intensity of 10^{15} Wcm^{-2} for 790 nm and 50 fs. The appearance potentials of $CS_2{}^{2+}$ and $CS_2{}^{3+}$ are 27.5 and 53.6 eV respectively [19]. This spectrum looks very similar to that of deuterated benzene with the 1^+ and 2^+ peaks being by far the strongest components and also an unambiguous $CS_2{}^{3+}$ signature being visible. Any other fragmentation is very small. There was however evidence for coulomb explosion in this molecule since small peaks of multiply charged C and S were present.

Finally in figure 4 the mass spectra of a number of different molecules are shown at various intensities in the IR for pulse widths less than 90 fs. For all the molecules presented here, the 1^+ and 2^+ ion peaks are the dominant entities and any other fragmentation is small. The spectrum for Xenon is also presented. A general theme from the present work seems to be emerging. For laser intensities in the infrared at intensities in the range $5x10^{13}$-10^{15} Wcm^{-2} the fragmentation for the molecules described in this paper is small. Multiply charged ions are evident up to 3^+ and for the hydrocarbon molecules, an envelope of 2^+ ions of (M-nH) entities is visible. Exceptionally the 3^+ ion for toluene was not seen. The characteristic envelope of 2^+ ions for the hydrocarbon molecules had intensity thresholds > $5x10^{13}$ Wcm^{-2}. The low degree of fragmentation observed in the present work is in agreement with the studies of DeWitt *et al* on aromatic molecules. These authors did not observe multiple charging in their spectra and this is also in accord with the present work since their maximum laser intensity was about $4x10^{13}$ Wcm^{-2}, marginally lower than the thresholds mentioned above.

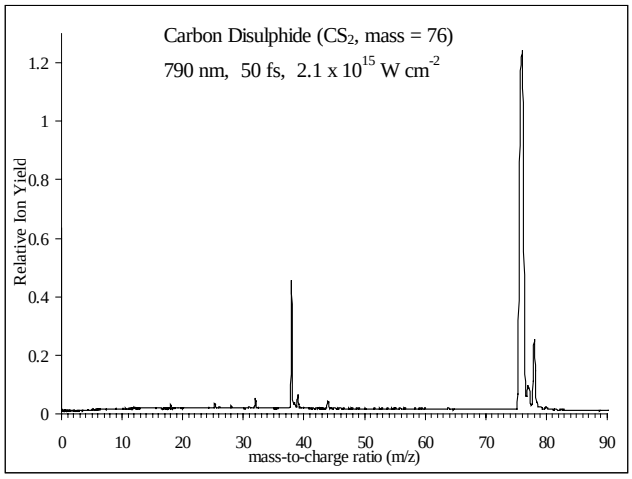

Figure 3. The mass spectrum of the linear molecule CS_2 with the single, double and triple ionised peaks visible. The laser conditions are similar to those described in figure1.

Conclusions

Under the intense laser irradiation reported in this letter, the polyatomic molecules which have been studied, show remarkable stability and electronic dynamics similar to that in atoms. Clearly ladder switching fragmentation of the type reported for ns pulses [1 - 3] is not taking place to any great degree.

The simplest model of the molecular behaviour in the strong IR laser fields observed in the present experiment is as follows. The molecules reach the 1^+ ion level by multiphoton processes during the rise time of the pulse. They then absorb more photons sequentially and reach the 2^+ and 3^+ levels either by tunnelling ionization or by barrier suppression [13]. This was the sequential mechanism proposed by Lambropolous [20] for multiple ionization of atoms by intense pulsed lasers. His calculations showed that multiply charged ions are only produced for laser intensities approaching 10^{14} $Wcm^{-2.}$ For sequential ionization, a charge state can be produced only after the previous charge state begins to volume saturate [21]. This would certainly describe the data in figure 2 where the onset of the 2^+ signal coincides with the flattening off of the parent ion intensity. It is thought that much of the intensity of the single

ionization peak comes from the lower intensity wings of the laser beam.

Coulomb explosion ionization is a possible mechanism for CS_2 since the multiply charged atoms of C and S are observed although at low intensities. No similar evidence for coulomb explosion is evident for the hydrocarbon molecules studied here. However an envelope of 2^+ cations is observed for these molecules and this shedding of hydrogen atoms at the 2^+ level or a mixture of charged and uncharged hydrogen atoms from the 3^+ level is a striking characteristic of this intensity regime.

Conventional coulomb explosion is unlikely to explain the present observations. For light molecules, multiply charged ions which lead to coulomb explosion are only transient species [13] while in the present work, the 2^+ and 3^+ parent ions have lifetimes at least of the order of the flight time in the TOF (about tens of μsecs). Any dissociation, particularly the shedding of hydrogen atoms, seems to be a rather gentle process similar to ordinary photodissociation after excitation to a predissociating electronic state. Newton has claimed that multiple ionisation is favoured for molecules which have sufficient numbers of nonbonding or delocalised electrons [19].

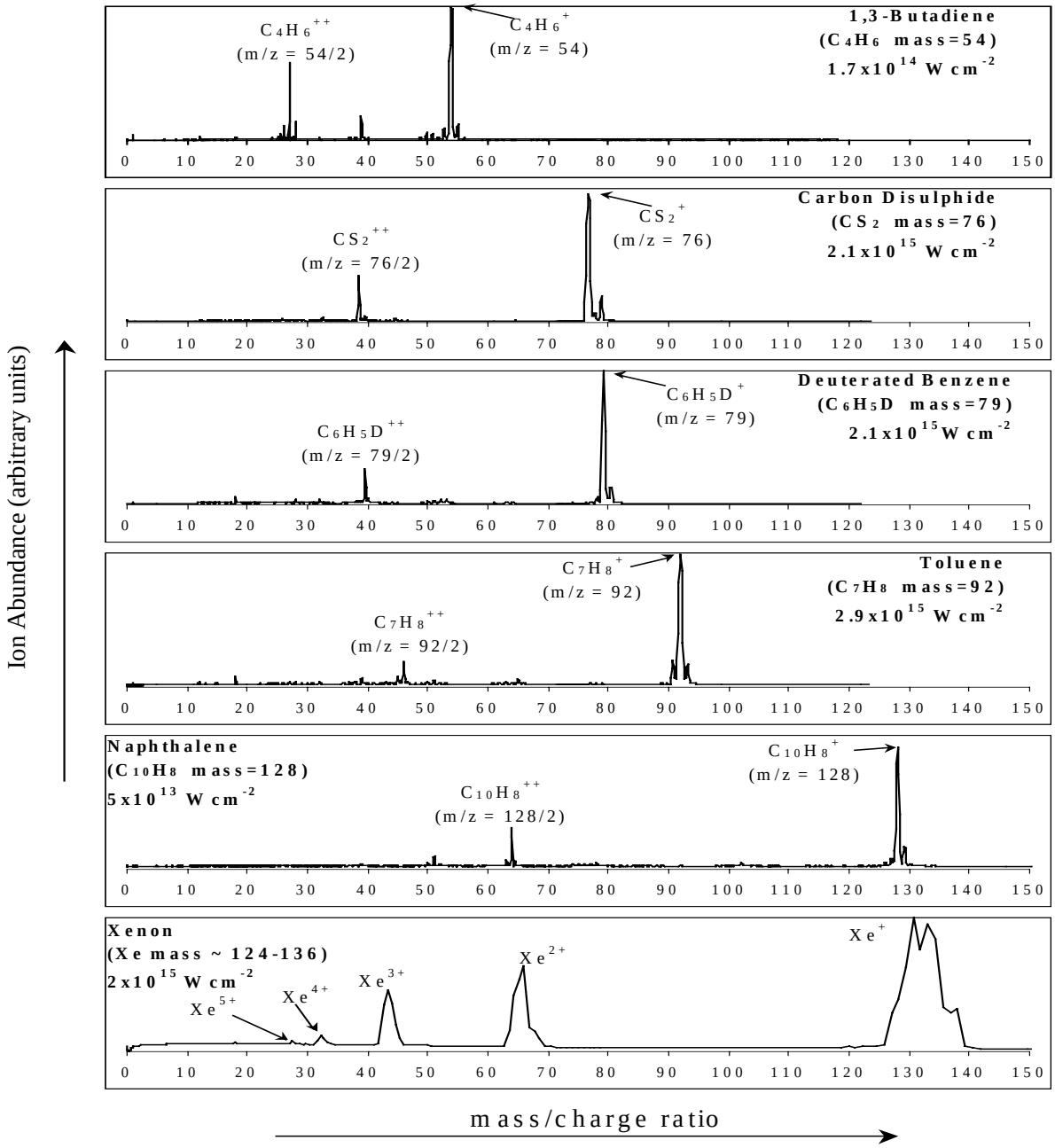

Figure 4. Mass spectra of polyatomic molecules. Laser conditions 5x 10^{13} Wcm^{-2} to 2x10^{15} Wcm^{-2}. The wavelength range is 750 -790 nm , pulse width 50-90 fs. This is compared with the Xe spectrum taken at the same intensity. The 1^+ and 2^+ charged parent peaks are the principle entities and any fragmentation is very small. This behaviour is similar to that of the inert atoms.

References

1. Zandee, L.; Bernstein, R.B.
J.Chem.Phys. 1979, 71, 1359

2. Boesl, U.
J.Phys.Chem. 1991, 95, 29493

3. Dietz, W.; Neusser, H.J.; Boesl, U.; Schlag, E.W.; Lin, S.H.
Chem.Phys. 1982, 66,105.

4. Ledingham, K.W.D.; Singhal, R.P.
Int.J.Mass Spectrom. Ion Processes, 1997, 163, 149.

5. DeWitt, M.J.; Levis, R.J.
J.Chem.Phys. 1995, 102, 8670.

6. DeWitt, M.J.; Peters D.W.; Levis R.J.
Chem.Phys. 1997, 218, 211.

7. Cornaggia, C.; Schmidt, M.; Normand D.
Phys.Rev.A 1995, 51, 1431

8. Cornaggia, C.
Phys.Rev.A. 1995, 52, R4328

9. Telebpour, A.; Larochelle, S.; Chin, S.L.
J.Phys.B: At. Mol.Opt.Phys. 1997, 30, L245

10. Hatherley, P.A.; Stankiewicz, M.; Codling,K.; Frasinski, L.J.; Cross, G.M.
J.Phys.B:At.Mol.Opt.Phys.1994, 27,2993.

11. Safvan, C.P.; Bhardwaj, V.R.; Ravindra Kumar; G.; Mathur, D.; Rajgara, F.A.;
J.Phys.B: At. Mol.Opt.Phys. 1996, 29, 3135.

12. Constant, E.; Stapelfeldt, H.; Corkum, P.B.
Phys.Rev.Lett. 1996, 76, 4140.

13. Codling, K.; Frasinski, L.J.
Contemp Physics,1994,35, 243.

14. Smith,D.J.; Ledingham, K.W.D.; Kilic, H.S.; McCanny, T.: Peng, W.X.; Singhal, R.P.; Langley, A.J.; Taday P.F.; Kosmidis, C.
Rapid Comm. Mass Spectrom. 1998,12, 813

15. Singhal, R.P.; Kilic, H.S.; Ledingham,K.W.D.; Kosmidis, C.; McCanny, T.;Langley,A.J.;Shaikh,W
Chem.Phys.Lett. 1996, 253, 81.

16. Kosmidis,C.Ledingham K.W.D.;Kilic,H.S. McCanny, T.; Singhal R.P.;Langley, A. J. Shaikh,W.
J.Phys.Chem.A. 1997, 101, 2264.

17. Kilic, H.S.; Ledingham, K.W.D.; Kosmidis,C.; McCanny, T.; Singhal, R.P.; Wang, S.L.; Smith, D.J.; Langley, A.J.; Shaikh, W.
J. Phys. Chem. A, 1997, 101, 17.

18. Dorman, F.H.; Morrison, J.D.;
J.Chem.Phys. 1961, 35, 575.

19. Newton, A.S.
J.Chem.Phys. 1964, 40, 607.

20. Lambropolous, P.
Phys. Rev.Lett., 1985, 55,2141.

21. Fittinghoff, D.N.; Bolton, P.R.; Chang, B.; Kulander, K.C.
Phys.Rev.Lett. 1992, 69, 2642.

Geometry modifications and alignment of H_2O in an intense femtosecond laser pulse

J H Sanderson, W A Bryan, A El-Zein, W R Newell.

University College London, Gower Street, London, WC1E 6BT. UK. Email ucapjhs@ucl.ac.uk

A J Langley, P F Taday.

CLRC Rutherford Appleton Laboratory, Chilton, Didcot, Oxon., OX11 0QX. UK.

Introduction

Modifications to the structure of a small molecule during laser induced Coulomb explosion is an active area of interest at present. Experiments have shown that the bond lengths of polyatomic molecules as large as SF_6 [1)] expand to double their normal value before multiple ionisation is complete. Evidence has been found to support bending of both the ground state [2, 3, 4)] and vibrationally excited [5)] CO_2 molecule and straightening of the initially bent SO_2 molecule [6)]. A more recent experiment indicated that SO_2 retains its bent structure [7)] for high ionisation channels. In the present experiment we use a momentum imaging technique developed by Hishikawa *et al* [7)] to examine the modification to the initially bent H_2O molecule in a 50 fs laser pulse of peak intensity 2.10^{15} W/cm^2.

Experimental

The 790 nm, 10 Hz laser used in the present experiment has been modified from that used in earlier studies [1, 4, 5)]. The incident laser beam enters the vacuum system, which has a base pressure 10^{-9} Torr, through a fused silica window and is reflection focussed using an f/5 parabolic mirror into the interaction region giving a near diffraction limited spot size, calculated to be 12 μm. The intensity was calculated from the spot size and the pulse energy of 750 J to peak at 2.10^{15} W/cm^2. The direction of the laser polarisation was controlled using a half-wave plate. The laser focus was situated in a central plane equidistant from two parallel grids separated by 20 mm, which formed the source region of a Wiley-McLaren type time-of-flight (TOF) mass spectrometer [8)], in which a 3 mm aperture was placed in front of the micro-channel plates [4)]. During the experiment the target gas pressure rose to 10^{-7} Torr and because of the increase in both the laser pulse energy and the focal spot size, the signal strength was one hundred times higher than in previous work [4)]. The signal from the channel plates was therefore fed directly into a Tektronix TDS 744A digital oscilloscope interfaced to a PC. The laser pulses were monitored as previously [4)] in order to minimise the effect of energy fluctuations. The polarisation direction was controlled by a half-wave plate, mounted in a rotation stage and driven by a stepping motor [9)]. The polarisation was rotated in 2° steps and a Time-of-flight, (TOF) spectrum were recorded at each step. Only one hundred laser pulses were needed to build up each spectrum and so a two dimensional matrix of TOF spectra from 0° to 360° could be built up in approximately 30 minutes.

Results

Figures 1 a, b and c show momentum maps [7)] of the observed atomic fragment ions, H^+, O^+ and O^{2+} constructed from spectra recorded at 2° intervals from 0° to 360°. The vertical axis is parallel to the laser polarisation direction. Clear information can be gained from these plots. Figure 1a shows a low momentum island, (< $10°10^3$ a.m.u. ms^{-1}) consisting of ions from the H^+ + OH (1,0) channel. The island is circular indicating that the angular distribution of these ions is isotropic. The crescent shaped islands, which consist of ions from the Coulomb channels (1,1,1) and (1,2,1), have a wide angular distribution, but are not isotropic. The grey intensity scale shows that these islands have their highest values at angles close to 0° and 180° which indicates that the Coulomb

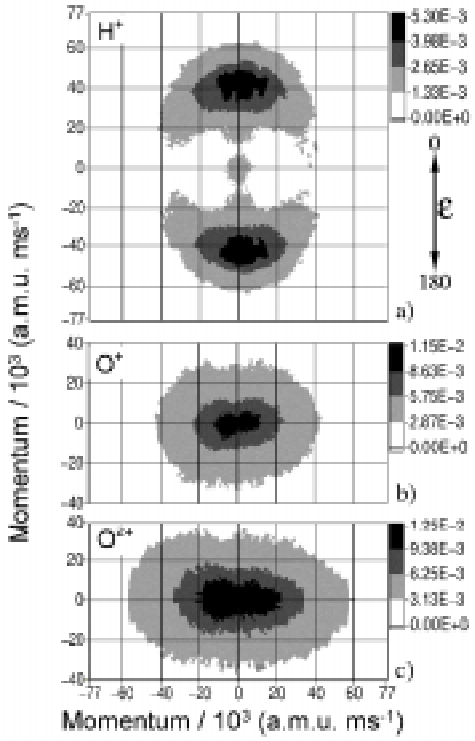

Figure 1. Momentum maps for the atomic fragment ions resulting from the Coulomb explosion of H_2O. The vertical axis is parallel to the laser field direction ε.

explosions result from H_2O molecules in which a certain amount of alignment exists between the H-H axis and the laser polarisation direction. We have fitted a function of the form $A\cos^n\theta$ to the H^+ angular distribution, at a momentum of $40°10^3$ a.m.u ms^{-1}, which is close to the highest point on the island (at 0° and 180°). The least squares fit gives a value of n = 4.5, which compares with n=12 for the (1,1,1) channel of CO_2 at the same laser intensity [4)].

Recent experiments with laser pulses of less than 100 fs and intensity greater than 10^{14} W/cm^2 have shown that the angular distributions of fragments from light diatomic molecules can not be explained simply by the higher ionisation rate of molecules which are aligned with the laser field [9, 10)]. This indicates that the laser field reorients light diatomic molecules on a femtosecond time scale. By contrast it was found that the massive I_2 molecule could not be reoriented on such a short time-scale. The H_2O molecule is light and so it is reasonable to assume that the origin of the angular distribution, observed here, is the reorientation of the H_2O molecule by the laser field. The static field induced dipole strengths parallel and perpendicular to the H-H axis have recently been calculated for a range of field strengths [11)]. These calculations suggest that at low laser intensity (≈10^{13} W/cm^2), the torques on the molecule associated with these dipoles are roughly equal and opposite, so that the molecule is not reoriented. The angular distributions of H^+ ions, most probably from the (1,0) channel, were measured

in that work and found to be isotropic. This observation is confirmed in the present work, as the low momentum H^+ ions must originate from a region within the focal spot where the intensity is low enough to result in only single ionisation channels such as (1,0). The calculations further showed that at higher intensities, the parallel induced dipole becomes dominant and so the molecule should be rotated, such that the H–H axis aligns with the laser field. This prediction is confirmed by the present result. The effect of opposing torques should reduce the amount of reorientation experienced by the molecule in comparison with more linear molecules such as CO_2, leading to a lower value of n as observed here. Furthermore the bent nature of H_2O is important in widening the angular distribution of the Coulomb channel, in a very simple way. If the H-H axis is completely aligned with the polarisation direction, the trajectories of the H^+ ions cannot be along the polarisation direction, because of the repulsion from the laterally offset oxygen ion. The bent nature of H_2O is deducible from figures 1b and 1c in which the O^+ and O^{2+} momentum plots are elliptical. In both cases the major axis of the ellipse is orientated at 90° to the laser polarisation direction. This indicates that the molecules aligned with the H-H axis along the polarisation direction repel the central oxygen ion at right angles to the polarisation direction; this is only possible from a bent geometry.

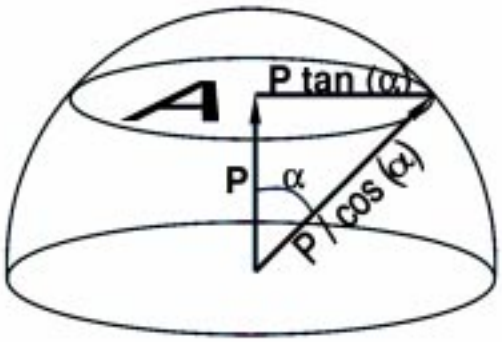

Figure 2. Momentum maps for the atomic fragment ions resulting from the Coulomb explosion of H_2O. The vertical axis is parallel to the laser field direction ε.

Further information about the molecular geometry can be extracted from the momentum maps, but first it is necessary to correct the data for the effect of the variation of detector acceptance angle with ion momentum. This variation has most effect on the oxygen ion maps in figures 1b and 1c, because the momenta of the oxygen fragments are small and so the acceptance angle becomes large, reaching $\pi/2$ for momenta close to zero. This means that the ion distributions appear more isotropic than is physically the case. Figure 2 shows the geometry, which must be considered for the correction procedure applied to each momentum point P on the map. In figure 2 the signal S measured at a particular momentum P is proportional to the momentum surface area A, defined by $\pi(P.\tan(\alpha))^2$, where α is the acceptance angle of the most energetic ion which can be detected with momentum $P/\cos(\alpha)$ and which can be calculated from the experimental geometry. The measured signal is divided by the factor $\pi\sin^2(\alpha)$ which is analogous to a solid angle correction. A fuller discussion of this and other correction procedures will be given elsewhere.

Figures 3a, b and c show the angular distributions of H^+, O^+ and O^{2+} respectively, after correction for the variation of acceptance angle. In figure 3a the central island is now not visible, but the Coulomb islands have not been greatly altered, as their momentum is high. The major difference is in figures 6b and 6c where removing the false isotropy has transformed the elliptical islands into 'bow-tie' shaped islands.

It is now possible to use the three corrected maps to deduce the

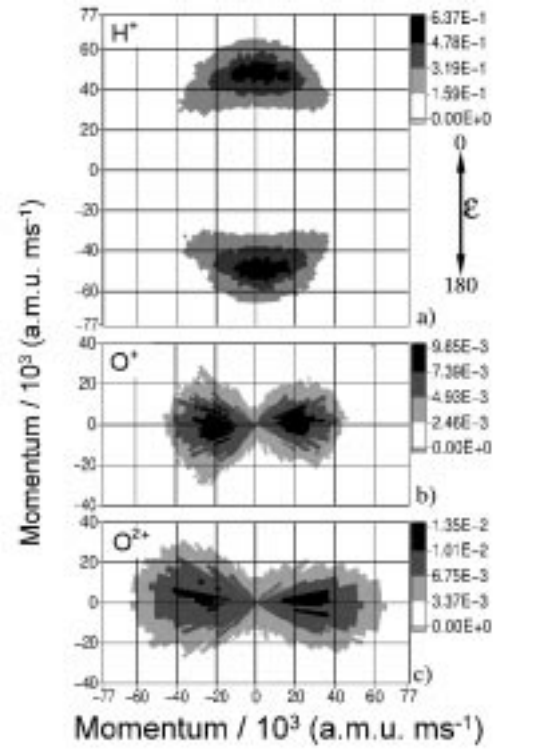

Figure 3. Momentum maps after correction for the finite collection angle of the detector

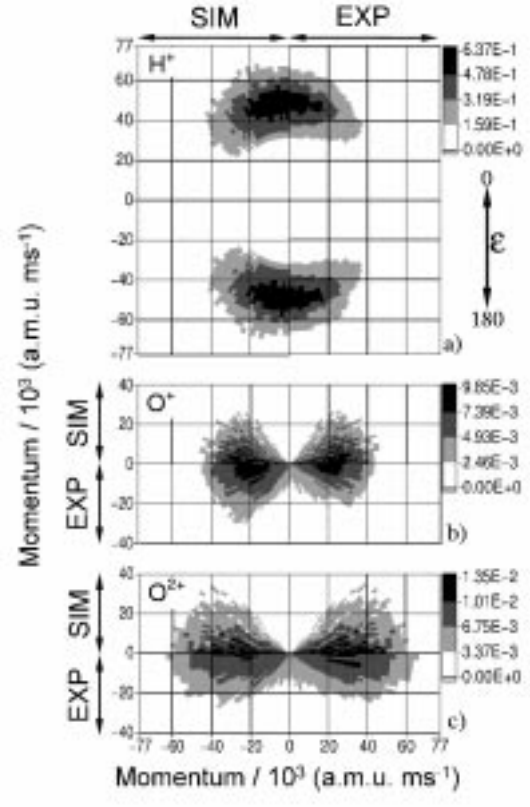

Figure 4. Comparison between experimental (EXP) and simulated (SIM) momentum maps.

geometry of the exploding molecule, by comparing them with maps derived from a Monte-Carlo simulation of the Coulomb explosion of the H_2O molecule from a distribution of geometries. A similar technique has been used previously [3] to determine molecular geometry from the islands of a double correlation map. In the present simulation, three independent distributions are chosen to represent the O-H bond length R, the H-O-H bond angle θ and the alignment angle ϕ between the H-H axis and the laser polarisation direction. The distributions used are either triangles or trapeziums for ease of calculation. The simulated O^+ map was derived from a set of R, θ, and ϕ distributions in which the molecule was allowed to explode into the (1,1,1) channel and the O^{2+} map was derived from a set of distributions in which the molecule exploded into the (1,2,1) channel. The simulated H^+ map contains contributions from both channels, weighted in accordance with the magnitudes of the O^+ and O^{2+} ion intensities of figure 3. For comparison with the experimental maps, the simulated maps were scaled using a free scaling parameter. The initial distributions chosen were consistent with the geometry of the neutral molecule, i.e. the θ distribution peaking at 104° and the R distribution peaking at 0.9 Å. Theses were not found to give a good agreement with the experimental map, and so were varied until the best agreement was found. Figures 4a, b and c show a comparison between the experimentally derived and the best simulated momentum maps. The general agreement is good with the simulated maps reproducing the shape of the islands and the positions of the highest ion signal in the experimental maps.

Figures 5a, b and c show the derived distributions for R, ϕ and θ. For both channels, the R distribution was found to peak at 2 Å, in good agreement with the critical distance theory [12, 13]. The alignment distribution ϕ narrows with increasing ionisation channel as expected [4]. This is for two reasons; better alignment is needed between the molecule and the field to produce the higher ionisation channel, and the greater field strength, which produces the higher channel, also gives rise to more reorientation. Triangular alignment distributions with FWHM of 60° and 40° were derived to describe the (1,1,1) and (1,2,1) channels of CO_2 [3], as compared to 70° and 60° respectively in the present work. The distributions are comparable and contrast with the measured FWHM for the angular distribution of fragments from the (2,1) channel of I_2 which, at 6 x 10^{14} W/cm^2 is greater than 90° [9]. The results are therefore consistent with reorientation of H_2O, but to a lesser extent than in H_2O than in CO_2, due to competition between the parallel and perpendicular torques. The maximum in the bond angle θ distribution is at 130° for the (1,1,1) and 140° for the (1,2,1) channel this compares with a most probable angle of 104° for the neutral molecule; even more striking is the fact that the bend angle distributions saturate at these values. Figure 5d also shows a comparison with θ_V the angle between the H^+ trajectories calculated with a multi-configurational self consistent field technique [14] for dissociating H_2O^{3+} and H_2O^{4+} excited by highly charged ion impact. These distributions describe the molecular ion geometries well, but the bond angles can not directly be derived from them, as the dissociation is not completely coulombic. Nevertheless the dissociation is close to coulombic and the θ_V distributions are a good approximation to the natural bond angle distributions and they show a low probability for large angles. In the present work the observation of high probabilities for large bond angles, between 130° and 180°, strongly indicates that the molecules have been straightened in the laser field. The phenomenon responsible for this straightening of the molecule may be bond angle softening [15], tentative evidence for which has been found in the photoelectron spectrum of H_2O at 532nm. Figure 6 shows the interaction potential as a function of θ for the H_2O^+ ion with the $\tilde{A}\ ^2A_1$ state lowered by the photon energy of 1.6 eV. This makes the crossing positions near to the centres of the wells of the X^2B_1 ground state and close to the most probable angle for H_2O^+ which is 120°. The process of bond angle softening occurs by a single photon transition from the ground state onto the $\tilde{A}\ ^2A_1$ state, the molecule then begins a large amplitude oscillation to the other crossing, where it emits a photon and returns to the ground state. The time scale for this motion is comparable to the rise time of the laser pulse. If the molecule is ionised near to the start of the laser pulse, which is likely, then

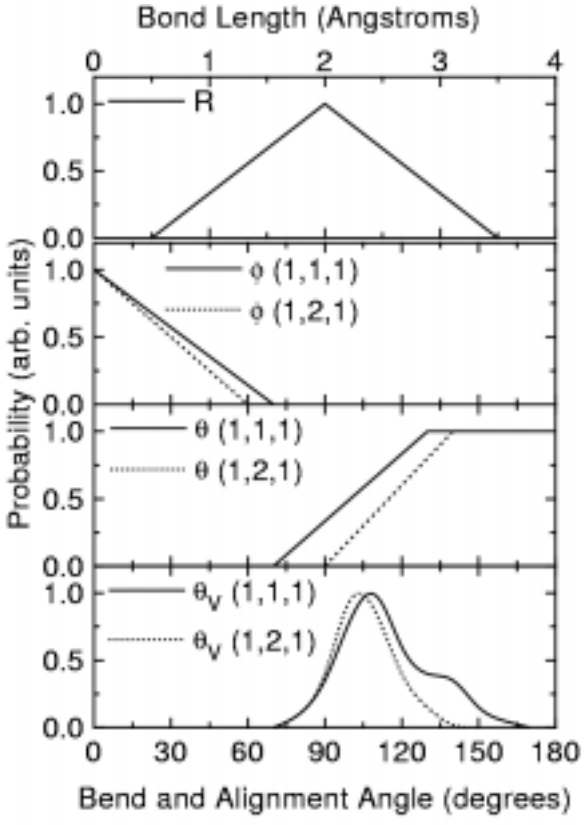

Figure 5. Distributions of the bond length R, alignment angle ϕ and bend angle θ used to generate the simulated map in figure 4. Also shown are the θv distributions calculated by Werner *et al* [14]

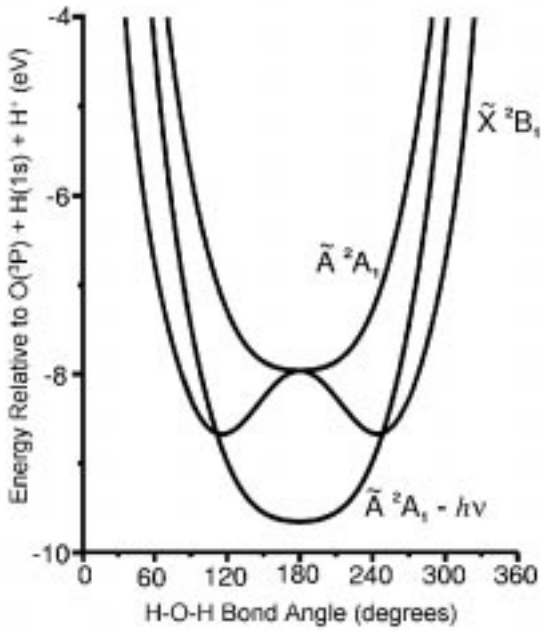

Figure 6. Interaction potential for H_2O^+ derived from Rottke *et al* [15], with the $\tilde{A}\ ^2A_1$ state shifted by the photon energy of 1.6eV

there is enough time for the ion to undergo this bending process before the peak intensity is reached, and Coulomb explosion takes place. The bend angle distribution would be modified in this process increasing the importance of large angles, as observed.

Conclusions

Using high intensity femtosecond laser pulses we have been able to excite the H_2O^+ molecule to high vibrational levels through a, single photon, bond angle softening process and observe the resulting nuclear motion, through Coulomb explosion, using a momentum mapping technique. This technique has also revealed stretching of the bonds, before Coulomb explosion, consistent with enhanced ionisation and alignment of the fragment ions, consistent with reorientation of the molecule in the laser field. Further theoretical studies of the bond angle softening process in a high intensity laser pulse would be beneficial.

References

1. J. H. Sanderson, R. V. Thomas, W. A. Bryan, W. R. Newell, A. J. Langley and P. F. Taday
J. Phys. B: At. Mol. Opt. Phys. 30 4499-4507 (1997)
2. C. Cornaggia, M, Schmidt and D. Normand
J. Phys. B: At. Mol. Opt. Phys. 27 L123 (1994)
3. C. Cornaggia
Phys. Rev. A 54 2555 (1996)
4. J. H. Sanderson, R. V. Thomas, W. A. Bryan, W. R. Newell, A. J. Langley and P. F. Taday
J. Phys. B: At. Mol. Opt. Phys. 31 L599-L606 (1998)
5. J. H. Sanderson, R. V. Thomas, W. A. Bryan, W. R. Newell, I. D. Williams, A. J. Langley and P. F. Taday
J. Phys. B: At. Mol. Opt. Phys. 31 L59-L63 (1998)
6. C. Cornaggia, F. Salin, C. Le Blanc
J. Phys. B: At. Mol. Opt. Phys. 29 L749-L754 (1996)
7. H. Hishikawa, A. Iwamae, K. Hoshina, M. Kono and K. Yamanouchi
Chem. Phys. Lett 282 283 (1998)
8. W. C. Wiley and I. H. McLaren
Rev. Scie. Instr. 26 1150-1157 (1955)
9. J. H. Posthumus, J. Plumridge, M. K. Thomas, K. Codling, L. J. Frasinski, A. J. Langley and P. F. Taday
J. Phys. B: At. Mol. Opt. Phys. 31 L553-L562 (1998)
10. Ch. Ellert, H. Stapelfeldt, E. Constant, H. Sakhai, J. Wright, D. M. Rayner and P. B. Corkum
Phil. Trans. R. Soc. Lond. A 356 329-344 (1998)
11. V. R. Bhardwaj, C. P. Safvan, K. Vijaylakshmi and D. Mathur
J. Phys. B: At. Mol. Opt. Phys 30 8321-8331 (1997)
12. J. H. Posthumus, A. J. Giles, M. R. Thompson, L. J. Frasinski, K. Codling, A. J. Langley and P. F. Taday
J. Phys. B: At. Mol. Opt. Phys. 29 L525 (1996)
13. T. Seideman, M. Yu. Ivanov and P. B. Corkum
Phys. Rev. Lett. 75 2819 (1995)
14. U. Werner, K. Beckord, J. Becker, H. O. Folkerts, H. O. Lutz
Nucl. Instr. And Meth. B 98 385 (1995)
15. H. Rottke, C. Trump and W. Sander
J. Phys. B: At. Mol. Opt. Phys. 31 1083-1096 (1998)

Dissociation of H_2^+ molecular ions by intense femtosecond laser pulses

I D Williams, B Srigengan, P McKenna.

Department of Pure and Applied Physics, The Queen's University of Belfast, Belfast, BT7 1NN. E-mail i.williams@qub.ac.uk

W R Newell, J Sanderson, W A Bryan, A El-Zein.

Department of Physics and Astronomy, University College London, London, WC1E 6BT

A J Langley, P F Taday.

CLRC, Rutherford Appleton Laboratory, Chilton, Didcot, Oxon., OX11 0QX

Introduction

A major development in atomic and molecular physics in the past decade has been the advances made in understanding the behaviour of matter in strong fields. Through the interaction of ultra-short pulses of intense radiation with atoms and molecules, new physical processes have been discovered. These include above threshold ionization and dissociation [1), 2)], Coulomb explosions [3)], bond softening [4), 5)], and vibrational population trapping [6), 7)]. The dynamics of molecules in laser fields [8)] with the discovery of pendular motion [9)] and alignment [10)] is also a new area of investigation.

Most recently a great deal of interest has been generated in the specific case of molecular ions in strong fields. For example it has been predicted that molecular ions are a far more efficient source of harmonic conversion than neutral atoms [11)]. Further motivation has been driven by the practical desire to be able to control chemical dynamics, *eg* isotope separation in HD^+ [12)]. As a result, a great theoretical effort has been expended on such studies, in particular for the simplest system of a single electron in a homonuclear diatomic potential, i.e. H_2^+ [13), 14), 15)].

To date, experimental measurements have all involved a two-stage process, where H_2 molecules are ionized to form H_2^+ by the same laser pulse that subsequently probes the molecular ion. Such a system has distinct disadvantages, primarily in that the vibrational population of the resulting H_2^+ ions varies with pulse intensity. This severely complicates efforts to map the interaction as a function of field strength. Although attempts have been made at characterising the initial vibrational state distribution of the ions through energy analysis of the ionized electrons, such a method is not possible at short pulse durations (typically for pulse durations less than 1 ps). It must also be considered that a purely sequential explanation of ionization followed by dissociation, for the neutral molecule H_2 may not be totally valid for ultra-short pulses. For example, one theory of the vibrational trapping phenomenon suggests that it results from the simultaneous interplay between ionization of the neutral molecule and dissociation via the formation of a coherent vibrational wavepacket [16)].

In order to enable the dissociation of H_2^+ to be investigated as a function of field strength, and to initiate a comprehensive study of the above mentioned phenomena, we have for the first time conducted an experiment where a pure ion beam is probed by intense femtosecond laser pulses.

Experimental arrangement

A schematic diagram of the experimental arrangement is shown in figure 1. A beam of H_2^+ ions, extracted from an oscillating electron type ion source, was momentum selected by a bending magnet and focussed through a differentially pumped chamber onto the point of interaction with a laser beam. H_2^+ beam currents of 500 nA at 2.5 keV were produced at the point of interaction where the background pressure was 5×10^{-10} mbar. A Ti:Sapphire oscillator, pumped by an argon ion laser, produces femtosecond pulses which are subsequently amplified using the chirped pulse amplification process to give 2 mJ pulses at 10 Hz. The laser, housed at the Rutherford Appleton Laboratory, delivers radiation pulses of 50 fs duration at a wavelength of 790 nm which are monitored using a single shot autocorrelator. Reflection focussed to a spot size of 4 μm diameter, laser intensities of approximately 10^{17} Wcm^{-2} can be produced. In the present work, due to the low density of H_2^+ ions, the laser was only focussed to a diameter of 0.1 mm with a correspondingly large confocal length of 15 mm. This gave a maximum pulse intensity at the point of interaction of 7×10^{13} Wcm^{-2}. Measurements were carried out for a series of pulse intensities in the range $(1\text{-}7) \times 10^{13}$ Wcm^{-2}, with the laser beam linearly polarized in a direction perpendicular to the plane containing the two beams.

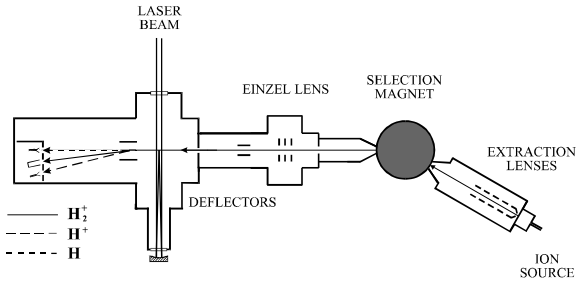

Figure 1. Schematic diagram of the laser-ion apparatus

Following laser dissociation of the H_2^+, the fragments H and H^+, which retain the initial ion velocity, are subjected to electrostatic deflection which separates the primary H_2^+ ions from the H^+ ions. The H_2^+ ions are monitored using a Faraday collector while the H^+ ions and the H neutrals are detected using channel electron multipliers. In addition to the spatial separation of the ions a time of flight analysis was also performed on the fragmenting products. The laser pulse provided the start pulse for the timing electronics with the ions timed over the 27 cm flight path between the point of interaction and the channel electron multiplier detectors.

Results and Discussion

In laser produced dissociative ionization of a neutral molecule, AB, it is accepted that the dissociative ionization and Coulomb explosion proceeds by the initial production of the parent ion AB^+ which subsequently expands to the critical internuclear separation R_c ($R_c > R_o$) before undergoing further sequential ionization as evidenced by Coulomb explosion measurements. This sequential ionization of AB^+ will also depend on the alignment and polarization of the molecular ion within the laser field. These are dynamical processes which produce an effective ionization potential for the molecular ion. There have been several recent investigations of laser produced dissociative ionization of the neutral H_2 molecule [17), 18), 19), 20)], using both single colour and phase-control, two-colour, photo dissociation in which the fragmentation channels (0,1) and (1,1) were monitored.

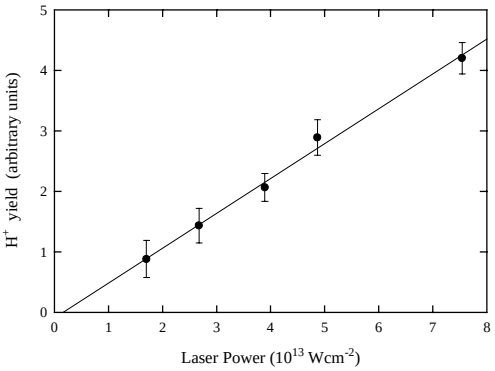

Figure 2. Proton yield due to dissociation in the (0,1) channel. Experiment (•). Linear regression (——).

Measurements of laser produced dissociative ionization of H_2^+ have been from experiments in which the molecule is first ionized to H_2^+ and sequentially probed in the same laser pulse. This procedure fails to decouple the primary ionization step ($H_2 \rightarrow H_2^+ + e$), in which the ionized electron is highly correlated with the parent H_2^+ molecular ion, and the subsequent dissociative ionization. The direct reactions involved in the laser produced dissociative ionization of H_2^+ in which a beam of H_2^+ molecular ions is the target are

$$H_2^+ (1s\,\sigma_g, v) + \text{LASER} \rightarrow H(n, l) + H^+$$

$$\rightarrow H^+ + H^+ + e$$

The production of protons in the (0,1) channel as a function of laser intensity is given in figure 2 over the laser intensity range of 1 to 7×10^{13} Wcm^{-2}. The Coulomb explosion channel (1,1) which has a predicted threshold [21] of 8×10^{13} Wcm^{-2} in H_2^+ is not observed. In the case of H_2 the (0,1) and (1,1) channels have thresholds of 9×10^{13} Wcm^{-2} and 1.5×10^{14} Wcm^{-2} respectively [17], whereas the observed threshold for the (0,1) channel in H_2^+ occurs at the much lower value of approximately 1×10^{13} Wcm^{-2}.

The slope of the graph in figure 2 is approximately linear indicating a first or low order laser interaction process. The fragmentation can be produced via multiphoton absorption or tunneling, and these processes can be distinguished by the value of the Keldysh parameter γ. When $\gamma > 1$ multiphoton dissociative ionization is more likely whereas when $\gamma < 1$ a tunneling mechanism is more likely. However with the H_2^+ in the ground state and an associated laser pondermotive potential of 5.2 eV the Keldysh parameter is 1.5. This value is intermediate and even if the H_2^+ was in a high vibrational level γ would still be greater than unity. However since at least 15 photons would be required to dissociatively ionize H_2^+ from the ground state, and figure 5 does not show a corresponding non-linearity, then we should conclude that a tunneling process is more likely.

References

1. A Giusti-Suzor *et al*
   Phys. Rev. Lett., 64 515, (1990)
2. A Zavriyev *et al*
   Phys. Rev. A, 42 5500, (1990)
3. K Codling *et al*
   J. Phys. B: At. Mol. Opt. Phys., 22 L321, (1989)
4. P H Bucksbaum *et al*
   Phys. Rev. Lett., 64 1883, (1990)
5. G Jolicord and O Atabek
   Phys. Rev. A, 46 5845, (1992)
6. A Giusti-Suzor and F H Mies
   Phys. Rev. Lett., 68 3869, (1992)
7. G H Yao and S-I Chu
   Chem. Phys. Lett., 197 413, (1992)
8. B Friedrich and D Herschbach
   Phys. Rev. Lett., 74 4623, (1995)
9. G R Kumar *et al*
   Phys. Rev. A, 53 3098, (1996)
10. J H Sanderson *et al*
    J. Phys. B: At. Mol. Opt. Phys., 31 L599, (1998)
11. T Zuo and A D Bandrauk
    Phys. Rev. A, 48 3837, (1993)
12. E Charron *et* al
    Phys. Rev. Lett., 75 2815, (1995)
13. A Giusti- Suzor *et al*
    J. Phys. B: At. Mol. Opt. Phys., 28 309, (1995)
14. M Plummer and J F McCann
    J. Phys. B: At. Mol. Opt. Phys., 29 4625, (1996)
15. M Plummer and J F McCann
    J. Phys. B: At. Mol. Opt. Phys., 30 L401, (1997)
16. A Zavriyev *et al*
    Phys. Rev. Lett., 70 1077, (1993)
17. M R Thompson *et al*
    J. Phys. B: At. Mol. Opt. Phys., 30 5755 (1997)
18. J Zhu and W T Hill III
    J. Opt. Soc. Am. B, 14 2212, (1997)
19. Y L Shao *et al*
    J. Phys. B: At. Mol. Opt. Phys., 29 5421, (1996)
20. G N Gibson *et al*
    Phys. Rev. Lett., 79 2022, (1997)
21. J H Posthumus
    Private communication (1998)

Laser-induced molecular reorientation and geometry modification in a high intensity 55fs laser pulse

W A Bryan, A El-Zein, J H Sanderson, W R Newell.

University College London, Gower Street, London, WC1E 6BT. UK. Email ucapwab@ucl.ac.uk

A J Langley, P F Taday.

CLRC Rutherford Appleton Laboratory, Chilton, Didcot, Oxon., OX11 0QX. UK.

Introduction

The development of tabletop femtosecond lasers has allowed dramatic progress in the understanding of the behaviour of small molecules in intense electric fields. Coulomb explosion[1)] in an intense laser field has allowed the study of modifications in the structure and orientation of a range of molecules.

We have performed a number of experiments on a range of small molecules. Reorientation in the laser field has been studied for CO_2 and SF_6 using a simple technique. The enhanced ionisation model has been investigated in the case of three triatomic molecules, namely CO_2, N_2O and OCS. The Covariance mapping technique[2)] has been used in this case. Presented here is the first observation of the Coulomb explosion of OCS in a femtosecond laser pulse. The modification of the bond-angle of these molecules has been observed using an ion-momentum imaging technique[3)].

Experiment

Intensities of 2 x 10^{15} W/cm^2 generated by a 50 fs laser pulse at 790 nm, with pulse energy of 1mJ have been used in the present work. These pulses have been reflection-focussed by a f/5 mirror to a spot size calculated to be 12 μm in diameter. This focus is situated equidistantly between two grids, which form the source region of a Wiley-McLaren time-of-flight (ToF) mass spectrometer[4)], situated in a vacuum system with a base pressure of 10^{-9} Torr. When the target gas is allowed into the vacuum system, the pressure rises to 10^{-7} Torr. Ions produced by the ionisation of the target gas are detected by a pair of micro-channel plates, the output of which is fed directly into a Tektronix TDS-744A digital storage oscilloscope (DSO). The DSO and PC are interfaced via an AT: GPIB link, with software written in a graphical programming language (G) used to control data acquisition and processing. The laser pulse energy is gated with a photodiode monitoring a reflection from the input window to the vacuum system in order to eliminate fluctuations. The apparatus used here has been described previously.[6, 9)]

Two different apparatus configurations have been used in these experiments. Firstly, a 3 mm aperture is placed directly in front of the micro-channel plates to limit the angular acceptance of the instrument; ions are only detected if their momentum is along the detector axis. This configuration has been used in the experiments examining the angular dependence of the ions emitted during Coulomb explosion. When examining the fragmentation channels using Covariance mapping, the aperture is removed.

Results

The results of these experiments are presented in four stages. Initially, the focussed laser-intensity is calibrated with respect to the measured pulse energy by examining the ionisation stages in Xenon. A time-of-flight spectrum of Xenon is presented in figure 1; the presence of eight stages of ionisation is consistent with a peak laser intensity of 2 x 10^{15} W/cm^2 at a laser pulse energy of 1 mJ [5)]. In this experiment, no aperture is used in front of the channel plates.

The question of molecular reorientation is now addressed. It has been shown that many molecules preferentially dissociate along

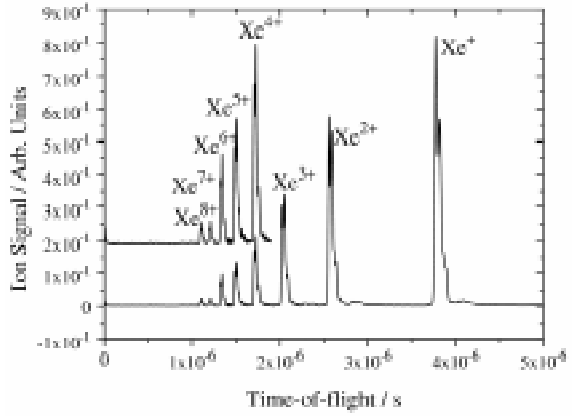

Figure 1. Time-of-flight spectrum of Xenon, showing eight stages of ionisation, relating to a focussed intensity of 2 x 10^{15} W/cm^2

the laser polarisation direction. Recent experiments under similar conditions have measured the ionic fragments from laser-induced Coulomb explosion of CO_2, SO_2, H_2 and H_2O with respect to laser polarisation direction[6, 7, 8 and 9)].

Figures 2 and 3 show time-of-flight (ToF) spectra taken with linearly and circularly polarised light. Figure 2 shows ToF spectra for CO_2, and figure 3 for SF_6. In both cases, two spectra are presented in each figure. Firstly, the laser pulse energy is set to 0.5 mJ, and a ToF spectrum is taken with linear polarisation. The polarisation direction is parallel to the detector axis. Secondly, the laser power is set to 1 mJ, and a quarter-wave plate is inserted into the beam before entrance into the vacuum system. This converts the linear polarisation to circular polarisation.

In both figures, the subscripts F and B describe whether the component of the momentum along the detector axis was initially in the direction of the detector (F) or away from the detector (B). The term 'vertical' in figures 2 and 3 implies that

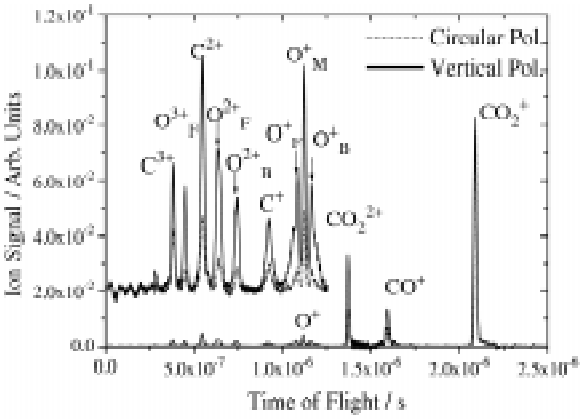

Figure 2. Time-of-flight spectra of Carbon Dioxide taken with both circularly and linearly polarised laser pulses. See text for discussion.

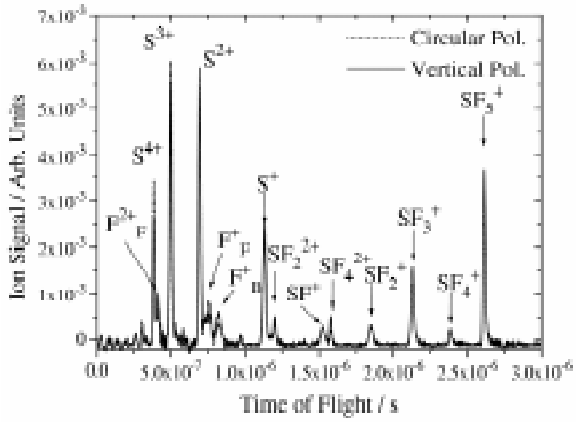

Figure 3. Time-of-flight spectra of Sulphur Hexafluoride taken with both circularly and linearly polarised laser pulses. See text for discussion.

the polarisation is parallel to the spectrometer axis. By reducing the laser pulse energy in the first experiment, the component of the electric field strength (ε) along the detector axis is the same for both linear and circular polarisation. Therefore, if the ion signal produced in both experiments is comparable, the ion intensity is due to the electric field ε in that direction. However, if the ion signal intensity is increased with linear polarisation, then molecular reorientation is implied, as the number of ions reaching the detector is enhanced by the linear polarisation.

In the case of CO_2, it can be seen that all of the atomic ion fragments exhibit a substantial increase in signal strength in the presence of the linearly polarised laser pulse. This indicates that CO_2 is reoriented before the Coulomb explosion of the molecule. The enhancement of the atomic ion signal strength indicates that molecules in a region of the laser focus of sufficient intensity to ionise past CO_2^+ can be reoriented. At the electric field strengths produced in the focus, the field-induced dipole moment parallel to the inter-nuclear axis is dominant over the perpendicular moment. The sum of these moments couples with the applied field to produce a torque on the molecules; this torque makes rotation occur. Conversely, experiments on the massive I_2 molecule have shown that rotation does not occur in the laser pulse, because the large moment of inertia of the molecule prevents rotation, despite the coupling.

As shown in figure 3, the ion signal strengths produced in the ionisation of SF_6 under both circular and linear polarisation are similar for all of the ions. Previous experiments using SF_6 have shown that the SF_6^+ ion is unstable, and so not observed[10, 11]. When a comparison is made between the results for CO_2 and SF_6, it is clear that the heavier molecule does not rotate to the same extent. This is apparent from the lack of significant difference between circular and linear polarisation. As in the case of I_2, the mass of the SF_6 molecule prevents significant rotation despite the coupling of the induced moments. A more detailed analysis comparison will be made later.

Covariance Mapping

The enhanced ionisation model describes how the inter-atomic bonds of molecules as large as SF_6 in a short (fs) intense ($>10^{15}$ W/cm^2) laser pulse stretch to a critical distance, around double the initial values[10]. Seideman *et al*[13] and Posthumus[14] have defined enhanced ionisation as follows. In the leading edge of the laser pulse, electrons are removed until the first repulsive state is reached. At this point, the inter-atomic bonds expand to around double their initial value. When the atoms in the molecule approach this point, the probability of ionisation is greatly increased. Depending on the electric field strength present, the molecule is then further ionised, and Coulomb explosion takes place.

The Covariance mapping technique allows unambiguous identification of the ionisation channels produced by the laser field. Previous experiments have examined the fragmentation of a variety of molecules, including CO_2 [15, 16 and 18] and N_2O[17]. Presented here are Covariance maps taken at 790 nm with a 55 fs pulse. Figures 4, 5 and 6 show Covariance maps of CO_2, N_2O and OCS respectively. Each map is built up over around 10000 laser shots. The Covariance maps presented here are double-covariance maps, therefore conservation of momentum must be used to identify the fragmentation channels. As has been shown before for CO_2 and SO_2 [7] amongst others, the momenta of the ions allow the separation of the ions before Coulomb explosion to be calculated. We have calculated the pre-explosion inter-nuclear separations of the ionisation channels and have found that the Coulomb explosion of CO_2,

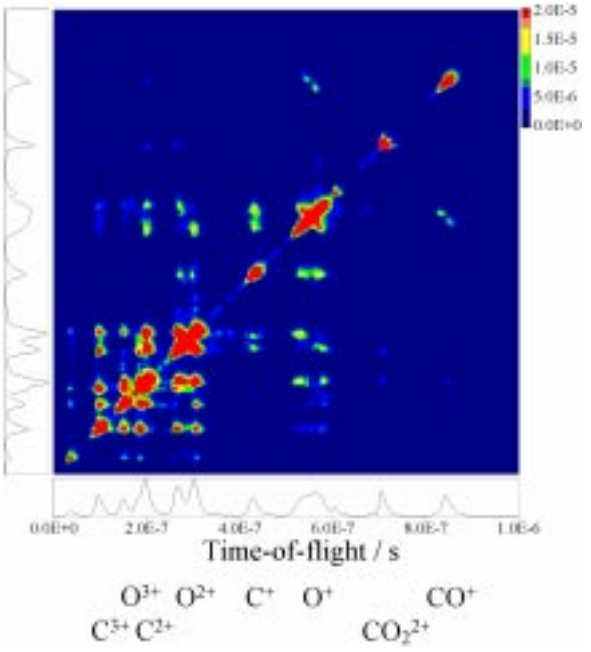

Figure 4. Covariance map of Carbon Dioxide taken with 790 nm 55 fs laser pulses at an intensity of 2 x 10^{15} W/cm^2.

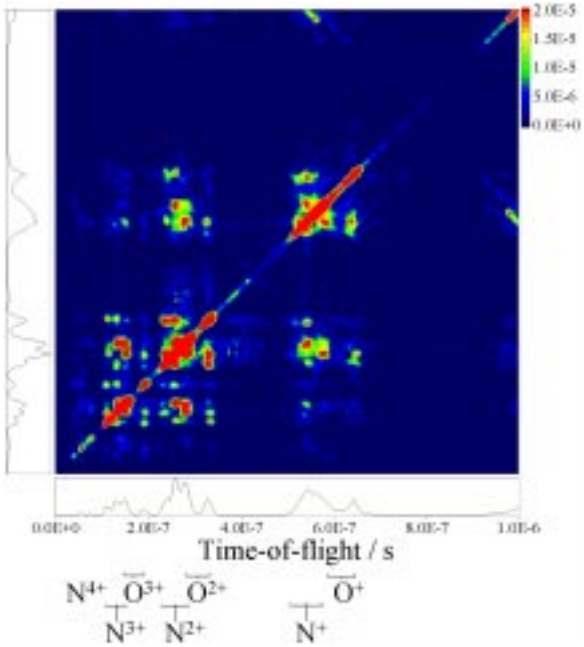

Figure 5. Covariance map of Nitrous Oxide taken with 790 nm 55 fs laser pulses at an intensity of 2 x 10^{15} W/cm^2.

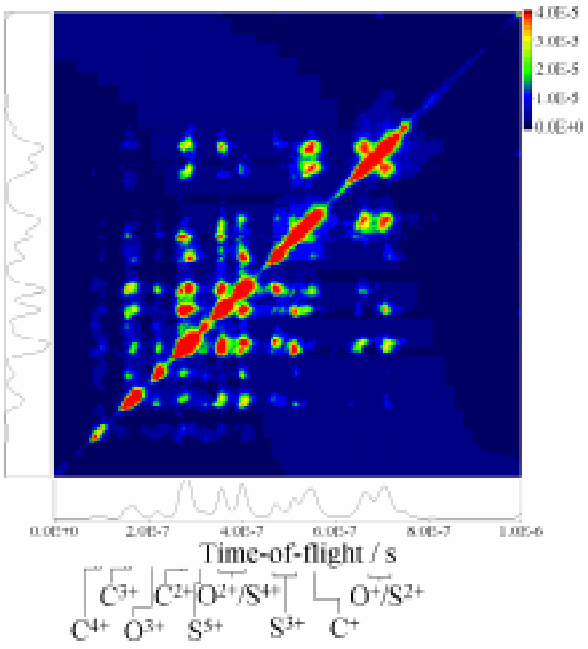

Figure 6. Covariance map of Carbonyl Sulphide taken with 790 nm 55 fs laser pulses at an intensity of 2 x 10^{15} W/cm^2.

N_2O and OCS is consistent with the enhanced ionisation model. The results of the analysis of the CO_2, N_2O and OCS data will be presented in more detail elsewhere.

Ion-Momentum Imaging

So far, we have observed molecular reorientation and bond-length modification. Modifications to the inter-atomic bond-angles are also of interest at the present time. Evidence has been found to support bending of both ground state[6, 16, 18] and vibrationally excited CO_2 [12], straightening of the initially bend

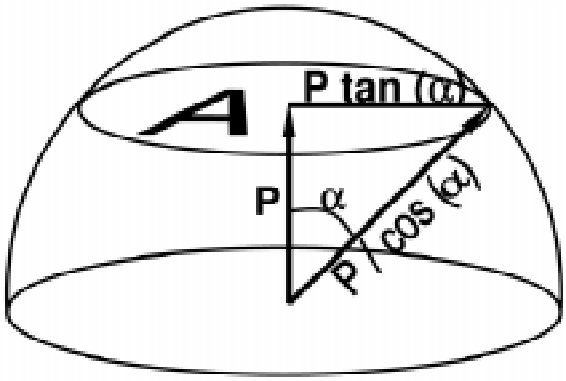

Figure 7. Correction geometry used for the finite collection angle of the detector. The Ion signal S at each point of momentum P is proportional to area A. The angle α is the acceptance angle of the most energetic ion which can be detected with momentum P / cos (α). This is calculated from the experimental geometry.

SO_2 [7] and H_2O [9] molecules. In the experiment on the H_2O molecule, we have used an Ion-momentum imaging (IMI) technique[3] to examine the straightening of H_2O under the same laser conditions. The IMI technique involves collecting ToF spectra at different angles between the axis of the spectrometer and the direction of the laser polarisation. The laser polarisation direction is rotated using a half-wave plate mounted in a rotation stage, driven by a stepper motor, which rotates at 0.1 degrees per second, thus rotating the laser polarisation direction by 0.2 degrees per second. Spectra are recorded over ten second intervals, so each spectrum is the average ion signal over 100 laser shots. The half-wave plate is allowed to rotate through 180 degrees, allowing a matrix of ToF spectra to be built up from 0 to 360 degrees with respect to the spectrometer axis.

An intrinsic instrumental factor that must be taken into account is the variation in detector angular acceptance with both ion

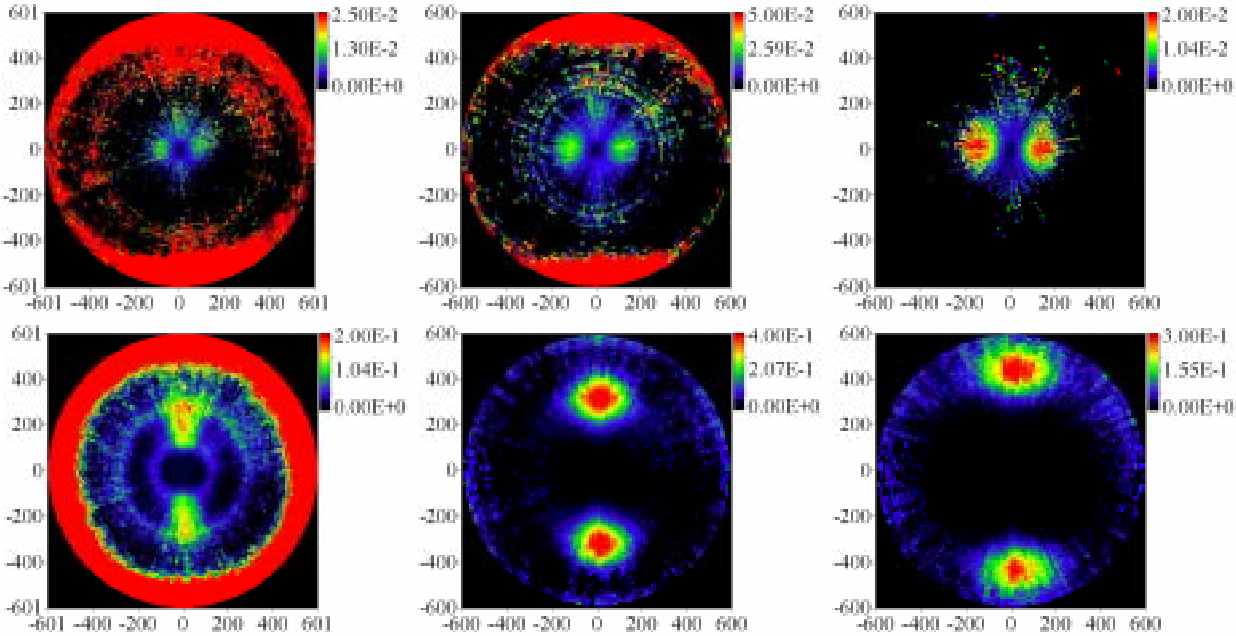

Figure 8. IMI plots of the laser-induced Coulomb explosion of Carbon Dioxide following correction for the finite collection angle of the detector. X and Y axes are ion momentum in a.m.u. ms^{-1} x 10^3 and the Z axis is corrected ion signal strength in arbitrary units. Top row from left – C^+, C^{2+} and C^{3+}. Bottom row from left – O^+, O^{2+} and O^{3+}. The laser polarisation direction is vertically up the page. Note that the circular red areas on the C^+ and C^{2+} IMI plots are unrelated to the C^+ and C^{2+} ions. The area of interest in each plot are the green lobes across the page. The same is true of the O^+ IMI plot: the circular red area around the edge of the plot is unrelated to the O^+ ion. The observation of carbon ions emitted perpendicular rather than parallel to the laser polarisation direction indicates that the molecules must be bent by the laser field before Coulomb explosion takes place.

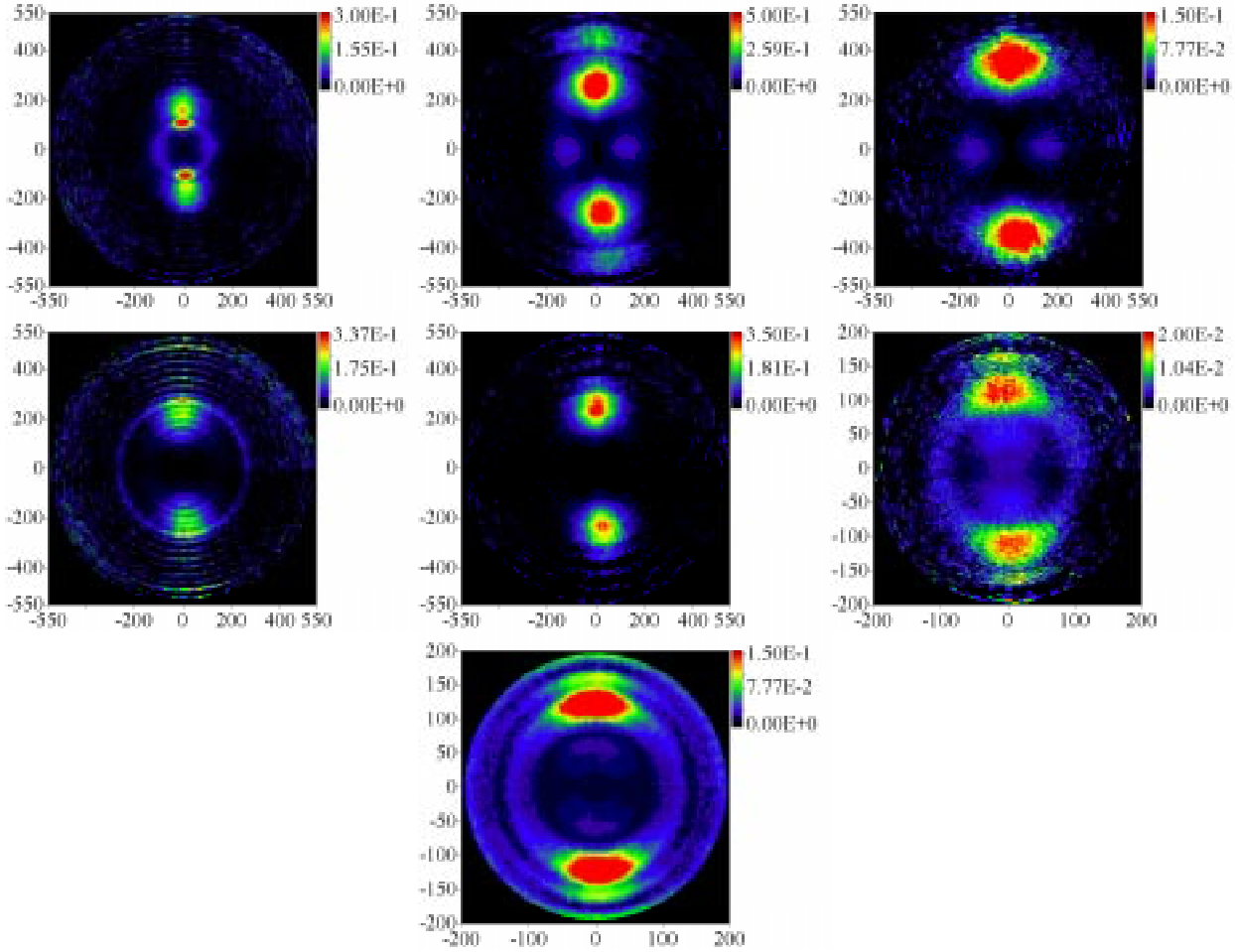

Figure 9. IMI plots of the laser-induced Coulomb explosion of Nitrous Oxide following correction for the finite collection angle of the detector. X and Y axes are ion momentum in a.m.u. ms^{-1} x 10^3 and the Z axis is corrected ion signal strength in arbitrary units. Top row from left – N^+, $N^{2+}$and N^{3+}. Middle row from left – O^+, O^{2+} and N^{2+}. Bottom row NO^+. The laser polarisation lies vertically up the page. The nitrogen ion plots show two populations, one parallel to the laser polarisation and another perpendicular with much lower momentum. The O^+ ion shows an instrumental 'ringing' effect. Despite this effect, it is clear that the oxygen ions are emitted along the polarisation. The perpendicular population of nitrogen ions indicates bending.

charge-to-mass ratio and initial momentum. The manifestation of this effect is to enhance the low-momentum ion signal with respect to those with higher momentum. This effect must be removed from the spectra before quantitative analysis can take place. Figure 7 shows the collection geometry used to correct the ion signal for the finite collection angle of the detector. This correction technique has been used in previous work [9] to remove the effect of the instrument. The corrected ToF data can then be represented on a three-dimensional polar plot. The angle axis is equal to the angle between the ToF axis and the laser polarisation direction. The radial axis is the ion momentum in a.m.u. ms^{-1} x 10^3 and the corrected ion signal strength is represented by a colour.

This polar representation of the corrected ToF data forms the basis of the Ion-Momentum Imaging (IMI) technique. The initial momentum of the ions is represented as a colour, and allows calculations to be made of the bend-angles and bond-lengths before Coulomb explosion. Figures 8,9 and 10 show corrected IMI plots of CO_2, N_2O and OCS. It is important at this point to reinforce the point of the observation of the previous experiment: CO_2 is rotated by the laser field. We have performed a similar experiment on the N_2O molecule and have again observed rotation; this data will be published later. In the case of these molecules being rotated by the laser field, then the outer ions will be emitted along the polarisation direction.

The three molecules examined here have a linear ground state configuration. If these linear configurations were maintained during Coulomb explosion, it would be expected that the middle ion would have no momentum perpendicular to the inter-atomic bonds. Therefore, the momentum of the middle ion would depend on the mass and charge of the outer ions.

Hence, in the case of the symmetric CO_2 molecule, the carbon ion would have negligible momentum if the two oxygen atoms where ionised by the same amount (symmetric channel, for example 1,1,1 or 2,2,2). The carbon ion would have momentum parallel to the lowest charged ion if the ionisation of the molecule were asymmetric (for example 2,2,3). However, both N_2O and OCS are asymmetric, so a linear configuration before Coulomb explosion would generally lead to the central ion being emitted in the direction of the lightest outer ion. For N_2O, the middle nitrogen would be expected to move away from the oxygen by virtue of the higher mass of the oxygen atom. For OCS, the middle carbon atom will move in the direction of the outer oxygen atom, again, by virtue of the considerably more massive sulphur atom.

However, it is clear from figures 8 to 10 that a linear configuration is not possible for the three molecules in this experiment. The carbon ions in figure 8 clearly have a non-zero component of momentum perpendicular to the trajectory of the oxygen ions; furthermore, the momentum parallel the oxygen ions is far less then in the perpendicular case. To detect both energetic oxygen ions in the direction of the laser polarisation and carbon ions emitted perpendicular to the laser polarisation implies two important behaviours. The oxygen ions indicate

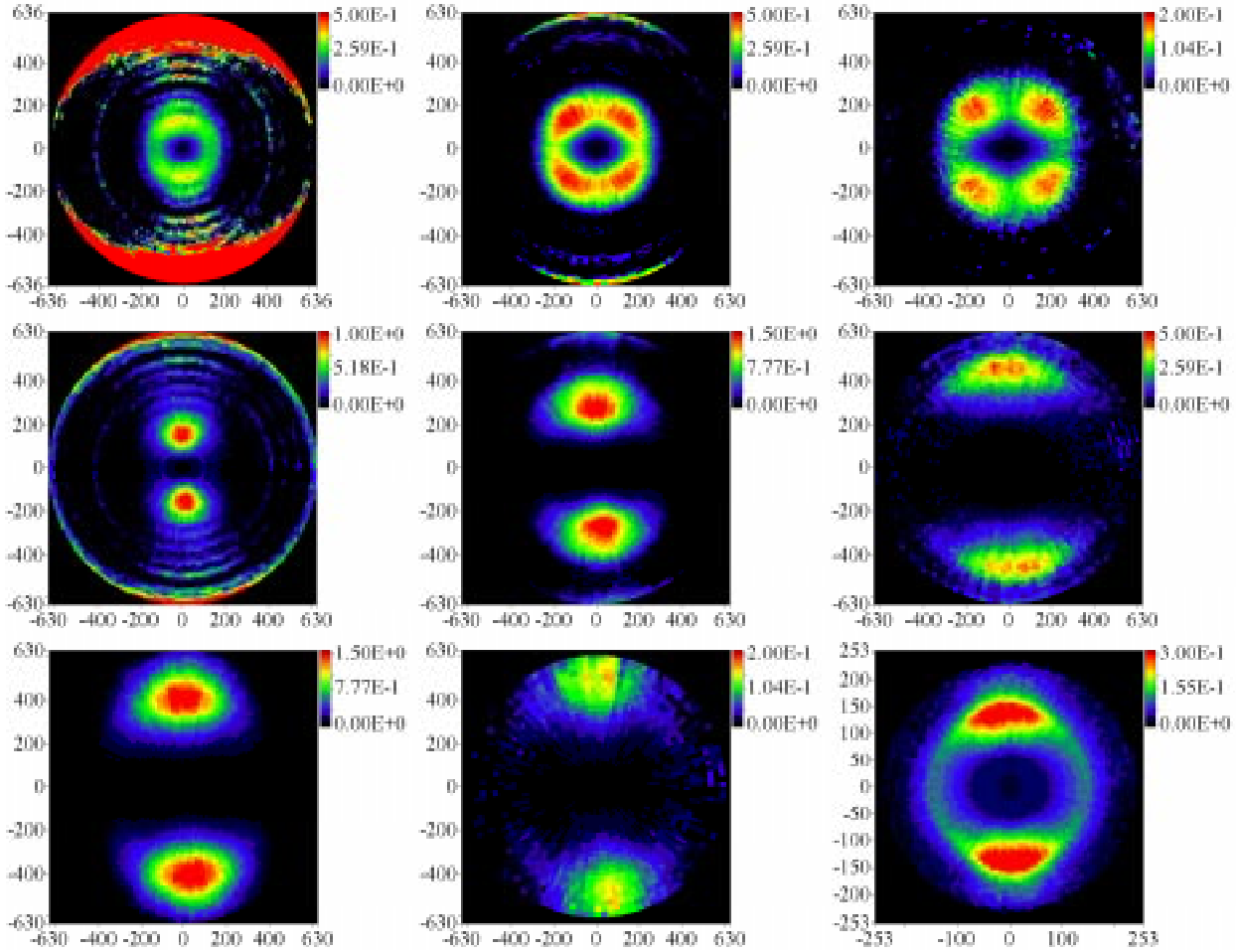

Figure 10. IMI plots of the laser-induced Coulomb explosion of Carbonyl Sulphide following correction for the finite collection angle of the detector. X and Y axes are ion momentum in a.m.u. ms^{-1} x 10^3 and the Z axis is corrected ion signal strength in arbitrary units. The laser polarisation direction lies vertically up the figure. Top row from left – C^+, C^{2+} and C^{3+}. Middle row from left – O^+/ S^{2+}, O^{2+}/ S^{4+} and O^{3+}/ S^{6+}. Bottom row from left – S^{3+}, S^{5+} and CO^+. As with figures 8 and 9, the red area on the circumference of the C^+ plot is unrelated to the C^+ ion, and there is instrumental 'ringing' present. The area of interest is the central green island. The same applies to the C^{2+} ion and the O^+ plot, where the areas of interest are near the centre and are red. Notice that all of the oxygen and sulphur ions travel along the laser polarisation, whereas the emission of the carbon ions is almost isotropic for the first ionisation stage. The higher stages exhibit a four-fold symmetry, indicating that the ions are emitted at an angle (not 90 degrees) to the O-S axis. This again indicates bending of the molecule by the laser.

that the initially randomly-orientated molecules have been largely rotated towards the laser polarisation; this should also be compared to the results of the experiment using the circularly polarised laser pulse. Secondly, the direction of the laterally emitted carbon ions indicates that the molecule has been bent either during or before the ionisation process begins. Importantly, the molecule must be bent before Coulomb explosion takes place. We have observed similar results at a lower intensity[6], but there is a considerable increase in the quality of the experimental data presented here. Also, note that the C^{2+} IMI plot in figure 8 contains a contribution from the O^{3+} ion. However, this does not hinder interpretation.

N_2O has also been found to exhibit signs of bending before Coulomb explosion. This can be seen in figure 9, specifically the nitrogen ion IMI plots. Each of the IMI plots show two distinct populations: ions from the centre of the molecule are emitted perpendicular to the laser polarisation, and ions from the end of the molecule are emitted along the polarisation. The distinction can be made by the fact that the ions emitted parallel to the polarisation have considerably higher momentum than those emitted perpendicular. As is the case with the carbon ions from CO_2, the IMI plots of the middle ion have little signal in the direction of the laser polarisation. This leads to the conclusion that the N_2O molecule is bent by the laser field.

Analysing the OCS IMI plots in figure 10 is more difficult due to the charge-to-mass degeneracy of the oxygen (mass 16) and sulphur (mass 32) ions. This makes quantitative analysis more difficult. However, the IMI plots of the central carbon ions lead to the same conclusion as with CO_2 and N_2O. These ions are not emitted in the same direction as the outer oxygen and sulphur ions due to the laser-induced bending of the molecule. In the case of the carbon ions from OCS, there is four-fold reflection symmetry. This is due to the carbon ions being emitted at some angle to the O-S axis. The asymmetry of the OCS molecule means that the carbon is emitted towards the oxygen ion, but not perpendicular to it. This effect becomes more pronounced with the higher fragmentation channels.

Conclusion

The rotation of the triatomic molecule CO_2 has been observed for the first time. A comparison to the behaviour of the more massive SF_6 molecule have been made; the SF_6 molecule is observed not to align to the extent of the CO_2 molecule. The coupling of the laser-induced dipole moments with the electric filed of the laser is sited as an explanation. The SF_6 molecule is thought to be too massive to allow the torques produced by this coupling to produce rotation.

Enhanced ionisation has been studied using the Covariance mapping technique for three triatomic molecules, namely CO_2, N_2O and OCS.

The effect of a linearly polarised laser pulse on the same three initially linear triatomic molecules has been studied, and modification to the bend-angle has been found in all three cases. This conclusion is reached after observing the emission of the central ion at a non-zero angle to the laser polarisation. A bent geometry is therefore possible.

Acknowledgements

This work was made possible with the financial support of the Engineering and Physical Sciences Research Council.

Dr. P. F. Taday and Dr. A. J. Langley of the Rutherford Appleton Laboratory are gratefully acknowledged for their dedicated assistance.

We would also like to thank Dr. J. H. Posthumus for continued interest in this work and the loan of the rotation stage.

References

1. K. Codling and L. J. Frasinski
J. Phys. B: At. Mol. Opt. Phys. 26 793 (1993) and references therein.
2. L. J. Frasinski, K. Codling and P. A. Hatherly
Science 246 1029 (1989)
3. H. Hishikawa, A. Iwamae, K. Hoshina, M. Kono and K. Yamanouchi
Chem. Phys. Lett. 282 283 (1998)
4. W. C. Wiley and I. H. McLaren
Rev. Scie. Instr. 26 1150-1157 (1955)
5. S. Augst, D. Strickland, D. D. Meyerhofer, S. L. Chin and J. H. Eberly
Phys. Rev. Lett. 63 2212 (1989)
6. J. H. Sanderson, R. V. Thomas, W. A. Bryan, W. R. Newell, A. J. Langley and P. F. Taday
J. Phys. B: At. Mol. Opt. Phys. 31 L599-L606 (1998)
7. C. Cornaggia, F. Salin, C. Le Blanc
J. Phys. B: At. Mol. Opt. Phys. 29 L749-L754 (1996)
8. J. H. Posthumus, J. Plumridge, M. K. Thomas, K. Codling, L. J. Frasinski, A. J. Langley and P. F. Taday
J. Phys. B: At. Mol. Opt. Phys. 31 L553-L562 (1998)
9. J. H. Sanderson, A. El-Zein, W. A. Bryan, W. R. Newell, A. J. Langley and P. F. Taday
Phys. Rev. A Submitted for publication.
10. J. H. Sanderson, R. V. Thomas, W. A. Bryan, W. R. Newell, A. J. Langley and P. F. Taday
J. Phys. B: At. Mol. Opt. Phys. 30 4499-4507 (1997)
11. C. Lynga, A. L'Huillier and C. G. Wahlstrom
J. Phys. B: At. Mol. Opt. Phys. 29 3293-3302
12. J. H. Sanderson, R. V. Thomas, W. A. Bryan, W. R. Newell, I. D. Williams, A. J. Langley and P. F. Taday
J. Phys. B: At. Mol. Opt. Phys. 31 L59-L63 (1998)
13. T. Seideman, M. Yu. Ivanov and P. B. Corkum
Phys. Rev. Lett. 75 2819 (1995)
14. J. H. Posthumus, A. J. Giles, M. R. Thompson, L. J. Frasinski, K. Codling, A. J. Langley and W. Shaikh
J. Phys. B: At. Mol. Opt. Phys. 29 L525 (1995)
15. L. J. Frasinski, P. A. Hatherly, K. Codling, M. Larsson, A. Persson and C. G. Wahlstrom
J. Phys. B: At. Mol. Opt. Phys. 27 L109-L114 (1994)
16. C. Cornaggia, M. Schmidt and D. Normand
J. Phys. B: At. Mol. Opt. Phys. 27 L123-L130 (1994)
17. L. J. Frasinski, P. A. Hatherly and K. Codling
Phys. Rev. A 156 227-232 (1991)
18. C. Cornaggia
Phys. Rev. A 54 2555 (1996)

Dissociative Ionization and Angular Distributions of CS_2 using ultra intense laser beams

K W D Ledingham, P Graham, R P Singhal, D.J Smith, T McCanny.

Department of Physics & Astronomy, University of Glasgow, Glasgow, G12 8QQ, Scotland, UK.

A Langley, P F Taday.

CLRC Rutherford Appleton Laboratory, Didcot, Oxon., OX11 0QX., England, UK.

C Kosmidis.

Department of Physics, University of Ioannina, Ioannina, GR-45110, Greece.

Introduction

From developments in laser generation of light pulses, very intense (>10^{16} W/cm^2), ultrashort (< 150 fs) pulses, made possible by the impact of CPA (Chirped Pulse Amplification) techniques [1], allows the experimental investigation of non-linear phenomena via "dressed" states induced by the laser-molecule interaction.

One of these is the alignment and subsequent ionization of a molecule. A very large electric field associated with the laser light, which can be used to induce dipole moments, aligns or orientates the ions along the polarization vector of the electric field. The degree of orientation depends upon the strength of the electric field, and the magnitude of the polarizability of the ion. Studies of the angular distributions of CS_2 at intensities on the order of 10^{12}-10^{14} W/cm^2 have been previously undertaken [2, 3] with pulse widths of 35 ps, and it was now sought to extend this for intensities of the order 10^{15}-10^{16} W/cm^2 using pulse widths of 50-100 fs.

Sanderson et al [4] have recently studied the alignment and bending of CO_2 molecules by intense femtosecond laser pulses at 60 fs and 750 nm. They measured the angular distributions of the CO_2 fragment ions.

Experimental

The TOF apparatus has been described in detail elsewhere [5]. Briefly, CS_2 was admitted effusively from an inlet system into a high-vacuum chamber, pumped to a base pressure of 1×10^{-8} Torr. CS_2 pressure was of order 1×10^{-5} Torr. The TOF system (figure 1) is a conventional linear system, the field-free length being 1.2 m, and an Einzel lens fitted to increase ion extraction. Ions are detected by an electron multiplier connected to a LeCroy 9304 digital oscilloscope.

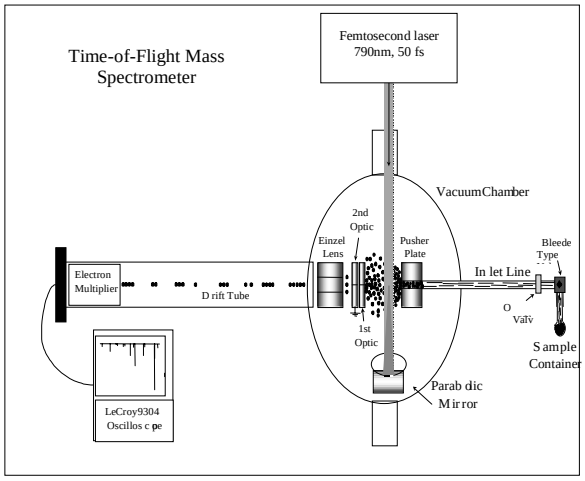

Figure 1. TOF system with effusive gas sample and focused with a mirror to the centre of the ion optics.

The laser system used is based on a Spectra Physics Ti:S oscillator pumped by an argon ion laser [6]. It produces 50 fs pulses at 790 nm, and energy/pulse of 2 mJ, after being stretched, amplified in a 7 mm long Ti:S rod (Crystal Physics), which is pumped by a Nd:YAG (Spectra Physics) laser, before being re-compressed to 50 fs. The repetition rate was 10 Hz. Pulse widths for 750 nm were 50 fs, whilst that for 375 nm were 90 fs.

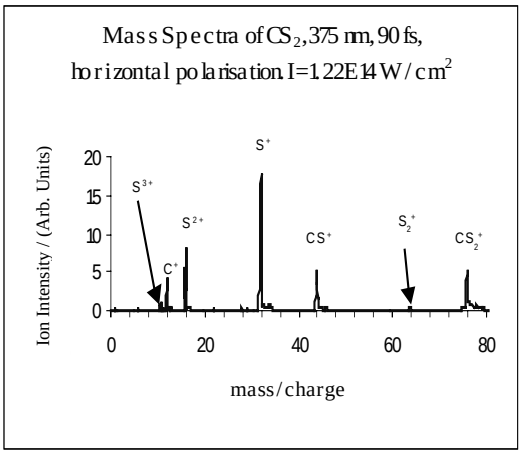

Figure 2. Mass spectra at 375 nm showing a number of multiply charged S ions. The fragmentation at 750 nm is considerably reduced

Results and discussion

A typical mass spectrum of CS_2 at 375nm is shown, (figure 2). It can be seen that there is considerable fragmentation, as the parent ion is not the dominant peak, even at these short pulse widths (fragmentation was pronounced at ns time-scales, but reduced for fs studies [7]). It was noted that the intensities are not the same for horizontal and vertical polarization, a consequence of the molecular alignment. The S^+ peak is the most pronounced in both polarisations. It is also possible that post dissociative ionization could occur for some fragments, although it may be a weak process given the short pulse durations.

The dominant peaks for the horizontal case are: CS_2^+, CS^+, S^{2+}, and C^+, all of approximately equal intensity. There are also S^{3+} and S^{4+} peaks present. Other dominant peaks in the vertical spectra are: C^+, CS_2^+, and CS^+, in decreasing order and a significant C^{2+} peak, as well as a S^{2+}, CS^{2+}, S^{3+}, and a tentative CS_2^{3+} peak. The different sulphur isotopes are present with the correct isotopic abundances. For both polarizations, at 375 nm, it has been observed that there is a sizeable S_2^+ peak occurring at m/z=64. This may come about, by transitions to states with bent geometrical configurations, (which cannot be as easily accessed at 750 nm).

Typical mass spectra for 750 nm, relative to that for 375 nm, have less pronounced fragmentation. The parent ion is dominant for both polarization orientations. The strongest

fragment ions present in the vertical case are: CS^+, CS_2^{2+}, S^+, and C^+ ions. There are also smaller CS^{2+}, S^{2+}, and C^{2+} ion peaks. In the horizontal spectra, there are: CS^+, CS_2^{2+}, S^+, S^{2+}, and C^+ primary fragment ions, with smaller CS^{2+}, S^{3+}, and C^{2+} ions present.

CS_2 is believed to be linear under 750 nm irradiation, due to the near absence of any peak at m/z = 64, i.e., S_2^+. This moiety is thought to be produced when CS_2 has a bent structure, and thus the 2 peripheral S-atoms are sufficiently close to bond with each other, and break from the C-atom. The lack of the S_2^+ ion is consistent with the idea that no bent geometrical states of the CS_2 molecule, or its ion, can be excited above 532 nm, and also the observation of Mathur et al. [3], who noticed that no S_2^+ ions were produced when irradiated by 532 nm, 35 ps pulses.

Angular distributions for S^{2+}, and C^{2+} are presented, (figures 3-4). It has been seen that all fragments are anisotropic, even the C-atom at 790 nm, where an isotropic distribution would be expected from this 'stationary' central atom. The C-distributions are, however, perpendicular to the polarization-vector, for 395 and 790 nm. Bhardwaj et al. [8], when considering bent triatomics such as NO_2, explain the perpendicular NO distribution by the directional components of the induced dipole moment of NO_2, whose parallel component is bigger than the orthogonal component, even for small fields, produced in the rising-edge of the pulse. In linear triatomics the fragments should all align along the field direction. The CS and the CS_2 distributions are essentially isotropic.

Since the majority of carbon ions can be detected at angles orthogonal to the axis of polarization, this presents a way of distinguishing the fragments coming from the explosive dissociative ionization of CS_2.

Finally, angular distributions were carried out for up to C^{3+} and S^{5+}, possible with the higher intensities used. It was noticed that they were narrower for each successive charge-state, illustrating that the degree of alignment is stronger, as the electric field needed to produce the higher charge states will cause more of an alignment, and also due to the higher polarization value of the ions. The results are at variance with earlier distributions of CS_2 ions obtained by Kumar et al, using 35 ps [2] and this discrepancy is at present being studied extensively.

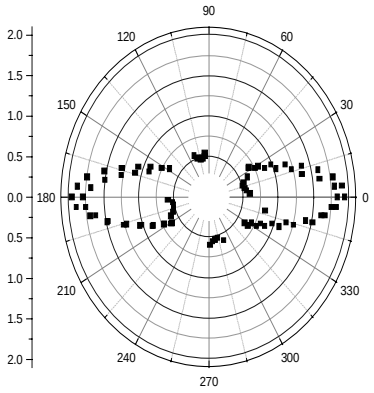

Figure 3. S^{2+} Distribution and all other S^{n+} distributions are similar. The angular distributions of all the S ions are directed along the direction of polarisation of the laser.

Conclusions

The results herein support the view that one charge-state starts when the previous one has saturated. Increasing the laser intensity merely increases the volume of production of an ion. Angular distributions were worked out by varying the polarization direction. It is noted that higher charge state ions have narrower distributions, as expected, and the results indicate alignment of the molecule. Finally, mass spectra were obtained at 375/395 nm and 750/790 nm, and fragmentation was found to be relatively increased at the shorter wavelength. This has also been observed for C_7H_6O [9], and C_4H_6 [10].

Production of the S_2^+ ion, indicative of exciting the parent to states with a bent geometrical structure, was also increased at 375 nm. For certain conditions at 790 nm, it was found that the ionization behaved very atomic-like, i.e., little fragmentation and multiple-charged parent ions [11]. This phenomenon has also been observed for both CH_3I, and 1-3 Butadiene [10].

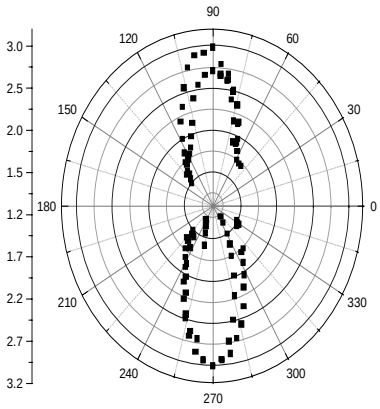

Figure 4. C^{2+} Distribution and all other C^{n+}distributions. It can be seen that the carbon ions unlike S ions, are distributed in a direction at right angles to the laser polarisation.

References

1. Strickland D and Mourou G,
   Opt. Commun., 56, 219 (1985)

2. Kumar G R, Gross P, Safvan C P, Rajgara F A, and Mathur D,
   J. Phys. B: At. Mol. Opt. Phys., 29, L95-L103 (1996)

3. Mathur D, Kumar G R, Safvan C P and Rajgara F A,
   J. Phys. B: At. Mol. Opt. Phys., 27, L603-L610 (1994)

4. Sanderson JH, Thomas RV, Bryan WA, Newell WR, Langley AJ, Taday PF.
   J.Phys. B At Mol Opt. Phys. 31, L599-L606, 1998.

5. Ledingham K W D, Kilic H S, Kosmidis C, Deas R M, Marshall A, McCanny T, Singhal R P, Langley A J and Shaikh W,
   Rapid Commun. Mass Spectrom., 9, 1522 (1995)

6. Taday P F, Mohammed I, Langley A J, and Ross I N, to be published

7. Ledingham, KWD and Singhal,RP,
   Int.J.Mass Spectrom and Ion Processes, 163, 149, 1997.

8. Bhardwaj V R, Safvan C P, Vijayalakshmi K and Mathur D,
   J. Phys. B: At. Mol. Opt. Phys., 30, 3821-3831 (1997)

9. Smith D J, Ledingham K W D, Kilic H S, McCanny T, Peng W X, Singhal R P, Langley A J, Taday P F and Kosmidis C,
   J. Phys. Chem. A, 102, 2519, 1998.

10. Graham P, Ledingham K W D, Singhal R P, Smith D J, McCanny T, Langley A J and Taday P F,
    to be published

11. Ledingham K W D, Singhal R P, Smith D J, McCanny T, Graham P, Kilic H S, Peng W X, Wang S L, Langley A J, Taday P F, and Kosmidis C,
    J. Phys. Chem. A, 102, 3002-3005 (1998)

Characterisation of the lsf x-ray source for Microscopy

A G Michette, C J Buckley, S J Pfauntsch, N I Khaleque*, P Edmundson, G S Dermody[#].

Centre for X-Ray Science, Department of Physics, King's College London, Strand, London WC2R 2LS

** Now at Research Systems UK*

[#] Now at DERA Fort Halstead, Sevenoaks, Kent

I C E Turcu[ϕ], W Shaikh.

CLRC Rutherford Appleton Laboratory, Chilton, Didcot, Oxon., OX11 0QX

[ϕ] Now at JMAR Research, San Diego, CA, USA

Introduction

In order to assess the capability of the Laser for Science Facility x-ray source for microscopy it is important to understand the emission characteristics. The source was last characterised in 1992 [1], since when it has been significantly upgraded [2], and thus a full characterisation of the source was needed. This has been done using six target materials (Mylar, aluminium, copper, silver, tungsten and gold) and three diagnostic instruments (a pinhole camera, a transmission grating spectrometer and a flat-field reflection grating spectrometer). Here, the pinhole camera images and transmission grating spectra of the Mylar tape target are presented.

The data were recorded on Shanghai 5F soft x-ray film, which has been calibrated by Tallents *et al.* [3], and were subsequently digitised using a microdensitometer. The film calibration showed that the incident x-ray flux I (in photons per square micrometre) is related to the exposure D (optical density) of the film by

$$I = -K \ln\left(1 - \frac{D}{D_{\text{sat}}}\right) \tag{1}$$

where D_{sat} is the saturation density of the film. The values determined were $D_{\text{sat}} = 2$ and $K = 2.78$ photons μm^{-2}. However, it is known that the characteristics of Shanghai 5F film can vary from batch to batch. The calibration was therefore checked by exposing the film to x-ray pulses generated by different numbers of laser shots, typically one to several tens for pinhole images and several hundred to a few thousand for transmission grating spectra. The saturation density was then varied until the incident flux varied linearly with the number of shots. This indicated that, for the film used, $D_{\text{sat}} = 2$ was a good value.

The Pinhole Camera

The pinhole camera used a 5 µm diameter pinhole and the images were recorded on film 11 cm behind the pinhole. A 100 nm silicon nitride membrane coated with 200 nm of aluminium prevented UV and visible emission of the source from fogging the film. The camera was used to study the plasma under the following conditions:

with 20 torr of helium in the target chamber to give the source size for the unfiltered Mylar spectrum;

5–15 torr of nitrogen acting as a filter to isolate (primarily) the Lyman α line of hydrogen-like carbon (λ = 3.37 nm);

20 torr of helium plus 200–400 nm of calcium fluoride to try to isolate the He_α line of helium-like carbon (λ = 4.02 nm). This was not very successful as the Lyman α line was still more intense than the He_α.

Images were taken for all of the above using single and eight pulse trains of laser pulses.

A typical pinhole image, using the eight pulse train which will be used for the x-ray microscope, is shown in figure 1a.

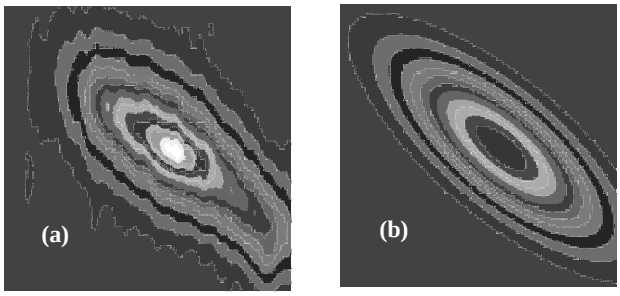

Figure 1. (a) Pinhole camera image taken in one laser shot (8 pulses) with 20 torr He. (b) Reconstruction of the image.

The elongation is mostly caused by the viewing angle used — along the target normal, where the emission is maximum, with the target surface at 45° to the incoming laser beam The images were fitted to two dimensional distributions using the Pearson VII peak function [4] which, in one dimension, is

$$f(x) = H\left[1 + \left\{\frac{2(x - x_0)\sqrt{2^{1/M} - 1}}{w}\right\}^2\right]^{-M} \tag{2}$$

where H is a normalisation constant, x_0 is the centre of the distribution, w is the full width at half maximum (FWHM) and M is known as the Pearson parameter. This distribution is a good approximation to a Voigt function (i.e., a convolution of Gaussian and Lorentzian distributions) but is computationally much less expensive. For large M the Pearson VII distribution approximates to a Gaussian (and the fit is insensitive to M), while as M approaches one it tends to a Lorentzian. The fit to the image of figure 1(a) is shown in figure 1(b). The source sizes w_s (FWHM) corresponding to the fitted pinhole image FWHMs w_f were calculated from the pinhole camera magnification taking into account the penumbral blurring caused by the finite diameter p of the pinhole

$$w_s = \frac{s(w_f + p) + pf}{f} \tag{3}$$

where s is the source to pinhole distance and f is the pinhole to film distance. The fitted source size for the eight pulse train is (41±4) µm by (19±2) µm, or (29±3) µm by (19±2) µm when the viewing angle is corrected for. The remaining elongation is due to a subsequently discovered misalignment of the multiplexer so that the pulses were not all focused to the same place.

The fitted FWHM source size for the single pulse train also shows a slight elongation, probably due to the ribbon shape of the incoming laser beam. Images recorded after the multiplexer alignment was improved are more symmetrical but appear to indicate a larger source size. This is because they were recorded over five shots and it has subsequently been discovered that the tape drive was causing an oscillation of the target surface with an amplitude of ≈ 10 µm. This was caused by incorrect tape

tension and by target debris in the clutch, which can easily be rectified by regular servicing or replacement. The fitted source sizes do not vary significantly with filter type, indicating that there is no strong spatial dependence in the emission of the main spectral lines.

The Transmission Grating Spectrometer

The transmission grating spectrometer used a ~200 nm period grating 10.75 cm from the source, protected by a 100 nm Si_3N_4 membrane coated with 200 nm of aluminium. The spectra were recorded on film 22.75 cm from the grating. The grating was made by electron beam lithography on a 100 nm Si_3N_4 membrane followed by nickel electroplating over an area of ≈100×100 µm. This would have given a poor (geometrical) spectral resolution which was increased by using a 25 µm pinhole before the grating. For the source sizes presented in table 6 this gave a wavelength spread $\Delta\lambda \approx 0.08$ nm, still poor but the grating had high efficiency. Higher resolution spectra have been obtained using the flat-field spectrometer.

Spectra were recorded using the same gas / filter combinations as for the pinhole camera images; typical spectra are shown in figure 2 which shows the effect of nitrogen filtering. The line widths are predominantly due to instrumental broadening. The recorded spectra also contain lines due to higher order diffraction from the grating. Comparing the intensities in the various diffraction orders allows the diffraction grating efficiency to be determined as a function of wavelength, taking the phase modulating effect of the nickel into account.

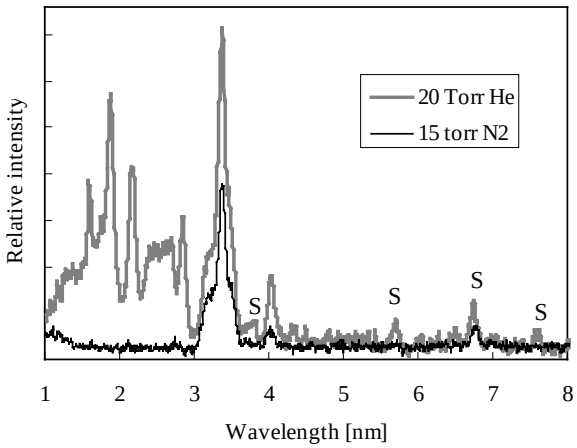

Figure 2. Spectra recorded using the eight pulse train with 20 torr He and 15 torr N_2 filters. Lines marked S are due to second order diffraction from the grating. Other second and higher order lines are too small to be seen easily or lie beneath first order lines.

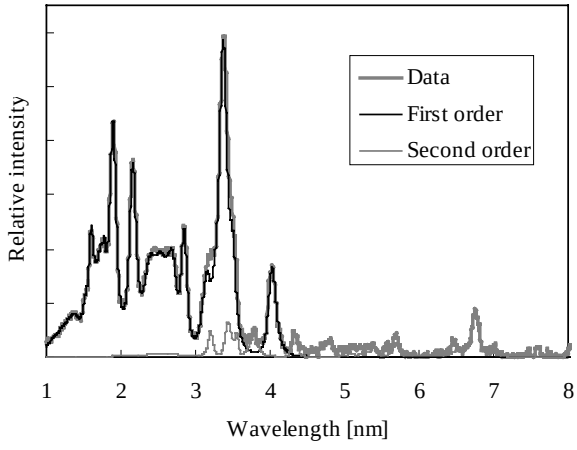

Figure 3. Recorded spectrum from the single pulse train with 20 torr He and the corresponding fit. For clarity, only the first two diffraction orders are shown.

The spectra were fitted using the Pearson VII function for each spectral line, equation (2) with x replaced by the wavelength λ. The fit parameters are not directly correlated to line broadening processes but this is not important here as the purpose is to determine the absolute x-ray emission in each spectral line. The recombination edges were modelled by triangular functions convolved with Lorentzians, as convolution with a Pearson VII function is tedious. A typical fit is shown in figure 3; the fitted lines typically had Pearson M values in the range 1–2, i.e., the line shapes approximated to Lorentzians.

Conclusions

The analysis presented above is still not complete, and so any conclusions must be considered as preliminary. However, the spectral line intensities of the single pulse spectrum are, after taking the diffraction grating efficiency and filter transmission into account, compatible with those predicted by a model calculation [5]. The intensity in the Lyman α line of the eight pulse spectrum is compatible with the goal of single pulse per pixel imaging in the scanning x-ray microscope.

References

1. MS Schulz
PhD thesis, University of London (1991)

2. ICE Turcu, IN Ross, P Trenda, C W Wharton, R A Meldrum, H Daido, M S Schulz, P Fluck, AG Michette, A P Juna, JR Maldonado, H Shields, GJ Tallents, L Dwivedi, J Krishnan, D L Stevens, T L Jenner, D Batani & H Goodson
Applications of Laser Plasma Radiation, Proc. SPIE **2015** 243–260 (1993)

3. GJ Tallents, J Krishnan, L Dwivedi, D Neely & ICE Turcu
Applications of X-Rays Generated from Lasers and Other Bright Sources, Proc SPIE **3157** 281–290 (1997)

4. WP Elderton & NL Johnson,
Systems of Frequency Curves (London: Cambridge University Press, 1969)

5. P Edmundson
PhD thesis, University of London (1998)

Characterisation of a picosecond laser plasma source in the Extreme UV wavelength band

R Stuik, L A Shmaenok, F Bijkerk.

FOM – Institute for Plasma Physics, PO Box 1207, 3430 BE Nieuwegein, The Netherlands. Email stuik@rijnh.nl

A A Sorokin.

Ioffe Physical Technical Institute, St Petersburg 194021, Russia

I C E Turcu, W Shaikh, N Spencer.

CLRC Rutherford Appleton Laboratory, Chilton, Didcot, Oxon., OX11 0QX.

Introduction

Extreme Ultra Violet lithography is considered a likely successor of the current deep-UV lithographic techniques in semiconductor industry. For this application a bright source of monochromatic light with a wavelength in the range between 10 and 20 nm is needed. An appropriate candidate is the laser plasma; a very bright point source, also in this wavelength range. Optimisation of yield of a laser plasma is needed in order to use this source as efficient as possible. Much research has been done on this subject at longer pulse lengths (5-25 ns), e.g. [1, 2]. So far, shorter pulses, usually resulting in high temperature plasmas, have not often been studied. In this work, several experiments have been carried out with the FOM Institute for Plasma Physics Rijnhuizen (Nieuwegein, The Netherlands), to provide a characterisation of the RAL picosecond laser plasma source [3] in the EUV band. A calibrated diagnostic unit for detection of radiation at 13.7 nm wavelength was employed.

Experimental

The characterisation of the picosecond plasmas was done at 13.7 nm, in the wavelength band that will be used in future EUVL applications. The laser plasma was generated using the RAL picosecond laser system. A pulse train of 6 picosecond pulses of 20 mJ laser light of 248 nm generated a laser plasma with temperatures of a few hundred eV. These temperatures combined with high electromagnetic radiation levels of the laser are sufficient to generate x-rays with energies of several tens of eVs up to several keVs. A small energy band ($E/\Delta E \approx 25$) centred at 90 eV (13.7 nm) was selected using a multilayer mirror. The mirror consisted of 40 bi-layers of Mo/Si on a spherical substrate with 32 cm radius of curvature. The plasma was imaged on a PIN diode by this multilayer mirror. The diode was covered with a filter consisting of 50 nm Si_3N_4 and 100 nm Nb. This filter suppresses visible/UV by a factor of 10^4. All elements (mirror, filter and detector) were absolutely calibrated for the wavelength under observation at the PTB beam line at Bessy (Berlin) and the Institute for Physics of Microstructures (Nizhny Novgorod).

For a few experiments, also a streak camera was used to investigate the time structure of the plasma at the wavelength of 13.7 nm. The scheme used was analogous to the absolute calibration measurements, with the cathode of the streak camera replacing the PIN diode. This way, a time resolution of a few tens of picoseconds could be obtained.

The power density on target was varied using different methods of illumination:

- *Beam attenuation*: by inserting different quartz plates, the laser beam was attenuated over more than an order of magnitude while keeping the spot size constant. A second method to attenuate consisted of positioning a diaphragm in the beam, which changed somewhat the focal spot size.
- *Pulse duration*: Changing the oscillator cavity, a range in pulse duration's between 3 and 21 ps per pulse could be obtained. Since the energy per pulse did not change significantly over this range, almost an order of magnitude in pulse duration could be investigated.
- *Different lenses and lens defocusing*: Changing the spot size was achieved in two ways: By varying the focal distance of the lens and by defocusing the lens. It is noted that the error in the power density is somewhat larger due to imperfectness of the lens and a non-linear shape of the beam waist.

Moreover, two other parameters of importance to the Conversion Efficiency (CE) have been studied:

- *Pulse to pulse separation*: Previous measurements have shown [4], that a pre-pulse can influence the conversion efficiency of the main pulse. In a pulse train this situation may occur for every pulse, except the first. The influence of pulse-to-pulse separation has been investigated for discrete values of 1.8, 3.7 and 7.4 ns.
- *Target material*: Different target materials have different electron configuration and therefore different excitation and emission energies, giving different levels of radiation at the investigated wavelength.

For all these cases, the absolute CE was determined and for the pulse to pulse separation, also the time structure at wavelength was investigated using the streak camera. The target material was Cu tape, unless indicated otherwise.

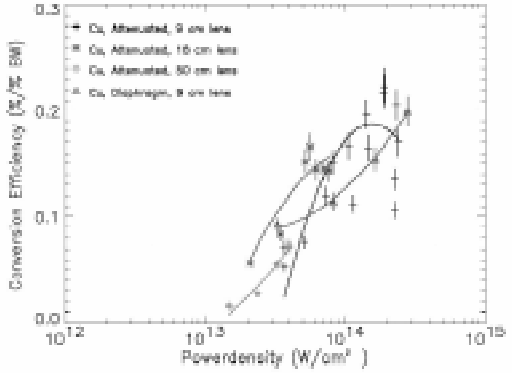

Figure 1. Dependence of the CE on power density for various lenses and beam attenuation schemes

Results

Figure 1 shows the dependence of the conversion efficiency on the power density as varied by attenuation of the beam for each of the three focal lengths used. All curves show a similar behaviour: The conversion efficiency increases with the power density, but above 10^{14} W/cm^2 the curves seem to top off. This could be an indication of a local optimum power density, but verification required an energy in the laser pulse beyond that of the current experimental conditions. The range of power densities of the 9 and 18 cm lens overlap, indicating that both lenses gave an approximately equal focal spot size. The range for the 50 cm lens is somewhat smaller due to high noise levels at the lower end of the power density range. As all lenses follow

the general curve, the conversion efficiency seems to be only dependent on the power density. Larger spots with higher energy result in similar CE values as smaller spots with low energy.

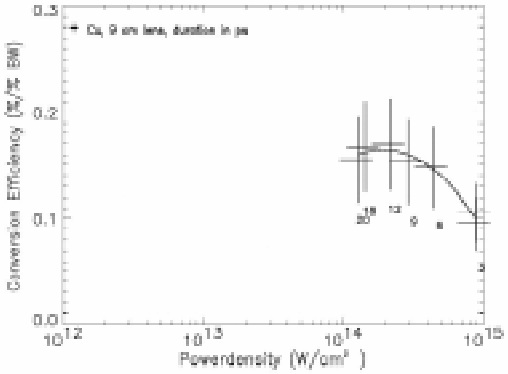

Figure 2. Dependence of CE on power density for different pulse duration's (annotated)

Using shorter pulses a higher power density can be investigated, up to almost 10^{15} W/cm^2 (figure 2). The plot shows an initial increase of the conversion efficiency with increasing power density, followed by a drop of the CE for even higher power densities. Combining figure 1 and 2, a local optimum is found at $2x10^{14}$ W/cm^2.

The conversion efficiency varies only slightly with the pulse-to-pulse separation, as shown in figure 3. Due to the small number of points combined with the relatively large errors on the data, the dependence of the conversion efficiency is not yet clear. There seems to be a slight increase in CE for longer pulse separations.

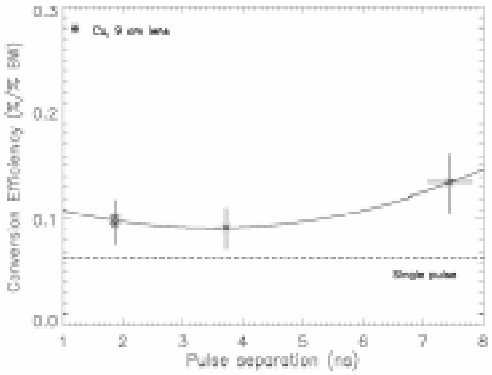

Figure 3. Dependence of conversion efficiency on the pulse-to-pulse separation (Horizontal line is a single pulse)

The material dependence is shown in figure 4. Four materials for three different lenses could be measured and a clear dependence of the conversion efficiency on the material and power density can be seen. For figure 4 only comparable conditions are used, explaining the lower maximum value for the copper target. From the materials investigated, gold shows the highest conversion efficiency. These results should be compared with results where longer pulses with lower power densities were used [2]. They observed increased emission where a K, L or M shell transition was close to the wavelength under investigation.

Conclusions

From the different schemes of scanning the power density on the target (attenuation, duration, lens focal distance and lens defocusing) coherent data could be obtained about the behaviour of the conversion efficiency on the power density. Combining figure 1 and 2 shows an optimum power density of $2x10^{14}$ W/cm^2 for copper targets. The conversion efficiency obtained at this value is 0.22%/% BW.

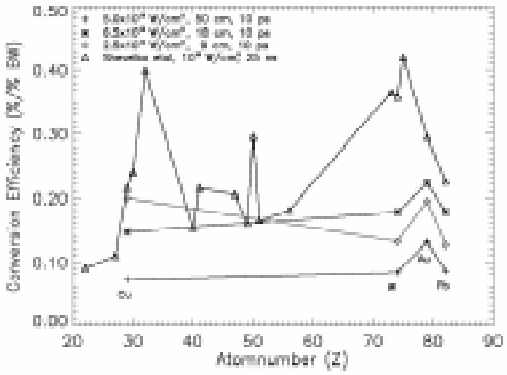

Figure 4. Dependence of the conversion efficiency on material and power density.

A certain trend can be seen in the conversion efficiency versus pulse-to-pulse separation plot (figure 3). For somewhat longer separation, the conversion efficiency seems to increase. Even at separations of more than 7 ns, some influence of the pre-pulse is visible (At infinite separation the CE should drop to the level of a single pulse).

For different materials the conversion efficiency follows the general trend already found in previous research at lower power density [2]. Gold has the highest conversion efficiency (0.22%/% BW at $2.5x10^{14}$ W/cm^2) under similar conditions, but the lack of variation of materials in this investigation leaves room for further material optimisation at these power densities (like Ge and Re for 10^{12} W/cm^2, see figure 4).

Future research could be focused on a better spread of elements in the periodic table, at a larger range of laser energies and focal spot sizes. From figure 1 we conclude that a higher pulse energy on target could confirm the optimum power density for these picosecond pulses.

Acknowledgements

We gratefully thank N. Takeyasu, S. Huntingdon and the supporting staff of RAL for their assistance in operating the laser and the building of the set-up. E. Louis and N.N. Salashchenko are acknowledged for the supply of the multilayer EUV mirrors and A.G. Michette and S.J. Pfauntsch for sharing their beam time at RAL with us. This work was financially supported by the LSF at RAL, the EC and FOM (the Foundation for Fundamental Research on Matter), STW (the Netherlands Technology Foundation) and INCO-Copernicus.

References

1. R C Spitzer et al
   J Appl Phys 79(5) 2251(1996)
2. A P Shevelko et al
   Physica Scripta, 57 576(1998)
3. I C E Turcu et al
   SPIE, 2015 243(1994)
4. L A Shmaenok et al
   SPIE, 2523 113(1995)

Spatio-Temporally Resolved Dual Laser Plasma Photoabsorption Studies of Thorium Plasmas with an Extreme UV Continuum Light Source

J T Costello, C McGuinness, L Dardis, C Moloney, O Meighan.

Centre for Laser Plasma Research (CLPR), School of Physical Sciences, Dublin City University, Dublin 9.
E-mail jtc@physics.dcu.ie

C L S Lewis, R O'Rourke, A MacPhee.

School of Mathematics and Physics, Queen's University of Belfast, Belfast BT7 1NN

I C E Turcu, C Danson, S Huntingdon, N Takeyasu, W Shaikh.

CLRC Rutherford Appleton Laboratory, Chilton, Didcot, Oxon., OX11 0QX

Introduction

When an extreme-ultraviolet (EUV) photon interacts with an atom or ion in a ground or excited state, in addition to valence electron excitation and/or ionization, several competing processes can take place involving inner shell and/or multiple electron excitations. Interpretation of the multi-electron dynamics of the excitation and decay processes requires theoretical models capable of handling the complex many-particle nature of the problem. The challenge to experimentalists is to devise techniques which can identify and measure accurately the various excitation and decay processes for atoms and ions in well described initial and final states. In addition to its fundamental interest, the study of photoexcitation/ ionization in this energy regime is also of considerable practical interest as the results are relevant to an understanding of many laboratory and astrophysical plasma processes. Furthermore, as atoms in molecules or condensed matter often exist in ionic form, measurements on their free atom or ion counterparts can prove helpful in elucidating the effects of the molecular or condensed matter host. Most recently, the discovery that nanoclusters can be formed in laser matter interactions [1)] has refocussed interest on free atom/ion spectra for comparative purposes.

For neutral atoms experimental techniques for photoionization are well developed and spectroscopies such as photoabsorption, fluorescence, photoion, photoelectron and coincidence measurements often combined with angular resolution have provided very detailed data on atomic excitation and decay dynamics [2)]. For ions the situation is much less satisfactory mainly due to the great difficulty in generating high density ion beams. An extremely versatile technique for the recording of photoabsorption spectra of atoms and ions is the Dual Laser Plasma (DLP) method [3)]. One laser plasma constitutes the 'sample' while the other becomes the XUV backlighting source. The DLP method has been used to study a wide variety of atomic and ionic species [4)] and has contributed to a number of significant advances in the field of atomic inner shell excitations over recent years [5)].

A key element of the DLP technique is the extensive 'line free' XUV continuum emission from laser plasmas of the rare-earth and neighbouring metals [6)] which provides a compact and economic alternative to a bending magnet or insertion device at a synchrotron radiation facility. In a previous experiment at RAL [7)] we showed that one could produce similar emission using 7 ps, 248 nm pulses with an upper limit of 750 ps on the duration. Since the time resolution of the DLP method is determined by the XUV pulse width one major goal of the current experiment was to better measure this parameter for some typical target plasmas (Sm, W, Au & Pb) and study its dependence on certain laser characteristics, in particular laser to ASE pulse energy ratio.

One of the most interesting entities to have been revealed via inner shell excitation is the so called 'Giant Resonance'. It is a characteristic of the collective nature of electron interactions in atoms and observed for $\Delta n = 0$ transitions in medium and high-Z atoms. Since first seen in the XUV spectra of the lanthanide solids in the mid 1960's they have received extensive theoretical and experimental study in atomic, molecular and solid state phases [8)]. Only two experiments on ions have been published [9, 10)] in the intervening thirty years or so and a half dozen or so on the actinides (ref. [11)] and refs. within). To date no experiment on photoionization of actinide ions has been published and in order to address this gap we decided look at 5d-photoionization along the Th isonuclear sequence.

Experimental setups

1. XUV Continuum Duration

A schematic of the experimental setup used to measure the XUV continuum pulse duration is shown in figure 1(a). 7 ps pulses from the frequency mixed output of a synchronously pumped dye laser were amplified up to ~ 20 mJ by double passing them through a KrF excimer laser. The KrF amplifier was triggered by a 10 Hz clock derived from the 82 MHz oscillator of the modelocked Nd-YAG laser. The output from the KrF amplifier was focused to an irradiance of ~ 10^{13} W/cm^2 *in vacuo* (10^{-5} Torr) onto rod targets via a f/7 fused silica plano-convex lens with a focal length of 35 cm. An optical low pass filter consisting of a pair of Ag coated mirrors oriented at a grazing angle of 10^o combined with an XUV transmission filter composed of thin films of Mo (0.185 μm), CH (0.159 μm) and the 0.1 μm formvar substrate of the streak camera CsI photocathode yielded an symmetric transmission curve with a peak transmission of 65% @ 115 eV and FWHM of ~ 75eV. The streaked image was read out by an image intensified CCD camera and the overall system time response was better than 60 ps.

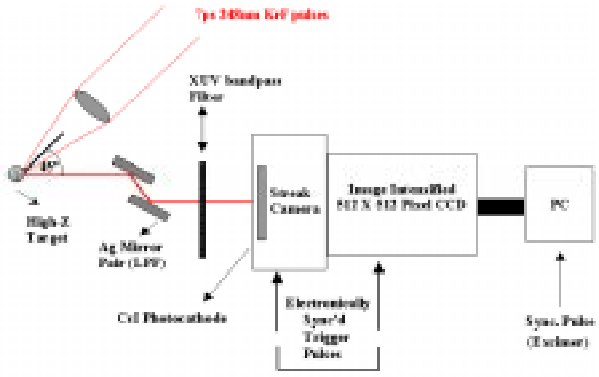

Figure 1 (a). Experimental Setup for extreme-UV continuum pulse duration measurements.

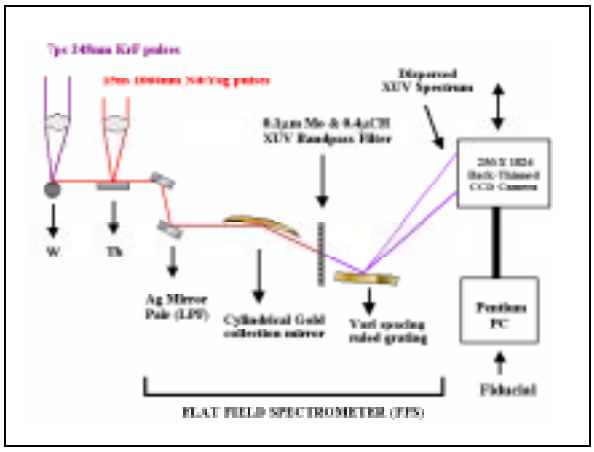

Figure 1 (b). Experimental setup for time and space resolved dual laser plasma (DLP) photoabsorption measurements.

2. Time Resolved Dual Laser Plasma Experiments

The setup used to record time integrated emission and time resolved photoabsorption spectra is shown in figure 1 (b). The thorium absorbing plasma was generated by focussing the 1064 nm/ 300 mJ/ 8 ns output pulse from a Q-switched Nd-YAG laser to a spot size of ~100 µm dia. via a f/5 lens (f = 12.5 cm). The 248nm/ 20 mJ/ 7ps pulse was synchronised to the Pockels cell of the Nd-YAG laser and, tightly focused onto a tunsten rod target, generated a backlighting XUV continuum with a variable delay and an inter laser pulse jitter of +/- 500 ps. An XUV prefilter, similar to the one used in the streak camera measurements virtually eliminated all photons above 200 eV thereby ensuring that the window of interest from 100 - 200 eV was free from order sorting problems. In addition the pre filter eliminated all scattered light permitting the measurement of reliable relative cross-sections. Transmitted XUV radiation was dispersed by a flat field spectrometer equipped with an ANDOR back thinned CCD which typically covered the 65 - 200 eV range with its 1024 pixel width. The spectral resolution achieved approached 250. The thorium target was affixed to a three axis mount which permitted us to probe different regions of the expanding plasma plume. The footprint of the XUV beam at the thorium target position was estimated to be < 100 µm V X 100 µm H as determined by the geometric acceptance of the spectrometer and its associated optics.

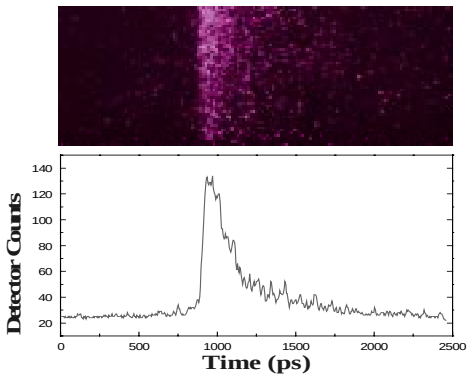

Figure 2. 2D and corresponding vertically binned CCD image of the streak from a tunsten plasma.

Results and Discussion

Comprehensive sets of measurements of both static and dynamic images were made for four target materials (Sm, W, Au & Pb). The static images were used to determine estimates of the streak camera instrument function for each set of data which is reasonably well approximated by a Gaussian curve of FWHM 60 ps or so. The results are summarised in table 1. and show the mean continuum pulse duration to be sub 200 ps or so and as low as 120 ps for a tungsten plasma. These values may be reduced by 10 - 15 ps after deconvolution of the streak camera response. At the irradiances used here one would expect plasma temperatures of 150 eV or so and ion velocities of ~10^7 cm/sec. Hence continuum emission times of 100 - 200 ps correspond to plasma emitting sizes of 10 - 20 µm or so.

Continuum Target	Average FWHM (ps)	Std Deviation (ps)
Lead	123	±42
Tungsten	176	±42
Samarium	183	±27
Gold	209	±34

Table 1.

It has been well established that the duration of X-ray emission from ultrashort pulse laser plasmas tends to increase in the presence of either ASE or controlled pre-pulses [12)] . In order to investigate the effect of a 20 ns ASE pedestal from the KrF amplifier on the continuum duration, a spatial filter with an adjustable iris was used to vary the ratio of ps laser to ASE energy (see figure 1). We found little dependence of XUV continuum duration on ASE level for ASE energy = 0.5 -> 2.0 times picosecond laser pulse energy. Since even at the lowest ASE level we could form a pre-plasma and given that the pre-plasma parameters did not vary much over the range of ASE energy available this observation is not too surprising. Unfortunately we could not eliminate the ASE to determine the the spectral purity and duration of continuum produced in a direct laser-solid target interaction. However, one would expect to observe a further pulse width reduction in this case.

We observed a marked dependence on picosecond laser pulse energy (figure 3). In case of tungsten, the continuum duration ranged from < 100 ps to almost 200 ps for pulse energies of 10 to 23 mJ or so. The growth of continuum duration with laser pulse energy appears to show a threshold at ~ 15 mJ and is very marked at the higher energy limit of the laser. This latter point explains the error of +/- 25% f.s.r. on the measurements given in table 1, since shot to shot fluctuations of up to +/-50% or so in the ps laser energy were not uncommon.

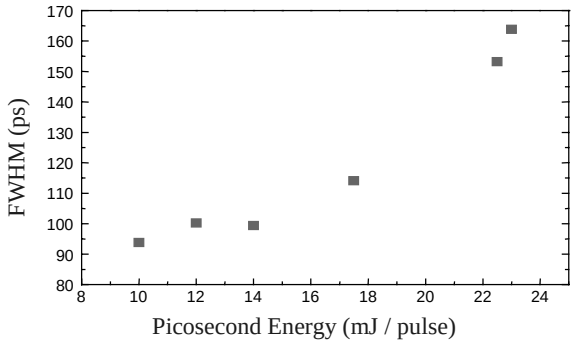

Figure 3. Dependence of extreme-UV continuum pulse duration on picosecond laser pulse energy.

The time evolution of XUV photoabsorption by laser produced thorium plasmas is shown in figure 4. The energy range chosen straddles the 5d-subshell ionization limits of thorium permitting the study of both 5d photoexcitation and photoionization.

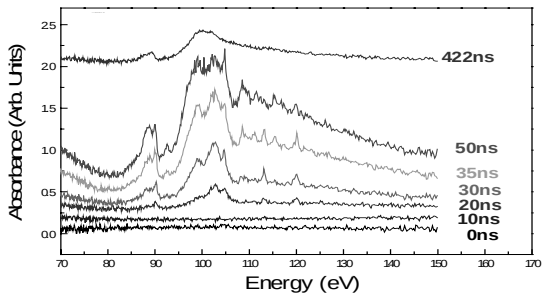

Figure 4. Time resolved extreme-UV photoabsorption spectra of a thorium plasma showing the transition from 'Giant Resonance' continuum absorption to discrete Rydberg like spectra with decreasing time delay.

At long times (> 400 ns) after the initiation of the thorium plasma the absorption spectrum exhibits two well defined features, a narrow one below the 5d ionizations limits and a broad and strong asymmetric one above the limits. There is no single simple interpretation of the spectrum. One approach which relies on the collective response of the atom's electron cloud to an external electromagnetic field [13] yields good agreement with the current photoelectric data and an earlier measurement using the long pulse DLP technique [14]. There is however a discrepancy in the width of each feature which was postulated to be due to low lying metastable states in thorium and in particular of the $6d^3 7s$ configuration. To test this point we have performed preliminary calculations using the RTDLDA code [15] which indicate that the observed spectrum does indeed exhibit contributions from both ground and metastable states of Th (see figure 5). It is clear from the figure that significant populations of thorium atoms appear to become 'frozen' in long lived metastable states. As of now we cannot say for certain whether metastables are formed in excitation of atomic thorium in the plume or in e - Th^+ recombination.

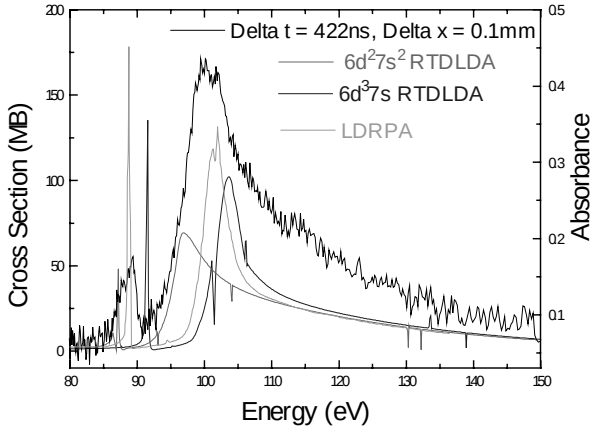

Figure 5. Comparison of measured 'Giant Resonance'with computed cross-sections of atomic thorium using collective atomic models:LDRPA [12] and RTDLDA [15]. The RTDLDA results indicate the presence of both ground and metastable state absorption.

As the inter-plasma time delay is shortened it can be seen that the character of the spectrum changes radically as the broad giant resonance becomes overlaid with discrete structure and Rydberg series develop. Such dramatic changes in oscillator strength distribution along an isonuclear sequence were observed only once before observed in 1981 for 4d - ε,nf excitations in the Ba /Ba^+ /Ba^{2+} isonuclear sequence using resonant laser excitation and ionization of Ba vapour [9]. Only very recently was this study extended to triply ionized La [10]. The data shown in figure 4 represent the first measurements along an actinide isonuclear sequence. A simple picture requires an alternative interpretation of 'giant resonances'.

f-electrons possess bi-well potentials separated by a potential barrier. In atomic thorium a 5f (^{1}P 'like') state lies above the 5d limits but trapped by the potential barrier while the 5f (^{3}P, ^{3}D 'like') states lie below the 5d limits and are located in the inner well of the potential. The higher nf states all lie in the outer well eliminating the possibility of 5d - nf (n>5) transitions. Thus the atomic spectrum of Th may be interpreted as comprising a 5d - 5f (^{3}P, ^{3}D) low energy resonance and a 5d - 5f (^{1}P) high energy 'giant resonance'. As the degree of ionisation is increased the f-waves begin to contract and the spectrum shows discrete structure overlaid on a giant resonance. Very suddenly all f-waves collapse into the inner well at which point the spectrum becomes a simple Rydberg series running up to the 5d ionization limits. We carried out a series of calculations on 5d - nl excitations with the Cowan suite of codes [16]. We concentrated on more highly ionised thorium ions (4+ -> 6+) which have relatively simple ground states. The results are shown in figure 6, where we show a comparison between a measured relative and computed absolute cross-sections.

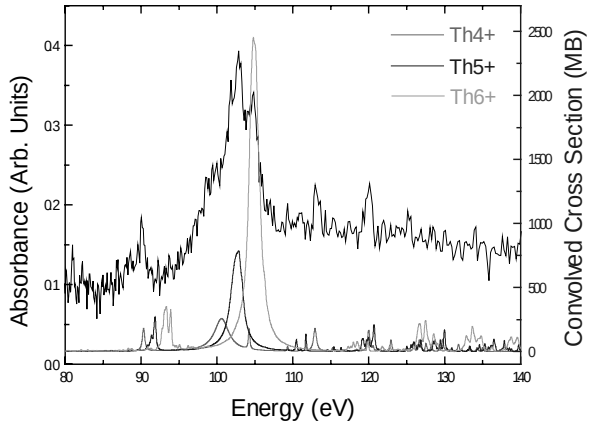

Figure 6. Photoabsorption spectrum at an interplasma delay of 20ns. The spectrum is compared with computed spectra for 4,5 & 6 time ionized thorium. The absorption is clearly due to predominantly five times ionized Th ions.

It is clear that the spectrum is an admixture of all three ion stages and dominated by the main 5d - 5f transition which absorbs most of the 5d-spectrum's oscillator strength.

References

1. A A Seraphin et al
J.Appl.Phys **80**, 6429 (1996)

2. V Schmidt,
Rep.Prog.Phys. **55**, 1483 (1992)

3. P K Carroll and E T Kennedy,
Phys.Rev.Lett **38**, 1068 (1977)

4. J T Costello et al.,
Phys.Scr **T34**, 77 1991

5. E T Kennedy, J T Costello and J-P Mosnier,
J.Electron.Spec.Relat.Phenom **79**, 283 (1996)

6. P K Carroll et al.,
IEEE,J.Q.Electron **QE-19**, 1807 (1983)

7. O Meighan et al.,
Appl.Phys.Lett **70**, 1497 (1997)

8. "Giant Resonances in Atoms, Molecules and Solids",
Eds. J-P Connerade et al., (Plenum: 1987)

9. T B Lucatorto et al.,
Phys.Rev.Lett **47**, 1124 (1981)

10. U Koble et al.,
Phys.Rev.Lett **74**, 2188 (1995)

11. P K Carroll and J T Costello,
J.Phys.B **20**, L201 (1987)

12. J C Kieffer and M Chaker,
J.X-ray.Sci.Tech **4**, 312 (1994)

13. G Wendin,
Phys.Rev.Lett **53**, 724 (1984)

14. P K Carroll and J T Costello,
Phys.Rev.Lett **57**, 1581 (1986)

15. D A Liberman and A Zangwill,
Comput.Phys.Commun **32**, 75 (1984)

16. R D Cowan,
ftp://t4.lanl.gov/pub/cowan

Generation of optically triggered-magnetic field pulses for use in pump-probe experiments

R J Hicken, J Wu.

Department of Physics, The University of Exeter, Stocker Road, Exeter, EX4 4QL,UK. Email R.J.Hicken@exeter.ac.uk

Introduction

Photoconductive switch structures may be used to generate magnetic field pulses for use in pump-probe experiments [1]. When triggered with a sub-picosecond optical pulse, the switch generates a current pulse with a sub-picosecond rise time. The associated magnetic field pulse may then be used to pump dynamical magnetic processes in thin film samples. The response of the material is probed by means of a time resolved measurement of the Magneto Optical Kerr rotation. In this report we describe the fabrication and testing of suitable photoconductive switch structures. We show also that the magnetic field pulses generated by the switch may be used to stimulate Ferromagnetic Resonance (FMR) oscillations in a ferromagnetic thin film sample.

The Photoconductive Switch

A schematic representation of a typical photoconductive switch structure is shown in figure 1. Conducting tracks of Au were deposited onto an intrinsic semi-insulating GaAs substrate by evaporation and patterned using a standard photolithographic lift-off technique. The switch is in essence a biased parallel wire transmission line. The Au tracks in the main part of the transmission line, where the sample was overlaid, had a width and separation of 125 µm. The transmission line was connected to large Au pads to which wires and surface mount components were attached with silver paint. By matching the terminating impedance to the characteristic impedance of the transmission line it is possible to control the amplitude of reflections from the power supply end of the line.

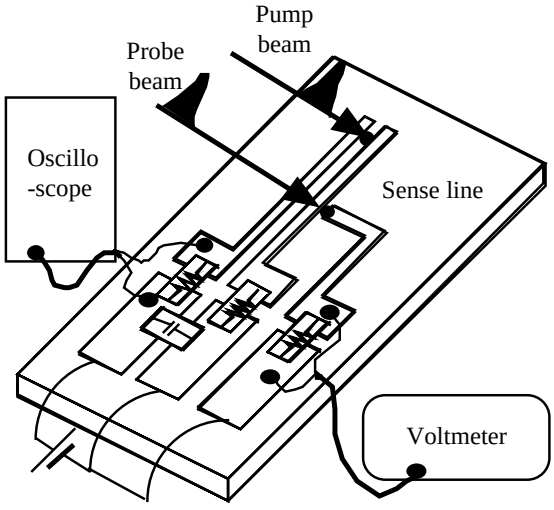

Figure 1. A schematic representation of a typical photoconductive switch structure is shown.

The switch is triggered by focusing an optical pump pulse onto the gap between the tracks. The photoexcited carriers cause the conductance of the gap to be reduced which causes a current pulse to propagate along the transmission line. If the switch is triggered close to its open circuit end, the resulting instantaneous reflection of the current pulse allows the height of the current pulse to be effectively doubled [1]. A fast oscilloscope was connected across one of the resistors in the main line so that the shape of the current pulse could be monitored continuously. An additional sense line has also been shown in figure 1. If a second time delayed optical pulse is focused on to the gap between the sense line and the main line then some of the current in the main line may be diverted into the sense line. Let us assume that the conductivity in each of the two gaps has the same time dependence. By measuring the integrated current in the sense line as a function of the time delay between the two optical pulses, an autocorrelation measurement of the temporal profile of the current pulse may be obtained.

Testing the Switch

Measurements were made using a standard optical pump-probe apparatus. The light source was a diode-pumped mode locked Ti:sapphire laser that produced 100 fs pulses at a repetition rate of 82 MHz. The average power output was approximately 1 W at the operating wavelength of 800 nm. Each pulse from the laser was divided into pump and probe parts by means of a beamsplitter. The length of the pump beam path was varied by reflecting the beam from a glass corner cube mounted on a stepper motor driven translation stage. We chose to vary the length of the pump beam path because the detector used for the measurements on the magnetic sample was found to be particularly sensitive to any motion of the probe beam.

The form of the trace acquired by the oscilloscope when the switch was triggered by the pump beam is shown in figure 2. The wave form has a period of 12 ns corresponding to the repetition rate of the laser. The apparent rise time of each pulse is determined by the sample rate of the oscilloscope, while the long tail results from the long recombination time of the GaAs substrate. In general the tail is not of a simple exponential form, suggesting that small partial reflections of the pulse still occur at the ends of the transmission line. The results of autocorrelation measurements made with the sense line are shown in figure 3.

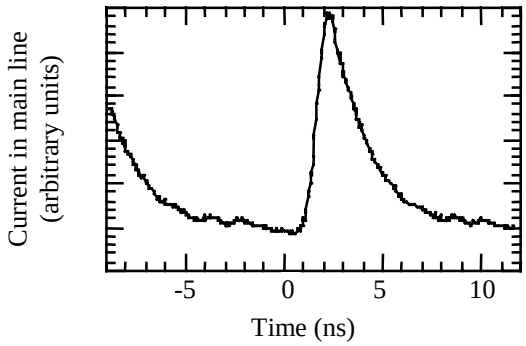

Figure 2. The current in the main line as measured by a fast oscilloscope is shown.

Fits to figures 2 and 3 indicate that the current in the switch exhibits an exponential time decay. The time constant obtained from the fits was approximately 2 ns in each case and is of the same order as the expected recombination time of the GaAs substrate. In practice the oscilloscope was found to be the more useful diagnostic tool since the effect of adjusting the position of the pump beam spot could be immediately observed.

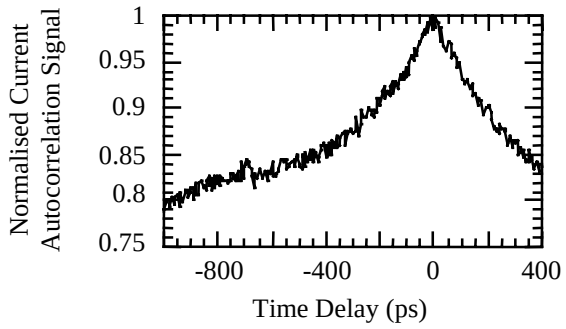

Figure 3. Integrated current is plotted against time delay for autocorrelation measurements made with the sense line.

Observation of Ferromagnetic Resonance

The magnetic field generated by the switch is most intense in the region immediately above the surface of the GaAs substrate. The structure MgF_2(1000Å)/ Fe(250Å)/ MgF_2(100Å) was therefore deposited directly onto the switch. Each layer was grown by evaporation at a background pressure of 10^{-6} mbar. However it was necessary to briefly vent the vacuum system between the growth of the different layers. Some oxidation of the Fe is therefore to be expected. The first MgF_2 layer was designed to prevent the Fe layer short-circuiting the transmission line. The upper MgF_2 layer was intended to protect the Fe from the atmosphere while allowing optical access. The Kerr rotation of a p-polarised probe beam was measured with an optical bridge constructed around a polarising beamsplitter. The pumping magnetic field was modulated either by chopping the pump beam or by applying an ac voltage to the switch. The use of phase sensitive detection allowed the Kerr rotation to be measured with microdegree resolution.

The pumping magnetic field typically had a peak value of 1 Oe while its orientation could be varied simply by scanning the probe beam across the transmission line. The pumping magnetic field is expected to lie roughly parallel to the plane of the substrate above the Au tracks and perpendicular to the plane elsewhere. A static magnetic field was applied in the plane of the sample. Measurements were made with this field either parallel or perpendicular to the plane of incidence. Figure 4 shows typical results for the case that a static field was applied perpendicular to the plane of incidence and the pumping field lies in the plane of the sample and perpendicular to the static field. The static field strength was 400 Oe and the maximum rotation was about 1000 μdeg.

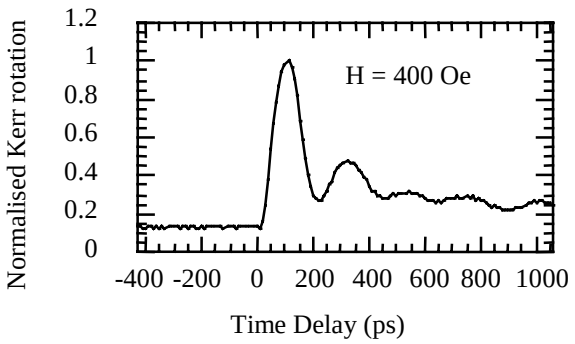

Figure 4. The Kerr rotation is plotted against time delay for a 250Å Fe film

In order to confirm the magnetic origin of the oscillations in figure 4 the strength of the static magnetic field was varied. The field dependence of the oscillation frequency has been plotted in figure 5. The motion of the magnetisation may be described by the Landau-Lifshitz equation and its solution for small amplitude oscillations is well known[2]. This yields the formula shown in figure 5 where the magnetomechanical ratio γ is related to the g-factor by the expression $\gamma = \pi g(2.80)\mathrm{MHz/Oe}$. By assuming the parameter values shown in the figure, the formula was used to generate the theoretical curve. We note that the fitted value of the magnetisation is strongly reduced with respect to that of bulk Fe, which we attribute to the partial oxidation of the Fe layer.

In principle the shape of the oscillations observed in figure 4 can be calculated. This is not a trivial exercise since the Kerr rotation depends upon more than one component of the time dependent magnetisation vector [3] and the values of a large number of material parameters must be known. However we can see that the measurement technique allows the frequency of oscillation and the damping of the magnetisation to be directly quantified.

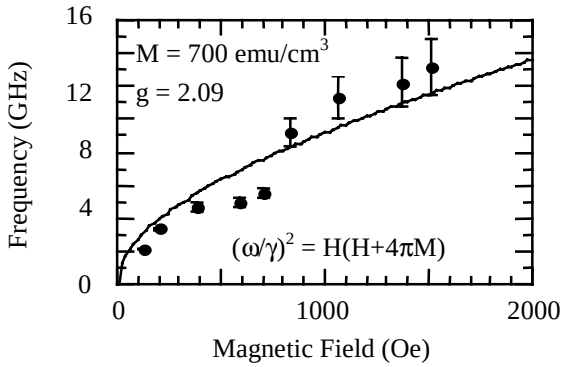

Figure 5. FMR frequency is plotted against static magnetic field strength.

Conclusion

In conclusion, we have demonstrated that a photoconductive switch may be used to generate magnetic field pulses and that these may in turn be used to observe FMR oscillations in optical pump-probe experiments. The pump-probe spectroscopy technique has many advantages over existing experimental techniques such as microwave resonance and Brillouin Light Scattering for the observation of magnetic resonance phenomena and it may become the technique of choice for studies of miniature lithographically defined structures.

We gratefully acknowledge the financial support of the EPSRC, assistance with sample preparation from Mr D. J. Jarvis, and many stimulating discussions with Dr C. D. H. Williams.

References

1. M. R. Freeman, R. R. Ruf, and R. J. Gambino, IEEE Trans. Magn., 27 4840, (1990)

2. A. H. Morrish, "The Physical Principles of Magnetism", Krieger, New York (1980).

3. J. Zak, E. R. Moog, C. Liu, and S. D. Bader, J. Appl. Phys. 68, 4203, (1990).

A Study of the Subcellular Localisation of Photosensitisers in V79/4 Fibroblasts and Model Systems by Time-Resolved Fluorescence Microscopy

D I Pattison, A J MacRobert.

National Medical Laser Centre, University College London Medical School, London

A D Waite, D Phillips.

Department of Chemistry, Imperial College of Science, Technology and Medicine, London

K Henbest, A W Parker.

CLRC Rutherford Appleton Laboratory, Chilton, Didcot, Oxon., OX11 0QX

C de Lara, P O 'Neill.

MRC Radiation and Genome Stability Unit, Harwell, Didcot, Oxon

Introduction

Photodynamic therapy (PDT) using photosensitising drugs is a promising minimally invasive technique for the destruction of tumours and diseased tissue without the use of major surgery. A number of photosensitisers are currently under scrutiny, and many second generation photosensitisers are based on metallo-phthalocyanines or chlorins. The intrinsic fluorescence of these photosensitisers enables studies of the intracellular localisation of these drugs by fluorescence microscopy. However, it is known that the fluorescence lifetime of the drugs is affected by factors such as aggregation and binding to proteins. The use of the confocal fluorescence lifetime imaging microscope (CFLIM) at the Rutherford Appleton Laboratory allows the spatial distribution, and the environment of the photosensitisers to be quantified. The data presented here expands on previous work at the Rutherford Appleton Laboratory with the anionic photosensitiser, di-sulphonated aluminium phthalocyanine ($AlPcS_2$). In addition, two further photosensitisers have been investigated, which have been studied previously with steady-state fluorescence microscopy by other groups. These are the cationic complex, pyridyl zinc phthalocyanine (ZnPPC), which has been found to have a higher cellular uptake than anionic sensitisers, and 5,10,15,20-meta-tetra(hydroxyphenyl)chlorin (m-THPC or Foscan).

Experimental Details

The CFLIM apparatus has been described previously. However, some of the studies reported below were acquired with an upgraded image intensifier (loaned by Kentech Instruments), which enhanced the signal-to-noise ratio in time-gated mode, and provided greater image quality with much faster acquisition times. This resulted in less light exposure of the sample, reducing the effects of photobleaching and unwanted destruction of the sample.

Sepharose beads (50 - 150 µm in diameter) were used as model systems to allow characterisation of the photosensitisers. The beads were stained with the sensitisers by leaving them in an aqueous solution of the desired photosensitiser (ca. 10 - 20 µM) for between 30 s and 4 h depending on the sensitiser used. The beads showed strong uptake of all three photosensitisers, with $AlPcS_2$ yielding the most fluorescent beads. Once stained the beads were suspended in gelatine in specially constructed Petri dishes with a cover slip base for study under the microscope.

For the preparation of cells the facilities at the Medical Research Council (MRC) were used to grow V79/4 Chinese Hamster fibroblasts to log phase. The cells were stained with the required photosensitiser (typically 25 µM for ZnPPC and $AlPcS_2$) in phosphate buffered saline (PBS) at 37 ^{o}C and 5% CO_2 for ca. 1 hour. The cells were subsequently rinsed 3 times with PBS, before investigation under the microscope.

Results

Model Systems

A sample was prepared by mixing beads stained with either $AlPcS_2$ or m-THPC. The beads were stained separately under conditions that resulted in similar fluorescence intensities, independent of the stain used. The use of time-resolved fluorescence imaging allowed differentiation of the beads by their lifetimes, with a lifetime of ca. 4.8 ns for those stained with $AlPcS_2$, and 8.5 ns for the m-THPC stained beads figure 1a).

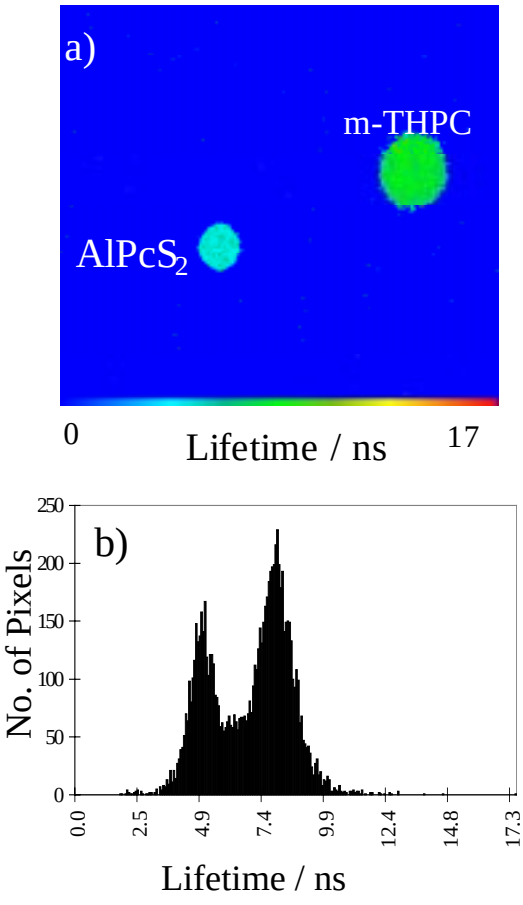

Figure 1. Sepharose Beads Stained With AlS_2Pc and m-THPC; a) lifetime image; b) histogram of lifetimes

The histogram showing the distribution of lifetimes (figure 1b) within the calculated lifetime map clearly demonstrates the bimodal distribution of lifetimes in the sample. This illustrates the ability of both the microscope system itself, and the analysis software, to accurately determine two completely different lifetimes within the same sample.

Cells with $AlPcS_2$

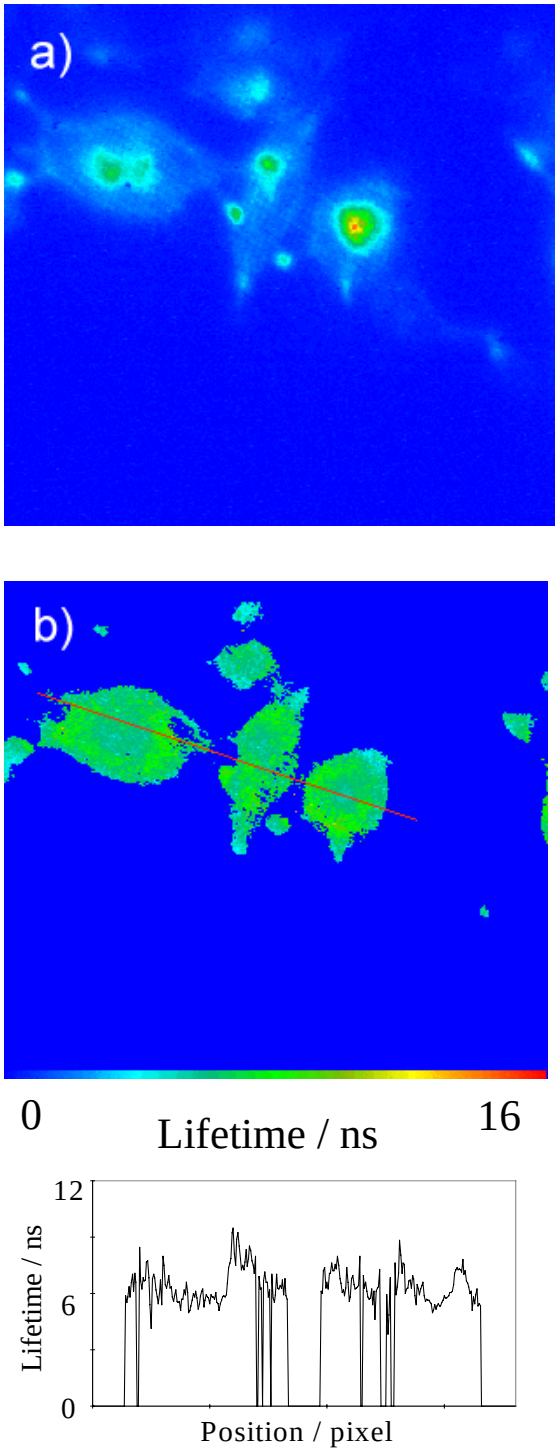

Figure 2. AlPcS2 in V79/4 cells; a) time-gated image (0.5 ns after excitation pulse) showing localisation of fluorescence; b) fluorescence lifetime map; c) lifetime profile along red line in lifetime map

The experiments previously undertaken with $AlPcS_2$ in cells have been repeated with the new Kentech gated image intensifier to obtain clearer images. For the first time during these experiments we have been able to measure time-gated fluorescence images with the resolution required to observe the localisation of $AlPcS_2$ within the cells (figure 2). This localisation had previously only been seen in steady-state measurements due to the deterioration of the image quality upon changing to time-gated mode.

The calculated lifetime maps have an average lifetime of ca. 6.5 ns which is longer than that observed previously, but there is evidence for a shorter lifetime in the Golgi apparatus and nuclear envelope, than in the surrounding cell. However, single pixel analysis of the images provided no evidence for the biexponentiality observed previously in cells, but this may be due to insufficient light exposure resulting in low degrees of relocalisation within the cell, relative to that observed in earlier experiments.

Cells with ZnPPC

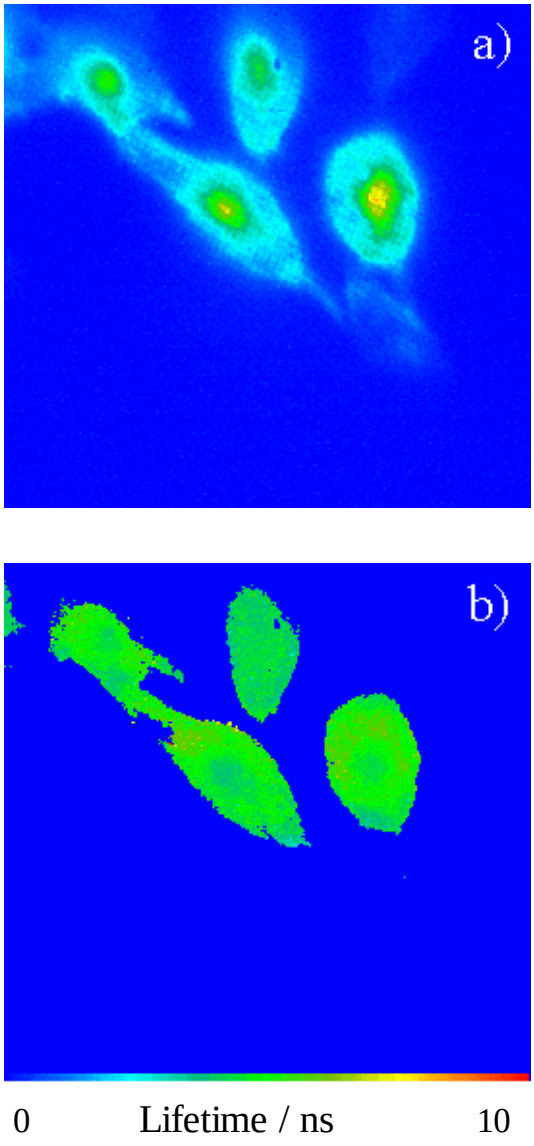

Figure 3. V79/4 Fibroblasts stained with 25mM ZnPPC for 1 hr; a) time-gated image after 0.5 ns; b) fluorescence lifetime map

Previous studies of ZnPPC in RIF-1 cells by steady-state fluorescence microscopy showed that ZnPPC localises predominantly in lysosomes, with extensive relocalisation following exposure to light.

The experiments undertaken with the CFLIM system at RAL were performed to give further insight into the species present within the cells (monomeric, dimeric or aggregated ZnPPC), and on the mechanisms involved during relocalisation of the ZnPPC, as well as providing a parallel cell line to compare the behaviour of ZnPPC.

The time-gated fluorescence images obtained showed little localisation of the ZnPPC within the cells, and we propose that the light levels required to measure these images were sufficient to induce the relocalisation processes. However, the lifetime maps show little variation over the cell between bright and dark areas, with an average lifetime of 2.5 - 3.0 ns (figure 3). The staining conditions were varied with concentrations from 10 - 50 μM ZnPPC in PBS, but there was little change in the measured lifetimes.

An interesting observation, was that staining in growth medium rather than PBS resulted in much slower uptake of the ZnPPC, but still there was no discernible difference in the measured lifetimes. Prolonged light exposure of the cells, leads us to tentatively propose a shortening of the fluorescence lifetime. These results are promising, but further experiments are required in order to determine the exact nature of ZnPPC in cells, and crucially experiments with much less light exposure must be undertaken to give the insight we require.

Summary

The initial localisation and subsequent photo-induced relocalisation of phthalocyanine photosensitisers in V79/4 cells has been studied by time-resolved fluorescence microscopy. The changes in the lifetimes of the drugs upon relocalisation appear to be minimal, but further studies with reduced light exposure are expected to show differing lifetime distributions, particularly with ZnPPC. The usefulness of the CFLIM technique has been highlighted in a model system, consisting of beads stained with different photosensitisers, where it is difficult to differentiate the beads by fluorescence intensities alone, but they are easily differentiated by their lifetimes.

Acknowledgements

We would like to thank the BBSRC and EPSRC for providing funding for this work. We are also very grateful to Prof. S. Brown and Dr D. Vernon (University of Leeds) for their kind contribution of the ZnPPC required for these studies.

References

1. D Scully, R B Ostler, D Phillips, P O'Neill, K M S Townsend, A W Parker, A J MacRobert, Bioimaging, 5 9-18 (1997)

2. S R Wood, J A Holroyd, S B Brown, Photochem, Photobiol, 65 397-402 (1997)

3. R Hornung, B Jentsch, N E A Crompton, U Haller, H Walt, Lasers in Surgery and Medicine, 20 443-450. (19997)

4. R B Ostler, A D Scully, A Waite, K Henbest, C de Lara, D I Pattison, A J MacRobert, D Phillips, A W Parker, CLF RAL Annual Report, 180-181 (1996-1997)

Antioxidant function of lipoamide and dihydrolipoic acid studied by laser flash photolysis and time-resolved resonance raman spectroscopy

R H Bisby.

Department of Biological Sciences, University of Salford, Salford M5 4WT. Email R.H.Bisby@biosci.salford.ac.uk

A W Parker.

CLRC Rutherford Appleton Laboratory, Chilton, Didcot, Oxon., OX11 0QX

Introduction

By virtue of their reducing properties, thiols are regarded as having antioxidant [1)] and radioprotective [2)] properties. Although in nature (dihydro)lipoamide functions mainly as a cofactor in the pyruvate dehydrogenase complex, both dihydrolipoic acid and lipoic acid and derivatives have been intensively investigated as potentially useful therapeutic antioxidants [3, 4)]. In model systems both compounds have been shown to scavenge reactive oxygen species (ROS) such as singlet oxygen [5)], hypochlorous acid and the trichloromethylperoxyl radical [6)], and hydroxyl radicals [6, 7)]. In addition lipoic acid may chelate redox-active transition metal ions [6, 8)].

There have been few physiochemical studies of reactions between both of these compounds and ROS. Pulse radiolysis has been used to study both the one-electron oxidation and reduction of dihydrolipoate and lipoate respectively to the lipoate radical anion ($RSSR^{\cdot-}$) [9)]. Asmus and Bonifacic have shown the one-electron oxidation of disulfides to a radical cation ($RSS^{+\cdot}$) [10)] and have estimated the reduction potential of the lipoate radical cation $RSS^{+\cdot}$/RSS couple as 1.10 V vs SHE [11)], some 300 mV lower than for that for non-cyclic disulfides and a result of the small dihedral CS-SC angle in the five-membered ring of lipoic acid [12)].

The triplet excited state of duroquinone (^{3}DQ) is usually regarded as mainly π-π^* in nature, but its reactivity with ethanol and isopropanol [13, 14)] implies at least partial n-π^* character in polar solvents. The triplet may then be a model for peroxyl and alkoxyl radicals, which are important free radical intermediates in lipid peroxidation. We have previously studied the oxidation of a number of antioxidants by ^{3}DQ and have found it to react rapidly ($k_2 \sim 10^9$ dm^3 mol^{-1} s^{-1}) with dihydrolipoic acid in ethanol solution and to be a useful one-electron oxidant for the study of antioxidant radicals by time-resolved resonance Raman (TR^3) spectroscopy [15, 16)].

Materials and Methods

Experiments were undertaken in the Nanosecond Laboratory at the Lasers for Science Facility. Laser flash photolysis employed a Lumonics PM-846 XeCl laser emitting a 10 ns pulse at 308 nm. The laser output was attenuated to approximately 5-10 mJ pulse^{-1} in order to minimise triplet-triplet decay of excited duroquinone and all samples were deoxygenated by bubbling with argon. Transient absorption measurements were made using a conventional kinetic single beam spectrometer consisting of tungsten lamp (Oriel), monochromator (Bentham, model TM310) and photomultiplier detection (Hamamatsu R905). Time-resolved resonance Raman spectra were obtained using the apparatus previously described [18)]. The pump pulse was the frequency-tripled output of a Continuum Sunlight Nd:YAG laser at 355 nm (5 ns, ~1 mJ) and the probe pulse was obtained from a Lumonics XeCl pumped dye laser (Lambda-Physik FL3002) at 440 nm (10 ns, ~0.5 mJ). Raman spectra were measured with a Spex Triplemate 1877 and a back-illuminated liquid nitrogen cooled CCD array (Princeton Instruments). Calibration was with the toluene Raman spectrum and is accurate to ± 2 cm^{-1} and spectral manipulations were performed with the Princeton CSMA software.

Results and Discussion

a) Kinetics of triplet duroquinone reactions

When excited by the 308 nm output of the XeCl laser, the initial singlet excited state of duroquinone undergoes rapid (ca 20 ps) and efficient (ϕ = 0.91) intersystem crossing [17)] to the triplet state which is a strong oxidant [18)]. In an acetonitrile/water (1:1) solution ^{3}DQ (λ_{max} 480 nm) decays with a first order rate constant (k_0) of about 2 x 10^5 s^{-1}. The pseudo first order decay (k') of ^{3}DQ increases in the presence of added reactive solute, S. The value of the second order rate constant k_r was determined from the slope of a plot of k' versus [S] according to equation (1).

$$k' = k_0 + k_r[S] \qquad (1)$$

The inset to figure 1 shows a second order plot for the oxidation of dihydrolipoate (DHLA) by ^{3}DQ at pH 7.7 from which a value for k_r of (2.09 ± 0.06) x 10^9 dm^3 mol^{-1} s^{-1} was obtained. During these measurements it was noted that on repeated pulse illumination of these solutions at higher laser intensity the rate of decay of ^{3}DQ increased, implying the formation of a more reactive product. This is confirmed by the plot in the inset to figure 1 for the reaction of ^{3}DQ with lipoamide (LA) at pH 7.7, from which k_r = (4.72 ± 0.08) x 10^9 dm^3 mol^{-1} s^{-1}. Hence at pH 7.7 ^{3}DQ reacts more than twice as rapidly with LA as with DHLA. Below pH 6 the rate constant for reaction of ^{3}DQ with dihydrolipoate is independent of pH with a value of 1.1 x 10^9 dm^3 mol^{-1} s^{-1} but above neutral pH the rate constant increases indicating a much higher reactivity of the thiolate anion. The results are consistent with the reported average pK_a of the thiol groups of DHLA of 10.7 [19)]. The results in figure 1 indicate that at pH 7, quenching of ^{3}DQ is due almost entirely to the undeprotonated form of DHLA. It is rather unexpected that the reactivity of ^{3}DQ with the disulfide (LA) is higher than with the

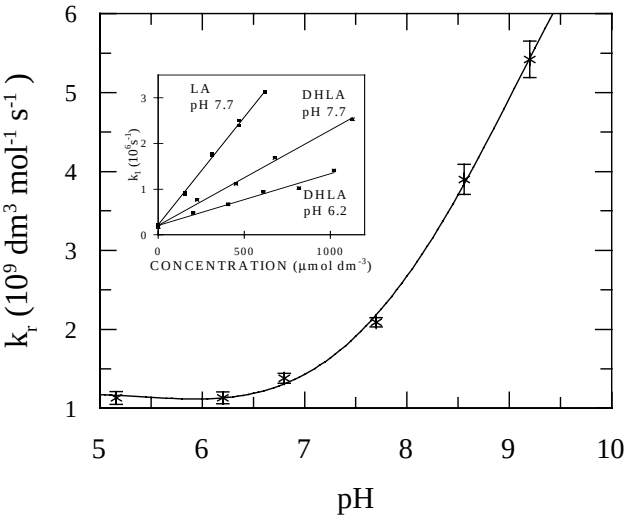

Figure 1. Effect of pH on the second order rate constant, k_r, for reaction of triplet duroquinone with dihydrolipoate in phosphate (10 mmol dm^{-3}) buffered water/acetonitrile (50:50 v/v). INSET: plots of pseudo first order rate constants (k') for reaction of triplet duroquinone with lipoamide (LA) and dihydrolipoate (DHLA).

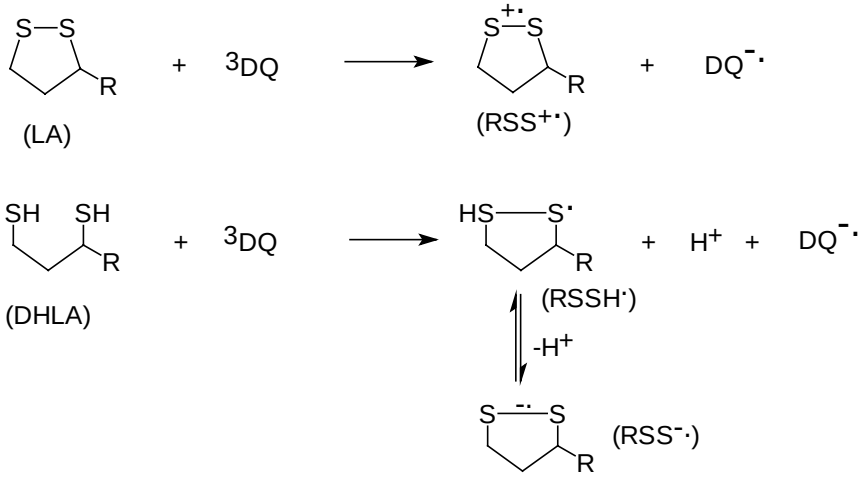

SCHEME 1

thiol form (DHLA), but this is supported by the previous observation that the $CCl_3O_2^{\cdot}$ radical reacts nearly 8 times faster with lipoic acid than with DHLA [6].

Scheme 1 shows that the reaction of ^{3}DQ with LA is expected to be a simple electron transfer. Reaction of the DHLA in the undeprotonated form (pH << pK_a ~ 10.7) involves both electron and proton loss to generate initially the monoprotonated radical (i.e $RSSH^{\cdot}$) which may undergo further proton loss to give the cyclic disulfide radical anion ($RSS^{-\cdot}$). This is confirmed by the results of experiments in which D_2O replaced H_2O in the solvent. The $k(H_2O)/k(D_2O)$ ratio for the reaction of ^{3}DQ with LA has a value (Table) of ~1 indicative of a simple electron transfer without the involvement of a proton or hydrogen atom. In contrast the reaction ^{3}DQ with DHLA at pH 5.2 (involving exclusively the undeprotonated form) has a $k(H_2O)/k(D_2O)$ ratio of ~2 clearly indicating the involvement of a proton in the reaction mechanism. The activation energies for reaction of ^{3}DQ with LA and DHLA are 10.1 ± 0.7 and 4.2 ± 1.5 kJ mol^{-1} respectively. These small values are expected for reactions whose rates approach the diffusion-controlled limit. The Table shows that the slower reaction of ^{3}DQ with DHLA, whilst having a lower experimental energy and enthalpy of activation, has a considerably more negative entropy of activation than the reaction of ^{3}DQ with LA. This entropic control of the slower reaction of ^{3}DQ with DHLA is to be anticipated for a reaction in which both a proton and electron are removed from the reductant, and in which the transition state may be ordered to include a molecule of water.

b) Transient absorption and resonance Raman spectra

Transient absorption spectra obtained by laser flash photolysis for reaction of ^{3}DQ with both DHLA and LA at pH 7.7 were consistent with one-electron oxidation of the substrate and showed the decay of ^{3}DQ (λ_{max} 480 nm) and formation of the durosemiquinone radical anion, $DQ^{-\cdot}$ (λ_{max} 440 nm). In the reaction of ^{3}DQ with LA the $DQ^{-\cdot}$ radical yield is lower than in the case of DHLA. The product spectra from reaction of ^{3}DQ with DHLA were stable on the tens of microseconds timescale, whilst those from reaction with LA decayed with a lifetime of approximately 15 μs. This is insufficient to account for the lower yield of the $DQ^{-\cdot}$ absorption and suggests that relatively efficient back electron transfer occurs from within the geminate ($DQ^{-\cdot}$:$RSS^{+\cdot}$) radical ion pair. In the spectrum obtained at 5 μs after reaction of ^{3}DQ with LA there appeared to be an additional component underlying the spectrum of $DQ^{-\cdot}$ ascribed to the lipoamide radical cation ($RSS^{+\cdot}$, Scheme 1) which has a more intense and broader spectrum than $DQ^{-\cdot}$, but which is also centred at 440 nm [11].

TABLE

	Dihydrolipoic acid	Lipoamide
k_r , dm^3 mol^{-1} s^{-1}	(1.13 ± 0.08) x 10^9 (pH 5.2)	(4.72 ± 0.08) x 10^9
$k(H_2O) / k(D_2O)$	1.97 ± 0.23	0.972 ± 0.021
Activation Energy*, ΔE_a	4.2 ± 1.5	10.1 ± 0.7
Enthalpy of Activation*, $\Delta H^{\ddagger}$	1.7 ± 1.5	7.6 ± 0.7
Entropy of Activation*, $\Delta S^{\ddagger}$	-62 ± 2	-34 ± 1

*In units of kJ mol^{-1}

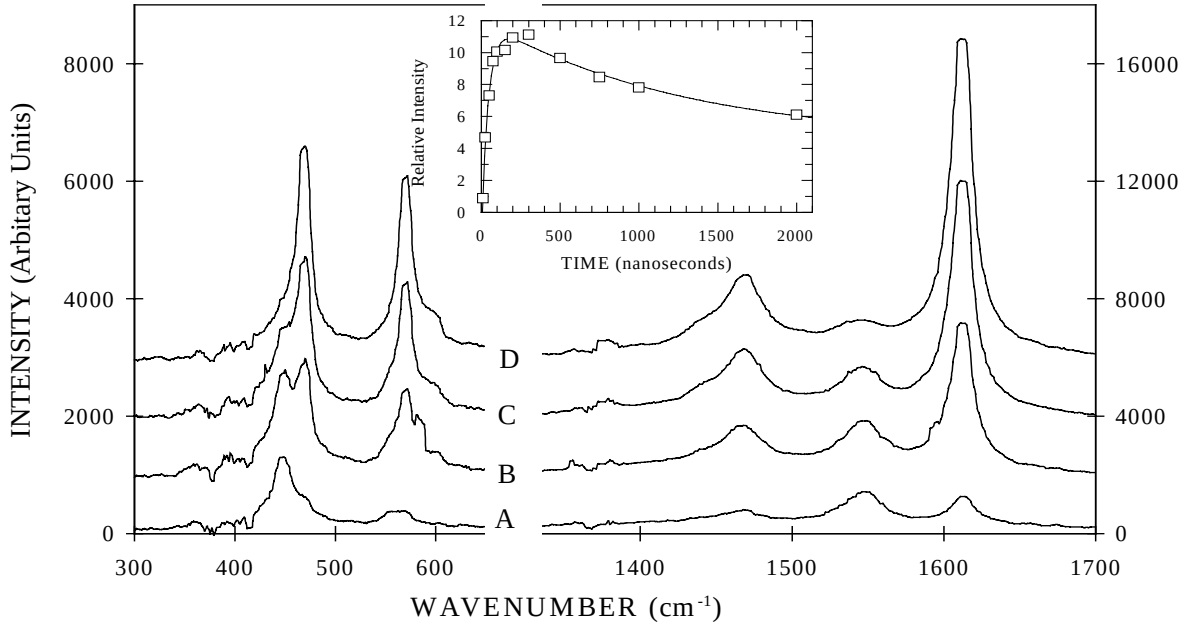

Figure 2. Time-resolved resonance Raman spectra measured from acetonitrile/water (50:50 v/v) solutions of duroquinone (5 mmol dm-3) with lipoamide (2 mmol dm-3) buffered to pH 7.7 with phosphate (10 mmol dm-3). Delays between the pump (355 nm) and probe (440 nm) laser pulses were 5 ns (A); 25 ns (B); 50 ns (C); and 100 ns (D). Background solvent spectra (measured using only the probe pulse) have been subtracted. INSET: Intensity of the durosemiquinone radical anion peak at 1613 cm^{-1} as a function of delay time between pump and probe pulses.

Resonance Raman spectroscopy was also used to investigate the reaction between ^{3}DQ and LA. ^{3}DQ was formed by a 355 nm pump laser pulse and the Raman spectrum of reaction intermediates probed after a variable time delay by a second laser pulse at 440 nm, chosen to be in resonance with both the durosemiquinone radical anion and the lipoamide radical cation ($RSS^{+\cdot}$) absorption spectra. Figure 2 shows resonance Raman spectra in which the ^{3}DQ bands at 1548 cm^{-1} and 448 cm^{-1} decay with increasing time delay (from 5 to 100 ns) between pump and probe pulses and the concomitant formation of $DQ^{-\cdot}$ bands at 469, 570, 1470 and 1613 cm^{-1}. The latter two bands are assigned to the C-O and C=C stretching vibrations respectively of the durosemiquinone radical anion [15]. The time course of formation of the $DQ^{-\cdot}$ band at 1613 cm^{-1} (Inset to figure 2) shows that the peak intensity is reached at 200 ns, and like the transient absorption spectra indicates that the products decay over a period of microseconds.

Inspection of the TR^3 spectrum in figure 2 at a time delay of 100 ns (trace D) shows a shoulder on the higher wavenumber side of the 570 cm^{-1} band which cannot be ascribed to the durosemiquinone radical. In order to observe possible contributions from the LA disulfide radical cation, the TR^3 spectrum of $DQ^{-\cdot}$ (obtained from reaction of ^{3}DQ with sodium ascorbate under identical conditions - the ascorbate radical does not absorb at 440 nm and has not been observed by TR^3 spectroscopy [20]) was subtracted from the TR^3 spectrum from reaction of ^{3}DQ with lipoamide. The resulting expanded spectrum in Figure 3 reveals peaks at 298, 326, 598 and 1191 cm^{-1} . These are assigned to the lipoamide disulfide radical cation. Artifact peaks due to poor subtraction of solvent (acetonitrile) bands are indicated by an asterisk. The strongest peak in the lipoamide disulfide radical cation spectrum at 598 cm^{-1} is assigned to the S-S stretching mode, which in lipoic acid in methanol solution occurs [21, 22] at 504 cm^{-1} . The increase in vibrational frequency upon oxidation of the disulfide to the radical cation is consistent with the formation of the stronger three electron bond in the radical resulting from interaction of the singly occupied orbital on the sulfur atom representing the primary site of oxidation and an lone pair of electrons on the other sulfur atom [11, 12]. This contrasts with the situation in the disulfide radical anions such as $(SCN)_2^{-\cdot}$ in which the additional odd electron occupies a σ^* orbital causing considerable weakening of the S-S bond and a reduction in the vibrational frequency of the S-S bond[23] from 490 cm^{-1} in $(SCN)_2$ to 218 cm^{-1} in $(SCN)_2^{-\cdot}$. There appear to be no discernible bands in figure 3 attributable to the C-S stretches in the region of 700 cm^{-1}, although in the Raman spectra of lipoic acid and lipoamide these are less intense than the S-S band [21, 22]. The band at 1191 cm^{-1} is believed to be the first overtone of the S-S stretching vibration at 598 cm^{-1}. Series of overtones have been observed in the spectra of $(SCN)_2^{-\cdot}$ and dihalide radicals [23]. At present it is not possible to unambiguously assign the two bands at lower frequency (298 and 326 cm^{-1}) but we believe these to be either C-S bending modes or alkyl expansions pertaining to deformations of the C-C framework.

A full account of this work has recently been published [24].

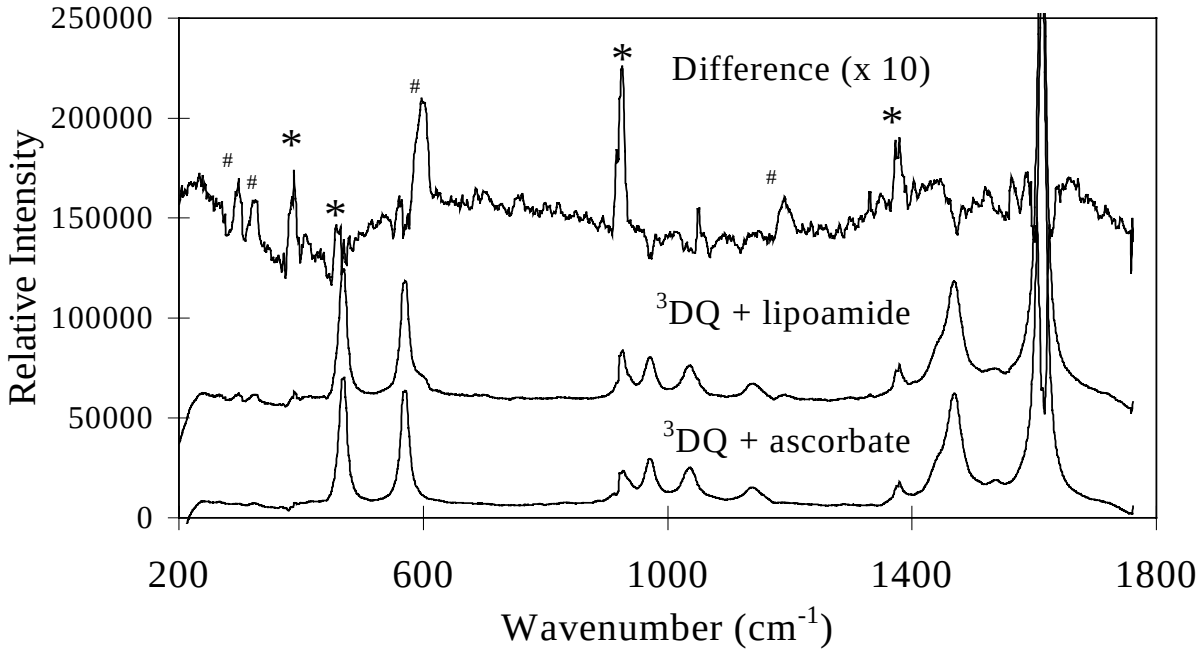

Figure 3. Time-resolved resonance Raman spectrum of the lipoamide disulfide radical cation, obtained as the difference between the TR3 spectra obtained from reaction of triplet duroquinone with lipoamide and ascorbate. Both of the latter spectra were obtained with 1 ms delay between pump (355 nm) and probe (440 nm) pulses and are shown after subtraction of the solvent (probe-only) spectra. Marked bands in the difference spectrum represent either real spectral components ascribed to the lipoamide disulfide radical cation, marked (#), or artefact bands, marked (*), which are due to slight band intensity mismatch of solvent bands between the subtracted spectra.

Acknowledgment

This work was supported by the Biotechnology and Biological Research Council (BBSRC).

References

1. O.I.Aruoma *et al*
Free Rad. Biol. Med. 6, 593 (1989).
2. C. von Sonntag The Chemical Basis of Radiation Biology, Taylor and Francis, London (1987).
3. L.Packer *et al*
Free Rad. Biol. Med. 19, 227 (1995).
4. G.P.Biewenga, G.R.M.M.Haenen, and A.Bast
Gen. Pharmac. 29, 315 (1997).
5. T.P.A.Devasagayam *et al*
Chem-Biol. Interactions 86, 79 (1993).
6. B.C.Scott *et al*
Free Rad. Res. 20, 119 (1994).
7. S.Matsugo *et al*
Biochem. Mol. Biol. Int. 37, 375 (1995).
8. M.R Baumgartner *et al*
Inorg. Chim. Acta 252, 319 (1996).
9. S.W.Chan et al
Biochim. Biophys. Acta 338, 213 (1974).
10. M.Bonfacic and K.-D.Asmus
J. Phys. Chem. 80, 2426 (1976).
11. M.Bonfacic and K.-D.Asmus
J. Chem. Soc. Perkin Trans. II 1805 (1986).
12. H.Bock *et al*
Chem. Ber. 113, 3208 (1980).
13. E.Amouyal and R.Bensasson
J. Chem. Soc., Faraday Trans. 72, 1274 (1976).
14. S.Nagaoka and K.Isihara
J. Amer. Chem. Soc. 118, 7361 (1996).
15. R.H.Bisby, and A.W.Parker
J. Amer. Chem. Soc. 117, 5664 (1995).
16. R.H.Bisby *et al*
Free Rad. Biol. Med. 20, 411 (1996).
17. F.Wilkinson *et al*
J. Phys. Chem. Ref. Data 24, 663 (1995).
18. R.Scheerer and M.Gratzel
J.Amer. Chem. Soc. 99, 865 (1977).
19. I.M.Gascoigne and G.K.Radda
Biochim. Biophys. Acta 131, 498 (1967).
20. R.H.Schuler
Radiat. Phys. Chem. 43, 417 (1994).
21. H.E.van Wart *et al*
Proc. Natl. Acad. Sci. USA 70, 2619 (1973).
22. H.E.van Wart, H.E. and H.A.Scheraga
J. Phys. Chem. 80, 1823 (1976).
23. R.Wilbrandt
Chem. Phys. Lett. 60, 315 (1979).
24. R.H.Bisby and A.W.Parker
Biochem. Biophys. Res. Commum., 244, 263 (1998).

Irradiation of DNA with 193 nm light yields damage mainly at Guanine as detected by Excision Enzymes

T Melvin, S M T Cunniffe, P O'Neill.

MRC Radiation and Genome Stability Unit, Harwell, Didcot, Oxfordshire OX11 0RD. Email p.oneil@har.mrc.ac.uk

A W Parker.

CLRC Rutherford Appleton Laboratory, Chilton, Didcot, Oxon., OX11 0QX

T Roldan-Arjona.

Universidad de Cordoba, 14071-Cordoba, Spain

Introduction

Exposure of DNA to ionising radiation results in chemical modifications caused by two different processes i) direct ionisation of the DNA molecule, the direct effect, and ii) damage from radical species produced in the vicinity of the DNA, the scavengeable (indirect) effect. The advent of short wave ultraviolet lasers has enabled the study of the direct ionisation processes without the interaction of the ionisation products of water. Photoionisation of aqueous solutions of DNA with 193 nm laser light results in the formation of a photoejected electron via a monophotonic process.[1] The DNA radicals formed by photoionisation are proposed precursors of low yields of single strand breaks (ssb),[2] which we have confirmed using Rayleigh light scattering experiments. [3] Further, migration of the electron loss centres to guanine has been demonstrated thereby enriching the yield of guanine radicals. Radical product(s) formed at guanine are indeed the precursor(s) of strand breakage which occurs in yields of less than 1% of the photoionisation events.[2,4,5] Since, the majority of the damage, produced from photoionisation of DNA, is not prompt single strand breakage, the question arises as to whether base modifications are the major damages.

A method for quantitative determination of the base modifications formed within plasmid DNA was employed using enzymes which are selective for different damage sites and create a single strand breakage at the site of the damage. Damage identified from formation of the guanine radical cation induced by 193 nm light in DNA includes (i), frank single strand breakage (ssb),[2,6] (ii) alkali labile ssb[2] and (iii) 8-oxo-7,8-dihydroguanine.[4] Recently, 193 nm irradiation of plasmid DNA has been demonstrated to cause damage, which is excised by *Escherichia coli* formamidopyrimidine-DNA glycosylase (Fpg),[5] an enzyme known to excise oxidised purine modifications, including 8-oxo-7,8-dihydroguanine and 2,6-diamino-4- hydroxy-5-formamidopyrimidine (FapyGua), and it additionally has a β,δ-lyase activity that nicks DNA at apurinic/apyrimidic (AP sites).[7] The present study was done to determine whether damage, caused by exposure of DNA to 193 nm light, is targeted specifically at guanine, or whether other nucleic acid bases are damaged by photo-processes or photo-ionisation events. The yields and the base specificity for damage excised by Fpg, *Escherichia coli* endonuclease III (Nth), and *bacteriophage* T4 endonuclease V (T4 endo V) were investigated. Nth is known to excise oxidised pyrimidine damages,[7,8] whereas T4 endo V is known to excise pyrimidine photodimers.[8] which may be induced by ionisation and photo-processes of DNA. Excision enzymes have proved useful tools for the determination of both the yield and the nucleic acid base specificity for various damaging agents, since the site of nucleic acid base damage is revealed as a gap/ssb. The purpose of this study is to identify whether nucleic acid base damage occurs at specific 'hot spots' in DNA as a result of the 'direct' effects of ionising radiation, such as γ-radiation.

Results

Aqueous solutions of plasmid DNA were irradiated with 193 nm light, then assayed for yields of strand breakage, before and after treatment with either Fpg, Nth or T4 endo V (for full experimental details see ref. 5,9). The dependence on fluence of the cc DNA fraction of plasmid DNA in an aqueous solution containing 1mmol dm^{-3} sodium perchlorate, under oxic and anoxic conditions, irradiated with 193 nm light followed by post exposure treatment with Nth and T4 endo V is linear. The quantum yields of 193 nm light induced damage excised by the enzymes are shown in the table 1. The yield of Fpg sensitive damage, measured as ssb, is ~20 times that for prompt ssb in plasmid DNA irradiated with 193 nm light.[5] Lower yields of damage, representing ~5x the yield of prompt ssb, are excised by Nth from the plasmid DNA irradiated with 193 nm light. Thus much larger yields of base modification than frank ssb result from base radical cations. The yield of cyclobutylpyrimidine dimers induced by irradiation of plasmid DNA with 193 nm light and excised by the *micrococcus* UV endonuclease, was previously determined to be 1.65 x 10^{-3} in air saturated solutions.[6,10] This yield of photodimers is slightly greater than reported here using T4 endo V (see table 1).

damage/electrons	Quantum yields/10^{-4}	
	air	argon
photo-electrons		860
prompt ssb	1.5	0.9
Fpg excised damage[5]	33.1	23.8
Nth excised damage	7.3	6.2
T4 endo V excised damage	5.5	8.2

Table 1 Quantum yields of damage by exposure of pUC-18 plasmid DNA to 193 nm light

The base sequence specificity of the enzyme sensitive sites induced by 193 nm light was determined using Fpg, Nth and T4 endo V. An aqueous solution containing a 5'-^{32}P-end labelled restriction cut fragment of double stranded DNA, of known sequence, was irradiated with 193nm light (for conditions see ref. 2). The base specificities of ssb (lane i) and enzyme-induced ssb (lanes ii-iv) induced in DNA by 193nm light are shown in the Figure. The enzyme -induced ssb were introduced after incubation of the 193nm irradiated DNA with Fpg (lane ii), Nth (lane iii) and T4 endo V (lane iv) as shown in the Figure. Lanes v and vi show the Maxam Gilbert cleavage sequence for G/A and C respectively. Treatment of un-irradiate DNA with these proteins does not result in the formation of ssb. As shown previously,[2] 193 nm irradiation of DNA results in prompt ssb exclusively at the guanine moieties (lane i) but the distribution of ssb is not the same for all the guanines, reflecting

an inflence of local structure. Damage excised by Fpg protein yields a gap (single-strand break) in the duplex (lane ii) exclusively at guanine. The relative yields of damage excised by Fpg compared with that cleaved by the hot piperidine treatment are very similar. The amount of damage of guanine in the form of prompt ssb, hot alkali labile damage and Fpg excision damage is greatest for neighbouring guanine residues unless this duplex has a 3' thymine residue. The distribution of damages as ssb at guanine is non-random with a dependence on neighbouring base sequence which is similar for both Fpg sensitive sites and hot alkali labile sites. The absolute quantity of hot alkali sensitive lesions, compared with that for Fpg sensitive lesions is lower.

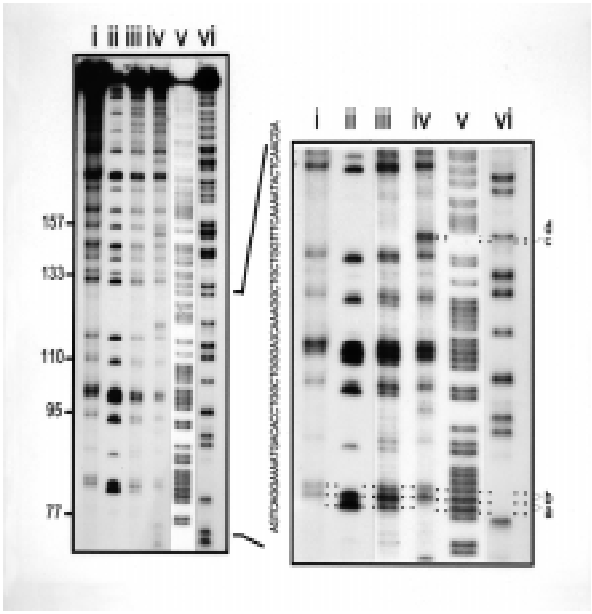

Figure 1. The base sequence specificity of prompt and enzyme induced ssb in DNA by 193 nm light; frank ssb (i), Fpg (ii), Nth (iii), T4 endo V (iv) and Maxma Gilbert lanes for A/G (v) and C (vi).

Damage in DNA irradiated with 193 nm light is also excised by Nth at guanine sites, but not detected at pyrimidine sites, (figure 1, lane iii). There is no evidence for excision of any oxidative pyrimidine damage, which would have been excised by Nth if present. The fact that guanine residue damages are excised by the Nth was unexpected. However, excision of damage at guanine by Nth has been previously reported for UV and also γ-irradiated DNA samples.[11)] At each Nth excision site, two fragments were observed. One fragment has an electrophoretic mobility similar to that of the fragment formed by prompt ssb (figure, lane i) and the other fragment has a mobility similar to that formed after Fpg treatment (lane ii). Unlike Fpg, which cleaves the apurinic/apyrimidinic (AP) site by a β,δ-elimination resulting in total removal of the damaged nucleoside.[7)] Nth cleaves the AP site by a β-elimination pathway to yield a 3'-α,β-unsaturated aldehyde terminus; this 3'- end group is unstable under standard polyacrylamide gel electrophoresis conditions. Loss of some of the 3'-heat-labile end-group yields a DNA fragment, which migrates through the gel to the same distance as the respective Maxam Gilbert sequences or Fpg treated samples. Samples with an intact 3' α,β-unsaturated aldehyde terminus migrate to a comparable distance to that of the fragments generated by prompt ssb. The sequence dependence on the yield of 193 nm light induced damage excised at guanine by Nth follows a similar trend as that for the prompt ssb, Fpg damage and hot alkali labile damage. It is therefore suggested that the damage precursor is common, and most likely a guanine radical cation.[3)]

The sample treated with T4 endo V (figure 1, lane iv) contains fragments with a similar electrophoretic mobility as that for the samples in lane i (prompt ssb), consistent with prompt ssb at the guanine site. Also fragments of lengths consistent with cleavage of damage sites at thymine residues were observed (i.e. figure 1, label c, within the sequence GGTTTC, two bands are detected, from two thymine dimer products).

In summary, irradiation of DNA with 193 nm light results in damage, which is localised predominantly at guanine; the yield of photo-damage such as pyrimidine dimers is relatively minor at this wavelength. The formation of prompt ssb is only a minor process compared with that for base damage formation. Photoionisation of DNA yields radical cations of all the nucleic acid bases, the subsequent migration to the most easily oxidised base, guanine,[2,12)] occurs and results in 'targeted' damage at this site. The findings indicate that a common precursor to the damage is involved reflecting the similarity in the sequence distribution of the damage. These results indicate that damage at guanine and the sequence dependent yields are a signature for *direct ionisation*, which is a major component of the damaging effect of exposure to cellular systems to ionising radiation.

References

1. L P Candeias, P O'Neill, G D D Jones, and S Steenken, Int.J.Rad.Biol., 61 15, (1992)
2. T Melvin, M A Plumb, S W Botchway, P O'Neill and A W Parker Photochem.Photobiol., 61 584, (1995)
3. T Melvin, S W Botchway, A W Parker and P O'Neill J.Am.Chem.Soc., 118 10031, (1996).
4. Cullis P.M., Malone, M.E. and Merson-Davies, L.A. J. Am. Chem. Soc. 118, 2775-2781(1996)
5. T Melvin, S Cunniffe, D Papworth, T Roldan-Arjona and PO'Neill Photochem. Photobiol. 65 660, (1997)
6. I E Kochevar and L A Buckley Photochem. Photobiol., 51 527, (1990)
7. E C Friedberg, G C Walker and W Siede DNA Repair and Mutagenesis, ASM Press, Washington D.C. (and references therein) (1995)
8. H E Krokan, R Standal and G Slupphaug Biochem.J., 325 1, (1997) (and references therein)
9. T Melvin, S M T Cunniffe, P O'Neill, A W Parker and T Roldan-Arjona Nucleic Acids Research, (1998) submitted for publication
10. I G Gut, R Farmer, R C Huang and I E Kochevar Photochem. Photobiol., 58 313, (1993)
11. D E Helland, P W Doetsch and W A Haseltine Mol.Cel.Biol., 6 1983, (1986)
12. T Melvin, S W Botchway, A W Parker and P O'Neill J.Chem.Soc., Chem.Commun., 653-654, (1995)

A Study of Upconversion Emission from Er(3+) Co-doped with Yb(3+) into Sol-Gel Silica Glasses Under Infrared Excitation

R Withnall, A Newport, P Riby, A Vecht.

School of Chemical and Life Sciences, University of Greenwich, Wellington Street, Woolwich, London SE18 6PF

Introduction

There is currently a great deal of interest in sol-gel glasses doped with lanthanon ions because they have potential applications ranging from solid-state lasers to electronic displays. Indeed there is currently a need for these materials as specific glasses in optoelectronic communication as well as for novel real time 3D displays and a range of security inks. In order for infrared radiation to be converted into visible light by the phosphor, two-photon absorption must take place. This can happen if the lanthanon ion dopant possesses an energy level which is above the ground state by an amount of energy equal to that of an infrared quantum and a second energy level which is above the ground state by twice this amount. Visible light is emitted when the ion relaxes radiatively from the second energy level down to the ground state.

The Er^{3+} ion has such a distribution of energy levels, and has thus been chosen as the luminescer in these studies. The Er^{3+} ion has a valence electron configuration of $4f^{11}$ having a $^4I_{15/2}$ ground state and low-lying excited states of $^4I_{13/2}$, $^4I_{11/2}$, $^4I_{9/2}$, $^4F_{9/2}$, $^4S_{3/2}$, $^2H_{11/2}$, $^4F_{7/2}$ and $^2H_{9/2}$ as shown in figure 1 [1]. The $^2H_{9/2} \rightarrow {}^4I_{15/2}$, $^4S_{3/2} \rightarrow {}^4I_{15/2}$ and $^4F_{9/2} \rightarrow {}^4I_{15/2}$ transitions give rise to the emission of light centred on 410, 550 and 660 nm respectively [2]. We are interested in maximising the upconversion efficiency of this visible emission by optimising the composition and preparative conditions of Er^{3+} doped sol-gel silica glasses, thereby making them useful in optoelectronic devices.

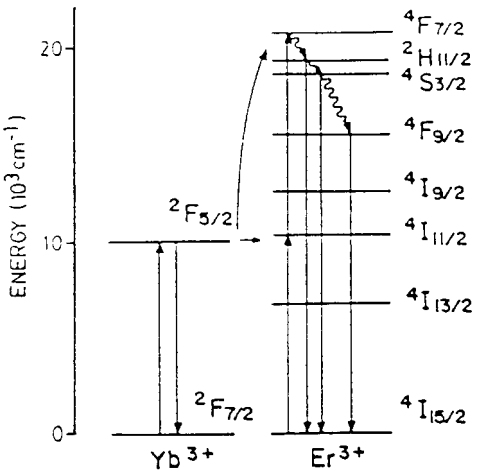

Figure 1. Low-lying energy levels of Er^{3+} and Yb^{3+}.

The green upconversion emission from Er^{3+} ions doped into sol-gel silica glasses has recently been studied using red light (λ = 647.1 nm) excitation from a krypton ion laser which excites the Er^{3+} ion into its $^4F_{9/2}$ level [2]. However commercial application of these phosphors would benefit greatly if the excitation could be provided by an infrared diode laser, thus it is important to study the visible upconversion luminescence under infrared excitation. As the absorption cross-section of the $^4I_{15/2} \rightarrow {}^4I_{11/2}$ transition is smaller than that with red light ($^4I_{15/2} \rightarrow {}^4F_{9/2}$), Yb^{3+} has been co-doped into the samples so as to act as sensitiser.

The Er^{3+} and Yb^{3+} co-doped sol-gel silica glass samples have been prepared by the phosphors group at the University of Greenwich using a modified literature procedure [3]. The infrared light excitation was provided by a 3900 Ti: sapphire laser pumped by a Millennia Nd:YAG laser (Spectra-Physics).

Results

Infrared laser light (λ = 974 nm) was focused on to polished samples down to a spot size of ca. 30 μm diameter (laser power at sample = ca. 50 mW) and visible luminescence was collected at 90° to the exciting laser beam. The collected light was imaged on to the entrance slit (slit width = 200 μm) of a Spex 1877 Triplemate spectrometer equipped with holographic gratings blazed at 500 nm and a Princeton EG&G intensified photodiode array detector. Wavelength dispersed visible emission was detected with this set-up only for Er^{3+} and Yb^{3+} co-doped glasses which had been subjected to fluoridization (by treatment with 45% aqueous HF), as can be seen in figures 2, 3 and 4 for the red, green and blue regions respectively. This can be explained by the decrease in phonon energies of the sol-gel matrices upon partial conversion of the oxide to a fluoride, thus increasing the luminescence yield relative to non-radiative processes.

Optimum concentrations of Yb^{3+} and Er^{3+} were found to be approximately 0.85 and 0.13 mole % respectively in order to maximise the luminescence yield. Higher concentrations of Er^{3+} result in concentration quenching of the emission. Exposure of the fluoridized samples to the infrared laser beam resulted in prompt red, green and blue emissions with the green and blue emissions growing stronger over a period of some minutes. Furthermore, the green and blue emissions were stronger relative to the red at high power densities.

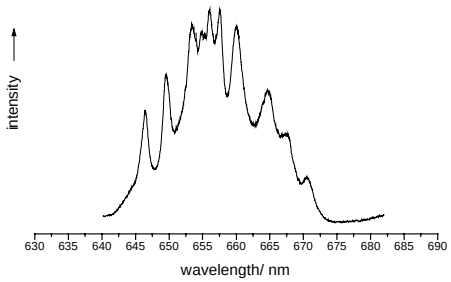

Figure 2. Spectrum of the red emission corresponding to the $^4F_{9/2} \rightarrow {}^4I_{15/2}$ transition.

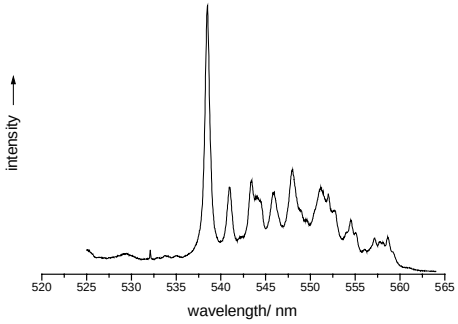

Figure 3. Spectrum of the green emission corresponding to the $^4S_{3/2} \rightarrow {}^4I_{15/2}$ transition.

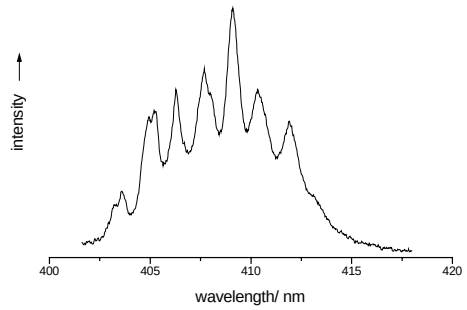

Figure 4. Spectrum of the blue emission corresponding to the $^2H_{9/2} \rightarrow {}^4I_{15/2}$ transition.

These observations may be explained by a saturation of the $^4I_{15/2} \rightarrow {}^4I_{11/2}$ transition at high power densities. This is also consistent with the observed photon dependence of the emission. A plot of log(emission intensity) versus log(excitation power) for the green emission gives a straight line with a slope of 1.15 ± 0.05 (see figure 5) rather than a value of ca. 2 which is expected for a biphotonic process. Similar values are also measured for the slopes of the lines obtained for the red and blue emissions. The value of the slope of the line for the green emission increases to 1.65 ± 0.05 (see figure 6) when the incident light flux is reduced by ca. 10^5 on removing the focusing lens, thereby avoiding saturation.

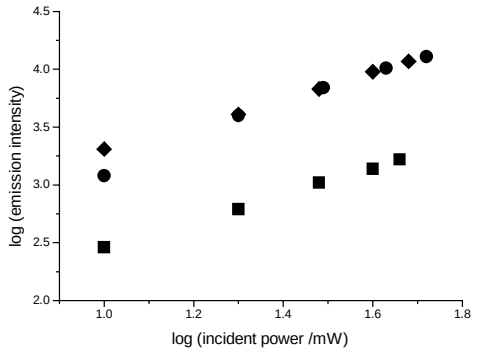

Figure 5. Intensity dependence of the 410 (squares), 550 (circles) and 660 nm (diamonds) bands.

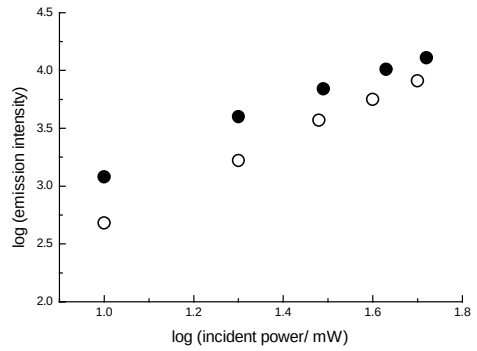

Figure 6. Intensity dependence of the 550 nm band at high incident light flux (solid circles) and low incident flux (open circles).

In conclusion, these measurements have enabled us to compare the efficiencies of the upconversion phosphor-doped sol-gel silica glasses which have been synthesised so far at the University of Greenwich. The effects of varying the concentrations of the lanthanon ion dopants and the extent of fluoridization of the matrix have been determined.

References

1. M.A. Chamarro and R. Cases
J. Luminescence 46, 59-65 (1990).

2. W. Xu, S. Dai, L.M. Toth, G.D. Del Cul and J.R. Peterson,
J. Phys. Chem. 99, 4447-4450 (1995).

3. D. Moutonnet, R. Chaplain, M. Gauneau, Y. Pelous and J.L. Rehspringer,
Materials Science and Engineering B9, 455-457 (1991).

Investigation of the DNA damage action spectra using laser-plasma generated monochromatic VUV photons

M Folkard, K M Prise.

Gray Laboratory Cancer Research Trust, PO Box 100, Mount Vernon Hospital, Northwood, Middx, HA6 2JR

W Shaikh, I C E Turcu.

CLRC Rutherford Appleton Laboratory, Chilton, Didcot, Oxon., OX11 OQX

Introduction

One of the fundamental aims of radiation biology is to develop a complete mechanistic description of the processes and subsequent biological effects that follow the initial energy deposition by ionizing radiation. Radiations can produce a variety of damage within the DNA helix. Of these, double-strand breaks (where both strands of the helix are broken within a few base pairs) can lead to lasting damage via the production of mutations, chromosome aberrations, genetic changes and ultimately cell killing. In this study, we have developed techniques for irradiating dry plasmid DNA using monochromatic vacuum-UV radiation in the energy range 7-25 eV. Using gel electrophoresis, it possible to quantify the yield of single-strand and double-strand breaks induced in the DNA sample following exposure to the radiation. Through these studies, we can establish the 'action spectra' for the induction of single-strand and double-strand breaks as a function of energy. The vacuum-UV energy region is an important region to study for several reasons: It is known that the most frequent local energy depositions in the DNA helix (i.e. by individual, or clusters of ionizations) are on the order of a few tens of electron volts, and that sparsely-ionizing radiations produce very few energy depositions >200 eV. Also, for some theoretical studies it is assumed that the minimum energies required to produce single-strand and double-strand breaks are about 17 eV and 50 eV respectively, although there is little experimental evidence to support this. Some data has been acquired by the Gray Laboratory Group using vacuum-UV photons from the 2 GeV electron synchrotron at CLRC Daresbury Laboratory. Data acquired so far suggest much lower energy thresholds for strand-break induction than had been assumed previously.

Increasingly, the emphasis of synchrotron facilities worldwide is towards higher photon energies, and the vacuum-UV plasma light source represents the only viable alternative with the versatility required for these experiments. A three week period was allocated in which to undertake a feasibility study to see if the Rutherford Laboratory vacuum-UV light source can be used for this work. During this period, we were successful in demonstrating that the VUV plasma light source facility can be used to quantify the action of radiation on DNA in terms of the amount of energy deposited at the site of damage, with particular emphasis on low-energy depositions below 25 eV.

Methods

For these experiments, we will utilize model plasmid DNA systems where we can easily quantify both single- and double-strand breaks. Undamaged plasmid DNA exists as a closed loop of double-stranded DNA in a so-called 'supercoiled' condition. If one, or more single-strand breaks are produced (i.e. by ionizing radiation), the molecular topology relaxes to an 'open-circular' form. If a double-strand break is produced, then the DNA assumes a 'linear' form. The fraction of supercoiled, open-circular and linear forms of DNA are readily quantified using established gel-electrophoresis techniques. By measuring the loss of supercoiled DNA, and the formation of linear DNA, it is possible to estimate the fraction of single-strand and double-strand breaks produced.

Vacuum-UV radiation is generated using a pulsed laser, focused on to a copper target to generate a plasma that emits a broad spectrum of photons from a few eV, to a few hundred eV [1)]. A concave holographic grating is used to select photons of appropriate energy at the sample position. The input and exit slits to the grating are opened fully, to maximize the intensity, and the area available for exposure of the sample. As a consequence, the energy bandwidth (10%) is poor, but is acceptable for this study.

Below 11.5eV, a LiF window is used to block second order radiation from the plasma and to protect the monochromator grating from debris generated by the plasma. Initial problems were experienced due to the LiF window rapidly coating (with debris) and attenuating the beam. This was resolved by flushing the chamber with near-atmospheric helium gas, which is completely transmitting below about 22eV. Above 11.5eV, the LiF window was removed. The dose-rate was seen to diminish with increasing energy from 12eV to 20eV. This was believed to be due to the grating not being completely clean, which is more detrimental at higher energies.

Plasmid DNA is spread as a dry monolayer, over a 5mm square area of a glass coverslip. This is placed in the vacuum and exposed to a range of doses, up to 10^{14} photons/cm^2 (typically, this takes about 3 minutes). The dose to the DNA is estimated using a NIST-calibrated silicon photodiode, located at the sample position prior to an exposure. At the time, no monitoring detector was installed, therefore the diode was used to measure the dose-rate, and exposures to the DNA were given as timed irradiations.

After all the samples are exposed, gel electrophoresis is used to ascertain the induction of DNA single-strand breaks and double-strand breaks formed. In the available period of time, two energies were studied: 9eV and 15eV.

Results

The results of this preliminary experiment were highly favorable; demonstrating that outputs of at least 10^{12} photons/s/cm^2 at 10% bandwidth could be achieved. This is sufficient for a range of experiments.

A dose-effect was clearly seen at 9eV and at 15eV, but could not be reliably quantified as it was not possible to determine the dose delivered precisely without either a stable dose-rate or a dose-monitoring arrangement.

Reference

1. Stuik - Facility Annual Report 1997-1998 Rutherford Appleton Laboratory Investigation of the DNA damage action spectra using laser-plasma generated monochromatic VUV photons.

Facility Developments

1) Vulcan

2) Titania

3) Instrumentation

4) Laser R&D

5) Lasers *for* Science Facility

Evaluation of a novel front end amplification technique for Vulcan

J Collier, C Hernandez-Gomez, I Ross, P Matousek, C Danson, J Walczak.

CLRC Rutherford Appleton Laboratory, Chilton, Didcot, Oxon., OX11 0QX. Email j.collier@rl.ac.uk

Introduction

Recently, a novel amplification technique for ultra short pulses has been proposed and explored in detail in a theoretical paper by Ross *et al* [1]. The technique, based on non-linear optics, is known as *Optical Parametric Chirped Pulse Amplification (OPCPA).* It has a number of features that, in principle, make it highly attractive. Primarily it offers extremely large gains simultaneously with extremely large bandwidths. Additional attractions are virtually no spatial and temporal phase distortion of the amplified pulse, reduced amplified spontaneous emission levels (equivalent), small optical material lengths and an inherent simplicity of implementation. In this paper we present an evaluation of the technique as a front end amplifier for the ultra short pulse amplification chain of the Vulcan system. Such a system could replace the existing amplification in Nd:glass (phosphate) and additionally have a wider impact as direct replacement of regenerative amplifiers on large scale CPA facilities.

The OPCPA Technique

An ultra short pulse is stretched in time by applying a large dispersion to it. This results in a chirped pulse, with the different frequency components present in the pulse distributed in time. This pulse, termed the seed pulse, is then amplified through optical parametric amplification where energy from a narrowband pump pulse is transferred to the seed pulse through the direct coupling of these fields in a non linear optical crystal. In the process of amplification, a third field is necessarily generated, known as the idler field, to conserve photon energy and momentum. In order to efficiently transfer energy between the pump and signal/ idler fields, all frequencies must propagate through the crystal at equal speed, a condition known as the phase matched condition. The natural dispersion of the crystal would normally prevent this process from occurring but by exploiting the birefringence that most crystals exhibit it is possible to achieve phase matching by choosing appropriate polarization and propagation directions. In the completely phase matched case with gains greater than about 10, the process gain *G* is given by equation (1)

$$G = e^{k\sqrt{I}} \qquad (1)$$

where *k* is a gain coefficient that depends on the crystal used and the optical frequencies involved and *I* is the pump intensity. For reasonable pump intensities and BBO or LBO crystals, gains of the order 10^5 to 10^7 are feasible. Furthermore, by appropriate choice of crystal and geometry it is possible to achieve the phase matched condition simultaneously over a very large range of seed/ idler frequencies. The high gains and broad bandwidths thus make it an excellent amplification process for ultra short pulses.

System Description

The experimental configuration for the OPCPA scheme is shown in figure 1. There are four main elements- an oscillator, stretcher, the OPA and a set of diagnostics. The seed pulse is generated by a commercial Kerr Lens modelocked oscillator [2] using Ti:Sapphire as the active medium. It produces an 80 MHz pulse train of 5 nJ, 120 fs pulses of which one is used.

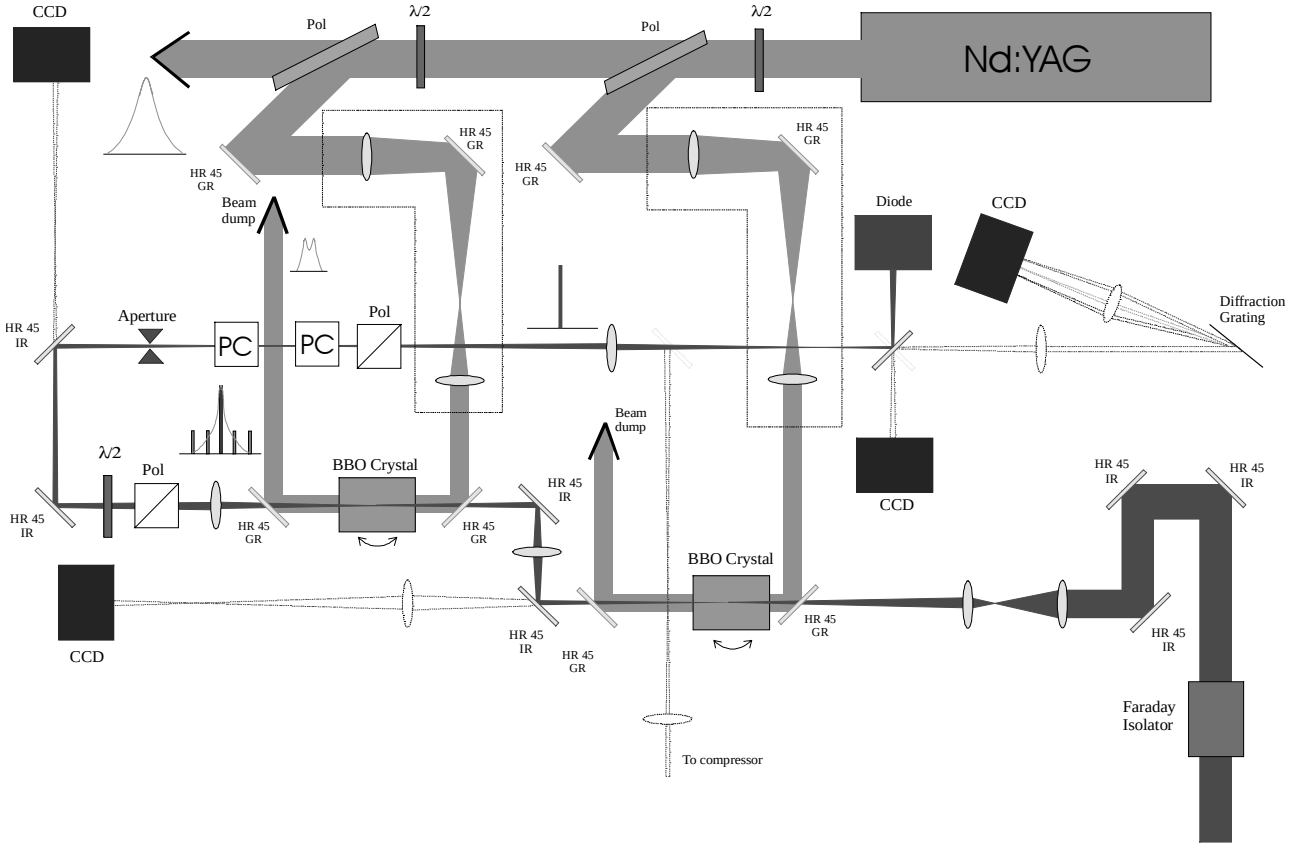

Figure 1. OPCPA Schematic

The pulse has FWHM bandwidth of 15 nm centred at 1053 nm. This pulse is stretched in time using the Vulcan system stretcher. This is a telescopic stretcher which is formed by a pair of 1740 lines/mm diffraction gratings separated by a confocal telescope. The telescope produces an effective grating separation of 3.5 m, which, when operated at 72.9^{o} incidence angle produces a group velocity dispersion of approximately 150 ps/nm. In the process of being stretched the pulse suffers a hard spectral clip by one of the stretcher lenses which causes a reduction in bandwidth to 6 nm resulting in a 900 ps stretched pulse duration. This limitation in bandwidth does not represent a problem for its normal use in the Vulcan laser system due to substantial gain narrowing, but it does place a limitation on this evaluation of the OPCPA technique. A Faraday rotator is placed at the output of the stretcher in order to isolate the OPCPA amplifier from the oscillator. The overall oscillator to OPCPA energy transmission efficiency is 10 % resulting in 0.4 nJ seed pulses.

The OPCPA amplifier was designed to operate with two individual amplification stages as shown in figure 1. The maximum individual stage gain is ultimately limited by fluence damage threshold of the mirrors and other optics to approximately 10^4. The implication of this is that in order to obtain gain saturation using a modest Nd:YAG laser, either two stages or a double pass configuration are required. Two stages were chosen for simplicity and versatility. The two stages have slightly different configurations. The seed and pump beams are co-linear in the first stage and non co-linear in the second stage.

The pump pulses are generated by a commercial Q-switched Single Longitudinal Mode (SLM) seeded Nd:YAG operating at 532 nm [3]. It produces a 15 Hz pulse train of 250 mJ -5.9 ns pulses. The output of Nd:YAG pump laser is split using a combination of waveplates and polarisers to produce the pump pulses for the two stages. The SLM cavity is required to ensure a smooth pulse profile in time, because any temporal modulations in the pump beam will translate into spectral modulations in the amplified signal due to the chirped nature of the seed. The pump and seed pulses are synchronised in time using a SRS delay unit. The beam path of the pump and seed beams is such to ensure suitable temporal overlap in both crystals.

The pump beam is collimated in the first stage using a 3.3 demagnification telescope, which transports the spatially flat near field at the output of the Nd:YAG laser onto the first crystal. The near field diameter is 1.9 mm and the maximum pump pulse energy in is 60 mJ, which results in a 2.1 J/cm^2 fluence and a 300 MW/cm^2 maximum pump intensity for the 5.9 ns pump pulses. In the second stage the pump beam is also demagnified by a 3.3 telescope. However, in this case the inter lens separation of the telescope is slightly smaller, which results in the pump beam being slightly converging onto the crystal, the pump beam is characterised by more of a Gaussian shape although is not operated quite in the farfield. The pump beam diameter is 1.3 mm FWHM. The pump pulse has a 52 mJ maximum energy, a 3.9 J/cm^2 fluence and thus a 650 MW/cm^2 maximum intensity. The pump is vertically polarized.

The seed is injected using a 2.5 demagnification telescope adjusted such that the seed is operated in the far field in the first crystal. By placing a 15 cm focal lens between the stages it ensures that the seed is also operated at the far field in the second stage. The seed has a Gaussian type spatial shape with a FWHM diameter of 0.35 mm in both stages. The seed beam is horizontally polarised and is injected through the back of the final pump steering mirror as shown in figure 1. Near field profiles are shown in figure 2.

In both stages the crystals used were BBO because of their high non linear coefficient. This means, however, that there is a significant walk off between the pump and seed beams and a relatively low angular acceptance for the process. Both crystals were 15 m long and have a 7 mm × 7 mm cross sectional area. The crystals were mounted inside temperature controlled ovens and phase matching was achieved by angle tuning.

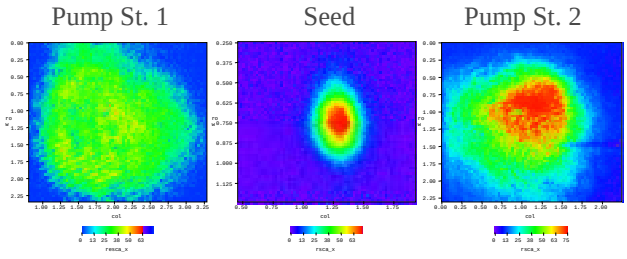

Figure 2. Near Field Profiles

In the first stage the pump is spatially large in comparison to the seed and thus by suitable choice of the position of the seed with respect to the pump one can compensate for the effect of the 3.2 degrees internal walk off angle. This ensures that the seed beam always lies spatially within the pump beam and thus interacts with it over the full length of the crystal. In the second stage the seed and pump have a comparable size and certainly the seed would walk outside the pump diameter. The reduction in pump diameter was necessary to provide a sufficient intensity increase to achieve saturation. This could not be achieved by increasing the pump energy due to air breakdown in the relay telescope. To partially compensate for the walkoff the pump and seed beams were thus set non co-linear with a 1.2° internal included angle in order to increase the gain length.

Gain Measurement

The energy gain of the system was measured using a combination of a fast photodiode and suitably calibrated neutral density filters. To ensure that no spatial integration occurred the measurements were conducted in a magnified image plane of the relevant crystal surface. This meant that the small active area of the photodiode only recorded the gain in the very centre of the seed pulse. The gains for each individual stage as a function of absolute pump intensity are shown in figure 3 and that of the combined stages in figure 4. Each point is the average of 64 pump laser shots With a maximum absolute intensity of 350 MW cm^{-2} for Stage 1 the observed gain was approximately 2400 and for Stage 2 with a maximum intensity of 650 MW cm^{-2} the observed gain was approximately 8000. Also plotted on figure 3 is the gain that could be expected on the basis of equation (1) for these intensities.

It is clear from figure 3 that the more efficient stage configuration was that of Stage 1, despite having a lower absolute gain at the peak intensity available to it. Stage 1 was configured with a pump that was collimated with a flat spatial intensity profile and such that the effects of walkoff were negligible. The stage was co-linear and operated close to degeneracy which means that both the signal and idler fields will walk off from the pump field at equal rates. However, the pump beam size was appreciably larger than the signal / idler size and furthermore appreciably larger than the distance that the seed / idler field would walk off. Thus, the signal / idler field always saw a constant intensity over the whole crystal length despite the walk off. It is therefore unsurprising that there is also a good agreement between the measured gain and that predicted by Equation 1. The penalty for this configuration is that the intensity (and thus the gain) is limited to a maximum of 350 MWcm^{-2}.

The situation for Stage 2 is more complex. The gain efficiency of the stage is somewhat reduced with respect to Stage 1 and furthermore there is a substantial disagreement between the values measured and those predicted by equation (1). The reason for this is subtle. Equation (1) assumes that the intensity of the pump field is spatially constant. This is not true in Stage 2 because the effects of walkoff are not negligible. The pump beam has a Gaussian type shape with a FWHM diameter that is not only comparable to that of the seed/ idler size but also comparable to the walkoff distance for the seed. The

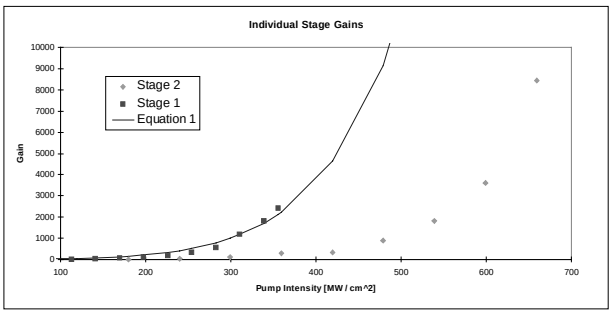

Figure 3. Individual Stage Gains

assumption therefore that the intensity is constant over the length of the crystal is clearly not valid. Furthermore, because the stage is configured to be non co-linear the effective walkoff for the signal occurs at a different rate to that of the idler. This walkoff of both the signal and the idler at different rates, taken in conjunction with the non constant pump intensity, can be considered to be a loss mechanism for the signal and the idler which are not present in the first stage. An estimation of the expected gain of Stage 2 is thus more complex and requires a numerical analysis. We have performed such an analysis for the specific configuration of Stage 2 which indicates that a reduction in gain by a factor of 4 could be expected over that predicted by equation (1) when operated at the highest pump intensities available of 650 $MWcm^{-2}$ consistent with experimental observation.

One final point is that the lack of the total collimation of the pump beam in the second stage has only a small effect on the gain, despite possessing a spatially varying convergence that can lie outside the acceptance angle of BBO. This is because the overall gain of the process is low when compared to the gains ($>10^{12}$) needed for a process such as second harmonic generation which is that generally that used in the measurement of the 'acceptance angle'.

Figure 4 shows the gain of both stages as a function of Stage 2 pump intensity with Stage 1 operated at it maximum gain. At higher intensities, a significant departure in overall gain is observed over what could be expected on the basis of the gains of the individual stages. At the highest Stage 2 intensity, a maximum gain of ~$2x10^6$ is measured when a gain of ~$2x10^7$ should be possible on the basis of the producted gains of the individual stages presented in figure 3. This difference arises due to the saturation of Stage 2. Figure 5 which is the temporal profile of a small spatial section of the pump beam imaged onto the photodiode illustrates this saturation, with the almost total depletion of the pump energy in the relevant time window. The saturation of Stage 2 is desirable because this not only means that the system is extracting the maximum amount of energy possible but it also leads to an increase in stability as described later. This is the primary reason why the stage was configured with a smaller pump beam size because as explained earlier this was the only way to increase the intensity and thus gain to a level that would saturate. In saturating Stage 2, one has to be careful because under these pump depletion conditions the transfer of energy between pump and seed can be cyclic and energy will start to flow back from the seed to the pump field. However, despite the relatively heavy saturation indicated by figure 4 we did not observe any reconversion.

The average output pulse energy of the amplified seed pulse measured under these saturated conditions is typically 0.33 mJ per pulse. This represents an extraction efficiency of approximately 0.6 % from the 50 mJ Stage 2 pump pulse. This is relatively low but consistent with the expectations of this test configuration for the OPCPA technique.

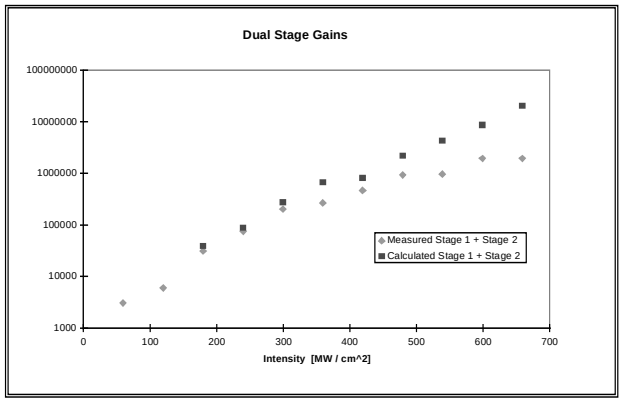

Figure 4. Combined Stage Gains

Bandwidth Measurement

The bandwidth of the OPCPA technique under the conditions in this evaluation should be very large of the order 1200 cm^{-1} (120 nm) [1]. The potential bandwidth of the process under optimum conditions could be of the order 4000 cm^{-1} (400 nm). However, as previously explained the bandwidth available in the seed pulse was limited by the stretcher to 6 nm. Figure 6 illustrates the bandwidth gain of the system when operated with these 6 nm seed pulses. Two points are evident. In the case of no saturation (by attenuating the seed pulse) with a total gain of $2x10^7$ there is virtually no difference between the seed and amplified pulse bandwidth. The slight asymmetry arises from the fact that the seed pulse is not exactly located at the centre of the pump pulse in time. Because the seed pulse is chirped and

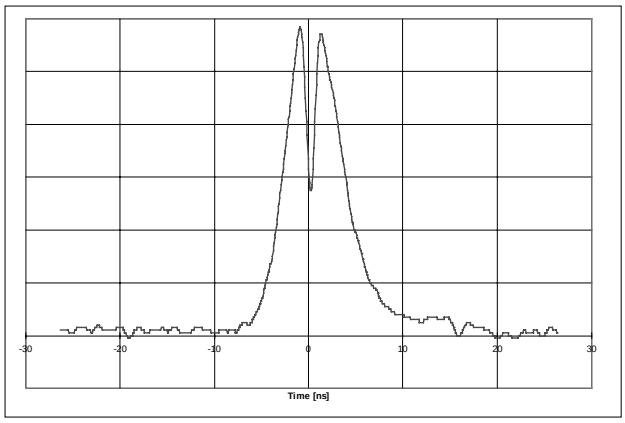

Figure 5. Pump Saturation

the gain is high this slight asymmetry in the temporal pump intensity results in a slight spectral asymmetry in the amplified seed pulse. However, in the case of saturation, with a gain of $2x10^6$ the output spectral bandwidth is flat and slightly broader as would be expected.

In order to examine the process when used with much higher bandwidths, a test bandwidth was generated by directly injecting the 100 fs output pulses from the seed oscillator into a length of single mode optical fibre. The fibre length was approximately 500 m. Strong self phase modulation occurred in the first few metres of the fibre and resulted in an increase in the FWHM spectral bandwidth of the seed pulses from 12 nm to more than 50 nm. The remaining length of fibre served to temporally stretch this bandwidth to approximately 0.5 ns. The output from this fibre was then injected as the seed pulse into the OPCPA system. Figure 7 is the resultant measured gain bandwidth of the system, however modified by the mirror coatings and other optics. A gain of approximately 10^6 was achieved across a bandwidth of more than 50 nm.

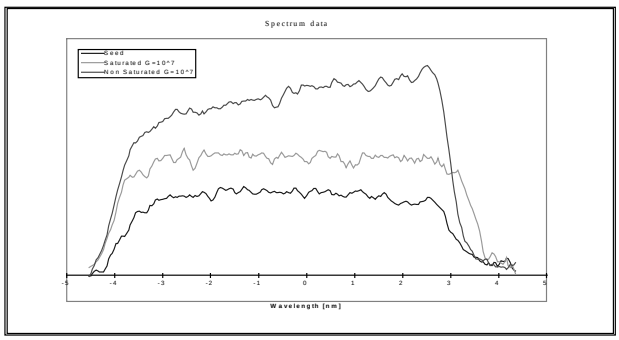

Figure 6. Pulse Bandwidth

Stability Measurement

The shot to shot energy stability of the system was assessed by recording relative energies of 2000 consecutive shots at a number of different locations in the amplifier scheme using a SRS Boxcar Amplifier and PC. The 2000 shots were then histogramed and the results are displayed in figure 8. Four histograms are shown. The relative output energies of Stage 1 and 2 when operated independently, the relative output energies of Stage 1 and 2 when operated together and the relative output energies of the pump laser inside a 1 ns window. Clearly, the stability of the individual stages is poor with more than 80 % of

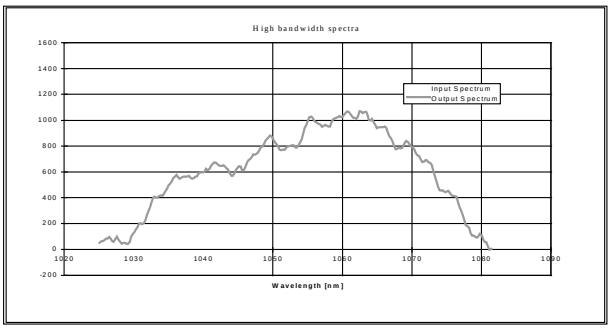

Figure 7. Test Bandwidth

shots lying within approximately ±25% of the mean. However, when operated together the stability, which one would expect to degrade on the basis of the independent measurement to approximately ±50%, markedly improves to approximately ±10%. This is a direct result of the relatively strong saturation of Stage 2. In fact the stability of the system becomes ultimately limited by the stability of the pump laser inside the equivalent 1 ns windows as also evident from figure 8.

Pulse Compression Measurement

The 6 nm pulse bandwidth illustrated in figure 6 was compressed using a double pass compressor. The pulse length was recorded using a single shot autocorrelator. The result is shown in figure 9, illustrating a compressed pulse length of approximately 1 ps. This is consistent with a Fourier transform of the spectral shape illustrated in figure 6 demonstrating that there is no disruption of the linear chirp through the OPCPA process.

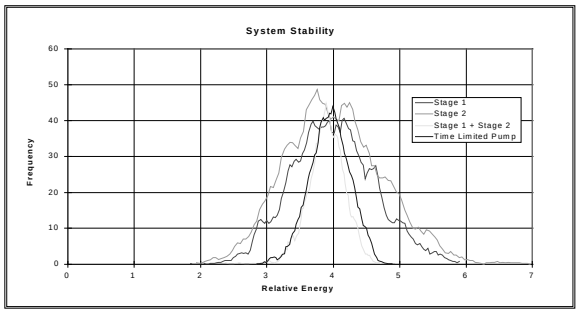

Figure 8. Stability Data

Conclusion

We have demonstrated the OPCPA technique and have achieved gains greater than 10^7 with no observable gain narrowing over at least 50 nm at 1053 nm. We have achieved saturated output energies of the order 1 mJ and demonstrated energy stability of ± 10%. We have compressed an OPCPA amplified pulse to its transform limit. The feasibility of an OPCPA system as an ultrabroad band front end pre-amplifier for Vulcan has been established and a dedicated system is now under construction.

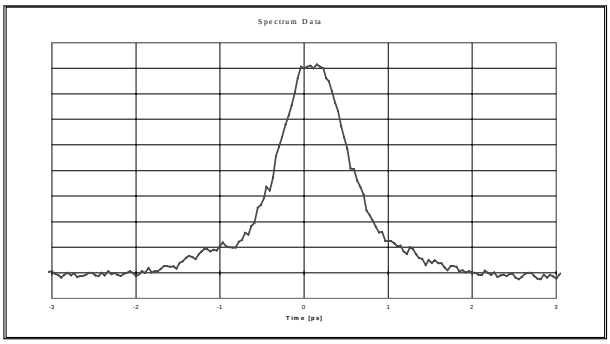

Figure 9. Autocorrelation of Compressed Pulse

References

1. Ross *et al*, Ops. Comm 144 (1997) 125-133
2. Specta Physics “Tsunami”
3. Spectra Physics Model GCR-150

Multi-terawatt Frequency Doubling of Picosecond Pulses for Plasma Interactions

D Neely, R Allott, J L Collier, C N Danson, A Djaoui, C B Edwards, P Flintoff, P Hatton, M Harman, M H R Hutchinson D A Pepler, I N Ross, T Winstone.

CLRC Rutherford Appleton Laboratory, Chilton, Didcot, Oxon., OX11 0QX.

F Amiranoff, V Malka, M Salvati.

LULI, Ecole Polytechnique, France

E L Clark, A E Dangor, K Krushelnick, A Modena, Z Najmudin, M Santala, M Tatarakis.

Imperial College, Prince Consort Road, London, UK

C Clayton, D Gordon.

UCLA, Los Angeles, California, US

G Malka.

University of Orsay, France

Introduction

An investigation was carried out to select the optimum scheme for frequency doubling the 1054 nm sub picosecond Vulcan chirped pulse amplified (CPA) beam. Conversion efficiency tests were initially carried out on small aperture KDP (type 1) crystals at a range of incident intensities up to 3 x10^{11} W/cm^2 giving the optimum crystal thickness for pulses in the 0.3 to 3 ps region. The conversion efficiency and resultant focal spot quality obtained using a large aperture 140 x 89 mm drive beam and 4 mm thick type 1 crystal were measured. The effect of B-integral on the frequency doubled beam quality was studied and is shown not to be the dominant cause of the observed beam break-up. During this experiment a frequency doubled beam line was commissioned and delivered pulses of over 10 TW onto target for an electron acceleration experiment[1)].

Background

Chirped Pulse Amplification [2)] has allowed major advances in the study of ultra-high intensity interactions with matter. Frequency doubling CPA laser systems offers a route to investigate laser matter interactions in a new regime. Interest in using such a beam arises in a number of cases: production of high harmonics, collisionally excited soft X-ray lasers[3)], electron accelerator experiments [4)] etc. The laser contrast can have a substantial effect on the interaction physics involved, as a poor contrast, particularly before the peak of the pulse, leads to the beam interacting with a pre-formed plasma of large scale lengths [5)]. In CPA systems the final contrast achieved on target is usually determined by one of three things: amplified spontaneous emission (ASE), pre-pulses derived from the pulse generator or pre-amplifier, or spectral clipping in the compressor. Frequency doubling offers a potential method of significantly improving contrast levels due to the non-linear nature of the process. In this paper measurements of doubling efficiency and focal beam quality will be presented.

Efficient frequency doubling of large aperture infrared beams at an intensity of a few GWcm^{-2} was described by Linford et al [6)]. Intensities of few GWcm^{-2} are typical at the output stages of a glass laser system prior to recompression. It would therefore be possible to efficiently frequency convert the beam prior to compression. However, unfavorable scaling of the grating damage threshold with wavelength severely constrains the final pulse energy. The alternative scheme is to frequency double after the compression gratings, which avoids this limitation and is the approach adopted by the authors.

Type I KDP crystals, whose phase matching condition produces almost equal group velocities for the fundamental and second harmonic components were used. To ensure high contrast ratio on the target it is essential to eliminate any unconverted fundamental component in the final beam. Type I frequency conversion produces orthogonally polarised fundamental and second harmonic components. These orthogonally polarised components are relatively easy to separate using polarisation sensitive reflective mirrors.

Doubling Efficiency

In order to determine the most appropriate crystal length and operating intensity regime for the large aperture CPA beam, a number of frequency doubling conversion efficiency measurements were carried out on small 25 mm diameter aperture KDP crystals. The crystal lengths were 2 and 4 mm and were operated at a range of incident intensities up to 300 GWcm^{-2}. The incident infrared and converted green beam energy was measured using absorption calorimeters. The data is presented in figure 1. The majority of the data was obtained using a 1 ps CPA pulse, although a number of points were obtained using a 2.5 ps YLF pulse. The data shows that a 4 mm crystal gives optimum conversion efficiency at an irradiance of ~150 GWcm^{-2} and the optimum conversion efficiency for a 2 mm thick crystal is at an intensity greater than 250 GWcm^{-2}. The lines in the figure are fits to all of the conversion efficiency data points using a power series expansion in IL^2, where I is the intensity and L the crystal thickness. Frequency doubling was theoretically examined by Armstrong[7)] where conversion efficiency was shown to scale as a function of IL^2. However,

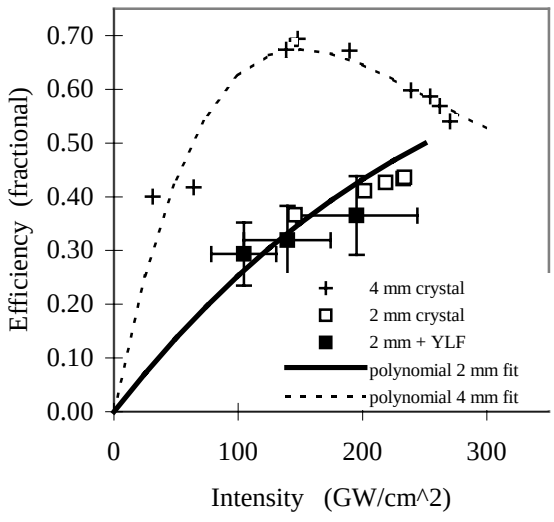

Figure 1. Second harmonic conversion efficiency for 2 and 4 mm thick KDP type 1 crystals as a function of 1054 nm pulse intensity. The fits were generated from a single polynomial (see text) and scaled as crystal thickness squared to fit both sets of data.

when calculating the conversion efficiency, Armstrong did not include the effects of the intensity dependent refractive index change, as this effect was negligible in the range he considered. In our measurements significant intensity dependent refractive index changes are present and therefore preclude us from using a simple fit to IL^2. Thus, a single polynomial function, C(I,L) of the form

$$C(I[GWcm^{-2}],L[mm]) = \sum a_n(IL^2)^n \qquad (1)$$

for both the 2 and 4 mm crystals at both pulse lengths is used. The fitting coefficients have values of a_1=7.379 x 10^{-04}, a_2=-2.804 x 10^{-07}, a_3=4.489 x 10^{-11}, a_4=-3.302 x 10^{-15} and a_5=9.181 x 10^{-20} and the fit applies in the range $5 < IL^2 < 50$ GW.

This method of fitting allows us to extrapolate from the measured data into parameter areas in crystal length and intensity that were not directly measured. For example, figure 2, generated on the basis of the fits, explores the possibilities of using the same and different crystals over a variety of different pulse lengths for fluences that represent the design range for the Vulcan compression gratings. It shows that for the current laser system under normal operating fluences with a 700 fs pulse a 2 mm crystal is the optimum choice. However, there are significant problems associated with the manufacture of a 2 mm thick crystal with an aperture of sufficient size (150 mm x 90 mm) and of reasonable optical quality. The thinnest commercial crystal available[8] at the time was 4 mm manufactured with a circular aperture of 157 mm. While not being optimum in terms of frequency doubling efficiency this crystal was the closest match available and was installed on the Vulcan system. A transmission interferogram for this crystal is shown in figure 3. The crystal has a 100 mm chord, which gives the fringe shift visible along the top of the image. The $\lambda/6$ @ 1053 nm wavefront distortion represents to the best of our knowledge an unparalleled quality for such an aperture thin crystal.

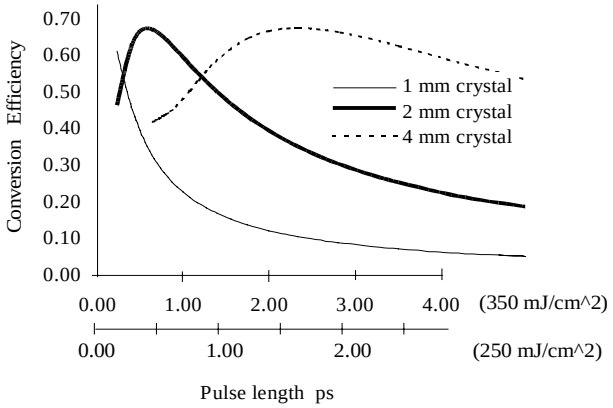

Full beam frequency doubling tests were carried out with this crystal**.** Calorimeter measurements taken during full energy laser shots demonstrated identical efficiencies to the 4 mm small aperture data shown in figure 1 to within experimental uncertainties. The second harmonic pulse length, measured, using a second order autocorrelator was 0.68 ± 0.1 ps when using a 0.7 ps 1053 nm drive pulse.

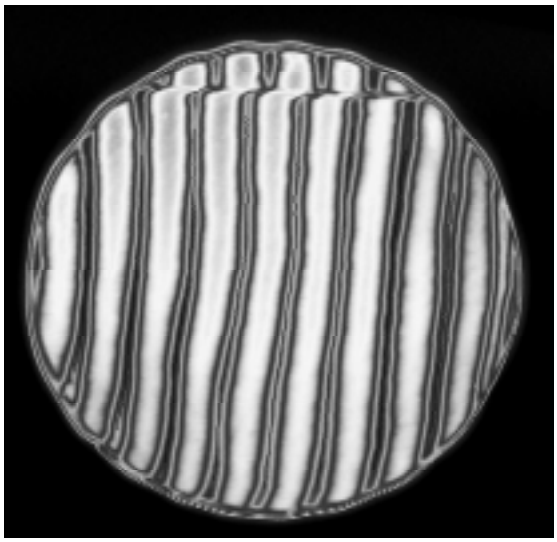

Figure 3. Interferogram of 157 mm diameter 4mm thick KDP crystal.

Far Field Quality

Figure 4 illustrates the far field of the frequency doubled beam at a low drive intensity of 0.1 $GWcm^{-2}$ (and thus low conversion) and figure 5 illustrates the far field at a high drive intensity of 200 $GWcm^{-2}$. The far field clearly degrades in the high intensity case and fragments into a number of spots distributed in the focal plane. Radial integration of this focal plane distribution indicates that the frequency doubled beam under the conditions of high fundamental intensity is ~5 times diffraction limited. As a comparison, previous studies on the fundamental beam have indicated that the beam is approximately 2.5 times diffraction limited. The implication of this result is that there is a significant amount of non-linear phase accumulation, or B integral [9], in the frequency doubled beam, arising both from an incident pump beam carrying a B integral of 1 and the propagation of the coupled fields through the crystal. To estimate the B integral in the frequency doubled beam a simple stepwise numerical integration was carried out[10] using published values of the coefficient of non linear refractive index[11, 12] This indicated that the expected value of B for the frequency doubled beam under these conditions would be 2.1. Again, previous studies[10] at 1053 nm have indicated that typically a B greater than 14 is required to produce a 5 times diffraction limited spot, and even under these relatively high values of B no fragmentation occurs. It seems unlikely therefore that B integral alone is responsible for the break up of the second harmonic far field under these conditions.

Discussion

The second harmonic conversion efficiency dependence on intensity obtained here are generally in good agreement with the measurements of Chien et al[10] who used a slightly shorter 500 fs pulse and 26 mm diameter KDP crystals. Chien et al observed no degradation of focusability with type I frequency doubling but did observe some degradation when using a pre-delay scheme and type II doubling. This is similar to the work reported here, where it was only through measurement of the ~x5 larger beam (and hence more sensitive) frequency doubled far-field that an observation of degradation of focusability was made. In earlier work by Eckardt & Reintjes[13] it is interesting to note the rapid spectral and temporal pulse break-up introduced by using a crystal, which is thicker than optimal. Their work clearly shows that significant reconversion occurs primarily at the peak of the pulse leading to energy loss and pulse distortion. It is interesting to speculate that in an

analogous fashion similar spatial and angular beam perturbations may have been introduced in the present work where the crystal used was thicker than optimum. If the beam break up is due to this, a simple solution might be to slightly detune the crystal delaying peak conversion to the end of the crystal and hence avoiding significant reconversion effects. Although detuning a crystal generally tends to lower the maximum achievable conversion, in the present case where B ~ 2 it should be possible to counterbalance these effects.

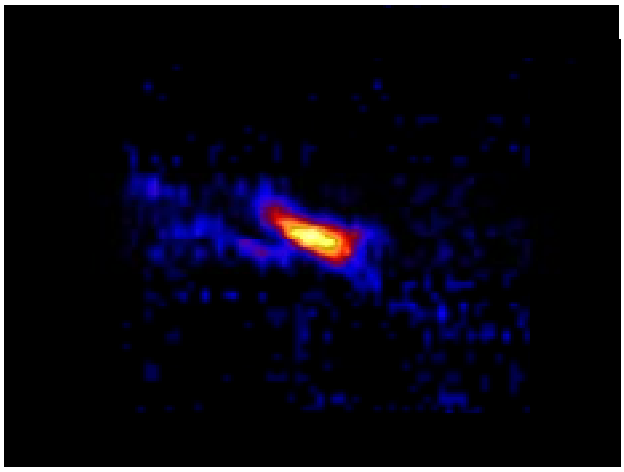

Figure 4. Far-field intensity distribution of the frequency doubled beam obtained at an incident fluence 0.1 GWcm^{-2}.

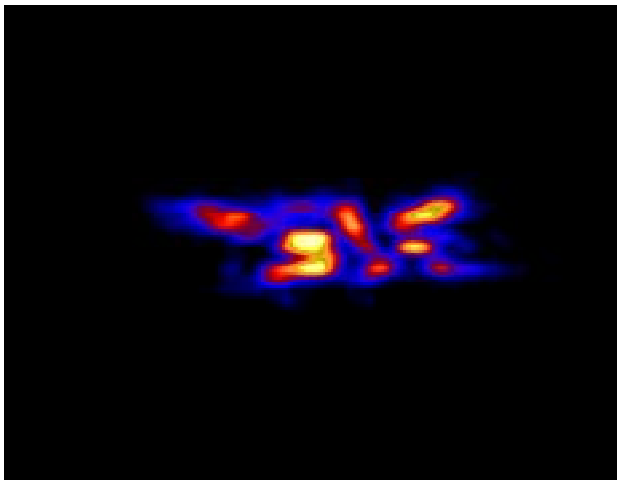

Figure 5. Far-field intensity distribution of the frequency doubled beam obtained at an incident fluence onto the crystal of 200 GWcm^{-2}.

Frequency doubling can be considered in an analogous manner to optical parametric amplification as a process in which gain is generated at the frequency doubled wavelength. Phase matching over a range of ΔK could potentially produce ~5 times diffraction limited beam size far-fields which would be in line with the observed measurements. This effect would be more observable for large diameter thin crystals as is the present case. However, it is not clear why break-up in the far-field should be observable.

The change in the energy within the wings of the far-field as the irradiance is increased could be due to driving the crystal at saturation in the centre (causing reconversion) of the beam and making the far-field significantly more sensitive to aberrations at the edges of the beam. The far-field would therefore degrade at higher drive irradiances where the effect would be dominant, as it is known that beam quality is poorer in the periphery than at the centre. An adaptive optic based compensation system is presently under design and will be implemented prior to re-testing the system.

Conclusion

Efficient frequency doubling of the large aperture Vulcan CPA beam was demonstrated with pulses of over 10 TW being delivered to target. Future work using a thinner 2 mm crystal that is optimal for the sub ps Vulcan pulses is presently underway. Break-up of the far-field was observed and it was demonstrated that this is not entirely attributable to B-integral effects. Additional work is underway to examine the cause of the far-field degradation and it is hoped that the addition of adaptive optic compensation to the drive beam will significantly help in isolating the various contributions.

Acknowledgements

The authors would like to thank the operations and support staff of the Central Laser Facility. This work was funded by the Engineering and Physical Science Research Council and through the EU TMR contract ERB FMGE CT950053.

References

1. Z. Najmudin et al, ECLIM 1998
2. D Strickland & G Mourou. 1985 Opts. Comm., 56, 219-221.
3. M. P. Kalachnikov et al 1998 Phys. Rev. A, 57, No.6, 4778-4783
4. Modena, A. et al 1995, Nature 377, 606.
5. G. T. Tsakiris et al, 1998 Proc. of the XXV ECLIM, Formia, Italy
6. G. J. Linford et al, Applied Optics, 21, No 20, p3633-3643, 1982
7. J. A. Armstrong et al. 1962 Phys. Rev. 127, 6, 1918.
8. Crismatec, B.P. 521-77794 Nemours Cedex - France
9. Seigman, 'Lasers', University Science Books, 1986
10. D. Neely et al, 1998, SPIE Proc. of the SSLAICF, Monterey, USA, 1998
11. C. Y. Chien et al. Opt. Let. Vol. 20, No. 4 p353-355, 1995.
12. T. Ditmire et al 1996 J. Opt. Soc. Am. B, Vol. 13, No. 4, p649-655.
13. R. C. Eckardt & J. Reintjes 1994 IEEE J. Q. Electronics, Vol. QE-20, No. 10 p1178-1187.

Wavefront Analysis of the Vulcan Laser System

C Hernandez-Gomez, J Collier, S Hawkes, C Danson, I Ross, T Winstone, D Pepler.

CLRC Rutherford Appleton Laboratory, Chilton, Didcot, Oxon., OX11 0QX. Email c.hernandez-gomez@rl.ac.uk

Introduction

In the amplification of an ultra-short pulse the wavefront quality is of fundamental importance because it is this that determines the focusability of the beam and thus the on target intensity. The focusability of the CPA beam line on the high power laser Vulcan was characterised recently and found to be three times the diffraction limit [1]. This result indicated that it would be possible to achieve even higher intensities, because improvement in the spot size towards the diffraction limit would have a significant effect on the focused intensities -as the spot diameter decreases the focused intensities increase. Thus, a measurement of the wavefront quality of the CPA was initiated using a radial shear interferometer [2]. The wavefront was studied for the alignment beam and for single shots under a variety of different configurations. The primary aim of the study was to determine the origin of the wavefront aberrations and whether they were static (optics), dynamic (thermal) or transient (shot related) in nature and therefore to identify ways of their correction.

Wavefront Characterization

The interferometer was placed in the diagnostic suite for the CPA beamline located after the 150 mm amplifier. The interferograms obtained were recorded on video tape and post processed using a commercial software package [3]. An Optical Path Difference (OPD) map of the wavefront is generated from an individual interferogram, the shape of which is then subsequently represented using a Zernike polynomial analysis. Zernike polynomials have a number of useful properties for this application and have a long tradition of use in classical optical aberration analysis.

The wavefront $W(\rho,\theta)$ can be described by a series of Zernike polynomials $R_n^m(\rho)\cos(m\theta)$ and $R_n^m(\rho)\sin(m\theta)$ defined for an optical system with a circular pupil of unit radius where $R_n^m(\rho)$ is a polynomial in ρ of order n and azimuthal frequency m, with (ρ,θ) the polar coordinates of any point located in the pupil.

The wavefront can be written as expansion of these polynomials,

$$W(\rho,\theta)=\sum_{n=0}^{x}\sum_{m=0}^{n}[2(n+1)/(1+\delta_{m0})]^{1/2}R_n^m(\rho).(c_{nm}\cos m\theta+s_{nm}\sin m\theta)$$

Where c_{nm} and s_{nm} are the expansion coefficients, n and m are positive integers including zero, $n\text{-}m\geq 0$, δ_{ij} is a Kronecker delta.

Individual Zernike aberrations are orthogonal and balanced meaning that the variance across the aperture is minimized by the introduction of lower order aberrations. Additionally, excepting for the lowest order polynomial ($n=0$) the mean value for each aberration is zero. These polynomials can be normalised (thus becoming orthonormal) by choosing the right definition for the constants. These properties mean that the expansion coefficients represent the standard deviation of each individual aberration across the pupil for each term. This series has an infinite number of terms and there is no standard way of ordering them. In this study the ISO scheme was chosen [4, 5]. Finally, it is necessary to decide how many Zernike terms to take into account. This is a tradeoff between adequately

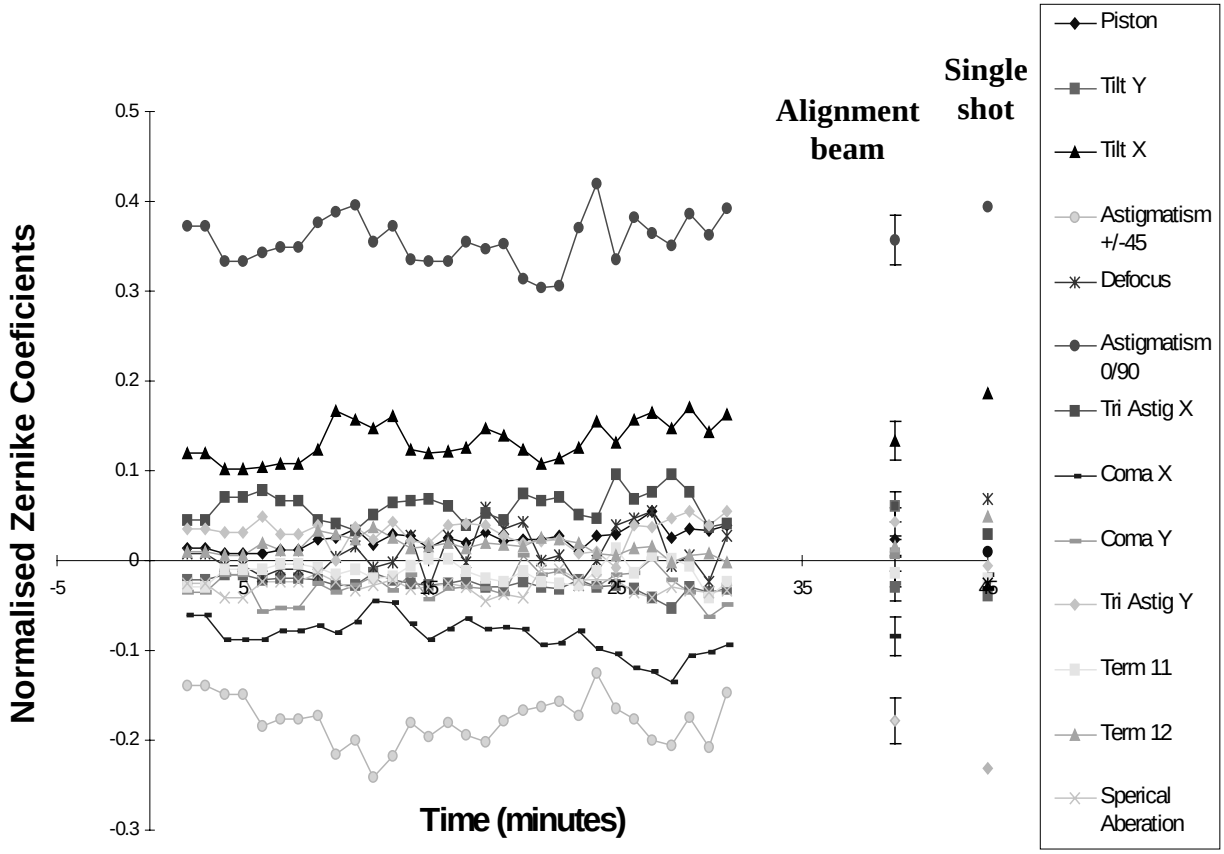

Figure 1. Values for the 13 Zernike terms for the alignment beam and their mean values and standard deviations

representing the wavefront at the expense of the loss of higher order mode information and computer processing time. In this study, we stopped the 13th ISO term ($n=4$). Some of these terms corresponds to well known aberrations, such as astigmatism, coma and spherical aberrations.

Analysis

The first part of this analysis was to determine whether the alignment beam can be used as a good reference of the wavefront quality present on a single shot. This is important to determine whether the wavefront aberrations on a single shot are comparable to the mean value of the aberrations on the alignment beam, for a fixed period of time prior to the shot. Figure 1 shows the values for the 13 Zernike terms for the alignment beam and their mean values and standard deviations. It also shows the values for these terms for the single shot fired immediately after. The analysis clearly shows different values of the wavefront aberrations over this period of time arising primarily from air movement. From figure 1, it is reasonable to conclude that the mean value of the Zernike terms obtained with the alignment beam is representative of the values obtained for the wavefront aberrations on a single shot to within one standard deviation of these values. Furthermore figure 1 shows that the largest contributions are from terms four and six which are the terms that represent astigmatism. The next largest terms are eight and nine which represent coma.

These results demonstrate that the wavefront is predominately aberrated by a fixed optical source. As the beam propagates through the amplifier chain it encounters different optics, some of which such as the disk amplifiers possess asymmetry and could be the origin of the apparent fixed astigmatism. There is a small contribution to wavefront distortion due to air movement, as the beam propagates partly through air and not in an enclosed beam line.

Astigmatic Shot Recovery

The Vulcan laser system fires one shot every 20 minutes. This shot rate was empirically determined using previous studies of the energy transmitted through a pinhole to determine when the beam quality has recovered sufficiently to enable another shot. The shot recovery time is minimised by the use of a set of blowers that cool the amplifier for 15 minutes after each shot. Astigmatism is of special interest as it is the main contribution to the aberrated wavefront. It is possible to describe classical aberrations that are represented by two Zernike coefficients, such as astigmatism, by the orientation in degrees and RMS magnitude. The magnitude is obtained by summing the appropriate normalised Zernike coefficients in quadrature.

The wavefront aberrations for the 20 minutes recovery time after a single shot were analysed. Figure 2 shows the magnitude and orientation of astigmatism for the alignment beam after a single shot for a 35 minute period.

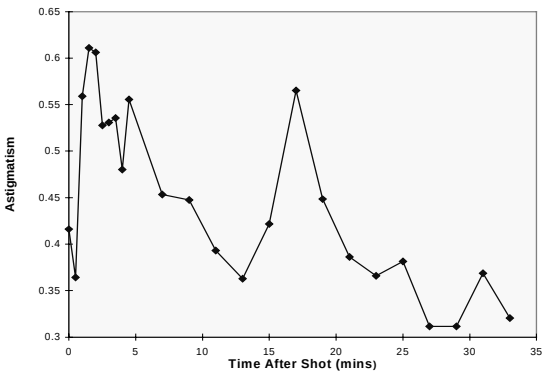

Figure 2a. Magnitude of astigmatism following a single shot

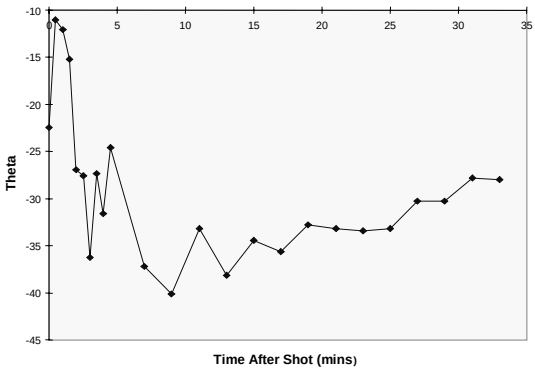

Figure 2b. Orientation of astigmatism after a single shot

The results of this analysis shows that a secondary astigmatism is introduced such that the value of magnitude for this aberration increases by approximately 50%. It returns to its value prior to the shot after a period of about 25 minutes. A rotation of the axis of astigmatism of about 10 degrees can also be observed which also recovers to its original value after a similar time. This result confirms that the wavefront could potentially be improved by deliberately introducing a controlled amount of astigmatism to compensate that introduced in the system optics. One feature of special interest can be observed in these figures and this is the effect of the blowers switching off after 15 minutes. The magnitude of astigmatism increases for a short time when the blowers are switched off.

Shot Sequence

An evaluation of any accumulation of thermal wavefront errors was performed by monitoring the wavefront for a series of 8 consecutive single shots fired on a 20 minutes cycle, although on a normal operational schedule the Vulcan laser system is

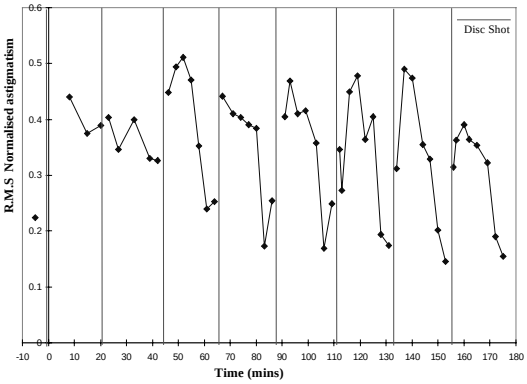

Figure3a. Magnitude of astigmatism in a sequence of single shots.

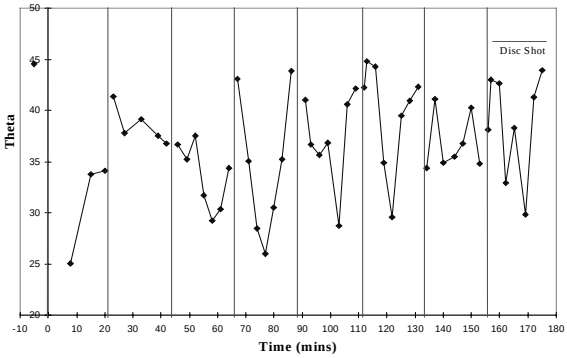

Figure 3b. Orientation of astigmatism in a sequence of single shots.

usually fired with intervals longer than 20 minutes. Figure 3 shows the astigmatism magnitude and orientation and figure 4 shows the magnitude for coma. The graph for the magnitude of the astigmatism shows an increase for the first two shots and it is only in the rest of the shots that the magnitude increases but it recovers to its nominal value after twenty minutes. The trend for the orientation of the astigmatism is very similar. For the first three shots the orientation changes to a value of ~35 degrees and it is only after the third shot that the orientation changes, but consistently recovers after 20 minutes. This shows that it is possible to correct the astigmatic wavefront by introducing a controlled amount of astigmatism whose magnitude and orientation would not have to be altered in a normal operational day.

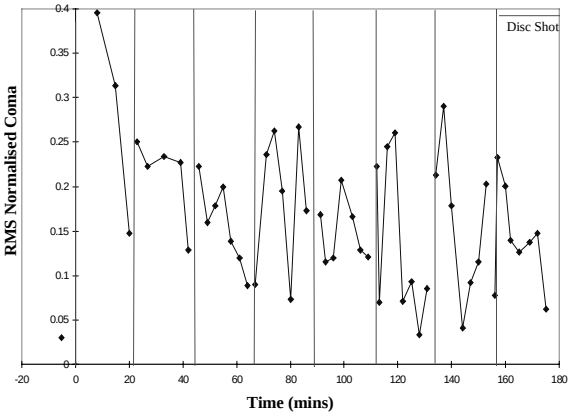

Figure 4. Magnitude of coma in a sequence of single shots.

When looking at the magnitude of coma, it increases for the first two shots although the trend during the sequence is to decrease to its initial value. The next residual aberration is triangular astigmatism, figure 5 shows the values of this aberration for the series of shots. The results show that the magnitude increases for the first two shots but the trend during the sequence is to decrease to a lower value than its initial value.

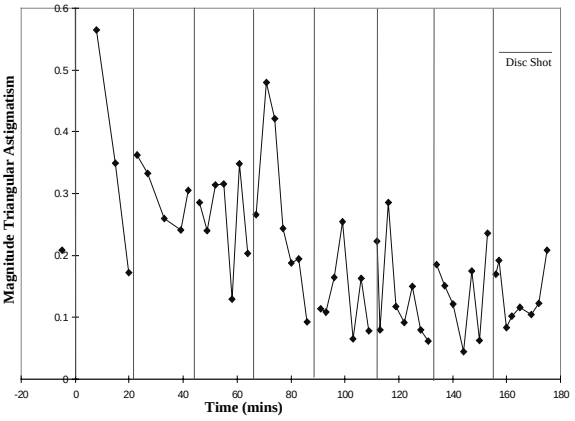

Figure 5. Magnitude of triangular astigmatism in a sequence of single shots

Defocus was also studied for this series the results plotted in figure 6 show how this term increases after the shot and recovers, but after the trend is to decrease as the number of shots increases, however in the case of defocus it is compensated for in the target areas.

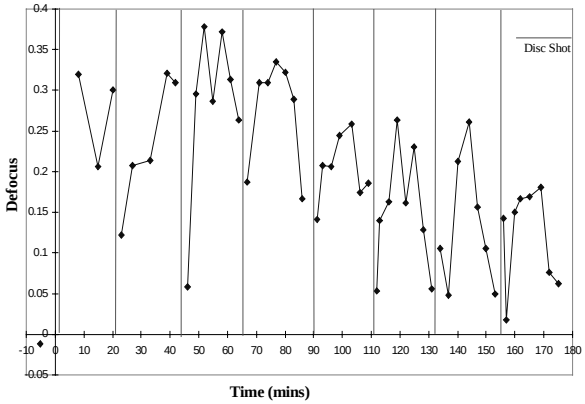

Figure 6. Defocus in a sequence of single shots

Conclusion

We can conclude from this study that the wavefront on the CPA line is predominately aberrated by a fixed optical source. It also shows that the main aberration is astigmatism. The Vulcan laser can be fired every twenty minutes, this analysis shows how the magnitude and orientation of astigmatism recover in this period of time. Therefore the wavefront could potentially be improved by deliberately introducing a controlled amount of astigmatism to compensate that introduced by the system optics. The results obtained in the series of shots show that the wavefront does not change significantly in a normal operational period and therefore the correction of the wavefront with a static corrector would be feasible.

References

1. C N Danson, 'Characterisation of the Vulcan CPA beam giving intensities of 10^{19} W cm^{-2}'
   Central Laser Facility Annual Report 1995-1996,
   Rutherford Appleton Laboratory

2. C. Hernandez-Gomez, A Radial Shear Interferometer
   Central Laser Facility Annual Report 1997-1998,
   Rutherford Appleton Laboratory

3. Fringe Analysis / Wavefront - 'FRIN' *from* Oxford Framestore Applications, Oxford, U.K.

4. V. N.Mahajan,' Zernike Circle Polynomials and Optical Aberrations of Systems with Circular Pupils'
   Engineering and Laboratory Notes in Optics and Photonics News 5, December 1994.

5. V.N. Mahajan,' Zernike AnnularPolynomials and Optical Aberrations of Systems with Annular Pupils'
   Engineering and Laboratory Notes in Optics and Photonics News 5, November 1994.

Vulcan Intensity Increase by Wavefront Quality Improvement

C Hernandez-Gomez, J Collier, S Hawkes.

CLRC Rutherford Appleton Laboratory, Chilton, Didcot, Oxon OX11 0QX. Email c.hernandez-gomez@rl.ac.uk

Introduction

The improvement of the wavefront quality can be achieved by deliberately introducing into the amplification chain a controlled amount of an aberration in such a way as to cancel the aberration that is intrinsically present in the chain. The deliberate introduction of such a controlled aberration may be done in a dynamic or static way. Dynamic correction is versatile, enabling the correction of any aberration. It is however also complex and expensive. Because the previous study had shown the primary aberration to be astigmatism of fixed characteristics, a static correction of just this aberration was undertaken.

Wavefront Correction with a Static Corrector

Following a recent analysis of the wavefront quality of the chirped pulse amplification line of the Vulcan laser system [1], it was considered that it might be possible to improve the wavefront quality and thus achieve a focal spot size closer to diffraction limit. The results of the study showed that the main contribution to the aberrated wavefront was an astigmatism of fixed magnitude and orientation that remained constant in character on a shot to shot basis. Initial calculations indicated that the removal of this fixed astigmatism in the wavefront would reduce the focal spot size by at least a factor of two. This would mean an increase of intensity by factor of four and would potentially make it possible to achieve intensities greater than 10^{20} W cm^{-2}.

To correct the wavefront two elements are required: a wavefront sensor and a wavefront corrector located at suitable points in the beam path. The wavefront sensor chosen was a radial shear interferometer [2] as used in the wavefront study. This was located at the output end of the amplification chain prior to the beam entry into the target areas. The wavefront corrector used was a deformed standard infrared mirror. An almost perfect artificial astigmatism can be created over the central two thirds of its diameter by bending this mirror using 4 micrometers as shown in figure 1. To achieve this, the mirror was placed into a specially designed mount. Prior to installing the mirror, the correct amount of astigmatism was introduced into the mirror by placing it in an interferometer and adjusting the micrometers. After each adjustment a Zernike polynomial analysis was conducted and the micrometers further adjusted such that the quadrature sum of the two appropriate Zernike coefficients governing astigmatism were identical to that determined from the system study. An approximate 1.5 λ peak to-valley (p-v) astigmatism was introduced with a residual non astigmatic distortion of 0.2 λ p-v. This mirror was installed replacing the retro mirror at one end of the CPA beamline double pass disk amplifier and rotated to minimise the appropriate astigmatic Zernike terms of the wavefront recorded by the interferometer at the output of the beam line.

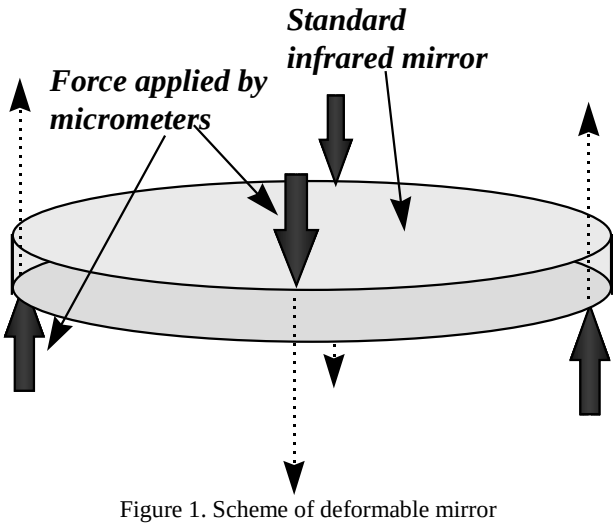

Figure 1. Scheme of deformable mirror

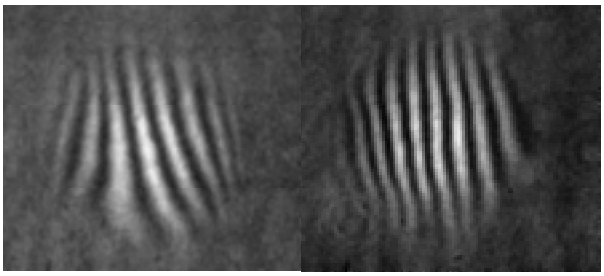

Figure 2. Interferograms of beam 8 before and after the installation of static corrector

Interferograms of the wavefront prior to and after the installation of the wavefront corrector are shown in figure 2. Without the static corrector the wavefront showed 1.5 λ p-v error. The corrected wavefront showed a 0.6 λ p-v error. A far field monitor was also installed at the output of the CPA line. Far fields of the alignment beam with and without the static corrector were also recorded. These far fields were processed to obtain radial integrations, the results of which are shown in figure 3. The figure shows an in increase of intensity by a factor of 4.

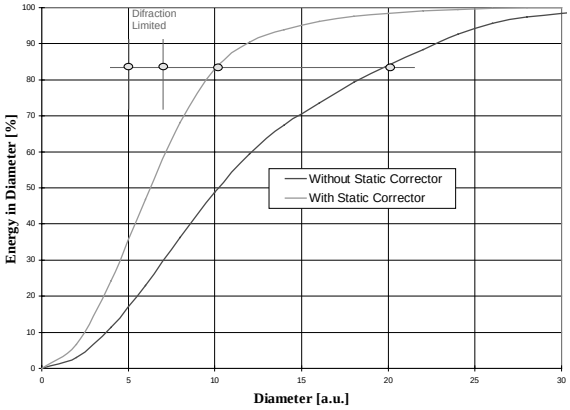

Figure 3. Radial Integration of Far Fields

Finally it should be noted that the CPA beamline is rectangular apodized to match the grating compressor aperture. Corrected wavefront interferograms recorded with the apodized beam indicate a 0.35 λ p-v wavefront error and far fields recorded after the grating compressor show a virtually diffraction limited spot diameter with the CW alignment beam.

References

1. C. Hernandez-Gomez, 'Wavefront Analysis of the Vulcan Laser System', Central Laser Facility Annual Report 1997-1998, Rutherford Appleton Laboratory

2. C. Hernandez-Gomez, 'A Radial Shear Interferometer' Central Laser Facility Annual Report 1997-1998, Rutherford Appleton Laboratory

Large Optics and Small F Numbers: Further Developments in the Vulcan Ultra-High Intensity Interaction Facility

R Allott, J Collier, C Danson, P Flintoff, M Harman, P Hatton, C Hernandez-Gomez, D Neely, T Winstone.
CLRC Rutherford Appleton Laboratory, Chilton, Didcot, Oxon., OX11 0QX. Email R.Allott@rl.ac.uk

Introduction

The commissioning of the target area for the Phase 1 petawatt upgrade of the Vulcan facility was reported last year[1]. At that stage the new large aperture diffraction gratings had not been delivered. This article reports on the installation of the new CPA compression gratings and the subsequent use of new fast focusing optics designed to handle the increased beam dimensions. The combination of the large gratings and fast optics further increases the intensity delivered to target.

Installation of New Large Aperture Diffraction Gratings

The new large aperture diffraction gratings (Jobin Yvon) have dimension 420 mm x 210 mm, 1740 lines/mm and are gold coated holographic in nature. The resulting beam has dimension 190 mm x 110 mm allowing up to 80 J to be delivered to target.

Figure 1. 420 mm x 210 mm Diffraction Grating

Installation of the gratings required the re-design of the CPA diagnostics suite based on a 280 mm diameter lens aspherised to give wavefront aberration <λ/10 @ 633 nm to accept the full beam and the commissioning of a new full beam interferometer[2] for on-line analysis of the reflected wavefront after the compressor. Alignment tolerances for such a large compression system are tight in particular for optimum performance (pulse length < 500 fs) the parallelism has to be set to within 50 μrad. The figure below shows the reflected wavefront quality of the first CPA grating in the first order which is <λ/6 @ 633 nm over 80% of the total area.

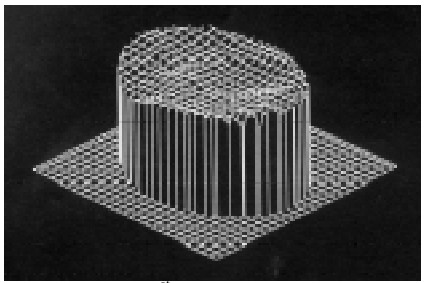

Figure 2. Plot of 1st Order Reflected Wavefront

Achieving Ultra-High Intensities: Fast Focusing Optics

In order to achieve intensities of 10^{19}-10^{20} Wcm^{-2} the focal spot diameter must be of the order 10 μm or less. This requires excellent beam quality (< 3 x diffraction limited) and fast optics <F3. Two focusing optics have been specified and purchased. The first is an F3 off-axis parabola (SORL) 230 mm square, focal length 600 mm, reflected wavefront <λ/8 @ 633 nm. The second is an F1.5 on-axis parabola (Optical Surfaces Ltd.) 255 mm x 130 mm, focal length 225 mm, reflected wavefront <λ/8 @ 633 nm. Both parabolas are HR coated for 1053 nm and 527 nm (SLS Optics). The incredible quality of these optics achieved over very large apertures is a testament to the skills of our optical suppliers.

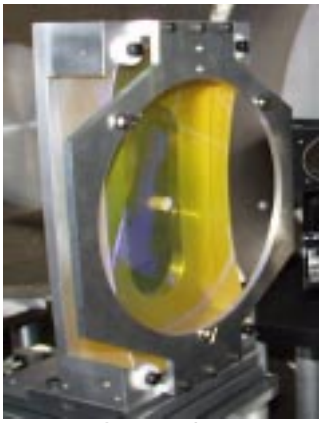

Figure 3. Large Aperture F1 On-Axis Parabola

Overall system Performance

The dimensions of the new CPA gratings allows the energy delivered to target to almost double. Coupled with the excellent surface quality of the gratings and focusing optics the intensity has been measured[3] at $5x10^{19}$ Wcm^{-2}. An adaptive optic is currently under test[4] to further improve the beam quality (<1.5x diffraction limited) and we thereby expect to exceed an intensity of 10^{20} Wcm^{-2} on target.

Applications

With the potential to deliver intensities up to 10^{20} Wcm^{-2} the ultra-high intensity interaction facility opens up a wealth of novel and exciting plasma physics. For example high harmonic production, nuclear activation, parametric instabilities, electron acceleration, relativistic effects and measurement of ultra-high magnetic fields. Also studies relating to the fusion programme, in particular the fast igniter scheme, are in progress.

References

1. D Neely et al CLF Annual Report RAL-TR-97-045 p194
2. C Hernandez-Gomez et al , A Radial Shear Interferometer, CLF Annual Report 1997/98, Rutherford Appleton Laboratory
3. C Danson et al, The Generation of Focused Intensities of $5x10^{19}$ $Wcm^{-2,}$ accepted for publication in Laser and Particle Beams, 1998
4. C Hernandez-Gomez et al, Vulcan Intensity Increase by Wavefront Quality Improvement, CLF Annual Report 1997/98, Rutherford Appleton Laboratory

Cerberus, a redesigned network interlock system for use with the Vulcan and Astra lasers and throughout the CLF

C J Reason, W Lester, E Divall.

CLRC, Rutherford Appleton Laboratory, Chilton, Didcot, Oxon., OX11 0QX. Email C.J.Reason@rl.ac.uk

Introduction

During the operation of the gas laser Sprite, a networked interlock system was specified, written, installed and commissioned called Cerberus (after the multi-headed dog guarding the gateway to Hades in Greek mythology). This was based on a single PC and a number of Intel processor cards based in 80186 chips, in STE crates linked on a token ring (arcnet) network. This has been described elsewhere [1), 2)] . This operated successfully on Sprite and Titania.

The interlock system on the Vulcan laser has component parts dating back to the original installation of Vulcan (some 20 or more years). This has become increasingly difficult to maintain and extend so it was decided to install an interlock system similar to that on Titania. Also the Astra (HPHR) project would need a new interlock system. It was decided to take this opportunity to update the components, change the network and introduce some additional rules to make the operational aspects of the system more user friendly.

Changes to the hardware

The cost of assembling an interlock station (processor, video card, display, digital IO, networking, a crate and power supply) was investigated and found to be substantially higher than purchasing a basic PC with a digital IO board. It was therefore decided to base the interlock system round a number of PC's with 192 way digital IO boards. This made the programming and networking of the stations much simpler. The specification of the PC was the minimum available from the laboratory supplier (16 Mbytes of memory, a 2 Gbyte hard disk, around 200 MHz speed, a sound card, a networking card, and the usual keyboard, mouse, floppy disk etc. capable of running DOS) although this was an over specification.

The signal conditioning, signal routing and interlock control system have been implemented in eurocrate in a modular format which gives a uniform look and feel to each area.

Changes to the network

The original Cerberus system was based on a token ring network. This was chosen because the timings on this type of network are deterministic, allowing us to predict the timing response of the network. After installation, a problem was discovered. As the token was always present on the network, electrical noise from the operation of the laser was picked up by the wires and the token destroyed. This meant that one of the stations was lost. The time taken to rebuild the network was longer than the required response time of the interlock system and the watchdog timeouts (i.e. just under one second). During operation, the interlock system shut down after most laser shots. A proprietary circuit was developed to detect this lost token and force a rebuild of the network in a much shorter times-scale than the watchdog timeout. This worked successfully.

It was decided to change the network to Ethernet in the new system because it is a wider standard than arcnet, is easily available and inexpensive. Its normal state is quiescent (in particular at the time of a shot) unless it is carrying a message. The probability that any electrical pickup will resemble a valid message packet is vanishingly small so noise will be rejected by the system. If the noise coincides with a valid package, then the package can be re-sent after just a few micro-seconds.

The reason Ethernet was rejected at first was it was thought that the timings would not be deterministic (because of the collision detection mechanism). However if the system is isolated and operated in a mode with handshakes (such that only the main computer can put messages on the Ethernet and then waits for a reply from a station before sending another message) then Ethernet timings become deterministic. The new system is operated in this mode.

If noise turns out to be a problem, it will be trivial to convert the network to fibre optic operation.

The operating system and the code

The operating system used is DOS (version 6.2) because this is easily available on a PC and is not a multitasking operating system. Thus when the interlock code is running, nothing can interrupt it, making the timings of the code deterministic. All versions of Windows have some foreground / background tasking, making them unsuitable for this application.

The code is written in Pascal (Borland Turbo Pascal Version 7). This was chosen because it is strongly typed and its structure allows for a simple mapping between the interlock rules and code statements.

New rules

A number of additional rules are incorporated to facilitate the operation of the system without compromising the safety:

- The rooms in which a particular laser can produce a hazard are specified by the Laser Responsible Officer (LRO). This covers the case where it is impossible that a laser can produce a hazard in a room even when there is a clear beam path.
- Shutters are specified to be fast or slow by the LRO depending on the time they take to close being less than or greater than the watchdog time (typically 0.25 sec.). The hazard will propagate through a slow shutter but not through a fast shutter. Thus a tripped room will not cause an adjacent room to trip if they are separated by a fast shutter.
- A scheme has been devised for completely enclosed lasers. Such a laser will not cause a hazard in the room.
- The concept of a 'shot' has been extended to high power operation for lasers that operate in CW mode or at a high rep. rate.

Status

The Cerberus system is currently installed and running on Astra and will be installed on Vulcan during the first half of 1999.

References

1. Cerberus: a laser interlock system using Arcnet by
P Gottfeldt and C J Reason.
Computing and Control Engineering Journal, December 1993. P 281.

2. Cerberus, A Computerised Interlock System for the Sprite Laser by
C J Reason, C J Hooker, P Gottfeldt and W J Lester.
CLF Annual Report 1992 (RAL-92-020) p 143.

Characterisation of the Titania Raman Front End

E J Divall, C J Hooker, J M D Lister.

CLRC Rutherford Appleton Laboratory, Chilton, Didcot, Oxon., OX11 0QX

Introduction

When Titania came on line as an operational laser system in 1996 it was run solely as a single beam CPA machine. Later in 1997 the optical hardware was upgraded to enable the system to run in Raman mode, using twenty KrF beams to amplify a single Raman pulse. The Raman upgrade also required modifications to the front end to provide seed pulses of 30 or 60 ps, at both the pump (248.6 nm) and Raman (268 nm) wavelengths. (The pulse length can be changed by installing different hardware in the oscillator.) In many respects the new Raman front end is a cross between the old Raman system and the existing CPA one[1)]. Its layout is shown in figure 1.

Ultra-violet generation

The source laser for the Raman front end is an Argon ion pumped Tsunami (Spectra-Physics Ltd) producing an 82 MHz train of 30 ps pulses at 746 nm - one pulse every 12 ns. The average power from this laser was initially set to 950 mW (11.5 nJ/pulse). This pulse train passes through a 40 mm dye cell filled with a solution of Rh 700 in methanol and pumped by four beams from a frequency doubled Nd:YAG laser running at 8.3 Hz. The four beams are all split from a single original 6 ns pulse, but delayed by 1 ns intervals to give an averaging effect in the dye. This gives an overall pump pulse of approximately 9 ns, which is shorter than the 12 ns interval between Tsunami pulses so that only one of these is selected and amplified. A final stage of amplification takes place in a Ti-sapphire rod, also pumped by the Nd:YAG laser. This amplifier uses an arrangement of mirrors and double bi-prisms to steer the beam through the rod 8 times[2)]. Together these amplifiers raise the energy of a single pulse to 10 mJ.

Two BBO crystals are used to frequency triple the red pulses to 248.6 nm. The crystals used are approximately 7 mm square and 2.5 mm thick. The energy of the third harmonic pulses is 1 mJ in a 4 mm diameter beam.

After the tripling crystals a 2.5 m air spatial filter is used to produce a near-diffraction limited beam which is recollimated at 6 mm diameter.

Discharge laser

Initial calculations showed that there would be enough KrF energy after the tripling crystals to saturate Titania following splitting and amplification in Sprite. Experiments have shown that more energy is needed in the seed pulse to saturate Titania fully. The tripling crystals are already operating near the non-linear limit, so the UV pulses are single-pass amplified in a KrF discharge laser (LPX105). This provides the necessary energy at the cost of a slight reduction in beam quality which, fortunately, is not important on a Raman system where the KrF pulses are only used as pump beams and do not travel to target.

Raman generation

A 50% mirror is used to split the KrF beam in two: one half becomes the KrF seed pulse and the other is used to generate the Raman beam. Initially both are amplified by a single pass through the LPX105 discharge laser. The KrF seed pulse is delayed by 6 ns before entering the amplifier to minimize the energy variations resulting from timing jitter. This beam is then expanded to 20 mm and fed through to the multiplexer room. The Raman generating pulse is split into two. One beam is sent through the discharge laser for a second pass and becomes the pump beam for the first Raman amplifier. The other passes though an iris and is focused in a 2.6 m tube of methane (at 2.2 bar) to generate the seed Raman beam. The iris is used to control the input beam energy - too great an intensity loses efficiency as higher order Stokes frequencies are generated. A prism and pinhole arrangement is used as a spectral filter to remove the remaining KrF and other unwanted frequencies. The Raman seed beam is then spatially filtered before being amplified in the first Raman amplifier, another tube filled with methane at 2 bar. It enters this tube almost colinearly with the pump beam, so that they interact for the full length of the amplifier. After amplification this Stokes beam is also fed through to the multiplexer room.

Tsunami performance

For optimum Raman conversion it is important to have a stable transform-limited oscillator. Measurements with the autocorrelator showed the Tsunami pulse length and stability to be dependent on the pump power (figure 2). To give 60 ps pulses the Argon ion laser was run at 8.5 W. However this configuration was found to give poorer quality UV pulses, which were believed to give poorer conversion efficiency in the main Raman amplifiers as a consequence of the input pulses not being transform-limited. We therefore set up a streak camera and spectrometer to measure the pulse length and bandwidth of the frequency-tripled pulses, making sure that the spectrum and

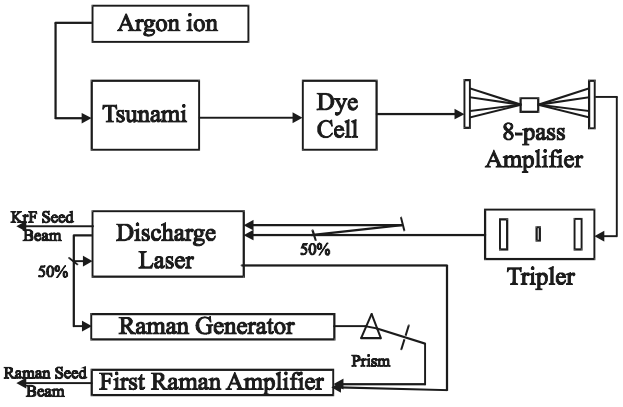

Figure 1. Schematic diagram of the Raman front end

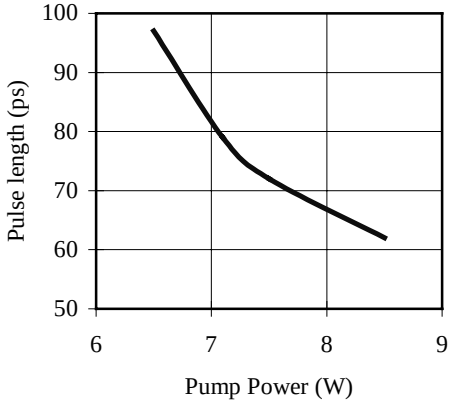

Figure 2. Tsunami pulse duration as a function of pump power

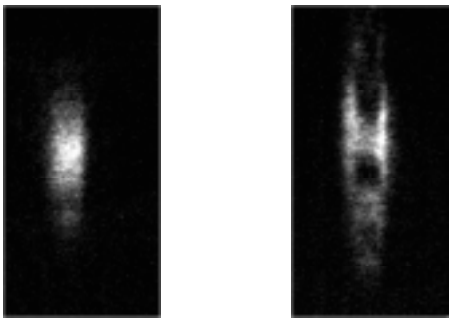

Figure 3. Low intensity (left) and high intensity (right) streaked images of the output from the tripler

streak were captured simultaneously, as there were significant pulse-to-pulse variations.

The tripler showed a 10% efficiency in converting from 746 nm to 248.6 nm. Replacing the BBO crystals with KDP (approx. 2 cm thick) made no difference to the tripling efficiency.

Using a streak camera it was found that there were significant unwanted non-linear effects present in both the KDP and BBO crystals. If the incident red intensity was increased beyond 1.3×10^9 W/cm^2 then the pulse temporal profile showed a distinct break up into two parts, (see figure 3). The spectrum was slightly broadened, but the effect on the spectrum was far smaller than on the pulse profile. This was greatly reduced by increasing the beam divergence through the 8-pass amplifier, which reduced the intensity at the crystals. Neither the air focus in the spatial filter nor the amplification in the discharge laser had any measurable effect on the spectrum or streak.

By plotting the time-bandwidth product of the pulses as a function of energy out of the TiS amplifier, we were able to establish a maximum operating power which still gave pulses reasonably close to the transform limit, (see figure 4). However, although individual pulses were all close to the transform limit, under some conditions successive pulses could vary in length by ±25%, with a corresponding variation in bandwidth. It became apparent that the stability of the pulse length and the spectral width varied with the pump power to the Tsunami. By experiment we found that the least fluctuation in both quantities occurred at a pump power of 7.2 W, so this was chosen as the operating point for the laser.

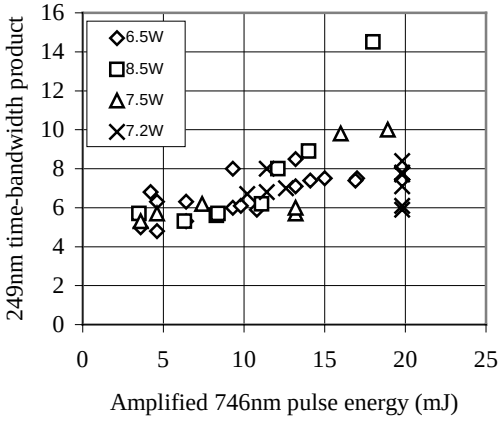

Figure 4. Time-bandwidth product after the tripler as a function of 746 nm pulse energy and Tsunami pump power

Conclusions

After the modifications described, the 60 ps pulses generated by the Titania front end were nearly transform-limited and were both spectrally and temporally smooth.

References

1. J M D Lister, E J Divall, G J Hirst, T M J Kendall, A K Kidd, I N Ross, CLF Annual Report 1996/7, RAL-TR-97-045 pp.202-203 (1997)

2 I N Ross et al, 'Multipass optical system', Patent No. 9517755.6 (Aug 1995)

Design of Handling and Testing Equipment for Titania and Sprite Laser Cells

S Hancock, B E Wyborn.

CLRC Rutherford Appleton Laboratory, Chilton, Didcot, Oxon., OX11 0QX. Email S.Hancock@RL.AC.UK

Introduction

Operational experience on the Titania laser revealed a need to improve the controlled procedures for the foiling, testing, assembly, and installation of the gas laser cells used in the Titania and Sprite KrF amplifiers**.**

Specialised equipment has been designed to improve the handling and testing of these cells and is described in further detail in this article. It should be noted that the Titania and Sprite cells are different in their physical dimensions, in their assembly and sealing arrangements, and in their method of installation. The design of the new equipment caters for these differences.

Foiling

New jigs have been designed to adequately support both cells during each facet of the foiling procedure, from the initial cleaning, through the etching procedure, to final gluing of the foils to the cells. Transportation of the cells between buildings after cleaning and etching has also been refined to eliminate possible contamination.

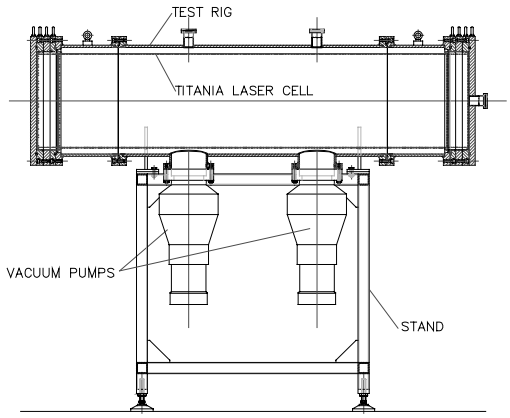

Figure 1. Titania laser cell in new test rig

Testing

A new rig has been purpose designed to test each of the foiled cells. Confidence in the test facility is essential to ensure confidence in the completed assemblies.

Figure 1 shows the test rig consisting of a 500 mm diameter vacuum vessel and ancillary equipment. This vessel is manufactured from either stainless steel or mild steel nickel-plated to minimise outgassing during use, thus giving confidence that gauge readings are representative of the actual cell integrity.

The test vessel is supported such that the loading of each cell can be carried out without any fear of damage taking place during the handling procedure. Each end of the vessel was required to give easy access for leak detection equipment to be used with confidence. A secondary vacuum test can be carried out, by sealing the central void with additional end flanges and pumping the internal space. The resulting pressure difference gives further information to establish the cell's integrity. The stand will also support such ancillary equipment that may be required to carry out all necessary operations on each cell.

Assembly

Once the cell has been satisfactorily tested various mechanical components are assembled into position before installation. At this stage of the procedure the cell is at a vulnerable state. The glued foils have been pre-formed to the shape of the hibachi grid, and can be accidentally damaged, therefore the carefully designed assembly jig offers as much protection to the vulnerable areas as possible but still allows easy access for the assembly as required. Figure 2 shows the Titania cell ready for installation on this assembly jig.

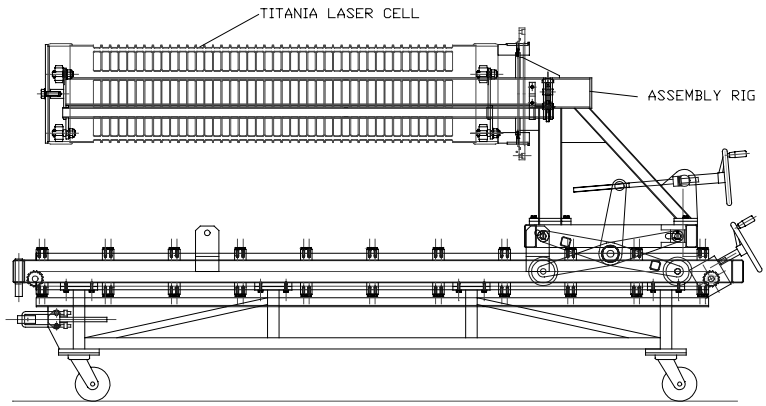

Figure 2. Titania cell ready for installation

High Energy Operation of Titania for Materials Processing

G J Hirst, E J Divall, A K Kidd.

CLRC Rutherford Appleton Laboratory, Chilton, Didcot, Oxon., OX11 0QX. Email G.J.Hirst@RL.AC.UK

Introduction

The optical layout of Titania for materials processing was described in last year's Annual Report[1]. The aim was to deliver 20 ns 249 nm pulses with up to 1 J cm^{-2} fluence and maximum possible fluence uniformity across a large area (up to 125 mm diameter). The scheme used three beam lines, temporally multiplexed through the Sprite and Titania amplifiers and then demultiplexed to target. The beam on each one was image-relayed from a plane near the output of a quasi-ASE source in the Front End Room.

Diagnostics

The diagnostic suite used to monitor the system performance is shown schematically in figure 1. Because the beams are image-relayed it is necessary to carry out the monitoring in a plane which is equivalent to the target plane. The large beam size requires the use of a large beam splitter and the only such optic available to us was a 15 mm thick uncoated silica flat. This has ~4% Fresnel reflectivity on both its front and back surfaces and must be used at near-normal incidence to prevent the front-reflected and back-reflected images from being significantly displaced in the equivalent plane. Near-normal operation requires, in turn, that the beam splitter be placed a long way (~10 m) from the target plane to allow the incident and reflected beams enough distance to separate.

The important performance parameters are fluence uniformity (time-integrated), pulse energy (time- and space-integrated) and temporal pulse shape (space-integrated). The fluence uniformity is measured by imaging the fluorescence from a glass flat onto a CCD camera. The glass flat is illuminated by light taken from the diagnostic beam using a 3 mm thick uncoated silica splitter. Pulse energy is measured using a pyroelectric detector (Molectron model no J50) with a lens to reduce the beam size. This is again fed from a splitter in the diagnostic beam. The temporal pulse shape is measured by a vacuum photodiode (ITL model no TF1850).

For some experiments a 2 cm × 2 cm mask is used just before the target plane. Under these circumstances corresponding masks are placed just before the equivalent diagnostic planes.

System performance

The maximum specified fluence of 1 J cm^{-2} can be reached quite comfortably when the system is operating optimally. As the gas mixtures in the lasers age, however, the output does fall. Furthermore the shot-to-shot reproducibility worsens as gain saturation becomes a less effective stabiliser. The fluence can be controlled by inserting attenuators into one or more of the beam lines. An order of magnitude reduction in the fluence can be achieved this way although the temporal pulse shape and the fluence uniformity may be changed somewhat. When the irradiated area is just 2 cm × 2 cm the fluence can be doubled by spatially splitting each full beam into two and overlapping the two samples at the target.

The temporal pulse shape on each beam line follows that of the ASE source (with some sharpening of the rising edge and reduction of the intra-pulse modulation as a result of gain saturation in Titania). The modulation can be reduced further by adjusting the demultiplexing delays on the individual beam lines. The FWHM of the pulse is typically 15 ns measured at the target.

The fluence uniformity has, to date, only been measured within a 2 cm × 2 cm aperture. Over this area the peak to valley fluence variation is 10-20% of the average fluence. The causes of the spatial nonuniformity appear to be, in decreasing order of importance, i) nonuniformity in the source, ii) fringes caused by diffraction (or, possibly, interference) and iii) nonuniformity in the amplifers' gain. The most straightforward way of improving the fluence uniformity would be to improve the source, by increasing both the spatial uniformity and the incoherence (increased incoherence would lead to increased intrinsic divergence which would improve the spatial averaging through the amplifier chain). The price to be paid for this would be an increased gain requirement in the amplifier chain and a reduced depth of field at the target plane.

References

1. G J Hirst, E J Divall, A K Kidd and J M D Lister Central Laser Facility Annual Report 1996-7, RAL-TR-97-045, 208 (1997)

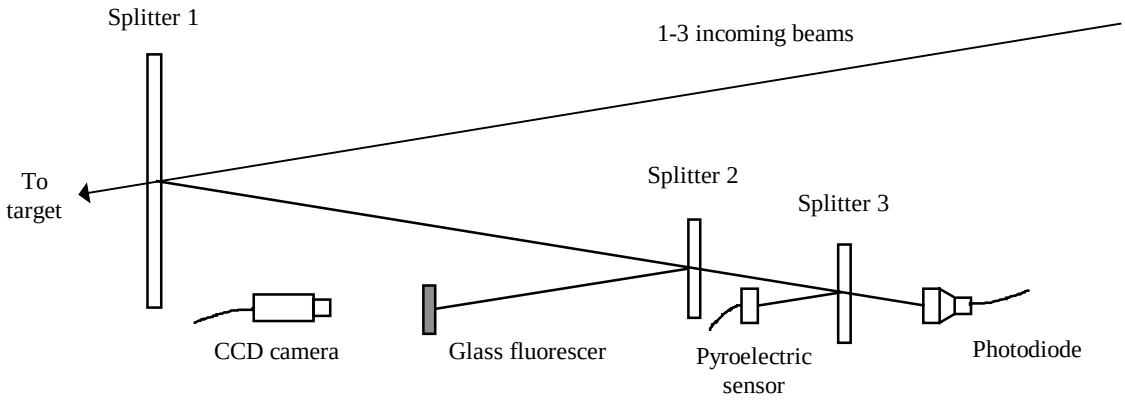

Figure 1. Layout of the Titania diagnostics suite in Materials Processing mode

Performance of the Titania Power Raman Amplifiers

C J Hooker, E J Divall, G J Hirst, A K Kidd, J M D Lister.

CLRC Rutherford Appleton Laboratory, Chilton, Didcot, Oxon., OX11 0QX. Email C.J.Hooker@RL.AC.UK

Introduction

Operation of Titania in Raman mode commenced in May 1997, following a lengthy installation period in which 120 large-aperture mirrors and other optics were installed on the frameworks in the multiplexing area [1]. The gas cells for the two Raman amplifiers, RAT2 and RAT3, were installed on their frameworks, and the pre-assembled float-glass lightguides mounted inside them. The other main elements of the Raman beamline were the two Vacuum Spatial Filters (VSFs), each 18 metres in length. The second of these, VSF2, is placed between the two Raman amplifiers as an expander, and also ensures the input to the final amplifier is as close to diffraction-limited as possible. The pump energy for RAT2 is derived from two beams from Titania, which for reasons of synchronisation are numbers 1 and 2; two 75 mm mirrors are placed in each beam to obtain four beams of the correct size for the 60 mm lightguide. RAT3 is pumped by beams 5 to 24 from Titania, which are arranged in four groups of five, above, below and to either side of the axis of the amplifier at an average angle of three degrees to it. The output of RAT3 is sent through an evacuated beam pipe into the target area.

Initial performance

The early performance of the laser was characterised by low output energy from both Raman amplifiers. The maximum recorded output from RAT2 was 420 mJ, but the output was very erratic, with 200 mJ being more typical, and the greatest conversion efficiency was 18%, far less than the expected value. The near-field of the output Stokes beam exhibited horizontal and vertical striations, suggesting imprinting of pump non-uniformities. The oscillator beam at the output of VSF2, following RAT2, appeared smooth and diffraction-limited; on a shot, however, the transmission of this VSF was very low. The output from RAT3 on full shots was also quite variable, but the maximum output was just over 10 J, irrespective of input energy, pump energy or variations in the partial pressure of methane in the amplifier.

Performance analysis and system modifications

The erratic performance of RAT2 contrasted strongly with the apparently clamping on the output of RAT3, and it was presumed that these two effects had different causes. Variations in the spectrum of the oscillator pulses might account for the former, and some combination of Two-Photon Absorption (TPA), the "pancake" effect, spectral broadening of the Stokes in the second VSF and insufficient gain length in RAT3 itself might explain its poor output. The throughput of VSF2 reached its theoretical value only after the cell was flushed with helium and evacuated, and decreased gradually over time thereafter. This was consistent with a leak in the pipework causing a build-up of air pressure, and subsequent self-focusing of the beam which reduced the transmission through the pinhole.

Calculations of TPA in the RAT3 windows showed that although significant, it should not reduce the available pump energy so much that the output was only 10 J, and would not account for the clamping of the output. An absorption measurement made on one of the windows using the oscillator output gave a value for the TPA coefficient of 0.066 ± 0.01 cm GW^{-1}: the accepted value is 0.07 cm GW^{-1}.

With a pump beam angle of 3 degrees, the pancake effect causes an apparent pulse stretching of 28 ps across the 16 cm aperture of the lightguide, which would almost double the effective pulse length near the edges of the guide, and might result in loss of conversion efficiency. Finally, although computer modelling of the amplifiers had shown that a length of 1 m was sufficient to saturate the output of RAT3, if the gain were reduced by some other effect, an increase in length might be needed to obtain the expected output energy.

Campaign for improved performance

The first stage of the campaign involved the changes to the front end and the introduction of better operating procedures described elsewhere in this report [2]. These resulted in stable, near-transform-limited pulses of approximately 60 ps duration being fed into the main amplifier chains. As the poor performance of RAT2 was one of the main concerns in the previous run, its pump energy was boosted by removing the 50% beamsplitters in beams 1 and 2 after Sprite, which doubled the input to Titania on those beams, significantly increasing the pump energy to RAT2, although the number of pump beams to RAT3 was reduced from 20 to 18.

To ensure there would be sufficient gain-length in RAT3 this time, the amplifier housing was extended, and a second 1 m section of lightguide installed. A more accurate pressure gauge was fitted at the same time, so the overall gain could be controlled by varying the methane partial pressure.

Better diagnostics of the Raman amplifier pump energies were set up, using photodiodes to monitor the Rayleigh-scattered light from the beams just before they entered the amplifiers. To minimise the effects of light scattered from elsewhere in the room, the diodes were fitted with 249 nm interference filters and enclosed in boxes with carefully-designed light baffles. Although the laser pulse length was 60 ps, the scattered light reaching the diode originated from a volume of ~20 cm length swept out by the beam, effectively stretching the pulse seen by the diode to around 1 ns: this avoids overloading the diode. After calibration against a conventional calorimeter, the diode signals gave energies accurate to ±5%, with the advantage that no splitter plate had to be placed in the beam. An additional Rayleigh diode, with a 268 nm filter, was installed at the output of the second VSF, to measure the Stokes input to the final Raman amplifier. A number of leaks in the pipework of the VSF were eliminated and, to ensure a good vacuum, a turbomolecular pump was installed close to the centre section, giving typical pressures near the pinhole of $<5 \times 10^{-4}$ torr.

Performance of RAT2

With the changes described and seed pulses of better spectral quality, the performance of RAT2 was dramatically improved. Pump energies of 2 - 2.5 J were obtained, and after the timing had been optimised Stokes output energies were typically in the region of 1 J, with a maximum of 1.4 J. This corresponds to a pump-to-Stokes conversion efficiency of around 60%, which is similar to that achieved previously in the Sprite system. As expected, the transmission of VSF2 was more consistent as a result of the better vacuum, and on most shots it was close to the calculated value of 68%.

Performance studies of RAT3

Once RAT2 was working correctly, some shots were taken on RAT3 to carry out a timing scan. This showed an almost constant Stokes output of around 10 J over the timing range, the same maximum energy that was obtained previously. The small-signal gain was measured by blocking the pump beams to RAT2 so that the input to RAT3 consisted of the oscillator pulse alone. The output energy was between 9 and 9.4 J, which

from an input energy estimated at 30 μJ corresponds to a gain of 3.7×10^5. In fact, as the output was near the saturation level this is not the small-signal gain, which is clearly larger still.

One concern from the previous run was the amount of TPA loss in the windows of RAT3, which are 3 mm thick silica. One pump beam was dedicated to investigating this, using a pair of calorimeters to measure the energy in a 25 mm diameter portion of the beam before and after its passage through the amplifier (filled with helium for this experiment). Comparison of the ratio of the signals when all the beams were present with that when only the test beam was present gave a net transmission of 84%, or a loss of 16%, due to TPA in the two windows. This is the expected value for a thickness of 6 mm of silica at an intensity of 4.5 $GWcm^{-2}$ (54 J of pump energy). The transmission with 1 bar of methane in the cell was only 24%; this increased rapidly as either the number of beams or the partial pressure of methane in the cell were reduced. The pump energy was either being absorbed in the amplifier, or scattered so that most of it did not strike the calorimeter.

Pump beam spectral measurements

A simple etalon spectrometer was constructed to monitor the spectrum of one pump beam after passage through the amplifier: beam 5 was chosen because it has the longest air-path after Titania, and would be most likely to show any non-linear effects. During alignment, and to measure the front end spectrum, a kinematically-mounted HR mirror was used at the input, and the signal from the CCD camera integrated over about a hundred pulses. On shots, the mirror was replaced by an uncoated flat on a second kinematic mount, aligned at the same angle, while the mirror itself was moved into the beam to act as an attenuator, giving an overall reduction in sensitivity of $\sim 10^6$.

Spectra were recorded during the amplifier transmission measurements described above. With pure helium in RAT3, the amplified spectrum was not significantly different from that of the oscillator, but with 1 bar of methane the spectrum was broadened by a factor which was typically between 2 and 3. Transmission measurements were made with various proportions of methane (mixed with helium) in the cell, and the amount of spectral broadening was generally greater with higher methane concentrations and higher pump energies.

Spectra recorded when there was an input Stokes signal to RAT3 were still broadened, but also showed a narrow absorption feature. The width of this feature was the same within error limits as that of the KrF oscillator spectrum, and the interpretation is that it represents depletion of the pump radiation lying within the bandwidth accessible to the Raman process. Since the seed Stokes pulse is generated from the oscillator, the correspondence of the width of the feature with the oscillator spectrum is not surprising. The output of the amplifier varied with methane concentration, from 9.4 J at 100% up to a maximum of 16.2 J at 47%. On further reduction of the methane concentration the output energies became smaller again. Spectral broadening could easily account for the clamping of the output energy, if it redistributes the pump energy so that the amount available within the Raman bandwidth is more or less constant.

Higher Stokes phenomena

Previous work with Raman lasers [3, 4] had shown the significance of second Stokes in limiting the output of the amplifiers. A mini-spectrometer on a PC card with a fibre-optic input was used to examine the output from RAT3 to determine what other wavelengths were present. This clearly showed three lines: KrF, first Stokes and second Stokes, with the last being stronger than the first Stokes. To examine the angular distribution of these wavelengths, a lens of 4.3 m focal length

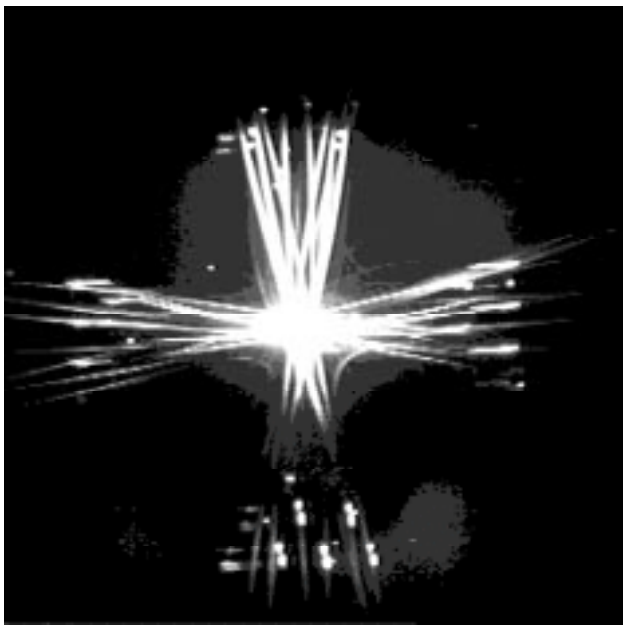

Figure 1. Far-field output of RAT3 with high gain

was placed just after RAT3, with a pair of glass plates (uncoated) at 45° immediately after it to provide ~100× attenuation. The far-field image of the amplifier output was received on a large screen of card at the focus of the lens and viewed with a CCD camera. A typical image is shown in figure 1.

The central spot is the first Stokes. The groups of spots and short straight lines are pump radiation that has been transmitted directly through the guide or reflected from the slightly curved walls. The long curved rays are second Stokes generated by the interaction of scattered Stokes with the phonon waves in the methane [4]. Once generated, the second Stokes is amplified at the expense of the first Stokes. On shots taken with no Stokes input, the spectrometer showed both pump and first Stokes, and a large, diffuse area of self-generated Stokes emission was observed in the far-field. Calorimeter measurements showed this contained over a joule of energy.

The length of RAT3 was reduced to the original 1 m, and the measurements were repeated with 100% methane in the amplifier. The second Stokes rays were absent, and there was no indication of self-generated first Stokes. However, the maximum output energy was still around 10 J. The etalon spectrometer was set up to record two parts of beam 5: one from before the amplifier in addition to the one transmitted. These spectral measurements showed the transmitted intensity was depleted by a factor of 25, compared with a factor of only 4 obtained from the calorimeter data. The best conversion efficiency was 22%. At the time of writing these discrepancies in the energy balance measurements have not been resolved, and the poor performance of RAT3 remains unexplained.

References

1. D A Bates et al,
   CLF Annual Report 1996-7, RAL TR-97-045, p.206, (1997)
2. E J Divall, C J Hooker, J M D Lister,
   See elsewhere in this Report
3. C J Hooker, E J Divall, G J Hirst, J M D Lister, M J Shaw, D C Wilson,
   CLF Annual Report 1994-5, RAL TR-95-025, p.94 (1995)
4. C J Hooker, E J Divall, G J Hirst, J M D Lister, M J Shaw, D C Wilson,
   Phys. Rev Lett., 74 4197 (1995).

Redesign of the Sprite Pulse Forming Lines (PFLs)

A K Kidd, P E Hatton, G J Hirst.

CLRC Rutherford Appleton Laboratory, Chilton, Didcot, Oxon., OX11 0QX

Introduction

As a consequence of the Titania upgrade begun in 1995, the Sprite amplifier is now required to accommodate a longer optical pulse train [1]. Making allowance for amplifier fill time, switch jitter and gain risetime, the amplification of 48 pulses of 1.5 ns separation means that the electrical pulse length seen by the electron beam diodes has been increased from 60 ns to 120 ns. No modifications were carried out on the laser-triggered PFL switches or on the diodes themselves, but the physical length of the PFLs was doubled from 1.05 m to 2.1 m. This increase in length, coupled with the removal of the water capacitor when the Marx generator was replaced, has increased the PFLs' electrical charge time by more than a factor of 7 to 1.5 µs. Although the PFLs are charged to the same voltage as before, the increased charge time places additional electrical stress on the switch insulator [2]. Problems have arisen during the past two years with laser triggering and insulator tracking. Six insulators have shattered on different switches in that time. In order to improve pulsed power reliability and reduce operational down-time, we undertook a re-design of the PFLs.

Mechanical design

The re-design was undertaken under the constraints of retaining as much of the existing hardware as was practical in order to save money and time. We have used the existing switch housing (aluminium), output section and trigger beam optics. The solution arrived at is shown in figure 1.

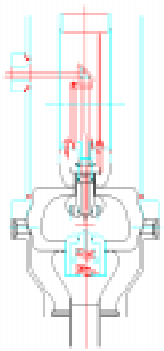

Figure 1. The new Sprite PFL design

Salient points of the design include:

The PFLs are made from aluminium. The electrode inners are brass enclosed in stainless steel outers. The insulator is cast from a single piece of epoxy resin block for which ε_r is 3.3.

The gradual curvature of the insulator surface away from the cathode diverts debris, resulting from shots, away from regions of high electric field. The higher electrical stress on the insulator makes reliable laser triggering particularly important. Unlike the Titania switch design (which uses two disk insulators) it was not possible to see directly into the Sprite switch to ensure a laser spark was present. The porthole on the side of the new switch housing does allow this provided the insulator surface is polished in this region.

Electrical design

The electrical design focused on reducing the electrical stress by reshaping the switch insulator. The insulator's radial dimensions are constrained by those of the switch housing but there is scope for modification in other directions. Specifically, the curvature and/or angle of orientation of the insulator may be changed to improve the electrostatic field grading along the water/insulator interface. The electrostatic field distribution was modelled using the two-dimensional MagNet [3] software package. The results are shown in figure 2.

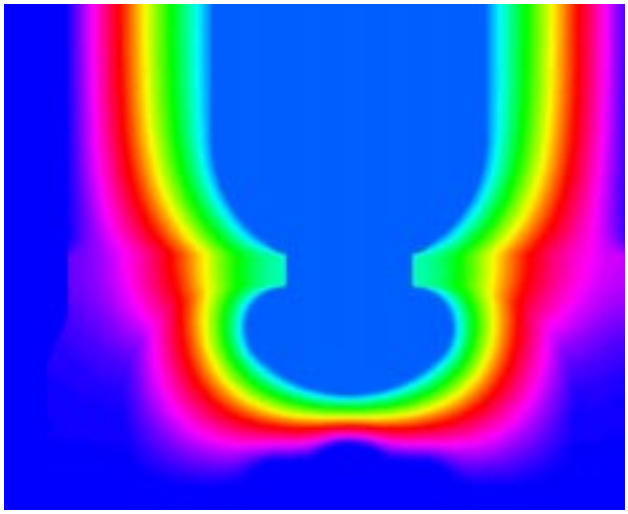

Figure 2. Equipotential lines in the redesigned Sprite switch

The main improvement of this design is that the shape of the cathode shields the triple junction (gas/insulator/electrode) from high electric fields. The field at the triple junction (which tends to be one of the weakest points in any high voltage insulating system) is very much lower than that of the current design (15 $kVcm^{-1}$ compared with 38 $kVcm^{-1}$). Furthermore, the gradual curve on the insulator produces a more gradual field distribution along the insulator gas interface. The peak electric field occurs 1-2 cm along the curved surface and is 90 $kVcm^{-1}$ (compared with the current 110 $kVcm^{-1}$). All figures are for a Marx charge voltage of 60 kV. It was found that no significant improvement in electric field uniformity was possible by angling the reverse side of the insulator due to the overriding influence of the inner surface.

Summary

An electrostatic modelling package has been used to predict the performance of proposed improvements to the Sprite switch and compare it with that of the existing design. This procedure paid particular attention to the electric fields at the triple junction and the water/insulator interface. The triple point electric field is 60% lower than with the existing design and the peak electric field along the insulator surface is 20% lower. The resulting design uses the current switch housing and should allow the Sprite laser system to be operated more reliably than at present.

References

1. S Angood et al
Specification for the TITANIA KrF laser system

2. RAL report No. RL-94-014, (1994). J C Martin
Nanosecond pulse techniques
Proc IEEE, 80 934,(1992).

3. Infolytica Ltd MagNet version 5.2
68 Milton Park, Abingdon, Oxon. OX14 4RX.

Measurements of Helium Purity in the Titania Stokes Delay Line

A Boba, C E Marker, E J Divall, G J Hirst.

CLRC Rutherford Appleton Laboratory, Chilton, Didcot, Oxon., OX11 0QX. Email G.J.Hirst@RL.AC.UK

Introduction

The Titania laser has two modes of operation - CPA and Raman. The Raman mode requires an optically delayed Stokes beam to seed the single-shot Raman amplifier system. The delay is produced in a helium-filled beam pipe with a set of mirrors at each end, allowing the Stokes beam to pass back and forward within the pipe nine times. Helium is used because it has a very low nonlinear refractive index therefore preventing any spectral or spatial distortion of the beam. (These would lead to energy losses when the beam reaches the amplifiers.) The objective of the following experiment was to find an accurate method of measuring the purity of the helium which falls, over a period of weeks, as air leaks into the beam pipe.

Experiment

The speed of sound in helium is very different from that in air (greater by a factor of approximately three). It was therefore decided to investigate the use of an ultrasonic measuring device to quantify the relative amounts of the two gases. The only foreseeable problems were in placing the transducer securely inside the pipe without obstructing any of the beam paths and ensuring that it would still function properly after the pipe had been pumped out to a vacuum then refilled to a pressure of one atmosphere several times over.

The transducer was removed from an ultrasonic "tape measure" (RS Components stock no 198-4511) and fixed onto a small mirror mount to allow for directional adjustments. The transducer and mount were then fitted onto the mirror array at one end of the beam pipe. Gas-tight Lemo plugs and sockets were used to connect the transducer to its electronic display which would remain outside the pipe. With the beam pipe filled with air the mount was adjusted to give a reading on the display which coincided with the measured distance from the transducer to the far end of the pipe i.e. 12.05 m.

The pipe was then sealed and the contents were pumped out to a vacuum before being refilled with helium. A reading was taken from the display and recorded. The contents of the pipe were then pumped out again and 10 mbar of air was let in before the pipe was filled to 1 bar with helium. Another length reading was taken. This was repeated several times to give measured lengths for 0 - 10% of air mixed with the helium. The results are compared with the theory in figure 1.

The expected effective length of the pipe (i.e. the reading on the display) was calculated using the following formulae:

$$\text{Effective length} = \text{True length} \times \frac{\text{Speed of sound in air}}{\text{Speed of sound in gas mixture}}$$

$$\text{Speed of sound in gas mixture} = \sqrt{\frac{\gamma \times \text{Pressure}}{\text{Density}}}$$

$$\text{Density} \approx \text{Density of air} \times p + \text{Density of helium} \times (1-p)$$

where p is the partial pressure of air in bar

$$\text{Ratio of specific heats, } \gamma \approx 1 + \frac{R}{C_v(\text{air}) \times p + C_v(\text{helium}) \times (1-p)}$$

and:

Pressure = 101325 Pa

Density of air = 1.184 kg m^{-3}

Density of helium = 0.1664 kg m^{-3}

$$C_v(\text{air}) = \frac{5R}{2}$$

$$C_v(\text{helium}) = \frac{3R}{2}$$

Conclusions

Figure 1 shows that the measured lengths followed the line of the theoretical lengths within a few centimetres up to an air fraction of 6%. However above 7% the readings became very erratic and differed from the theory by more than 10 cm. One possible explanation for this could be that due to the density difference the air was sinking to the bottom of the pipe and the gas mixture was separating. This effect would be expected to get worse as the amount of air in the pipe increased.

The ultrasonic tape measure was found to measure the air fraction accurately for values up to 6%. Since spectral effects occur when only a few percent of air has leaked into the pipe the device works well enough to indicate when refilling is necessary.

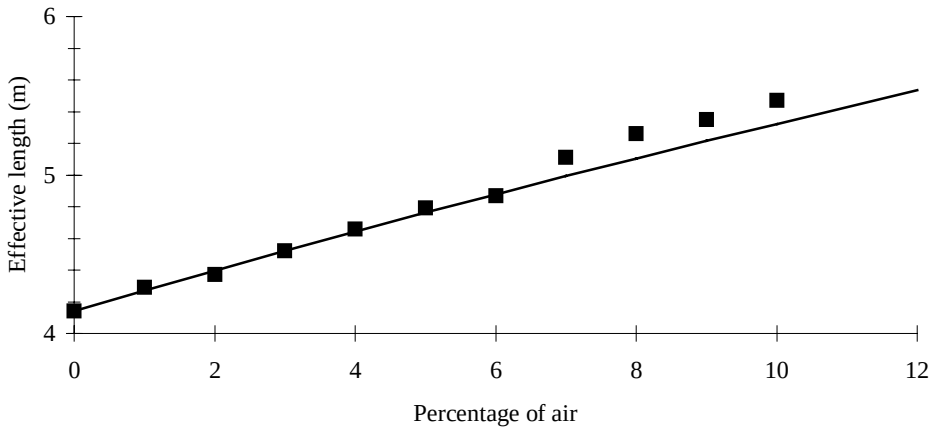

Figure 1. Measured and theoretical lengths as a function of percentage of air

A Radial Shear Interferometer

C Hernandez-Gomez, J Collier, C Danson.

CLRC Rutherford Appleton Laboratory, Chilton, Didcot, Oxon., OX11 0QX. Email C.Hernandez-gomez@rl.ac.uk

Introduction

An interferometer has been developed for use on the Vulcan laser system based on a radial shear concept. The interferometer has a number of intrinsic features which make it ideally suited for use with Vulcan. Some of the important features are: it is self referencing and therefore does not require an additional high quality reference wavefront, it is of a common path design which not only produces a very stable interference pattern but combined with its self imaging properties make it ideal when used with ultra short pulses.

Description

Radial shear interferometers have been used in the past for wavefront sensing [1), 2)]. The interferometer designed for the wavefront analysis is shown schematically in figure 1. High contrast fringe patterns are produced by the interference of two beams which are propagated clockwise and anticlockwise through the device.

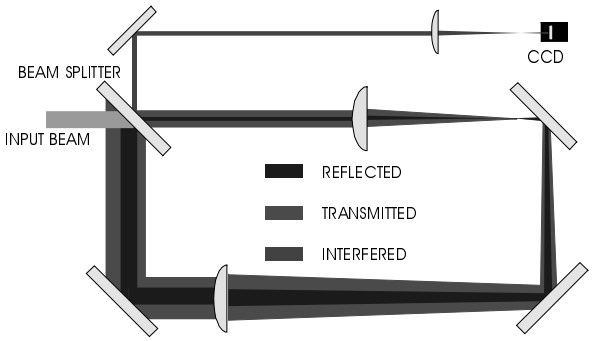

Figure 1. Radial shear interferometer

The interferometer is designed for a 30 mm diameter linearly polarized input laser beam and is constructed from λ\10 peak to valley optics at 1053 nm. The input beam passes through a suitably orientated waveplate to ensure that at the 45° uncoated BK7 beam splitter it is 's' polarized. The split ratio at the beam splitter is thus 90% transmitted and 10% reflected. The transmitted beam is expanded in diameter by a factor of three using a confocal telescope, while the reflected beam is reduced in diameter by the same factor. When the expanded beam passes through the beam splitter for the second time only 90% of it is transmitted and similarly 10% of the compressed beam is reflected. This split ratio and telescope magnification results in an equal intensity irrespective of the direction of propagation.

Interference takes place on the beam splitter between the whole spatial extent of the compressed beam and a small fraction of the expanded beam. The wavefront gradients are assumed to be sufficiently small in the input beam so that over the small interfering fraction of the expanded beam there is a perfectly flat or spherical wavefront. Any sphericity can be removed by adjustment of the telescope separation. Special care is taken in the design so that the beam splitter is imaged back onto itself and this coupled with the equal intensity in each beam ensures a 100% fringe visibility. The interference pattern is imaged onto a CCD camera with a typical output as shown in figure 2. The fringe pattern is then processed to reconstruct the wavefront using a software package [3)]. The corresponding wavefront error map generated from the fringe pattern shown in figure 2 is illustrated in figure 3.

The fringes produced by an interferometer describe the actual wavefront of the laser beam. Perfectly straight fringes describe a perfectly flat wavefront, any deviations from straight fringes

Figure 2. Interference pattern

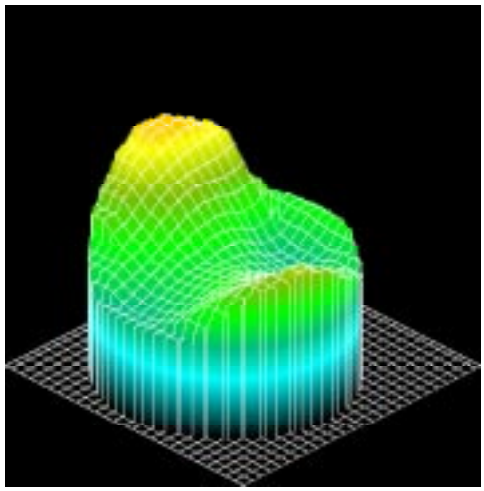

Figure 3. Reconstructed wavefront

represent the wavefront errors. The change in distance from one fringe to the next indicates the change in phase of the wavefront. An Optical Path Difference (OPD) map of the wavefront generated from an interferogram is a plot of the spatial variation in the fringe separations. The software package analyses the light and dark fringes and plots the phase changes on the wavefront as a false colour (OPD) map and expresses results in terms of Root Mean Square (RMS) and Peak-to-Valley (P-V) distortions, in units of wavelength.

References

1. D Malacara,
   Optical Shop Testing, 1978 (John Wiley and Sons), Chapter 5

2. C B Edwards, P Lee, M Tatarakis,
   'Single Shot Wavefront Measurement of sub-ps Laser Pulses', SPIE Vol 2375

3. Fringe Analysis / Wavefront - 'FRIN' *from* Oxford Framestore Applications, Oxford, U.K.

The Von Hamos Spectrometer - a hard X- ray diagnostic

M Notley, A Damerell, J Leach, D Neely.
CLRC Rutherford Appleton Laboratory, Chilton, Didcot, Oxon., OX11 0QX

G Tallents, J Lin, R Smith, S J Pestehe.
Physics Dept., University of Essex, Colchester

Introduction

A Von Hamos[1] X-ray crystal spectrometer was designed and manufactured for use on an experiment to investigate the properties of laser produced plasmas. The experiment was carried out using the Titania high power laser system and aimed to investigate the characteristics of a high density Iron plasma in local thermodynamic equilibrium[2]. The targets used were Aluminium doped Iron-Mylar coated slabs which were designed to give a tamped (short time) plasma containing the spectra of both Iron and Aluminium. The spectrum of Aluminium is well known and can therefore be used to diagnose the conditions under which the Iron spectra are produced. The spectrometer was designed to collect information from the He–β and Lyman-α lines of the Aluminium spectrum. This report describes to the design and performance of the instrument.

The Von Hamos Spectrometer Design

The important and significant difference between the Von Hamos design compared with other crystal spectrometers currently employed at the CLF is the use of a curved rather than a flat crystal to significantly enhance collection efficiency. A crystal of dimension 20 mm x 50 mm and radius of curvature of 65 mm was implemented in our design in order to collect information from the 2-8 Å region of the x-ray spectrum, with special interest in 6.05 Å and 6.65 Å - the He-β and Ly-α lines of Aluminium. This shape of crystal allows 2 orders of magnitude greater collection of flux from the plasma source than that obtainable by a flat crystal of similar dimension. The crystal used to obtain data from the specific region of interest was PET (Petraethylate) 100 which has a 2d lattice spacing of 8.74 Å.

The instrument consists of an adjustable mounting for the crystal onto which a cleaved crystal of 0.2 mm was curved and attached. Also a platform holding a mounting plate for either film or CCD and a housing, prevent stray light and hot electrons from interfering with the data of interest, were incorporated. The spectrometer forms 1-D image data due to the geometry of the optics (figure 1). It can also record data on a single shot basis by the use of an 16 bit X-ray CCD camera[3] or film.

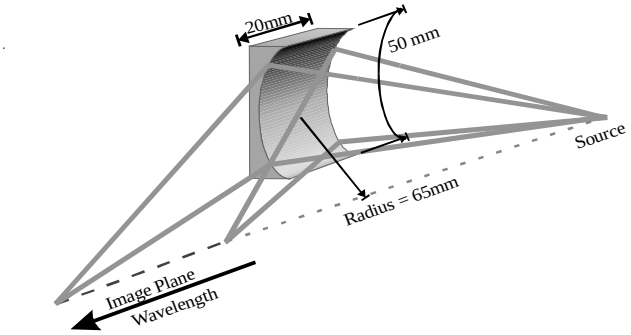

Figure 1. Diagram showing the geometry of the Von Hamos design of spectrometer using a cylindrically curved crystal.

Data collection from other regions of the x-ray spectrum is possible with the current spectrometer design by using x-ray crystals with different lattice spacings as shown by figure 2 or by changing the radius of curvature to increase or decrease the focal range.

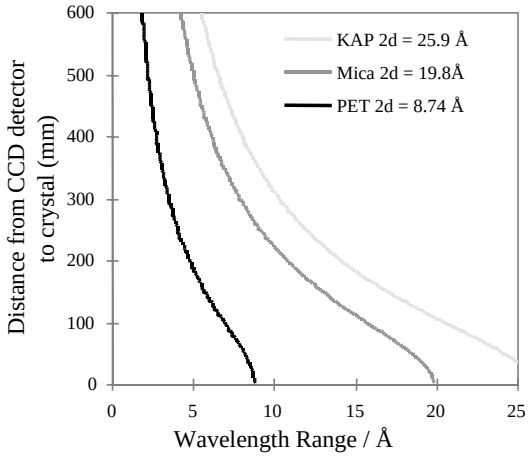

Figure 2. Graph showing the wavelength ranges available using different crystals and the distances necessary for focusing.

The radius of curvature used for the current design allowed a specific spectral range between 6 and 6.8 Å to be detected by the CCD. The experiment required that the He-β and Ly-α lines of Aluminium be detected simultaneously and they therefore had to fit spatially within the 28 mm length of the CCD chip and still be within focal range.

Instrument Performance

The spectrometer was installed and its performance assessed throughout its use in the experiment. The efficiency of the instrument was measured to be 2×10^{-4} in the wavelength region of interest (see figure 3). This is dependent on the collected solid angle (10^{-4} sr at a distance of 130mm from the source), the integrated reflectivity of the crystal [4), 5)] , the sensitivity of the CCD Chip[5)] (~50% of incident photons) and the transmission of the filters used (99.6%).

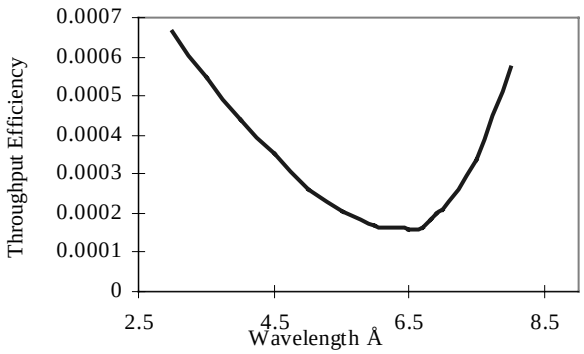

Figure 3. Graph showing the throughput efficiency of the instrument when used with a 16 bit CCD [3)] & Beryllium Filter

Figure 4 shows a typical spectrum obtained with the spectrometer. Via comparison of the Aluminium spectrum with that of Germanium lines of known width, the wavelength resolution of the instrument was ascertained to be better than 10 mÅ (although resolution was not a major factor concerned in the design of the instrument).

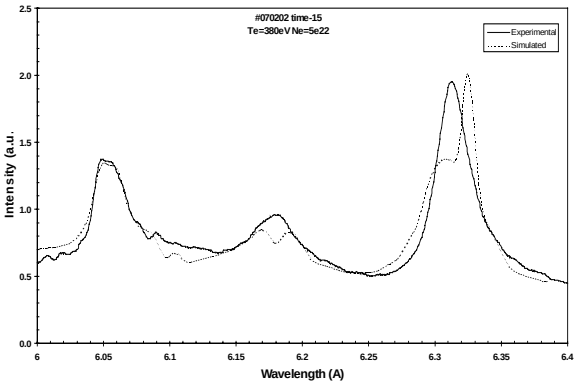

Figure 4. Graph showing a typical spectrum obtained using the spectrometer including a theoretical code plot

A spectrum as detected by the CCD is shown in figure 5. This image was recorded by diffraction from the first PET crystal used which was found to be striated causing multiple 1-D images.

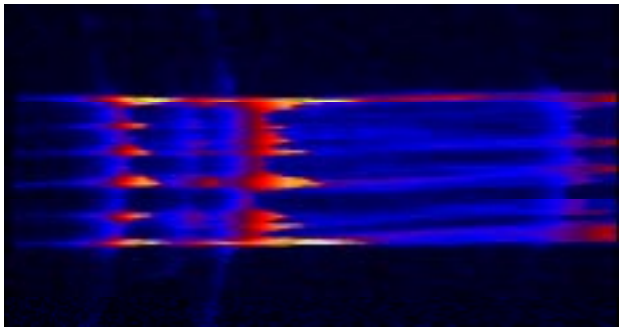

Figure 5. Spectrum as seen by the CCD from an imperfect PET crystal - the striations causing multiple spectral recordings.

The imperfections in the structure of this crystal severely limited the performance of the spectrometer. Therefore another crystal was installed which gave considerably better results (see figure 6). It was cleaved in-house and is estimated to have a thickness of 0.2 mm. To prevent the stresses caused by attaching the crystal along its whole length to the mount it was curved and fixed only at its edges which avoided the problem of striation, but as curvature is still not perfect the data can be seen to contain a dispersed spectral recording.

A perfect spectrogram would contain just one single row of intensity peaks due to the spectral lines. The dispersed spectrum in figure 6 may arise from the curvature of the crystal being different at the points where it was fixed to the mount from the rest of the crystal causing the one row of peaks to spread out.

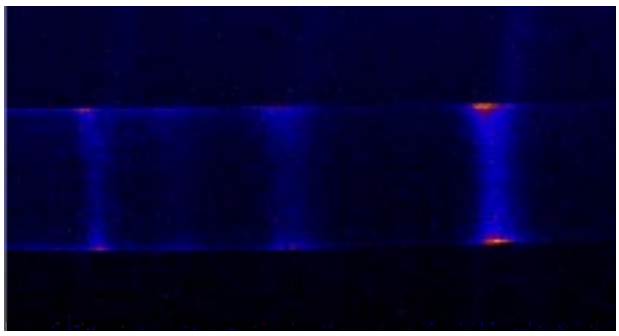

Figure 6. Spectrum as seen by the CCD from the second PET crystal - the imperfections causing a dispersed spectrum.

Crystal quality has a large part to play in the image quality of the data and there are many factors in this including surface quality, how smoothly curved the crystal is, reflectivity, rocking curve effects and quality of the internal structure.

Limitations of the instrument arise from factors such as the source size, crystal resolving power and crystal quality. Initially the image quality and resolution of the instrument were not as high as seen in the figure 4.

Theoretically the crystal is capable of easily resolving the Al spectrum (dependence of rocking curve, lattice structure and position of the reflective layer).

Conclusions

The spectrometer performed very well and recorded the results as per specification enabling single shot collection of data from the region of interest. In the future it will be possible to adapt the design for different spectral regions by use of different crystals and by changing the radius of curvature of the mount.

The initial design included mounting capabilities for either a CCD detector or a film back providing versatiltiy in data collection.

The crystal quality is difficult to perfect and is the factor which can most affect the images. Future developments should concentrate on finding a method to successfully bend crystals without introducing any deformation into internal structure.

References

1. L. Von Hamos,
Z. Krystallogr 101 17 (1939)

2. R.Smith , G. Tallents, S.J Pestehe, G. Hirst, J.Lin, S. Rose, M. Tagviashvili
"A spectroscopic analysis of near solid density plasmas"
CLF Annual Report 1998

3. Instaspec CCD camera including a 1024x256 pixel chip supplied by ANDOR Technology, Belfast

4. A. Burek, University of California
"Crystals for Astronomical X-ray Spectroscopy"
Space Science Instrumentation 2, 53 1976

5. N.G. Alexandrop & G. Cohen
"Crystals for Stella spectrometers".
Applied Spectroscopy Vol 28 No. 2 1974

6. A.Macphee
PhD Thesis 1997, QUB, Belfast

Principles and possibilities for optical parametric chirped pulse amplifiers

I N Ross, P Matousek, M Towrie, A J Langley, J L Collier.

CLRC Rutherford Appleton Laboratory, Chilton, Didcot, Oxon., OX11 0QX. Email I.N.Ross@rl.ac.uk

Introduction

There has been much interest in the generation of extremes in high power, pulse duration and intensity through the application of the technique of chirped pulse amplification (CPA) in laser systems[1)-6)] and this has opened up for investigation new areas of research as well as extending the work in existing areas. In different systems centred around Nd:glass and Ti:sapphire reported powers have reached 1 PW[7)] with intensities on target exceeding 10^{20} W/cm^2 and pulse durations down to 30 fs, and it is expected that this is close to the limit for these laser systems.

One limitation with these systems is the level of prepulse intensity which can significantly perturb the target prior to arrival of the main pulse. This is especially difficult in experiments using solid targets which may have plasma generation thresholds below 10^{10} W/cm^2 and hence require pulse contrast ratios more than 10^{11} . Existing systems have not been able to meet this requirement except by using harmonic generation after the laser.

It is clear that, if the energy continues to be limited by compressor grating technology, then the route to yet higher powers lies through a reduction in pulse duration, and this requires an amplifier with increased gain bandwidth at high energy. Such an amplifier exists and is well known. It is the optical parametric amplifier (OPA).

Properties of optical parametric chirped pulse amplifiers

The scheme under consideration is that in which an OPA is pumped by a beam from a laser (possibly Nd:glass, Ti:sapphire, Nd:YAG, KrF etc.) operating in an energy efficient mode. This will commonly lead to a pump beam with relatively narrow spectral bandwidth and long pulse duration, typically about 1 ns, and the OPA is then used to amplify a large bandwidth and chirped 'signal' pulse of equal pulse duration prior to re-compression[8)-10)]. This scheme will be referred to as optical parametric chirped pulse amplification (OPCPA).

Bandwidth

The gain bandwidth of an OPA can be estimated using the analytical solution of the coupled wave equations in the slowly varying envelope approximation and assuming flat top spatial and temporal profiles and no pump depletion. The intensity gain (G) and phase (φ) of the amplified signal beam are given[11)] by:

$$G = 1 + (\gamma L)^2 \left(\frac{\sinh B}{B}\right)^2$$

$$\varphi = A - \tan^{-1}\frac{A \tanh B}{B} \qquad (1)$$

where: $A = \Delta kL/2$; $B = \sqrt{(\gamma L)^2 - (\Delta kL/2)^2}$

gain coefficient(γ) = $4\pi d_{eff}\sqrt{I_p / 2\varepsilon_0 n_p n_s n_i c \lambda_s \lambda_i}$

phase mismatch (ΔkL)= ($\underline{k}_p$-$\underline{k}_s$-$\underline{k}_i$)L

and where: L = amplifier length; d_{eff} = effective nonlinear coefficient; I_p = pump intensity

The phase mismatch is calculated from the material index curves, noting that in the case being considered the pump wavelength is effectively monochromatic and conservation of energy demands that $\omega_p = \omega_s + \omega_i$.

A number of ways of realising broad bandwidth gain have been discussed and demonstrated in the literature[12)-15)]. Two of particular relevance to the OPCPA are:

a) The case of near-collinear geometry which applies for all crystals and pump wavelengths which are compatible with a type I process. The FWHM gain spectral bandwidth as calculated using equation (1) shows large variations with wavelength and crystal and can be very large as demonstrated in figure 1(a) for KDP and LBO. Maximum bandwidth is achieved by operating with a small phase mismatch at the degeneracy point.

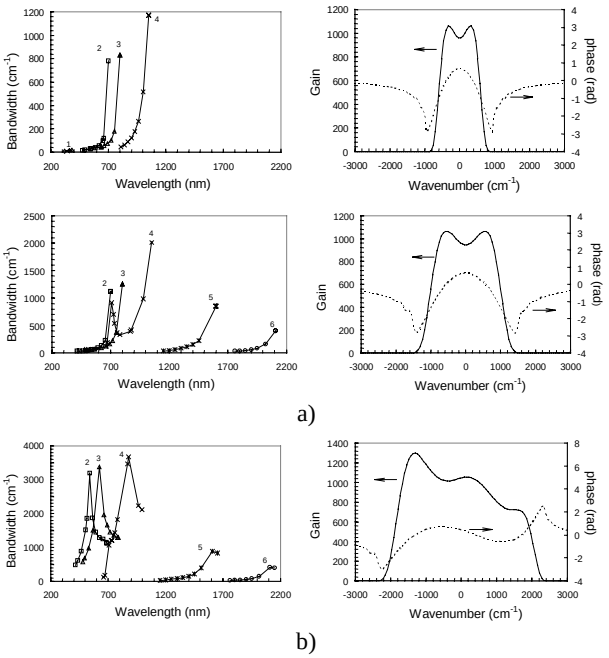

Figure 1. Dependence of the OPA gain bandwidth (FWHM) on the signal wavelength for (a) KDP and LBO in collinear geometry and for (b) LBO in optimised non-collinear geometry, calculated for the pump wavelengths (1) 249 nm, (2) 351 nm, (3) 400 nm, (4) 526 nm, (5) 800 nm and (6) 1053 nm and pulse duration 0.5 ns. Lower curves show gain and phase calculated for the maximum bandwidth in case 4. A small phase mismatch has been introduced to maximise the gain bandwidth. The crystal length was adjusted for x1000 gain at fluencies of 1 and 1.5 J/cm^2 for KDP and LBO respectively

b) The second case is for an optimised non-collinear geometry. For an angle (α) between pump and signal beams, the phase matching angle is calculated for the centre signal wavelength and the bandwidth again calculated using equation (1). The maximum bandwidths (for optimised values of α) are plotted in figure 1(b).

Figure 1 shows that very large gain bandwidths are possible in OPAs at a variety of wavelengths.

There is a 'gain-narrowing' effect in OPCPAs due to the generally non-flat pump temporal profiles rather than the usual effect arising from the spectral gain distribution. This results in a reduction in pulse duration of the amplified chirped signal

(and hence also its bandwidth) leading to longer pulses after re-compression. Although it is not generally possible to have a flat-top pump pulse profile this effect can be reduced to an acceptable level if the OPCPA is heavily saturated and if the crystal is detuned to slightly reduce the gain for the central wavelength.

Pulse duration

The shortest possible pulse duration after re-compression of the amplified chirped pulse is given by the Fourier transform of the output spectrum, taking into account both the spectral gain and phase as shown in figure 1. For the example of LBO in non-collinear geometry, figure 2 shows that pulses as short as 7 fs are possible.

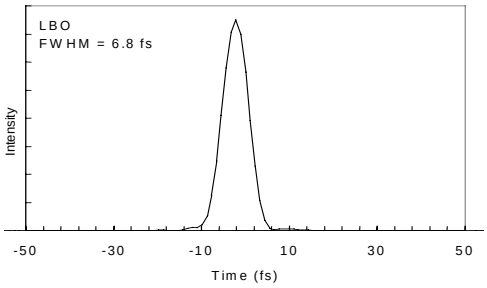

Figure 2. Pulse temporal profile for a 5 fs pulse amplified in LBO, corresponding to the spectral gain and phase of figure 1(b). The phase terms up to the 3rd order have been removed.

There are also contributions to the spectral phase from the compressor and from group velocity dispersion and self phase modulation, and these can reduce the fidelity of the re-compressed pulse as calculated for figure 2. However, calculation of these contributions for the OPCPA indicate that they can be kept acceptably small.

Energy capacity

For the proposed OPCPA systems the maximum output signal energy is given by:

$$E_s = \eta_s F_D A \qquad (2)$$

where A = crystal area; F_D = pump beam fluence limit, normally set at, for example, 50% of the damage threshold; η_s = pump to signal energy optical parametric efficiency.

The efficiency can be calculated by solving the coupled wave equations for the case of pump depletion, see for example Armstrong et al[11]. An important feature of the process is that the efficiency is cyclic with the parameter $I_P L^2$, not asymptotic as for example with second harmonic generation, indicating that as $I_P L^2$ is increased beyond the 100% point energy begins to flow back into the pump beam. Consequently it is not possible to achieve complete conversion for real beams which do not have flat intensity profiles in space and time. For example, simulations indicate[16] a maximum efficiency of 32% into the signal beam for flat-top spatial and Gaussian temporal profiles, and this has been confirmed by experiment[17].

Higher efficiencies are possible[16] and have been demonstrated[14] by profiling of the input pump and signal beams.

As an example KDP, which can be grown to sizes > 30 cm, can be operated without optical damage at mean fluences up to ~2 J/cm^2 . If η= 30%, then the signal beam energy can be amplified to more than 400 J, assuming the availability of the necessary 1330 J of pump energy.

Gain

A high gain is desirable in a high power amplifier as it reduces the amount of material in the beam (minimising the nonlinear effects and effects of dispersion) and reduces the physical length of the system (giving less aberration from air).

As examples, if the materials BBO, LBO and KDP are pumped with 0.5 ns pulses at 526 nm and at intensities below the damage threshold, the gain coefficients are respectively 12, 12, and 2.4 cm^{-1}. A system, as outlined below, designed for a small signal gain of $4x10^{11}$ has less than 5 cm of material in three amplifiers and may be genuinely tabletop in size. These coefficients can be compared to typical values for Nd:glass and Ti:sapphire of 0.1 and 2.3 cm^{-1} respectively.

Beam quality

The compact size of the OPA amplifier helps to minimise aberrations on the signal beam. Two further features of the OPA are also significant for beam quality.

One is the property of the OPA which allows efficient amplification of an un-aberrated signal beam without transfer of pump beam phase aberrations. The only requirement on pump beam aberrations is that the pump beam divergence must be less than the phase matching angular tolerance. For large beams with KDP at close to collinear geometry the pump beam can be many times the diffraction limit.

The second feature of an OPA is the absence of significant thermal aberration. This follows from its 100% quantum efficiency and from an absence of significant absorption at the pump, signal and idler wavelengths. Such a system could operate very close to the diffraction limit.

Beam contrast

It is important in any system to assess the contributions which reduce the final pulse contrast. These come from ASE, prepulses or imperfectly compressed pulses. For conventional laser gain media, the ASE intensity on target is given in the limit of high gain by:

$$I_{ASE} = \frac{F_s}{16F^2\tau_{RAD}} . \frac{\Delta\lambda_{ASE}}{\Delta} . G \qquad (3)$$

where G = net small signal gain; F_s = saturation fluence; F = F.No. of focusing optic; τ_{RAD} = upper state radiative lifetime; $\Delta\lambda_{ASE}$ = ASE spectral bandwidth; Δ = laser gain bandwidth

For a PW Nd:glass laser with a Ti:sapphire front end this gives an estimated value of $I_{ASE} \approx 1.3.10^{12}$ W/cm^2 .

For the OPCPA the ASE intensity on target is given for high gain by

$$I_{ASE} = \frac{\pi}{4F^2} . \frac{h\nu.\Delta\nu}{\lambda^2} . G \qquad (4)$$

where: $\frac{h\nu.\Delta\nu}{\lambda^2}$ = noise source (1 photon/mode)[18]

In this case for a PW system the estimated ASE intensity on target is 7 x 10^{11} W/cm^2, a factor of 17 less than for Nd:glass.

In addition, unlike most conventional amplifiers, the gain window in an OPCPA is no longer than the pump pulse duration which is the same length as the signal pulse in the amplifier (typically 1 ns). Consequently only prepulse ASE and noise on the signal within the gain time window will be amplified.

Practical OPCPA designs

We present two practical designs of OPCPA system with very different specifications to show that the scheme can offer significant advantages over existing systems in very different regimes.

A 'simple' millijoule system

A typical design and calculated performance are illustrated in figure 3. This scheme has wide application as a short pulse CPA amplifier in femtosecond systems. It can be regarded as a less complex alternative or replacement to for example regenerative and multi-pass Ti:sapphire amplifiers, and offers better performance by providing higher gain bandwidth, lower group velocity dispersion, lower B-integral, lower thermal distortion and higher contrast ratio.

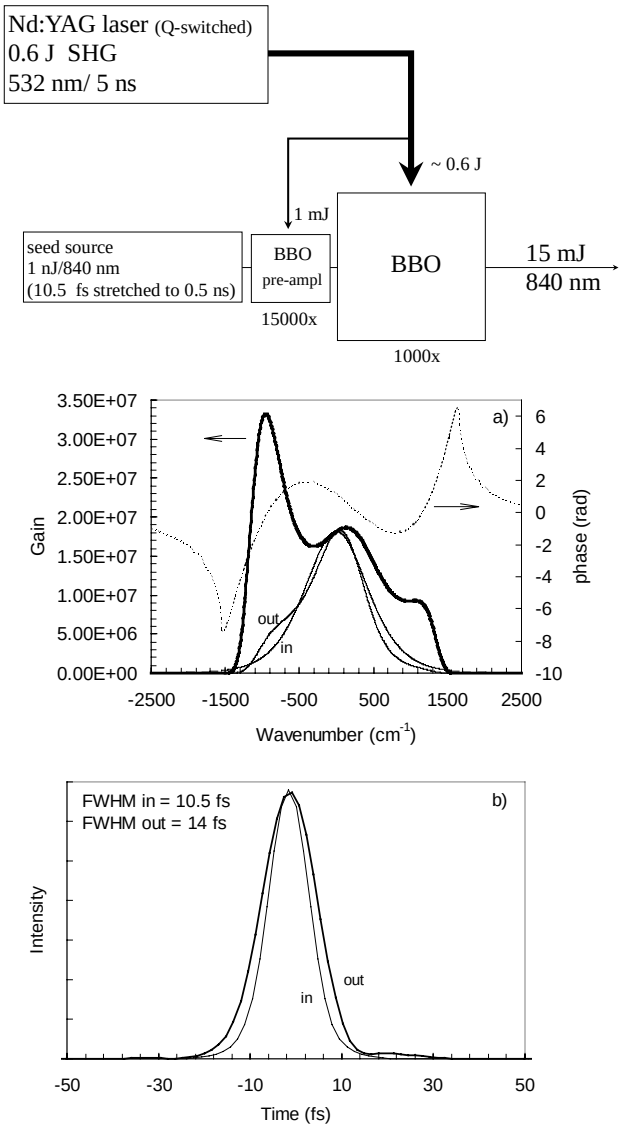

Figure 3. OPCPA design for a 600 mJ frequency doubled Nd:YAG laser. (a) The total gain and phase, together with the assumed input pulse spectrum and the spectral gain. (b) Fourier transform of the input and output pulses. The phase terms up to the 3rd order have been removed.

Maximum power and intensity using a large Nd:glass laser

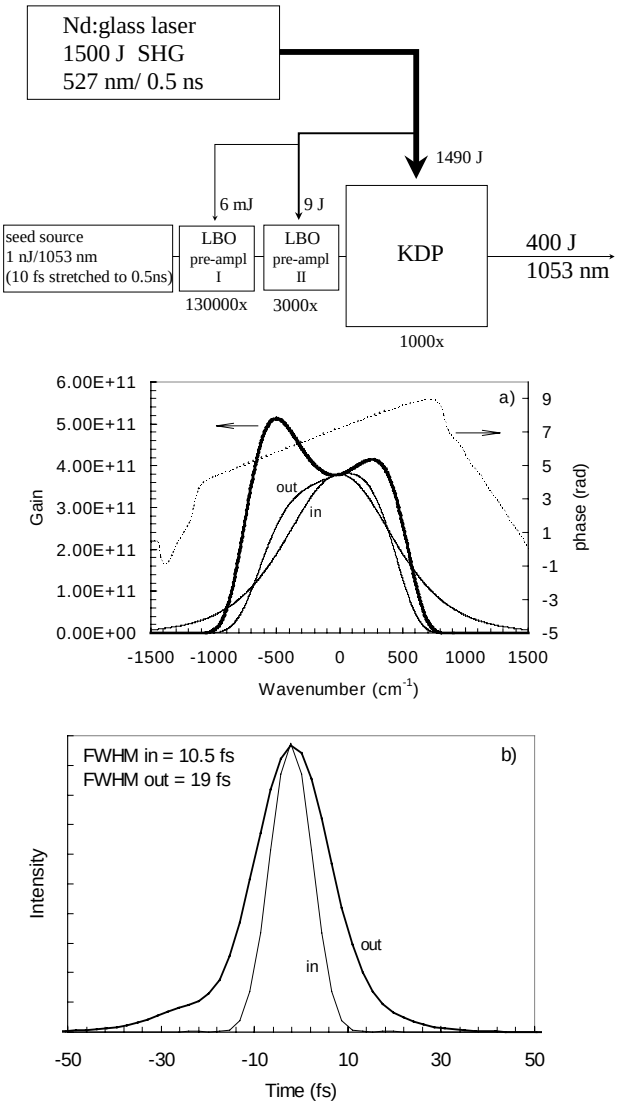

Figure 4. Petawatt OPCPA design pumped by a high power Nd:glass laser. (a) The total gain and phase together with the assumed input pulse spectrum and the system spectral gain. (b) Fourier transforms of the input and output pulses. The phase terms up to the 3rd order have been removed.

This scheme, shown in figure 4, uses as pump source the second harmonic of the high energy available from a Nd:glass laser. This type of laser has excellent characteristics as a pump laser because it operates with best energy efficiency for spectrally narrow pulses of duration well suited to efficient compression using available large area gratings. The laser output energy was taken to be 3 kJ since it provides at the second harmonic an energy close to the maximum that a single beam OPCPA can use consistent with the largest available crystals (~30 cm) and measured damage thresholds (~2 J/cm^2). The OPCPA system is a three stage amplifier with a total net gain of 4x10^{11}. The final 'power' amplifier is KDP type I working close to degeneracy and slightly non-collinear to enable downstream angular separation of pump, signal and idler beams. The signal source is a modelocked Ti:sapphire oscillator spectrally broadened and chirped by self phase modulation in an optical fibre. After transmission through a pulse stretcher the pulse duration is 0.5 ns. The final OPCPA amplifier is assumed to yield a 30% extraction efficiency giving an output energy of ~ 400 J which is within the capacity of the largest available commercial compressor gratings. Assuming a single pass compressor with

70% throughput and a further 20% loss due to spectral clipping on the gratings[19], 224 J is available for focusing to target.

The pulse duration achievable on target is determined by the product of the source bandwidth and the OPCPA gain bandwidth, combined with other effects in the compressor[20]. We can expect an oscillator bandwidth of 1000 cm^{-1} since this is achieved with commercial Ti:sapphire lasers. Figure 4 shows, for the OPCPA system, the calculated output spectrum which Fourier transforms to a pulse of duration 19 fs, also shown in figure 4. Based on examples given in [19], and assuming gratings flat to $\lambda/200$ cm^{-1} rms, the estimated pulse duration on target is 21 fs. With 224 J in 21 fs, the power on target is 11 PW.

It is more difficult to estimate the achievable intensity on target because of uncertainties in the realisable quality of optics. However, taking into account the optical simplicity of the OPCPA scheme an output beam < 1.5 x DL can be expected. Out of flatness errors of $\lambda/200$ cm^{-1} rms on the compressor gratings and similar errors on the focusing paraboloid may be expected to result in a 2 x DL spot on target, yielding, for an F/1 paraboloidal focusing mirror, an expected intensity on target of $2x10^{23}$ W/cm^2.

Conclusions

There are exciting new possibilities for achieving very high power and intensity and very short pulse duration using optical parametric chirped pulse amplifiers. Their favourable properties, particularly the parametric gain bandwidth and the availability of large aperture devices, offer the prospect of reaching much higher powers and intensities than have so far been considered. These amplifiers may also be included in many smaller short pulse laser systems both reducing their complexity and cost and giving enhanced performance.

References

1. D.Strickland and G.Mourou
   Opt. Comm. **56**, 219, (1985)
2. C.Rouyer et al
   Opt.Lett. **18**, 214, (1993)
3. C.Barty, C.Gordon and B.Lemoff
   Opt.Lett. **19**, 1442, (1994)
4. C.N.Danson et al
   Opt.Comm. **103**, 392-397, (1993)
5. O.Martinez
   JOSA **B3**, 929, (1986)
6. M.Perry and G.Mourou
   Science **264**, 917, (1994)
7. M.Perry
   Science and Tech. Rev., 4, (1996)
8. I.N.Ross, P.Matousek, M.Towrie, A.J.Langley, J.L.Collier,
   Opt. Comm. **144**, 125, (1997)
9. A.Dubeitis, G.Jonasauskas, A.Piskarskas,
   Opt. Comm. **88**, 437, (1992)
10. A.Galvanauskas, A.Hariharan, D.Harter, M.A.Arbore, M.M.Feyer,
    CLEO'97 Baltimore, (1997)
11. J.Armstrong, N.Bloembergen, J.Ducuing and P.Pershan
    Phys.Rev. **127**, 1918, (1962)
12. P.DiTrapani et al
    JOSA B **12**, 2237, (1995)
13. A.Piskarskas, A.Stabinis and A.Yankauskas
    Sov. Phys. Usp. **29**, 969, (1986)
14. J.Liu, G.Zhou and S.Pyo
    JOSA B **12**, 2274, (1995)
15. J.Wang, M.Dunn and C.Rae
    Opt.Lett. **22**, 763, (1997)
16. I.Begishev et al
    Sov.J.Quant.Electr. **20**, 1100, (1990)
17. B.Bareika et al
    Sov.Tech.Phys.Lett. **12**, 78, (1986)
18. D.Kleinmann
    Phys.Rev. **174**, 1027, (1965)
19. I.Ross, M.Trentleman and C.Danson
    App. Opt. **36**, 9348, (1997)
20. C.Fiorini et al
    IEEE JQE **30**, 1662, (1994)

Optical parametric chirped pulse amplification - experimental progress

K Osvay.

Department of Optics and Quantum Electronics, JATE University, Dom ter 9, Szeged H-6720, Hungary

I N Ross.

CLRC Rutherford Appleton Laboratory, Chilton, Didcot, Oxon., OX11 0QX. Email I.N.Ross@rl.ac.uk

Introduction

Having established the principles of optical parametric chirped pulse amplification (OPCPA) and its potential for major enhancement of existing laser facilities[1)], it was necessary to embark on an experimental programme, initially at a small scale, to verify the theoretical predictions and establish sufficient confidence to initiate a larger scale development programme.

The principle aims of the experiments were to confirm the predicted gain, gain bandwidth and extraction efficiency for both LBO and BBO optical parametric amplifiers in non-collinear geometry, using both chirped and unchirped signal pulses.

Experimental arrangement

The layout of the experiment is shown on figure 1. For measuring the non-collinear amplification bandwidth the signal pulses were provided by a tuneable OPO-OPA laser (Continuum Sunlite) with a pulse duration of 2.3 ns. For the preliminary test of OPCPA and saturation, sub-50 fs pulses from a Ti:S laser were used. In both cases we used the 5 ns second harmonic pulses from a Q-switched seeded Nd:YAG laser as pump pulses.

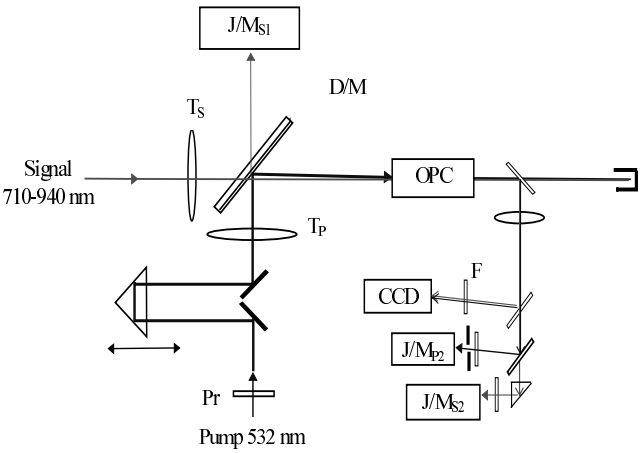

Figure 1. Experimental layout for measuring the amplification of a non-collinear and non-degenerate OPCPA system.

The measurement of broadband spectral amplification was carried out in the following way. The phase matching angle of the optical parametric crystal (OPC) was aligned to a central signal wavelength. Changing the wavelength of the signal, the amplification and pump depletion were measured using the J/M_{S1}, J/M_{S2} and $J/M_{P1,}$ J/M_{P2} power meters, respectively. In the case of the fs signal pulses, the spectral amplification was measured using a monochromator / photodiode instead of J/M_{S2} power meter.

Spectral amplification with tuneable signal pulses

Figure 2 shows the measured spectral amplification in LBO for collinear (a) and non-collinear (b) geometry. The central wavelength and the effective pump intensity were 830 nm and 490 MW/cm^2, respectively. In agreement with the theory, it can be seen that the amplification bandwidth increased enormously while the peak gain dropped only slightly.

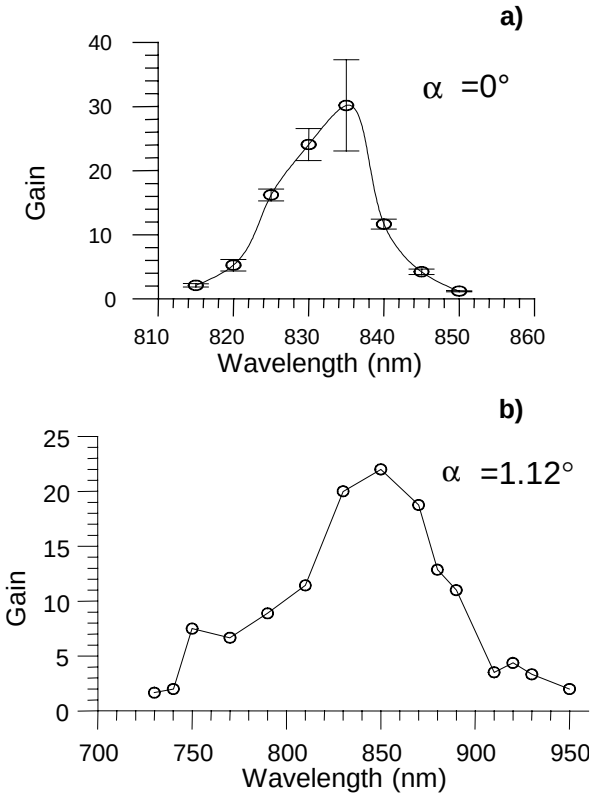

Figure 2. Bandwidth of optical parametric amplification in LBO for collinear (a) and non-collinear (b) interacting pulses.

Measuring the spatial beam distribution of the interacting beams as well as the input and output energies, the efficiency of the process could be calculated. Using a 15 mm long BBO crystal at a pump intensity of 430 MW/cm^2, we have managed to deplete the pump and obtain an efficiency of 57 %, close to the theoretical maximum.

Amplification of fs pulses

The 811 nm, 50 fs signal pulses were too short to be amplified directly in 15 mm BBO because of pump depletion, so they have been chirped and stretched to 1.6 ps in a slab of SF10 glass. The spectral amplification was determined by comparing the unamplified and amplified spectra. The bandwidth of a collinear OPA (figure 3a) is slightly broader than it would be expected from the theory. The reason for this is the strong depletion of the pump which results in a saturation effect similar to that of traditional amplifiers.

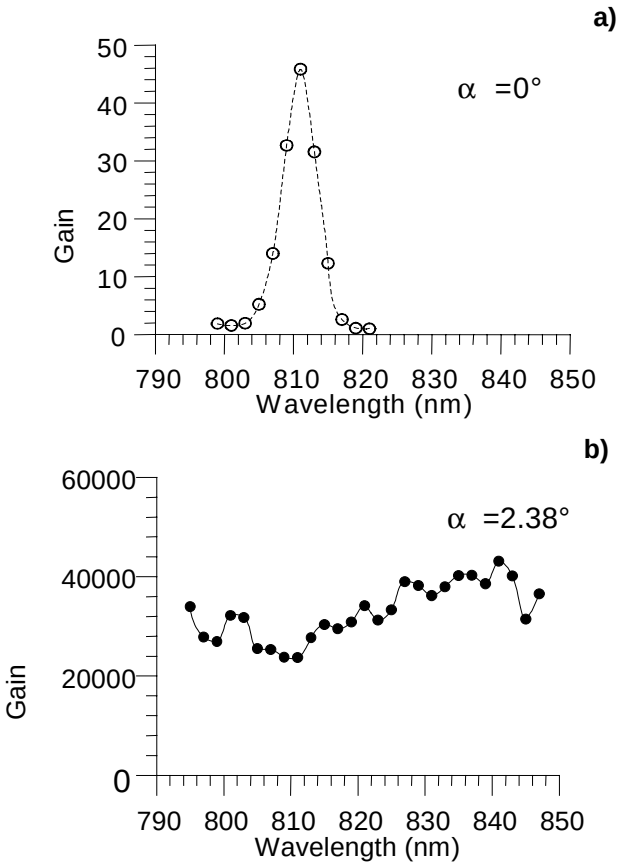

Figure 3. The bandwidth of an optical parametric amplifier in collinear (a) and non-collinear (b) geometry.

Working with an OPA at a non-collinear angle close to the condition of the broadest spectral amplification, the full spectrum of our 50 fs pulse can be amplified (figure 3b). The very high gain could only be measured with a substantial reduction of the incoming signal energy prior to amplification. Even in the case of 10^{-3} attenuation of the nJ signal pulses the comparison with the theoretically achievable bandwidth (figure 4) shows, however, a slight depletion at and around the central wavelength.

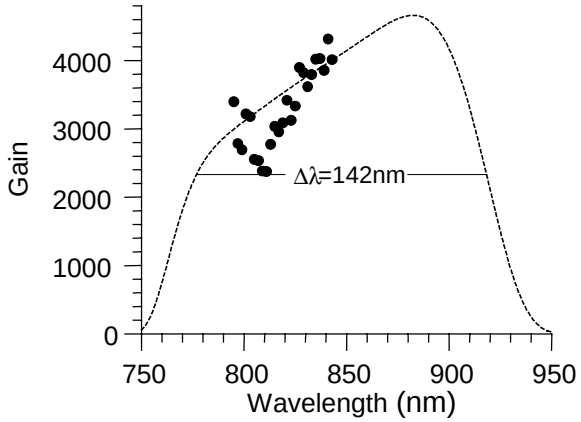

Figure 4. The measured (dotted) and calculated (solid) gain of a BBO OPA in non-collinear geometry.

Determination of the limits

There are several effects which limit the maximum achievable gain of an OPA, namely damage threshold of the crystal, threshold of optical parametric lasing in the crystal, group velocity dispersion and lateral walk-off. In the course of the experiment the damage threshold of the crystals and the self-lasing threshold have been measured:

LBO: no multiple shot damage occurred up to the flux of 6.4 J/cm^2 or to the corresponding intensity of 1.3 GW/cm^2. Because of the low non-linear coefficient and hence modest gain, no self lasing was observed.

BBO: there are several examples of damage threshold data in the literature but these are not consistent. The possible reason of this uncertainty is the extreme sensitivity of BBO to the method and the rapidity of crystal growing. Our BBO (purchased from CASIX) survived many thousands shots of 5.6 J/cm^2- (1.1 GW/cm^2) and also a few shots of 8 J/cm^2 (1.6 GW/cm^2). At the geometry and crystal used the inclination to self lasing was, however, fairly high and always happened when the pump intensity exceeded the intensity of 1.1 GW/cm^2.

References

1. I.N.Ross, P.Matousek, M.Towrie, A.J.Langley, J.L.Collier, Opt. Comm. **144**, (1997), 125

Progress in adaptive optics for laser beam phasefront control

C J Hooker, C J Reason, I N Ross, M J Shaw, N M Tucker.

CLRC Rutherford Appleton Laboratory, Chilton, Didcot, Oxon., OX11 0QX. Email C.J.Hooker@RL.AC.UK

Introduction

The development programme aimed at producing a working adaptive optical phasefront corrector has continued throughout the year, and we have made significant improvements to both the hardware and the software. We have also changed our approach to correcting wavefront errors, abandoning the original idea of direct curvature correction, and substituting a more general technique based on the response matrix of the adaptive mirror. This has the potential to overcome a problem which appeared insoluble under our previous approach.

Improvements to the hardware

The early version of the corrector, described in last year's Annual Report[1], needed two PCs running different operating systems, one to capture and analyze the Hartmann image and the other to control the adaptive mirror. These two machines have now been replaced by a single 200MHz Pentium PC running Windows NT4, and the original Turbo Pascal software has been translated into the Delphi language to provide a simple and elegant user interface. The other major change is in the wavefront sensor, which was formerly a simple Hartmann plate with a screen several metres away, imaged by a CCD camera. This has been replaced by a Shack-Hartmann-type sensor in which an array of computer-generated Fresnel zone plates is used instead of the conventional array of lenses. The array was made using techniques developed for the fabrication of random phase plates for focal spot shaping on Vulcan[2]. The zone plates have a principal focal length of 7 m, and their centres lie on the same 5 mm grid as the apertures of the original Hartmann plate; in consequence, each individual plate has only two complete zones: a clear central zone and an opaque second zone. The main lens has a focal length of about 1 m. The pattern of foci formed by the combination fits within the CCD chip, and consists of spots with FWHM diameters of 8 - 10 pixels, which is a good size for accurate centroiding. The spots are well-separated, and there are only very weak interference peaks between adjacent spots, so identification of the spots is easy and the background illumination level is low. The ability of the sensor to measure small spot displacements is increased by a factor M, defined as the ratio of the original beam size to the size of the spot array on the camera.

The accuracy of centroiding was checked by measuring the position of a spot before and after making a small, calibrated, displacement. A glass plate in the beam just in front of the camera was tilted through a known angle, moving the spots by a calculated distance on the CCD. Displacements as small as 1/50 of a pixel could be made by this technique, and the accuracy of determining the centroid of a spot was found to be typically ±1/10 of a pixel. A check was also made on the mirror relaxation routine, which is designed to restore the mirror to a standard condition after it has been deformed in any way. An oscillating voltage with an exponentially-decaying envelope is applied simultaneously to all actuators, so the mirror is taken repeatedly around its hysteresis cycle at ever-decreasing amplitude, the entire process taking a few seconds. After deformation and subsequent relaxation, the Hartmann spots return reproducibly to within about 1/10 pixel of their original positions, i.e. within the limits of the measurement accuracy.

Improvements to the software

The first change to the software was the conversion to Windows NT, which mainly required the installation of different drivers for the framestore board and the output interface. The change to Delphi from Turbo Pascal was more fundamental, in that large parts of the original program handling the user interface were discarded in favour of the Delphi interface structure. The routines for analyzing an image: identifying and centroiding spots, calculating slopes, wavefront curvature and optical path differences, and those for manually applying voltages to the actuators and the all-important relaxation procedure were retained. New code was written to control the process of generating the matrix and reading the inverted matrix back into the main program. A suite of diagnostic routines was written to export data from the program into Excel files for analysis; these routines were customised and added to as the process of debugging the code progressed.

Mirror control algorithm

Our first attempts at controlling the mirror by measuring and correcting the local curvature within the beam area, and then using the outer actuators to apply slope corrections to the beam edges, were partly successful[1]. However, we were unable to develop an algorithm for the edge slope correction which could be incorporated into the control loop, so we abandoned this approach in favour of one using the slope influence matrix, **H**, defined by:

$$\mathbf{s} = \mathbf{H}\,\mathbf{v} \qquad (1)$$

where **s** is the vector of slopes in x and y, and **v** is the voltage vector. **s** has x- and y-elements for each Hartmann spot (e.g. 200 elements for a 10 x 10 Hartmann array), and **v** has as many elements as there are actuators (60 in our prototype mirror). To measure **H**, the mirror is relaxed to its standard condition, a voltage of +64 V is applied to the first actuator, the image captured, the spots centroided and the slopes at each point calculated. If a slope matrix is being constructed, the slope data are written directly to a file, otherwise the slopes are further processed to yield curvatures or OPDs which are written to the file instead. The mirror is relaxed once more, and the whole process repeated with the same voltage applied to the next actuator. This continues until the effect of each individual actuator on the mirror has been recorded. One column of **H** is generated for each actuator, so the final matrix has 200 rows and 60 columns. The elements of **H** are scaled by 1/64 to correspond to unit applied voltage on the actuators.

The matrix **H** tells us the slopes that are produced for a given distribution of voltages on the mirror. However, in the control situation we require just the opposite: given a set of measured slopes (or curvatures or OPDs), we ask what voltage distribution will best reproduce the quantities we observe. Applying such a distribution to the mirror with the sign reversed should result in the best possible single-step correction of the beam. We thus seek the matrix $\mathbf{H}^{\dagger}$ which satisfies:

$$\mathbf{v} = \mathbf{H}^{\dagger}\mathbf{s} \qquad (2)$$

where $\mathbf{H}^{\dagger}$ is known as the pseudoinverse of **H** (the inverse $\mathbf{H}^{-1}$ is not defined since **H** is not a square matrix).

The set of equations (2) represent a common problem in linear mathematics of an overdetermined system, i.e. there are many more equations than there are unknowns. There are well established techniques for handling such systems which use least squares methods for finding a solution that minimises the error in $\Sigma(\mathbf{Hv} - \mathbf{s})^2$. The solution so obtained will yield a pseudoinverse matrix, and hence a voltage vector which gives a best fit to the observed slopes.

The most stable way to solve the least squares problem is called "singular value decomposition" or SVD. It is routinely available in linear mathematics libraries such as NAG or LAPACK, and is included in Numerical Recipes and in the *Mathematica* package. The SVD of the matrix **H** is given by:

$$\mathbf{H} = \mathbf{U}\mathbf{S}\mathbf{V}^{\mathbf{T}} \quad (3)$$

where **U** and **V** are orthogonal matrices and **S** is a diagonal matrix the elements of which (s_i) are all positive or zero. The positive elements are known as the singular values of **H**. The key property of an orthogonal matrix is that its inverse is the same as its transpose, and hence the pseudoinverse of **H** is given by:

$$\mathbf{H}^{\dagger} = \mathbf{V}\mathbf{S}^{\dagger}\mathbf{U}^{\mathbf{T}} \quad (4)$$

where $\mathbf{S}^{\dagger}$ is diagonal with elements:

$$s_i^{\dagger} = s_i^{-1} \text{ if } s_i > 0,\ s_i^{\dagger} = 0 \text{ if } s_i = 0\ . \quad (5)$$

Using *Mathematica* on a 200MHz Pentium PC, the SVD of a 200 by 60 matrix takes about ten seconds. Subsequent manipulations include transposing the matrices U and V, and adjusting the values s_i before multiplying the matrices together to obtain the pseudoinverse. The final matrix is saved in a file from which it is read into an array in the main program. The computation carried out in the control loop is the multiplication of the measured slope vector by $\mathbf{H}^{\dagger}$ to give the control voltage vector, and this step can be very fast. At the time of writing the system has not been shown to work in closed-loop mode, either to remove the wavefront distortion introduced by the residual curvature of the adaptive mirror itself, or to actively correct imposed errors in the wavefront.

This matrix method of control has a number of advantages in principle. It is extremely direct, since if slopes are used it requires no computation on the wavefront sensor data apart from the single matrix multiplication. However, it does not need to be restricted to slope control and will work just as well with phase or curvature sensors. It is tolerant of addressing errors because the location of the actuator on the beam and its effect are determined experimentally. The determination of the influence function matrix and the computation of its pseudoinverse can be done quite quickly under software control and can be used to recalibrate the correction system. Effects such as ageing of actuators and new beam alignments can be rapidly accounted for. It does, however, rely on the linearity of the system to obtain the best fit solution. Unfortunately, piezoelectric transducers are not linear devices and in fact show significant hysteresis. There are two ways to cope with this problem. One is to neglect it and rely on closed loop operation to arrive at the best wavefront after a few cycles. The other way is to introduce a lineariser into the piezo drive circuits. If this can be done with reasonable economy of computation so that the loop time is not greatly increased, then this approach will lead to a significantly faster system.

Future plans

Once the control software has been debugged and the entire AO system is capable of stable closed-loop operation, it is intended to construct a larger mirror for installation on the Vulcan CPA beam. The actual mirror will require multiple pieces of PZT, as the largest single piece available is 70 mm square, which is too small for the 108 mm beam diameter. Some development will be needed to ensure that the mirror stiffness remains constant across the boundaries between PZT segments. The design of the actuator layout will take into account which aberrations contribute most to the overall wavefront distortion, to give the best match between the modes of the mirror and the errors.

References

1. M J Shaw, C J Hooker, C J Reason and T Kaneko
Central Laser Facility Annual Report 1996-97, RAL Report TR-97-045, pp213-215.

2. D A Pepler, C N Danson, I N Ross and S A Edwards
RAL Technical Report RAL-TR-95-033 (July 1995)
and references therein.

Efficient frequency mixing using chirp compensation

K Osvay*, I N Ross.

CLRC Rutherford Appleton Laboratory, Chilton, Didcot, Oxon., OX11 0QX. Email C.J.Reason@RL.AC.UK

**On leave from Dept. of Optics & Quantum Electronics, JATE University, Dóm tér 9, Szeged H-6720, Hungary*

Introduction

The main limitation to efficient broadband frequency conversion originates from the dispersion of the non-linear crystal. To overcome such severe restrictions on efficiency, an alternative technique in theory[1)] has been proposed in which the generating beams to be mixed in the nonlinear material are chirped at different chirp rates such that the phase matching condition can be met at all times.

For experiments scaling physical and chemical phenomena with pulse length, it would be extremely useful if the pulse duration is easily varied. Spectral shaping of ultrashort pulses provides this possibility at the expense of poor temporal contrast due to spectral diffraction on the mask.

In this paper we show experimentally that the bandwidth and the spectral position of a pulse generated by frequency mixing can be independently tuned by changing the chirp of and the delay between the generating pulses, respectively.

Theory

In our description of the broadband scheme we consider a collinear type I mixing process, where the ordinary $\omega_1<\omega_2$ waves generate the extraordinary ω_3 wave. The frequencies are assumed varying with time. For perfect generation the total phase mismatch of the process $\Delta\psi=0$ should be satisfied in time and in space simultaneously. This requirement can be fulfilled by introducing a chirp (β_1, β_2) into the initial fields, so it can be interpreted as chirp-assisted group velocity matching (CGV). The ratio of these necessary chirps is determined by the group velocities of the interacting waves, while their optimum values are set by GVD as well as by the need for high conversion efficiency[1)].

Narrow band operation can be described more easily on the basis of the above picture. If the two generating pulses are substantially stretched by approximately the same amount but with opposite sign, there are only very few frequency pairs satisfying the phase matching condition and this results in narrow generated bandwidth. Moreover, a change of delay between the input pulses gives rise to a spectral tuning of the generated field within the achievable largest generated bandwidth. It is worth noting that in this tunable narrow band case an increase of the crystal length leads to an increase of efficiency along with narrowing the generated bandwidth. This description of the CGV scheme applies equally in the case of type II processes.

Experimental

The theoretical predictions have been tested by an experiment carried out using 50 fs pulses from a Ti:S oscillator. The 744 nm beam is negatively stretched (down-chirped) by a double pass prism stretcher, then split into two. One part of the beam is overcompressed by glass slabs while the other part remains unchanged in pulse duration but its polarisation is rotated. Recombining the two beams after appropriate timing and focusing weakly into a 0.65 mm type II BBO crystal the generated 372 nm spectrum along with the generating 744 nm spectra have been recorded. Measurement of both generated and input powers established the efficiency.

The overall figure of merit of this new scheme can be defined as the product of the generated bandwidth and the efficiency. Figure 1 shows the essential summary of the series of measurements carried out at different chirps of the generating pulses. The ratio of the chirps β_1/β_2 have been calculated from the measured pulse durations. The length of the longer pulse (τ_2) unchanged in the course of each series is also shown. It can be seen that in agreement with the theory the peak of the bandwidth-efficiency product (i) increases with less stretched generating pulses; (ii) occurs at lower chirp ratio when the pulses are less stretched and (iii) there is a factor of 40 between the lowest and highest figure of merit obtained in the experiment[2)]. The broadest bandwidth is generated around $\beta_1/\beta_2\approx-3$ whereas the narrowest tuneable pulses obtained at -1.

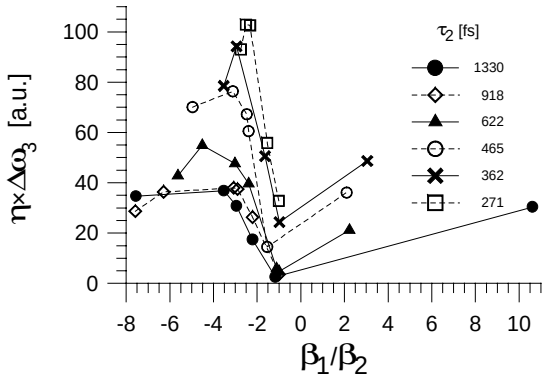

Figure 1. The product of the generated bandwidth and the efficiency vs. the chirp ratio of the generating pulses.

An example of the spectral tuning achieved in our experiment is plotted in figure 2. Since the process depends on the interacting bandwidths, the delay is given in units of the generating bandwidth $1/\Delta\omega_0$. The generated bandwidth is kept almost constant over the whole tuning range with the spectral tuning resolution of 2.4 cm^{-1}, which could be easily improved by several orders of magnitude by using a longer crystal and more highly stretched generating pulses.

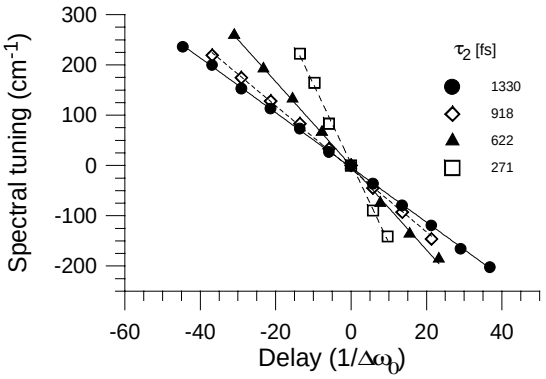

Figure 2. Spectral tuning ranges from the experiment.

References

1. K.Osvay, I.N.Ross, J.Opt.Soc.Am. B **13** (1996) 1431

2. K.Osvay, I.N.Ross, submitted (1998)

Intense Terawatt Laser Facility for Femtosecond Atomic and Molecular Science

P F Taday, I Mohammed, A J Langley, I N Ross.
CLRC Rutherford Appleton Laboratory, Chilton, Didcot, Oxon., OX11 0QX.

K Codling.
Department of Physics, University of Reading, Whiteknights, READING, Berks. RG4 6AF.

K W D Ledingham.
Department of Physics and Astronomy, University of Glasgow, Glasgow,G12 8QQ.

W R Newell.
Department of Physics and Astronomy, University College of London, Gower Street, London, WC1E 6BT.

S Preston.
Department of Physics, University of Oxford, Oxford.

D Riley, I Williams.
Department of Physics and Mathematics, Queen's University of Belfast, Belfast.

Introduction

The combination of titanium-doped sapphire (Ti:S) laser technology with chirped-pulse amplification (CPA)[1)] techniques has set new standards in high-power femtosecond pulse generation in recent years. Figure 1 illustrates the essential features of CPA. A femtosecond pulse derived from an oscillator is stretched in a grating stretcher to a few hundred picoseconds. After amplification in a medium such as Ti:sapphire, a grating compressor is used to recover the original short duration input pulse. This technique is essential if high energy amplification is to be achieved without encountering nonlinear distortion of the amplified beam or destroying the fidelity of the pulse. Pulses as short as 20 fs are now available with terawatt peak powers, at repetition rates of 10–50 Hz,[2-5)] and with multigigawatt peak power at kilohertz rates. This progress in laser technology has opened the way to investigating and exploiting a wide range of high-field phenomena in the intensity range 10^{17} -10^{19} Wcm^{-2} using small-scale laboratory size laser systems.

Here we report on phase I of the development of a table-top terawatt laser system for experiments in atomic and molecular physics.

The laser system

Figure 2 shows an overview of the laser system. A Spectra Physics Ti:S oscillator is pumped by a large frame argon-ion laser. The oscillator produces 50 fs pulse at 790 nm with about 10 nJ per pulse. The pulses are stretched to about 200 ps in an all-reflective stretcher comprising 1500 lines/mm gratings and concave mirror (ROC = 730 mm), shown in figure 3. The grating stretcher has been designed to take advantage of the Littrow geometry for minimum aberration. The angle of incident $\phi_{Littrow}$ is given by

$$\sin\phi_{Littrow} = \frac{\lambda}{2d}$$

where λ is the wavelength of the laser and d is the line spacing. For a 1500 line/mm grating used in our configuration, $\phi_{Littrow} = 36^0\ 52''$. Currently the system is being run in a near Littrow configuration with plans later in the year to convert both the stretcher and compressor to the Littrow geometry.

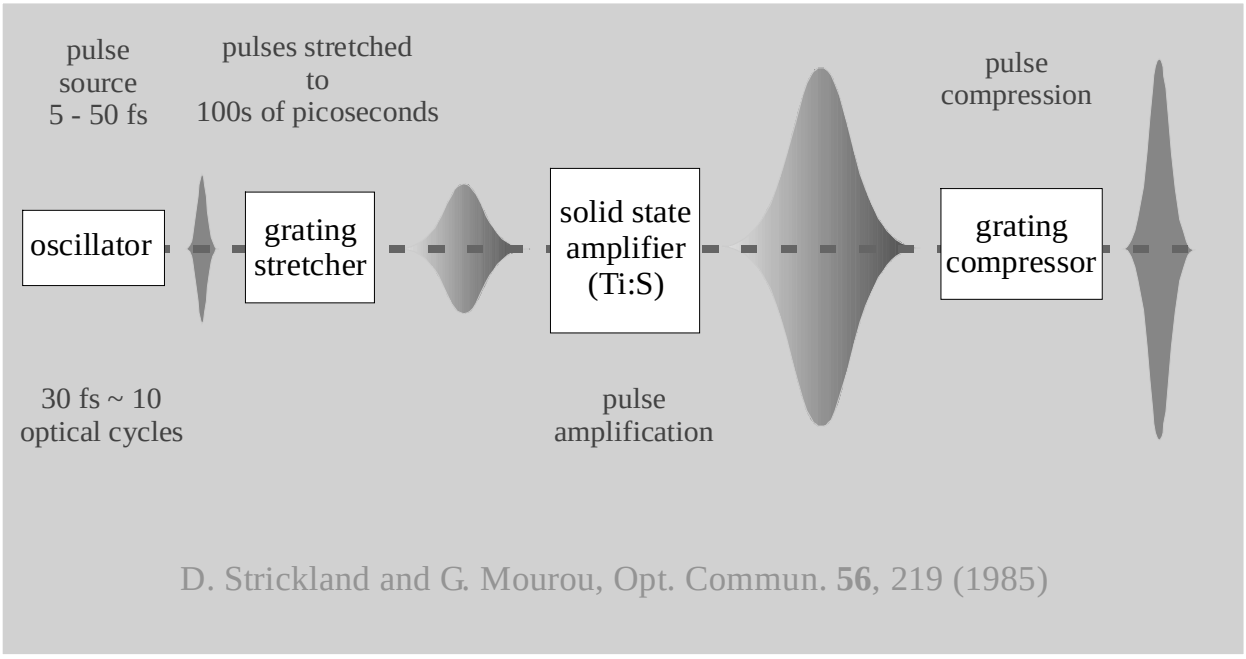

Figure 1. The concept of chirped-pulse amplification in a solid state amplifier

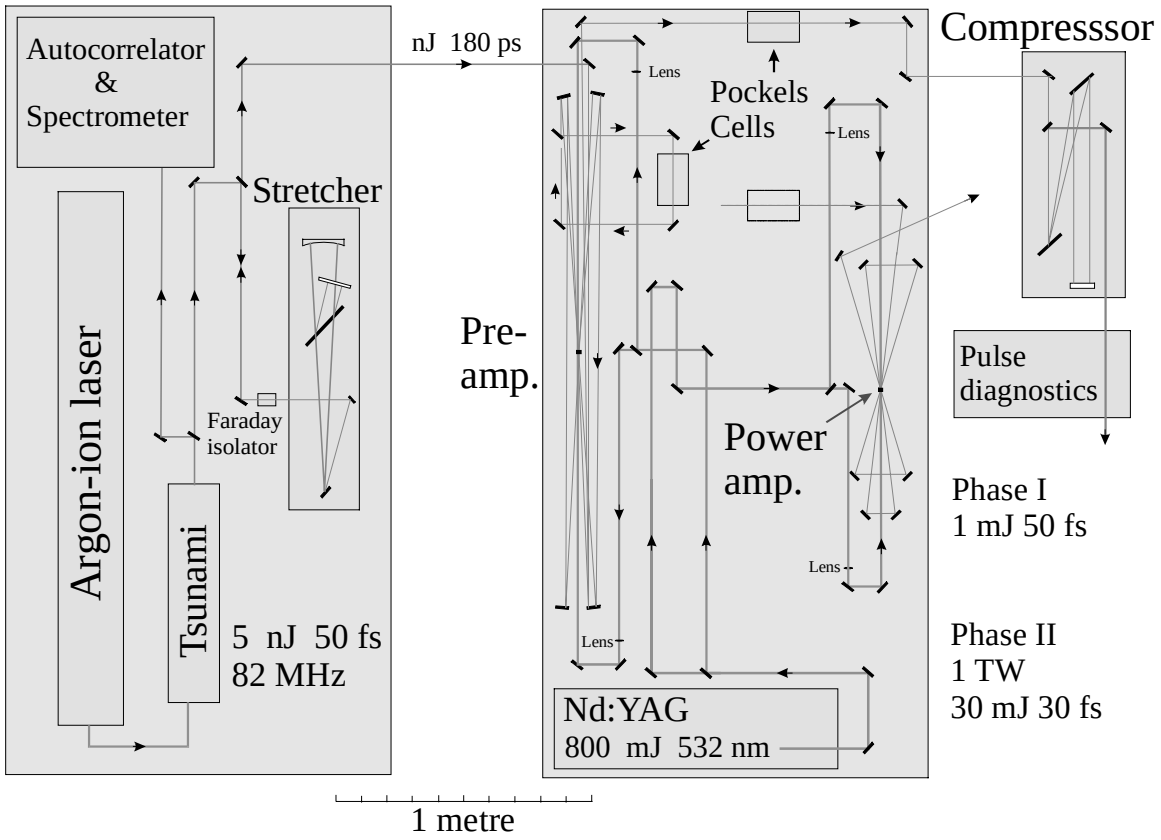

Figure 2. The table-top terawatt system at the Rutherford Appleton Laboratory

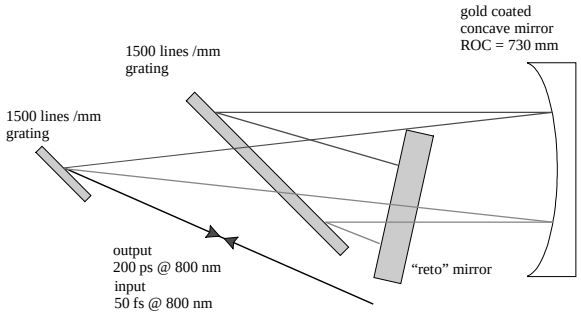

Figure 3. Stretch design for the terawatt programme

The oscillator is isolated from down-beam reflections by passing the beam through a Faraday rotator placed before the stretcher. This allows the input and output beams in the stretcher to be co-linear for minimum beam aberration. The Faraday isolator also directs the stretched pulse beam to the amplifier.

The preamplifier

The stretched pulses are amplified in a multi-pass confocal amplifier. This consists of four spherical mirrors (ROC = 2000 mm) and a 7 mm long Ti:S rod (Crystal Systems. FOM=150 and α_{514} = 4.8) pumped with 67 mJ from a Spectra Physics GCR 270-10 Nd:YAG laser. After the first five passes the pre-amplified pulse train is extracted from the amplifier and passed through a pulse picker to reduce the repetition rate from 82 MHz to 10 Hz. The selected pulse is then reinjected into the amplifier to boost its energy to about 2 mJ. The amplifier provides a total net gain of 4 x 10^6. The beam is then expanded to 4 mm in Galilean telescope prior to compression.

For current user experiments the pulses are compressed to 50 fs using a pair of 1500 lines/mm gratings in a parallel arrangement. The stretcher and compressor were set up using rapid scanning autocorrelators with unamplified oscillator pulses to test that the stretched pulses were successfully recompressed to 50 fs duration. Figure 4 shows autocorrelator traces obtained before stretching and after compression. The small difference is due to different autocorrelators being used for the input and output pulses. Amplified pulses were also monitored on a single shot autocorrelator. A typical autocorrelation is shown in figure 5. We plan to undertake high-dynamic range autocorrelation measurements in order to determine the contrast of the compressed pulse.

The spatial beam quality was determined by focusing the beam through a 50 μm pinhole with a 500 mm focal length lens. The beam was found to be about 1.5 times the diffraction limit.

The spectrum of the amplified beam shown in figure 6 is slightly redshifted from that of the unamplified pulses due to gain pulling towards the gain maximum at 795 nm. The

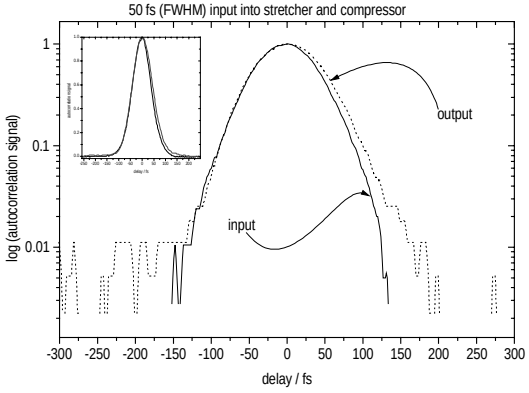

Figure 4. Rapid scanning autocorrelation traces of unstretched 50 fs oscillator pulses and pulses after the compressor. The insert shows a linear plot of the autocorrelation.

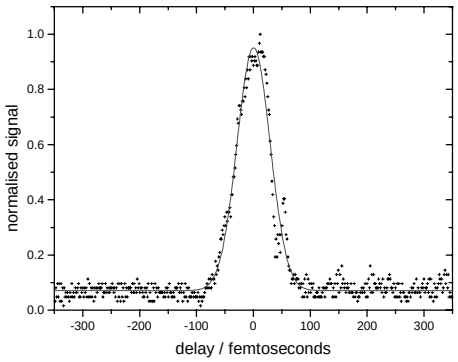

Figure 5. Single shot autocorrelation of the amplified laser pulse

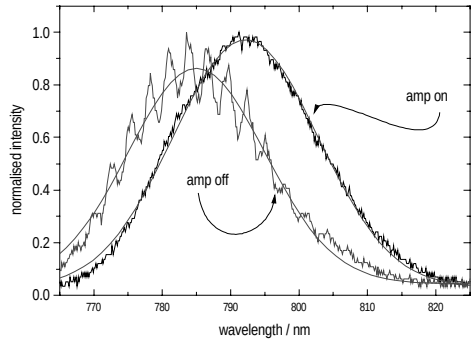

Figure 6. Spectrum of amplified pulse

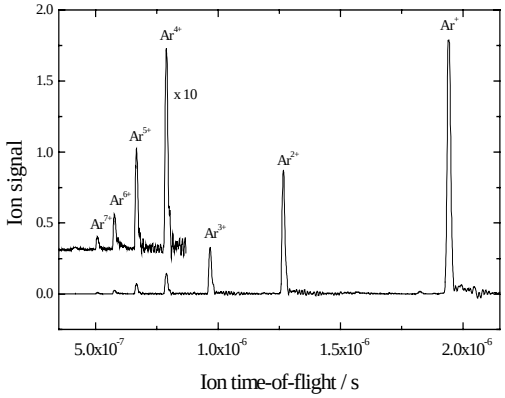

Figure 7. Time-of-flight spectrum of argon

modulation on the unamplified beam is due to a waveplate placed in the system to allow the measurement to occur.

Figure 7 show the time-of-flight spectrum of argon after interacting with the intense femtosecond laser pulse. The observation of the Ar^{7+} shows that we can obtain, with f/3.5 focusing, intensities greater than 10^{16} Wcm^{-2}.

Proposed development of a TW power amplifier

A power amplifier, yet to be commissioned, will comprise a four pass "bow-tie" configuration pumped by the remaining 650 mJ from the Spectra Physics GCR Nd:YAG. We expect to obtain about 100 mJ from this amplifier. The parameters of the Ti:S rod used in the amplifier will be similar to that in the preamplifier.

With 6.5 W average pump power incident on the Ti:sapphire crystal we expect to observe some thermal lensing. The thermal lens has a focal length, f_t given by

$$f_t = \frac{2k\pi\varphi^2}{P_0 dn}$$

where k = thermal conductivity of the rod, φ is the radius of the pumped area, P_0 is the average power of the pump laser absorbed as heat into the rod, and dn is the change of refractive index with respect to temperature. For our system we expect $f_t \approx 35$ m (k = 0.33 $Wcm^{-1}K^{-1}$ and dn = 12.6 x 10^{-6} K^{-1} for Ti:S) which will result in a diminishing beam size though the amplifier if not corrected by the insertion of a suitable negative lens.

The amplified beam will be expanded before compression to a diameter of between 20-25 mm in order to reduce the fluence on the compressor gratings to well below the damage threshold of 100 mJ/cm^2.

In addition we need to consider the intensity dependent nonlinear phase contribution better known as self-phase modulation. A measure of this is given by

$$\psi(t) = \frac{2\pi n_2}{\lambda}\int I(t,l)dl$$

where n_2 is the nonlinear refractive index of the material (for air n_2=3 x 10^{-19} cm^2 W^{-1} and for fused silica n_2=3 x 10^{-16} cm^2 W^{-1}). The equation, known as the "B-integral", is related approximately to the nonlinear group delay by $d\phi/d\omega = B/dv$, where dv is the spectral half-width. If, for example, we take B=1 and assume a pulse bandwidth of 20 nm then an additional optical delay of 17 fs is obtained. Since the intensity varies across the beam there would also be phase distortion resulting in poor beam quantity. In short, for this as in other high power pulsed laser systems, the B-integral should remain below a value of 1. The design parameters will be selected to ensure that this condition is obtained.

Other developments to be undertaken

The Spectra Physics Ti:sapphire oscillator will be replaced with a 20 fs all solid state mirror dispersion controlled system pumped by a frequency doubled cw diode-pumped Nd:YVO_4 laser.

The preamplifier will be pumped by a Continuum SureLite Nd:YAG custom built to provide 150 mJ at 532 nm with a pulse duration of 22 ns. The lengthened pulse duration over a standard 8-10 ns Nd:YAG should reduce the likelihood of damage to the Ti:S amplifying crystal.

To aid identification of phase distortions in the amplified pulses we will be building a device to obtain frequency-resolved optically-gated (FROG) measurements

Summary

We have demonstrated the amplification of 50 fs pulses to the millijoule level at 10 Hz repetition rate. The system has performed well for five scheduled experiments (see articles elsewhere in this CLF Annual Report). We have outlined our objective of generating terawatt pulses before the end of the year.

Table 1 summarises the achieved laser performance in phase I and the expected performance after phase II of the development programme to be completed by September 1998.

Figure 8 shows Dr Ian Williams from the Queen's University, Belfast setting up an experiment in the Femtosecond Science Laboratory.

	Phase I	Phase II
Pulse energy	1 mJ	>40 mJ
Pulse duration	50 fs	40 fs
Peak power	20 GW	>1 TW
Focused intensity (f/2)	$>10^{16}$ Wcm^{-2}	$>5x10^{17}$ Wcm^{-2}
Wavelength	800 nm	800 nm
Repetition	10 Hz	10 Hz

Table 1. Summary of performance

Acknowledgments

The authors wish to thank Dr Roy Newell and his group from University College London for the time-of-flight measurements of argon during their scheduled experiments at the CLF. We would also like to thank Dr Ken Ledingham and his group from the University of Glasgow for the use of vacuum apparatus in undertaking some test measurements.

References

1. D. Strickland and G. Mourou, Opt. Commun. **56,** 219 (1985).
2. J. Squier, F. Salin, G. Mourou, and D. Harter, Opt. Lett. **16,** 324 (1991).
3. J. D. Kmetec, J. J. Macklin, and J. F. Young, Opt. Lett. **16,** 1001 (1991).
4. K. Yamakawa, H. Siraga, Y. Kato, and C. P. J. Barty, Opt. Lett. **16,** 1593 (1991).
5. T. B. Norris, Opt. Lett. **17,** 1009 (1992).
6. J. V. Rudd, G. Korn, S. Kane, J. Squier, G. Mourou, and P. Bado, Opt. Lett. **18,** 2044 (1993).
7. J. P. Zhou, C. P. Huang, M. M. Murnane, and H. C. Kapteyn, Opt. Lett. **20,** 64 (1995).
8. C. P. J. Barty, T. Guo, C. Le Blanc, F. Raksi, C. Rose-Petruck, J. Squier, K. R. Wilson, V. V. Yakovlev, and K. Yamakawa, Opt. Lett. **21,** 668 (1996).
9. C.P. J. Barty, C. L. Gordon III, and B. E. Lemoff, Opt. Lett. **19,** 1442 (1994).
10. J. P. Chambaret, C. Le Blanc, G. Cheriaux, P. Curley, G. Darpentigny, P. Rousseau, G. Hamoniaux, A. Antonetti, and F. Salin, Opt. Lett. **21,** 1921 (1996).
11. Lenzer, Ch. Spielmann, E. Wintner, F. Krausz, and A. J. Schmidt, Opt. Lett. **20,** 1397 (1995).
12. S. Backus, J. Peatross, C. P. Huang, M. M. Murnane, and H. C. Kapteyn, Opt. Lett. **20,** 2000 (1995).
13. I.N. Ross, A.J. Langley and P.F.Taday, to be published.
14. P. Georges, F. Estable, F. Salin, J.P. Poizat, P. Grangier and A.Brun, Opt. Lett. **16**(3) 144 (1991).

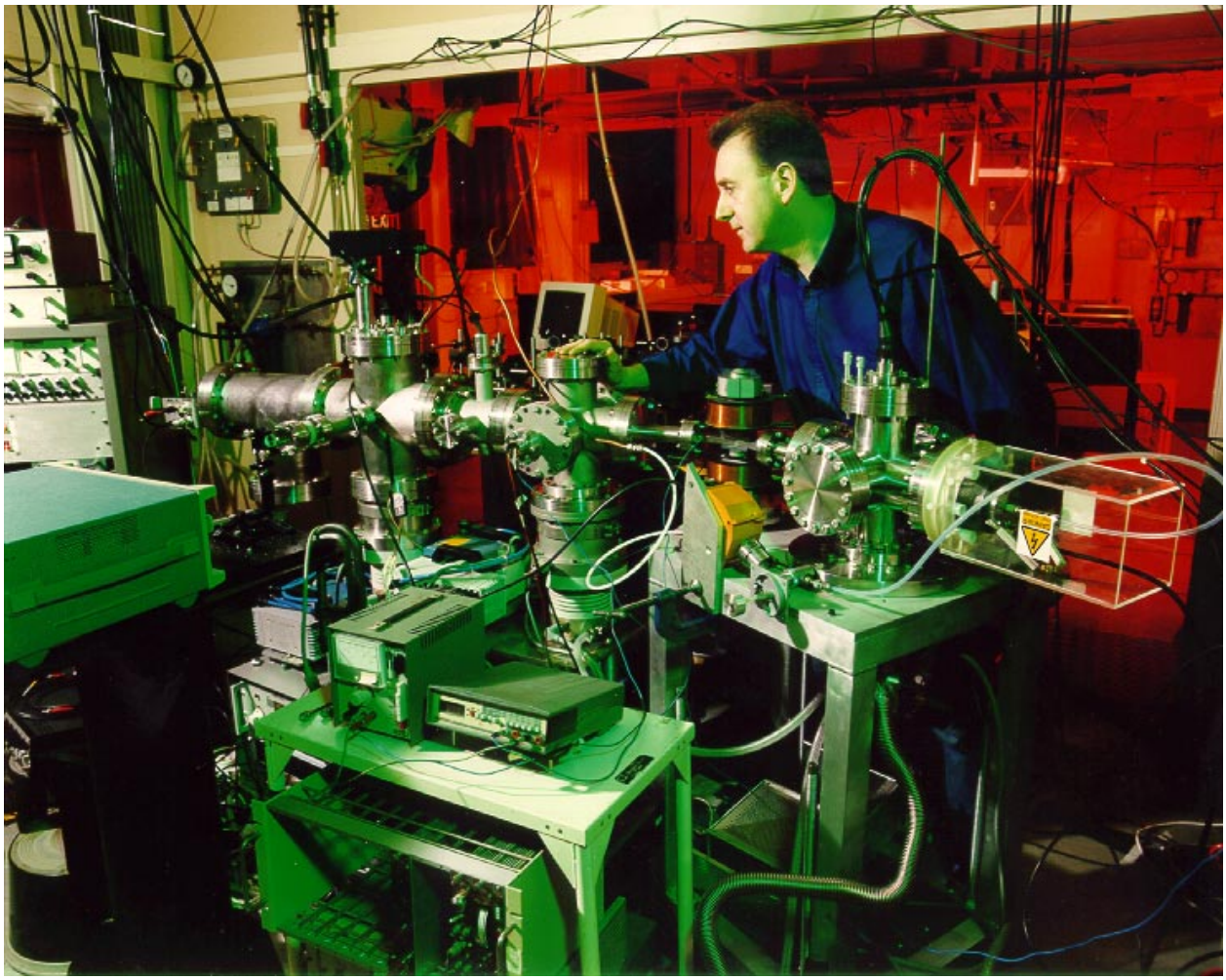

Figure 8. Dr Ian Williams from the Queen's University, Belfast setting up an experiment in the Femtosecond Science Laboratory.

Dual Diode Array System for Transient Absorption Spectroscopy

M Towrie, P Matousek, A W Parker, S Jackson.

CLRC Rutherford Appleton Laboratory, Chilton, Didcot, Oxon., OX11 0QX. Email M.Towrie@rl.ac.uk

R H Bisby.

Biosciences Division, Science Research Institute, Peel Building, University of Salford, M5 4WT

Introduction

Femtosecond transient absorption spectroscopy is a technique for interrogating electronic transitions of photochemically prepared short lived intermediates. In combination with the structural information obtained from picosecond transient resonance Raman spectroscopy (ps-TR^3) it provides a powerful tool for studying solution phase systems and disentangling complex data.

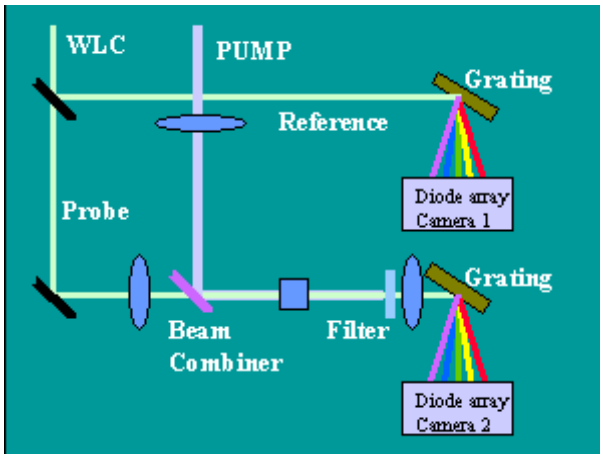

We have recently commissioned a state-of-the-art dual diode array transient absorption system at the Lasers for Science Ultrafast Spectroscopy Laboratory to enhance the capability of the existing ps-TR^3 apparatus. The system was custom built to our specifications by Laser 2000 Ltd/Cronin Electronics GmbH and enables the simultaneous detection of transient absorption signals across a wide spectral range. Fast electronics accomplishes real-time pulse-to-pulse data normalization. This system has the same sensitivity as the single channel system used previously but gives two orders of magnitude higher signal-to-noise than the previous multichannel CCD detector arrangement.

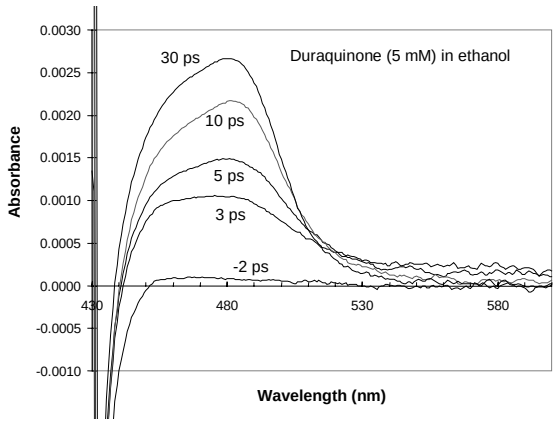

Figure 1. Transient absorption spectrum of duraquinone (5 mM) in ethanol at various time delays. The pump wavelength was 400 nm (accumulation time was 10 mins for each spectrum).

Specifications

- absorbance sensitivity $< 10^{-3}$
- repetition rate 0.8 kHz
- time-resolution 500 fs
  (unremoved chirp ~2 ps/100 nm)
- number of channels 512 px/array
- current wavelength range
  probe 420-700 nm
  (to be extended)
  pump (OPA) 205-2200 nm
- pump pulse energy ~ 1 μJ
- spectral resolution ~15 nm
- detection window ~200 nm

The detection system yields the transient absorption spectra at given time delay (see figure 1) obtained by probing using white-light continuum. At the same time the data contains the kinetic information which can be viewed by plotting the absorbance signal versus time delay at any given wavelength (see figure 2).

The ps/fs optical parametric amplifier (OPA) system at the front end gives virtually unlimited choice of pump wavelength (220 - 2200 nm, > 1 μJ).

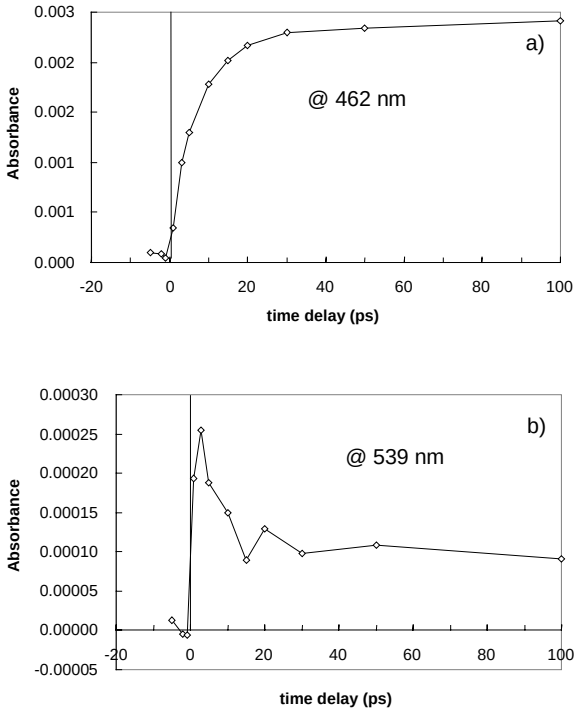

Figure 2. Sections through transient absorption data shown in figure 1 at different wavelengths.

SCHEDULES AND OPERATIONAL STATISTICS

1) Vulcan

2) Titania

3) Lasers *for* Science Facility – RAL Based

4) Lasers *for* Science Facility – Laser Loan Pool

Vulcan Operational Statistics

D A Pepler.

CLRC Rutherford Appleton Laboratory, Chilton, Didcot, Oxon., OX11 0QX, UK. Email D.A.Pepler@RL.AC.UK

In this reporting period (April '97 to March '98) a major facility development programme, namely the Phase I Petawatt upgrade, was commissioned and fourteen other experiments have been conducted. The majority of the experiments were for EPSRC with one experiment for the EU TMR Large Scale Facilities access programme. A broad range of experiments have taken place with a good level of laser shots. The majority of the experiments have been in the two main target areas; west (TAW) and east (TAE).

A total of 8868 shots were fired during the year with 4795 shots into the laser area for test or alignment purposes and 4073 shots delivered to the target areas. These are comparable to last year's totals (5027 into the laser area and 4679 into the target area). The total number of shots has fallen by a little more than 9%. Nonetheless a total of 1497 disc amplifier shots were fired for laser-plasma interaction studies.

Experimental set-ups continue to increase in complexity and about 60% of the shots into the target areas were required to establish beam timings, crystal tunings and to set-up and calibrate the instruments and establish the required experimental conditions.

Table 1 indicates the full statistics for the experimental programme giving totals for the number of shots fired, target shots (disc shots) and failed target shots for each individual experiment and area (maintenance weeks not shown). Chart 1 indicates the relative breakdown of the target shots fired into each area.

No significant down time was experienced during the year with only odd days being lost due to pulse timing, capacitor bank, or rod amplifier problems.

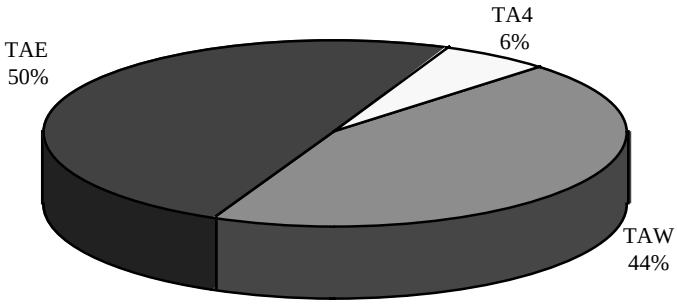

Chart 1 Relative number of target shots per area

EXPERIMENTAL PERIOD Apr '97 - Mar '98	EXPERIMENT (Total number of shots - Target shots - Failed target shots)		
	TAE	TAW	TA4
31 Mar - 27 Apr	Phase I Petawatt		
28 Apr - 11 May	Holhraum (516 - 102 - 2)	Petawatt commissioning (445 - 39 - 0)	
12 May - 8 June			Ultra Dense plasma studies (265)
16 June - 29 June	X-ray laser radiography (152-96-5)	X-ray laser (380-76-2)	
30 June - 27 July			
4 Aug - 17 Aug	X-ray scattering (317 - 130 - 2)	Spectroscopy (118 - 102 - 0)	
18 Aug - 14 Sept			
22 Sept - 5 Oct	Holhraum (520 - 130 - 4)	Short pulse propagation (336 - 77 - 3)	
6 Oct - 2 Nov			Ultra Dense plasma studies
10 Nov - 23 Nov	X-ray laser (167 - 146 - 1)	Solid target interaction (176 - 111 - 3)	
24 Nov - 21 Dec			
5 Jan - 18 Jan	X-ray laser radiography (196-163-5)	EU TMR experiment (262 - 125 10)	
19 Jan - 15 Feb			
23 Feb - 8 Mar	X-ray scattering (295 - 94 - 6)	Spectroscopy (193 - 106 - 6)	
9 Mar - 5 Apr			
Totals	(2163 - 861 - 25)	(1910 - 636 - 24)	(265)

Table 1. VULCAN statistics for the year ending March '98

Titania Operational Statistics

E J Divall, G J Hirst, A K Kidd, J M D Lister, C E Marker.

CLRC Rutherford Appleton Laboratory, Chilton, Didcot, Oxon., OX11 0QX. Email E.J.Divall@RL.AC.UK

Scheduled operations

The second year of operations on Titania saw an increased amount of scheduled experimental time (see Table 1.). In all eight experiments were run, totaling 35 weeks, a 60% increase over 1996/7. Seven of the experiments were scheduled for the EPSRC. The remaining one formed part of the EU TMR programme. The laser was operated in CPA mode and, for the first time, in Raman and Materials Processing modes.

The remaining time was devoted to routine maintenance, scheduled shutdowns and to detailed investigation of system performance, in particular of the CPA far-field beam quality and of the Raman amplifier energy conversion efficiency. Both of these parameters were improved significantly during the year.

There was some unscheduled downtime associated with pulsed power failures, mainly on the Sprite preamplifier. This problem was being addressed at the end of the year with a redesign of the Sprite PFL switches, described in more detail elsewhere in this report.

Experiment	Institution	Dates (incl Setup)	Laser Configuration	Pulse Duration	Pulse Energy (typical)	Target Shots
Raman commissioning	RAL (Shaw)	1.4.97-11.5.97	Raman	30 ps	8 J	345
Solid target interactions	RAL (Norreys)	12.5.97-22.6.97	Raman	30 ps	8 J	81
Materials processing	Nottingham Trent (Thomas)	30.6.98-6.7.97	MP	15 ns	1 J cm^{-2}	47
Raman commissioning	RAL (Shaw)	28.7.97-7.9.97	Raman	30 ps	8 J	234
Femtosecond acceleration	FSU Jena (Sauerbrey)	13.10.07-23.11.97	CPA	350 fs	300 mJ	91
High energy density X-ray source	Essex/RAL (Tallents & Rose)	5.1.98-15.2.98	CPA	350 fs	300 mJ	214
X-ray spectroscopy	Oxford (Wark)	16.2.98-8.3.98	CPA	350 fs	300 mJ	50
Materials processing	Nottingham Trent (Thomas)	16.3.98-22.3.98	MP	15 ns	1 J cm^{-2}	31

Table 1. Scheduled experiments on Titania

Schedule of RAL-Based Experiments at the Lasers *for* Science Facility 1997/98

Date	Femtosecond Science Laboratory	Laser Microscope Laboratory	Nanosecond Science Laboratory	Ultrafast Spectroscopy Laboratory	X-Ray Laboratory	Date
31-Mar-97	**FREY** (Southampton)					31-Mar-97
07-Apr-97	Studies of atmospheric aerosol material by surface SHG		**MAINTENANCE**		**MICHETTE/ BUCKLEY/TURCU** (KCL/RAL)	07-Apr-97
14-Apr-97			**COMMERCIAL CONTRACT**	**TRUSCOTT/ PARKER** (Keele/RAL)	Laboratory Scanning X-ray Microscope	14-Apr-97
21-Apr-97	FL4C3/96	**JONES/MOUNT** (Edinburgh)		Solvent Dependence of the picosecond TR3 Spectra of Carotenoids	XU5P4/97	21-Apr-97
28-Apr-97		Photophysics of Novel Electropolymerised Indoles		US2C4/97	**THOMAS/STEVENS/ CRANTON** (Not'hm Trent) Materials Engineering for Electro-luminescent Displays XU6M4/97	28-Apr-97
05-May-97			**SCHOLES/PHILLIPS / PARKER** (Imperial College/RAL)		**BIJKERK/ SHMAENOK/STUIK** (FOM, Holland)	05-May-97
12-May-97		LM2C4/97	Resonance Raman Excitation Profiles of Chromophore Aggragates	**FEMTOSECOND AND TRANSIENT ABSORPTION DEVELOPMENT**	Optimisation of Narrowband Extreme Ultraviolet Source for Applications in Lithography	12-May-97
19-May-97	**TERAWATT FEMTOSECOND DEVELOPMENT**					19-May-97
26-May-97			NS2C4/97		XU5P1/97	26-May-97
02-Jun-97		**MACROBERT/ PHILLIPS** (UCL/Imperial)	**TRUSCOTT/ PARKER/ TAVENDER** (Keele/RAL)		**CAIRNS/ FITZGERALD/ LAWRENSON** (Dundee)	02-Jun-97
09-Jun-97	**GR/L37458**	Time-Resolved Fluorescence Bio-imaging	Time-Resolved Resonance Raman Studies of Carotenoid Radical Cations	**BROWN** (UCL) Femtosecond Kinetics of ESIPT in 3-hydroxyflavones	Manufacture of Next-Generation Photomasks for Electronic Devices and Sensors XU2M4/97	09-Jun-97
16-Jun-97		LM3B4/97		US1C4/97	**WILSON/TURCU** (Heriot Watt/RAL)	16-Jun-97
23-Jun-97			NS4C4/97		Diamond Etching with the Laser Plasma X-ray Source XU7M4/97	23-Jun-97
30-Jun-97			**CREST**			30-Jun-97
07-Jul-97		**BEEBY/FAULKNER** (Durham)	**MAINTENANCE**		**FOLKARD/PRISE/ MICHAEL** (Gray Lab)	07-Jul-97
14-Jul-97		Time-Resolved Imaging of Biological Systems using Neodymium Complexes LM1C4/97	**BISBY** (Salford)	**TRUSCOTT/ PARKER** (Keele/RAL)	Focused laser plasma generated vacuum-UV X-rays to determine the action-spectra for the induction of DNA damage for low-energy photons XU3B4/97	14-Jul-97
21-Jul-97			Time-Resolved Resonance Raman Spectroscopy and laser flash photolysis	Solvent Dependence of the picosecond TR3 Spectra of Cartenoids		21-Jul-97
28-Jul-97					**COSTELLO/ MCGUINESS** (DCU, Dublin)	28-Jul-97

Continued…

Date	Femtosecond Science Laboratory	Laser Microscope Laboratory	Nanosecond Science Laboratory	Ultrafast Spectroscopy Laboratory	X-Ray Laboratory	Date
04-Aug-97			**ROSS/MATOUSEK/ DANSON** (RAL)	**PHILLIPS/PARKER** (IC)	Spatially Temporally resolved dual laser plasma photoabsorption with extreme UV continuum light source	04-Aug-97
11-Aug-97			Optical Parametric Chirped Pulse Amplifiers NS3AP1/97	TR3 studies of charge transfer		11-Aug-97
18-Aug-97			**SIMPSON/TOWRIE/ GRIFFITHS** (Oxford/RAL)		XU6P1/97	18-Aug-97
25-Aug-97			Energy Transfer and Laser Induced Photolysis of Physisorbed Molecules on Dielectric surfaces using Infrared and Ultraviolet lasers NS4C1/97	US2C1/97	**MAINTENANCE WEEK**	25-Aug-97
01-Sep-97					**MILANI/BATANI** (Milan, Italy)	01-Sep-97
08-Sep-97				**LONG/BRADLEY** (Sheffield)	Differential, two colour X-ray radiobiology in yeast cells	08-Sep-97
15-Sep-97				Emission dynamics under high excitation in polymers		15-Sep-97
22-Sep-97		**JONES/MOUNT** (Edinburgh)	**ROSS/MATOUSEK/ DANSON** (RAL)	US1P1/97	XU7P1/97	22-Sep-97
29-Sep-97		Photophysics of novel electro-polymerised Indoles	Optical Parametric Chirped Pulse Amplifiers	**VLCEK** (Queen Mary)	**O'NEILL** (MRC)	29-Sep-97
06-Oct-97		LM01C1/97	NS3BP1/97	Dynamics of metal-ligand bond splitting	DNA modification by 193 nm light XU2B1/97	06-Oct-97
13-Oct-97		**MacROBERT** (UCL)	**MAINTENANCE WEEK**	US3C1/97	**CRANTON/THOMAS /STEVENS** (Nottingham Trent) Materials engineering for high efficiency full colour TFEL devices XU9AN1/97	13-Oct-97
20-Oct-97		Confocal fluorescence lifetime imaging microscopy	**PHILLIPS/PARKER** (IC/RAL)	**PHILLIPS/PARKER** (IC/RAL)	**MICHETTE/ BUCKLEY/TURCU** (KCL/RAL)	20-Oct-97
27-Oct-97	**LANGLEY/ROSS/ TADAY/ CODLING/NEWELL/ RILEY/ WILLIAMS/ PRESTON** (RAL/Reading/ Glasgow/UCL/QUB/ Oxford) Femtosecond Laser Post-development Pilot Experiments FL3P1/97			TR3 Studies of Charge Transfer US5AC2/97		27-Oct-97
03-Nov-97		LM02B1/97	TR3 Studies of Charge Transfer	**SETA** (CNRS France) Photoinduced absorption studies in porphyrin triads US8C1/97	Laboratory Scanning X-ray Microscope	03-Nov-97
10-Nov-97		**JONES/MOUNT** (Edinburgh)	NS2 1/97			10-Nov-97
17-Nov-97		Photophysics of novel electro-polymerised Indoles	**BISBY** (Salford)		XU1P1/97	17-Nov-97
24-Nov-97	**NEWELL/WILLIAMS/ SANDERSON** (UCL/QUB)	LM01C1/97	Time-Resolved spectroscopy of protein-Radical enzymes NS01B1/97	**KLUG** (IC) Evaluation and application of an ultra-short laser produced X-ray source	**CRANTON/THOMAS /STEVENS** (Nottingham Trent) Materials engineering for high efficiency full colour TFEL devices XU9BN1/97	24-Nov-97

Continued…

Date	Femtosecond Science Laboratory	Laser Microscope Laboratory	Nanosecond Science Laboratory	Ultrafast Spectroscopy Laboratory	X-Ray Laboratory	Date
01-Dec-97	Interaction of femtosecond pulses with ground state and excited		**PHILLIPS/PARKER** (IC/RAL)		**CAIRNS/ FITZGERALD/ LAWRENSON** (Dundee)	01-Dec-97
08-Dec-97	molecules & +ve ions		TR3 Studies of Charge Transfer	US9P1/97	The manufacture of next generation photmasks for electronic devices and sensors XU1AP2/97	08-Dec-97
15-Dec-97	FL2AP2/97		NS3AC2/97	**PHILLIPS/PARKER** (IC/RAL) US5BC2/97	**O'NEILL/MELVIN/ PARKER** (MRC/RAL) XU2AM2/97	15-Dec-97
22-Dec-97	**CHRISTMAS**	**CHRISTMAS**	**CHRISTMAS**	**CHRISTMAS**	**CHRISTMAS**	22-Dec-97
29-Dec-97						29-Dec-97
05-Jan-98	**FRASINSKI/ CODLING** (Reading)		**PHILLIPS/PARKER** (IC/RAL)	**PHILLIPS/PARKER** (IC/RAL)	**MAINTENANCE**	05-Jan-98
12-Jan-98	Multiphoton dissociative ionization of H2 with	**JONES/MOUNT** (Edinburgh)	TR3 Studies of Charge Transfer	TR3 Studies of Charge Transfer	**O'NEILL/MELVIN/ PARKER** Hole migration in DNA XU2BM2/97	12-Jan-98
19-Jan-98	ultrashort 3rd harmonic Ti:S laser pulses	Photophysics of novel electro-polymerised Indoles LM3C2/97	NS3BC2/97	US5C2/97	**MICHETTE/ BUCKLEY/TURCU** (KCL/RAL)	19-Jan-98
26-Jan-98			**MAINTENANCE**	**FERREIRA** (Lisbon, Portugal)		26-Jan-98
02-Feb-98	FL1P2/97	**MacROBERT/ PHILLIPS** (UCL/IC)		Photophysics of cyanine dyes	Laboratory Scanning X-ray Microscope	02-Feb-98
09-Feb-98	**NEWELL/WILLIAMS/ SANDERSON** (UCL/QUB)	Confocal fluorescence lifetime imaging microscopy		US6C1/97		09-Feb-98
16-Feb-98	Interaction of femtosecond			**OELKRUG** (Tubingen, Germany)		16-Feb-98
23-Feb-98	pulses with ground state and excited molecules & +ve ions	LM4B2/97		Photoinduced absorption in highly ordered films	XU3P2P/967	23-Feb-98
02-Mar-98	FL2BP2/97	**JONES/MOUNT** (Edinburgh)		US7C1/97	**CRANTON/THOMAS /STEVENS** (Nott'm) Electroluminescent displays XU4E2/97	02-Mar-98
09-Mar-98	**Commissioning of ultrashort pulse oscillator**	Photophysics of novel electropolymerised Indoles	**O'NEILL/MELVIN/ PARKER** (MRC/RAL) Reaction of excited state nucleic acid bases with oxygen NS1AM2/97	**FREY** (Southampton)	**CAIRNS/ FITZGERALD/ LAWRENSON** (Dundee) The manufacture of next generation	09-Mar-98
16-Mar-98				Investigation of surface chemistry using SHG	photmasks for electronic devices and sensors	16-Mar-98
23-Mar-98		LM3C2/97		US3C2/97	XU1BP2/97	23-Mar-98

Schedule of the Lasers *for* Science Facility's Laser Loan Pool 1997/98

Date	NSL1	NSL2	NSL3	NSL4	NSL5	NSL6	CWL1	CWL2
April 7	**ASHWORTH** **Bristol**		**WHITEHEAD** **Manchester**		**McKENDRICK** **Edinburgh**	**SIMONS** **Oxford**	**FRENCH** **Liverpool**	**WITHNALL** **Greenwich**
14		**JONES**						
21	**LP1C2/96**	**Edinburgh**	**LP9 C2/96**		**LP5 C2/96**	**LP4C3/96**	**LP1M3/96**	**LPB3/96**
28				**TURBERFIELD**				
May 12	Detection and identification of low-	**LP2B3/96**		**Oxford**		Charge separation & the primary processes in acid base catalysis		Study of upconversion emmission from Er(3+) Co-doped with Yb(3+) into sol-gel silica glasses under IR light excitation
19		Laser desorption supersonic jet spectroscopy of tyrosine peptides		**LP5P3/96**				
26	lying electronic states of transition metal compounds using laser induced grating spectroscopy		extended		**SIMS/SMITH** **Birmingham**			
June 9			UA	The fabrication and assessment of 3-D photonic crystals	**LP2C4/97**		**POTTON** **Salford**	
16								
23					Reactive processes in the gas phase at ultralow temperatures		**LP5P197**	
30							Adaptive signal processing using photochromic glass spatial filter	
July 14			**GORRY** **Manchester**					
21								
28	**COSTELLO** **X-RAY 3 wks**		**LP2C197**			**SIMONS** **Oxford**		*Tests of Tsunami Millennia system* RAL + **ROSS** **RAL** **NS03P1/97**
Aug. 11			An investigation of the inelastic scattering and trapping / desorption of Br2 + GaAs (100)					
18								
25	**SIMS** **Birmingham**	**DENNING** **Oxford**		**HANCOCK** **Oxford**		**LP6C197**		
Sept. 8								
15	**LP7C197**	**LP1C197**		**LP4C197**		Charge separation in hydrated molecular clusters.		
22					**GRAHAM** **QUB**			
29	Reactive processes in gas phase at ultra-low temperatures: reactions of C-atoms	The correlation crystal field in lanthanide spectroscopy		Reaction dynamics with monoenergetic atoms	**LP3P197**			Optical parametric amplification of chirped pulses
Oct. 6								
13					Detection of sputtered atoms			
21								
28						Extended		
Nov. 3								
10			Div. Heads Extension					
17								
24								**HICKEN** **Exeter**
Dec. 8							**FRENCH** **Liverpool**	
15								**LP6P2/97**
22							**Div. Head**	
29						**HANCOCK** **Oxford**		Generation of optically triggered magnetic field pulses with ultrafast rise times
Jan. 12	**ELLIS** **Leicester**	**POWIS** **Nottingham**	**GEORGE** **Nottingham**	**SMITH** **Birmingham**			High speed filming of flow dynamics surrounding a plasma plume during laser induced plasma deposition	
19						**LP5C2/97**		
26	**LP2C2/97**	**LP7C2/97**	**LP3C2/97**					
Feb 2				**LP9C2/97**	**GRAHAM** **QUB**	Reaction dynamics with monoenergetic atoms		
9	Stimulated emission pumping spectroscopy of the alkali monoxides	Competitive dynamical processes in UV excited polyatomic molecules	Time resolved spectroscopy in inonventional conventional and supercritical fluids	Rovibrational energy transfer and rotational effects on bimolecular reactions				
16								
23					EXTENSION			
Mar 2								
9								
16					MAINTENANCE & REPAIR			
23								
30								**HICKEN** **Exeter**
Apr 6							**GILKES**	

PUBLICATIONS

1) Science – High Power Laser Programme

2) Science – Lasers *for* Science Facility Programme

3) Facility Developments

Science - High Power Laser Programme

JOURNAL PUBLICATIONS, BOOKS AND PUBLISHED PROCEEDINGS

A Behjat, G J Tallents, D Neely
The characterization of a high-density gas jet
J Phys D-Applied Physics **30** (20) 2872-2879 (1997)

A D Badger, R Evans, F Fallies, T A Hall, M H Mahdieh, P Audebert, J-C Gauthier, J-P Geindre, A Djaoui, A Antonetti, A Mysyrowicz
Femtosecond laser driven shock waves
Advances in Laser Interaction with Matter and Inertial Fusion, Proceedings of 24th ECLIM Eds G Velarde, J M Martinez-Val, E Minguez, J M Perlado, publ World Scientific 661-664 (1997)

A R Bell, J R Davies, S Guerin, H Ruhl
Fast-electron transport in high intensity short-pulse laser light at relativistic intensities
Plasma Physics and Controlled Fusion **39** (5) 653-659 (1997)

M Borghesi, A Giulietti, D Giulietti, L Gizzi, A Macchi, D Neely, O Willi
Underdense plasmas from thin films: production, interferometric characterisation and short-pulse interaction studies
Advances in Laser Interaction with Matter and Inertial Fusion, Proceedings of 24th ECLIM Eds G Velarde, J M Martinez-Val, E Minguez, J M Perlado, publ World Scientific 581-584 (1997)

M Borghesi, A J MacKinnon, L Barringer, L A Gizzi, C Meyer, O Willi
Propagation of a short laser pulse in preformed plasmas at relativistic intensities
Advances in Laser Interaction with Matter and Inertial Fusion, Proceedings of 24th ECLIM Eds G Velarde, J M Martinez-Val, E Minguez, J M Perlado, publ World Scientific 633-636 (1997)

R E Burge, G E Slark, M T Browne, X-C Yuan, P Charalambous, X-H Cheng, C L S Lewis, A MacPhee, D Neely
Spatial coherence of x-ray laser emission from neonlike germanium after prepulse
JOSA B-Optical Physics **14** (10) 2742-2751 (1997)

J R Davies, A R Bell, M G Haines, S M Guerin
Short-pulse high-intensity laser-generated fast electron transport into thick solid targets
Phys Rev E **56** (6) 7193-7203 (1997)

T Ditmire, E T Gumbrell, R A Smith, A Djaoui, M H R Hutchinson
Time-resolved study of nonlocal electron heat transport in high temperature plasmas
Phys Rev Letts **80** (4) 720-723 (1998)

D L Foulis, S J Rose, T D Beynon
Transient multicentre electronic structure in dense plasmas
J Quant Spectr & Rad Trans **58** (4-6) 577-583 (1998)

D Gordon, K C Tzeng, C E Clayton, A E Dangor, V Malka, K A Marsh, A Modena, W B Mori, P Muggli, Z Najmudin, D Neely, C Danson, C Joshi
Observation of electron energies beyond the linear dephasing limit from a laser-excited relativistic plasma wave
Phys Rev Letts **80** (10) 2133-2136 (1998)

M J Grout, G J Pert, A Djaoui
Propagation effects in optical-field-induced gas mixture breakdown for recombination x-ray lasers
J Phys B-Atomic Molecular and Optical Physics **31** (1) 197-207 (1998)

D J Heading, A Machacek, L C Whitford, A J Varney, J S Wark, R W Lee, R Stamm, B Talin
Rapid generation of approximate optical spectra of dense cool plasmas
J Quant Spectr & Rad Trans **58** (4-6) 619-626 (1997)

D J Heading, J S Wark, R W Lee, R Stamm, B Talin
Comparison of the semiclassical and modified semiempirical method of spectral calculation
Phys Rev E **56** (1) 936-946 (1997)

D Hoarty, A Iwase, C Meyer, J Edwards, O Willi
Characterization of laser driven shocks in low density foam targets
Phys Rev Letts **78** (17) 3322-3325 (1997)

D H Kalantar, L B DaSilva, S G Glendinning, F Weber, B A Remington, S V Weber, E Wolfrum, M H Key, D Neely, N S Kim, J S Wark, J Zhang, C L S Lewis, A McPhee, J Warwick, A Demir, J Lin, R Smith, G J Tallents, J P Knauer
Measurements of laser imprint by XUV radiography using an X-ray laser
Advances in Laser Interaction with Matter and Inertial Fusion, Proceedings of 24th ECLIM Eds G Velarde, J M Martinez-Val, E Minguez, J M Perlado, publ World Scientific 164-167 (1997)

N S Kim, A Djaoui, M H Key, J S Wark, D Neely, S G Preston, M Zepf, C G Smith, A A Offenberger
Numerical modelling of the optical field ionized nitrogen recombinant XUV scheme
Advances in Laser Interaction with Matter and Inertial Fusion, Proceedings of 24th ECLIM Eds G Velarde, J M Martinez-Val, E Minguez, J M Perlado, publ World Scientific 511-514 (1997)

D H Kalantar, M H Key, L B DaSilva, S G Glendinning, B A Remington, J E Rothenberg, F Weber, S V Weber, E Wolfrum, N S Kim, D Neely, J Zhang, J S Wark, A Demir, J Lin, R Smith, G J Tallents, C L S Lewis, A MacPhee, J Warwick, J P Knauer
Measurements of direct drive laser imprint in thin foils by radiography using an x-ray laser backlighter
Physics of Plasmas **4** (5 Pt2) 1985-1993 (1997)

R J Kingham, A R Bell
Enhanced wakefields for the 1D laser wakefield accelerator
Phys Rev Letts **79** (24) 4810-4813 (1997)

J Y Lin, G J Tallents, A Demir, S B Healy, G J Pert
Optimization of double drive pulse pumping in Ne-like Ge x-ray lasers
J Appl Phys **83** (4) 1863-1868 (1998)

A Lorenz, A K L Dymoke-Bradshaw, A E Dangor
Optical multi-frame system with one gated intensifier as a diagnostic for high-speed photography
Measurement Science & Technology **8** (6) 676-678 (1997)

V Malka, A Modena, Z Najmudin, A E Dangor, C E Clayton, K A Marsh, C Joshi, C N Danson, D Neely, F Walsh
Second harmonic generation and its interaction with relativistic plasma waves driven by forward Raman instability in underdense plasmas
Physics of Plasmas **4** (4) 1127-1131 (1997)

D Neely, P Norreys, M Zepf
A high efficiency soft X-ray and optical spectrometer design
Advances in Laser Interaction with Matter and Inertial Fusion, Proceedings of 24th ECLIM Eds G Velarde, J M Martinez-Val, E Minguez, J M Perlado, publ World Scientific 669-672 (1997)

P V Nickles, M Schnurer, M P Kalachnikov, W Sandner, V N Shlyaptsev, C N Danson, D Neely, E Wolfrum, J Zhang, A Behjat, A Demir, G J Tallents, P J Warwick, C L S Lewis
Transient inversion XUV lasers in Ti and Ge
Soft X-ray lasers and applications II, Eds J J Rocca, L B Da Silva, SPIE **3156** 80-85 (1997)

P A Norreys, C N Danson, A P Fews, F N Beg, A R Bell, A E Dangor, P Lee, M Tatarakis, M E Glinsky, B A Hammel
Maximum ion energy and hot electron temperature measurements for picosecond solid target interactions between 10^{17} W cm^{-2} and 10^{19} W cm^{-2}
Advances in Laser Interaction with Matter and Inertial Fusion, Proceedings of 24th ECLIM Eds G Velarde, J M Martinez-Val, E Minguez, J M Perlado, publ World Scientific 613-616 (1997)

P A Norreys, A P Fews, F N Beg, A R Bell, A E Dangor, P Lee, M B Nelson, H Schmidt, M Tatarakis, M D Cable
Neutron production from picosecond laser irradiation of deuterated targets at intensities of 10^{19} W cm^{-2}
Plasma Physics and Controlled Fusion **40** (2) 175-182 (1998)

P K Patel, J S Wark, D J Heading, A Djaoui, S J Rose, O Renner, A Hauer
Simulation of X-ray line transfer in a cylindrically expanding plasma
J Quant Spectr & Rad Trans **57** (5) 683-694 (1997)

P K Patel, J S Wark, O Renner, A Djaoui, S J Rose, D J Heading, A Hauer
Experimental and simulated profiles of the Al XIII Ly-α resonance line from a cylindrically expanding plasma
J Quant Spectr & Rad Trans **58** (4-6) 835-844 (1997)

S G Preston, D M Chambers, R S Marjoribanks, P A Norreys, D Neely, M Zepf, J Zhang, M H Key, J S Wark
Generation of bright, extreme-ultraviolet harmonic radiation from a krypton fluoride laser
J Phys B-Atomic Molecular and Optical Physics **31** (5) 1069-1082 (1998)

M Protopapas, C H Keitel, P L Knight
Atomic physics with super-high intensity lasers
Reports on Progress in Physics **60** (4) 389-486 (1997)

U W Rathe, C H Keitel, M Protopapas, P L Knight
Intense laser-atom dynamics with the two-dimensional Dirac equation
J Phys B-Atomic Molecular and Optical Physics **30** (15) L531-L539 (1997)

O Renner, E Krousky, D Salzmann, P Sondhauss, E Forster, A Djaoui, K Eidmann
Search for plasma shifts in higher transition lines of aluminum Lyman series
Advances in Laser Interaction with Matter and Inertial Fusion, Proceedings of 24th ECLIM Eds G Velarde, J M Martinez-Val, E Minguez, J M Perlado, publ World Scientific 340-343 (1997)

O Renner, D Salzmann, P Sondhauss, A Djaoui, E Krousky, E Forster
Experimental evidence for plasma shifts in Lyman series of aluminum
J Phys B-Atomic Molecular and Optical Physics **31** (6) 1379-1390 (1998)

O Renner, P Sondhauss, D Salzmann, A Djaoui, M Koenig, E Forster
Measurement of the polarization shifts in hot and dense aluminum plasma
J Quant Spectr & Rad Trans **58** (4-6) 851-857 (1997)

D Riley, R A Smith, A J Mackinnon, O Willi, M H R Hutchinson
Interaction of high intensity picosecond laser pulses with large preformed plasmas
Laser and Particle Beams **16** (1) 101-113 (1998)

S J Rose, D L Foulis, P Gauthier
The effect of transient molecules on the bound-bound contribution to the radiative opacity at the centre of the Sun
J Phys B-Atomic Molecular and Optical Physics **31** (4) L127-L133 (1998)

B Rus, P Zeitoun, T Mocek, S Sebban, M Kalal, A Demir, G Jamelot, A Klisnick, B Kralikova, J Skala, G J Tallents
Investigation of Zn and Cu prepulse plasmas relevant to collisional excitation x-ray lasers
Phys Rev A **56** (5) 4229-4241 (1997)

G J Tallents, J Y Lin, A Demir, A Behjat, R Smith, J Zhang, E Wolfrum, J S Wark, M H Key, C L S Lewis, A G MacPhee, S P McCabe, P J Warwick, D Neely, S B Healey, G J Pert, P V Nickles, M P Kalachnikov, M Schnurer
X-ray laser enhancement with multipulsing
Soft X-ray lasers and applications II, Eds J J Rocca, L B Da Silva, SPIE **3156** 30-41 (1997)

M Tatarakis, F N Beg, P Lee, A E Dangor, S Moustaizis
X-ray emission from plasmas generated by 450 femtosecond excimer laser pulses
Physica Scripta **55** (6) 651-653 (1997)

J S Wark, S J Rose, P K Patel, A Djaoui, O Renner, A Hauer
Astrophysically relevant experiments on radiation transfer through plasmas with large velocity gradients
Physics of Plasmas **4** (5 Pt2) 2004-2010 (1997)

P J Warwick, C L S Lewis, S McCabe, A G MacPhee, A Behjat, M Kurkcuoglu, G J Tallents, D Neely, E Wolfrum, S B Healy, G J Pert
A study to optimise the temporal drive pulse structure for efficient XUV lasing on the J=0-1, 19.6 nm line of Ge XXIII
Opt Comm **144** (4-6) 192-197 (1997)

E Wolfrum, M H Key, D Neely, S J Rose, A Demir, J Lin, R Smith, G J Tallents, D H Kalantar, B A Remington, S V Weber, N S Kim, J Zhang, C L S Lewis, A McPhee, J Warwick
Measurement of single mode imprint by XUV laser radiography
Advances in Laser Interaction with Matter and Inertial Fusion, Proceedings of 24th ECLIM Eds G Velarde, J M Martinez-Val, E Minguez, J M Perlado, publ World Scientific 168-171 (1997)

E Wolfrum, J Wark, J Zhang, D Kalantar, M H Key, B A Remington, S V Weber, D Neely, S Rose, J Warwick, A MacPhee, C L S Lewis, A Demir, J Lin, R Smith, G J Tallents
Measurement of single mode imprint in laser ablative drive of a thin Al foil by extreme ultraviolet laser radiography
Physics of Plasmas **5** (1) 227-233 (1998)

N C Woolsey, J S Wark
Modeling of time resolved x-ray diffraction from laser-shocked crystals
J Appl Phys **81** (7) 3023-3037 (1997)

N C Woolsey, D Riley, E Nardi
Kilovolt x-ray scattering from a plasma
Rev Sci Instr **69** (2 Pt1) 418-424 (1998)

W Yu, M Y Yu, J Zhang, Z Xu
Harmonic generation by relativistic electrons during irradiance of a solid target by a short-pulse ultraintense laser
Phys Rev E **57** (3 PtA) R2531-R2534 (1998)

M Zepf, M Castro-Colin, D Chambers, S G Preston, J S Wark, J Zhang, C N Danson, D Neely, P A Norreys, A Dyson, A E Dangor, P Lee, M Bakarezos, P Loukakos, S Moustaizis, A P Fews, P Gibbon
Irradiance scaling of harmonics from solid targets
Advances in Laser Interaction with Matter and Inertial Fusion, Proceedings of 24th ECLIM Eds G Velarde, J M Martinez-Val, E Minguez, J M Perlado, publ World Scientific 601-604 (1997)

J Zhang, A G MacPhee, J Lin, E Wolfrum, R Smith, C N Danson, M H Key, C L S Lewis, D Neely, J Nilsen, G J Pert, G J Tallents, J S Wark
A saturated X-ray laser beam at 7 nanometres
Science **276** (5315) 1097-1100 (1997)

J Zhang, A G MacPhee, J Y Lin, E Wolfrum, J Nilsen, T W Barbee, C N Danson, M H Key, C L S Lewis, D Neely, R M N O'Rourke, G J Tallents, R Smith, G J Pert, J S Wark,
Recent progress in nickel-like X-ray lasers at RAL
Soft X-ray lasers and applications II, Eds J J Rocca, L B Da Silva, SPIE **3156** 53-64 (1997)

J Zhang, A G MacPhee, J Lin, E Wolfrum, R Smith, C Danson, M H Key, C L S Lewis, D Neely, J Nilsen, G J Pert, G J Tallents, J S Wark, P J Warwick
Optimisation of drive pulse configuration for a Ni-like Sn X-ray laser at 12 nm
Phys Letts A **234** (6) 410-414 (1997)

J Zhang, A G MacPhee, J Nilsen, J Lin, T W Barbee, C N Danson, M H Key, C L S Lewis, D Neely, R M N O'Rourke, G J Pert, R Smith, G J Tallents, J S Wark E Wolfrum,
Demonstration of saturation in a Ni-like Ag x-ray laser at 14 nm
Phys Rev Letts **78** (20) 3856-3859 (1997)

PUBLICATIONS IN PRESS AT END OF 1997/8

D Batani, A Bernardinello, V Masella, F Pisani, M Keonig, J Krishnan, A Benuzzi, S Ellwi, T A Hall, P A Norreys, A Djaoui, D Neely, S Rose, P Fews, M H Key
Propagation in compressed matter of hot electrons created by short intense lasers
Superstrong Fields in Plasmas, Eds M Lontano, G Mourou, F Pegoraro, E Sindoni AIP Conf Proc **426** 372-376 (1998)

A R Bell, J R Davies, S M Guerin
Magnetic field in short-pulse high-intensity laser-solid experiments
Phys Rev E **58** (2PtB) 2471-2473 (1998)

M Borghesi, A J MacKinnon, A R Bell, R Gaillard, O Willi
Megagauss magnetic field generation and plasma jet formation on solid targets irradiated by an ultraintense picosecond laser pulse
Phys Rev Letts **81** (1) 112-115 (1998)

M Borghesi, A J Mackinnon, R Gaillard, O Willi, A A Offenberger
Guiding of a 10-TW picosecond laser pulse through hollow capillary tubes
Phys Rev E **57** (5 PtA) R4899-R4902 (1998)

M Borghesi, A J Mackinnon, R Gaillard, O Willi, A Pukhov, J Meyer-ter-Vehn
Large quasistatic magnetic fields generated by a relativistically intense laser pulse propagating in a preionized plasma
Phys Rev Letts **80** (23) 5137-5140 (1998)

R E Burge, G E Slark, M T Browne, X-C Yuan, P Charalambous, Z An, X-H Cheng, C L S Lewis, A G MacPhee, D Neely,
Time dependence of the spatial coherence of the 23.6- and 23.2-nm radiation from the germanium soft-x-ray laser
JOSA B-Optical Physics **15** (5) 1620-1626 (1998)

A C Cefalas, P Argitis, Z Kollia, E Sarantopoulou, T W Ford, A D Stead, A Marranca, C N Danson, J Knott, D Neely
Laser plasma x-ray contact microscopy of living specimens using a chemically amplified epoxy resist
Appl Phys Letts **72** (25) 3258-3260 (1998)

C E Clayton, K-C Tzeng, D Gordon, P Muggli, W B Mori, C Joshi, V Malka, Z Najmudin, A Modena, D Neely, A E Dangor
Plasma wave generation in a self-focused channel of a relativistically intense laser pulse
Phys Rev Letts **81** (1) 100-103 (1998)

C N Danson, P V Nickles, R Allott, A Behjat, J Collier, A Demir, M P Kalachnikov, M H Key, C L S Lewis, D Neely, D A Pepler, G J Pert, M Schnurer, W Sandner, V N Shlyaptsev, G J Tallents, P J Warwick, E Wolfrum, J Zhang
Implementation of a CPA line focus travelling-wave for highly efficient saturated lasing of Ne-like Ti and Ge
Superstrong Fields in Plasmas, Eds M Lontano, G Mourou, F Pegoraro, E Sindoni AIP Conf Proc **426** 473-478 (1998)

A Djaoui
Time-dependent hydrogenic ionization model for non-LTE mixtures
J Quant Spectr & Rad Trans - accepted for publication

T Ditmire, P K Patel, R A Smith, J S Wark, S J Rose, D Milathianaki, R S Marjoribanks, M H R Hutchinson
keV x-ray spectroscopy of plasmas produced by the intense picosecond irradiation of a gas of xenon clusters
J Phys B-Atomic Molecular and Optical Physics **31** (12) 2825-2831 (1998)

P Gauthier, S J Rose, P Sauvan, P Angelo, E Leboucher-Dalimier, A Calisti, B Talin
Modeling the radiative properties of dense plasmas
Phys Rev E **58** (1) 942-950 (1998)

E T Gumbrell, R A Smith, T Ditmire, A Djaoui, S J Rose, M H R Hutchinson
Picosecond optical probing of ultrafast energy transport in short pulse laser solid target interaction experiments
Phys Plasmas **5** (10) 3714-3721 (1998)

T A Hall, S Ellwi, D Batani, A Bernardinello, V Masella, M Koenig, A Benuzzi, J Krishnan, F Pisani, A Djaoui, P Norreys, D Neely, S Rose, M H Key, P Fews
Fast electron deposition in laser shock compressed plastic targets
Phys Rev Letts **81** (5) 1003-1006 (1998)

K A Janulewicz, P V Nickles, M P Kalachnikov, M Schnurer, W Sandner, S B healy, G J Pert, P J Warwick, C L S Lewis, C N Danson, D Neely, E Wolfrum, A Behjat, A Demir, G J Tallents
Saturation in transient gain scheme of collisionally pumped germanium X-ray laser
Superstrong Fields in Plasmas, Eds M Lontano, G Mourou, F Pegoraro, E Sindoni AIP Conf Proc **426** 491-496 (1998)

M P Kalachnikov, P V Nickles, M Schnurer, W Sandner, V N Shlyaptsev, C Danson, D Neely, E Wolfrum, J Zhang, A Behjat, A Demir, G J Tallents, P J Warwick, C L S Lewis
Saturated operation of a transient collisional x-ray laser
Phys Rev A **57** (6) 4778-4783 (1998)

A J Mackinnon, M Borghesi, A Iwase, O Willi
Interaction of intense laser pulses with preformed density channels
Phys Rev Letts **80** (24) 5349-5352 (1998)

E Nardi, Z Zinamon, D Riley, N C Woolsey
X-ray scattering as a dense plasma diagnostic
Phys Rev E **57** (4) 4693-4697 (1998)

D Riley
Time dependent modelling of K-shell emission lines from laser produced plasmas
J Quant Spectr & Rad Trans **60** (2) 221-230 (1998)

S J Rose
The non-LTE excitation/ionization code GALAXY
J Phys B-Atomic Molecular and Optical Physics **31** (9) 2129-2144 (1998)

M Tatarakis, J R Davies, P Lee, P A Norreys, N G Kassapakis, F N Beg, A R Bell, M G Haines, A E Dangor
Plasma formation on the front and rear of plastic targets due to high-intensity laser-generated fast electrons
Phys Rev Letts **81** (5) 999-1002 (1998)

P J Warwick, C L S Lewis, M P Kalachnikov, P V Nickles, M Schnurer, A Behjat, A Demir, G J Tallents, D Neely, E Wolfrum, J Zhang, G J Pert
Observation of high transient gain in the germanium x-ray laser at 19.6 nm
JOSA B-Optical Physics **15** (6) 1808-1814 (1998)

M Zepf, G Pretzler, U Andiel, D M Chambers, A E Dangor, P A Norreys, J S Wark, I Watts, G D Tsakiris
Optimising harmonics from solid targets
Superstrong Fields in Plasmas, Eds M Lontano, G Mourou, F Pegoraro, E Sindoni AIP Conf Proc **426** 264-269 (1998)

M Zepf, J Zhang, D M Chambers, A E Dangor, A G MacPhee, J Lin, E Wolfrum, J Nilsen, T W Barbee Jr, C N Danson, M H Key, C L S Lewis, D Neely, P A Norreys, S G Preston, R M N O'Rourke, G J Pert, R Smith, G J Tallents, I F Watts, J S Wark
Recent progress in coherent XUV generation at RAL
Superstrong Fields in Plasmas, Eds M Lontano, G Mourou, F Pegoraro, E Sindoni AIP Conf Proc **426** 499-508 (1998)

CONFERENCE PRESENTATIONS

SPIE Soft X-Ray Lasers and Applications II, San Diego, USA (July 1997)

P V Nickles, M Schnurer, M P Kalachnikov, W Sandner, V N Shlyaptsev, C N Danson, D Neely, E Wolfrum, J Zhang, A Behjat, A Demir, G J Tallents, P J Warwick, C L S Lewis
Transient inversion XUV lasers in Ti and Ge

G J Tallents, J Y Lin, A Demir, A Behjat, R Smith, J Zhang, E Wolfrum, J S Wark, M H Key, C L S Lewis, A G MacPhee, S P McCabe, P J Warwick, D Neely, S B Healey, G J Pert, P V Nickles, M P Kalachnikov, M Schnurer
X-ray laser enhancement with multipulsing

J Zhang, A G MacPhee, J Y Lin, E Wolfrum, J Nilsen, T W Barbee, C N Danson, M H Key, C L S Lewis, D Neely, R M N O'Rourke, G J Tallents, R Smith, G J Pert, J S Wark,
Recent progress in nickel-like X-ray lasers at RAL

Topical Workshop on Fast Ignition of Fusion Targets, MPQ Garching, Germany (September 1997)

M Zepf, M Castro-Colin, D Chambers, M H Key, S G Preston, J Zhang, J S Wark, C N Danson, D Neely, P A Norreys, A Dyson, P Lee, A E Dangor, A P Fews, P Gibbon, S Moustaizis
Hole boring velocities for picosecond 10^{19} W cm^{-2} interactions with solid targets

M Borghesi, A J MacKinnon, A R Bell, L Barringer, R Gaillard, C Meyer, O Willi
Laser channelling and magnetic field generation in preformed plasma

P A Norreys, A Djaoui, M Tatarakis, P Lee, F N Beg, A R Bell, A E Dangor, A P Fews
Electron energy transport measurements for picosecond 10^{19} W cm^{-2} interactions with solid targets

D Batani, V Masella, A Bernardinello, M Keonig, J Krishnan, F Pisani, A Benuzzi, T Hall, S Ellwi, P Norreys, A Djaoui, D Neely, S Rose, P Fews, M Key
Measurement of electron transport through shock-compressed plasmas

P A Norreys, M D Cable, T C Sangster, M J Moran, T W Phillips, M B Nelson, J A Koch, K B Wharton, D Pennington, M H Key, S P Hatchett, A P Fews, F N Beg, P Lee, M Tatarakis, A E Dangor, H Schmidt
Neutron measurements on VULCAN and NOVA

S J Rose, C B Edwards
Short pulse laser development at the Rutherford Appleton Lab

International Conference on Superstrong Fields in Plasmas, Varenna, Italy (August/September 1977)

C N Danson, P V Nickles, R Allott, A Behjat, J Collier, A Demir, M P Kalachnikov, M H Key, C L S Lewis, D Neely, D A Pepler, G J Pert, M Schnurer, W Sandner, V N Shlyaptsev, G J Tallents, P J Warwick, E Wolfrum, J Zhang
Implementation of a CPA line focus travelling-wave for highly efficient saturated lasing of Ne-like Ti and Ge

K A Janulewicz, P V Nickles, M P Kalachnikov, M Schnurer, W Sandner, S B Healy, G J Pert, P J Warwick, C L S Lewis, C N Danson, D Neely, E Wolfrum, A Behjat, A Demir, G J Tallents
Saturation in transient gain scheme of collisionally pumped germanium X-ray laser

M Zepf, J Zhang, D M Chambers, A E Dangor, A G MacPhee, J Lin, E Wolfrum, J Nilsen, T W Barbee Jr, C N Danson, M H Key, C L S Lewis, D Neely, P A Norreys, S G Preston, R M N O'Rourke, G J Pert, R Smith, G J Tallents, I F Watts, J S Wark
Recent progress in coherent XUV generation at RAL

IoP National Quantum Electronics Conference (QE13), Cardiff, UK (September 1997)

J Zhang, A MacPhee, J Lin, E Wolfrum, J Nilson, T W Barbee, C Danson, M H Key, C L S Lewis, D Neely, R M N O'Rourke, G J Pert, R Smith, G J Tallents, J Wark, J S Warwick
New developments in Ni-like X-ray lasers at RAL

Applied Optics and Optoelectronics 1998, Brighton, UK (March 1998)

M M Notley, A Damerell, C Danson, J Leach, D Neely, J Lin, S J Pestehe, R Smith, G Tallents, M Zepf
Recent Instrumentation Developments for X-ray Emission Spectroscopy

Science - Lasers for Science Facility Programme

JOURNAL PUBLICATIONS, BOOKS AND PUBLISHED PROCEEDINGS

P Albertano, M Belli, P di Lazzaro, A Ya Faenov, F Flora, A Grilli, F Ianzini, T Letardi, A Nottola, L Palladino, T Pikuz, A Reale, L Reale, A Scafati, M A Tabocchini, I C E Turcu, K Vigli-Papadaki
Atmospheric pressure soft X-ray source for contact microscopy and radiobiology applications
Applications of X-rays generated from lasers and other bright sources Ed G A Kyrala SPIE **3157** 164-175 (1997)

R M Allott, I C E Turcu, N Lisi, N Spencer, W Shaikh, A Wybrew, S Wang, R Donovan, K Lawley, K Ledingham, M Folkard, K Prise
Continuously tuneable, high flux, VUV beamline constructed on a picosecond KrF laser plasma source
Applications of X-rays generated from lasers and other bright sources Ed G A Kyrala SPIE **3157** 138-147 (1997)

M Ballerini, M Milani, M Costato, F Squadrini, I C E Turcu
Life science applications of focused ion beams (FIB)
European Journal of Histochemistry **41** (S2) 89-90 (1997)

R H Bisby, A W Parker
Antioxidant reactions of dihydrolipoic acid and lipoamide with triplet duroquinone
Biochem Biophys Res Commun **244** (1) 263-267 (1998)

R A Brownsword, A Canosa, B R Rowe, I R Sims, I W M Smith, D W A Stewart, A C Symonds, D Travers
Kinetics over a wide range of temperature (13-744K): rate constants for the reactions of CH(v=0) with H_2 and D_2 and for the removal of CH(v=1) by H_2 and D_2
J Chem Phys **106** (18) 7662-7677 (1997)

R A Brownsword, I R Sims, I W M Smith, D W A Stewart, A Canosa, B R Rowe
The radiative association of CH with H_2: a mechanism for formation of CH_3 in interstellar clouds
Astrophys J **485** (1) 195-202 (1997)

A N Brunton, G W Fraser, J E Lees, I C E Turcu
Metrology and modeling of microchannel plate X-ray optics
Appl Opt **36** (22) 5461-5470 (1997)

N Cain, M O'Neill, J E Nicholls, T Stirner, W E Hagston, D E Hashenford
Photoluminescence of CdTe/CdMnTe multiple quantum wells excited near the Mott transition
Journal of Luminescence **75** (4) 269-275 (1997)

A Canosa, I R Sims, D Travers, I W M Smith, B R Rowe
Reactions of the methylidene radical with CH_4, C_2H_2, C_2H_4, C_2H_6 and but-1-ene studied between 23 and 295 K with a CRESU apparatus
Astron Astophys **323** (2) 644-651 (1997)

M Costato, A Pozzi, D Batani, A Conti, A Masini, M Milani, F Previdi
Selective soft X-rays interaction on the metabolism of eukaryotic cells
Physica Medica **13** (S1) 263-264 (1997)

B Dance
Deep 3D structures produced by soft X-ray lithography
Semiconductor International June 1997 217-218 (1997)

B Dance
Lasers' leading lights in communication
Practical Wireless May 1997 44-48 (1997)

M R Davidson, G J Berry, J A Cairns, A G Fitzgerald, B Lawrenson, J Thomson, I C E Turcu, W Shaikh, N Spencer, R M Allott, N Takeyasu
Novel route for the production of X-ray masks from a range of organometallic films
Microelectronic Engineering **41/42** 279-282 (1998)

T Fournier, S M Tavender, A W Parker, G D Scholes, D Phillips
Competitive energy and electron transfer reactions of the triplet state of 1-nitronaphthalene: a laser flash photolysis and time resolved resonance Raman study
J Phys Chem A **101** (29) 5320-5326 (1997)

P L James, I R Sims, I W M Smith
Rate coefficients for the vibrational self-relaxation of NO($X^2\Pi$, v=3) at temperatures down to 7K
Chem Phys Letts **276** (5,6) 423-429 (1997)

P L James, I R Sims, I W M Smith
Total and state-to-state rate coefficients for the rotational energy transfer in collisions between NO($X^2\Pi$) and He at temperatures down to 15K
Chem Phys Letts **272** (5,6) 412-418 (1997)

N Khaleque, A G Michette, C J Buckley, S J Pfauntsch, S D Saville
Development of a laboratory based scanning x-ray microscope
Cell Vision **4** (2) 114-5 (1997)

H S Kilic, K W D Ledingham, D J Smith, S Wang, C Kosmidis, T McCanny, R P Singhal, A J Langley, W Shaikh
The photo-dissociative pathways of nitromethane using femtosecond laser pulses at 375 nm
Resonance Ionization Spectroscopy 1996 Eds N Winograd, J E Parks AIP Conf Proc **388** 395-398 (1997)

A I Magunov, A Faenov, I Skobelelev, T Pikuz, D Batani, M Milani, A Conti, A Masini, M Costato, A Pozzi, E Turcu, R Allot, N Lisi, M Koenig, A Benuzzi, F Flora, T Letardi, L Palladino, A Reale
X-ray spectra of excimer-laser-produced high density plasmas
Advances in Laser Interaction with Matter and Inertial Fusion, Proceedings of 24th ECLIM Eds G Velarde, J M Martinez-Val, E Minguez, J M Perlado, publ World Scientific 67-70 (1997)

A I Magunov, A Ya Faenov, I Yu Skobelelev, T A Pikuz, D Batani, M Milani, A Conti, A Masini, M Costato, A Pozzi, E Turcu, R Allott, N Lisi, M Koenig, A Benuzzi, F Flora, T Letardi, L Palladino, A Reale
Formation of X-ray line emission spectra of excimer laser produced plasmas
Physica Scripta **55** (4) 478-482 (1997)

S Martin, C A Feely, J T Sheridan, V Toal
High efficiency diffractive optical elements recorded in a self-developing photopolymer material
Proceedings of Applied Optics and Optoelectronics 1998, Ed K T V Grattan, publ IoP Publishing 157-162 (1998)

A Masini, D Batani, F Previdi, A Conti, F Pisani, C Botto, F Bortolotto, F Torsiello, E Turcu, R Allott, N Lisi, M Milani, M Costato, A Pozzi, M Koenig
X-ray irradiation of yeast cells
Applications of X-rays generated from lasers and other bright sources Ed G A Kyrala SPIE **3157** 164-175 (1997)

P Matousek, A W Parker, D Phillips, G D Scholes, W T Toner, M Towrie
A picosecond time-resolved resonance raman study of S_1 cis-stilbene
Chem Phys Letts **278** (1-3) 56-62 (1997)

P Matousek, D L A de Faria, R E Hester, J N Moore, A W Parker, W T Toner, M Towrie
Anti-Stokes picosecond time-resolved resonance Raman spectroscopy in the study of singlet excited trans-stilbene
Proceedings of the 7th International Conference on Time-Resolved Vibrational Spectroscopy 1995, Santa Fe, New Mexico, Los Alamos, **LA-13290-C** 255-256 (1997)

P Matousek, A W Parker, M Towrie, W T Toner
The picosecond timescale relaxation of photoexcited quaterphenyl in solution
J Chem Phys **107** (23) 9807-9817 (1997)

A Michette
X-Ray microscopy: the state of the art and future prospects
Cell Vision **4** (2) 113-114 (1997)

A G Michette
Projected advances in laboratory soft x-ray systems and their applications
J X-ray Sci Technol **7** (2) 98-116 (1997)

A W Parker, D Phillips, M Towrie, P Matousek, E Vauthey
Photo-initiated electron transfer reactions studied by TR^3 spectroscopy
Proceedings of the 7th International Conference on Time-Resolved Vibrational Spectroscopy 1995, Santa Fe, New Mexico, Los Alamos, **LA-13290-C**, 249-250 (1997)

J H Posthumus, K Codling, L J Frasinski, M R Thompson
The field-ionization Coulomb explosion of diatomic molecules in intense laser fields
Laser Phys **7** (3) 813-825 (1997)

D Riley, A J Langley, P F Taday, W Shaikh, I McCormack
Reflectivity experiments with 60 femtosecond laser pulses
J Phys D-Applied Physics **31** (5) 515-518 (1998)

J H Sanderson, R V Thomas, W A Bryan, W R Newell, I D Williams, A J Langley, P F Taday
High intensity femtosecond laser interactions with vibrationally excited CO_2
J Phys B-Atomic Molecular and Optical Physics **31** (2) L59-L64 (1998)

J H Sanderson, R V Thomas, W A Bryan, W R Newell, I D Williams, A J Langley, P F Taday
Multielectron dissociative-ionization of SF_6 by intense femtosecond laser pulses
J Phys B-Atomic Molecular and Optical Physics **30** (20) 4499-4507 (1997)

G D Scholes, P Matousek, A W Parker, D Phillips, M Towrie
Inner sphere reorganisation dynamics accompanying charge transfer in cyanoterphenyl
J Phys Chem A **102** 1431-1437 (1998)

I W M Smith
Kinetics and energy partitioning in complex forming reactions between neutral species
Berichte der Bunsen Gesellschaft - Phys Chem Chem Phys **101** (3) 516-523 (1997)

D L Stevens, S J Marsden, M A Hill, I C E Turcu, R Allott, D T Goodhead
The separation of spatial and temporal effect of high LET radiation
Microdosimetry - an Interdisciplinary Approach
Eds D T Goodhead, P O'Neill, H G Menzel, 195-7 publ Royal Society of Chemistry (1997)

G M Sweeney, A Watson, K G McKendrick
Rotational and spin-orbit effects in the dynamics of $O(^3P_j)$ + hydrocarbon reactions I: Experimental results
J Chem Phys **106** (22) 9172-9181 (1997)

G M Sweeney, K G McKendrick
Rotational and spin-orbit effects in the dynamics of $O(^3P_j)$ + hydrocarbon reactions II: Models for spin-orbit propensities
J Chem Phys **106** (22) 9182-9189 (1997)

G J Tallents, J Krishnan, L Dwivedi, D Neely, I C E Turcu
Film calibration for soft X-ray wavelength
Applications of X-rays generated from lasers and other bright sources Ed G A Kyrala SPIE **3157** 281-290 (1997)

M R Thompson, M K Thomas, P F Taday, J H Posthumus, A J Langley, L J Frasinski, K Codling
One and two-colour studies of the dissociative ionization and Coulomb explosion of H_2 with intense Ti:sapphire laser pulses
J Phys B-Atomic Molecular and Optical Physics **30** (24) 5755-5772 (1997)

W T Toner, P Matousek, A W Parker, M Towrie
Resonance Raman study of the relaxation of photoexcited molecules in solution on the picosecond timescale
Atomic Physics Methods in Modern Research, publ Springer-Verlag, Berlin, 151 (1997)

I C E Turcu, R M Allott, C M Mann, C M Reeves, I N Ross, N Lisi, B J Maddison, S W Moon, P Prewett, J T M Stephenson, A W S Ross, A M Gundlach, B Koek, P Mitchell, P Anastasi, C McCoard, N S Kim
X-ray micro- and nanofabrication using a laser-plasma source at 1 nm wavelength
J Vac Sci Technol B **15** (6) 2495-2502 (1997)

I C E Turcu, C M Mann, S W Moon, B J Maddison, R Allott, N Lisi, S E Huq, N S Kim
X-ray micromachining of deep 3D terahertz waveguide components using a laser-plasma source at 1 nm wavelength
Applications of X-rays generated from lasers and other bright sources Ed G A Kyrala SPIE **3157** 291 299 (1997)

JOURNAL PUBLICATIONS, BOOKS AND PUBLISHED PROCEEDINGS 1996/7

M Chown
X-ray lens brings finer chips into focus
New Scientist No 2037, p18, 6 July (1996)

M S C Foley, A Beeby, A W Parker, S M Bishop, D Phillips
Photophysics of disulphonated aluminium phthalocyanine in reverse micelles of aerosol-OT
J Photochem Photobiol B: Biology **38** (1) 18-24 (1997)

PUBLICATIONS IN PRESS AT END OF 1997/8

D Batani, M Milani, G Leoni, A Conti, A Masini, F Pisani, M Costato, A Pozzi, E Turcu, R Allott, N Lisi, F Cotelli, C Lora Lamia Donin, M Moret
Yeast cell metabolic oscillations investigated by soft X-ray irradiation
Submitted to Phys Rev Letts (1998)

D Batani, M Milani, G Leoni, A Conti, A Masini, F Pisani, M Costato, A Pozzi, E Turcu, R Allott, N Lisi, F Cotelli, C Lora Lamia Donin, M Moret
Yeast cells response to soft X-rays from laser-plasmas
Accepted for publication in Vuoto Science and Technology (1998)

G J Berry, J A Cairns, M R Davidson, D R G Rodley, J Thomson, I C E Turcu, W Shaikh
1 nm X-ray lithography using novel mask fabrication technique
Rev Sci Instr 69 (9) 3350-3352 (1998)

R H Bisby, S A Johnson, A W Parker, S M Tavender
Time Resolved resonance Raman spectroscopy of the carbonate radical
J Chem Soc Faraday Trans **94** (15) 2069-2072 (1998)

G R Kennedy, C-L Ning, J Pfab
The 355nm photodissociation of jet-cooled CH_3SNO: alignment of the NO photofragment
Chem Phys Letts **292** (1,2) 161-166 (1998)

K W D Ledingham, R P Singhal, D J Smith, T McCanny, P Graham, H S Kilic, W X Peng, S L Wang, A J Langley, P F Taday, C Kosmidis
Behaviour of polyatomic molecules in intense infrared laser beams
J Phys Chem A **102** (18) 3002-3005 (1998)

I K Lednev, T-Q Ye, P Matousek, M Towrie, P Foggi, F V R Neuwahl, S Umapathy, R E Hester, J N Moore
Femtosecond time-resolved UV-visible absorption spectroscopy of trans-azobenzene: dependence on excitation wavelength
Chem Phys Letts **290** (1-3) 68-74 (1998)

A Masini, D Batani, F Previdi, M Milani, M Costato, A Pozzi, E Turcu, R Allott, N Lisi
Influence on yeast cell metabolism of irradiation with soft X-rays from a laser plasma source
Submitted to Phys Rev E (1998)

M Milani, M Ballerini, G Baroni, D Batani, S Cozzi, L Ferraro, M Costato, F Salsi, A Pozzi, F Squadrini, I C E Turcu, R Allot, N Lisi, W Shaikh, S Hughes
Differential two colour X-ray radiobiology of membrane/cytoplasm in yeast cells and lymphocytes
Advances in Optical Biophys SPIE **3256** 195-205 (1998)

A D Scully, R B Ostler, A J MacRobert, A W Parker, C de Lara, P O'Neill, D Phillips
Laser line-scanning confocal fluorescence imaging of the photodynamic action of aluminium and zinc phthalocyanines in V79-4 Chinese hamster fibroblasts
Photochem and Photobiol **68** (2) 199-204 (1998)

D J Smith, K W D Ledingham, H S Kilic, T McCanny, W X Peng, R P Singhal, A J Langley, P F Taday, C Kosmidis
Ionization and dissociation of benzaldehyde using short intense laser pulses
J Phys Chem A **102** (15) 2519-2526 (1998)

G D Scholes, I R Gould, A W Parker, D Phillips
Time-resolved resonance Raman and molecular-orbital studies of charge-separation and intramolecular reorganisation
Chem Phys **234** (1-3) 21-34 (1998)

I C E Turcu, B Dance
X-rays from laser-plasmas: generation and applications
Publ John Wiley & Sons (1998)

CONFERENCE PRESENTATIONS

Time Resolved Vibrational Spectroscopy International Conference VIII, Oxford, UK (April 1997)

R H Bisby, S A Johnson, A W Parker, S M Tavender
Time-resolved resonance Raman studies of radicals from 4-aminoresorcinol as models for the active site radical intermediate in copper amine oxidase

T Fournier, G D Scholes, I R Gould, S M Tavender, D Phillips, A W Parker
Triplet 1-nitronaphtalene and competitive energy and electron transfer reactions with trans-stilbene

P Matousek, A W Parker, D Phillips, G D Scholes, W T Toner, M Towrie
ps-TR^3 spectroscopy of S_1 cis-stilbene in solution

G D Scholes, P Matousek, M Towrie, A W Parker, D Phillips
Time evolution of mode-specific reorganisation accompanying intramolecular charge transfer

G D Scholes, I P Mercer, D R Klug, D Phillips, T Fournier, A W Parker
Resonance Raman studies of the nexus between energy and charge transfer in 9, 9'-bianthryl

S M Tavender, S A Johnson, D Balsom, A W Parker, R H Bisby
Time resolved resonance Raman spectroscopy of the carbonate radical

W T Toner, P Matousek, A W Parker, M Towrie
Picosecond Raman excitation profile and transient absorbance spectrum of S_1 quaterphenyl in solution

Royal Society Discussion Meeting on Ultrafast Processes in Chemistry and Biology, London, UK (April 1997)

M R Thompson, M K Thomas, J H Posthumus, L J Frasinski, K Codling, A J Langley, P F Taday
Multiphoton ionisation, dissociation and Coulomb explosion of H_2 with short, intense laser pulses

41st International Conference on Electron, Ion and Photon Beam Technology and Nanofabrication, Dana Point, USA (May 1997)

I C E Turcu, R M Allott, C M Mann, C M Reeves, I N Ross, N Lisi, B J Maddison, S W Moon, P Prewett, J T M Stephenson, A W S Ross, A M Gundlach, B Koek, P Mitchell, P Anastasi, C McCoard, N S Kim
X-ray micro- and nano-fabrication using a laser-plasma source at 1 nm wavelength

European Workshop on Laser Applications in Chemistry, Barcelona, Spain (June 1997)

A W Parker
Chemical applications of lasers at the Central Laser Facility, Rutherford Appleton Laboratory

A W Parker
Time-resolved resonance Raman spectroscopy: intermediates, mechanisms and dynamics

20th International Conference on the Physics of Electronic and Atomic Collisions, Vienna, Austria (July 1997)

J H Sanderson, R V Thomas, W A Bryan, W R Newell, I D Williams, A J Langley, P F Taday
High intensity laser fragmentation of vibrationally excited CO_2

International Workshop on Photoionisation IWP97, Chester, UK (July 1997)

S L Wang, K P Lawley, R J Donovan, K W D Ledingham, T McCanny, R P Singhal, R Allott, N Spencer, W Shaikh, I C E Turcu
Applications of VUV radiation from laser-produced plasmas for molecular photoionisation and ion-pair production

Applications of X-Rays Generated from Lasers and Other Bright Sources, San Diego, USA (July/August 1997)

P Albertano, M Belli, P di Lazzaro, A Ya Faenov, F Flora, A Grilli, F Ianzini, T Letardi, A Nottola, L Palladino, T Pikuz, A Reale, L Reale, A Scafati, M A Tabocchini, I C E Turcu, K Vigli-Papadaki
Atmospheric pressure soft X-ray source for contact microscopy and radiobiology applications

R M Allott, I C E Turcu, N Lisi, N Spencer, W Shaikh, A Wybrew, S Wang, R Donovan, K Lawley, K Ledingham, M Folkard, K Prise
Continuously tuneable, high flux, VUV beamline constructed on a picosecond KrF laser plasma source

A Masini, D Batani, F Previdi, A Conti, F Pisani, C Botto, F Bortolotto, F Torsiello, E Turcu, R Allott, N Lisi, M Milani, M Costato, A Pozzi, M Koenig
X-ray irradiation of yeast cells

G J Tallents, J Krishnan, L Dwivedi, D Neely, I C E Turcu
Film calibration for soft X-ray wavelength

I C E Turcu, C M Mann, S W Moon, B J Maddison, R Allott, N Lisi, S E Huq, N S Kim
X-ray micromachining of deep 3D terahertz waveguide components using a laser-plasma source at 1 nm wavelength

International Centennial Symposium on the Electron, Cambridge, UK (September 1997)

G J Berry, J A Cairns, M R Davidson, P R Drapacz, Y C Fan, A G Fitzgerald, D R G Rodley and J Thompson
The production of metal structures for the next-generation electronic devices by electron-induced decomposition of a new range of organometallic compounds

ROMOPTO'97: Fifth Conference on Optics, Bucharest, Romania (September 1997)

I C E Turcu, C M Mann, S W Moon, B J Maddison, R M Allott, N Lisi, S E Huq, N S Kim
X-ray micromachining with a laser-plasma source at 1 nm wavelength

Conference of the Italian Physical Society (SIF), Como, Italy (1997)

M Milani, M Costato, D Batani, E Turcu, D T Goodhead
Two colour soft X-ray differential radiobiology of membrane/cytoplasm in yeast cells

Discussion Meeting On Ultrafast Chemical Phenomena - Indian Institute of Science, Bangalore, India (March 1998)

A W Parker, M Towrie, P Matousek, D Phillips, G D Scholes, W T Toner, R H Bisby
Time resolved resonance Raman spectroscopy and transient absorption measurements using an ultrafast optical parametric amplifier: an update

Applied Optics and Optoelectronics 1998, Brighton, UK (March 1998)

S Martin, C A Feely, J T Sheridan, V Toal
High efficiency diffractive optical elements recorded in a self-developing photopolymer material

CONFERENCE PRESENTATIONS 1996/97

2nd Spectral Line Shapes, Firenze, Italy (June 1996)

M Magunov, I Skobelev, V Dyakin, A Faenov, T Pikuz, D Batani, A Mauri, A Reale, F Flora, E Turcu, et al.
X-ray spectral line shapes for the excimer-laser-produced high density plasma diagnostics

Proceedings of the XVth International Conference on Raman Spectroscopy, Pittsburgh, USA, (August 1996)

M Towrie, P Matousek, A W Parker, P F Taday, W T Toner
Two 40 kHz repetition rate independently tunable synchronised femtosecond pulses generated in the visible using optical parametric amplifiers

INTERNAL PUBLICATIONS

M Milani, D Batani, F Bortolotto, C Botto, G Baroni, S Cozzi, L Ferraro, A Masini, F Pervidi, M Balerini, M Costato, A Pozzi, F Salsi, R Allott, N Lisi, E Turcu
Differential two colour X-ray radiobiology of membrane/cytoplasm yeast cells
EU TMR Large Facilities Access Programme, Contract No ERBFMGECT950053, RAL Report RAL-TR-98-011 (1998)

PATENTS

I C E Turcu, I N Ross, F O'Neill
Laser-excited X-ray source
United States patent No. 5,654,998, (1997)

I N Ross, P Matousek, M Towrie, A J Langley, J L Collier
Optical parametric chirped pulse amplifier
Provisional patent (1997)

THESES

Alessandra Masini (Laura Thesis, University of Milan 1996)
Analisi della risposta metabolica di cellule all'irraggiamento con X molli

Nadia Correale (Laura Thesis, University of Milan 1997)
Caratterizzazione di cellule di lievito saccharomyces cerevisiae e loro utilizzo per irradiazione con raggi X

Francesca Salsi (Laura Thesis, University of Modena 1997)
Spettroscopia NMR di sospensioni cellulari sottoposte ad irragiamento di X-molli

I C E Turcu (PhD, University of London 1997)
Generation and application of X-rays from excimer laser-produced plasmas

Giuliana Baroni (Laura Thesis University of Milan 1998)
Riposta metabolica di cellule a radiazione ionaizzante

Fulvia Bortolotto (Laura Thesis, University of Milan 1998)
Spettroscopia di raggi X soffici prodotti da una sorgente laser-plasma e dosimetria X su cellule di lievito

INVITED LECTURES

A W Parker
Research into photodynamic therapy for treating cancer
Interview on BBC *News Night* (June 1997)

P F Taday
Intense femtosecond laser interactions at the Rutherford Appleton Laboratory
University of Oxford (February 1998)

I C E Turcu
Applications of laser-plasma X-ray radiation in science and technology
Max Plank Institute Fur Quantenoptik, Garching, Germany, (December 1997)

I C E Turcu
High brightness picosecond X-ray source and its applications
Physics Department, Bucharest Technical University, Bucharest, Romania (September 1997)

I C E Turcu
X-ray micro- and nano-fabrication with a laser-plasma source at 1nm wavelength
Centre for X-ray Lithography, University of Wisconsin at Madison, USA (1997)

I C E Turcu
X-ray micro- and nano-fabrication with a laser-plasma source at 1nm wavelength
Massachusetts Institute of Technology, Boston, USA (May 1997)

I C E Turcu
X-ray micro- and nano-fabrication with a laser-plasma source at 1nm wavelength
Universita di Roma, *Tor Vergata* Facolta di Ingegneria, Dipartimento di Sciennze e Technologie Finische ed Energetiche, Rome, Italy (October 1997)

Laser Development

JOURNAL PUBLICATIONS, BOOKS AND PUBLISHED PROCEEDINGS

R M Allott, I C E Turcu, N Lisi, A Whybrew
Bright, continuously tunable, VUV plasma source generated by a high repetition rate picosecond laser
QELS '97 Technical Digest, OSA Technical Digest Series 157 (1997)

R Allott, S Angood, C Beckwith, G Booth, J Collier, C N Danson, A Damerell, C B Edwards, J Ellwood, P Exley, P Flintoff, J Govans, S Hancock, P Hatton, S Hawkes, D Hitchcock, M H R Hutchinson, M H Key, C Hernandez-Gomez, J Leach, W Lester, D Neely, P Norreys, M Notley, D Pepler, C Reason, D A Rodkiss, M Stainsby, M Trentelman, J Walczak, T Winstone, R Wyatt, B Wyborn
10^{20} W cm^{-2} to target with the upgraded Vulcan laser system
Proceedings of Applied Optics and Optoelectronics 1998, Ed K T V Grattan, publ IoP Publishing 219 (1998)

C N Danson, S Angood, L J Barzanti, N Bradwell, J Collier, A R Damerell, C B Edwards, C Johnson, M H Key, D Neely, M Nightingale, P A Norreys, D A Pepler, D A Rodkiss, I N Ross, P Ryves, N Thompson, M Trentelman, F N Walsh, E Wolfrum, R W Wyatt
Design and characterization of the VULCAN Nd:glass laser to give focused intensities of >10^{19} W cm^{-2}
Solid state lasers for application to inertial confinement fusion: second annual international conference, Ed M Andre, SPIE **3047** 505-515 (1997)

C Danson, N Bradwell, L Barzanti, J Collier, A Damerell, C B Edwards, C Johnson, M H Key, D Neely, M Nightingale, D A Pepler, I N Ross, P Ryves, C Stephens, N Thompson, M Trentelman, E Wolfrum, F Walsh, R Wyatt
Characterisation of the Vulcan Nd:glass laser for multi-terawatt operation
Advances in Laser Interaction with Matter and Inertial Fusion, Proceedings of 24th ECLIM Eds G Velarde, J M Martinez-Val, E Minguez, J M Perlado, publ World Scientific 523-526 (1997)

C Hernandez-Gomez, J Collier, C N Danson, C B Edwards, S Hawkes, D A Pepler, I N Ross, T B Winstone
Interferometric measurement and analysis of the wavefront quality of the Vulcan laser facility
Proceedings of Applied Optics and Optoelectronics 1998, Ed K T V Grattan, publ IoP Publishing 325 (1998)

G J Hirst
Progress toward ultrahigh intensities with the Titania krypton fluoride laser system
CLEO '97 Technical Digest, OSA Technical Digest Series **11** 523 (1997)

I N Ross, P Matousek, M Towrie, A J Langley, J L Collier
The prospects for ultrashort pulse duration and ultrahigh intensity using optical parametric chirped pulse amplifiers
Opt Comm **144** (1-3) 125-133 (1997)

I N Ross, M Trentelman, C N Danson
Optimisation of a chirped pulse amplification Nd:glass laser
Appl Opt **36** (36) 9348-9358 (1997)

M Trentelman, I N Ross, C N Danson
Finite size compression gratings in a large aperture chirped pulse amplification laser system
Appl Opt **36** (33) 8567-8573

PUBLICATIONS IN PRESS AT END OF 1997/8

C N Danson, J Collier, D Neely, L J Barzanti, A Damerell, C B Edwards, M H R Hutchinson, M H Key, P A Norreys, D A Pepler, I N Ross, P F Taday, W T Toner, M Trentelman, F N Walsh, T B Winstone, R W W Wyatt
Well characterized 10^{19} W cm^2 operation of VULCAN - an ultra-high power Nd:glass laser
J Mod Opt **45** (8) 1653-1669 (1998)

C B Edwards, C N Danson, M H R Hutchinson, D Neely, B Wyborn
200 TW upgrade of the Vulcan Nd:glass laser facility
Superstrong Fields in Plasmas, Eds M Lontano, G Mourou, F Pegoraro, E Sindoni AIP Conf Proc **426** 485-490 (1998)

D Neely, D M Chambers, C N Danson, P A Norreys, S G Preston, F Quinn, M Roper, J S Wark, M Zepf
A multi-channel soft X-ray flat-field spectrometer
Superstrong Fields in Plasmas, Eds M Lontano, G Mourou, F Pegoraro, E Sindoni AIP Conf Proc **426** 479-484 (1998)

M Towrie, A W Parker, W Shaikh, P Matousek
Tunable picosecond optical parametric generator-amplifier system for time resolved Raman spectroscopy
Measurement Science & Technology **9** (5) 816-823 (1998)

H L Offerhaus, C B Edwards, W J Witteman
Single shot beam quality (M^2) measurement using a spatial Fourier transform of the near field
Opt Comm **151** (1-3) 65-68 (1998)

CONFERENCE PRESENTATIONS

Time Resolved Vibrational Spectroscopy International Conference VIII, Oxford, UK (April 1997)

M Towrie, P Matousek, A W Parker, W Shaikh
Tunable picosecond OPAs for TR^3 spectroscopy

QELS'97, Baltimore, USA (May 1997)

R M Allott, I C E Turcu, N Lisi, A Whybrew
Bright, continuously tunable, VUV plasma source generated by a high repetition rate picosecond laser

CLEO'97, Baltimore, USA (May 1997)

G J Hirst
Progress toward ultrahigh intensities with the Titania krypton fluoride laser system

International Workshop on Adaptive Optics for Industry and Medicine, Shatura, Russia (June 1997)

M J Shaw, I N Ross, C J Reason, D A Pepler, C N Danson, T Kaneko, C J Hooker
Active control of phase distortions in high power laser systems

International Conference on Superstrong Fields in Plasmas, Varenna, Italy (August/September 1977)

C B Edwards, C N Danson, M H R Hutchinson, D Neely, B Wyborn
200 TW upgrade of the Vulcan Nd:glass laser facility

D Neely, D M Chambers, C N Danson, P A Norreys, S G Preston, F Quinn, M Roper, J S Wark, M Zepf
A multi-channel soft X-ray flat-field spectrometer

IoP National Quantum Electronics Conference (QE13), Cardiff, UK (September 1997)

J Collier, D A Pepler, C N Danson, I N Ross, C B Edwards, P Exley, T B Winstone, J Elwood, D Hitchcock
The measurement of the wavefront quality of the VULCAN laser system - adaptive optic possibilities

J Collier, D A Pepler, C N Danson, I N Ross, C B Edwards, T B Winstone, J Elwood, P Exley, D Hitchcock, M Stainsby, C Beckwith, M Stainsby, C McCoard, D Neely, R Allott, M Trentelman
The Vulcan laser system 250 TW upgrade - ultra high power pulse diagnostics

C N Danson, S Angood, L Barzanti, J Collier, A Damerell, C B Edwards, S Hancock, P Hatton, M H R Hutchinson, M H Key, W Lester, C McCoard, D Neely, D A Pepler, C Reason, D A Rodkiss, I N Ross, W Toner, M Trentelman, F N Walsh, T B Winstone, E Wolfrum, R W W Wyatt, B Wyborn
VULCAN: a unique system delivering 250 TW and focused to give intensities of 10^{20} W cm^{-2}

D Neely, M Trentelman, C N Danson, C Beckwith, C L McCoard, J L Collier, C B Edwards, D A Pepler, M Stainsby, F N Walsh
Frequency doubling of picosecond pulses on the Vulcan large aperture CPA laser system

Applied Optics and Optoelectronics 1998, Brighton, UK (March 1998)

R Allott, S Angood, C Beckwith, G Booth, J Collier, C N Danson, A Damerell, C B Edwards, J Ellwood, P Exley, P Flintoff, J Govans, S Hancock, P Hatton, S Hawkes, D Hitchcock, M H R Hutchinson, M H Key, C Hernandez-Gomez, J Leach, W Lester, D Neely, P Norreys, M Notley, D Pepler, C Reason, D A Rodkiss, M Stainsby, M Trentelman, J Walczak, T Winstone, R Wyatt, B Wyborn
10^{20} W cm^{-2} to target with the upgraded Vulcan laser system

C Hernandez-Gomez, J Collier, C N Danson, C B Edwards, S Hawkes, D A Pepler, I N Ross, T B Winstone
Interferometric measurement and analysis of the wavefront quality of the Vulcan laser facility

PANEL MEMBERSHIP & CLF STRUCTURE

PANEL MEMBERSHIP

HIGH POWER LASER DIRECT ACCESS PANEL 1997/98

Professor G J Pert (Chairman)
Department of Physics
University of York

Dr K Burnett
Department of Physics
University of Oxford

Dr J-C Gauthier
LULI
Paris, France

Secretary: Dr G Hirst
Rutherford Appleton Laboratory

Mr P C Thompson
AWE
Aldermaston

Professor S Rose
Clarendon Laboratory
University of Oxford

Professor M G Haines
Plasma Physics Group
Imperial College

Mrs C Exton
Cross Programme Group
EPSRC

LASERS *for* SCIENCE FACILITY PANEL 1997/98

Professor D Phillips (Chairman)
Department of Chemistry
Imperial College

Dr R Bisby
Department of Biological Sciences
University of Salford

Dr C Wharton
Department of Biochemistry
University of Birmingham

Professor K Codling
Department of Physics
University of Reading

Secretary: Dr A Langley
Rutherford Appleton Laboratory

Professor F Wilkinson
Department of Chemistry
Loughborough University

Dr R Devonshire
Department of Chemistry
Sheffield University

Professor J A Cairns
Department of Applied Physics and Electronic and Mechanical Engineering
University of Dundee

Mrs P Backway, Mrs C Exton
Cross Programme Group
EPSRC

CLF EURO EXPERIMENTS PANEL 1997/98

Professor C L S Lewis (Chairman)
Department of Pure and Applied Physics
Queen's University of Belfast

Professor C Fotakis
Institute of Electronic Structure and Laser
FORTH, Greece

Professor D Phillips
Department of Chemistry
Imperial College

Secretary: Mr C Danson
Rutherford Appleton Laboratory

Dr E Rachlew-Kallne
Department of Physics
Royal Institute of Technology, Sweden

Dr G Matthieussent
Laboratoire Physique Gaz et Plasmas, Universite Paris XI - CNRS, France

Dr R Sigel
Max-Planck-Institut fur Quantenoptik
Garching, Germany

CENTRAL LASER FACILITY STRUCTURE